Medical Radiology · Diagnostic Imaging
Series Editors: Hans-Ulrich Kauczor · Paul M. Parizel · Wilfred C.G. Peh

Yoshiharu Ohno
Hiroto Hatabu
Hans-Ulrich Kauczor *Editors*

Pulmonary Functional Imaging

Basics and Clinical Applications

MOREMEDIA

Springer

Medical Radiology

Diagnostic Imaging

Series Editors

Hans-Ulrich Kauczor
Paul M. Parizel
Wilfred C. G. Peh

The book series Medical Radiology - Diagnostic Imaging provides accurate and up-to-date overviews about the latest advances in the rapidly evolving field of diagnostic imaging and interventional radiology. Each volume is conceived as a practical and clinically useful reference book and is developed under the direction of an experienced editor, who is a world-renowned specialist in the field. Book chapters are written by expert authors in the field and are richly illustrated with high quality figures, tables and graphs. Editors and authors are committed to provide detailed and coherent information in a readily accessible and easy-to-understand format, directly applicable to daily practice.

Medical Radiology - Diagnostic Imaging covers all organ systems and addresses all modern imaging techniques and image-guided treatment modalities, as well as hot topics in management, workflow, and quality and safety issues in radiology and imaging. The judicious choice of relevant topics, the careful selection of expert editors and authors, and the emphasis on providing practically useful information, contribute to the wide appeal and ongoing success of the series. The series is indexed in Scopus.

For further volumes: http://www.springer.com/series/4354

Yoshiharu Ohno • Hiroto Hatabu
Hans-Ulrich Kauczor
Editors

Pulmonary Functional Imaging

Basics and Clinical Applications

Springer

Editors
Yoshiharu Ohno
Department of Radiology
Fujita Health University
School of Medicine
Toyoake, Aichi
Japan

Hiroto Hatabu
Department of Radiology
Brigham and Women's Hospital
and Harvard Medical School
Boston, MA
USA

Hans-Ulrich Kauczor
Diagnostic and Interventional Radiology
German Center of Lung Research
Ruprecht-Karls-University Heidelberg
Heidelberg, Baden-Württemberg
Germany

ISSN 0942-5373 ISSN 2197-4187 (electronic)
Medical Radiology
ISBN 978-3-030-43538-7 ISBN 978-3-030-43539-4 (eBook)
https://doi.org/10.1007/978-3-030-43539-4

© Springer Nature Switzerland AG 2021
This work is subject to copyright. All rights are reserved by the Publisher, whether the whole or part of the material is concerned, specifically the rights of translation, reprinting, reuse of illustrations, recitation, broadcasting, reproduction on microfilms or in any other physical way, and transmission or information storage and retrieval, electronic adaptation, computer software, or by similar or dissimilar methodology now known or hereafter developed.
The use of general descriptive names, registered names, trademarks, service marks, etc. in this publication does not imply, even in the absence of a specific statement, that such names are exempt from the relevant protective laws and regulations and therefore free for general use.
The publisher, the authors, and the editors are safe to assume that the advice and information in this book are believed to be true and accurate at the date of publication. Neither the publisher nor the authors or the editors give a warranty, expressed or implied, with respect to the material contained herein or for any errors or omissions that may have been made. The publisher remains neutral with regard to jurisdictional claims in published maps and institutional affiliations.

This Springer imprint is published by the registered company Springer Nature Switzerland AG
The registered company address is: Gewerbestrasse 11, 6330 Cham, Switzerland

Foreword

One of the most beautiful sounds in the world is when a mother first hears her newborn child's cry announcing its life for the entire world to enjoy. We all owe a debt to our mothers which cannot be repaid. However, we can strive to make the world a better place to live for those around us and help to improve the health of those struggling with disease.

The sequence of physiological changes that the newborn undergoes in order to make its first cry is the key to understanding the complex relationship that exists between the lungs and the rest of the body. The amniotic fluid must be absorbed by the alveoli and inhaled air must replace it. This happens because of the lower pressure in the pulmonary venous system during the first breath as the patent foramen ovale and the ductus arteriosus close while the pulmonary lymphatics help to remove the amniotic fluid. This allows room air from the first breath to gain entrance by diffusion to the alveoli for gas exchange. In a nutshell, our independent life on this earth begins with the ability to exchange carbon dioxide for oxygen. Without the ability to breathe, we are no longer able to maintain consciousness and die.

Systematic study of the lungs started with John West and his seminal work on the relationship between oxygenation and lung physiology. West and his colleagues showed that the upper lobes are more oxygenated and alkaline and the lower lobes are better perfused and are less well oxygenated. Hence, the preference of *Mycobacterium tuberculosis* for the upper lobes. In fact, all occupational lung diseases involving particulates have a preferential distribution to the upper lobes for this reason. Ewald Weibel pioneered the concept of symmorphosis. Weibel and his colleagues experimentally showed that form is commensurate to the overall functional needs of the organism and that the lung is unusual in the degree of its redundant capacity.

The COVID-19 pandemic has changed the world forever. The public is now painfully aware that a viral pneumonia can be fatal even for those that have few comorbid risk factors. In this book, you will find the next generation

of scholars using quantitative imaging to unlock the secrets of the lung and the many diseases that affect its function. For young researchers, pulmonary functional imaging is an exciting area of endeavor, and I feel certain that the information contained in these passages will stand the test of time.

Mark L. Schiebler
Department of Radiology,
UW-Madison School of Medicine
and Public Health, Madison, WI, USA

Preface

The morphological evaluation of the lung is important due to the close relationship between structural changes of the lung with pathology and pathophysiology of pulmonary diseases. These correlations are the foundation for diagnostic imaging modalities including chest radiography and computed tomography (CT), which play a significant role in the diagnosis and management of the patient with pulmonary disease. However, the underlying disease process may result primarily in a change in pulmonary function without substantial changes in pulmonary morphology or structure, especially in the early phase of the disease. In such cases, the traditional pulmonary imaging approaches may not provide enough insight into underlying disease process. Thus, imaging of pulmonary physiology and pathophysiology has been pursued for the best clinical practice in patients with various pulmonary diseases since the 1960s. However, traditional nuclear medicine studies have not been applied in routine clinical practice as broadly as CT. Therefore, pulmonary functional imaging is put forward as new research and diagnostic tool mainly to overcome the limitations of mere morphological assessments as well as functional evaluation based on traditional nuclear medicine approaches.

In the last several decades, technical advancements and application of various contrast media including gas agents in CT and magnetic resonance (MR) imaging as well as medical image processing have been very groundbreaking. Many researchers have been striving to translate pulmonary functional imaging into routine clinical practice. However, knowledge of these new technical advancements is still limited among many chest radiologists, pulmonologists, thoracic surgeons, radiation oncologists, and technologists. Furthermore, traditional nuclear medicine has shifted from planar imaging to single-photon emission tomography (SPECT) or SPECT fused with CT (SPECT/CT), and some investigators have also applied positron emission tomography (PET) or PET fused with CT (PET/CT) with different tracers.

This book covers (1) basics of pulmonary physiology and pathophysiology; (2) introduction of currently applicable nuclear medicine, CT, and MRI techniques as well as image analysis methods, (3) clinical applications of pulmonary functional imaging by nuclear medicine, CT, MRI, and artificial intelligence in various pulmonary diseases, and (4) future directions of pulmonary functional imaging.

We believe that this book will support a deeper and clearer understanding of pulmonary functional imaging for the readers and provide opportunities for the introduced new techniques to be applied broadly in the clinical practice of diagnostic radiology and pulmonary medicine.

Toyoake, Aichi, Japan — Yoshiharu Ohno
Boston, Massachusetts, United States — Hiroto Hatabu
Heidelberg, Baden-Württemberg, Germany — Hans-Ulrich Kauczor

Contents

Anatomical Basis for Pulmonary Functional Imaging 1
Tomoyuki Hida and Hiroto Hatabu

Pulmonary Function Tests 11
Toyohiro Hirai

Basics and Clinical Application of CT for Pulmonary Functional Evaluation 21
Hyun Woo Goo, Hyungjin Kim, and Jin Mo Goo

Basics and Clinical Application of MR Assessment of Pulmonary Hemodynamics and Blood Flow 47
Sebastian Ley

Basics and Clinical Application of the MR Assessment of Ventilation 59
Sean B. Fain, Katherine Carey, Gregory P. Barton, and Ronald L. Sorkness

Principles and Clinical Applications of Respiratory Motion Assessment Using 4D Computed Tomography and Magnetic Resonance Imaging 91
Tae Iwasawa

Pulmonary Functional Imaging, Basics and Clinical Application of Nuclear Medicine and Hybrid Imaging 107
Marika Bajc, Dinko Franceschi, and Ari Lindqvist

Functional Assessment of COPD 125
Hye Jeon Hwang, Sang Min Lee, and Joon Beom Seo

Structure-Function Imaging of Asthma: Airway and Ventilation Biomarkers 153
Andrea L. Barker, Rachel L. Eddy, Hannah Yaremko, Miranda Kirby, and Grace Parraga

Functional Assessment of Cystic Fibrosis Lung Disease 175
Mark O. Wielpütz

Functional Assessment of Pulmonary Venous Thromboembolism 207
Edwin J. R. van Beek and Andrew J. Swift

Multimodality Imaging of Pulmonary Hypertension: Prognostication of Therapeutic Outcomes 225
Lindsay Griffin, Andrew J. Swift, Nanae Tsuchiya, Christopher François, Marc Humbert, Gideon Cohen, and Mark L. Schiebler

Functional Assessment of Lung Cancer and Nodules 259
Yoshiharu Ohno, Hisanobu Koyama, Kazuhiro Murayama, and Takeshi Yoshikawa

Computational Approach toward Pulmonary Functional Imaging . . 299
William D. Lindsay Jr, Nicholas J. Tustison, and James C. Gee

Image-Based Phenotyping, Deep Learning (DL), and Artificial Intelligence (AI) Applications in Clinical and Research Radiology and Chest Imaging 319
Vladimir I. Valtchinov, Joon Beom Seo, Tomoyuki Hida, and Hiroto Hatabu

Future of Pulmonary Functional Imaging 337
Yoshiharu Ohno and Hiroto Hatabu

Anatomical Basis for Pulmonary Functional Imaging

Tomoyuki Hida and Hiroto Hatabu

Contents

1 **Introduction** ... 1

2 **Histogenesis** ... 2

3 **Lung Parenchyma** ... 3
3.1 Lung Alveoli and Alveolar Ducts ... 3
3.2 Respiratory Bronchiole ... 4

4 **Lung Interstitium** ... 4
4.1 Pulmonary Vessels ... 4
4.2 Alveolar Capillary Beds and Venules ... 5
4.3 Pulmonary Lymphatics ... 6

5 **Pulmonary Secondary Lobules** ... 8

6 **Pulmonary Anatomical and Functional Analysis** ... 8

7 **Conclusions** ... 9

References ... 10

Abstract

Respiration is an unconscious but essential activity for us to maintain our lives. Lungs are the organs that play the most important role of gas exchange between blood and air, referred to as external respiration. The function and morphology of the lungs are inseparable and the understanding of pulmonary morphology and microstructure is essential for the interpretation of pulmonary functional imaging fully. In this chapter, we provide radiology- and histology-based lung morphology and correlation with physiology for the understanding of pulmonary functional imaging.

T. Hida (✉) · H. Hatabu
Center for Pulmonary Functional Imaging, Brigham and Women's Hospital and Harvard Medical School, Boston, MA, USA
e-mail: thida@radiol.med.kyushu-u.ac.jp

1 Introduction

Respiration is an unconscious but essential activity for us to maintain our lives. Lungs are the organs that play the most important role of gas

© Springer Nature Switzerland AG 2021

Y. Ohno et al. (eds.), *Pulmonary Functional Imaging*, Medical Radiology Diagnostic Imaging,
https://doi.org/10.1007/978-3-030-43539-4_1

exchange between blood and air, referred to as external respiration. The abnormalities and diseases of the lungs result in respiratory functional failure with various degrees by the causes. Interstitial pneumonitis (IP) and chronic obstructive pulmonary disease (COPD) are examples of diseases associated with respiratory functional failure. Vascular abnormalities such as pulmonary artery embolism and pulmonary edema with cardiac failure can also have an influence on pulmonary function. Not only these diseases but also pneumonia, atelectasis, tumor, and postoperative changes of the respiratory tract, and even aging, can affect the respiratory function adversely. For exact diagnosis, evaluation of the severity, and following appropriate treatment, assessment of the respiratory function of the patients with the respiratory disorder is important. Spirometry is one of the most useful tools for assessment, which allows us to evaluate obstructive and restricted pulmonary disorder. However, the results depend on the patient's condition. This test can measure mainly whole lung function, but it is not always enough for detection and evaluation to focal lung functional failure. Lung ventilation-perfusion scintigraphy is also an example and one of the most useful methods of diagnosis for pulmonary embolism, which uses single-photon emission computed tomography (SPECT).

Correspondence between pulmonary function and morphology has been studied, and recent progress of radiological equipment including computed tomography (CT) and magnetic resonance imaging (MRI) shows highly reflection of the pathologic features of lung diseases, and the possibility of future aspects of imaging analysis of pulmonary function (Itoh et al. 2001, 2004; Hatabu et al. 2002). Based on their high resolution and objectivity, these are expected to provide more objective data of pulmonary function and may refer localization of the respiratory disorder on the order of much smaller than subsegment (Webb 2006; Nishino et al. 2014). The function and morphology of the lungs are inseparable and the understanding of pulmonary morphology and microstructure is essential for the interpretation of pulmonary functional imaging fully. In this article, we provide radiology- and histology-based lung morphology and correlation with physiology for the understanding of pulmonary functional imaging.

2 Histogenesis

Lungs are a pair of spongy organs, which are air-filled and work for gas exchange between blood and air. The lungs are made up of numerous microstructures including bronchiole, alveolar duct, alveoli (called parenchyma), interalveolar septa, pulmonary vessels, bronchial artery, and lymphatics (called non-parenchyma). The characteristic structures of the lung are the result of millions of years of evolution.

Lungs develop from endoderm and mesoderm (Schoenwolf et al. 2014; Schittny 2017; Mullassery and Smith 2015). Endoderm is lining the respiratory diverticulum and gives rise to the epithelium and glands of trachea, bronchi, bronchiole, and alveoli. The connective tissue, cartilage, airway and vascular smooth muscles of the lungs are derived from the surrounding splanchnic mesoderm. Lung development and maturation can be divided into pseudoglandular, canalicular, saccular, and alveolar phases. Lung buds proliferate and branch in the surrounding splanchnic mesenchyme during pseudoglandular phase, and branching continues until all of the segmental bronchi have been formed. All major lung structures involved in the airway are formed by the end of this phase. Then, canaliculi, which compose the proper respiratory part of the lungs, branch out of the terminal bronchioles. In this canalicular phase, the terminal bronchiole divides to form several respiratory bronchioles, and consequently these respiratory bronchioles divide into several alveolar ducts. Alteration of the epithelium and the surrounding mesenchyma is also seen. The capillaries begin to invade into the mesenchyma and surround the acini. In the lumen, the cuboidal epithelial cells lining the

respiratory structures differentiate into type I and type II pneumocytes. Type I pneumocytes line most of the inner surface area of the alveolar ducts and sacculi and type II pneumocytes begin to secrete small amounts of surfactant. First future air-blood barriers are formed during this phase and fetal breathing movements may begin. Then, the terminal airways grow in length and width and form saccules, which represents the last subdivision of the passages that supply air. This saccular phase sees thinning of connective tissue between the airspaces and further maturation of the surfactant system. After that, the formation of secondary septa, which divides alveolar ducts into terminal alveoli, is seen in the final stage of lung development. Microvascular maturation also occurs in parallel to alveolarization. This alveolar phase, which maximizes the gas exchange surface area, begins in the last few weeks of the pregnancy and continues until 8–10 years postnatally (Mullassery and Smith 2015).

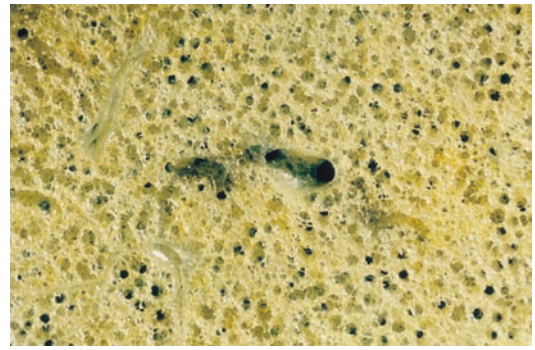


Fig. 1 A low power magnified view of the specimen shows a secondary lobule, in which the bronchiole locates in the center, and pulmonary veins and interlobular septa distribute in the boundary. Large cavities constitute alveolar ducts, and the smaller ones are alveoli. (Adapted with permission from reference Itoh et al. (2001))

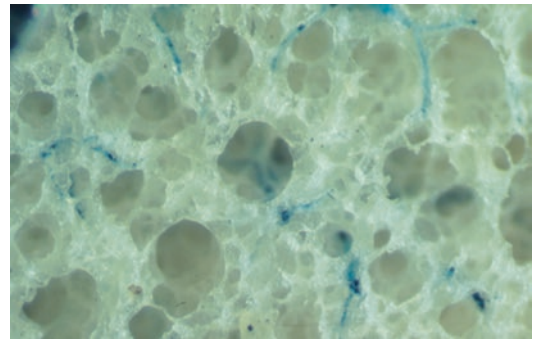


Fig. 2 A magnified view of the specimen shows alveolar ducts and alveoli. The alveoli show a polygonal shape and have orifices into alveolar ductal spaces. (Adapted with permission from reference Itoh et al. (2001))

3 Lung Parenchyma

3.1 Lung Alveoli and Alveolar Ducts

Lung parenchyma is the component for gas exchange and usually includes alveoli, alveolar ducts, and respiratory bronchioles (Schoenwolf et al. 2014). Acinus is the most important unit of pulmonary function that refers to all the lung parenchyma distal to the terminal bronchiole, and usually has 2–5 generations of respiratory bronchioles, alveolar ducts, alveolar sacs, and alveoli. Figure 1 reveals numerous air-containing passages and intervening fine structures, corresponding to alveolar duct and alveoli, respectively. The airways have approximately 23 generations of dichotomous branching from the trachea to alveoli. Central bronchioles can be identified up to eighth or older by high-resolution CT. There are 300–500 million alveoli in the lungs of a human adult, with a combined internal surface area of approximately 75 m^2, which is roughly the same size as a tennis court (Rhoades and Bell 2017). The overall shape of alveoli is polyhedral, and 7–8 alveoli surround the alveolar ductal lumen (Fig. 2). The interalveolar septum is seen between adjacent alveoli.

The detailed structure of alveoli and alveolar ducts has been written by Itoh et al. (2001, 2004). Histologically, every alveolar septal membrane appears as a line. Three-dimensionally, it is possible to distinguish alveolar ductal lumen, alveolar entrance, the lateral wall of the alveolus, and dome of the alveolus. The diameter of the ductal

lumen is 0.3 mm, and the mean size of the alveolus is 0.2 mm. The alveolar duct length is about 1 mm in the long axis. The inner surface of the alveolar duct is covered by a sheet of alveoli. The shape of each alveolar entrance is polygonal like a honeycomb, which is ideal for maximizing cell volume in a limited space. The honeycomb structure is composed of a single layer of alveoli, but in the lung parenchyma, the alveoli walls are double-layered. Every lateral wall of the alveolus joins to the apex of the alveolar dome. The double-layered alveolar sheets hold alveolar domes in common. This common histologic image defines the two-dimensional architectural unit of lung parenchyma. A small hole called Kohn pore can be seen in the alveolar dome. The alveolar ducts are characterized by frequent branching, and the pattern of branching is different from that of a bronchiole, as there is no spur. Histologically, there is an architectural unit forming a network in the parenchymal space and surrounding the alveolar duct (Fig. 3). The lumen of the alveolar duct is surrounded by polygonal alveoli, and the overall shape of the alveolar duct is polygonal, while the overall shape of the similarly sized bronchiole is cylindrical. This implies that the alveolar duct has an ideal overall shape for maximizing lung function. The histologic image in Fig. 3 demonstrates that the number of alveolar ducts is much greater than that of the bronchioles.

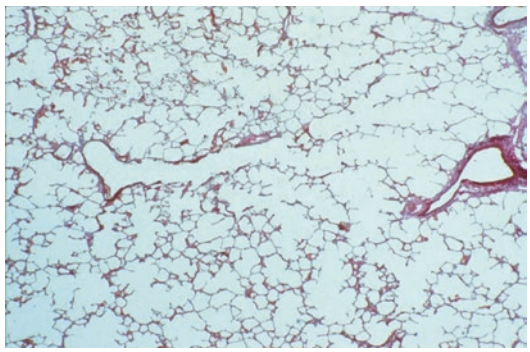


Fig. 3 A histological section shows a number of alveolar ducts with transition from the bronchiole. A greater number of alveolar ducts are seen compared with that of bronchioles. A part of the interlobular septa is seen in the periphery. (Adapted with permission from reference Itoh et al. (2001))

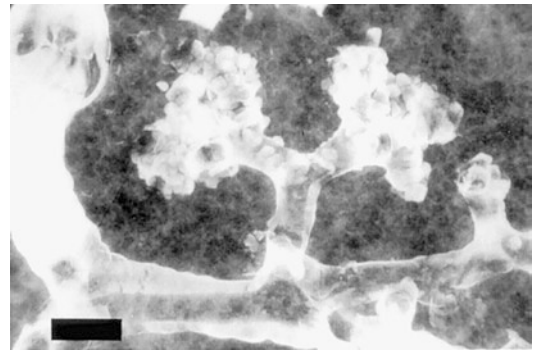


Fig. 4 A contact radiograph shows terminal and respiratory bronchioles with alveolar ducts opacified with barium sulfate. The alveoli have orifices into the respiratory bronchioles. (Adapted with permission from reference Itoh et al. (2001))

3.2 Respiratory Bronchiole

Respiratory bronchiole is usually included in lung parenchyma and called the transitional zone (Itoh et al. 2001, 2004). It is because the wall is partly replaced by alveoli and contributes gas exchange. Respiratory bronchioles split into several alveolar ducts, which terminate in alveolar sacs and individual alveoli (Fig. 4). The distance is constant from the respiratory bronchiole to the nearest septal structures of the secondary lobule. The wall of the respiratory bronchiole is remote from the pulmonary artery and is replaced by a double sheet of alveoli where they abut the recurrent branch of the alveolar duct.

4 Lung Interstitium

4.1 Pulmonary Vessels

There are two circulatory systems of blood supply in the lungs: pulmonary and bronchial vessels. Pulmonary arteries are located in the center of secondary lobules together with bronchioles that run parallel to them, while pulmonary veins are located in the margins of the lobules together with interlobular septa (Figs. 5 and 6). On CT images, pulmonary arteries of 200–300 μm in diameter are visualized. Figures 7 and 8 show numerous small lateral branches of bronchi

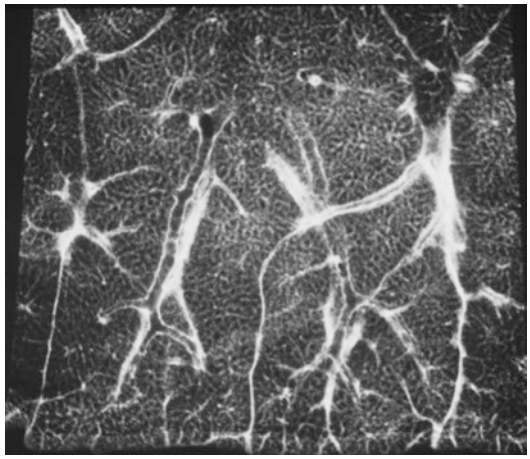


Fig. 5 A radiograph of 1-mm-thick specimen shows the secondary lobules, of which pulmonary arteries are located in the center and pulmonary veins are in the periphery. Terminal and respiratory bronchioles are observed as tubular structures accompanying the pulmonary arteries. Alveolar regions are visualized as fine reticular opacities. (Adapted with permission from reference Itoh et al. (2001))

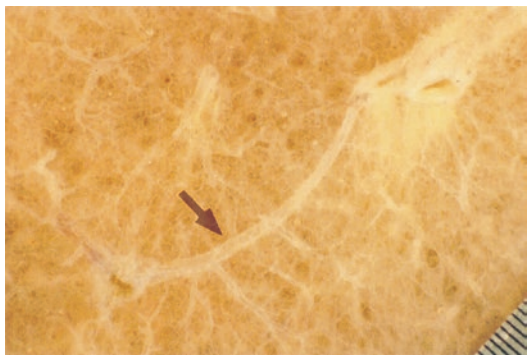


Fig. 6 A fixed specimen of a resected fixed lung specimen obtained during surgery shows bronchus and pulmonary artery (right upper) and pulmonary vein (left lower). A pulmonary vein connecting them (arrow) is observed, which receives blood from the alveolar region. (Adapted with permission from reference Itoh et al. (2001))

besides the regular dichotomous pattern of branching. There are a greater number of pulmonary artery branches than lateral branches of bronchi. The fact indicates that there could be small pulmonary artery branches that are not accompanied by bronchi. However, the pulmonary arteries must be accompanied by bronchioles in distant areas of the peripheral region. Bronchial circulation provides a rich

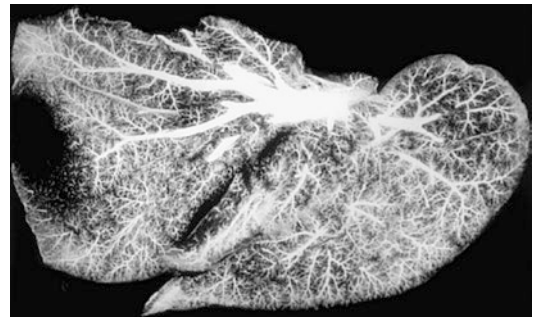


Fig. 7 A pulmonary arteriography with barium sulfate demonstrates a great number of small lateral branches originating from bronchi besides the regular dichotomous pattern of branching. (Adapted with permission from reference Itoh et al. (2001))

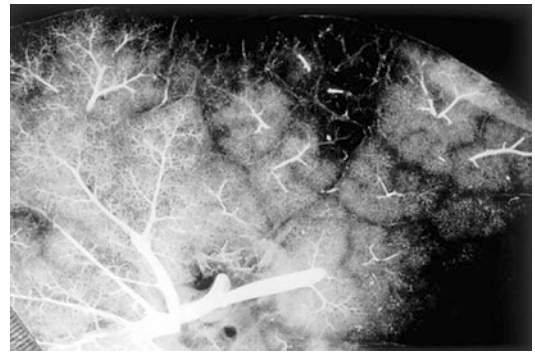


Fig. 8 A pulmonary arteriography using a higher concentration of barium sulfate than in Fig. 9 visualizes pulmonary arteries which run through the center of secondary lobules. The edges of the secondary lobules are partially opacified. (Adapted with permission from reference Itoh et al. (2001))

blood supply to the bronchi, large vessels, hilar lymph nodes and visceral pleura from bronchial arteries and communicating vessels between the pulmonary vein and the bronchial venous plexus. Bronchial veins are located around a bronchoarterial sheath, which communicates directly with the adjacent pulmonary vein, which gives off a small branch to the neighboring airways.

4.2 Alveolar Capillary Beds and Venules

Figure 9 shows the alveolar capillary, which is one of the important structural components of

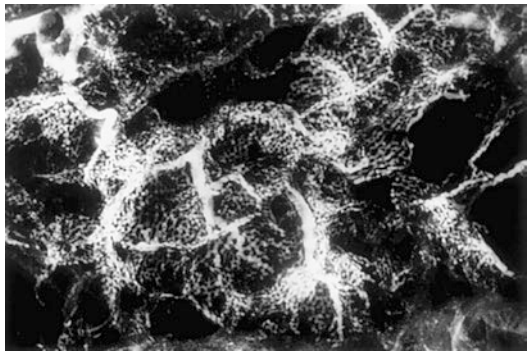


Fig. 9 A radiograph of 300-μm-thick specimen shows alveolar capillary vessels filled with barium sulfate. Capillary vessels reside in the alveolar walls. (Adapted with permission from reference Itoh et al. (2001))

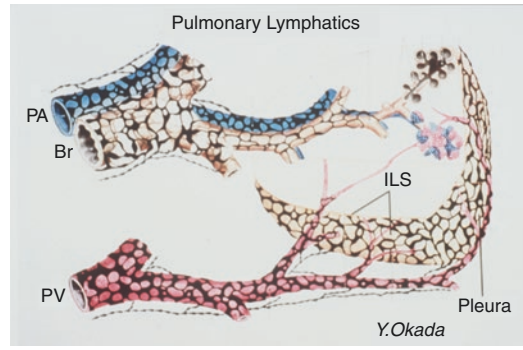


Fig. 10 The figure shows the distribution of pulmonary lymphatics. The pulmonary lymphatics do not exist in the alveolar region. Br, bronchus; ILS, interlobular septa; PA, pulmonary artery; PV, pulmonary vein. (Adapted with permission from reference Itoh et al. (2001))

the interalveolar septum (Itoh et al. 2001, 2004). The capillary beds extend to 50% of the volume of the septum. The alveolar capillary shows a dense network which is composed of a number of irregular polygons. 10% of alveoli meet non-parenchymal structures, such as pulmonary vessels (Weibel 1979). A number of alveoli abut the pulmonary vein. Because gas diffusion does not occur towards the pulmonary vessel, the alveolar dome contiguous to the vessel is a single-faced alveolar wall, instead of usual double-layered sheets. In contrast, the interalveolar septum is a double-faced alveolar wall, which enables gas exchange on both sides. As blood flows through the capillaries, oxygen diffuses from the alveolar space into the blood in conjunction with carbon dioxide diffusing from the blood into the alveolar space. Alveolar capillaries are connected to post- or pre-capillary small vessels. These small vessels occupy part of the limited interstitial space between the alveolar ducts and typically are located in the corner where four alveolar ducts gather. This corner called a ridge in solid geometry is ideal for blood vessel distribution.

4.3 Pulmonary Lymphatics

Pulmonary lymphatics defend the lungs from airborne particles and microorganisms and allow a local influx of liquid to clear and clean inflamed

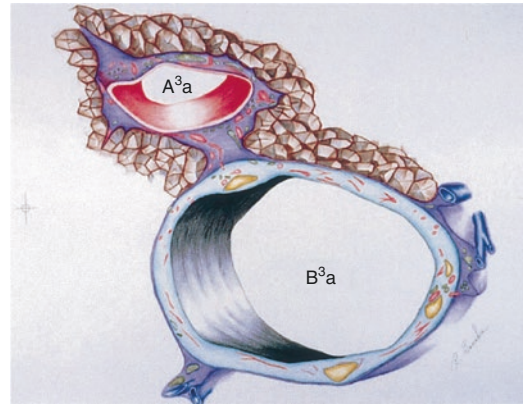


Fig. 11 The figure shows lymphatics (green) and bronchial artery circulation (red) in the bronchial wall. The structures around the pulmonary artery are also described. (Adapted with permission from reference Itoh et al. (2001))

or damaged tissue (Schraufnagel 2010). Figures 10 and 11 show the distribution of pulmonary lymphatic channels (Itoh et al. 2001). They distribute centrally along with the bronchovascular bundle towards the center of the lobules and peripherally within the interlobular septa and subpleural pulmonary tissues, but are not seen in the alveolar region. Subpleural lymphatic structures are sandwiched between air and lung parenchyma (Itoh et al. 2004). Three-dimensional CT demonstrates a rich network of lymphatics as a number of polygonal patterns (Figs. 12 and 13).



Fig. 12 A three-dimensional computed tomography of a resected left upper lobe obtained during surgery shows interlobular septa and lymphatics located on the surface of the lung. Pleural indentation caused by lung adenocarcinoma is observed. (Adapted with permission from reference Itoh et al. (2001))

As the reticular and linear structures of lymphatics are on the pulmonary side of the pleura, the lung surface is smooth while it appears to be irregular (Fig. 14). The size of the lymphatic systems expands to a varying degree in response to such conditions as an excess fluid load, cancer, or inflammation.

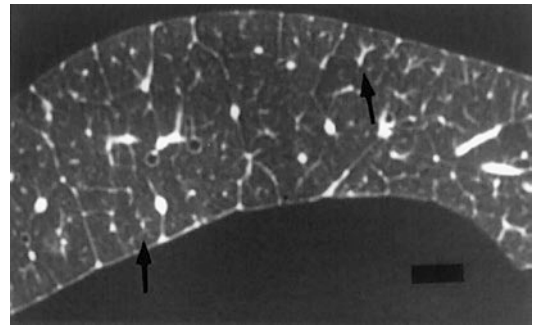


Fig. 14 The axial computed tomography corresponding to Fig. 6 demonstrates pulmonary arteries in the center of the secondary lobules (arrows), and pulmonary veins and interlobular septa in the periphery. (Adapted with permission from reference Itoh et al. (2001))

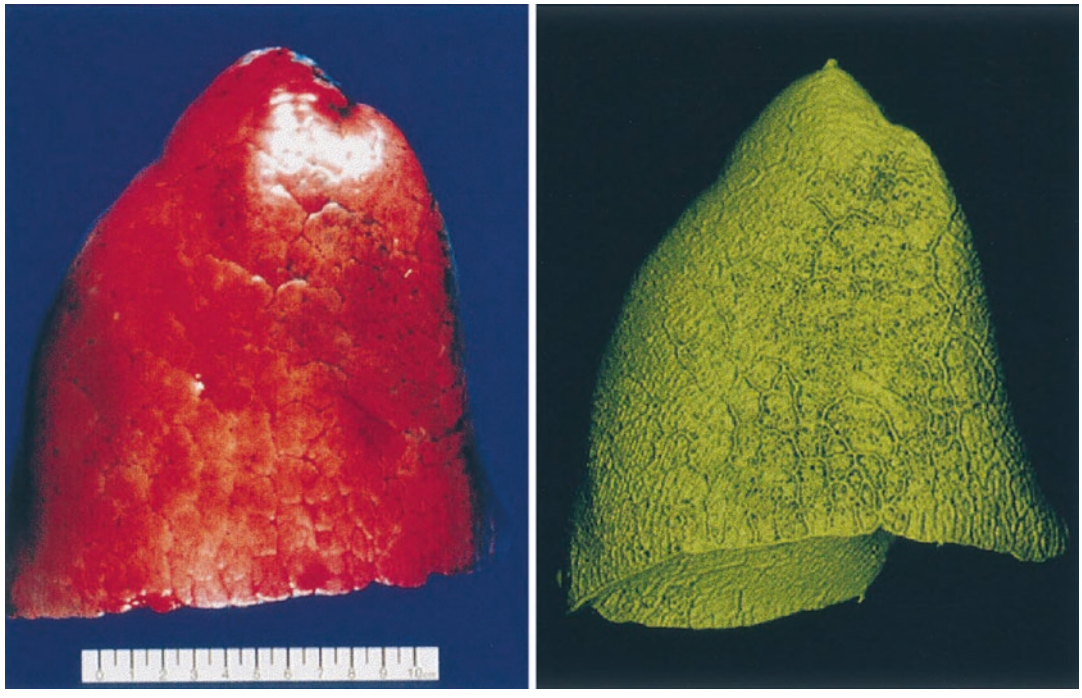


Fig. 13 An inflated, unfixed right lower lobe obtained during a surgical resection (left) and a corresponding three-dimensional computed tomography (3D-CT, right). The polygonal pattern is consistent between specimen and 3D-CT. Although the lung surface looks irregular, it is smooth because the polygonal pattern is a subpleural structure. (Adapted with permission from reference Itoh et al. (2001))

5 Pulmonary Secondary Lobules

The lungs are made up of such various and numerous anatomical microstructures, and there is a limitation to describe all of these microstructures in even recent radiological equipment. Therefore, secondary nodules are the basic and most important unit used for diagnosis and functional analysis of the lungs (Webb 2006; Nishino et al. 2014). This is the key to high-resolution CT terminology, and also the key to an understanding of the correlation between pulmonary morphology and function.

Secondary lobules measure between 1 and 2.5 cm in diameter and are composed of 5–15 acini and 30–50 primary lobules (Webb 2006). They are irregularly polyhedral in shape bounded by the interlobular septa that are continuous with the peribronchovascular interstitium and pleura (Fig. 15). Each secondary lobule is supplied by a lobular bronchiole and a pulmonary artery branch in the center and is drained by the pulmonary veins that form in the periphery of the lobule and pass through the interlobular septa (Fig. 16). Pulmonary lymphatics also run within the interlobular septa. Interlobular septa are at the lower limit of thin-section CT resolution. Under normal conditions, a few of these thin septa are visible in the lung periphery, usually anteriorly or along mediastinal pleural surfaces, but tend to be inconspicuous. Lung diseases have been classified with relation to the anatomy of the secondary lobules based on radiologic-pathologic correlation (Webb 2006; Nishino et al. 2014). Pathologic alterations in secondary lobular anatomy include interlobular septal thickening and diseases with peripheral lobular distribution, centrilobular and panlobular abnormalities, which can be visualized on thin-section CT scans. The recognition and analysis of which component of the secondary lobule is involved help us to diagnose the lung abnormalities and to narrow the differential diagnosis in such as diffuse lung diseases.



Fig. 15 A magnified view of the specimen shows interlobular septa, which is rarely exposed in the plane because the cut direction is parallel to the septa. (Adapted with permission from reference Itoh et al. (2001))

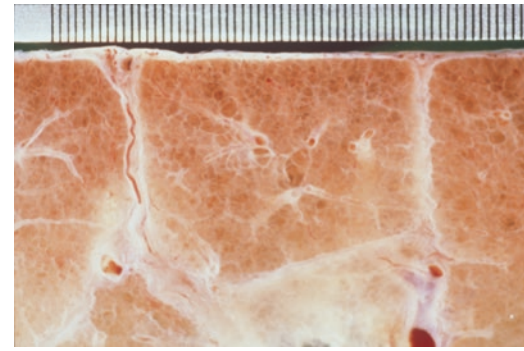


Fig. 16 A fixed specimen shows secondary lobules, of which bronchioles and pulmonary arteries are seen in the center, and pulmonary veins and interlobular septa are located in the margins. (Adapted with permission from reference Itoh et al. (2001))

6 Pulmonary Anatomical and Functional Analysis

An understanding of lung morphology and their ultrastructures that are believed to contribute for the pulmonary function is necessary and essential for effective pulmonary functional imaging. Assessment of pulmonary function by using radiological imaging has been tried for many years. As one of the examples of pulmonary functional imaging, pulmonary ventilation and perfusion SPECT using 81 m Kr and 133 Xe gases is still one of the most effective examinations for evaluation of pulmonary embolism and obstructive pulmonary diseases. Recent development in radiology such as CT and MR imaging technology allows investigating different aspects

of lung function, such as ventilation, perfusion, gas exchange, and respiratory mechanics from these morphological images. These techniques are useful not only for diagnosis but also for evaluation of severity, cause, and factors of lung diseases.

Recent development of CT equipment makes it possible to describe the detail of pulmonary morphology (Kakinuma et al. 2015). In the future, high-resolution CT imaging may describe the detail of microstructures smaller than acini. The morphological analysis on chest CT images may also make it possible to analyze the functional analysis of the lungs. As is well known, analysis for low attenuation area on chest CT images is very useful for diagnosis of emphysema. Inhalation/exhalation CT imaging is one of the most useful tools to evaluate respiration activity (Matsuoka et al. 2008; Koyama et al. 2016). Combination of inhalation and exhalation CT images makes it possible to visualize focal respiration such as ground-glass opacities that reflects an amount of air in secondary nodules or acini and air trapping which reflects obstruction of the bronchiole. These findings are useful for diagnosis and evaluation of severities of lung diseases such as hypersensitivity pneumonia, obstructive bronchitis, and COPD. Dual-energy CT, which utilizes two separate energy sets to examine the different attenuation properties of matter, having a significant advantage over traditional single energy CT, may make it possible to evaluate the focal pulmonary function with iodine-distribution imaging (Lapointe et al. 2017). Quantification of the respiratory activity of the lung using CT images and comprehension of segmental respiratory function is also useful for radiation therapy (Faught et al. 2017). Radiation therapy avoiding the high respiratory function area will reduce normal lung damages and be effective for tumor treatment. Radiation pneumonitis will be also avoided better by using pulmonary functional imaging.

Another aspect of pulmonary function, pulmonary perfusion analysis is also important and can be also evaluated by CT imaging. The analysis is useful not only for the detection of focal changes of pulmonary perfusion in such as pulmonary embolism but also for differential diagnosis of pulmonary nodules (Ohno et al. 2015). In a sense, visualization of pulmonary vessels for surgery may be included in the so-called functional imaging.

The recent revolutionary development of MR imaging techniques has opened a new window for the functional assessment of the lungs. MR imaging has become a feasible modality for the functional assessment of the lung including perfusion, ventilation, and biomechanics. Hyperpolarized gas image acquisition of MR imaging by using such as 129-Xenon and 3-Helium has been used to visualize the status of gas distribution and ventilation of airways and alveoli (Liu et al. 2014). These analyses will be used for evaluation of ventilation disorder such as pulmonary emphysema and bronchial asthma. It has been reported that there is a correlation between O_2-enhanced MR imaging, and forced expiratory volume in a second and diffusion ability (Ohno et al. 2011). O_2-enhanced MR imaging is applied for evaluation of pulmonary emphysema and bronchial asthma and may be also used for the prediction of the postoperative pulmonary function for lung cancer patients.

Dynamic analysis of the lungs is also one of the progress of pulmonary functional imaging (Yamada et al. 2017). Dynamic chest X-ray imaging reveals the movement of the diaphragms in the respiration and may be also useful for the analysis of pulmonary function. This method can be achieved at standing or sitting position and is thought to be useful for dynamic analysis of the lungs in normal condition, compared to CT and MR images that need lying position for imaging. About lungs, construction of the lungs is thought to be uneven—for example, surface towards ribs moves smoothly, and surface towards diaphragm moves bigger than any other sites. The analysis of the kinetics of the lungs will be also useful for the diagnosis and evaluation of various lung diseases.

7 Conclusions

Lung function is inseparable from its characteristic architecture, namely pulmonary alveolar structures. Knowledge of the morphology of the

lungs is essential for understanding the morphologic-functional relationship of the lungs and for effective pulmonary functional imaging.

Acknowledgments This chapter is written based upon the author's previous collaborative works with Professor Harumi Itoh, a great chest radiologist and an educator. This chapter is dedicated to Dr. Harumi Itoh, an emeritus professor and the first dean of School of Medical Sciences, Fukui University.

References

Faught AM, Miyasaka Y, Kadoya N et al (2017) Evaluating the toxicity reduction with computed tomographic ventilation functional avoidance radiation therapy. Int J Radiat Oncol Biol Phys 99(2):325–333. https://doi.org/10.1016/j.ijrobp.2017.04.024

Hatabu H, Uematsu H, Hasegawa I, Itoh H (2002) MR-pathologic correlation of lung specimens. Eur J Radiol 44(3):210–215

Itoh H, Nakatsu M, Yoxtheimer LM, Uematsu H, Ohno Y, Hatabu H (2001) Structural basis for pulmonary functional imaging. Eur J Radiol 37(3):143–154

Itoh H, Nishino M, Hatabu H (2004) Architecture of the lung: morphology and function. J Thorac Imaging 19(4):221–227

Kakinuma R, Moriyama N, Muramatsu Y et al (2015) Ultra-high-resolution computed tomography of the lung: image quality of a prototype scanner. PLoS One 10(9):e0137165. https://doi.org/10.1371/journal.pone.0137165

Koyama H, Ohno Y, Fujisawa Y et al (2016) 3D lung motion assessments on inspiratory/expiratory thin-section CT: capability for pulmonary functional loss of smoking-related COPD in comparison with lung destruction and air trapping. Eur J Radiol 85(2):352–359. https://doi.org/10.1016/j.ejrad.2015.11.026

Lapointe A, Bahig H, Blais D et al (2017) Assessing lung function using contrast-enhanced dual-energy computed tomography for potential applications in radiation therapy. Med Phys 44(10):5260–5269. https://doi.org/10.1002/mp.12475

Liu Z, Araki T, Okajima Y, Albert M, Hatabu H (2014) Pulmonary hyperpolarized noble gas MRI: recent advances and perspectives in clinical application. Eur J Radiol 83(7):1282–1291. https://doi.org/10.1016/j.ejrad.2014.04.014

Matsuoka S, Kurihara Y, Yagihashi K, Hoshino M, Watanabe N, Nakajima Y (2008) Quantitative assessment of air trapping in chronic obstructive pulmonary disease using inspiratory and expiratory volumetric MDCT. Am J Roentgenol 190(3):762–769. https://doi.org/10.2214/ajr.07.2820

Mullassery D, Smith NP (2015) Lung development. Semin Pediatr Surg 24(4):152–155. https://doi.org/10.1053/j.sempedsurg.2015.01.011

Nishino M, Itoh H, Hatabu H (2014) A practical approach to high-resolution CT of diffuse lung disease. Eur J Radiol 83(1):6–19. https://doi.org/10.1016/j.ejrad.2012.12.028

Ohno Y, Koyama H, Matsumoto K et al (2011) Oxygen-enhanced MRI vs. quantitatively assessed thin-section CT: pulmonary functional loss assessment and clinical stage classification of asthmatics. Eur J Radiol 77(1):85–91. https://doi.org/10.1016/j.ejrad.2009.06.027

Ohno Y, Nishio M, Koyama H et al (2015) Solitary pulmonary nodules: comparison of dynamic first-pass contrast-enhanced perfusion area-detector CT, dynamic first-pass contrast-enhanced MR imaging, and FDG PET/CT. Radiology 274(2):563–575. https://doi.org/10.1148/radiol.14132289

Rhoades RA, Bell DR (2017) Medical physiology: principles for clinical medicine, 5th edn. Wolters Kluwer Law & Business, Philadelphia, p 968

Schittny JC (2017) Development of the lung. Cell Tissue Res 367(3):427–444. https://doi.org/10.1007/s00441-016-2545-0

Schoenwolf GC, Bleyl SB, Brauer PR, Francis-West PH (2014) Larsen's human embryology, 5th edn. Elsevier Health Sciences, Oxford, England

Schraufnagel DE (2010) Lung lymphatic anatomy and correlates. Pathophysiology 17(4):337–343. https://doi.org/10.1016/j.pathophys.2009.10.008

Webb WR (2006) Thin-section CT of the secondary pulmonary lobule: anatomy and the image—the 2004 Fleischner lecture. Radiology 239(2):322–338. https://doi.org/10.1148/radiol.2392041968

Weibel ER (1979) Fleischner lecture. Looking into the lung: what can it tell us? Am J Roentgenol 133(6):1021–1031. https://doi.org/10.2214/ajr.133.6.1021

Yamada Y, Ueyama M, Abe T et al (2017) Time-resolved quantitative analysis of the diaphragms during tidal breathing in a standing position using dynamic chest radiography with a flat panel detector system ("Dynamic X-Ray Phrenicography"): initial experience in 172 volunteers. Acad Radiol 24(4):393–400. https://doi.org/10.1016/j.acra.2016.11.014

Pulmonary Function Tests

Toyohiro Hirai

Contents

1 **Introduction** 12

2 **Spirometry** 12

3 **Lung Volumes** 14

4 **Diffusing Capacity** 16
4.1 Measuring Method 16
4.2 Interpretation of D_{LCO} 17

5 **Other Pulmonary Function Tests** 17
5.1 Reversibility Test 17
5.2 Bronchoprovocation Test 17
5.3 Arterial Blood Gas Analysis 18
5.4 Respiratory Impedance 18
5.5 Field Walking Tests 18
5.6 Clinical Assessment of Dyspnea 18

6 **Summary** 19

References 19

Abstract

Pulmonary function tests provide quantitative assessment of physiological properties in respiratory system including the lungs and chest wall. Spirometry is the first step as a screening and diagnostic test to investigate the existence and severity of obstructive or restrictive ventilatory disorders. Second is the measurement of lung volumes. Another technique is used to measure functional residual capacity, because absolute gas volume remaining in the lungs cannot be measured using spirometer. Measurements of lung volumes enable us to evaluate the changes in the mechanical balance between the lungs and chest wall, due to pulmonary or extrapulmonary diseases. As the next step, diffusing capacity for carbon monoxide can be measured to assess the

T. Hirai (✉)
Department of Respiratory Medicine, Graduate School of Medicine, Kyoto University, Kyoto, Japan
e-mail: t_hirai@kuhp.kyoto-u.ac.jp

© Springer Nature Switzerland AG 2021

Y. Ohno et al. (eds.), *Pulmonary Functional Imaging*, Medical Radiology Diagnostic Imaging,
https://doi.org/10.1007/978-3-030-43539-4_2

capacity of the lung to exchange gas across the alveolar-capillary interface. Arterial blood gases that reflect the final output from respiratory system as the organs for gas exchange are introduced for the diagnosis of respiratory failure and acid-base disturbances. Additional pulmonary function tests including bronchoprovocation test, the measurement of respiratory impedance, and field walking tests (the 6-min walk test, incremental shuttle walk test, and endurance shuttle walk test) may be performed for further examinations in specific clinical circumstances. All these pulmonary function tests are useful for the assessment of pulmonary diseases in the clinical settings and clinical researches, especially in conjunction with morphological assessment using image diagnosis.

1 Introduction

Pulmonary function tests have the following characteristics compared with image diagnosis: they provide physiological characteristics of the lungs as quantitative values, and they are useful for the assessment of the disease severity, changes in functions during disease process, indication and effects of therapy, and also comparison with healthy subjects using the predicted values. Generally, pulmonary function tests reveal the parameters of physiological function for whole lungs, and do not describe the specific locality of the diseased area, while image diagnosis is able to provide normal and diseased areas visually. However, pulmonary function tests must contribute to the understanding of pathophysiology in pulmonary diseases, especially in conjunction with image diagnosis.

Table 1 shows major pulmonary function tests. They consist of measurements to evaluate pulmonary function including ventilation and gas exchange. In this section, some of basic function tests will be described to be useful for the understanding of functional imaging.

Table 1 Major pulmonary function tests

A. Ventilation functions
1. Spirometry
2. Lung volumes
3. Resistance and compliance
B. Gas exchange
1. Arterial blood gas analysis
2. Diffusing capacity
C. Others
1. Field walking tests
6-min walk test, shuttle walk test
2. Reversibility test
3. Bronchoprovocation test

2 Spirometry

Spirometry is the most classical and basic test of pulmonary function. It can be easily introduced and has been widely performed in usual clinical settings. Spirometer is simple equipment to measure and record changes of mouth flow with time, and the volume is calculated by integral of the flow. All spirometric measurements should be performed according to the official statement (Pellegrino et al. 2005; Miller et al. 2005) of the American Thoracic Society (ATS) and the European Respiratory Society (ERS) that describes the issues for standardization of spirometry including requirements for equipment, and within- and between-maneuver evaluation. At least three acceptable maneuvers are necessary to obtain accurate measurements.

For the measurements using spirometer, there are two kinds of maneuvers, slow and forced vital capacity maneuvers (SVC and FVC maneuver, respectively). SVC maneuver is performed to evaluate static characteristics of lungs by measuring lung volumes including vital capacity (VC). Figure 1 shows time tracing of lung volume in SVC maneuver. Decreased VC less than lower limit of the normal range (or 80% of predicted value) is defined as restrictive ventilatory impairment (Table 2). On the other hand, FVC maneuver provides the characteristics of dynamic ventilation including forced vital capacity (FVC) and forced expiratory volume in one second (FEV_1) (Fig. 2). FEV_1/FVC less than lower limit of normal (or 0.7) is defined as obstructive

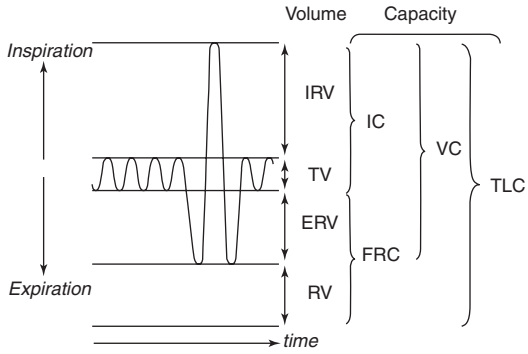


Fig. 1 Time tracing of lung volume in slow vital capacity (SVC) maneuver. After stable tidal breathing repeated several times, maximum inspiration after complete expiration, and maximum expiration again are slowly performed, and then the subject can relax back to tidal breathing. Lung volumes consist of four basic volume fractions: IRV, TV, ERV, and RV, whereas capacities are compartments composed of two or more volumes. TV (tidal volume): the volume of air entering and leaving the lungs during breathing at physiologic rest; *IRV* inspiratory reserve volume; *ERV* expiratory reserve volume; RV (residual volume): the volume of air that remains in the lungs due to the collapse of all small airways after maximum expiration; VC (vital capacity) = ERV + TV + IRV. FRC (functional residual capacity) = RV + ERV: the volume of air remaining in the lungs after a normal, physiologic expiration. IC (inspiratory capacity) = TV + IRV. TLC (total lung capacity) = RV + ERV + TV + IRV: the total volume of the lungs at maximal inspiration

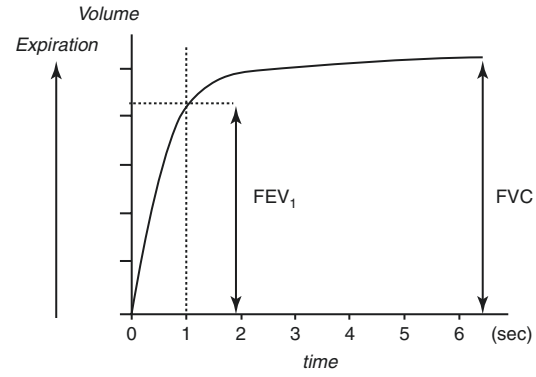


Fig. 2 Time tracing of lung volume in forced expiration, where expiation starts at time 0. *FEV_1* forced expiratory volume in 1 s, *FVC* forced vital capacity. The subject requires forced expiration for 6 s or more

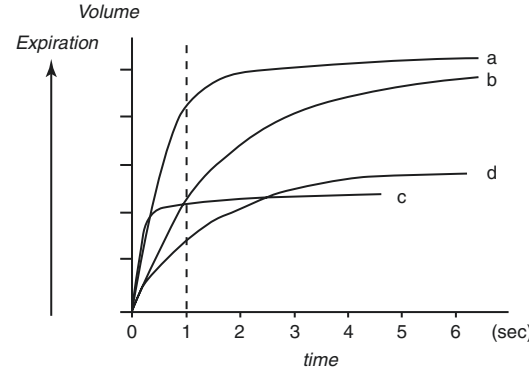


Fig. 3 Comparison of time tracings of lung volume in forced expiration among various ventilatory impairments. Expiation starts at time 0. a: normal, b: obstructive impairment (e.g., COPD), c: restrictive impairment (e.g., pulmonary fibrosis), d: mixed impairments of obstruction and restriction, or severe obstructive impairment (e.g., severe COPD)

Table 2 Typical examples of ventilatory disorders

A. Restrictive ventilatory impairments
1. Low lung volume
Interstitial pneumonia, pulmonary fibrosis
Lung resection
Atelectasis
2. Restricted ventilation
Chest wall deformity
Obesity
Neuromuscular diseases
B. Obstructive ventilatory impairments
Chronic obstructive pulmonary disease (COPD)
Asthma
Bronchiolitis obliterans
Lymphangioleiomyomatosis (LAM)
Pneumoconiosis

ventilatory impairment (Table 2). Figure 3 shows various patterns of ventilatory impairments with reduced FEV_1 in forced expiration. Low FEV_1 derives from obstructive, restrictive, or both ventilatory impairments. It is noted that the patients with severe COPD (severe emphysema) show low FEV_1 with reduced FVC as described later (see Sect. 3).

Flow-volume curve is another description in FVC maneuver (Fig. 4). This curve provides several parameters such as peak expiratory flow and the mean forced expiratory flow between 25% and 75% of the FVC (FEF25–75%). However, it is more important to recognize the shape of the curve, because some lung diseases provide

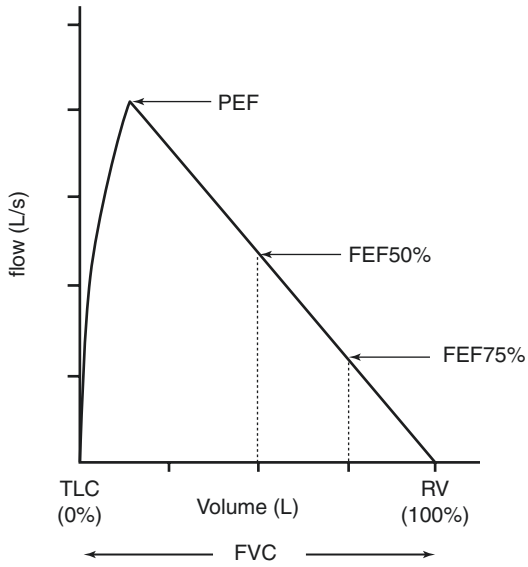


Fig. 4 Schematic explanation of flow-volume curve in FVC maneuver Mean forced expiratory flow between 25% and 75% of FVC is known as FEF25–75%. *PEF* peak expiratory flow, $FEF_{X\%}$ instantaneous forced expiratory flow when X% of the FVC has been expired, *TLC* total lung capacity, *RV* residual volume, *FVC* forced vital capacity

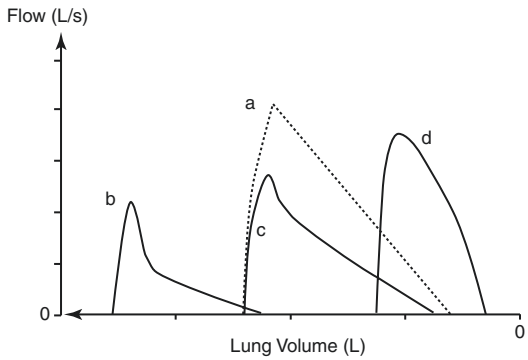


Fig. 5 Typical examples of flow plotted against absolute lung volume in healthy subject and patients with obstructive or restrictive lung diseases. a; normal, b: COPD, c: bronchial asthma, d: pulmonary fibrosis

different and typical patterns of the flow-volume curves (Fig. 5). In patients with COPD, a concave shape is typical on the flow–volume curve with a proportionally greater reduction in FEF75%. On the other hand, the flow–volume curve in patients with pulmonary fibrosis shows a convex pattern with a reduced VC and a normal or slightly

Table 3 Severity of airflow limitation in COPD (GOLD classification)

Degree of severity	Post-bronchodilator FEV_1
GOLD 1: Mild	$FEV_1 \geq 80\%$ predicted
GOLD 2: Moderate	$50 \leq FEV_1 < 80\%$ predicted
GOLD 3: Severe	$30 \leq FEV_1 < 50\%$ predicted
GOLD 4: Very severe	$FEV_1 < 30\%$ predicted

GOLD Global initiative for chronic obstructive lung disease

increased FEV_1/FVC. The flow-volume display is also useful for checking whether the maneuver has performed properly.

Spirometric measurements are dependent on many factors including age, gender, height, and race. Thus, reference values (equations) that are derived from large groups of healthy subjects can be used to compare the measurements among patients or subjects with different age and height using percent of predicted values. Ideally, race-specific reference values (equations) should be used. Percentage of predicted values is also used for the evaluation of disease severity. For example, severity of airflow limitation in COPD suggested by Global Initiative for Chronic Obstructive Lung Disease (GOLD) is classified on the basis of percent predicted value of post-bronchodilator FEV_1 (Table 3) (available at https://goldcopd.org/gold-reports/). This classification derives from the fact that FEV_1/FVC may not reflect the disease severity because not only FEV_1 but also FVC can decrease in the patients with advanced COPD.

3 Lung Volumes

Lung volumes can be determined by the mechanical balance between the lungs and chest wall, which is the relationship between pressure-volume curve of the lungs and that of the chest wall. To evaluate the lung volume fractions is useful for the diagnosis and understanding of pathophysiology in pulmonary diseases.

Spirometry is not able to provide total lung capacity (TLC), functional residual capacity (FRC), and residual volume (RV), because spirometer can measure the volume of air entering

and leaving the lungs, and it is not possible to measure absolute volume of air remaining in the lungs. Thus, other tests are necessary, and usually the measurement of FRC is introduced (Wanger et al. 2005). Once FRC is determined, TLC and RV can be calculated using FRC and spirometric parameters. Table 4 shows the methods for the measurement of FRC. Gas dilution method is the test using a known volume and fraction of gas (Helium (He) or Nitrogen), which is not nearly absorbed in blood, as a tracer gas. This test may not reflect the volume of air in the poorly ventilated areas (e.g., bulla) of the lungs during tidal breathing. On the other hand, body plethysmograph can measure whole thoracic gas volume including the poorly ventilated areas of the lungs, and generally FRC measured using body plethysmograph is more than that using gas dilution method in the patients with lung diseases such as severe COPD and large bullae. Measurements of TLC using body plethysmograph correlate well with those measured by chest computed tomography when the subject holds his breath after maximum inspiration during the scan.

Table 4 Methods for measurement of functional residual capacity (FRC)

1. Gas dilution method
A. Closed circuit method (Helium Dilution Test)[a]
B. Open circuit method (Nitrogen Washout)[b]
2. Body plethysmography[c]
3. Radiological method (Chest CT)

[a]The lung volume (FRC) at the time the subject is connected to the closed circuit with a known gas volume (V1) and helium fraction (F1) is calculated from the helium fraction at the time of equilibration (F2) as follows:
$V1 \times F1 = (V1 + \mathrm{FRC}) \times F2$
$\mathrm{FRC} = V1\,(F1 - F2)/F2$
because helium gas is not nearly absorbed in blood
[b]The subject breaths 100% oxygen through one-way valve to wash out the nitrogen (N_2) from the lungs, and the expired gas is collected to measure the volume and N_2 fraction. The lung volume at the start of washout (FRC) is calculated using the initial alveolar N_2 concentration and the amount of N_2 washed out
[c]The subject is seated inside a whole-body plethysmograph (so-called "body box") and breaths through a mouthpiece with pneumotachograph. The thoracic gas volume (FRC) can be calculated using the changes in mouth pressure and plethysmograph (box) pressure on the basis of Boyle's law

Figure 6 shows typical examples of lung volumes in healthy subject and patients with obstructive or restrictive lung diseases, though the details in changes of lung volumes may vary with disease severity in each patient. In elderly subjects, RV and FRC increase with age, but TLC remains stationary, and consequently VC decreases. In severe obesity, RV remains within normal limits, whereas significant decrease in FRC is seen as body mass index (BMI) increases. Restrictive lung diseases such as pulmonary fibrosis show that lung volumes are all decreased as a result of restricted expansion. Respiratory muscle weakness such as neuromuscular diseases increases RV and decreases TLC and VC. In obstructive lung diseases such as COPD, RV and TLC increase reflecting pulmonary hyperinflation as a

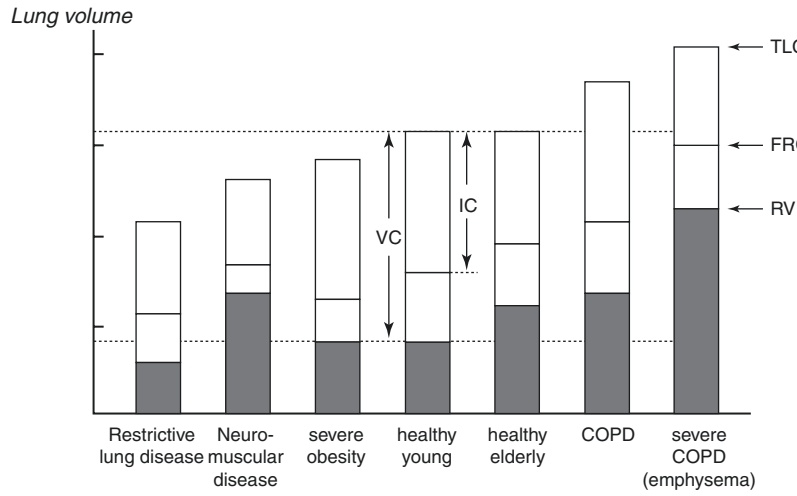


Fig. 6 Typical examples of lung volumes in healthy subject and patients with obstructive or restrictive lung diseases. *VC* vital capacity, *IC* inspiratory capacity, *RV* residual volume, *FRC* functional residual capacity, *TLC* total lung capacity

result of air trapping. In severe emphysema, TLC does not increase as much as increase in RV as the result that VC and IC decrease.

4 Diffusing Capacity

The test of diffusing capacity reflects the function of gas exchange in the lung. Atmospheric gas is transferred from inhaled air to blood in pulmonary capillaries across the thin membrane (0.2–0.3 μm) of alveolus by diffusion according to the gradient of gas concentration. The amount of gas transferred is proportional to the surface area and the difference in partial pressure of gas, and is inversely proportional to the thickness of the alveolar-capillary membrane (Fig. 7).

4.1 Measuring Method

To assess diffusing capacity, carbon monoxide (CO) is usually used as a tracer gas, because CO content in venous blood can be neglected and CO has high affinity with hemoglobin. The single-breath method (Fig. 8) (Macintyre et al. 2005; Graham et al. 2017a, b) is commonly used to obtain diffusing capacity for carbon monoxide (D_{LCO}), which is the volume of CO transferred in milliliters per minute per mmHg of alveolar partial pressure. During 10-second breath holding after full inspiration of test gas including known concentrations of CO and He, CO can be transferred to blood in pulmonary capillaries. Transfer coefficient of the lung (KCO) is measured as a concentration fall in alveolar CO per minute per

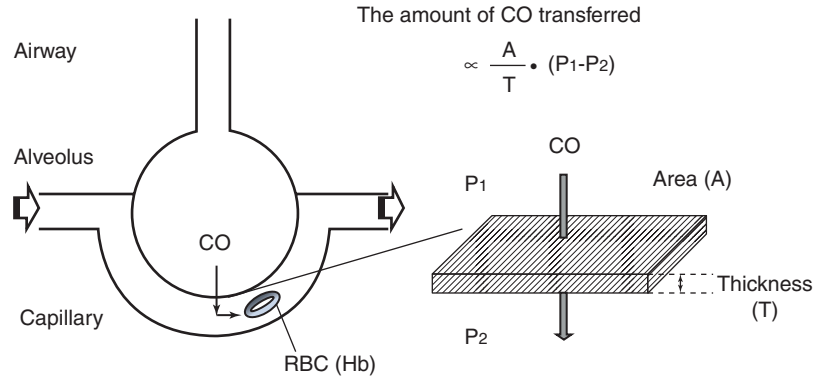


Fig. 7 Schematic explanation of diffusing capacity. P_1, P_2: partial pressure of gas in alveolus and capillary, respectively. The difference between P_1 and P_2 is the driving pressure for diffusion. *RBC* red blood cell, *Hb* hemoglobin

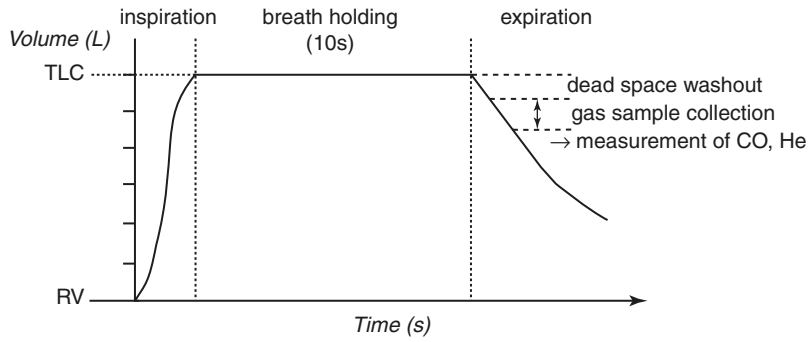


Fig. 8 Single breath D_{LCO} maneuver. After a maximum expiration to residual volume (RV), the subject inhales the test gas (0.3% CO, 10% helium, oxygen, and nitrogen) rapidly to total lung capacity (TLC), and holds his breath for 10 s. During this breath holding, the partial pressure of CO in alveolar gas can be decreased as transferring CO to red blood cells in pulmonary capillaries. An alveolar sample of the exhaled gas is collected after dead space washout (0.75–1.0 L) to measure the fractions of CO and He gas. He gas is used to calculate the alveolar volume (VA)

partial pressure of CO. Alveolar volume (VA) is obtained from the changes in He gas concentration, and finally D_{LCO} is calculated as the product of KCO and VA.

It should be noted that this method may not be able to apply for the patients with low VC and severe lung disease because of the requirement of 10-second breath holding and expired lung volume for washout and sample collection, though recent advanced equipment can improve D_{LCO} measurement by the continuous measurement technology using rapidly responding gas analyzer (Graham et al. 2017a, b).

4.2 Interpretation of D_{LCO}

The measured D_{LCO} can be affected not only by alveolar surface area and thickness but also by the volume of blood and the concentration of hemoglobin (Hb) in pulmonary capillaries (Table 5). Thus, D_{LCO} is also known as the transfer factor for carbon monoxide (TLCO), because the measured value does not solely reflect the diffusing properties of the lung. In COPD patients, the extent of low attenuation area on chest CT images, which reflects pulmonary emphysema, correlates well with D_{LCO} (Morrison et al. 1989; Gould et al. 1991). In interstitial pulmonary fibrosis, D_{LCO} has significant correlation with the disease prognosis (Plantier et al. 2018). Patients with combined pulmonary fibrosis and emphysema (CPFE) show the significant reduction of D_{LCO}, with the preservation of spirometric values and lung volumes that derive from a counterbalance between the restrictive effects of pulmonary fibrosis and the hyperinflation by emphysema (Papaioannou et al. 2016). The restrictive ventilatory disorders by spirometry with normal D_{LCO} may suggest extrapulmonary causes such as neuromuscular disease and pleural thickening. High D_{LCO} is associated with asthma, obesity, and intrapulmonary hemorrhage.

Here, it is important to interpret the measured values of D_{LCO} in conjunction with KCO. Although KCO is mathematically equal to D_{LCO}/VA, D_{LCO}/VA does not represent the correction for alveolar volume. It should be noted that D_{LCO} depends not only on alveolar volume but also on pulmonary blood flow. In pulmonary emphysema, both D_{LCO} and D_{LCO}/VA are decreased, while in patients who have undergone lung resection (e.g., pneumonectomy) and have the healthy remaining lung, D_{LCO} is decreased and D_{LCO}/VA is increased because of the increase in blood flow per alveolar unit.

Table 5 Clinical examples of low diffusing capacity (D_{LCO})

1. Decrease in diffusing area
lung resection, emphysema (COPD), atelectasis
2. Increase in diffusing distance
interstitial lung diseases, lung edema, microvascular dilatation (hepatopulmonary syndrome, pulmonary arteriovenous malformation)
3. Decrease in microvascular blood volume
decrease in cardiac output (heart failure), decrease in microvascular bed (vasculitis, micro-thrombosis, pulmonary hypertension)
4. Decrease in hemoglobin
anemia

5 Other Pulmonary Function Tests

5.1 Reversibility Test

Spirometry before and after bronchodilator [inhalation of β_2-stimulant (e.g., albuterol)] is used to evaluate the degree of airway reversibility. An increase in FEV_1 of more than 12% and greater than 0.2 L suggests significant bronchodilator responsiveness. Airway reversibility is one of the typical characteristics in asthmatic patients, though significant bronchodilator responsiveness cannot clearly discriminate between asthma and COPD.

5.2 Bronchoprovocation Test

Spirometry before and after bronchoprovocation challenges (e.g., inhaled methacholine of a starting delivered dose of 1–3 μg with subsequent doubling or quadrupling steps) is used to assess

the airway hyperresponsiveness (AHR) (Coates et al. 2017). AHR is defined as an increased sensitivity and exaggerated response to nonallergenic stimuli to cause airway narrowing, and is most commonly associated with asthma. Airway response is categorized from normal to marked AHR using the delivered dose of methacholine causing a 20% fall in FEV_1 (provocative dose (PD20)).

5.3 Arterial Blood Gas Analysis

Arterial blood gas analysis is useful for the assessment of respiratory failure and acid-base disorders. Hypercapnia ($PaCO_2$ > 45 Torr) reflects alveolar hypoventilation, because $PaCO_2$ is inversely proportional to alveolar ventilation.

5.4 Respiratory Impedance

Recently, the measurement of respiratory impedance using forced oscillation technique (FOT) (Oostveen et al. 2003) is widely used for physiological assessments, mainly of obstructive diseases such as bronchial asthma and COPD. Respiratory impedance, including resistance and reactance, can be measured using the relation between airway opening pressure and flow by imposing oscillation signals on normal breathing. Major component of respiratory resistance is airway resistance, whereas reactance reflects the elastic and inertial properties. Compared with spirometry, FOT is useful for the functional assessment of lung diseases especially for childhood asthma and adult severe COPD, because the FOT enables us to measure respiratory mechanics during tidal breathing without requiring an effort-dependent maneuver such as forced expiration. For example, the patients with asthma attack show the impedance values with increase in resistance and decrease in reactance, and they recover to normal ranges after inhalation of bronchodilator.

5.5 Field Walking Tests

Spirometry, measurements of lung volumes, and D_{LCO} as described above are all the tests for the subject at rest. Field walking tests (Holland et al. 2014; Singh et al. 2014) such as the 6-min walk test, incremental shuttle walk test, and endurance shuttle walk test are useful for evaluating functional exercise capacity in chronic respiratory disease. These tests can provide additional information on spirometry. For example, the patients with interstitial fibrosis often show oxygen desaturation and dyspnea on exercise even with normoxia at rest. The 6-min walking distance (6MWD) correlates more strongly with measures of peak work capacity and physical activity than with respiratory function, and shorter 6MWD correlates with an increased risk of mortality for patients with COPD, interstitial lung disease, and pulmonary hypertension.

5.6 Clinical Assessment of Dyspnea

Dyspnea is one of the common symptoms in patients with pulmonary diseases. Several questionnaires are available to assess the severity of dyspnea, such as the visual analog scale (VAS), the Borg scale (rating from 0 (Nothing at all) to 10 (Very, very severe)) (Borg 1982), and the Modified Medical Research Council (mMRC) dyspnea scale (Fletcher 1960) (Table 6). These

Table 6 Modified Medical Research Council (mMRC) dyspnea scale

Grade 0	I only get breathless with strenuous exercise
Grade 1	I get short of breath when hurrying on level ground or walking up a slight hill
Grade 2	On level ground, I walk slower than people of the same age because of breathlessness, or have to stop for breath when walking at my own pace
Grade 3	I stop for breath after walking about 100 yards or after a few minutes on level ground
Grade 4	I am too breathless to leave the house or I am breathless when dressing

scales can be used to evaluate the severity of dyspnea in baseline and future changes, for example, before and after exercise or medical treatment in chronic respiratory diseases.

6 Summary

In this section, common pulmonary function tests are briefly overviewed. The VC, FEV_1, and FEV_1/FVC ratio measured by spirometer are the basic parameters used to interpret lung function and classify into normal, obstruction, restriction, or mixed defect. The measurement of lung volumes can provide additional information to evaluate ventilator defect. For the next step, it is important to measure D_{LCO}. The measurement of D_{LCO} is useful to assess the causes of dyspnea or hypoxemia. Low D_{LCO} suggests gas exchange abnormalities such as COPD (emphysema), interstitial lung diseases, and pulmonary vascular diseases. All these pulmonary function tests must contribute to the understanding of pathophysiology in pulmonary diseases in conjunction with image diagnosis.

References

Borg GA (1982) Psychophysical bases of perceived exertion. Med Sci Sports Exerc 14:377

Coates AL, Wanger J, Cockcroft DW, Culver BH, Bronchoprovocation Testing Task Force, Carlsen K-H, Diamant Z, Gauvreau G, Hall GL, Hallstrand TS, Horvath I, de Jongh FHC, Joos G, Kaminsky DA, Laube BL, Leuppi JD, Sterk PJ (2017) ERS technical standard on bronchial challenge testing: general considerations and performance of methacholine challenge tests. Eur Respir J 49(5)

Fletcher CM (1960) Standardised questionnaire on respiratory symptoms: a statement prepared and approved by the MRC Committee on the aetiology of chronic bronchitis (MRC breathlessness score). BMJ 2:1665

Gould GA, Redpath AT, Ryan M, Warren PM, Best JJ, Flenley DC, MacNee W (1991) CT density correlates with measurements of airflow limitation and the diffusing capacity. Eur Respir J 4(2):141–146

Graham BL, Brusasco V, Burgos F, Cooper BG, Jensen R, Kendrick A, MacIntyre NR, Thompson BR, Wanger J (2017a) 2017 ERS/ATS standards for single-breath carbon monoxide uptake in the lung. Eur Respir J 49(1):1600016

Graham BL, Brusasco V, Burgos F, Cooper BG, Jensen R, Kendrick A, MacIntyre NR, Thompson BR, Wanger J (2017b) Executive summary: 2017 ERS/ATS standards for single-breath carbon monoxide uptake in the lung. Eur Respir J 49:1600016

Holland AE, Spruit MA, Troosters T, Puhan MA, Pepin V, Saey D, McCormack MC, Carlin BW, Sciurba FC, Pitta F, Wanger J, MacIntyre N, Kaminsky DA, Culver BH, Revill SM, Hernandes NA, Andrianopoulos V, Camillo CA, Mitchell KE, Lee AL, Hill CJ, Singh SJ (2014) An official European Respiratory Society/American Thoracic Society technical standard: field walking tests in chronic respiratory disease. Eur Respir J 44:1428–1446

Macintyre N, Crapo RO, Viegi G, Johnson DC, van der Grinten CP, Brusasco V, Burgos F, Casaburi R, Coates A, Enright P, Gustafsson P, Hankinson J, Jensen R, McKay R, Miller MR, Navajas D, Pedersen OF, Pellegrino R, Wanger J (2005) Standardisation of the single-breath determination of carbon monoxide uptake in the lung. Eur Respir J 26:720–735

Miller MR, Hankinson J, Brusasco V, Burgos F, Casaburi R, Coates A, Crapo R, Enright P, van der Grinten CP, Gustafsson P, Jensen R, Johnson DC, MacIntyre N, McKay R, Navajas D, Pedersen OF, Pellegrino R, Viegi G, Wanger J, ATS/ERS Task Force (2005) Standardisation of spirometry. Eur Respir J 26:319–338

Morrison NJ, Abboud RT, Ramadan F, Miller RR, Gibson NN, Evans KG, Nelems B, Müller NL (1989) Comparison of single breath carbon monoxide diffusing capacity and pressure-volume curves in detecting emphysema. Am Rev Respir Dis 139(5):1179–1187

Oostveen E, MacLeod D, Lorino H, Farré R, Hantos Z, Desager K, Marchal F, ERS Task Force on Respiratory Impedance Measurements (2003) The forced oscillation technique in clinical practice: methodology, recommendations and future developments. Eur Respir J 22(6):1026–1041

Papaioannou AI, Kostikas K, Manali ED, Papadaki G, Roussou A, Kolilekas L, Borie R, Bouros D, Papiris SA (2016) Combined pulmonary fibrosis and emphysema: the many aspects of a cohabitation contract. Respir Med 117:14–26

Pellegrino R, Viegi G, Brusasco V, Crapo RO, Burgos F, Casaburi R, Coates A, van der Grinten CP, Gustafsson P, Hankinson J, Jensen R, Johnson DC, MacIntyre N, McKay R, Miller MR, Navajas D, Pedersen OF, Wanger J (2005) Interpretative strategies for lung function tests. Eur Respir J 26:948–968

Plantier L, Cazes A, Dinh-Xuan AT, Bancal C, Marchand-Adam S, Crestani B (2018) Physiology of the lung in idiopathic pulmonary fibrosis. Eur Respir Rev 27(147):170062. https://doi.org/10.1183/16000617.0062-2017

Singh SJ, Puhan MA, Andrianopoulos V, Hernandes NA, Mitchell KE, Hill CJ, Lee AL, Camillo CA, Troosters T, Spruit MA, Carlin BW, Wanger J, Pepin V, Saey D,

Pitta F, Kaminsky DA, McCormack MC, MacIntyre N, Culver BH, Sciurba FC, Revill SM, Delafosse V, Holland AE (2014) An official systematic review of the European Respiratory Society/American Thoracic Society: measurement properties of field walking tests in chronic respiratory disease. Eur Respir J 44(6):1447–1478

Wanger J, Clausen JL, Coates A, Pedersen OF, Brusasco V, Burgos F, Casaburi R, Crapo R, Enright P, van der Grinten CP, Gustafsson P, Hankinson J, Jensen R, Johnson D, Macintyre N, McKay R, Miller MR, Navajas D, Pellegrino R, Viegi G (2005) Standardisation of the measurement of lung volumes. Eur Respir J 26:511–522

Basics and Clinical Application of CT for Pulmonary Functional Evaluation

Hyun Woo Goo, Hyungjin Kim, and Jin Mo Goo

Contents

1 **Introduction** 22

2 **Sources of Variation** 22
2.1 Radiation Dosage 24
2.2 Iterative Reconstruction Algorithm 24

3 **CT Lung Volumetry and Quantitative Parameters** 24
3.1 Lung Volume 26
3.2 Lung Densitometric Parameters and Airway Quantification 27
3.3 Pulmonary Vascular Volume 30

4 **Dual-Energy Computed Tomography** 30
4.1 Lung Perfusion 33
4.2 Lung Ventilation 35
4.3 Lung Ventilation and Perfusion 36
4.4 Thoracic Oncology 37

5 **Cine and Four-Dimensional Computed Tomography** 38

6 **Dynamic Perfusion Computed Tomography Assessment** 39
6.1 Dynamic Contrast-Enhanced CT with Perfusion Analyses 39
6.2 Dynamic First-Pass Contrast-Enhanced Perfusion Area-Detector CT 39

7 **Conclusion** 39

References 40

H. W. Goo
Department of Radiology and Research Institute of Radiology, University of Ulsan College of Medicine, Asan Medical Center, Seoul, South Korea

H. Kim · J. M. Goo (✉)
Department of Radiology, Seoul National University College of Medicine, and Institute of Radiation Medicine, Seoul National University Medical Research Center, Seoul, South Korea
e-mail: jmgoo@plaza.snu.ac.kr

Abstract

Pulmonary structures provide morphological basis for the vital functions to our body, which needs adequate airway flow, respiratory dynamics, lung ventilation, gas exchange, and lung perfusion closely interlinked with one another. For the CT evaluation of these functions, three-dimensional lung volumetry using the density mask techniques, dual-energy CT techniques, and cine and four-dimensional CT

© Springer Nature Switzerland AG 2021

Y. Ohno et al. (eds.), *Pulmonary Functional Imaging*, Medical Radiology Diagnostic Imaging,
https://doi.org/10.1007/978-3-030-43539-4_3

techniques may be used. To provide accurate and reproducible answers to clinical questions, we should first understand sources of variation influencing the results of these pulmonary functional CT exams. Then, we should know basic concepts, imaging techniques, and clinical applications of pulmonary functional CT. In addition to pulmonary anatomic details, pulmonary functional CT gives us new insights into lung physiology and ultimately opens new avenues in functional lung imaging.

1 Introduction

High-resolution three-dimensional (3D) thoracic anatomy provided by chest CT is now clinical routine and serves as the anatomical backbone for functional pulmonary evaluation. Radiologists need to go beyond pulmonary anatomy to truly evaluate pulmonary structures. This is because they support gas exchange as a vital body function, which comprises ventilation, perfusion, and diffusion of gases across the blood–gas interface. In addition, airways and respiratory muscles offer a crucial function to induce and maintain airflow in the lung. Pulmonary functional CT imaging in patients is challenging because of respiratory, cardiac, and patient motions in the thorax during the examination as well as complexities in data analysis and interpretation. This is why many studies on pulmonary functional CT imaging have been conducted in experimental and preclinical environments. Recently, translations from basic research to clinical application have been attempted, thanks to technical developments in CT data acquisition and analysis. In clinical studies, the radiation exposure of chest CT for pulmonary functional evaluation should be carefully optimized to ensure a favorable benefit–risk ratio by using various dose reduction techniques (Goo 2012). Compared with other imaging modalities used for pulmonary functional evaluation, such as nuclear medicine studies and MRI, CT has a higher spatial resolution, faster examination time, and wider availability. In this chapter, we will describe basics and clinical applications of CT for pulmonary functional evaluation, especially from clinical radiologists' point of view.

2 Sources of Variation

Sources of variation in pulmonary function evaluation using CT may be associated with patient-related factors, imaging-related factors, and algorithms for function evaluation (Coxson 2013; Hoffman et al. 2016). The imagers should acknowledge not only the effects of these factors on the results but also ways of troubleshooting to minimize these variations. Patient-related factors include patient age, lung inflation level, lung pathology, anatomical variation, sex, ethnicity, weight, height, and smoking status. Imaging-related parameters include CT scanner, slice thickness, reconstruction kernel, radiation dose, the use of iterative reconstruction algorithm, and the use of intravenous administration of contrast agent (Fig. 1). Examples are given in Table 1 for emphysema quantification. Basically, CT scanners should be calibrated on a regular basis, and inter-scanner differences in CT attenuation values can be reduced by being normalized to tracheal air density. Because of worldwide concerns about radiation risks from diagnostic CT imaging, the requirement of low-dose scanning is overwhelmingly emphasized. As a result, there would be a higher chance to use noisy CT images for pulmonary functional evaluation, particularly in obese patients (Fig. 2). Although there are only minor changes in mean lung density, a leftward shift in the CT density histogram may non-negligibly affect the results. This adverse effect of high image noise can be diminished by using iterative reconstruction algorithm instead of conventional filtered back projection for image reconstruction. In a recent study using an adult chest phantom (Lee and Goo 2018), chest CT images reconstructed with an iterative reconstruction algorithm, however, begin to show image quality degradation if radiation dose is used below 1.4 mGy in volume CT dose index.

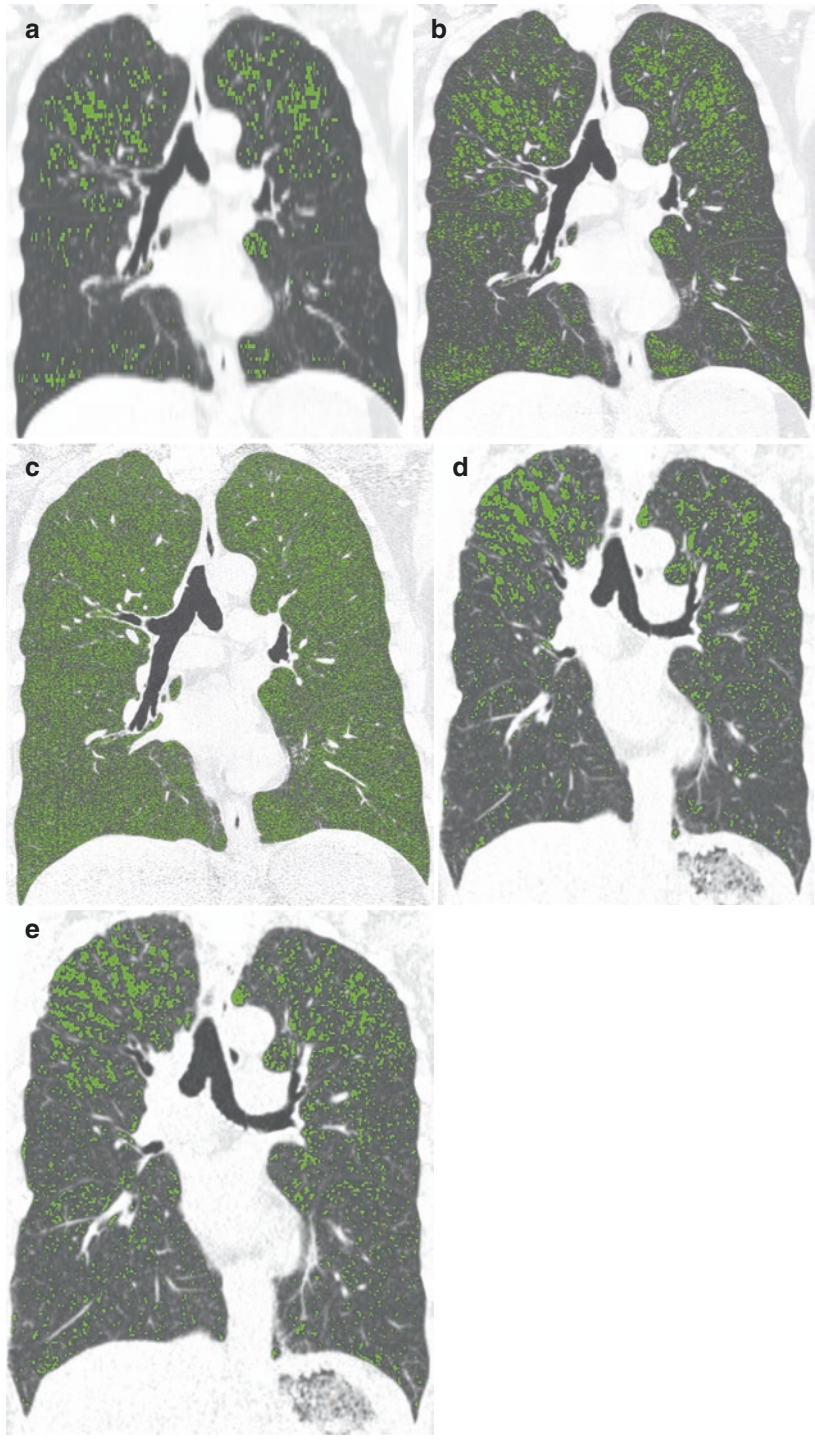


Fig. 1 (**a**–**c**) A patient with emphysema in the upper lobes. CT scan was reconstructed with standard kernel (B kernel; Philips Healthcare) at slice thicknesses of 3 mm (**a**) and 1 mm (**b**). Emphysema indices (EIs) were 4.9% and 14.1%, respectively. Sharp kernel reconstruction (YD) resulted in a substantial increase of EI (**c**; 35.1%). (**d**, **e**) Another patient with emphysema underwent a dual-source CT scan, and a single-tube reconstruction was conducted to obtain a reduced-dose scan. Reduced radiation dose also increases the EI. Specifically, full-dose CT (**d**) showed EI of 8.3%, while it was calculated as 10.4% at the quarter-dose scan (**e**)

Table 1 Sources of measurement variation for emphysema

Variation source	Situation	Effect on quantification	Source
Radiation dosage	Low-dose CT	Increase in %LAA	Gierada et al. (2007)
Slice thickness	Thin-section (1 mm)	Increase in %LAA	Gierada et al. (2007)
Reconstruction algorithm	Commercial iterative reconstruction algorithm from each vendor	Decrease in %LAA	Choo et al. (2014)
Reconstruction kernel	Sharp kernel	Increase in %LAA	Behrendt et al. (2008)
Contrast material	Contrast-enhanced CT	Decrease in %LAA	Heussel et al. (2010)
Quantification software	Commercial and in-house software programs	Limits of agreement from −25.5 to 18.8% for %LAA	Wielputz et al. (2014)

%LAA percentage low-attenuation area

Standardized lung inflation level is of critical importance to obtain reproducible results among different individuals and different time points. Unfortunately, such a standardized method is difficult to apply to patients in clinical practice, especially uncooperative patients. Also, post-processing algorithms for functional evaluation may influence the results. It is well known that the results of four-dimensional (4D) ventilation CT imaging considerably depend on deformable image registration algorithms used for the functional assessment.

2.1 Radiation Dosage

Increased image noise in low-dose CT scans may cause variations in the quantitative measurements. For example, low-dose CT may result in erroneous increase (i.e., overestimation) of percentage low-attenuation area (%LAA) for emphysema quantification (den Harder et al. 2018). Nevertheless, the variation caused solely by the radiation dosage level, when other acquisition parameters are fixed, would be small, and Nishio et al. (2012) reported that the mean difference of %LAA between low-dose and standard-dose CT scans was 1.98%. Gierada et al. (2007) also revealed that the mean difference at several thresholds for %LAA calculation was less than 3%. In addition, it was reported that the low-dose CT scans for lung cancer screening could be used for identification of the patients with chronic obstructive pulmonary disease (COPD) (Mets et al. 2011).

2.2 Iterative Reconstruction Algorithm

Iterative reconstruction algorithm alters the pixel value distribution of CT scans. Specifically, the mean of pixel value within a region-of-interest is preserved, but the standard deviation is reduced and the density histogram becomes more sharply peaked (Rodriguez et al. 2017). Consequently, this affects the quantitative measurements including emphysema quantification and airway measurement. Underestimation of %LAA when using the iterative reconstruction has been reported (Choo et al. 2014; Martin et al. 2017). In this context, one study suggested that higher Hounsfield units (HU) thresholds (e.g., −930 or −940 HU) for CT scans with iterative reconstruction could result in comparable emphysema measurements to the reference condition (filtered back projection at standard-dose CT) (den Harder et al. 2018). For the low-dose or ultralow-dose CT scans, application of the iterative reconstruction can counteract the effect of increased image noise. Several recent studies indicated that the low-dose CT scans with iterative reconstruction may potentially substitute for the standard-dose CT scans (Nishio et al. 2012, 2014).

3 CT Lung Volumetry and Quantitative Parameters

Lung volumes can be easily calculated from high-resolution isotropic 3D multi-detector row CT dataset, in which the voxel size is

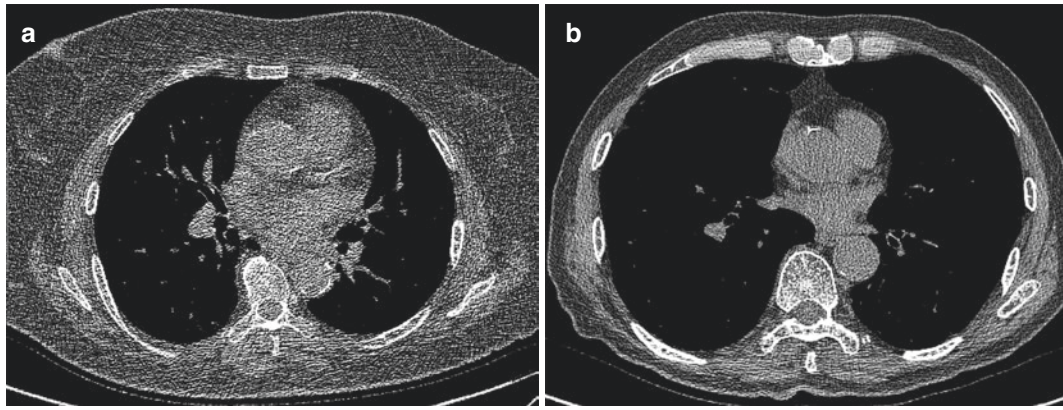


Fig. 2 Increased image noise or quantum mottle in a CT scan obtained from an obese woman (**a**) compared with a low-dose CT scan from a man with normal body habitus (**b**). Note that the same CT scanner and protocol were used for both patients

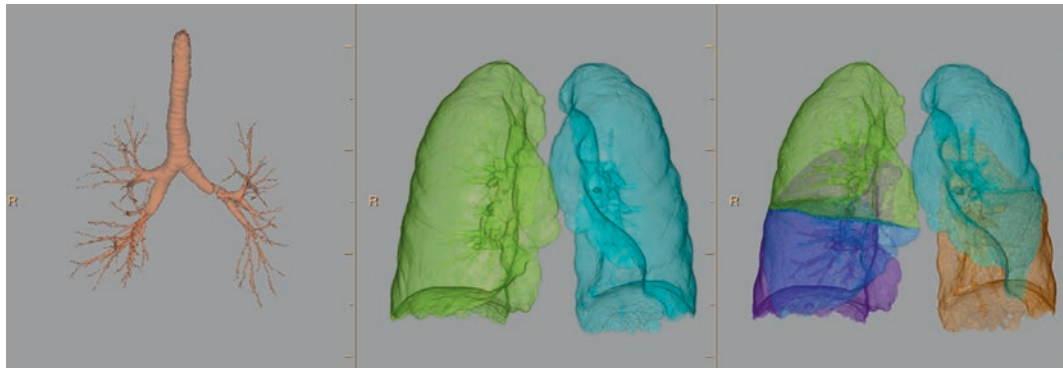


Fig. 3 An exemplary figure of a commercial software program (COPD application of IntelliSpace Portal, Philips Healthcare). This tool first extracts the airway and then performs lung segmentation followed by lobar segmentation (from left to right)

approximately 0.5 mm × 0.5 mm × 0.5 mm. The post-processing is now almost universally available in clinical workstations. Therefore, CT lung volumetry can be used as a routine clinical procedure. In the procedure, the upper threshold, usually in the range of −200 to −650 HU, is initially applied to extract air-containing structures including the lung and central airways from a 3D thoracic CT dataset (Fig. 3). The upper HU value should be adaptive rather than fixed depending on mean lung density especially in pediatric patients since mean lung density is relatively high in children during a proliferative lung growth period up to 8 years of age (Thurlbeck 1982; de Jong et al. 2003). A shallow lung inflation, which increases mean lung density, should also be considered in young children (Goo and Kim 2006). Subsequently, the central airways having similar CT densities should be excluded from the lungs (Fig. 3). Small differences (0.2–6.5%) in lung volumes were reported among different CT lung volumetry software packages (Nemec et al. 2015). On the contrary, substantial intraindividual variations, approximately 16%, in CT lung volumetry remain a challenge in interpreting the results (Haas et al. 2014). In this regard, standardization of lung volume during CT examination is desirable (Fuld et al. 2012). However, the systems proposed for the standardization are still too complicated for

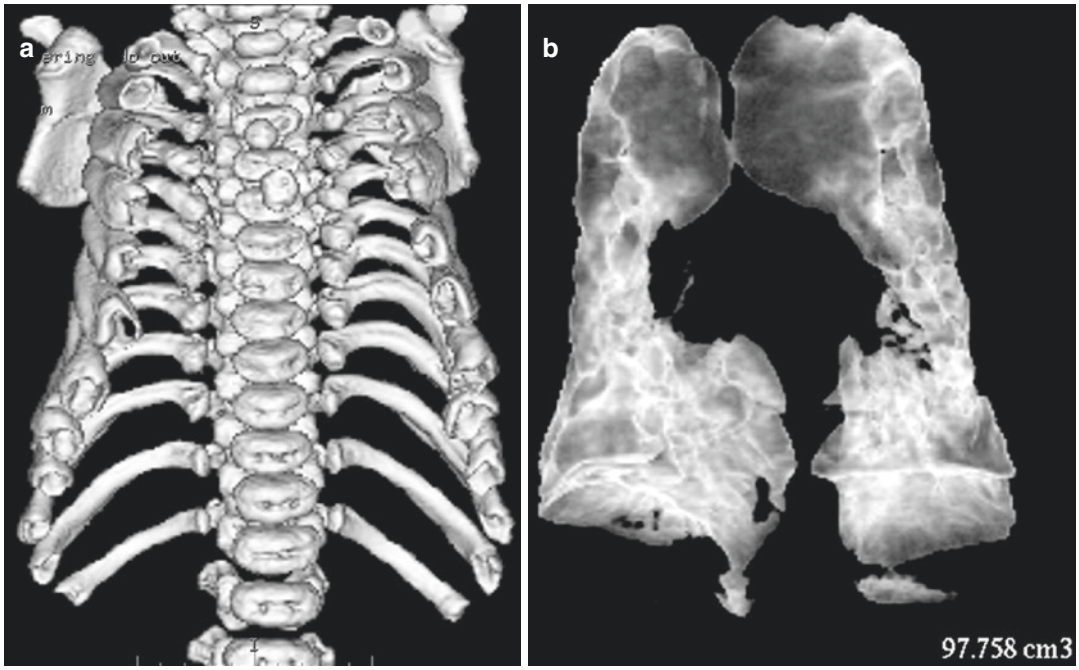


Fig. 4 CT lung volumetry in a child with asphyxiating thoracic dysplasia. Three-dimensional volume rendering CT images with an anterior view (**a**, the bony thoracic cages; **b**, the lungs) demonstrate the elongated hypoplastic thoracic cage, which is typical for the dysplasia, and the secondary lung hypoplasia

routine clinical use. In reality, proper respiratory instructions for CT examinations of the lungs are the best way to improve the quality of the examinations. In 64 adult patients with solitary pulmonary nodule who underwent CT lung volumetry, the authors suggested that normal lung capacity excluding an emphysema component is better than total lung capacity for preoperative lung function evaluation (Iwano et al. 2009). Non-contrast CT datasets are obviously preferred to contrast-enhanced ones for CT lung volumetry. Since intravenous injection of contrast agent increases mean lung density, the upper threshold for volumetry needs to be proportionally adjusted to obtain clinically relevant lung volumes.

3.1 Lung Volume

Lung volumes measured with CT show high correlations with pulmonary function test results (Iwano et al. 2009). Therefore, CT lung volumetry has been used to evaluate lung function in various pulmonary diseases, such as asthma (Cohen et al. 2008), COPD (Morimura et al. 2013), interstitial lung diseases (Yilmaz et al. 2011), bronchiolitis obliterans (Goo et al. 2010), neoplasms (Iwano et al. 2009; Matsuo et al. 2012), living lung donors (Chen et al. 2011), and deformed thoracic cages (Zeng et al. 2010; Sarwahi et al. 2014) (Fig. 4). Low-dose CT scans may be used for lung volumetry and pulmonary function estimation (Chen et al. 2014). It is noteworthy that the CT-based total lung capacity measured in the supine position is significantly smaller than the spirometry-based value measured in a sitting position because of diaphragm elevation in the supine position. An expiratory–inspiratory lung volume ratio may be used to determine the extent of resection and the treatment effect in lung volume reduction surgery for severe emphysema (Morimura et al. 2013). Lobar volumes from CT dataset can also be measured by utilizing a lobe segmentation method (Doel et al. 2015) (Fig. 5). In 111 adult patients with pulmonary neoplasms, the authors found that

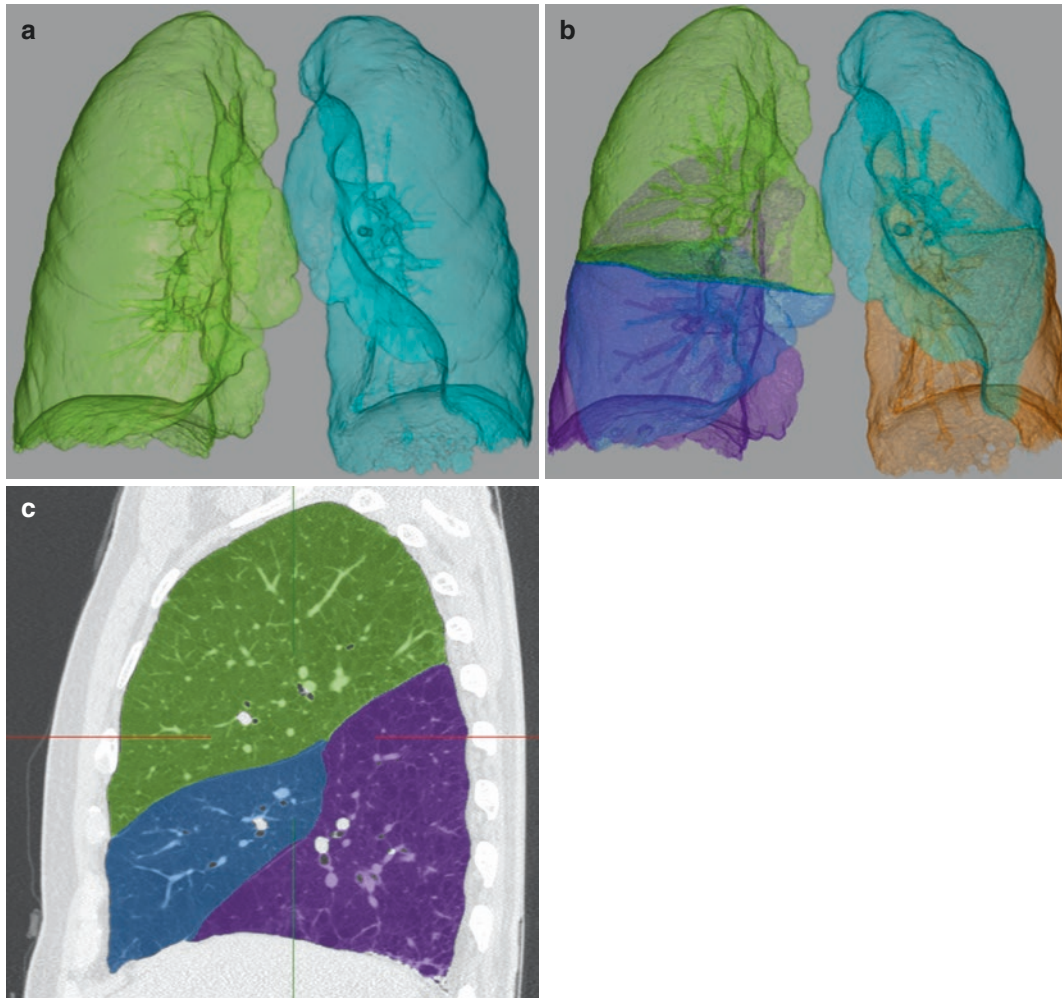


Fig. 5 Lung (**a**) and lobe (**b**, **c**) segmentation. Lobe segmentation can be performed automatically (**b**) and manual editing (i.e., re-drawing fissures) at axial, coronal, or sagittal images (**c**) may be required to adjust the lobar boundary

pulmonary function is influenced more by the normal lower lobe volumes than by the others (Matsuo et al. 2012).

3.2 Lung Densitometric Parameters and Airway Quantification

CT quantitative parameters have been investigated to evaluate functional pulmonary diseases including COPD and asthma (Table 2). A subset volume of low attenuating lesions, such as emphysema and air trapping, can be specifically quantified. To represent emphysema in COPD, such CT-based quantifications have been extensively evaluated by utilizing a cutoff value, e.g., −950 HU, generally at full inspiration (Fig. 6). The %LAA, the percentage of lung voxels with CT attenuation less than −950 HU, was an independent predictor for 8-year mortality in smokers according to Johannessen et al. (2013). Moreover, the so-called the 15th percentile (Perc15) is often defined as the 15th percentile point of the attenuation distribution curve on inspiratory scan. This parameter was associated with lung function decline and development of new airflow obstruction in heavy smokers (Mohamed Hoesein et al.

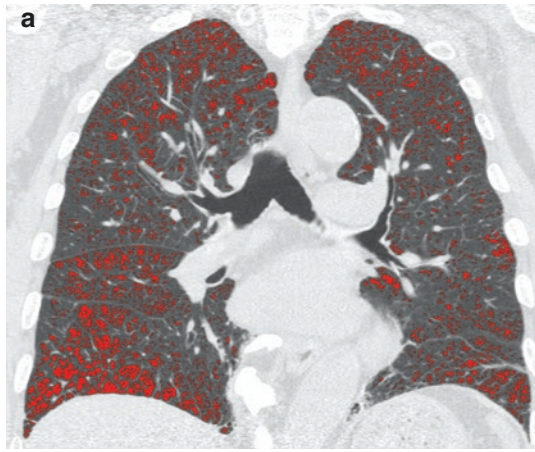
Table 2 Lung densitometric parameters and airway quantification for chronic obstructive pulmonary disease

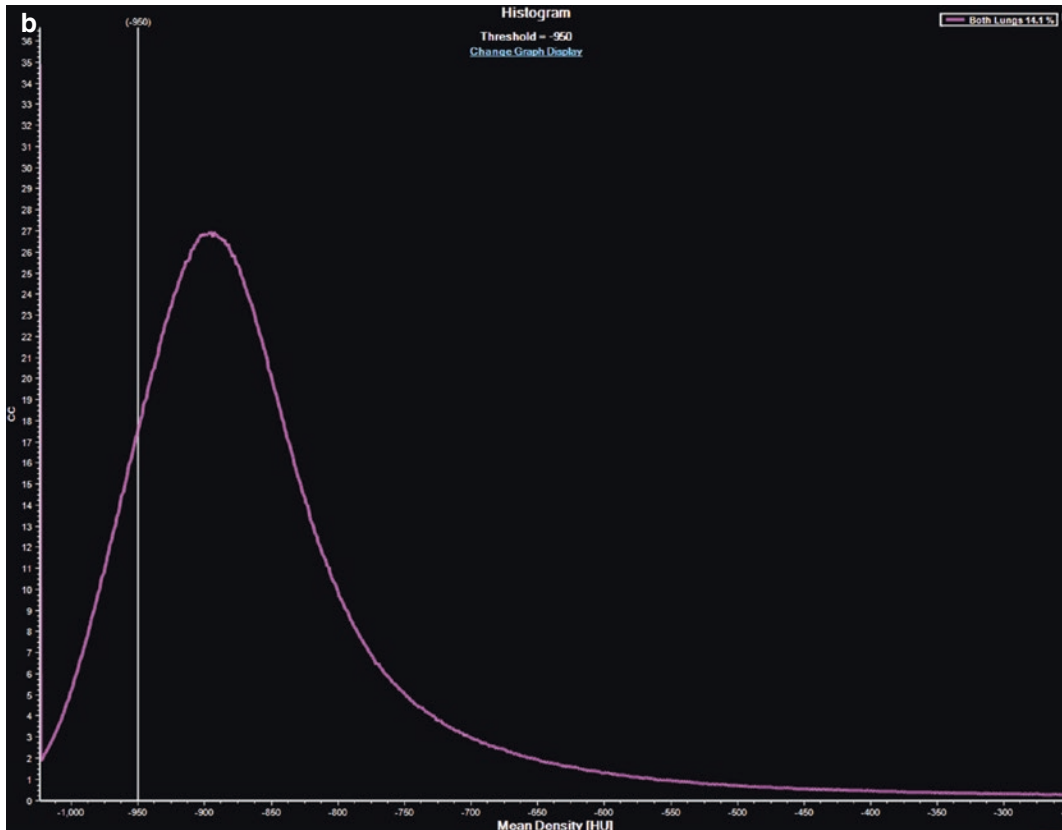
Category	Parameter	Explanation	Source
Emphysema measurement	%LAA	Percentage volume of pixels less than −950 HU relative to the lung volume	Johannessen et al. (2013)
	Perc15	15th percentile point of the attenuation distribution curve	Mohamed Hoesein et al. (2011)
Air trapping quantification	Expiration −856	Percentage volume of pixels less than −856 HU on expiration CT	Kim et al. (2015)
	Air trapping index	Volume fraction of the lung pixels in which the difference between the registered inspiratory and expiratory CT scans <50 HU	Kim et al. (2015)
	E/I ratio of mean lung density		Kim et al. (2015)
Airway measurement	Wall thickness	Cross-sectional wall thickness	Gierada et al. (2011)
	Wall area	Cross-sectional wall area	Gierada et al. (2011)
	Wall area percentage	Wall area divided by the cross-sectional airway area	Gierada et al. (2011)
	Pi10	Square root of wall area for a hypothetical airway with an internal perimeter of 10 mm	Johannessen et al. (2013)

E/I ratio expiratory-to-inspiratory ratio, *HU* Hounsfield units, *%LAA* percentage low-attenuation area, *Pi10* square root of wall area of a bronchus of internal perimeter 10 mm

2011). In contrast, expiratory scan is utilized to quantify lung lesions with air trapping in COPD and −856 HU is commonly used as a CT density threshold. By using nonrigid respiratory registration, lung lesions with air trapping can be quantified on subtraction images between pairs of inspiratory and expiratory CT scans (Kim et al. 2015; Goo 2013a), or simply, the expiratory-to-inspiratory ratio of mean lung density can be calculated (O'Donnell et al. 2004; Mets et al. 2012). The latter was associated with accelerated decline of lung function over time in heavy smokers and was independent of %LAA (Mets et al. 2013). In addition to general anesthesia with intubation and controlled ventilation, the prospectively respiratory-triggered sequential scan was recently reported as a less invasive approach to provide inspiratory and expiratory CT scans in free-breathing children (Goo and Allmendinger 2017; Goo 2018b). Gas and lung tissue volumes can be calculated separately in a software tool but their clinical significance remains to be determined (Nemec et al. 2015). Nevertheless, these densitometric approaches cannot reflect the distribution of emphysema. For example, paraseptal emphysema, which may not have considerable symptomatic and physiological consequences (Smith et al. 2014), cannot be differentiated from parenchymal (i.e., centrilobular) emphysema based on the densitometric parameters.

Airway remodeling results in airway wall thickening in both large and small airways, which is thought to be an independent component of airway flow limitation. To quantify airway dimensions, the airway tree is segmented, and then curved multiplanar images are reconstructed along the selected bronchial pathway to provide the airway dimensions (Fig. 7). In addition to the proportion of low-attenuation areas, the bronchial wall area showed a negative correlation with FEV1 and FEV1/FVC (Nakano et al. 2000). A smaller airway can be estimated by the regression line between the square root of the airway wall area and the internal perimeter (Pi) of the airway. Pi10 indicates the square root of wall area for an arbitrary airway with an internal perimeter of 10 mm (Fig. 8). Increased airway wall thickness reduced survival time in patients with more severe emphysema, although the airway wall thickness was not an independent predictor for mortality by itself (Johannessen et al. 2013).





Volumetric Measurements

	Volumetric Measurements		
	Emphysema Volume(cc) Threshold = -950 HU	Total Volume(cc)	Emphysema Ratio(%) Threshold = -950 HU
Both Lungs	681.1	4814.5	14.1
Right Lung	446.4	2716.1	16.4
Right Upper Lobe (RUL)	142.1	1208.8	11.8
Right Middle Lobe (RML)	118.9	503.3	23.6
Right Lower Lobe (RLL)	185.4	1004	18.5
Left Lung	234.7	2098.4	11.2
Left Upper Lobe (LUL)	132.6	1182.1	11.2
Left Lower Lobe (LLL)	102.1	916.3	11.1

Fig. 6 Coronal reformatted image shows color-coded overlay in red for the pixels below −950 Hounsfield units (**a**). The volume of those pixels and relative percentage (emphysema index) are calculated from each lobe and lung (**b**)

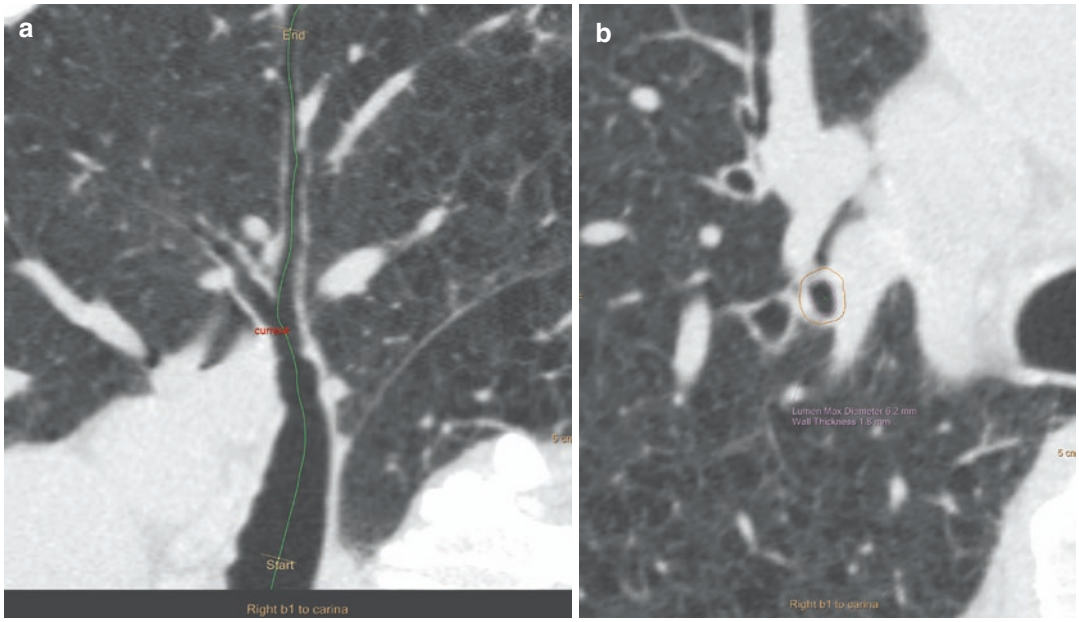


Fig. 7 Airway dimensional measurement. Curved planar reformation of the bronchial pathway from the carina to RB1 (**a**). Airway dimensions at the orthogonal cross-sectional plane are automatically calculated (**b**)

3.3 Pulmonary Vascular Volume

Recent studies (Goo and Park 2017; Goo 2018c) demonstrate that CT-based pulmonary vascular volume ratio obtained at the end-systolic phase shows a high correlation with the corresponding ratio measured with lung perfusion scintigraphy. As a result, a single contrast-enhanced cardiothoracic CT can offer such functional information, without additional radiation exposure, in addition to pulmonary vascular anatomy (Fig. 9). This volumetric ratio measured with cardiothoracic CT may be useful in patients with obstructive pulmonary vascular disease and pulmonary artery hypertension not only for the initial workup but also for follow-up after treatments.

In addition, pulmonary vessel volume itself may play a role as an imaging biomarker. Reduction in total pulmonary vascular volume, which was the volume of arteries and veins, was associated with lower left ventricular filling and dyspnea in ever-smokers (Aaron et al. 2017). Pulmonary vascular volume score, calculated as a percentage volume of pulmonary arteries and veins relative to the lung volume, was an independent predictor of mortality in patients with idiopathic pulmonary fibrosis (Jacob et al. 2017).

4 Dual-Energy Computed Tomography

Since the introduction of a dual-source CT scanner, the first clinical studies using dual-energy thoracic CT have been published in 2008 (Chae et al. 2008; Goo et al. 2008). Currently, several technical approaches, including dual tubes with or without beam filtration, rapid voltage switching of a single tube, and dual-layer detector with a single tube (Table 3), have been developed for acquiring dual-energy CT imaging (Goo and Goo 2017). These approaches have their own technical merits and demerits. Dual-source CT enables better material separation based on the two separate energy spectra. However, scatter radiation is a concern and correction is required.



	Average Inner Area (mm^2)	Average Inner Perimeter (mm)	Luminal Eccentricity	Average Wall Thickness (mm)	Wall Area (mm^2)	Wall Area %
Trachea	282.26	60.32	0.93	2.91	206.37	42.23
RMB	203.63	54.63	0.67	2.79	180.48	47.03
RUL	69.43	30.51	0.71	1.95	70.30	50.31
RB1	26.44	18.89	0.71	1.66	40.39	60.34

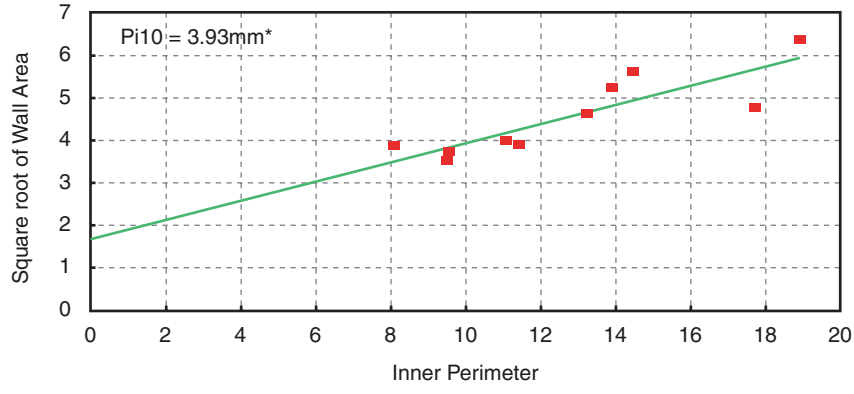
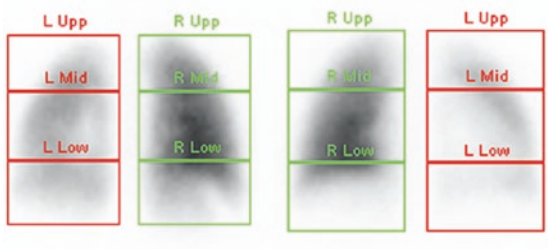


Fig. 8 Estimation of the square root of the wall area of the airway at Pi10. The square root of the wall area of the measured segments is plotted against its internal perimeter to produce Pi10, which is the square root of the wall area of the hypothetical airway with an internal perimeter of 10 mm



d



Perfusion

POST

(Counts)	Left	Right
Upper	061K	104K
Middle	138K	279K
Lower	079K	131K
Total	278K	514K

(% Ratios)	Left	Right
Upper	7.73	13.15
Middle	17.45	35.23
Lower	9.92	16.51
Total	35.10	64.90

ANT

(Counts)	Left	Right
Upper	053K	098K
Middle	088K	296K
Lower	042K	093K
Total	183K	487K

(% Ratios)	Left	Right
Upper	7.91	14.68
Middle	13.13	44.13
Lower	6.24	13.91
Total	27.28	72.72

Geometric Mean

(Counts)	Left	Right
Upper	057K	101K
Middle	108K	287K
Lower	056K	109K
Total	221K	496K

(% Ratios)	Left	Right
Upper	7.89	14.08
Middle	15.08	39.99
Lower	7.82	15.14
Total	30.79	69.21

Fig. 9 CT pulmonary vascular volume ratio. Three-dimensional volume rendering CT images with a posterior view (**a**, the whole cardiovascular structures; **b**, the lung vasculature; **c**, the lung vasculature with the lungs) show mildly diminished left pulmonary vascularity. The pulmonary vascular volume ratio (right:left = 71:29%) measured using CT is comparable to the lung perfusion ratio (right:left = 69:31%) measured using lung perfusion scintigraphy (**d**)

Table 3 Comparison of various dual-energy CT approaches

	Dual-source CT	Fast-kV-switching	Dual-layer detector
Hardware design	Two X-ray tubes with or without a tin filter	One X-ray tube with rapidly changing tube voltage	One X-ray tube with a dual-layer energy-resolving detector
Strength	Energy separation with beam filtration Separate tube current modulation	Projection-based processing	Projection-based processing Retrospective spectral analysis
Weakness	Image-based processing	No separate tube current modulation	Limited energy separation

Potential temporal gap between the two detectors is another issue. Single-source CT with rapid kilovoltage switching offers near simultaneous image acquisition for high- and low-energy spectra, but the overlap between the photon spectra is a limitation. Strength of a dual-layer detector CT scanner is that the high- and low-energy datasets can be obtained simultaneously and that dual-energy imaging is available from all image data only if a spectral base image is stored.

For functional thoracic dual-energy CT evaluation, exogenous materials should be given to patients, either by intravenous administration of iodinated contrast agent or inhalation of xenon or krypton gas (Kang et al. 2010; Goo 2013b). Of note, these contrast materials have relatively high atomic numbers resulting in a greater photoelectric effect at lower tube voltages. Material-specific dual-energy CT images are subsequently reconstructed by utilizing a material decomposition algorithm and can be used for the qualitative and quantitative assessments of regional lung perfusion and ventilation in various pulmonary diseases. Various artifacts, such as perivenous streak artifacts, beam-hardening artifacts, motion artifacts, and misregistration artifacts, may hamper image interpretation of dual-energy CT. Depending on a dual-energy scanning approach, a CT scanner model and an employed scan protocol, radiation dose of dual-energy thoracic CT may be lower than, comparable to, or higher than that of a single-energy thoracic CT (Henzler et al. 2012). Considering additional clinical benefits, the benefit–risk ratio of dual-energy thoracic CT performed with optimized protocols would be mostly favorable.

4.1 Lung Perfusion

In contrast-enhanced dual-energy thoracic CT, simultaneous evaluation of pulmonary arteries and lung perfusion considerably increases the detection of pulmonary embolism, especially for small peripheral pulmonary embolism (Goo 2010; Lu et al. 2012) (Fig. 10). Intravenous injection protocol of iodinated contrast agent needs to be optimized to reduce artifacts and improve image quality. In this regard, scanning delay slightly longer than that for conventional pulmonary CT angiography, tri-phasic injection protocol, and caudocranial scan direction are commonly used. Crucially, a shallow inspiratory level during breath-hold scanning is recommended to avoid poor pulmonary arterial enhancement resulting from excessive mixing with unenhanced inferior vena caval blood driven by the Valsalva maneuver associated with deep inspiration. The normal lung demonstrates homogeneous gravity-dependent iodine distribution on the iodine map (Felloni et al. 2017), while variably diminished iodine values may be seen in various pulmonary diseases, including pulmonary embolism, pulmonary artery stenosis, aberrant pulmonary arterial supply, pulmonary emphysema, and lung lesions with air trapping.

Typically, perfusion defects caused by acute occlusive pulmonary embolism on dual-energy iodine map are peripherally located, wedge-shaped, and in a segmental or lobar distribution. A recent study revealed that iodine map could help to detect segmental or even subsegmental pulmonary emboli (Weidman et al. 2018). Despite increased detection of small occlusive

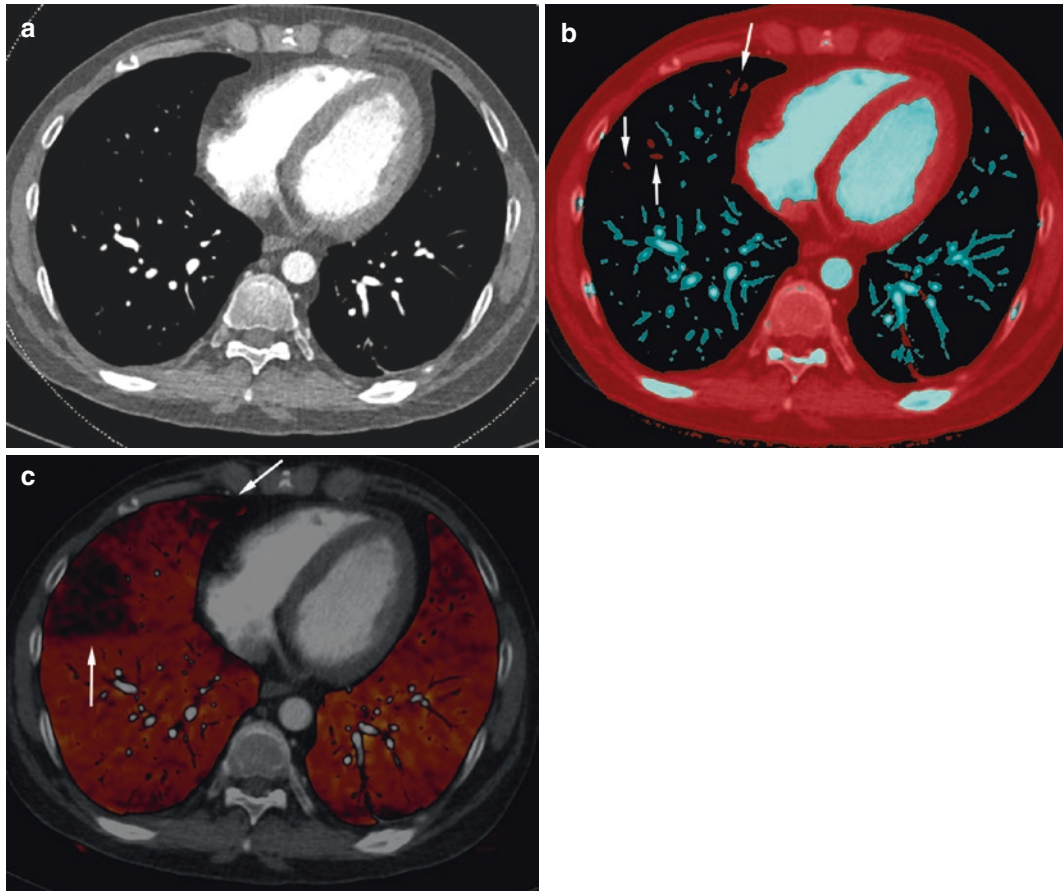


Fig. 10 Value of dual-energy CT technique in the evaluation of the pulmonary embolism. Pulmonary emboli are not visible on CT (**a**), but they are marked in red on pulmonary vessel view (**b**; arrows). Corresponding perfusion defects are also well visualized (arrows) on perfused blood volume map (**c**)

pulmonary embolism with dual-energy CT, its clinical significance is still controversial. Dual-energy CT has demonstrated higher diagnostic accuracy for detecting acute pulmonary embolism than perfusion scintigraphy (Zhang et al. 2009), MRI (Zhang et al. 2010), and planar SPECT and SPECT/CT (Yang et al. 2011) in a rabbit model with the histopathologic findings as the reference standard. In addition to the diagnosis of acute pulmonary embolism, dual-energy CT imaging has clinical implications for risk stratification, therapeutic surveillance, and prognostication. Dual-energy CT-based quantification of lung perfusion defects has been suggested as a marker of right heart strain (Chae et al. 2010a; Bauer et al. 2011). Moreover, color-coded lung vessel analysis utilizing a material labeling algorithm may be used to distinguish unenhanced small peripheral arteries typically with a diameter of 2 mm or less from enhanced ones, which is a cumbersome task in visual assessment only. In the dual-energy CT-based diagnosis of acute pulmonary embolism, we should be familiar with diagnostic pitfalls, including false negative findings in non-occlusive clots, false positive findings caused by other pulmonary diseases, and artifactual alterations in lung parenchymal iodine distribution.

A mosaic pattern of lung parenchymal iodine distribution on iodine map may be seen in patients with chronic pulmonary embolism. An excellent agreement between the dual-energy CT perfusion and ventilation/perfusion scintigraphy was observed (Masy et al. 2018). In addition,

calcifications within chronic clots and pulmonary artery walls can be detected on virtual non-contrast imaging. Delayed lung perfusion supplied by systemic arterial collaterals in chronic pulmonary embolism can be identified on two-phase dual-energy CT at the expense of additional radiation exposure to patients, which may help differentiate chronic pulmonary embolism from acute one (Hong et al. 2013). Of interest, chronic organized emboli showing higher iodine values can be distinguished from acute ones even with single-phase dual-energy CT (Kim et al. 2014). One recent study, which analyzed patients with chronic thromboembolic pulmonary hypertension, also reported that the lung perfused blood volume could serve as a useful surrogate for the mean pulmonary artery pressure and pulmonary vascular resistance obtained through the right heart catheterization (Takagi et al. 2016). In addition, for the patients with chronic thromboembolic pulmonary hypertension, the perfusion change after angioplasty could be monitored and quantified (Zhai et al. 2018).

In emphysema, contrast-enhanced dual-energy thoracic CT can provide emphysema quantification and regional perfusion evaluation using virtual non-contrast imaging and iodine map simultaneously (Lee et al. 2012). Moderate correlations between quantitative parameters on virtual non-contrast images and pulmonary function test results were observed (Lee et al. 2012).

4.2 Lung Ventilation

Xenon-inhaled dual-energy CT has been used for evaluating high-resolution regional and global lung ventilation function in addition to thoracic anatomic details in various pulmonary diseases (Fig. 11), including COPD (Park et al. 2010), combined pulmonary fibrosis and emphysema (Sugino et al. 2017), bronchial asthma (Chae et al. 2010b), bronchiolitis obliterans (Goo et al. 2010), and congenial hyperlucent lung lesions (Goo et al. 2011). In general, dual-energy CT-based parameters show high correlations with pulmonary function test results in these pulmonary diseases. To ameliorate transient anesthetic side effects of xenon gas caused by the dissolution of xenon in the blood, a mixture of 30%

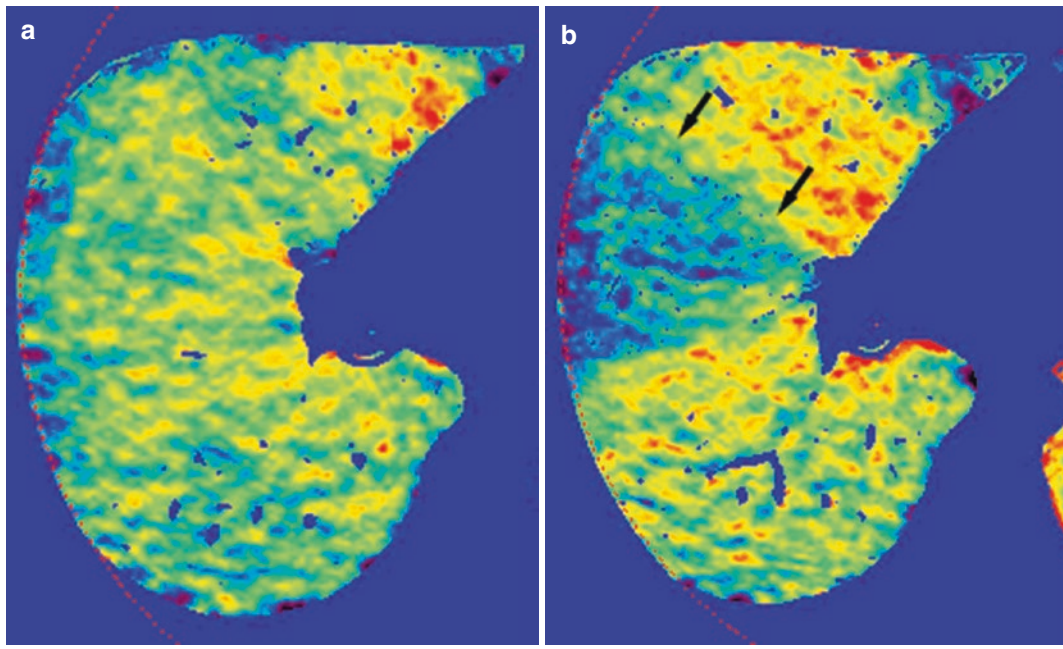


Fig. 11 Xenon-inhaled dual-energy CT. Xenon-inhaled CT shows no defect in the right lung at baseline (**a**) but shows a segmental defect in the right middle lobe (black arrows) after methacholine inhalation (**b**)

xenon and 70% oxygen is usually used for xenon-inhaled dual-energy CT (Chae et al. 2008; Goo et al. 2008). However, 30% xenon cannot completely abolish these adverse reactions and they have been reported in the range of 17–71%. Another shortcoming of xenon-inhaled dual-energy CT is that the cost of xenon gas required for the exam is too expensive to be used in clinical practice. Depending on clinical questions, target volume dynamic or whole lung static protocol may be utilized (Goo 2013b). Regarding whole lung static protocol, uniphasic wash-in scan or biphasic wash-in and washout scan may be used. Of interest, collateral ventilation can be demonstrated by using a dynamic protocol of xenon-inhaled dual-energy CT in bronchial atresia (Goo et al. 2008), bronchial obstruction (Chae et al. 2010c), and congenital hyperlucent lung lesions (Goo et al. 2011). In asthma, regional ventilation changes in response to a bronchoconstrictor or a bronchodilator can be assessed on dual-energy xenon map (Goo and Yu 2011; Kim et al. 2012). In 13 mechanically ventilated intensive care patients, xenon-inhaled dual-energy CT was helpful to identify bronchopleural fistula (Hoegl et al. 2013).

In most of the clinical studies using xenon-inhaled dual-energy CT, 30% xenon is continuously inhaled during 1–1.5-min wash-in periods not only to achieve maximal xenon concentration in the normal lung but also to reduce anesthetic side effects. In a study (Honda et al. 2012), whole lung static dual-energy CT performed after single vital-capacity inspiration of 35% xenon in four volunteers demonstrates lung parenchymal enhancement (21–30 HU) and anesthetic side effect (25%) comparable to the multiple-breath wash-in technique. Although the procedure is short and simple, the single-breath wash-in dual-energy CT images may not reflect lung ventilation with equilibrium state as well as collateral ventilation.

As an alternative inhaled contrast agent for dual-energy CT, stable krypton showed excellent clinical tolerance due to a lack of adverse effects (Hachulla et al. 2012). As expected when considering atomic number difference between the two materials ($Z = 54$ for xenon vs. $Z = 36$ for krypton), a considerably lower level of enhancement achieved by the highest possible krypton concentration (80%) than that achieved by 30% xenon, however, limits its clinical utility in evaluating regional lung ventilation.

It has been recognized that dual-energy-based whole lung static ventilation map is not predominantly superior to conventional CT densitometry in correlation with lung function test results (Park et al. 2010; Goo et al. 2010; Yanagita et al. 2013). In this regard, xenon-inhaled dual-energy CT should be judiciously utilized only when additional clinical benefits are strongly anticipated.

Lastly, xenon-enhanced ventilation CT scan can be achieved not only by the dual-energy CT but also by the subtraction technique, which subtracts unenhanced CT from the xenon-enhanced CT using nonrigid registration (Sase et al. 2010; Ohno et al. 2017a, b). The subtraction technique was shown to be a comparable method to the dual-energy CT and ventilation SPECT/CT for the assessment of pulmonary functional loss (Ohno et al. 2017a, b, 2018). Nevertheless, its added benefit to the conventional CT densitometry has not yet been analyzed in a prospective manner.

4.3 Lung Ventilation and Perfusion

A combined assessment of regional lung ventilation and perfusion is feasible with two-phase dual-energy CT with inhalation of xenon gas followed by intravenous administration of iodinated contrast agent in a single-imaging session (Thieme et al. 2010; Goo 2013b). It is noteworthy that lung perfusion scan in this two-phase dual-energy CT protocol should be performed usually 3–10 min after the switch from xenon inhalation to 100% oxygen inhalation to avoid residual xenon attenuation in the lung parenchyma on the iodine map. Nevertheless, an experimental study showed feasibility of a simultaneous single scan by using regional krypton and iodine concentrations (Hong et al. 2016).

Ventilation/perfusion (V/Q) match or mismatch can be evaluated in various lung lesions

including pulmonary embolism (Zhang et al. 2013) and severe emphysema (Hwang et al. 2016; Lee et al. 2017a, b) (Fig. 12). A recent study demonstrated improved V/Q mismatch after bronchoscopic lung volume reduction and suggested that the increased lung efficiency would be the underlying mechanism of improvement after lung volume reduction (Lee et al. 2017b). Lador et al. (2016) reported similar findings that increase in perfusion was observed in coil-free areas after bronchoscopic lung volume reduction. We need further clinical experiences to determine its clinical value.

4.4 Thoracic Oncology

In patients with lung neoplasms, dual-energy CT can add incremental functional information, such as tumor characterization and staging, therapeutic response evaluation (especially after anti-angiogenic therapies), and prediction of postoperative lung function (Sudarski et al. 2015; Goo and Goo 2017). The imaging technique offers quantitative measures of iodine and effective atomic number within primary thoracic tumors as well as regional and distant metastases, as surrogates of tissue vascularity and atomic composition, respectively. Specifically, iodine quantification has been shown to be a useful parameter for the differential diagnosis of lung lesions (benign vs. malignant; Zhang et al. 2016) as well as for the prediction of pathological grades (Iwano et al. 2015; Lin et al. 2018) and locoregional invasiveness in lung cancers (Shimamoto et al. 2016). A study by Baxa et al. (2016) reported that iodine quantification enabled early response evaluation in patients with non-small cell lung cancers receiving erlotinib. Interestingly, radiomics features extracted from the iodine overlay maps were also useful for the prognostication of patients who underwent

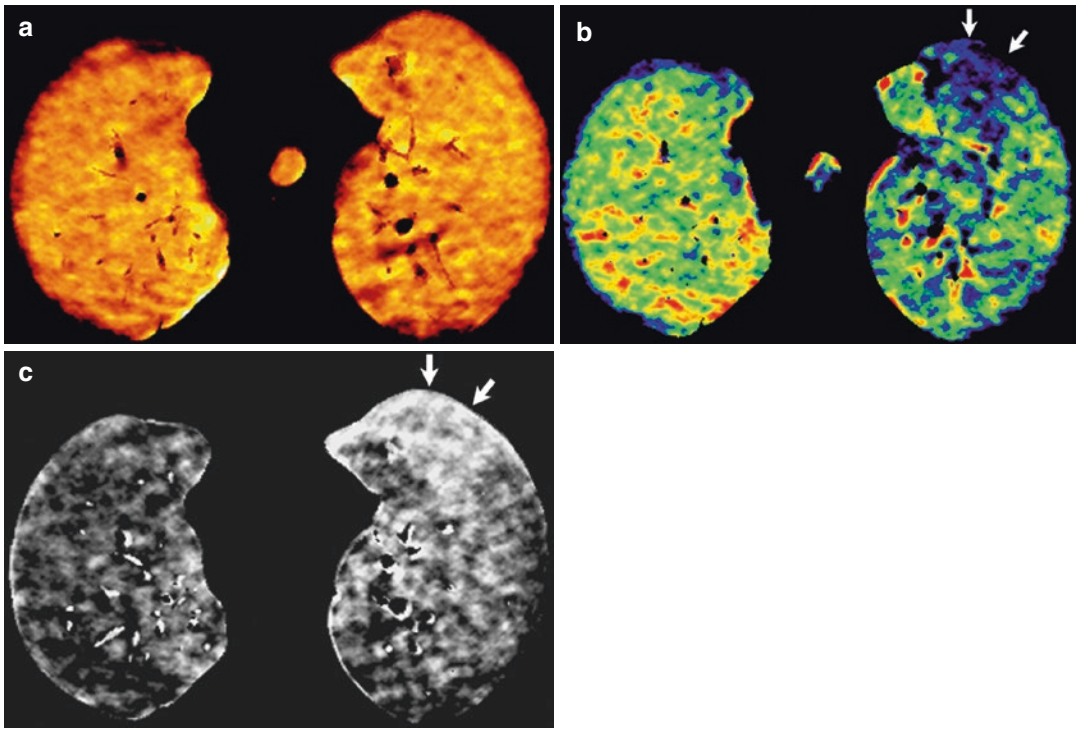


Fig. 12 Dual-energy lung ventilation, perfusion, and ventilation/perfusion (V/Q) maps. Xenon map (**a**) and iodine map (**b**) clearly depict a mismatched perfusion defect (arrows) in the anterior segment of the left upper lobe caused by thromboembolism. V/Q map (**c**) reveals increased values in the lesion

surgical resection of lung cancers (Choe et al. 2018). Furthermore, virtual non-contrast imaging helps differentiate calcifications or hemorrhage from iodine enhancement in the lesions. For example, iodine-related attenuation measurements can help identify enhancing components in anterior mediastinal lesions at a single scan and can enable discriminating benign cystic lesions from thymic epithelial tumors. This is particularly useful given the fact that the attenuations of intrathymic cysts are often higher than that of water (Araki et al. 2014).

5 Cine and Four-Dimensional Computed Tomography

Cine CT scan technique enables us to assess not only regional CT density changes but also tracheobronchial collapsibility throughout the respiratory cycle in adults and even in free-breathing pediatric patients (Goo and Kim 2006; Goo 2013c). Introduction of multi-detector row CT with a faster scan time and a greater longitudinal coverage up to 16 cm allows cine acquisition of high-resolution volumetric CT datasets, the so-called 4D CT (Fig. 13). By utilizing gapless 4D CT covering the entire thorax, we can overcome a technical limitation of cine CT in evaluating longitudinally moving or obliquely coursing structures. In addition, a more accurate CT densitometry is feasible on registered respiratory CT, and the expiration–inspiration ratio of mean lung density can be measured (Kim et al. 2015).

4D CT-based ventilation imaging can be produced by using deformable image registration algorithms based on either CT density or a Jacobian determinant that has its own merits and demerits (Kipritidis et al. 2016). The imaging technique has been principally utilized in radiation oncology for planning radiotherapy (Moorees and Bezak 2012). For respiratory-synchronized data acquisition, external surrogates, such as external marker, belt, and spirometer, are utilized and generally 10 respiratory phases are retrospectively reconstructed. However, the radiation dose of such retrospectively respiratory-gated CT is usually too high to be used for diagnostic purposes. Its technical validation has been conducted in healthy subjects (Pennati et al. 2014; Jahani et al. 2015) as well as patients with lung tumors and pulmonary emphysema (Yamamoto et al. 2011; Kanai et al. 2016). However, respiratory variation during 4D CT scans remains one of the main sources of error deteriorating the reproducibility of lung ventilation imaging (Yamamoto et al. 2012; Mistry et al. 2013). Errors resulting from respiratory variation are currently difficult to solve in clinical settings as previously mentioned. In this regard, 4D CT using a 320-slice CT scanner can provide a whole

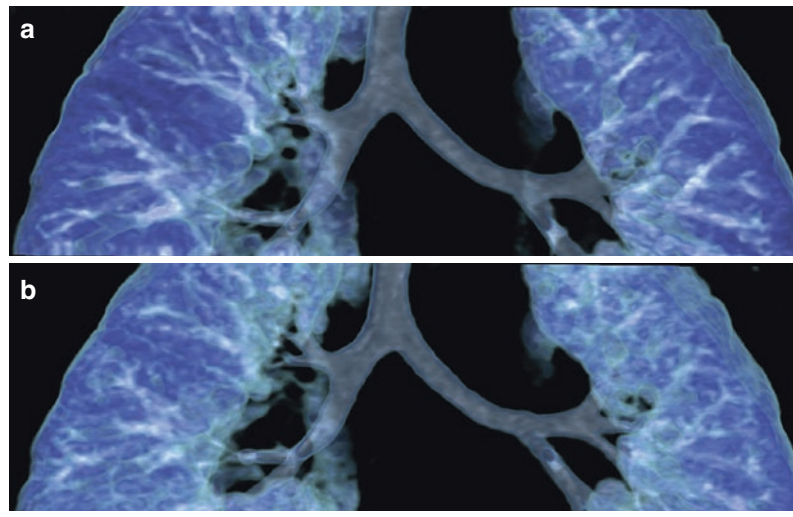


Fig. 13 Four-dimensional (4D) thoracic CT in a free-breathing child. Inspiratory (**a**) and expiratory (**b**) 4D CT images with anterior view show normal aeration in the lungs

thoracic dataset at the same respiratory phase because the entire thorax can be scanned in a single rotation (Kwong et al. 2015). This is an important step forward in technical advancement in 4D CT.

By utilizing 4D CT, initial experiences of dynamic evaluation of pediatric airway (Tan et al. 2013), lung cancer invasion into adjacent structures (Choong et al. 2015; Hashimoto et al. 2018), and pediatric diaphragm (Goo 2018a) have been reported. In addition, asynchrony in respiratory movements between the pulmonary lobes (Yamashiro et al. 2017) and abnormal cardiac compression during expiration (Xu et al. 2017) were observed in patients with COPD. Future studies are warranted to confirm these preliminary results and evaluate other clinical applications of 4D CT.

6 Dynamic Perfusion Computed Tomography Assessment

6.1 Dynamic Contrast-Enhanced CT with Perfusion Analyses

Dynamic contrast-enhanced (DCE) CT refers to the acquisition of multi-phase CT scans before and after the iodinated contrast material injection. Perfusion parameters including blood flow, blood volume, mean transit time, and peak enhancement can be obtained by analyzing the time-density curve for a given region-of-interest. These parameters and attenuation-based thresholds can be used for the diagnosis, response evaluation, and prognostic prediction of pulmonary diseases. A number of studies have demonstrated the diagnostic performance of DCE CT scans for the differentiation of lung nodules since the era of single-detector CT (Ohno et al. 2014). Diagnostic criteria including wash-in and washout thresholds had diagnostic sensitivity, specificity, and accuracy of 94%, 90%, and 92%, respectively (Jeong et al. 2005). Potential of DCE CT parameters for the treatment response evaluation after chemo- and/or radiotherapy has also been investigated by several researchers (Wang et al. 2009; Tacelli et al. 2013; Li et al. 2014). A concern regarding this technique would be the increased radiation dosage. Thus, justification and optimization should be considered for the perfusion studies which acquire a series of CT scans.

6.2 Dynamic First-Pass Contrast-Enhanced Perfusion Area-Detector CT

Advancement of CT technique enabled 256- or 320-row area-detector CT (ADCT). ADCT is able to perform dynamic first-pass perfusion given its wide coverage to encompass a whole organ without helical scanning and acquisition of isotropic volume data (Ohno et al. 2014). Dynamic first-pass perfusion CT is analyzed by constructing perfusion parameter maps using mathematical models such as the single- and dual-input maximum slope and single-input Patlak plot models (Ohno et al. 2016a, b). Importantly, selection of an appropriate mathematical model had a significant impact on the capability of a prediction model based on the perfusion indices (Ohno et al. 2016a, b).

One of the initial studies reported that the dynamic first-pass perfusion parameters were more accurate in diagnosing malignant lung nodules than the standardized uptake value derived from the positron emission tomography (Ohno et al. 2011). Dynamic first-pass perfusion CT was also useful for the treatment response prediction in non-small cell lung cancer patients treated with chemotherapy (Ohno et al. 2017a, b). Nevertheless, this novel technique is currently limited to specific CT scanners, and future studies are warranted to analyze and validate its clinical usefulness.

7 Conclusion

Thoracic CT utilizing various imaging techniques can provide important functional information, such as global lung function, a fraction of emphysema, a fraction of air trapping, lung

perfusion, lung ventilation, respiratory dynamics, and airway collapsibility. These enable quantitative and qualitative assessment of pulmonary diseases including COPD, idiopathic pulmonary fibrosis, and lung cancer in terms of diagnosis, response evaluation, as well as prognosis prediction. State-of-the-art CT technologies introduced in this chapter include dual-energy CT, 4D CT, and dynamic first-pass perfusion CT. Novel CT imaging would bring us new insights into lung physiology and ultimately opens new avenues in functional lung imaging. Nevertheless, clinical implication and added value to the current clinical practice should be further investigated.

References

Aaron CP, Hoffman EA, Lima JAC, Kawut SM, Bertoni AG, Vogel-Claussen J, Habibi M, Hueper K, Jacobs DR Jr, Kalhan R, Michos ED, Post WS, Prince MR, Smith BM, Ambale-Venkatesh B, Liu CY, Zemrak F, Watson KE, Budoff M, Bluemke DA, Barr RG (2017) Pulmonary vascular volume, impaired left ventricular filling and dyspnea: the MESA lung study. PLoS One 12:e0176180

Araki T, Sholl LM, Gerbaudo VH, Hatabu H, Nishino M (2014) Intrathymic cyst: clinical and radiological features in surgically resected cases. Clin Radiol 69:732–738

Bauer RW, Frellesen C, Renker M, Schell B, Lehnert T, Ackermann H, Schoepf UJ, Jacobi V, Vogl TJ, Kerl JM (2011) Dual energy CT pulmonary blood volume assessment in acute pulmonary embolism: correlation with D-dimer level, right heart strain and clinical outcome. Eur Radiol 21:1914–1921

Baxa J, Matouskova T, Krakorova G, Schmidt B, Flohr T, Sedlmair M, Bejcek J, Ferda J (2016) Dual-phase dual-energy CT in patients treated with erlotinib for advanced non-small cell lung cancer: possible benefits of iodine quantification in response assessment. Eur Radiol 26:2828–2836

Behrendt FF, Das M, Mahnken AH, Kraus T, Bakai A, Stanzel S, Gunther RW, Wildberger JE (2008) Computer-aided measurements of pulmonary emphysema in chest multidetector-row spiral computed tomography: effect of image reconstruction parameters. J Comput Assist Tomogr 32:899–904

Chae EJ, Seo JB, Goo HW, Kim N, Song KS, Lee SD, Hong SJ, Krauss B (2008) Xenon ventilation CT using a dual energy technique of dual source CT: initial experience. Radiology 248:615–624

Chae EJ, Seo JB, Jang YM, Krauss B, Lee CW, Lee HJ, Song KS (2010a) Dual-energy CT for assessment of the severity of acute pulmonary embolism: Pulmonary perfusion defect score compared with CT angiographic obstruction score and right ventricular/left ventricular diameter ratio. Am J Roentgenol 194:604–610

Chae EJ, Seo JB, Kim N, Song KS, Shin JH, Kim TH, Lee Y (2010c) Collateral ventilation in a canine model with bronchial obstruction: assessment with xenon-enhanced dual-energy CT. Radiology 255: 790–798

Chae EJ, Seo JB, Lee J, Kim N, Goo HW, Lee HJ, Lee CW, Ra SW, Oh YM, Cho YS (2010b) Xenon ventilation imaging using dual-energy computed tomography in asthmatics: initial experience. Investig Radiol 45:354–361

Chen F, Kubo T, Shoji T, Fujinaga T, Bando T, Date H (2011) Comparison of pulmonary function test and computed tomography volumetry in living lung donors. J Heart Lung Transplant 30:572–575

Chen H, Chen RC, Guan YB, Li W, Liu Q, Zeng QS (2014) Correlation of pulmonary function indexes determined by low-dose MDCT with spirometric pulmonary function tests in patients with chronic obstructive pulmonary disease. Am J Roentgenol 202:711–718

Choe J, Lee SM, Do KH, Lee JB, Lee SM, Lee JG, Seo JB (2018) Prognostic value of radiomic analysis of iodine overlay maps from dual-energy computed tomography in patients with resectable lung cancer. Eur Radiol. https://doi.org/10.1007/s00330-018-5639-0

Choo JY, Goo JM, Lee CH, Park CM, Park SJ, Shim MS (2014) Quantitative analysis of emphysema and airway measurements according to iterative reconstruction algorithms: comparison of filtered back projection, adaptive statistical iterative reconstruction and model-based iterative reconstruction. Eur Radiol 24:799–806

Choong CK, Pasricha SS, Li X, Briggs P, Ramdave S, Crossett M, Troupis JM (2015) Dynamic four-dimensional computed tomography for preoperative assessment of lung cancer invasion into adjacent structures. Eur J Cardiothorac Surg 47:239–243

Cohen J, Douma WR, van Ooijen PM, Willems TP, Dicken V, Kuhnigk JM, ten Hacken NH, Postma DS, Oudkerk M (2008) Localization and quantification of regional and segmental air trapping in asthma. J Comput Assist Tomogr 32:562–569

Coxson HO (2013) Sources of variation in quantitative computed tomography of the lung. J Thorac Imaging 28:272–279

De Jong PA, Nakano Y, Lequin MH, Merkus PJ, Tiddens HA, Hogg JC, Coxson HO (2003) Estimation of lung growth using computed tomography. Eur Respir J 22:235–238

den Harder AM, de Boer E, Lagerweij SJ, Boomsma MF, Schilham AMR, Willemink MJ, Milles J, Leiner T, Budde RPJ, de Jong PA (2018) Emphysema quantification using chest CT: influence of radiation dose reduction and reconstruction technique. Eur Radiol Exp 2:30

Doel T, Gavaghan DJ, Grau V (2015) Review of automatic pulmonary lobe segmentation methods from CT. Comput Med Imaging Graph 40:13–29

Felloni P, Duhamel A, Faivre JB, Giordano J, Khung S, Deken V, Remy J, Remy-Jardin M (2017) Regional distribution of pulmonary blood volume with dual-energy computed tomography: results in 42 subjects. Acad Radiol 24:1412–1421

Fuld MK, Grout RW, Guo J, Morgan JH, Hoffman EA (2012) Systems for lung volume standardization during static and dynamic MDCT-based quantitative assessment of pulmonary structure and function. Acad Radiol 19:930–940

Gierada DS, Guniganti P, Newman BJ, Dransfield MT, Kvale PA, Lynch DA, Pilgram TK (2011) Quantitative CT assessment of emphysema and airways in relation to lung cancer risk. Radiology 261:950–959

Gierada DS, Pilgram TK, Whiting BR, Hong C, Bierhals AJ, Kim JH, Bae KT (2007) Comparison of standard- and low-radiation-dose CT for quantification of emphysema. AJR Am J Roentgenol 188:42–47

Goo HW (2010) Initial experience of dual-energy lung perfusion CT using a dual-source CT system in children. Pediatr Radiol 40:1536–1544

Goo HW (2012) CT radiation dose optimization and estimation: an update for radiologists. Korean J Radiol 13:1–11

Goo HW (2013a) Advanced functional thoracic imaging in children: from basic concepts to clinical applications. Pediatr Radiol 43:262–268

Goo HW (2013b) Dual-energy lung perfusion and ventilation CT in children. Pediatr Radiol 43:298–307

Goo HW (2013c) Free-breathing cine CT for the diagnosis of tracheomalacia in young children. Pediatr Radiol 43:922–928

Goo HW (2018a) Four-dimensional CT of the diaphragm in children: initial experience. Korean J Radiol 19:111–118

Goo HW (2018b) Combined prospectively electrocardiography- and respiratory-triggered sequential cardiac CT in free-breathing children: success rate and image quality. Pediatr Radiol. https://doi.org/10.1007/s00247-018-4114-z

Goo HW (2018c) CT Pulmonary vascular volume ratio in children and young adults with congenital heart disease: the effect of cardiac phase. Pediatr Radiol. https://doi.org/10.1007/s00247-018-4120-1

Goo HW, Allmendinger T (2017) Combined ECG- and respiratory-triggered CT of the lung to reduce respiratory misregistration artifacts between imaging slabs in free-breathing children: Initial experience. Korean J Radiol 18:860–866

Goo HW, Chae EJ, Seo JB, Hong SJ (2008) Xenon ventilation CT using dual-source and dual-energy technique: dynamic ventilation abnormality in a child with bronchial atresia. Pediatr Radiol 38:1113–1116

Goo HW, Goo JM (2017) Dual energy CT: new horizon in medical imaging. Korean J Radiol 18:555–569

Goo HW, Kim HJ (2006) Detection of air trapping on inspiratory and expiratory phase images obtained by 0.3-second cine CT in the lungs of free-breathing young children. Am J Roentgenol 187: 1019–1023

Goo HW, Park SH (2017) Pulmonary vascular volume ratio measured by cardiac computed tomography in children and young adults with congenital heart disease: comparison with lung perfusion scintigraphy. Pediatr Radiol 47:1580–1587

Goo HW, Yang DH, Hong SJ, Yu J, Kim BJ, Seo JB, Chae EJ, Lee J, Krauss B (2010) Xenon ventilation CT using dual-source and dual-energy technique in children with bronchiolitis obliterans: correlation of xenon and CT density values with pulmonary function test results. Pediatr Radiol 40:1490–1497

Goo HW, Yang DH, Kim N, Park SI, Kim DK, Kim EAR (2011) Collateral ventilation to congenital hyperlucent lung lesions assessed on xenon-inhaled dynamic dual-energy CT: initial experience. Korean J Radiol 12:25–33

Goo HW, Yu J (2011) Redistributed regional ventilation after the administration of a bronchodilator and demonstrated on xenon-inhaled dual-energy CT in a patient with asthma. Korean J Radiol 12: 386–389

Haas M, Hamm B, Niehues SM (2014) Automated lung volumetry from routine thoracic CT scans: how reliable is the result? Acad Radiol 21:633–638

Hachulla AL, Pontana F, Wemeau-Stervinou L, Khung S, Faivre JB, Wallaert B, Cazaubon JF, Duhamel A, Perez T, Devos P, Remy J, Remy-Jardin M (2012) Krypton ventilation imaging using dual-energy CT in chronic obstructive pulmonary disease patients: initial experience. Radiology 263:253–259

Hashimoto M, Nagatani Y, Oshio Y, Nitta N, Yamashiro T, Tsukagoshi S, Ushio N, Mayumi M, Kimoto T, Igarashi T, Yoshigoe M, Iwai K, Tanaka K, Sato S, Sonoda A, Otani H, Murata K, Hanaoka J, Investigators of ACTIve Study Group (2018) Preoperative assessment of pleural adhesion by four-dimensional ultra-low-dose computed tomography (4D-ULDCT) with adaptive iterative dose reduction using three-dimensional processing (AIDR-3D). Eur J Radiol 98:179–186

Henzler T, Fink C, Schoenberg SO, Schoepf UJ (2012) Dual-energy CT: radiation dose aspects. AJR Am J Roentgenol 199:S16–S25

Heussel CP, Kappes J, Hantusch R, Hartlieb S, Weinheimer O, Kauczor HU, Eberhardt R (2010) Contrast enhanced CT-scans are not comparable to non-enhanced scans in emphysema quantification. Eur J Radiol 74:473–478

Hoegl S, Meinel FG, Thieme SF, Johnson TR, Eickelberg O, Zwissler B, Nikolaou K (2013) Worsening respiratory function in mechanically ventilated intensive care patients: feasibility and value of xenon-enhanced dual energy CT. Eur J Radiol 82:557–562

Hoffman EA, Lynch DA, Barr RG, van Beek EJ, Parraga G, Investigators IWPFI (2016) Pulmonary CT and MRI phenotypes that help explain chronic pulmonary obstruction disease pathophysiology and outcomes. J Magn Reson Imaging 43:544–557

Honda N, Osada H, Watanabe W, Nakayama M, Nishimura K, Krauss B, Otani K (2012) Imaging of ventilation with dual-energy CT during breath hold

after single vital-capacity inspiration of stable xenon. Radiology 262:262–268

Hong SR, Chang S, Im DJ, Suh YJ, Hong YJ, Hur J, Kim YJ, Choi BW, Lee HJ (2016) Feasibility of single scan for simultaneous evaluation of regional krypton and iodine concentrations with dual-energy CT: an experimental study. Radiology 281:597–605

Hong YJ, Kim JY, Choe KO, Hur J, Lee HJ, Choi BW, Kim YJ (2013) Different perfusion pattern between acute and chronic pulmonary thromboembolism: evaluation with two-phase dual-energy perfusion CT. AJR Am J Roentgenol 200:812–817

Hwang HJ, Seo JB, Lee SM, Kim N, Oh SY, Lee JS, Lee SW, Oh YM (2016) Assessment of regional xenon ventilation, perfusion, and ventilation-perfusion mismatch using dual-energy computed tomography in chronic obstructive pulmonary disease patients. Investig Radiol 51:306–315

Iwano S, Ito R, Umakoshi H, Ito S, Naganawa S (2015) Evaluation of lung cancer by enhanced dual-energy CT: association between three-dimensional iodine concentration and tumour differentiation. Br J Radiol 88:20150224

Iwano S, Okada T, Satake H, Naganawa S (2009) 3D-CT volumetry of the lung using multidetector row CT: comparison with pulmonary function tests. Acad Radiol 16:250–256

Jacob J, Bartholmai BJ, Rajagopalan S, Kokosi M, Nair A, Karwoski R, Walsh SL, Wells AU, Hansell DM (2017) Mortality prediction in idiopathic pulmonary fibrosis: evaluation of computer-based CT analysis with conventional severity measures. Eur Respir J 49(1):1601011

Jahani N, Choi S, Choi J, Iyer K, Hoffman EA, Lin CL (2015) Assessment of regional ventilation and deformation using 4D-CT imaging for healthy human lungs during tidal breathing. J Appl Physiol 119:1064–1074

Jeong YJ, Lee KS, Jeong SY, Chung MJ, Shim SS, Kim H, Kwon OJ, Kim S (2005) Solitary pulmonary nodule: characterization with combined wash-in and washout features at dynamic multi-detector row CT. Radiology 237:675–683

Johannessen A, Skorge TD, Bottai M, Grydeland TB, Nilsen RM, Coxson H, Dirksen A, Omenaas E, Gulsvik A, Bakke P (2013) Mortality by level of emphysema and airway wall thickness. Am J Respir Crit Care Med 187:602–608

Kanai T, Kadoya N, Ito K, Kishi K, Dobashi S, Yamamoto T, Umezawa R, Matsushita H, Takeda K, Jingu K (2016) Evaluation of four-dimensional computed tomography (4D-CT)-based pulmonary ventilation: the high correlation between 4D-CT ventilation and (81m)Kr-planar images was found. Radiother Oncol 119:444–448

Kang MJ, Park CM, Lee CH, Goo JM, Lee HJ (2010) Dual-energy CT: clinical applications in various pulmonary diseases. Radiographics 30:685–698

Kim EY, Seo JB, Lee HJ, Kim N, Lee E, Lee SM, Oh SY, Hwang HJ, Oh YM, Lee SD (2015) Detailed analysis of the density change on chest CT of COPD using non-rigid registration of inspiration/expiration CT scans. Eur Radiol 25:541–549

Kim SS, Hur J, Kim YJ, Lee HJ, Hong YJ, Choi BW (2014) Dual-energy CT for differentiating acute and chronic pulmonary thromboembolism: an initial experience. Int J Cardiovasc Imaging 30:113–120

Kim WW, Lee CH, Goo JM, Park SJ, Kim JH, Park EA, Cho SH (2012) Xenon-enhanced dual-energy CT of patients with asthma: dynamic ventilation changes after methacholine and salbutamol inhalation. AJR Am J Roentgenol 199:975–981

Kipritidis J, Hofman MS, Siva S, Callahan J, Le Roux PY, Woodruff HC, Counter WB, Keall PJ (2016) Estimating lung ventilation directly from 4D CT Hounsfield unit values. Med Phys 43:33

Kwong Y, Mel AO, Wheeler G, Troupis JM (2015) Four-dimensional computed tomography (4DCT): a review of the current status and applications. J Med Imaging Radiat Oncol 59:545–554

Lador F, Hachulla AL, Hohn O, Plojoux J, Ronot M, Montet X, Soccal PM (2016) Pulmonary perfusion changes as assessed by contrast-enhanced dual-energy computed tomography after endoscopic lung volume reduction by coils. Respiration 92:404–413

Lee CW, Seo JB, Lee Y, Chae EJ, Kim N, Lee HJ, Hwang HJ, Lim CH (2012) A pilot trial on pulmonary emphysema quantification and perfusion mapping in a single-step using contrast-enhanced dual-energy computed tomography. Investig Radiol 47:92–97

Lee KB, Goo HW (2018) Quantitative image quality and histogram-based evaluations of an iterative reconstruction algorithm at low-to-ultralow radiation dose levels: a phantom study in chest CT. Korean J Radiol 19:119–129

Lee SM, Seo JB, Hwang HJ, Kim N, Oh SY, Lee JS, Lee SW, Oh YM, Kim TH (2017a) Assessment of regional emphysema, air-trapping and xenon-ventilation using dual-energy computed tomography in chronic obstructive pulmonary disease patients. Eur Radiol 27:2818–2827

Lee SW, Lee SM, Shin SY, Park TS, Oh SY, Kim N, Hong Y, Lee JS, Oh YM, Lee SD, Seo JB (2017b) Improvement in ventilation-perfusion mismatch after bronchoscopic lung volume reduction: quantitative image analysis. Radiology 285:250–260

Li XS, Fan HX, Fang H, Huang H, Song YL, Zhou CW (2014) Value of whole-tumor dual-input perfusion CT in predicting the effect of multiarterial infusion chemotherapy on advanced non-small cell lung cancer. AJR Am J Roentgenol 203:W497–W505

Lin LY, Zhang Y, Suo ST, Zhang F, Cheng JJ, Wu HW (2018) Correlation between dual-energy spectral CT imaging parameters and pathological grades of non-small cell lung cancer. Clin Radiol 73:412.e1–412.e7

Lu GM, Zhao Y, Zhang LJ, Schoepf UJ (2012) Dual-energy CT of the lung. AJR Am J Roentgenol 199:S40–S53

Martin SP, Gariani J, Hachulla AL, Botsikas D, Adler D, Karenovics W, Becker CD, Montet X (2017) Impact of iterative reconstructions on objective and subjective

emphysema assessment with computed tomography: a prospective study. Eur Radiol 27:2950–2956

Masy M, Giordano J, Petyt G, Hossein-Foucher C, Duhamel A, Kyheng M, De Groote P, Fertin M, Lamblin N, Bervar JF, Remy J, Remy-Jardin M (2018) Dual-energy CT (DECT) lung perfusion in pulmonary hypertension: concordance rate with V/Q scintigraphy in diagnosing chronic thromboembolic pulmonary hypertension (CTEPH). Eur Radiol 28:5100–5110

Matsuo K, Iwano S, Okada T, Koike W, Naganawa S (2012) 3D-CT lung volumetry using multidetector row computed tomography: pulmonary function of each anatomic lobe. J Thorac Imaging 27:164–170

Mets OM, Buckens CF, Zanen P, Isgum I, van Ginneken B, Prokop M, Gietema HA, Lammers JW, Vliegenthart R, Oudkerk M, van Klaveren RJ, de Koning HJ, Mali WP, de Jong PA (2011) Identification of chronic obstructive pulmonary disease in lung cancer screening computed tomographic scans. JAMA 306:1775–1781

Mets OM, de Jong PA, van Ginneken B, Kruitwagen CL, Prokop M, Oudkerk M, Lammers JW, Zanen P (2013) CT air trapping is independently associated with lung function reduction over time. PLoS One 8:e61783

Mets OM, Zanen P, Lammers JW, Isgum I, Gietema HA, van Ginneken B, Prokop M, de Jong PA (2012) Early identification of small airways disease on lung cancer screening CT: comparison of current air trapping measures. Lung 190:629–633

Mistry NN, Diwanji T, Shi X, Pokharel S, Feigenberg S, Scharf SM, D'Souza WD (2013) Evaluation of fractional regional ventilation using 4D-CT and effects of breathing maneuvers on ventilation. Int J Radiat Oncol Biol Phys 87:825–831

Mohamed Hoesein FA, de Hoop B, Zanen P, Gietema H, Kruitwagen CL, van Ginneken B, Isgum I, Mol C, van Klaveren RJ, Dijkstra AE, Groen HJ, Boezen HM, Postma DS, Prokop M, Lammers JW (2011) CT-quantified emphysema in male heavy smokers: association with lung function decline. Thorax 66:782–787

Moorees J, Bezak E (2012) Four dimensional CT imaging: a review of current technologies and modalities. Australas Phys Eng Sci Med 35:9–23

Morimura Y, Chen F, Sonobe M, Date H (2013) Inspiratory and expiratory computed tomographic volumetry for lung volume reduction surgery. Interact Cardiovasc Thorac Surg 16:926–928

Nakano Y, Muro S, Sakai H, Hirai T, Chin K, Tsukino M, Nishimura K, Itoh H, Paré PD, Hogg JC, Mishima M (2000) Computed tomographic measurements of airway dimensions and emphysema in smokers. Correlation with lung function. Am J Respir Crit Care Med 162:1102–1108

Nemec SF, Molinari F, Dufresne V, Gosset N, Silva M, Bankier AA (2015) Comparison of four software packages for CT lung volumetry in healthy individuals. Eur Radiol 25:1588–1597

Nishio M, Matsumoto S, Ohno Y, Sugihara N, Inokawa H, Yoshikawa T, Sugimura K (2012) Emphysema quantification by low-dose CT: potential impact of adaptive iterative dose reduction using 3D processing. AJR Am J Roentgenol 199:595–601

Nishio M, Matsumoto S, Seki S, Koyama H, Ohno Y, Fujisawa Y, Sugihara N, Yoshikawa T, Sugimura K (2014) Emphysema quantification on low-dose CT using percentage of low-attenuation volume and size distribution of low-attenuation lung regions: effects of adaptive iterative dose reduction using 3D processing. Eur J Radiol 83:2268–2276

O'Donnell RA, Peebles C, Ward JA, Daraker A, Angco G, Broberg P, Pierrou S, Lund J, Holgate ST, Davies DE, Delany DJ, Wilson SJ, Djukanovic R (2004) Relationship between peripheral airway dysfunction, airway obstruction, and neutrophilic inflammation in COPD. Thorax 59:837–842

Ohno Y, Fujisawa Y, Koyama H, Kishida Y, Seki S, Sugihara N, Yoshikawa T (2017a) Dynamic contrast-enhanced perfusion area-detector CT assessed with various mathematical models: its capability for therapeutic outcome prediction for non-small cell lung cancer patients with chemoradiotherapy as compared with that of FDG-PET/CT. Eur J Radiol 86:83–91

Ohno Y, Fujisawa Y, Takenaka D, Kaminaga S, Seki S, Sugihara N, Yoshikawa T (2018) Comparison of Xenon-enhanced area-detector CT and Krypton ventilation SPECT/CT for assessment of pulmonary functional loss and disease severity in smokers. AJR Am J Roentgenol 210:W45–W53

Ohno Y, Koyama H, Fujisawa Y, Yoshikawa T, Seki S, Sugihara N, Sugimura K (2016b) Dynamic contrast-enhanced perfusion area detector CT for non-small cell lung cancer patients: Influence of mathematical models on early prediction capabilities for treatment response and recurrence after chemoradiotherapy. Eur J Radiol 85:176–186

Ohno Y, Koyama H, Lee HY, Miura S, Yoshikawa T, Sugimura K (2016a) Contrast-enhanced CT- and MRI-based perfusion assessment for pulmonary diseases: basics and clinical applications. Diagn Interv Radiol 22:407–421

Ohno Y, Koyama H, Matsumoto K, Onishi Y, Takenaka D, Fujisawa Y, Yoshikawa T, Konishi M, Maniwa Y, Nishimura Y, Ito T, Sugimura K (2011) Differentiation of malignant and benign pulmonary nodules with quantitative first-pass 320-detector row perfusion CT versus FDG PET/CT. Radiology 258:599–609

Ohno Y, Nishio M, Koyama H, Miura S, Yoshikawa T, Matsumoto S, Sugimura K (2014) Dynamic contrast-enhanced CT and MRI for pulmonary nodule assessment. AJR Am J Roentgenol 202:515–529

Ohno Y, Yoshikawa T, Takenaka D, Fujisawa Y, Sugihara N, Kishida Y, Seki S, Koyama H, Sugimura K (2017b) Xenon-enhanced CT using subtraction CT: basic and preliminary clinical studies for comparison of its efficacy with that of dual-energy CT and ventilation SPECT/CT to assess regional ventilation and pulmonary functional loss in smokers. Eur J Radiol 86:41–51

Park EA, Goo JM, Park SJ, Lee HJ, Lee CH, Park CM, Yoo CG, Kim JH (2010) Chronic obstructive pulmonary disease: quantitative and visual ventilation pattern

analysis at xenon ventilation CT performed by using a dual-energy technique. Radiology 256:985–997
Pennati F, Salito C, Baroni G, Woods J, Aliverti A (2014) Comparison between multivolume CT-based surrogates of regional ventilation in healthy subjects. Acad Radiol 21:1268–1275
Rodriguez A, Ranallo FN, Judy PF, Fain SB (2017) The effects of iterative reconstruction and kernel selection on quantitative computed tomography measures of lung density. Med Phys 44:2267–2280
Sarwahi V, Sugarman EP, Wollowick AL, Amaral TD, Harmon ED, Thornhill B (2014) Scoliosis surgery in patients with adolescent idiopathic scoliosis does not alter lung volume: a 3-dimensional computed tomography-based study. Spine (Phila Pa 1976) 39:E399–E405
Sase S, Nakano H, Suzuki H, Honda M (2010) Subtraction lung image for evaluating pulmonary ventilation in xenon-enhanced CT. Med Phys 37:4464–4474
Shimamoto H, Iwano S, Umakoshi H, Kawaguchi K, Naganawa S (2016) Evaluation of locoregional invasiveness of small-sized non-small cell lung cancers by enhanced dual-energy computed tomography. Cancer Imaging 16:18
Smith BM, Austin JH, Newell JD Jr, D'Souza BM, Rozenshtein A, Hoffman EA, Ahmed F, Barr RG (2014) Pulmonary emphysema subtypes on computed tomography: the MESA COPD study. Am J Med 127(94):e97–e23
Sudarski S, Hagelstein C, Weis M, Schoenberg SO, Apfaltrer P (2015) Dual-energy snap-shot perfusion CT in suspect pulmonary nodules and masses and for lung cancer staging. Eur J Radiol 84: 2393–2400
Sugino K, Kobayashi M, Nakamura Y, Gocho K, Ishida F, Isobe K, Shiraga N, Homma S (2017) Xenon-enhanced dual-energy CT imaging in combined pulmonary fibrosis and emphysema. PLoS One 12:e0170289
Tacelli N, Santangelo T, Scherpereel A, Duhamel A, Deken V, Klotz E, Cortot A, Lafitte JJ, Wallyn F, Remy J, Remy-Jardin M (2013) Perfusion CT allows prediction of therapy response in non-small cell lung cancer treated with conventional and anti-angiogenic chemotherapy. Eur Radiol 23:2127–2136
Takagi H, Ota H, Sugimura K, Otani K, Tominaga J, Aoki T, Tatebe S, Miura M, Yamamoto S, Sato H, Yaoita N, Suzuki H, Shimokawa H, Takase K (2016) Dual-energy CT to estimate clinical severity of chronic thromboembolic pulmonary hypertension: comparison with invasive right heart catheterization. Eur J Radiol 85:1574–1580
Tan JZ, Crossett M, Ditchfield M (2013) Dynamic volumetric computed tomographic assessment of the young paediatric airway: initial experience of rapid, non-invasive, four-dimensional technique. J Med Imaging Radiat Oncol 57:141–148
Thieme SF, Hoegl S, Nikolaou K, Fisahn J, Irlbeck M, Maxien D, Reiser MF, Becker CR, Johnson TR (2010) Pulmonary ventilation and perfusion imaging with dual-energy CT. Eur Radiol 20:2882–2889
Thurlbeck WM (1982) Postnatal human lung growth. Thorax 37:564–571
Wang J, Wu N, Cham MD, Song Y (2009) Tumor response in patients with advanced non-small cell lung cancer: perfusion CT evaluation of chemotherapy and radiation therapy. AJR Am J Roentgenol 193:1090–1096
Weidman EK, Plodkowski AJ, Halpenny DF, Hayes SA, Perez-Johnston R, Zheng J, Moskowitz C, Ginsberg MS (2018) Dual-energy CT angiography for detection of pulmonary emboli: incremental benefit of iodine maps. Radiology 289:546–553
Wielputz MO, Bardarova D, Weinheimer O, Kauczor HU, Eichinger M, Jobst BJ, Eberhardt R, Koenigkam-Santos M, Puderbach M, Heussel CP (2014) Variation of densitometry on computed tomography in COPD–influence of different software tools. PLoS One 9:e112898
Xu Y, Yamashiro T, Moriya H, Tsubakimoto M, Tsuchiya N, Nagatani Y, Matsuoka S, Murayama S (2017) Hyperinflated lungs compress the heart during expiration in COPD patients: a new finding on dynamic-ventilation computed tomography. Int J Chron Obstruct Pulmon Dis 12:3123–3131
Yamamoto T, Kabus S, Klinder T, Lorenz C, von Berg J, Blaffert T, Loo BW Jr, Keall PJ (2011) Investigation of four-dimensional computed tomography-based pulmonary ventilation imaging in patients with emphysematous lung regions. Phys Med Biol 56:2279–2298
Yamamoto T, Kabus S, von Berg J, Lorenz C, Chung MP, Hong JC, Loo BW Jr, Keall PJ (2012) Reproducibility of four-dimensional computed tomography-based lung ventilation imaging. Acad Radiol 19:1554–1565
Yamashiro T, Moriya H, Matsuoka S, Nagatani Y, Tsubakimoto M, Tsuchiya N, Murayama S (2017) Asynchrony in respiratory movements between the pulmonary lobes in patients with COPD: continuous measurement of lung density by 4-dimensional dynamic-ventilation CT. Int J Chron Obstruct Pulmon Dis 12:2101–2109
Yanagita H, Honda N, Nakayama M, Watanabe W, Shimizu Y, Osada H, Nakada K, Okada T, Ohno H, Takahashi T, Otani K (2013) Prediction of postoperative pulmonary function: preliminary comparison of single-breath dual-energy xenon CT with three conventional methods. Jpn J Radiol 31:377–385
Yang GF, Yang X, Zhang LJ, Zhu H, Chai X, Hu XB, Hu YX, Lu GM (2011) Pulmonary enhancement imaging with dual energy CT for the detection of pulmonary embolism in a rabbit model: comparison to perfusion planar scintigraphy, SPECT and SPECT-CT modalities. Acad Radiol 18:605–614
Yilmaz C, Watharkar SS, Diaz de Leon A, Garcia CK, Patel NC, Jordan KG, Hsia CC (2011) Quantification of regional interstitial lung disease from CT-derived fractional tissue volume: a lung tissue research consortium study. Acad Radiol 18:1014–1023
Zeng Q, Lai JY, Wang CJ, Cheng HY, Chu CC, Chang CJ, Chiu PH, Chen ZC, Chang PY (2010) A cross-sectional study of lung volume development in pectus excavatum patients: estimating the total lung volume from

chest computed tomograph using 3-dimensional volumetric reconstruction. J Pediatr Surg 45:2322–2327

Zhai Z, Ota H, Staring M, Stolk J, Sugimura K, Takase K, Stoel BC (2018) Treatment effect of balloon pulmonary angioplasty in chronic thromboembolic pulmonary hypertension quantified by automatic comparative imaging in computed tomography pulmonary angiography. Investig Radiol 53:286–292

Zhang LJ, Chai X, Wu SY, Zhao YE, Hu XB, Hu YX, Xue YB, Yang GF, Zhu H, Lu GM (2009) Detection of pulmonary embolism by dual energy CT: Correlation with perfusion scintigraphy and histopathological findings in rabbits. Eur Radiol 19:2844–2854

Zhang LJ, Lu L, Bi J, Jin LX, Chai X, Zhao YE, Chen B, Lu GM (2010) Detection of pulmonary embolism: comparison between dual energy CT and MR angiography in a rabbit model. Acad Radiol 17:1550–1559

Zhang LJ, Zhou CS, Schoepf UJ, Sheng HX, Wu SY, Krazinski AW, Silverman JR, Meinel FG, Zhao YE, Zhang ZJ, Lu GM (2013) Dual-energy CT lung ventilation/perfusion imaging for diagnosing pulmonary embolism. Eur Radiol 23:2666–2675

Zhang Y, Cheng J, Hua X, Yu M, Xu C, Zhang F, Xu J, Wu H (2016) Can spectral CT imaging improve the differentiation between malignant and benign solitary pulmonary nodules? PLoS One 11:e0147537

Basics and Clinical Application of MR Assessment of Pulmonary Hemodynamics and Blood Flow

Sebastian Ley

Contents

1 **Introduction** 47

2 **Basics** 48
2.1 Flow Measurements 48
2.2 Multidirectional Flow (4D Flow) 50
2.3 Perfusion 51
2.4 Non-contrast-Enhanced Pulmonary Perfusion 51
2.5 Contrast-Enhanced Pulmonary Perfusion 52

3 **Clinical Application** 54
3.1 2D Flow 54
3.2 4D flow 55
3.3 Perfusion 55

References 56

Abstract

The pulmonary arterial circulation is characterized by a low resistance setting. In case of obstruction of the pulmonary arterial vascular tree either intrinsic (like thrombotic material) or extrinsic (like compression like in emphysema), the resistance increases. Using MRI it is possible to characterize the changes in pulmonary arterial hemodynamics using through-plane or multidirectional phase-contrast flow measurements. For assessment of pulmonary perfusion, as one important aspect for oxygenation, different MR techniques are available. So far, more on a research side, non-contrast-enhanced perfusion techniques are being used allowing for visualization and quantification of perfusion. Clinically available and widely investigated are contrast-enhanced perfusion techniques.

S. Ley (✉)
Department of Diagnostic and Interventional Radiology, Chirurgisches Klinikum München Süd, Munich, Germany

Department of Radiology, Internistisches Klinikum München Süd, Munich, Germany
e-mail: ley@radiologie-ley.de

1 Introduction

The right heart is responsible for pumping the blood through the pulmonary arteries to ensure oxygenation. The pulmonary arterial circulation

© Springer Nature Switzerland AG 2021

Y. Ohno et al. (eds.), *Pulmonary Functional Imaging*, Medical Radiology Diagnostic Imaging,
https://doi.org/10.1007/978-3-030-43539-4_4

is a low resistance vascular system; therefore, the right ventricle is only required to generate a mean arterial pressure of 9–18 mmHg (Edwards 2009). In case of obstruction of any parts of the pulmonary circulation (central or subsegmental), the cross-sectional area of the pulmonary vascular tree will be reduced. In this case, the vascular resistance increases and the right ventricle has to work against this increase. This change has also an effect on the central pulmonary arteries and on the small, subsegmental pulmonary arteries. An increase in pulmonary arterial pressure can be assessed by echocardiography and as gold-standard by invasive right heart catheter (Hoeper et al. 2013). Using MR imaging two approaches are available for estimation of pulmonary pressure and blood flow. First, phase-contrast flow measurements allow for central flow and pressure estimation. Second, pulmonary perfusion allows for a 3D assessment of peripheral pulmonary perfusion distribution and quantification.

2 Basics

2.1 Flow Measurements

For assessment of global hemodynamics phase-contrast (PC) flow measurements are the most established MR techniques (Lotz et al. 2002; Gatehouse et al. 2005). Flow measurements are subdivided into through-plane measurements, were the flow through (2 directions) an image plane is assessed (2D PC flow), and multidirectional flow measurements, were all flow directions within a volume were assessed (i.e., turbulence flow) which is called 4D PC flow.

In principle, spins moving through a magnetic field acquire a phase shift of their phase of rotation. For linear field gradients, the amount of this phase shift Φ is proportional to the velocity of the moving spin (Moran et al. 1985). Phase shifts of stationary tissue are compensated for with the help of a bipolar gradient. Two image datasets are acquired, one with the signal intensities (magnitude image) and one with the phase information (phase image) for each voxel.

The target vessel is analyzed by drawing a region-of-interest in all frames. The velocity of all voxels is determined and by putting it in relation to the area the flow volume is determined. Taking all frames together, various parameters can be quantified like peak and mean velocity, antegrade blood flow, retrograde blood flow, net flow, and (change of) vessel diameter (Fig. 1).

A slice thickness of 6 mm is accepted standard with a balanced compromise between partial volume effects and signal-to-noise ratio. Regarding the in-plane resolution at least four true pixels are needed across the vessel diameter for 10% accuracy (Gatehouse et al. 2005).

2.1.1 Prospective and Retrospective Gating Techniques

Flow measurements are synchronized to the cardiac cycle, using the R-peak as trigger signal.

Prospective gating techniques wait for the trigger to start data acquisition. The acquisition time is set approximately 10% smaller than the RR-interval. This should avoid acquisition of data within the following RR-interval, and if the following R-peak is measured, the next data acquisition has to wait for the next trigger signal (R-peak) and measurement time would double. As a drawback, the flow on late diastole is not assessed since data are not sampled.

In retrospective gating techniques, data collection is done continuously throughout the whole cardiac cycle. The trigger signals are recorded parallel to the raw data allowing to assign the raw data to specific position within the cardiac cycle. With this technique, the complete cardiac cycle is assessed. Therefore, this technique is the most frequently used approach.

Both techniques require multiple cardiac cycles for data acquisition. Since there are always physiologic variations in the length of the cardiac cycles, the data have to be interpolated to represent an average cardiac cycle.

To obtain reliable values of peak velocity and flow in the great arteries, a minimum of 16 frames per RR-interval should be acquired. If a lower temporal resolution is used, peak velocity and flow will be underestimated.

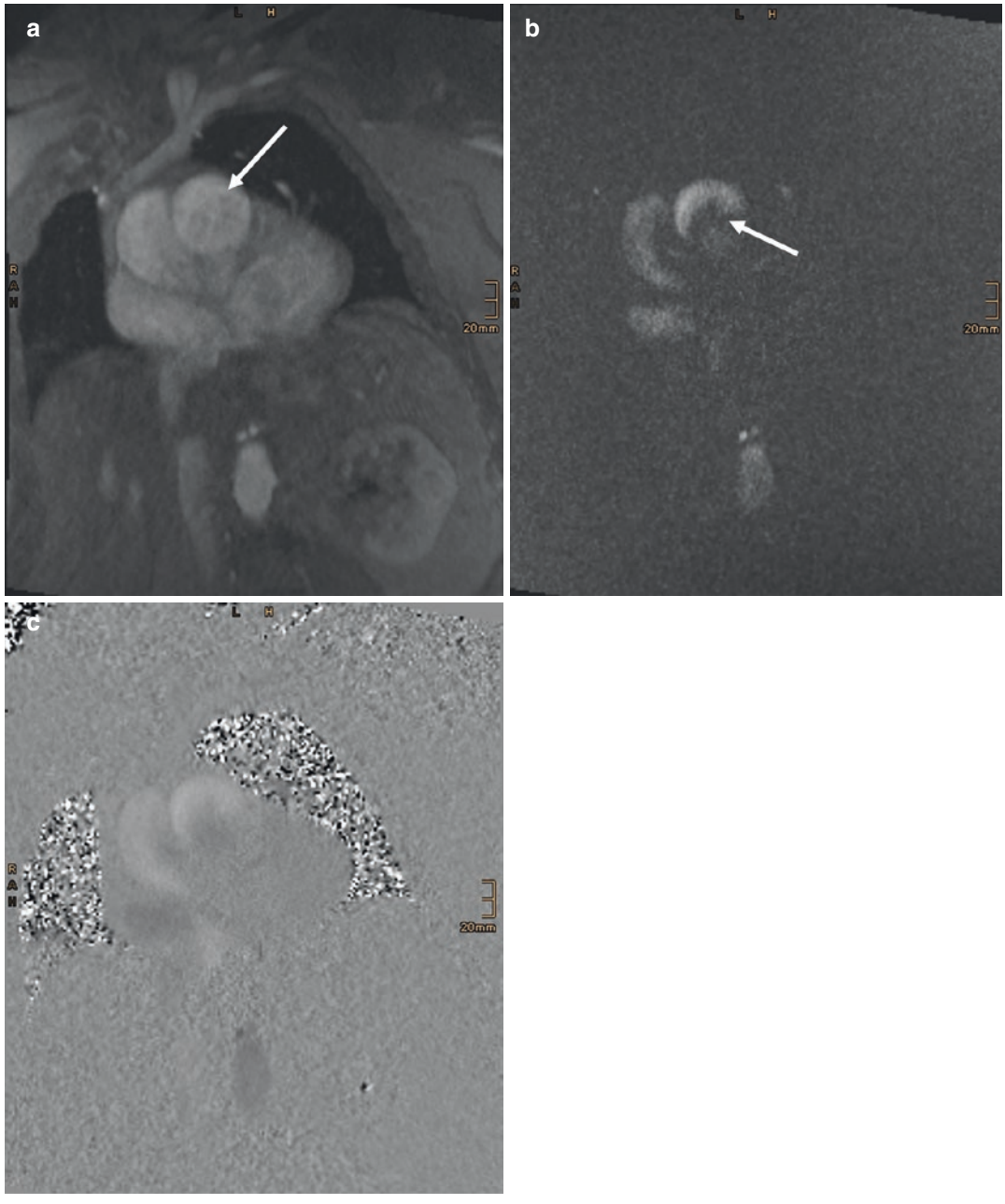


Fig. 1 Patient suffering from pulmonary arterial hypertension. Phase-contrast flow measurement of the pulmonary artery (arrow) is shown with the morphological image (**a**), the phase image (**b**), and the magnitude image (**c**). Especially in the phase image (**b**, arrow) the dephasing moments of the helical flow pattern are noticeable. Quantitative evaluation revealed a maximum velocity of 58 cm/s and a mean area of the pulmonary artery of 13.8 cm^2, both values indicative of pulmonary arterial hypertension

2.1.2 Errors and Limitations

Phase shifts were measured in angular degrees with a range of ±180°. To allow for a most accurate flow measurement, the user has to enter the expected velocity (cm/s; V_{enc} = velocity encoding gradient) before the sequence is executed. The

more accurate the velocity is estimated, the more accurate the true velocity is measured. With increase in V_{enc} the image noise (i.e., random error of phases) increases, resulting in random noise voxels within the vascular lumen. These noise voxels can lead to a false high (peak) velocity. The blood flow is the sum of all voxels and is less prone to errors. If the velocity range is set lower than the peak velocity in the vessel aliasing occurs. The affected voxels are usually displayed with an inverse color and thus easy to be identified. Using dedicated evaluation software, this error can be corrected for easily, if the overall velocity range does not exceed the velocity range chosen. However, it is safer to repeat the flow measurement with a modified V_{enc} than to correct the aliased dataset (Lotz et al. 2002).

In normal conditions, typical V_{enc} values are: ascending aorta 200 cm/s (expected peak velocity 100–160 cm/s), main pulmonary artery, and right/left pulmonary artery 180 cm/s (expected velocity 60–120 cm/s). It should be noted that in healthy adults 55% of pulmonary flow goes through the right pulmonary artery.

The measurement plane should be planned orthogonal to the vessel, requiring a double oblique planning. The true velocity is reduced by the cos of variance of the orthogonal image plane (measured velocity = true velocity * cos α). A deviation of up to 15° is tolerated as no significant differences to the real velocity or flow result.

A deviation from the true flow of 3.5–4.5% was estimated as the inborn technical error of phase-contrast measurement when a non-breath-hold cine gradient-echo sequence with prospective gating is used (Evans et al. 1993). Using retrospective gating a 3% deviation of the true flow was described (Lotz et al. 2002).

2.2 Multidirectional Flow (4D Flow)

As pointed out above, 2D flow provides time-resolved velocity information in a typically predominant direction of motion (Reiter et al. 2016). 4D flow assess the tridirectional velocity field in a volume of interest. For this purpose, a volume of interest has to be acquired and the flow settings have to be changed for acquisition of all flow directions (3 velocity components). Measuring tridirectional flow information doubles up imaging time compared to one-directional velocity encoding. Therefore, these techniques are acquired in free breathing. To compensate for artifacts due to respiratory motion, motion-compensating techniques or averaging has to be facilitated, again at the cost of imaging time. To cover the large thoracic vessels or the cardiac chambers with a reasonable spatial resolution of $2.5 \times 2.5 \times 2.5$ mm^3 and a temporal resolution of at least 50 ms 10–20 min acquisitions are required.

4D flow datasets contain complete flow information which require a dedicated post-processing software for visualization and quantification of flow. To visualize the complex flow pattern vector plots are commonly used. The lengths of the vectors present the velocity magnitude. The direction of the vectors represents the direction of flow (Fig. 2). Other possibilities for visualization are streamlines and particle traces.

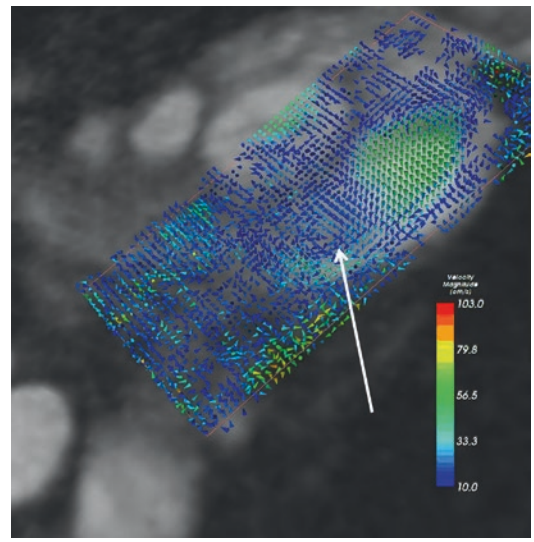


Fig. 2 Multidirectional flow in a patient with pulmonary hypertension during systole. The flow information are coded in vectors showing direction and color coded the velocity. In the proximal pulmonary artery a vortex is seen (arrow), indicative for an increased resistance

As 3D datasets are acquired, the orthogonal plane through the target vessel is generated during the post-processing.

2.3 Perfusion

Oxygenation is dependent on the match of perfusion and ventilation. For perfusion imaging the most established technique is lung perfusion scintigraphy using Tc-99 m-macro-aggregates of albumin (Zophel et al. 2009). However, this technique is not routinely available off-hours, and therefore other techniques are warrant being available 24/7. To cover the whole lung and allowing a 3D visualization only few techniques are available. Computed tomography as dual-energy technique allows for visualization of pulmonary perfusion; however, this technique is also not broadly available and applies a reasonable amount of radiation to the patient. On the other hand, MR scanners are broadly available and can be used for imaging 24/7. Using MR imaging two main approaches are available: without the use of contrast material and with application of contrast media (Ley and Ley-Zaporozhan 2012).

2.4 Non-contrast-Enhanced Pulmonary Perfusion

The major advantage of techniques without using contrast media is that they can be repeated indefinitely. This allows for pre- and post-intervention imaging as well as for monitoring disease progression. Some drawbacks have to be mentioned, more or less significant for the sequences discussed below. In general, the sequences are not routinely available on MR scanners. They require a regular cardiac cycle during imaging acquisition. Single-slice techniques and 5–8 slices have to be acquired to cover the whole lung with a limited resolution (like $5 \times 5 \times 30$ mm^3).

Arterial spin labeling (ASL) is successfully used for perfusion measurements in the brain. This technique requires one image with blood and tissue (where the arterial blood is saturated by a RF pulse) and one image without magnetic labeling. The subtraction results in a map of magnetization differences based on inflowing blood. The signal difference directly reflects local tissue perfusion. This technique was applied to the lungs with sequences called FAIR (Flow-sensitive Alternating Inversion Recovery) and FAIRER (FAIR with an Extra Radiofrequency pulse) (Mai and Berr 1999; Bolar et al. 2006; Martirosian et al. 2010). Cardiac triggering is required to ensure that all images are acquired at the same phase of the heart cycle. The pair of images (labeled and non-labeled) are acquired within one breath-hold of 20–27 s. Any change of anatomic position within this time period leads to "misregistration" artifacts. Furthermore, the extremely heterogeneous magnetic susceptibility of the lung tissue reduces the measurable signal from the lung parenchyma. The strong local gradients induced by the susceptibility differences between the alveolar air and the lung tissue lead to a rapid signal decay in gradient echo sequences.

Imaging of the lung parenchyma throughout the cardiac cycle reveals signal intensity changes. Using a half-Fourier single-shot turboSE (HASTE) sequence with ECG gating pulmonary perfusion was visualized by subtraction of the systolic and diastolic images (Tadamura and Hatabu 2001). Perfusion defects in an animal model of pulmonary embolism could be visualized similar to perfusion images acquired with contrast material.

A further development was the SEEPAGE (spin echo entrapped perfusion image) (Fischer et al. 2008; Kjorstad et al. 2014a). The most prominent feature of SEEPAGE is the possibility to obtain the perfusion image in a single shot due to a complete saturation of stationary background tissue before acquisition of the image. As a result, misregistration artifacts are avoided. Perfusion-weighted images can be obtained without any adjustment scans (Fig. 3). A complete SEEPAGE experiment takes less than 5 s, which makes the method applicable for a wide spectrum of patients with lung disease. A quantification of pulmonary perfusion is feasible by comparing the perfusion-weighted images to an additionally independently acquired reference scan (Fischer et al. 2008). Overall, these sequences have only been



Fig. 3 Non-contrast-enhanced perfusion (SEEPAGE) image of the lung in a sagittal orientation (with permission from Ley and Ley-Zaporozhan (2012)). The spatial resolution is $3.9 \times 3.9 \times 10\ mm^3$ allowing for visualization of the major and minor fissure

used in a few studies without broad application (Sommer and Bauman 2016).

More recently, a very promising technique has been developed facilitating assessment of pulmonary perfusion and ventilation without contrast media. Using fast acquisition with a balanced steady-state free-precession sequence (bSSFP) combined with nonrigid image registration, it is possible to observe regional changes of parenchyma density and visualize local alterations of the lung tissue. Using a Fourier decomposition method it is possible to separate the ventilation and the perfusion signal (Bauman et al. 2009). No ECG-triggering is required and the spatial resolution is about $3.5 \times 3.5 \times 15\ mm^3$. To cover the whole lung, approximately 1 min is required. This technique was successfully used for quantification of perfusion in volunteers and patients (Kjorstad et al. 2014b, 2015). However, these measurements also showed some limitations of the technique due to low SNR or image artifacts.

The overall sequence design was further advanced by adding a spoiled gradient-echo (GRE) sequence for advanced post-processing, named PREFUL (Perfusion Mapping With Phase-Resolved Functional Lung) (Voskrebenzev et al. 2018). Special post-processing steps with data filtering and nonparametric regression allowed for a robust calculation of perfusion maps allowing for quantification of perfusion. As drawback, this method applies arbitrary thresholds and requires manual classification of healthy lung regions.

2.5 Contrast-Enhanced Pulmonary Perfusion

Contrast-enhanced perfusion techniques are long-standing players in the field of perfusion imaging of the lung. They have been extensively assessed against standard techniques like scintigraphy, SPECT, and CT and thus are the best-validated technique nowadays (Sommer and Bauman 2016). Two large reviews of this topic present the techniques and post-processing algorithms in great detail (Ley and Ley-Zaporozhan 2012; Johns et al. 2017a). Therefore, at this point a brief description of the technique will be provided.

Application of an intravenous contrast shortens the T1 time of blood. Therefore, T1-weighted images can be acquired with short TE and TR times to visualize this effect. This was used early on for 3D MR angiograms using a gradient echo sequence. This technique used a high spatial resolution to visualize the peripheral pulmonary arteries and reasonable acquisition time of less than 10 s per 3D volume.

For assessment of pulmonary perfusion a rapid assessment of the images is required to clearly differentiate between the pulmonary arterial, parenchymal, pulmonary venous, and systemic arterial phases (Ohno et al. 2016). A temporal resolution of 0.5 s per dataset is currently feasible with a diagnostically acceptable spatial resolution (Johns et al. 2017a). In general,

2D and 3D datasets of the lung parenchyma can be acquired. As most of the pulmonary diseases are heterogenous, acquisition of 3D datasets is preferable for clinical purposes.

By applying parallel imaging and/or 3D view-sharing techniques such as TRICKS (Time-Resolved Imaging of Contrast KineticS), the temporal resolution was increased (view-sharing methods under-sample k-space and share missing k-space between datasets, giving a higher nominal temporal resolution) (Fink et al. 2004). This allows for assessment of T1-weighted dynamic contrast-enhanced perfusion images of the lungs as 3D datasets with higher temporal resolution with the risk of spatiotemporal interpolation artifacts.

Application of contrast material is mandatory for this technique. Regarding the injection technique and amount of contrast media applied is a field with great variation and discussion.

Unlike iodinated contrast agents, contrast concentration and signal intensity are not linearly related at higher concentrations (Puderbach et al. 2008; Veldhoen et al. 2016). Therefore, half of the standard dose of, i.e., gadobutrol (Gadovist®)—0.05 mL per kg patient weight is recommended followed by a saline chaser of at least 20 mL (Johns et al. 2017a). A more individualized approach suggests a weight adapted application: 0.3 mmol/mL Gd-DTPA for patients <70 kg and a concentration of 0.5 mmol/mL for patients ≥70 kg body weight (Ohno et al. 2007).

Injection speed is also of matter as a sharp bolus results in an optimal delineation of the different abovementioned vascular phases. Flow rates of 3–5 mL/s are commonly recommended (Ley and Ley-Zaporozhan 2012; Johns et al. 2017a; Fink et al. 2006).

For qualitative evaluation subtraction of a baseline dataset from a peak enhancement dataset is performed. This allows for rapid visualization of perfusion defects and their anatomical location (Fig. 4). However, any delayed perfusion

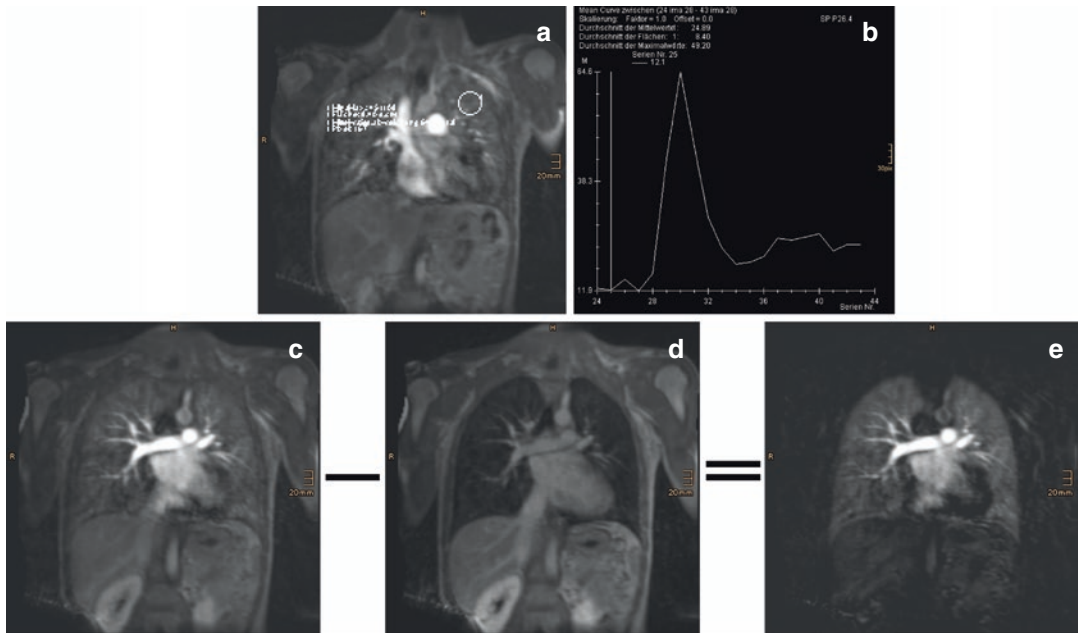


Fig. 4 The bolus passage of contrast media through the pulmonary circulation is imaged by a dynamic series of T1-weighted 3D sequences. For visualization purposes a region of interest is placed within the lung (**a**) to analyze the signal enhancement as the contrast media passes the lung parenchyma (**b**). To enhance the perfusion aspect and suppress the background tissue a subtraction of the dataset with the highest signal (**c**) and one without contrast media (**d**) is performed. The resulting 3D dataset allows for optimal visualization of perfusion (**e**)

areas are being counted as non-perfused. Therefore, more advanced visualization techniques are warranted to visualize the full information of these perfusion datasets.

For displayed maps and quantification of perfusion the arterial input function has to be determined in order to calculate the tissue response function (Wild et al. 2012). The arterial input function is usually determined in the central pulmonary artery and the tissue function is a region of interest of the lung parenchyma. Allying the adequate equations typical perfusion values like pulmonary blood flow, volume, and mean transit time can be calculated (Johns et al. 2017a). At this point it has to be mentioned that these equations assume a linear relationship between signal intensity and contrast media concentration. As mentioned above, for gadolinium-based contrast media this is only seen in a small range of low concentrations of contrast. This is a particular problem for the arterial input function as the contrast bolus passes in a compact bolus with the highest concentration, maybe exceeding the range of linearity. Therefore, the contrast media dose should be low enough to prevent this happening or a dual bolus approach should be chosen. With this a low-dose injection is performed to calculate the arterial input function followed by a second "diagnostic" contrast media application (Risse et al. 2006).

Once the AIF has been established, basically two mathematical solutions can be used to calculate the absolute perfusion parameters. First, using a model-free approach the signal time curve of a voxel can be converted to concentration time course from the assumption of a linear relationship between signal intensity and contrast concentration (Johns et al. 2017a). The concentration time-curves are fitted using the Gamma variate function to calculate the mean transit time and subsequently blood volume and blood flow (Levin et al. 2001). A more advanced post-processing for quantification of pulmonary perfusion is the indicator dilution theory (Risse et al. 2006; Meier and Zierler 1954) (Fig. 5).

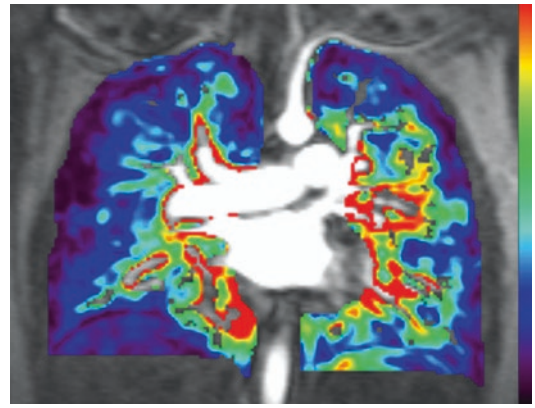


Fig. 5 Color-coded quantification of pulmonary blood flow [mL/min/100 mL]. The patient suffered from pulmonary hypertension, noticeable at the (homogenous) low blood flow in the lung periphery

3 Clinical Application

The application of flow and perfusion measurements in typical diseases like CF, COPD, PH, and CTEPH are covered elsewhere within this book.

Therefore, at this point overall clinical results are shown.

3.1 2D Flow

In case of an increase in pulmonary resistance, many flow-related parameters change. Over the linear portion of the pressure-diameter curve, normal pulmonary arteries distend ~2% of their initial diameter for each millimeter mercury increase in transmural pressure (Reeves et al. 2005). Therefore, the diameter of the main pulmonary artery is enlarged in pulmonary hypertension and a reduced distensibility is found. The main pulmonary artery distensibility can be calculated from the relative area change between systole and diastole as derived by the segmentation as performed for flow quantification. The absolute correlation between the area change and mPAP is moderate. However, the minimum area and area change can be used to identify a PH. A

minimum area ≥6.6 cm^2 enabled diagnosis of PAH with sensitivity/specificity of 93%/88%, and minimum area ≥6.0 cm^2 detected PVR > 3 WU with sensitivity/specificity of 96%/85% (Sanz et al. 2007). In line with these findings, results from the ASPIRE register showed that, in a population including all PH groups, mPAP ≥25 mmHg can be identified from a minimum area ≥ 6.0 cm^2 with sensitivity/specificity of 88%/66% (Swift et al. 2012).

Using 2D flow measurements, a decrease of velocity was found in patients with increased pulmonary resistance. However, a linear relationship between velocity measurements (peak or mean velocity) seems unlikely (Swift et al. 2013). Including all PH groups, a curvilinear (logarithmic) association of mean velocity with PVR was found. It was the standard 2D flow parameter with the strongest univariate correlation with PVR, irrespective of the cause and severity of PH (Garcia-Alvarez et al. 2011). In a large population study (603 MRI datasets in patients with pulmonary hypertension) different regression models were tested for assessment of pulmonary hypertension (Johns et al. 2018). Regression models of MR parameters allowed for identification of pulmonary hypertension (mPAP >25 mmHg) with a good sensitivity (93%) and specificity (79%). The limits of agreement of cardiac MRI models were found insufficient for accurate estimation of an individual mPAP value.

3.2 4D flow

The increase in pulmonary vascular resistance leads to a changed flow profile within the pulmonary arteries. Using 2D flow measurements a backward flow profile was observed in pulmonary hypertension which could not be explained. Nowadays, the 3D flow profile can be visualized by using 4D flow techniques. A flow vortex was found in pulmonary hypertension explaining the backward flow on 2D flow measurements. The duration of this vortical blood flow showed a linear relationship with mPAP and allowed for detection of patients with pulmonary hypertension (Reiter et al. 2015).

3.3 Perfusion

Clinical applications for non-contrast-enhanced MR perfusion techniques are performed in normal and patients suffering from cystic fibrosis and COPD.

In healthy volunteers the advanced arterial spin labeling technique SEEPAGE was compared to Fourier Decomposition technique (Kjorstad et al. 2014a). A good agreement between these two techniques was found with a mean difference between the methods of 0.2 mL/min/100 mL. The Fourier Decomposition technique was compared to contrast-enhanced perfusion MRI in patients with cystic fibrosis (Bauman et al. 2013). A visual scoring system was used to compare the two techniques, where a good agreement was found. The latest technical development of Fourier Decomposition technique (PREFUL) was compared to contrast-enhanced perfusion MRI in patients with COPD (Kaireit et al. 2018). The perfusion defects with both techniques were scored visually. An absolute and spatial agreement between the methods was found with a mild overestimation of perfusion defects in PREFUL of 5%.

As mentioned above, contrast-enhanced perfusion techniques have the longest history of validation. In 1999, one of the first comparison studies was published. Contrast-enhanced MR perfusion was compared to scintigraphy in patients with pulmonary embolism (Berthezene et al. 1999). Given the previously limited technical capabilities, the found sensitivity and specificity of 69% and 91% were a good clinical introduction of this technique. With current MR scanners an ideal sensitivity of 100% for detection of CTEPH was found, compared to a sensitivity of 97% for SPECT (Johns et al. 2017b).

Estimation of postoperative lung function in patients with lung cancer is an important clinical determent before surgery. Many studies evaluated the capability of MRI as an alternative to pulmonary scintigraphy. The overall results were all positive, like in a study by Ohno et al., where a correlation coefficient of postoperative FEV1 with $FEV1_{MRI}$ ($r = 0.93$, $p < 0.0001$) was better than that with $FEV1_{PS}$ ($r = 0.89$, $p < 0.0001$). The limits of agreement between postoperative FEV1 and predicted $FEV1_{MRI}$ ($0.9 \pm 0.4\%$) were smaller than those between postoperative FEV1 and predicted $FEV1_{PS}$ ($2.1 \pm 13.2\%$) (Ohno et al. 2004).

Also, contrast-enhanced perfusion MRI was able to quantify the differential pulmonary blood flow compared to scintigraphy (Molinari et al. 2006). Peak contrast enhancement outperformed more sophisticated quantification techniques like pulmonary blood flow and volume.

As the perfusion dataset represents a 3D angiographic dataset, segmentation of the central pulmonary arteries is possible (Rengier et al. 2016). Significantly increased volumes and diameters in patients with pulmonary arterial hypertension compared to healthy controls were found. Therefore, this approach may serve as an easy predictor for pulmonary hypertension.

References

Bauman G, Puderbach M, Deimling M et al (2009) Non-contrast-enhanced perfusion and ventilation assessment of the human lung by means of fourier decomposition in proton MRI. Magn Reson Med 62:656–664

Bauman G, Puderbach M, Heimann T et al (2013) Validation of Fourier decomposition MRI with dynamic contrast-enhanced MRI using visual and automated scoring of pulmonary perfusion in young cystic fibrosis patients. Eur J Radiol 82:2371–2377

Berthezene Y, Croisille P, Wiart M et al (1999) Prospective comparison of MR lung perfusion and lung scintigraphy. J Magn Reson Imaging 9:61–68

Bolar DS, Levin DL, Hopkins SR et al (2006) Quantification of regional pulmonary blood flow using ASL-FAIRER. Magn Reson Med 55:1308–1317

Edwards (2009) Normal Hemodynamic Parameters and Laboratory Values. Edwards Lifesciences. Available https://www.edwards.com/scin/edwards/sitecollectionimages/edwards/products/presep/ar04313hemodynpocketcard.pdf. Accessed Nov 1, 2018 2018

Evans AJ, Iwai F, Grist TA et al (1993) Magnetic resonance imaging of blood flow with a phase subtraction technique. In vitro and in vivo validation. Investig Radiol 28:109–115

Fink C, Bock M, Kroeker R, Requardt M, Ley S, Kauczor H-U (2004) Contrast-enhanced MRA with elliptic-centric view ordering and view sharing: theoretical considerations and application in patients with cardiopulmonary disease. In: Proceedings of the International Society for Magnetic Resonance in Medicine. International Society for Magnetic Resonance in Medicine, Kyoto, Japan, p 6

Fink C, Risse F, Semmler W, Schoenberg SO, Kauczor HU, Reiser MF (2006) MRI of pulmonary perfusion. Radiologe 46:290–299

Fischer A, Pracht ED, Arnold JF, Kotas M, Flentje M, Jakob PM (2008) Assessment of pulmonary perfusion in a single shot using SEEPAGE. J Magn Reson Imaging 27:63–70

Garcia-Alvarez A, Fernandez-Friera L, Mirelis JG et al (2011) Non-invasive estimation of pulmonary vascular resistance with cardiac magnetic resonance. Eur Heart J 32:2438–2445

Gatehouse PD, Keegan J, Crowe LA et al (2005) Applications of phase-contrast flow and velocity imaging in cardiovascular MRI. Eur Radiol 15:2172–2184

Hoeper MM, Bogaard HJ, Condliffe R et al (2013) Definitions and diagnosis of pulmonary hypertension. J Am Coll Cardiol 62:D42–D50

Johns CS, Kiely DG, Rajaram S et al (2018) Diagnosis of pulmonary hypertension with cardiac MRI: derivation and validation of regression models. Radiology. https://doi.org/10.1148/radiol.2018180603:180603

Johns CS, Swift AJ, Hughes PJC, Ohno Y, Schiebler M, Wild JM (2017a) Pulmonary MR angiography and perfusion imaging—a review of methods and applications. Eur J Radiol 86:361–370

Johns CS, Swift AJ, Rajaram S et al (2017b) Lung perfusion: MRI vs. SPECT for screening in suspected chronic thromboembolic pulmonary hypertension. J Magn Reson Imaging. https://doi.org/10.1002/jmri.25714

Kaireit TF, Voskrebenzev A, Gutberlet M et al (2018) Comparison of quantitative regional perfusion-weighted phase resolved functional lung (PREFUL) MRI with dynamic gadolinium-enhanced regional pulmonary perfusion MRI in COPD patients. J Magn Reson Imaging. https://doi.org/10.1002/jmri.26342

Kjorstad A, Corteville DM, Fischer A et al (2014a) Quantitative lung perfusion evaluation using Fourier decomposition perfusion MRI. Magn Reson Med 72:558–562

Kjorstad A, Corteville DM, Henzler T, Schmid-Bindert G, Zollner FG, Schad LR (2015) Non-invasive quantitative pulmonary V/Q imaging using Fourier decomposition MRI at 1.5T. Z Med Phys 25:326–332

Kjorstad A, Corteville DM, Henzler T et al (2014b) Quantitative lung ventilation using Fourier decomposition MRI: comparison and initial study. MAGMA 27:467–476

Levin DL, Chen Q, Zhang M, Edelman RR, Hatabu H (2001) Evaluation of regional pulmonary perfusion using ultrafast magnetic resonance imaging. Magn Reson Med 46:166–171

Ley S, Ley-Zaporozhan J (2012) Pulmonary perfusion imaging using MRI: clinical application. Insights Imaging 3:61–71

Lotz J, Meier C, Leppert A, Galanski M (2002) Cardiovascular flow measurement with phase-contrast MR imaging: basic facts and implementation. Radiographics 22:651–671

Mai VM, Berr SS (1999) MR perfusion imaging of pulmonary parenchyma using pulsed arterial spin labeling techniques: FAIRER and FAIR. J Magn Reson Imaging 9:483–487

Martirosian P, Boss A, Schraml C et al (2010) Magnetic resonance perfusion imaging without contrast media. Eur J Nucl Med Mol Imaging 37(1):52–64. online first

Meier P, Zierler KL (1954) On the theory of the indicator-dilution method for measurement of blood flow and volume. J Appl Physiol 6:731–744

Molinari F, Fink C, Risse F, Tuengerthal S, Bonomo L, Kauczor HU (2006) Assessment of differential pulmonary blood flow using perfusion magnetic resonance imaging: comparison with radionuclide perfusion scintigraphy. Investig Radiol 41:624–630

Moran PR, Moran RA, Karstaedt N (1985) Verification and evaluation of internal flow and motion. True magnetic resonance imaging by the phase gradient modulation method. Radiology 154:433–441

Ohno Y, Hatabu H, Higashino T et al (2004) Dynamic perfusion MRI versus perfusion scintigraphy: prediction of postoperative lung function in patients with lung cancer. AJR Am J Roentgenol 182:73–78

Ohno Y, Koyama H, Lee HY, Miura S, Yoshikawa T, Sugimura K (2016) Contrast-enhanced CT- and MRI-based perfusion assessment for pulmonary diseases: basics and clinical applications. Diagn Interv Radiol 22:407–421

Ohno Y, Murase K, Higashino T et al (2007) Assessment of bolus injection protocol with appropriate concentration for quantitative assessment of pulmonary perfusion by dynamic contrast-enhanced MR imaging. J Magn Reson Imaging 25:55–65

Puderbach M, Risse F, Biederer J et al (2008) In vivo Gd-DTPA concentration for MR lung perfusion measurements: assessment with computed tomography in a porcine model. Eur Radiol 18:2102–2107

Reeves JT, Linehan JH, Stenmark KR (2005) Distensibility of the normal human lung circulation during exercise. Am J Physiol Lung Cell Mol Physiol 288:L419–L425

Reiter G, Reiter U, Kovacs G, Olschewski H, Fuchsjager M (2015) Blood flow vortices along the main pulmonary artery measured with MR imaging for diagnosis of pulmonary hypertension. Radiology 275:71–79

Reiter U, Reiter G, Fuchsjager M (2016) MR phase-contrast imaging in pulmonary hypertension. Br J Radiol 89:20150995

Rengier F, Worz S, Melzig C et al (2016) Automated 3D volumetry of the pulmonary arteries based on magnetic resonance angiography has potential for predicting pulmonary hypertension. PLoS One 11:e0162516

Risse F, Semmler W, Kauczor HU, Fink C (2006) Dual-bolus approach to quantitative measurement of pulmonary perfusion by contrast-enhanced MRI. J Magn Reson Imaging 24:1284–1290

Sanz J, Kuschnir P, Rius T et al (2007) Pulmonary arterial hypertension: noninvasive detection with phase-contrast MR imaging. Radiology 243:70–79

Sommer G, Bauman G (2016) MRI methods for pulmonary ventilation and perfusion imaging. Radiologe 56:106–112

Swift AJ, Rajaram S, Condliffe R et al (2012) Diagnostic accuracy of cardiovascular magnetic resonance imaging of right ventricular morphology and function in the assessment of suspected pulmonary hypertension results from the ASPIRE registry. J Cardiovasc Magn Reson 14:40

Swift AJ, Rajaram S, Hurdman J et al (2013) Noninvasive estimation of PA pressure, flow, and resistance with CMR imaging: derivation and prospective validation study from the ASPIRE registry. JACC Cardiovasc Imaging 6:1036–1047

Tadamura E, Hatabu H (2001) Assessment of pulmonary perfusion using a subtracted HASTE image between diastole and systole. Eur J Radiol 37:179–183

Veldhoen S, Oechsner M, Fischer A et al (2016) Dynamic contrast-enhanced magnetic resonance imaging for quantitative lung perfusion imaging using the dual-bolus approach: comparison of 3 contrast agents and recommendation of feasible doses. Investig Radiol 51:186–193

Voskrebenzev A, Gutberlet M, Klimes F et al (2018) Feasibility of quantitative regional ventilation and perfusion mapping with phase-resolved functional lung (PREFUL) MRI in healthy volunteers and COPD, CTEPH, and CF patients. Magn Reson Med 79:2306–2314

Wild JM, Marshall H, Bock M et al (2012) MRI of the lung (1/3): methods. Insights Imaging 3:345–353

Zophel K, Bacher-Stier C, Pinkert J, Kropp J (2009) Ventilation/perfusion lung scintigraphy: what is still needed? A review considering technetium-99m-labeled macro-aggregates of albumin. Ann Nucl Med 23:1–16

Basics and Clinical Application of the MR Assessment of Ventilation

Sean B. Fain, Katherine Carey, Gregory P. Barton, and Ronald L. Sorkness

Contents

1 **Introduction** 60

2 **Theory and Rationale of Ventilation Imaging Using MRI** 61
2.1 Proton-Based Methods 64
2.2 MR Visible Gas Nuclei 70

3 **Clinical Research in Ventilation Imaging Using MRI** 75
3.1 Asthma and COPD 75
3.2 Clinical Research Using Dynamic Functional MRI 76
3.3 Pediatric Lung Disease: CF and Asthma 77
3.4 Applications in Lung Cancer 78

4 **Summary of Ventilation Imaging Using MRI** 80

References 81

Abstract

There is a growing motivation for imaging regional lung ventilation. Global measures of lung function such as spirometry are not able to distinguish patterns of obstruction and regional reversibility in response to intervention. Advantages of MRI for lung imaging include use of nonionizing radiation and flexibility for acquiring dynamic, multidimensional signal changes in response to changes in lung function. For these reasons, MRI is particularly attractive for longitudinal studies of chronic lung disease, especially in pediatric populations. There are two broad classes of ventilation imaging methods using MRI, which have

S. B. Fain (✉)
Departments of Medical Physics, Radiology, and Biomedical Engineering, University of Wisconsin, Madison, WI, USA
e-mail: sfain@wisc.edu

K. Carey, M.S. · G. P. Barton
Department of Medical Physics, University of Wisconsin, Madison, WI, USA

R. L. Sorkness
School of Pharmacy and Morris Institute for Respiratory Research, University of Wisconsin, Madison, WI, USA

© Springer Nature Switzerland AG 2021

Y. Ohno et al. (eds.), *Pulmonary Functional Imaging*, Medical Radiology Diagnostic Imaging,
https://doi.org/10.1007/978-3-030-43539-4_5

matured over the past decade: proton-based methods and direct imaging of exogenous gases using multinuclear MRI and spectroscopy. This chapter will provide a review of the theory and rationale of ventilation imaging with MRI, results of clinical research in ventilation MRI, and emerging methods of ventilation imaging. Proton MRI ventilation imaging techniques covered in this chapter include deformable image registration, Fourier decomposition, and oxygen-enhanced methods. This chapter also covers ventilation techniques utilizing MRI of visible gas nuclei, including hyperpolarized gas MRI and perfluorinated gas MRI.

1 Introduction

There is a growing motivation for imaging regional lung ventilation. Global measures of lung function such as spirometry are not able to distinguish patterns of obstruction and regional reversibility response to intervention. This is underscored by the appreciation that many common chronic lung diseases such as asthma and COPD are regionally heterogeneous and ventilation heterogeneity is itself considered a marker of disease severity (Glenny 2009). Moreover, spirometry is less reliable in pediatric lung diseases such as asthma and cystic fibrosis (CF), and a more precise regional assessment of disease pre- and post-intervention would improve therapy monitoring and new drug development (Altes et al. 2017a). However, imaging methods are typically more expensive than conventional markers of lung function, necessitating a more detailed understanding of the strengths and weaknesses of MRI methods and their role in improving understanding of disease progression. In several high-cost drug therapies and surgical intervention, MRI will aid in selection of patients via prospective phenotyping and in identifying nonresponders earlier to guide alternative approaches. Examples include biologic drug therapies, lung volume reduction surgery, valve placement, and bronchial thermoplasty.

There is an increasing variety of techniques for obtaining images of ventilation using MRI. Advantages of MRI for lung imaging include use of nonionizing radiation and flexibility for acquiring dynamic, multidimensional signal changes in response to changes in lung volume. For these reasons, MRI is particularly attractive for longitudinal studies of chronic lung disease, especially in pediatric populations. There are two broad classes of ventilation imaging methods using MRI which have matured over the past decade: proton-based methods and direct imaging of exogenous gases using multinuclear MRI and spectroscopy. From a clinical research perspective, proton-based methods are more cost-effective because they do not require additional hardware, software, and exogenous gases for contrast, but these cost advantages come with trade-offs in lung coverage and signal-to-noise ratio.

Several studies have shown measures of ventilation such as the ventilation defect percent (VDP) using hyperpolarized gases and oxygen-enhanced (OE) MRI correlate with disease severity, have a sensitive minimal clinically important difference (MCID) (Eddy et al. 2018), and are associated with outcomes such as exacerbations and lung function decline in COPD and asthma (Kirby et al. 2017; Mummy et al. 2018) and phenotypes such as eosinophilic asthma (Svenningsen et al. 2018). Despite these clear strengths, making full use of the regional ventilation information provided by MRI has, from a clinical perspective, been more challenging. In this regard, the hyperpolarized gas and OE techniques are most advanced, owing in part to their longer history in the field. But advances in proton-based techniques have accelerated recently suggesting promise for future applications.

This chapter is organized into three sections each addressing a different aspect of ventilation imaging using MRI: (1) Theory and Rationale—this section focuses on the theoretical and physical rationale for ventilation imaging including various MRI techniques for imaging ventilation and generic protocol details concerning acquisition design and protocols; (2) Clinical Research—this section summarizes clinical research results with an emphasis on larger studies that have

shown promise for ventilation MRI to provide clinical information beyond that available from conventional biomarkers; and (3) Overview—this compares and contrasts different approaches to ventilation MRI and touches on promising feasibility studies and clinical research studies in adult and pediatric lung disease applications.

2 Theory and Rationale of Ventilation Imaging Using MRI

Any method for evaluating lung ventilation ideally measures the airflow both into and out of the lungs both globally and through individual airway segments. The goal is therefore to estimate the volume of fresh air (V_f) flowing into a fixed reference volume (V_r) usually taken at end-expiration. The ratio of these volumes is known as the specific ventilation (SV) and can be thought of as the mixed fraction of the original reference lung volume and end-expiration that is replaced by fresh air (or a tracer gas) for each breath:

$$\mathrm{SV} = \frac{V_f}{V_r} \tag{1}$$

A related measure is the fractional ventilation (FV), which estimates the fraction of total lung volume that is made up of fresh air (or tracer gas) on end-inspiration, and can be expressed in terms of SV:

$$\mathrm{FV} = \frac{V_f}{V_r + V_f} = \frac{\mathrm{SV}}{1 + \mathrm{SV}} \tag{2}$$

Over time, global and regional delivery of V_f will reach an equilibrium under tidal breathing conditions that reflects the rate of gas delivery to the terminal bronchi and acini where gas exchange takes place. Using a tracer gas such as N_2, a dynamic multiple breath gas washout experiment can reveal global ventilation heterogeneity by fitting the exponential washout curves to reveal fast and slow exchange compartments that show different SV (Fig. 1). In lung disease such compartmental models are especially useful for detecting dead-space regions that emerge due to unmatched ventilation heterogeneity (Lewis et al. 1978).

However, the most common pulmonary function test (PFT) is spirometry, a set of global measures of airflow performed under a forced respiratory maneuver that is commonly used to

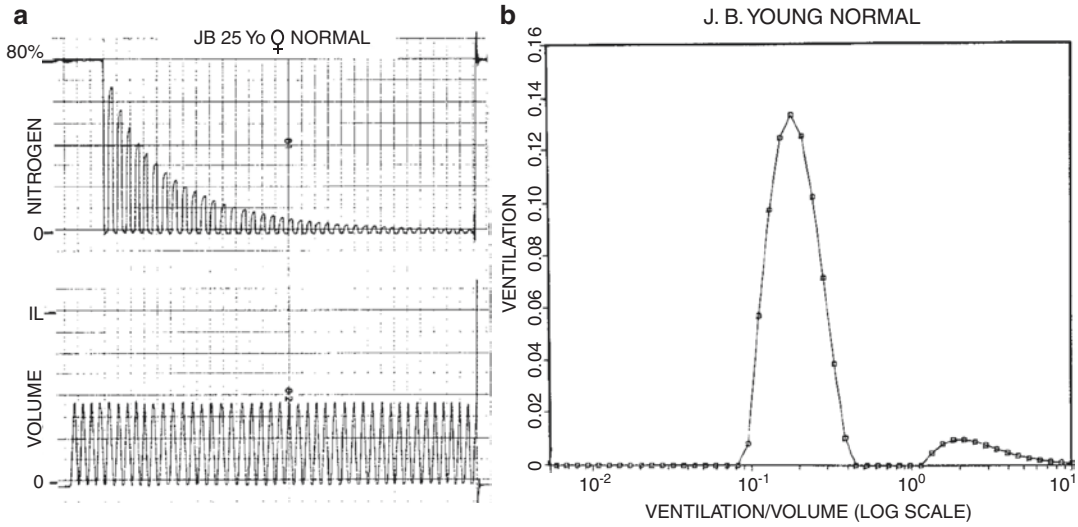


Fig. 1 (**a**) Nitrogen multi-breath washout (top) and volume (bottom) time curves for a healthy subject with (**b**) sample result from a 50-compartment model of the washout curve in the top of panel A. The high ventilation regions to the right of the main peak correspond to large airway dead-space, while the main peak captures regions of normal ventilation within the lung parenchyma. Adapted from (Lewis et al. 1978)

diagnose obstructive and restrictive lung disease. Spirometry is capable of measuring global airflow into and out of the lungs under different conditions, including passive (e.g., tidal breathing) and dynamic (e.g., forced exhalation) conditions. While spirometry measures can tell us something about the degree and type of (e.g., restrictive vs. obstructive) flow limitation, spirometry cannot provide regional information about which lung units are affected (e.g., apical vs. lower lobes or central vs. peripheral airways).

Much debate has been focused on whether imaging can provide quantitative information on ventilation. Most methods for imaging ventilation provide regional estimation of local obstruction (or restriction) with certain trade-offs, often in the absence of dynamic free breathing or under forced maneuvers. Consequently, most imaging methods are proportional to ventilation (e.g., acquired at breath-hold) or reflect steady-state information averaged over multiple respiratory cycles (e.g., acquired during steady-state tidal breathing). However, all the major modalities, including nuclear imaging and MRI, provide information that is limited either in spatial coverage or in dynamics of gas flow, making regional information more or less proportional to local ventilation. For example, MRI methods that depend on hyperpolarized gas inhalation (e.g., ^{3}He or ^{129}Xe mixed with N_2) are typically imaged rapidly during a short 10–15 s breath-hold and visualize so-called "ventilation defects" where the ^{3}He or ^{129}Xe gas does not fill obstructed regions of the lungs (Samee et al. 2003). Unfortunately, such ventilation defects do not capture delayed filling or gas wash-in or washout making the VDP measure proportional to a "worst case" estimate of late filling or totally obstructed lung regions.

Several steady-state methods such as OE MRI (Edelman et al. 1996; Ohno and Hatabu 2007) and Fourier decomposition (FD) (Bauman et al. 2009) typically suffer from low signal-to-noise ratio (SNR) and rely on averaging measures of ventilation over many tidal breathing cycles. However, these methods can capture dynamic filling by repeated breath-hold coaching or controlled breathing over many tidal breaths (Schreiber et al. 2001; Halaweish et al. 2013; Sa et al. 2010; Arai et al. 2018; Gutberlet et al. 2018) and can provide approximate measures of voxel-wise SV (Eq. 1) and FV (Eq. 2) at the expense of long scan times and post-processing complexity using deformable image registration (DIR) methods that can be difficult in severe disease. Therefore, the jury is still out as to whether obtaining more quantitative measures of regional ventilation is worth the additional effort and challenge in disease populations vs. more simple approximations. Both VDP and ventilated volume (VV) have been proposed for characterizing and quantifying ventilation using HP Xe MRI. Both indices correlate with global PFT's and disease severity (Woodhouse et al. 2005; Fain et al. 2008; Kirby et al. 2017; Mummy et al. 2018; Gutberlet et al. 2018), and clinical standard imaging modalities (V/Q SPECT-CT). However, the ventilation defect percent (VDP) (Fain et al. 2008) is a relatively simple metric which has found increasing application in clinical research and across multiple MRI ventilation methods:

$$\mathrm{VDP} = \frac{\mathrm{Ventilation\ Defect\ Volume}\left(\mathrm{HP\ MRI}\right)}{\mathrm{Total\ Lung\ Volume}\left(\mathrm{Proton\ MRI}\right)} \quad (3)$$

Most of these methods are either single breath-hold, such as HP gas MRI, or time averaged methods, such as OE of FD MRI, that are acquired over multiple tidal breaths and provide images that are proportional to ventilation and are not strictly quantitative in a physiologic sense. The reader is directed to several excellent reviews of this ongoing debate for further information (Hopkins et al. 2007; Miller et al. 2014). This chapter will take a pragmatic view and include both methods when they have reached a sufficient level of maturity for potential clinical characterization of obstructive and restrictive disease processes.

Methods for ventilation imaging with MRI can be broadly classified as either proton signal based or multinuclear signal based, typically using direct imaging of inhaled exogenous gases in the latter case. Proton-based techniques most often depend on signal intensity or mechanical

changes that are proportional to local lung inflation (Fig. 2). By contrast, multinuclear techniques image various exogenous gases directly, including fluorinated (commonly perfluoropropane, "PFP"), and hyperpolarized ^{3}He and ^{129}Xe gases (Fig. 3). The OE MRI techniques do not

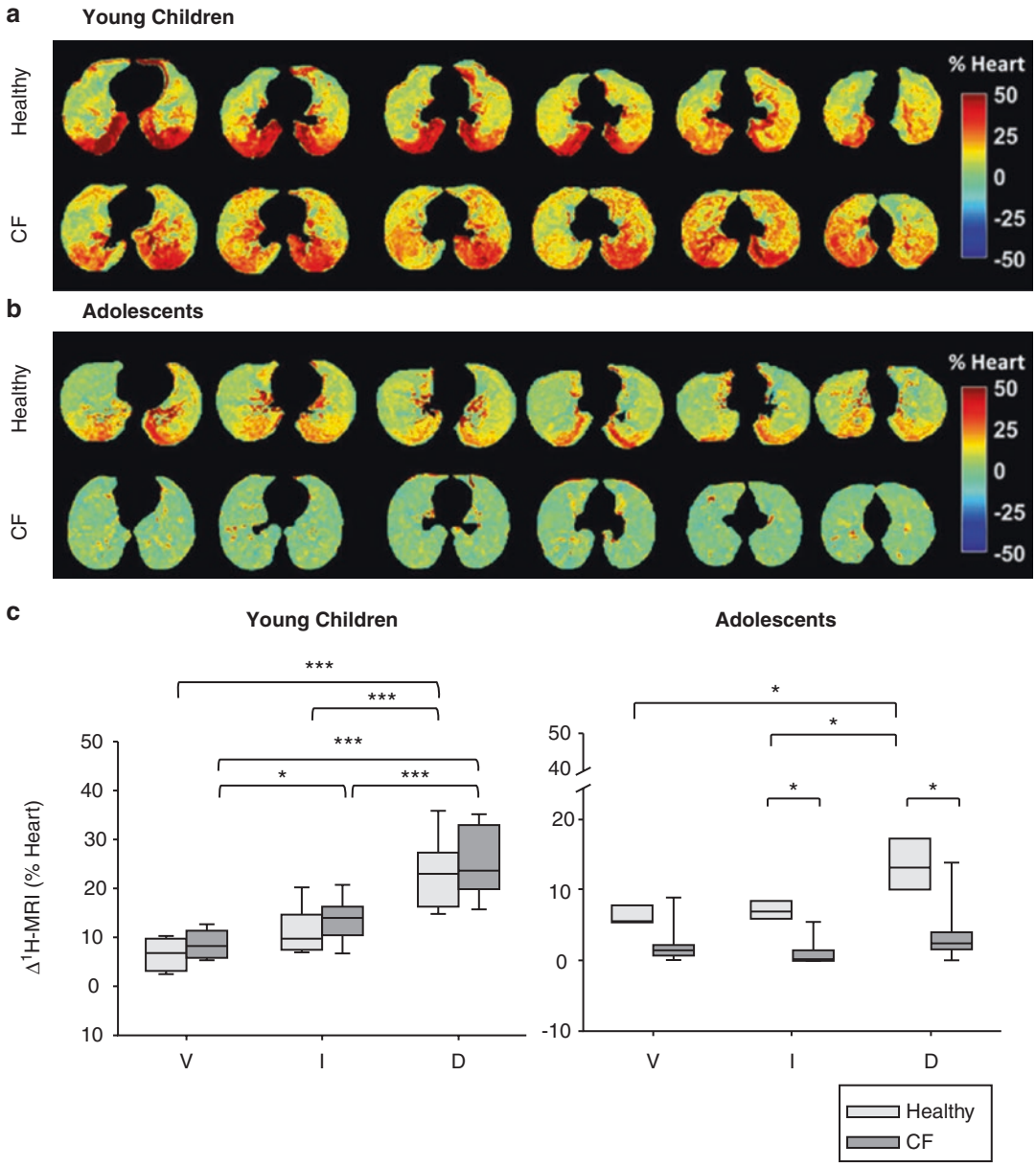


Fig. 2 (**a**) Maps of MR signal-intensity change of a representative healthy (top) and a representative CF (bottom) young child are shown from top diaphragm (left) to aortic arch (right) at equally spaced lung levels. (**b**) MR signal-intensity change maps of a representative healthy (top, FEV1 = 83%) and a representative CF adolescent (bottom, FEV1 = 96%) are shown from top diaphragm (left) to aortic arch (right) at equally spaced lung levels. Color scale indicates the proton-signal difference as a percentage of the mean heart signal. Gravity-dependent gradients in signal difference from the anterior to posterior are no longer seen in the CF adolescent. (**c**) This pattern was found to be significantly different in a group-wise comparison. Adapted from Pennati et al. (2018). Used with permission from the authors

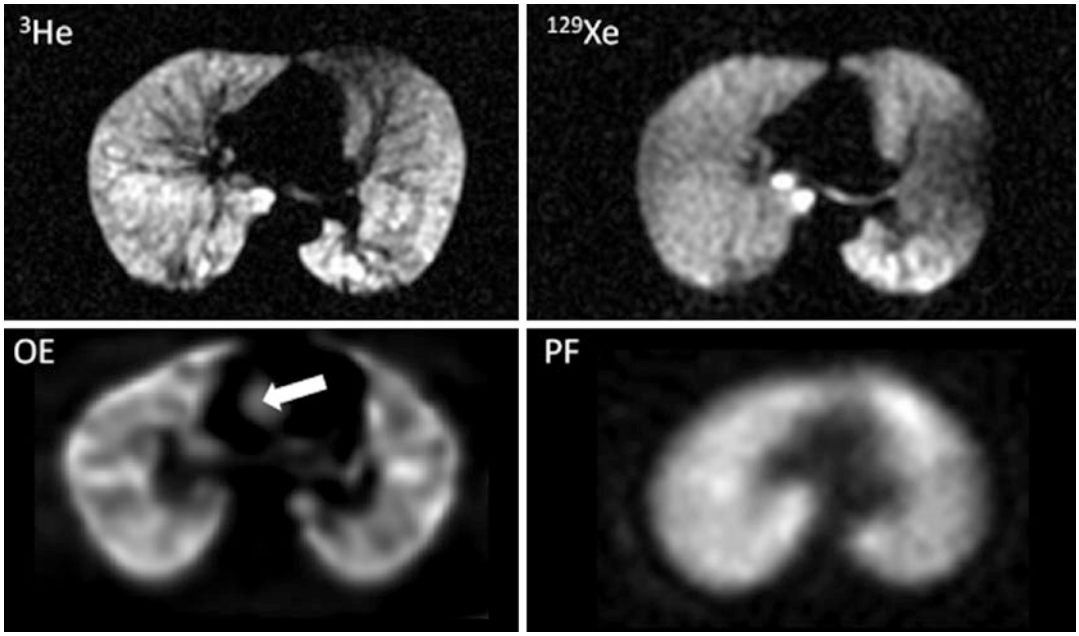


Fig. 3 Representative images of the four gas contrast agents: ^{3}He, ^{129}Xe, oxygen-enhanced (OE), and perfluorinated gas (PF). In the OE contrast image, enhancement extends beyond the lungs into the ascending aorta (arrow). Adapted from Ebner et al. (2017)

fall as neatly into these two areas in that they depend on inhalation of different fractions of oxygen gas (typically comparing normoxic (21% O_2) with 100% O_2 breathing), but are strictly proton based since they do not directly image the oxygen gas. The OE MRI methods instead depend on the indirect T1-weighted proton contrast change in proportion to the local variations in dissolved oxygen within the tissues and blood. OE MRI therefore shares some methodological attributes with both the proton-based and multinuclear-based MRI methods.

2.1 Proton-Based Methods

To detect the distribution of air throughout the lungs with conventional proton MRI, there are two basic strategies: methods that use change in lung signal intensity and methods that use change in lung mechanical deformation at different lung inflation volumes. Signal intensity varies with lung inflation because the lung tissue density and, to a lesser extent, T2* change as the alveolar volume changes locally. MRI is therefore performed either during free breathing or at specified breath-holds acquired at different lung inflation volumes. The more extreme the difference in lung inflation between end-expiratory and end-inspiratory breath-holds, the greater the relative change in signal improving the contrast-to-noise ratio (CNR). The CNR can also be improved by signal averaging over multiple tidal breaths during free breathing usually over a 10–20 min exam.

Specific measures of signal change at different lung inflation states are benefited by short echo times and fast imaging in general to reduce breath-hold time or improve temporal resolution during dynamic imaging. This is because of two well-known limitations of MRI for depicting lung parenchyma, including low proton signal density (i.e., rho ~0.2 g/cm^3) and the very short T2* of the lung parenchyma due to high local field inhomogeneities induced by the many air tissue interfaces of the alveolar structures in the parenchyma. The MR signal of parenchyma is much weaker than that of adjacent tissues (Wild et al. 2012). Tissue is diamagnetic and oxygen in the air is paramagnetic, leading to magnetic susceptibility differences at air-lung interfaces,

forming a static local field gradient at each air-lung interface that leads to rapid dephasing in gradient echo imaging (Wild et al. 2012). While not a requirement, the potential of such proton-based methods has been expanded by the development of faster, more stable, gradients and calibration methods to support robust non-Cartesian and Cartesian trajectory ultrashort echo time (UTE) MRI.

Obtaining ventilation images from signal intensity and mechanical variations depend on advanced post-processing, including deformable image registration (DIR) (Sotiras et al. 2013) and Fourier techniques (Bauman et al. 2009; Bauman and Bieri 2017) that, over the past decade, have been optimized for detecting local inflation. The application of these tools to estimate lung ventilation is described in more detail below.

2.1.1 Deformable Image Registration

Methods for estimating ventilation using DIR have gained traction due to their potential for deriving ventilation information from standard imaging protocols. The Jacobian of the DIR spatial transformation is defined as the determinant of the transformation's first derivative and represents the degree of magnification of volumes under the transformation (Wild et al. 2012). Jacobian maps have been used to estimate ventilation in 4D computed tomography (4DCT) (Reinhardt et al. 2008; Castillo et al. 2017) and the results have been shown to correlate with pulmonary function tests (Brennan et al. 2015) and to visually correspond with HP gas MRI ventilation (Mathew et al. 2012b). Prior work has used registered proton MRI in conjunction with signal differences to detect local ventilation abnormalities (Pennati et al. 2014, 2018), but deformable image registration transformation based methods, such as the Jacobian, have not been thoroughly investigated in proton MRI. However, signal intensity and deformational changes for direct estimation of ventilation represent a comparatively underdeveloped area of study in MRI that may be poised for new advances with the development of UTE MRI sequences for more robust parenchymal signal detection.

Given the lower signal intensity of the lung parenchyma in conventional MRI, constraints on possible DIR solutions are likely less controlled than for CT, and further study is needed to confirm DIR performance for MRI. Advances in diffeomorphic DIR algorithms that enforce topological constraints (i.e., differentiable, one-to-one mapping, with positive Jacobian) (Sotiras et al. 2013) seem to be empirically robust for mapping lung regions in a way that is consistent with changes in local lung inflation. However, while diffeomorphic DIR solutions are well constrained by anatomic markers, specific mappings are not unique (Castillo et al. 2017) such that there may be multiple DIR solutions that are within the spatial accuracy of a voxel but that yield different estimates of spatial deformation and signal change, and therefore different estimates of local ventilation. Some useful strategies employ grouping of similar lung inflation phases to improve SNR prior to the application of DIR between images at different respiratory phases (Voskrebenzev et al. 2017). In practice, proton-based techniques, all of which depend on DIR to varying degrees, seem to yield empirically robust results that are consistent with independently measured functional imaging techniques (Bauman et al. 2013b; Tahir et al. 2018).

2.1.2 Fourier-Based Methods

Fourier-based methods combine DIR with dynamic imaging to provide images of ventilation and perfusion (Bauman et al. 2009). Specifically, 2D dynamic images are acquired during free breathing to record the changes in signal intensity due to local variations in tissue density and T2* due to respiration at a temporal frequency of ~0.1 Hz (~5 breaths/min) in conjunction with cardiac pulsatility of the blood flow at ~1 Hz (~60 beats/min). The corresponding respiratory and cardiac temporal frequencies can be estimated for each voxel of a 2D multi-slice dynamic time course of images using the Fourier transform to isolate the relevant temporal frequencies using bandpass filters, in other words using Fourier power spectral analysis of the temporal frequencies of the finite-time Fourier transform (Fig. 4).

Basic feasibility of the original FD technique has been demonstrated with reproducibility studies performed 24 h apart in 16 healthy subjects.

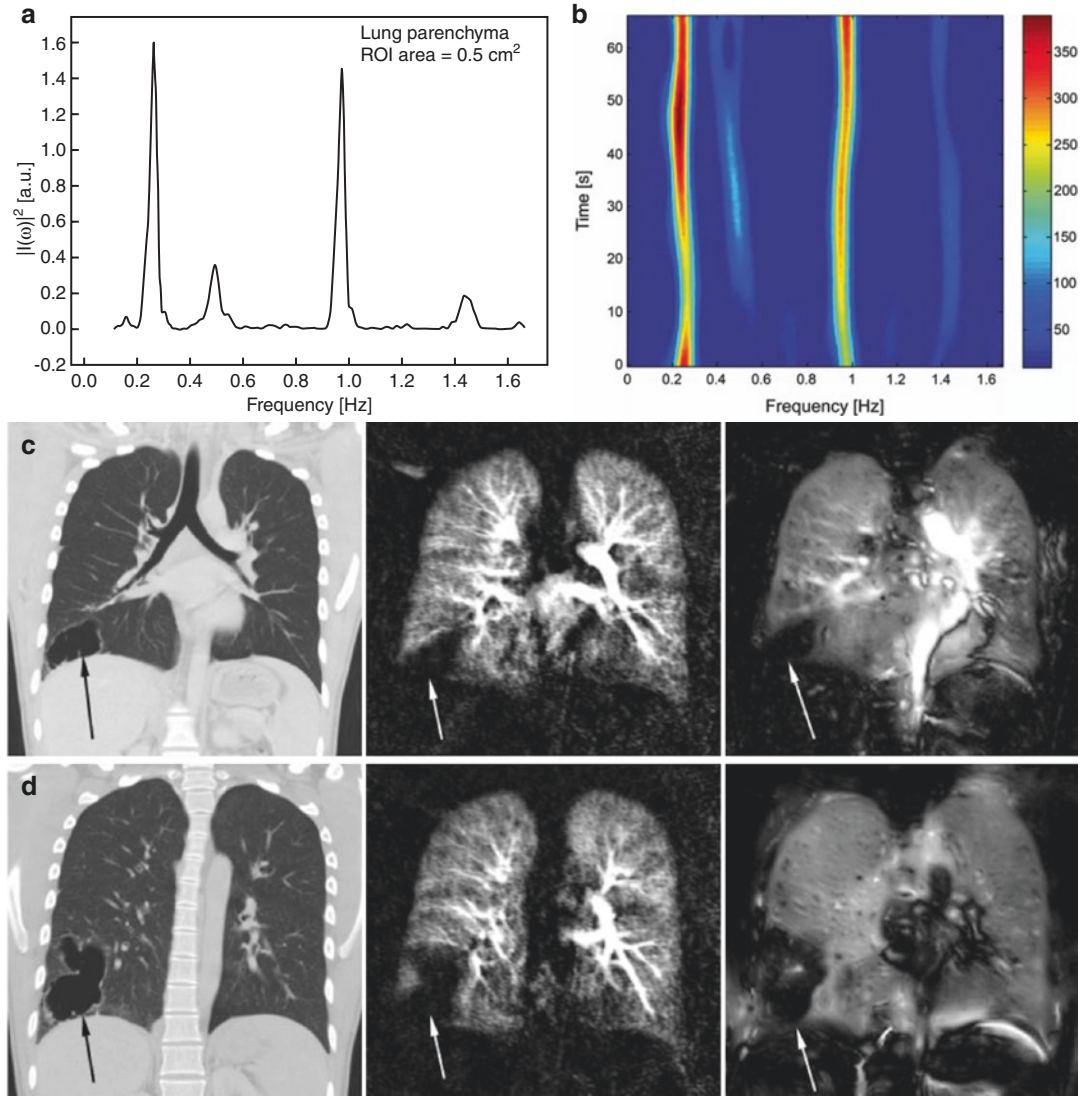


Fig. 4 (**a**, **b**) Short-time Fourier transform of the time-dependent signal intensity within a dynamic image voxel depicts characteristic frequencies at the respiratory and cardiac cycles and their associated harmonics. These spatial and temporal frequencies can be used to isolate images of ventilation and perfusion. (**c, d**) CT and MRI images from two coronal slices from a case of cystic parenchymal defect (arrows) mimicking a pulmonary embolism as seen on CT (left), corresponding dynamic contrast enhanced perfusion MRI (middle), and images of (**c**, right) perfusion and (**d**, right) ventilation obtained using the Fourier decomposition method. Adapted from Bauman et al. (2009). Used with permission from the authors

This study used the most common balanced steady-state free precession (bSSFP) acquisition method with parameters as summarized in Table 1. Findings showed strong ICC (0.94 for perfusion-weighted, and 0.86 for ventilation-weighted images), with minimal bias and good reproducibility especially for posterior slices. However, anterior slices are less consistently represented using FD techniques due to variations and inconsistencies in chest vs. diaphragm breathing that lead to inconsistency of breathing motion in the anterior slices over time. This remains a weakness of the technique with most studies confining coverage to 3 relatively thick

(10–15 mm) posterior coronal slices as a consequence. The most anterior slice reliably imaged is positioned to intersect the hilum so that the major pulmonary vessels and some portion of all 5 lung lobes are represented in the coronal ventilation and perfusion-weighted images. Additional validation studies demonstrated comparable perfusion-weighted images when compared to dynamic contrast-enhanced perfusion in young patients with CF indicating promise for pediatric applications without requiring gadolinium (Gd) contrast agents, and during a free-breathing exam without need for exogenous gas agents (Bauman et al. 2013a; Nyilas et al. 2018). Multiple sites have replicated the method to demonstrate good quality FV images using FD MRI in a variety of disease applications and cross-validated with reference standard MRI of ventilation using exogenous gas agents, including HP gas MRI (Capaldi et al. 2015, 2018) and ^{19}F MRI (Kaireit et al. 2018).

Technical advances have highlighted multiple pulse sequence solutions with sufficient temporal resolution and signal sensitivity to successfully reproduce this method at higher 3 T field strengths (Table 1). A range of techniques with varying degrees of SNR and CNR performance have been developed not all of which are sufficiently robust on all clinical scanners. The highest performing sequence is the ultra-fast bSSFP (UF-bSSFP) mostly due to its ability to rapidly acquire fractional echoes (TE of 0.7 ms) and longer signal recovery time (TW) between images. Conventional SPGR and modified transient SPGR (tSPGR) are less demanding on RF excitation and gradient performance and have reduced sensitivity to off-resonance artifacts and specific absorption rate (SAR) due to reduced overall RF energy deposition; both are advantages at the 3 T vs. 1.5 T field strength (Bauman et al. 2019). Methods thus far are typically multi-slice and 2D to trade-off sufficient temporal resolution against signal recovery between excitations to improve SNR.

Recent post-processing advances have built on the FD technique by fitting the ventilation and cardiac perfusion signals in the time-domain enabling estimation of both the local amplitude of signal change as well as regional phase differences to estimate temporal delays and time of arrival maps (Bauman and Bieri 2017; Voskrebenzev et al. 2018). Using self-gated methods similar to SENCEFUL (Fischer et al. 2014), self-gating in the time domain has enabled time to peak maps of ventilation and relative measures of regional V/Q with this non-contrast MRI approach (Voskrebenzev et al. 2018). The expanding utility of FD-based methods is quickly developing with quite promising recent advances suggesting wide dissemination is feasible to centers where gas agents are not available or in populations where such agents are not possible due to safety or logistical concerns.

2.1.3 Oxygen-Enhanced MRI

OE MRI, first proposed in 1996 by Edelman et al. (1996), shares similar advantages to FD in that the technique is free breathing, but with additional contrast derived from the introduction of oxygen as a T1 contrast agent. Oxygen gas diffuses easily into the tissues and blood and is easily available at high purity for very little

Table 1 Basic pulse sequences and parameters for FD estimation of ventilation and perfusion

Field strength	Pulse sequence	TR (ms)	TE (ms)	TW (ms)	Flip angle (deg)	RF spoiling phase (deg)	SNRL	CNRV	CNRQ
1.5 T	BSSFP	1.9	0.8	110	75				
	UFSSFP	1.45	0.67	178	65		73.3	33.2	36.2
	tSPGR	0.99	0.43	224	11	5	38.1	15.4	12.5
	SPGR	3.00	0.82	0	11	50	20.7	13.5	4.1
3 T	BSSFP								
	UFSSFP	1.34	0.57	185	30		31.2	16.5	11.3
	tSPGR	0.99	0.43	224	9	5	35.6	29.7	50.8
	SPGR	3.00	0.82	0	9	50	21.3	22.4	16.5

expense, adding high potential for clinical translation. Due to the paramagnetic effect of molecular oxygen, T1-shortening scales inversely with the inhaled concentration of oxygen (F_IO_2) (Hatabu et al. 2001) and is therefore proportional to local ventilation in steady-state conditions (Fig. 3), and to oxygen wash-in and washout under dynamic conditions. Usually, a dual acquisition is performed: one during inhalation of 21% O_2 (normal atmospheric oxygen concentration) and the other during inhalation of 100% O_2. Typically, proton spins in the vicinity of dissolved oxygen have a T1 difference of 8–15% (Edelman et al. 1996; Jakob et al. 2001; Chen et al. 1998; Loffler et al. 2000) between normoxic and hyperoxic acquisitions. The change in T1 that drives the OE effect, however, is not instantaneous as a function of F_IO_2. The changes in T1 driven by the physiological wash-in and washout follow an exponential curve, with estimates of the time constant ranging from as long as 45–80 s (Naish et al. 2005; Arnold et al. 2004; Bauman et al. 2018) to as low as 17–30 s. (Dietrich et al. 2010; Ohno et al. 2008b; Hatabu et al. 2001) Therefore, for static OE MRI, most researchers allow 1–2 min between changes in F_IO_2 to avoid transient effects. Well-ventilated regions of the lung show an oxygen-dependent signal enhancement; typically, a map of this signal enhancement is provided in units of percent signal enhancement, with recent extension with k-means segmentation approaches to include the VDP measure similar to that used for HP gas MRI methods (Zha et al. 2019).

The relatively long T1, short T2, and very short T2* (Table 2) of the lung must therefore be considered when designing MR sequences for OE MRI to ensure adequate T1 recovery and minimal phase dispersion. For both the conventionally used 2D inversion recovery single-shot fast spin echo (IR-SSFSE, also called IR-HASTE) and more recently introduced 3D radial UTE approaches, T1 effects dominate. The avoidance of T2* effects is the primary reason that fast spin echo (FSE) or single-shot fast spin echo (SSFSE) methods have formed the basis of most OE MRI to date. An inversion recovery (IR) prep pulse is typically used with FSE or SSFSE methods to increase T1-weighting. The inversion time (TI) is typically set to the null point of the lungs in the air-breathing image (Edelman et al. 1996; Stock et al. 1999; Ohno et al. 2002) or to maximize the CNR between the T1 recovery curves (Chen et al. 1998; Loffler et al. 2000; Dietrich et al. 2005; Mai et al. 2003; Muller et al. 2002). Centric view ordering is typically used to minimize the effects of T2 decay and provide better CNR in the OE image. Using this approach, the image of a single 2D slice can be acquired in a fraction of a second. Unfortunately, however, the very low SNR of OE MRI requires a longer acquisition time to allow sufficient signal averaging, usually on the order of 10+ minutes for a complete OE scan. Scan efficiency is therefore a priority to enable whole lung coverage in a reasonable scan time. Interleaved 2D slices combined with parallel imaging and half-Fourier reconstruction has enabled multi-slice 2D OE MRI using IR-SSFSE (Dietrich et al. 2005).

Important limitations to the conventional 2D IR and FSE approaches to OE MRI include limited thoracic coverage and long scan times. The combination of 3D radial UTE acquisition with OE MRI works to mitigate these limitations by improving SNR efficiency (e.g., no IR is needed), while providing whole lung coverage and reduced

Table 2 Basic pulse sequences and parameters for OE MRI estimation of ventilation

Scan method	Acquisition parameters						
	TR (ms)	TE (ms)	Flip angle (°)	FOV	Slice	In-Slice Spatial Resolution (mm^2)	TI (ms)
IR-SSFSE[a]	3200–5000	4	90	450 mm × 450 mm	10	2 × 2	900
3D radial UTE[b]	2.9–4.2	0.08–0.12	8	32 cm	3.2	3.2 × 3.2	N/A

[a]Inversion recovery single-shot fast spin echo
[b]Ultrashort echo time

cardiac motion sensitivity (Kruger et al. 2014a; Zha et al. 2018b; Sasaki et al. 2017). To move from 2D to 3D OE MRI, the signal averaging of repeated Cartesian acquisitions is no longer feasible due to time constraints. Instead, one strategy is to use a 3D radial center-out k-space trajectory (Kruger et al. 2014a; Togao et al. 2011; Johnson et al. 2012). Radial acquisitions are inherently robust against cardiac motion artifact due to inherent signal averaging because the center of k-space is acquired with every projection. Contrast is generated by a combination of competing T1 and T2* effects (Kruger et al. 2014a). Ultrashort echo time (UTE) with TE < 100 μs is chosen to maximize T1 contrast while minimizing T2* effects. The flip angle should be chosen to maximize CNR. Respiratory motion may be somewhat mitigated by both prospective respiratory gating to end-expiration and retrospective deformable image registration. Typical parameters for both IR-SSFSE and 3D UTE implementations are summarized in Table 2 (Kruger et al. 2014a, 2016).

Gradient echo sequences such as snapshot fast low-angle shot (FLASH) have also been used to perform rapid OE MRI T1 mapping at multiple O_2 concentrations to derive the oxygen transfer function (OTF) measure (Jakob et al. 2001, 2004; Arnold et al. 2004). The OTF is derived from the slope of the linear fit of oxygen concentration vs. R1 = 1/T1. In addition, T2* mapping (Pracht et al. 2005) has been explored because gradient echo sequences are very sensitive to T2* effects. Given this, it is crucial to use the shortest TE possible in order to mitigate T2* decay whenever T1-weighting or T1-mapping is desired. This is also the reason why gradient echo methods like the 3D radial UTE approach (Kruger et al. 2014a) have required ultrashort echo time implementations.

Furthermore, both respiratory and cardiac motion can cause significant artifacts and must be addressed either prospectively or retrospectively. Higher confidence in OE MRI signal has been demonstrated under respiratory triggering (Vaninbroukx et al. 2003). More recently, both respiratory and cardiac triggering have been implemented successfully for 2D OE-MRI (Dietrich et al. 2005; Molinari et al. 2007). Typically, non-rebreather facemasks are used with a constant flow of oxygen at 15 L/min (Renne et al. 2015b; Molinari et al. 2008). Even with the use of respiratory gating or triggering, lung volume varies with changes in F_IO_2 (Dripps and Comroe 1947). Since most complete OE MRI datasets take ten or more minutes to acquire, this fact combined with bulk patient motion can cause misregistration between the two sets of images. Initially, many researchers performed signal averaging by taking advantage of the large number of acquired images to blur the misregistration, particularly near the diaphragm (Jakob et al. 2001; Stock et al. 1999; Tadamura et al. 1997). Since then, Mai et al. demonstrated an improved correlation between the F_IO_2 input function and the OE MRI signal by using only the images with minimal divergence in diaphragm position (Mai et al. 2003). The majority of researchers have implemented this approach prior to signal averaging—in effect implementing a combination of both prospective and retrospective respiratory gating (Edelman et al. 1996; Chen et al. 1999; Dietrich et al. 2010; Molinari et al. 2007; Sa et al. 2010; Loffler et al. 2000). Another complementary approach to motion correction is deformable image registration, which has been shown in 2D OE MRI to improve consistency of signal and quantitative measures (Naish et al. 2005). More recently, diffeomorphic registration has been applied to 3D isotropic OE MRI (Kruger et al. 2014a), although no formal analysis on the efficacy of the technique in this context has yet been performed.

The ready availability of proton-based techniques including oxygen-enhanced and the freedom from dedicated multinuclear imaging hardware make OE MRI a promising research tool with high potential for clinical translation. The technique has shown strong correlations with other reference standards for pulmonary function such as PFT, CT, $\%DL_{CO}$, scintigraphy, and HP ^{3}He MRI (Zha et al. 2019; Arai et al. 2018). Recent advances in OE MRI with respect to lung coverage, improved spatial resolution and repeatability of semiquantitative estimates of VDP (Zha

et al. 2018b) and quantitative regional SV maps (Sa et al. 2010), as defined in Eq. 1, further support translation in a wide range of pediatric and adult lung diseases where imaging of the distribution and dynamics of a gas agent is preferred.

2.2 MR Visible Gas Nuclei

2.2.1 Hyperpolarized Gases

Hyperpolarized (HP) gas MRI allows for direct visualization of gas distribution in the lungs without the use of ionization radiation (Mugler and Altes 2013). While non-proton nuclei have the advantage that no background signal is present in the images, the gases used and technology necessary to image multinuclear frequencies are not widely available (Fain et al. 2010). Additionally, global quantities of HP ^{3}He are limited and quite costly, so HP gas MRI is migrating towards the use of HP Xenon-129 (^{129}Xe) (Mugler and Altes 2013). The technical challenges of this migration have been made easier by advances in ^{129}Xe SEOP polarization (Hersman et al. 2008; Ruset et al. 2006; Freeman et al. 2014; Stewart et al. 2015). Most typically HP ^{129}Xe MRI uses enriched ^{129}Xe isotope from the natural abundance of 26% to ~85% to compensate for lower achievable polarization compared to ^{3}He gas. All the major types of contrast-weighting achieved with ^{3}He MRI have now been replicated robustly with enriched HP ^{129}Xe (Mugler and Altes 2013; Ebner et al. 2017). While broadband hardware and dedicated RF coils are needed to implement the technology, access to polarizer technology is the primary barrier to translation. There are now two commercial companies developing HP ^{129}Xe polarizers and technology for lung imaging applications—Xemed LLC (http://www.xemed.com/) and Polarean (http://www.polarean.com/). In addition, an open source ^{129}Xe polarizer system that can be manufactured locally using 3D printing technology was introduced recently (Nikolaou et al. 2014; Nikolaou et al. 2013).

The HP gases are most commonly delivered as an anoxic gas mixture to the subject in the supine position starting from FRC lung volume followed by a 6–15 s breath-hold. The effective T1 time for imaging in the lungs is approximately 30 s due to mixing with paramagnetic oxygen residual in the lungs but allowing sufficient time for acquisition within a breath-hold or dynamically over a 30–60 second washout experiment (Horn et al. 2014). Extensive experience with HP ^{3}He MRI and now ^{129}Xe has shown that repeated inhalation of these gases is safe (Kirby and Parraga 2013; Altes et al. 2007; Lutey et al. 2008; Driehuys et al. 2012). The anesthetic effects of xenon are not a concern in adult subjects (Driehuys et al. 2012) but remain to be studied in pediatric lung disease. Since ^{3}He gas has been safely used in a wide range of pediatric studies (Driehuys et al. 2012; Altes et al. 2006; Cadman et al. 2013), it will likely remain an important contrast agent during the translation of ^{129}Xe to pediatric lung disease (Liszewski et al. 2013). Additionally, improved polarization methods for ^{129}Xe may reduce the required gas volume to approximately 200 ml, which may be sufficient to avoid anesthetic effects altogether (Stewart et al. 2015). Similar advances may also make the use of natural abundance HP ^{129}Xe MRI feasible, significantly reducing cost. There can be significant variation in lung inflation volume in pulmonary MRI studies. Normalization of the inhaled dose varies from specified fractions of vital capacity (VC) (Kirby and Parraga 2013), forced vital capacity (FVC) (Wang et al. 2008), total lung capacity (TLC) (Cadman et al. 2013; van Beek et al. 2009), to, most commonly, a fixed volume (typically 1 L) above FRC. As the field matures, there is a need to establish a consistent approach to allow comparison of studies across sites in a manner similar to parallel efforts in quantitative CT (Newell et al. 2013). In this regard, a consortium of HP ^{129}Xe MRI sites was recently formed to standardize approaches for gas delivery, acquisition, and post-processing analysis (https://cpir.cchmc.org/XeMRICTC).

Spin density images during breath-hold represent a snapshot of gas distribution depicting so-called "ventilation defects" in cases of obstructive disease (Fig. 5). The VDP, as defined in Eq. (3) above, is emerging as a general biomarker using various functional MRI methods but was first introduced for HP ^{3}He MRI as a semi-automated measure (Tustison et al. 2011; Kirby et al. 2012; He et al. 2016, 2018). Multiple

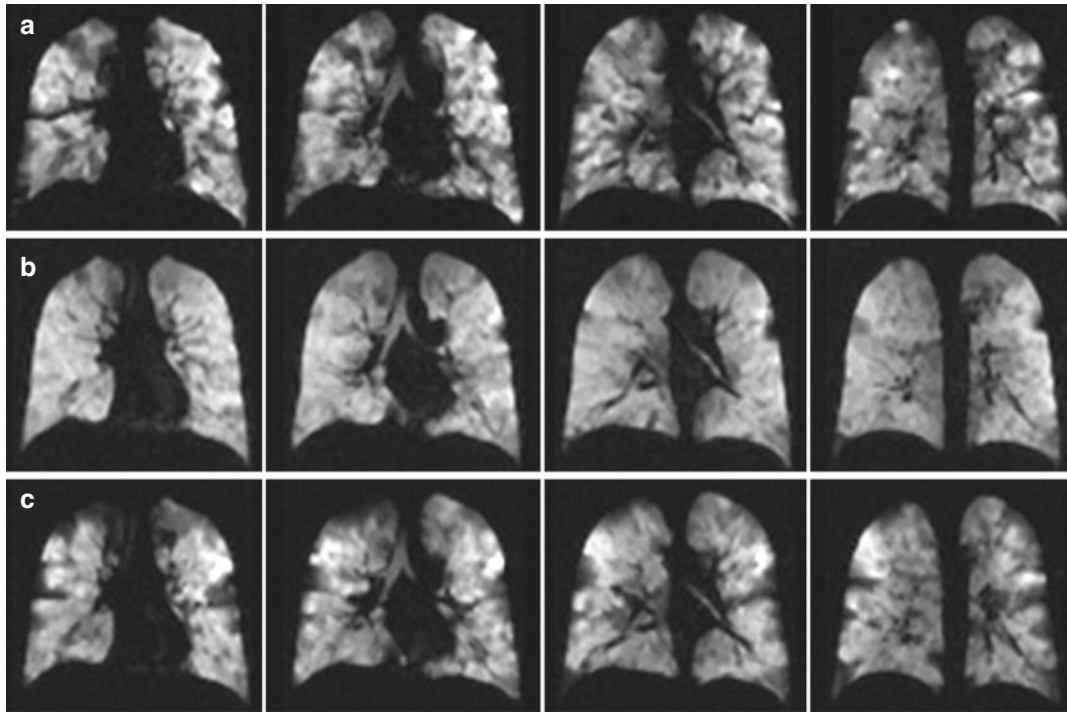


Fig. 5 Coronal hyperpolarized ^{3}He-MRI images of a CF patient in Part A. Typical images are shown. Following inhalation of the hyperpolarized gas, well-ventilated lung regions appear bright white, and poorly ventilated regions (termed "ventilation defects") appear dark gray/black. (**a**) Baseline (day 15): ppFEV1: 62.2; VDP: 48.4%. (**b**) End of 4 weeks of ivacaftor treatment (day 43): ppFEV1: 83.0; VDP: 17.4%. (**c**) End of 2 weeks of placebo washout (day 57): ppFEV1: 71.6; VDP 40.9%. Adapted from Altes et al. (2017a)

groups have demonstrated repeatability (He et al. 2016, 2018; Niles et al. 2013; de Lange et al. 2009; Kirby et al. 2011) and validity of the VDP measure compared to pulmonary function testing (Kruger et al. 2014b; Mathew et al. 2012a; Virgincar et al. 2013) and severity of disease (Virgincar et al. 2013; de Lange et al. 2006; Kirby et al. 2014; Mummy et al. 2018). Importantly, several studies have now directly compared HP ^{3}He and ^{129}Xe with respect to repeatability and equivalency of the VDP measure. Both ^{3}He and ^{129}Xe MRI methods show highly repeatable defects in asthma (Svenningsen et al. 2013) and COPD (Stewart et al. 2018), with the former showing repeated measures of reversibility pre−/post-bronchodilation. Of note, there is a bias towards larger values of VDP for HP ^{129}Xe MRI vs. ^{3}He MRI in the same individual that is likely attributable to the higher Xe gas density, but fundamental relationships to lung disease and severity appear to be equivalent if not more pronounced for HP ^{129}Xe MRI (Kirby et al. 2013b; Stewart et al. 2018). Although not discussed in this chapter, the relatively high solubility of ^{129}Xe in the lung tissues and blood enables estimates of gas exchange, further enhancing the utility of this exciting technology (Mugler and Altes 2013).

Images of ventilation correspond to spin density weighting. Most pulse sequences used for HP gas MRI use fast spoiled gradient echo (SPGR) acquisitions with Cartesian, spiral and radial acquisitions and low flip angle (Wild et al. 2003) or variable flip angles matched to the acquisition time (Zhao and Albert 1998; Wild et al. 2006) to more efficiently use the nonrecoverable HP gas signal. Both 2D multi-slice (de Lange et al. 1999; Wild et al. 2002) and 3D volumetric (Wild et al. 2004; Holmes et al. 2008) SPGR imaging are commonly used (Table 3). Voxel sizes are typically anisotropic with higher in-plane resolution (~2–4 mm) than slice

Table 3 Typical methods and pulse sequences for HP ^{129}Xe MRI

Parameter	2D	3D	3D Dynamic
Pulse sequence	2D SPGR	3D SPGR	3D Stack of spirals[a] (or stack of stars)
FOV (cm)	~40	~40	32
Phase FOV (cm)	0.8–1	1.0	1.0
Matrix	96 × 96	128 × 128	128 × 128
Pixel size (mm)	4 × 4	4 × 4	3 × 3
No. of slices	15–20	14–17	13
Slice thickness (mm)	15	15	15
Flip angle (°)	9	Variable	10
TR/TE (ms)	8–20/2.2–4.2	6.7/1.5	23/0.05
BW (kHz)	4–16 kHz	16	128
Xe Dose volume (ml)	300–1000 in 1 L total (Remainder N2 gas)	500 in 1 L total (Remainder N2 or 4He gas)	1000 in 1 L total (>99% 129× e gas)
Breath-hold duration	15–25 s	15	20

SPGR spoiled gradient recalled echo
"Stack of Spirals" and "Stack of Stars" refer to hybrid non-Cartesian sampling methods with spiral (radial) trajectory sampling in-plane and phase encoding in the slice direction
[a]2.5 s temporal resolution with 8 × 3D frames in a 20 s breath-hold

resolution (~1 cm). Most time-resolved methods for dynamic ventilation methods use sequential fast GRE acquisitions with centric view orders to better capture temporal dynamics at specific time points (Fischer et al. 2004; Horn et al. 2014). Parallel imaging has been proposed (Lee et al. 2006) and used (Dregely et al. 2013; Emami et al. 2013; Kadlecek et al. 2013) but widespread implementation has been slowed by hardware challenges associated with multi-channel and multinuclear applications on most clinical MRI systems. Several investigators have explored fast time-resolved 2D radial (Wild et al. 2003), spiral (Salerno et al. 2001; Doganay et al. 2018b) or 3D radial spoiled GRE sequences with isotropic resolution (Holmes et al. 2009), and constrained reconstruction (Holmes et al. 2009; O'Halloran et al. 2010; Ajraoui et al. 2013). As gradient performance improves, bSSFP has become feasible with good performance demonstrated recently by exploiting the high data acquisition and SNR efficiency of bSSFP (Wild et al. 2006).

2.2.2 Perfluorinated Gases

The use of fluorinated gas MRI to investigate lung function was first proposed by Heidelberger and Lauterbur in 1982 (Heidelberger and Lauterbur 1982). ^{19}F gas images of a phantom and excised rat lungs were successfully acquired with a radial free induction decay (FID) type acquisition. Since then, several groups have continued to investigate the use of inert ^{19}F compounds for ventilation imaging, most typically tetrafluoromethane (CF4), sulfur hexafluoride (SF6), hexafluoroethane (C2F6), or octofluoropropane (C3F8). Fluorinated gases are an attractive choice because the ^{19}F isotope is 100% naturally abundant, with a high gyromagnetic ratio on the order of that of ^{1}H (Ruiz-Cabello et al. 2011) and short T1 recovery time. Moreover, there is negligible background fluorine in the body; the fluorinated gases used have low water solubility (Kuethe et al. 2000), resulting in very little diffusion into the blood. In contrast to hyperpolarized gas contrast agents, fluorinated gases do not require hyperpolarization. Since these gases are used in thermal equilibrium, there is no polarization decay for extended imaging with multiple breath studies. The generally low cost of these gases combined with these imaging advantages make ^{19}F a cheaper alternative to HP gas MRI for direct imaging of gas distribution in the lungs that is especially useful for direct imaging of dynamic ventilation.

The most commonly used gases in ^{19}F MRI are sulfur hexafluoride (SF_6) and hexafluoroethane

(C_2F_6). These molecules each possess six symmetric chemically equivalent fluorine atoms. T1 and T2 values at or near the 1.5 T field strength are less than 6 ms for C_2F_6, and as low as 2 ms for SF_6. Another ^{19}F molecule, octofluoropropane (C_3F_8), more commonly "perfluoropropane" or PFP for short, is of interest because it possesses two additional fluorine atoms, providing greater spin density. However, due to the asymmetric structure of the molecule, not all atoms are chemically equivalent. The two extra atoms bound to the central carbon atom are chemically shifted by 48 ppm compared to the other six. This results in an image offset stemming from chemical shift off-resonance in the frequency domain and must be carefully managed to avoid image distortion (Laukemper-Ostendorf et al. 2002). The T1 and T2 of C_3F_8 are similarly short: between 8–16 ms depending on gas concentration (Chang and Conradi 2006). In general, the T1 relaxation in ^{19}F gases is dominated by spin-rotation interactions (161), such that T1–T2. Both T1 and T2 decay times depend upon the concentration of the gas itself and are generally short, on the order of a few milliseconds for ^{19}F. The short T2 can result in significant transverse signal decay between the RF excitation and readout, especially if the TE is long, but this trade-off is mitigated by the rapid T1 recovery, allowing larger flip angles and favoring UTE MRI approaches (Table 4).

For static and dynamic ventilation imaging, 2D FLASH sequences have been most commonly used (163–166) due to their short TR and TE. However, 3D radial methods that enable ultrashort TE (UTE) and high data acquisition efficiency (Table 4) have desirable qualities in terms of mitigating T2* decay while providing a generally superior SNR due to the large number of signal averages per unit time (Couch et al. 2013). Center-out radial FID acquisitions have been used for both 3D static and dynamic ventilation imaging (Kuethe et al. 2000; Couch et al. 2013; Kuethe et al. 1998). Recent methods have focused on mixtures of 79% PFP and 21% O_2 mixed in a 1 L Tedlar bag and inhaled with imaging over a 15 s breath-hold or dynamic imaging approaches under free breathing from a 30 L reservoir bag via closed facemask (Gutberlet et al. 2018). The latter enables measures of gas washin and washout that captures more realistic regional ventilation as compared to a fixed breath-hold. The total acquisition time of the gas washout takes ~5 minutes (i.e., until no ^{19}F gas is left in the lungs) (Table 5).

Table 4 Typical methods and pulse sequences for lung ^{19}F-Fluorinated gas MRI

Parameter	3D Breath-hold	3D Dynamic
Pulse sequence	3D Radial UTE*	3D Stack of spirals** (or stack of stars)
FOV (cm)	~40	32
Phase FOV (cm)	0.8–1	1.0
Matrix	96 × 96	128 × 128
Pixel size (mm)	4 × 4	3 × 3
No. of slices	15–20	13
Slice thickness (mm)	15	15
Flip angle (degrees)	9	10
TR/TE (ms)	8–20/2.2–4.2	23/0.05
BW (kHz)	4–16 kHz	128
19F Dose and volume (ml)	79% perfluoropropane (PFP) in 1 L total (Remainder O_2 gas)	79% PFP and 21% Oxygen mixed in a 30 L reservoir bag with tidal breathing by the subject via closed facemask
Breath-hold duration	15–25 s	20

UTE Ultrashort echo time

*"3D radial" refers to radial projections acquired on a spherical geometry typically reconstructed with re-gridding in spatial frequency (i.e., *k*-space) onto a Cartesian coordinate system with isotropic spatial resolution

**"3D Stack of spirals" refers to 2D planar spirals acquired with phase encoding steps in the third dimension to sample *k*-space. The 2D spirals are re-gridded as for radial projections but usually with aniostropic spatial resolution compared to the phase encoded dimension

Table 5 Comparison of the major functional MRI used for imaging of ventilation

	HP He-3 MRI	HP Xe-129 MRI	F-19 MRI	OE MRI	FD MRI
SNR	High	High	Low	Low	Medium
Breath-hold vs. Free breathing	Breath-hold	Breath-hold	Both	Free breathing	Free breathing
Cost	Very high	Medium	Medium	Low	Low
Hardware requirement	High	High	Medium	Low	Low
IND required	Yes	Yes	Yes	No	No
Scan length	Seconds	Seconds	Seconds to Minutes	10–20 minutes	10–20 minutes
Measurements	VV, VDP	VV, VDP	VDP, tau_out, FV	PSE, VDP, DPO2, tau_in, tau_out, SV	VDP, FV
Multi-center Repeatability established	Yes	No	No	No	No
Weighting	Ventilation	Ventilation, gas exchange	Ventilation	Ventilation	Ventilation and Perfusion
Strengths	Regional measures of emphysema/gas trapping and airway occlusion have high sensitivity for longitudinal and interventional assessments	Regional measures of emphysema/gas trapping and airway occlusion have high sensitivity for longitudinal and interventional assessments. Ability to image gaseous and dissolved phases enables assessment of gas exchange	Regional measures of emphysema/gas trapping and airway occlusion	Can be performed using conventional coils without additional gas preparation/ handling hardware	Can be performed using conventional coils without additional gas preparation/ handling hardware

3 Clinical Research in Ventilation Imaging Using MRI

3.1 Asthma and COPD

Since its inception as a medical imaging technology in the early 2000s, hyperpolarized gas MRI has steadily advanced as a method for imaging chronic obstructive lung diseases. In asthma, VDP has shown particular promise as a simple yet strong biomarker of obstruction with excellent correspondence to CT images of lung structure and function (Fain et al. 2008); regional VDP corresponds with sites of increased airway wall thickness (Svenningsen et al. 2014), and air trapping (Fain et al. 2008 #216; Capaldi 2016 #1466) on CT imaging. VDP is also associated with asthma exacerbations (Mummy et al. 2018) and high levels of granulocytes (Svenningsen et al. 2018).

The VDP as a semiquantitative biomarker has potential to assist in phenotyping populations enriched for less stable disease (Mummy et al. 2018) and inflammatory phenotypes (Svenningsen et al. 2018), suggesting that HP ^{129}Xe MRI can be helpful to reduce sample size for new drug trials. This is supported by several blinded rigorous validation studies of salbutamol/albuterol bronchodilation (Svenningsen et al. 2013), leukotriene inhibition (Kruger et al. 2014b; Niles et al. 2013), and shows promise for biologic therapy (Svenningsen and Nair 2017). In combination, these small well-designed pilot trials support a strong role for VDP using hyperpolarized ^{129}Xe MRI to provide a useful regional measure of ventilation that is informative as both a prescriptive and monitoring biomarker than whole-lung tests and clinical control questionnaires.

Moreover, the regional information afforded by VDP has motivated novel therapy and mechanistic approaches that exploit the regional character and longitudinal imaging safety profile of ventilation on MRI. Specifically, HP gas MRI has been proposed for image-guided bronchial thermoplasty (Cox et al. 2007; Thomen et al. 2015) and for investigating inflammation and tissue remodeling regionally in asthma (Zha et al. 2018a; Mummy et al. 2018), as well as the characterization of extent of involvement by lobe and valve placement in COPD (Matin et al. 2017; Snell et al. 2003; Mata et al. 2011; Mathew et al. 2012a).

In COPD both HP gas MRI and OE MRI have made significant contributions. Ohno et al. have found that PSE on OE MRI is lower and more heterogeneous in emphysema subjects compared to healthy normal subjects (Ohno et al. 2002; Ohno and Hatabu 2007), and pioneered the value of dynamic OE MRI for detecting differences in lung diffusing capacity (Ohno et al. 2002). In addition, a later trial comparing PSE as measured with OE MRI to functional lung volume (FLV) as measured with CT (Ohno et al. 2008a) in a pool of 160 smokers showed that OE MRI yielded a superior correlation coefficient to pulmonary function tests. Furthermore, PSE as measured with OE MRI correlated with disease severity classifications for emphysema (citation).

HP gas MRI have been performed in COPD (Salerno et al. 2002; Kirby et al. 2010; Virgincar et al. 2013), with a growing number of recent studies focusing on cystic fibrosis (CF) in children and adults (Mentore et al. 2005; Kirby et al. 2011; Paulin et al. 2014). Perhaps the greatest advantage of pulmonary MRI is for characterizing, or "phenotyping," disease progression and severity. In a 2-year longitudinal study of subjects with mild to moderate COPD, VDP increased in the absence of significant change in forced expiratory volume in 1 s (FEV1), suggesting progression detected by imaging but not conventional methods (Kirby et al. 2010). Similar to findings in asthma, the VDP in particular is associated with severe outcomes such as hospitalizations for exacerbations in mild to moderate COPD—an association that is not observed using conventional measures, including CT (Kirby et al. 2014). This work suggests the potential use of HP gas MRI to identify patients most likely to have severe outcomes at an earlier stage of disease progression. This, in turn, could allow more aggressive treatment to be targeted at these higher-risk individuals (Kirby et al. 2013a).

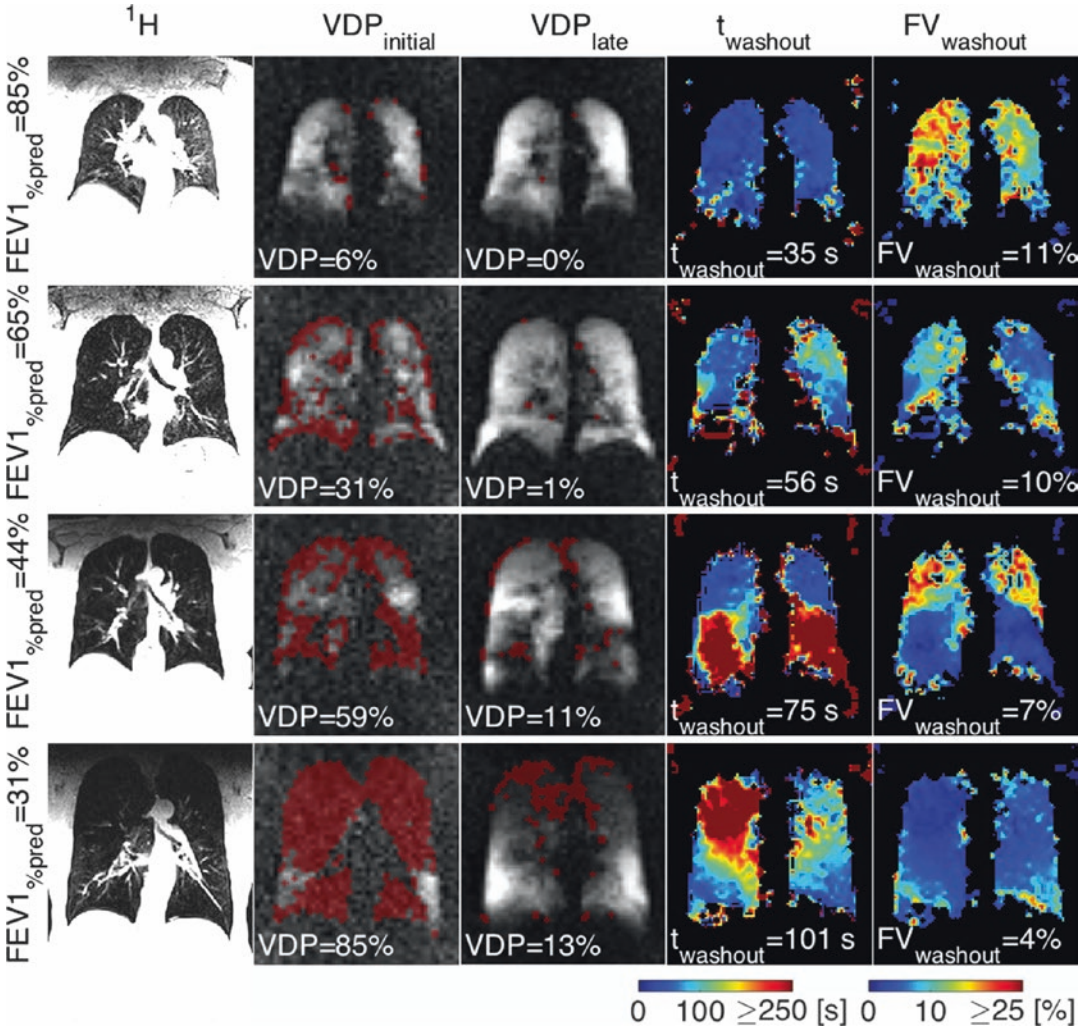


Fig. 6 Parametric images from dynamic ^{19}F MRI for four representative subjects (corresponding to GOLD stages I–IV from top to bottom row) demonstrating the percentage of lung involvement (VDP) differs markedly depending on early and late phase respiratory time points (VDP$_{initial}$ vs. VDP$_{late}$) due to delayed filling. Images show increased heterogeneity of regional lung ventilation with progression of disease for, from left to right, morphologic imaging, ventilation defect (red masks), and maps of washout times and FV assessed with dynamic ^{19}F gas washout MR imaging. Adapted from Gutberlet et al. (2018)

3.2 Clinical Research Using Dynamic Functional MRI

Building on the desire to characterize ventilation more fully than the binary depiction of ventilation defects, multiple dynamic methods based on OE, ^{19}F PFP, and HP ^{129}Xe MRI have been introduced. Recent work in COPD with dynamic ^{19}F MRI demonstrated the percentage of lung involvement differed markedly (Fig. 6) depending on when VDP was measured with respect to early and late phase respiratory time points due to delayed filling (Gutberlet et al. 2018). Multiple groups have pioneered dynamic measures derived using OE (Naish et al. 2005; Ohno et al. 2002) and ^{19}F (Halaweish et al. 2013; Gutberlet et al. 2018) MRI, including measurement of washout time and regional FV, with good repeatability

(Gutberlet et al. 2019) and increased sensitivity in asthma (Naish et al. 2005) and COPD (Ohno et al. 2002; Gutberlet et al. 2018). Dynamic modeling ^{19}F MRI of PFP gas signal washout results in highly repeatable FV and washout time measurements. FV derived from dynamic modeling of ^{19}F MRI of PFP washout is clearly reduced in COPD in these studies with expected regional apical predominance and strong correlation with global lung function (Gutberlet et al. 2019).

Using dynamic OE MRI, elegant mechanistic studies of obstruction and specific ventilation have been performed in healthy subjects under methacholine challenge to capture specific ventilation using the time course of several cycles of oxygen wash-in and washout. In similar dynamic OE studies, the oxygen wash-in slope was found to inversely correlate with $\%DL_{CO}$ in smoking-related COPD (Ohno et al. 2008b) and IPF (Muller et al. 2002). In a small study of mild/moderate and severe asthma, reduced oxygen wash-in time constant and mean peak enhancement were associated with greater severity (Kuo et al. 2014). In addition, in studies of lung volume reduction surgery candidates (Ohno et al. 2012) and asthma patients (Ohno et al. 2011, 2014), OE MRI showed equal or superior performance in detecting treatment effect and disease severity compared with PFT, CT, and/or nuclear medicine study. The OTF was shown to be highly reproducible (Triphan et al. 2017) and decrease in asthmatics after allergen challenge and correlated with the percentage of eosinophils in bronchoalveolar lavage at the site of challenge (Renne et al. 2015a).

Similarly, advances in fast stack of spirals imaging has enabled dynamic HP ^{129}Xe MRI that was found to strongly correlate on a lobar regional level with dynamic V/Q SPECT/CT using technetium 99 m DTPA (Doganay et al. 2018a), providing a strong regional validation of this approach that incorporates the high spatial resolution advantages of MRI with measures of gas wash-in and washout times. These methods demonstrate a maturation of the field with the potential to provide quantitative regional ventilation measures in the near future.

3.3 Pediatric Lung Disease: CF and Asthma

The lack of ionizing radiation using functional lung MRI has made it an exciting clinical research technique in cystic fibrosis and asthma, both important pediatric lung diseases. Studies in pediatric asthma have been limited (Teague et al. 2014) but show promise for detecting changes in VDP at early stages of disease and are likely to inform on the safe application of emerging biologic therapies in children (Altes et al. 2016) and improve understanding of the progression of asthma into adulthood (Cadman et al. 2013).

CF is an obstructive lung disease caused by infection, chronic inflammation, and mucus plugging due to the mutation in the cystic fibrosis transmembrane conductance regulator (CFTR) gene leading to impaired mucus clearance from the central airways. The genetic origin of this disease has an even more prominent pediatric component that leads to progressive loss of function due to chronic infection, inflammation, and airway mucus plugging. The consequence of these mechanisms of airway injury is highlighted in surveillance of subjects with CF in which areas of bronchiectasis and mucus plugging often correspond to perfusion defects that, unfortunately, become more prominent during and after exacerbation (Wielputz et al. 2014). Multiple small molecule "gain of function" drug therapies have been introduced in the past 5 years leading to promising improvements in some patients (Graeber et al. 2018) and the prospect of mitigating exacerbation events to stabilize function.

Multiple methodologies including proton-based and hyperpolarized gas techniques have shown promising results in small studies in CF. The development of small molecule therapies such as Ivacaftor have revolutionized the treatment of CF. HP ^{3}He MRI played an early role in characterizing the regional response to therapy in a small double blinded placebo-controlled study (Altes et al. 2017a). HP ^{3}He MRI revealed a strong regional response to therapy after 4 weeks, but also, interestingly, a return of defects at the same locations of the lungs 2 weeks of drug

washout (Fig. 5). The patterns observed point to a persistent injury in the lungs that is treatable but may not be totally reversible. These therapies are increasingly being delivered in younger patients where imaging methods would have value in establishing regional response (Altes et al. 2017a), especially in patients with less common CFTR mutations where benefit from the drugs targeting more common mutations may be assumed to have more marginal effect. Recently, the HP ^{129}Xe technique showed similar association with disease severity in studies of CF patients with average age of 12 years (Thomen et al. 2017; Rayment et al. 2019; Santyr et al. 2019). Besides its prominent role in CF, mucus plugging has also been implicated in central airway obstruction in asthma and could be another target for regional therapies guided by imaging (Dunican et al. 2018).

Proton-based methods, including FD and OE MRI methods, have been applied to early clinical research studies in CF. While HP gas MRI retains advantages for studies in very young children where the benefit of very rapid imaging during a short breath-hold or single tidal breath is required (Altes et al. 2017b), the free-breathing methods used by OE (Martini et al. 2018a, b) and FD MRI are generally well tolerated in children (Bauman et al. 2013a; Nyilas et al. 2018; Kaireit et al. 2017) and more widely available at CF centers. Short-term (1–2 day) repeatability of FV using the matrix pencil technique was very good (<5% difference) in 12 CF patients with mean age of 13 years (Bauman et al. 2013a; Nyilas et al. 2018). The use of DIR methods to estimate ventilation in CF using proton signal intensity (Fig. 2) has also showed promise in preliminary studies (Pennati et al. 2018).

In 2004, Jakob et al. (Arnold et al. 2004) measured the OTF (O'Sullivan et al. 2014) directly in a pool of 5 normal and 5 CF (Halaweish et al. 2013) subjects by repeating T1 measurements at various F_IO_2 using an IR-FLASH sequence. In normal subjects they found a homogeneous distribution of T1 under normoxic conditions, and a homogeneous decrease in T1 under hyperoxic conditions. However, CF subjects showed an inhomogeneous distribution of T1 under normoxic conditions. Under hyperoxic conditions the diseased lung regions (as measured with perfusion MRI) had a smaller OE-related decrease in T1 than the more normal lung regions. A recent study combining both the OTF and the FD technique corroborated these findings in a larger cohort of 16 CF patients with average age of 14 years (Kaireit et al. 2017). This study included an intervention with hypertonic saline therapy but did not detect difference between pre- and post-therapy images acquired 2 h after baseline. This result is consistent with an early study of hypertonic saline intervention using HP ^{3}He MRI (Mentore et al. 2005). Dynamic 3D OE MRI showed ΔPO_2, washout and wash-in times correlate with severity of pulmonary function tests and CT Brody score in an older cohort, median age of 25 years, of 21 CF patients (Martini et al. 2018a, b).

OE MRI with UTE (Zha et al. 2018b) using the VDP measure can also potentially overcome concerns about CT dose in pediatric patients and may provide a useful adjunct for more frequent longitudinal assessment in CF (Zha et al. 2019). An additional advantage of OE MRI using UTE is the inherent spatial alignment of the ventilation-weighted measures to structural UTE MRI (Fig. 7). This provides a means to gauge structure-function associations without interpolation errors associated with registration of parametric maps. For example, the juxtaposition of patterns of bronchiectasis and air trapping visualized on UTE with semiquantitative measures of regional ventilation defects from PSE maps depicts ventilation and perfusion defects local to areas of structural abnormality.

3.4 Applications in Lung Cancer

Lung cancer is the leading cause of cancer death in the world and 80% of all lung cancers are non-small cell carcinoma (NSCLC), which often are treated with thoracic radiotherapy. Loss of lung function, from tissue damage in surgery or radiation therapy, can lead to a lower quality of life following treatment.

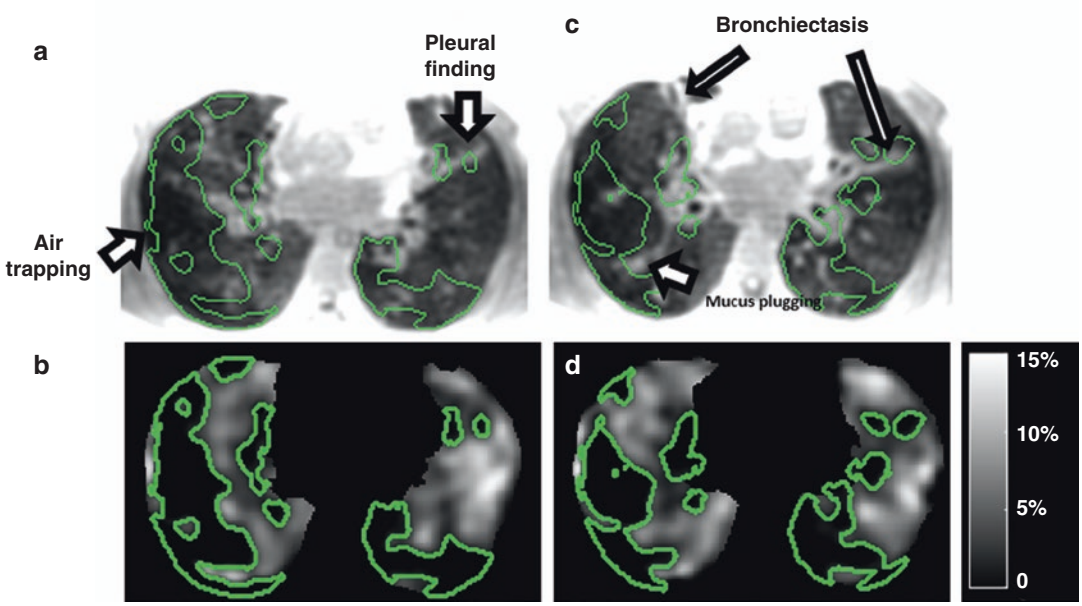


Fig. 7 The OE MRI derived using the same UTE images is spatially registered. Spatial associations between structural CF abnormalities on UTE MRI for a 37-year-old woman with cystic fibrosis (**a** & **c**) juxtaposed with (**b** & **d**) PSE defects on OE MRI simultaneously depict morphological (air trapping, pleural finding, bronchiectasis—arrows) and physiological (ventilation defects—green outline) abnormalities. Color bar indicates percent signal enhancement (PSE). Adapted from Torres et al. (2019)

Ohno et al. (2001) showed that mean PSE in 10 cancer subjects was lower than that in 7 healthy normal subjects, while the combination of cancer and emphysema in 8 subjects resulted in an even lower PSE. In an effort to segment localized ventilation defects, Nakagawa et al. (2001) compared OE MRI and contrast-enhanced perfusion MRI in 9 cancer and 6 pulmonary embolism (PE) subjects. The typical ventilation-perfusion mismatch expected in PE was observed. No ventilation defects were found in either case, even in the regions of clear perfusion defect shown on perfusion MRI. In a 2005 study of 30 cancer subjects, Ohno et al. (2005) demonstrated that OE-MRI was equal or superior to CT and nuclear scintigraphy in predicting post-surgical lung function as measured by FEV1.

Two commercial MRI-guided radiation therapy (RT) systems have been introduced: The Eleka Unity (https://www.elekta.com/unity), which uses a Phillips 1.5 T MRI system, and the ViewRay by MRIdian (https://viewray.com), which uses a Siemens 0.35 T MRI system. The MRIdian ViewRay is built around a low field magnet, which is favorable for lung MRI. There is potentially significant clinical benefit of integrating ventilation imaging into RT for reducing exposure of healthy ventilated lung tissues while increasing local dose to the lung tumor. As a consequence, there is an increasing clinical research focus on estimating ventilation from MRI lung images to guide radiation dose treatment planning in lung cancer with early efforts employing HP ^{3}He MRI (Ireland et al. 2007, 2008; Bates et al. 2009; Hodge et al. 2010; Tahir et al. 2014; Cai et al. 2011). Recently, focus has shifted to DIR techniques first introduced with 4DCT that use the Jacobian to estimate regional ventilation with comparison to HP ^{129}Xe MRI (Tahir et al. 2018). The development of UTE MRI introduces the possibility of applying similar DIR techniques to estimate regional ventilation also using the Jacobian in analogy to 4DCT. The application of these techniques to MRI-guided radiotherapy systems would allow tracking of ventilation changes at each radiation treatment.

4 Summary of Ventilation Imaging Using MRI

Prospective clinical studies in adults and children have recently multiplied as multiple MRI sources of ventilation contrast outlined above have become widely available. An array of methods to choose from with overlapping strengths and weaknesses have been shown to be feasible, repeatable, and valid compared to global and other image-based functional imaging methods. In general, MRI techniques play an important role in studying response to novel therapies where CT is a major concern. The primary impediment to integrating MRI methods into therapy monitoring across centers is standardization.

The various MRI approaches to measure regional ventilation have different strengths and weaknesses. The HP gas MRI techniques provide high SNR, can be used to image a short breath-hold, and, in the case of ^{3}He, have an established track record for repeatability in multi-center studies (e.g., Niles et al. 2013). The challenge of multi-center repeatability remains for all of the remaining techniques, although studies are underway including at least one expert group with chartered goal of improving and developing standards for quantitative biomarkers using HP ^{129}Xe (https://cpir.cchmc.org/XeMRICTC). Given the substantial benefits of other approaches, primarily in terms of reduced costs and complexity, similar efforts to establish utility across multi-center networks are warranted. In the short term, it is likely that different approaches will have utility for different applications depending on availability of hardware and MRI scanner make and model since access to disease populations will not always correspond to advanced technologies. In the long term, establishing a single method for lung ventilation imaging using MRI will require substantial cooperation and investment by the research and clinical communities and will therefore depend on the emergence of a strong clinical motivation for ventilation MRI that will most likely be in applications to pediatric disease.

Recently the minimal clinically important difference (MCID) of the VDP biomarker on HP ^{3}He MRI was estimated from cross-sectional data (Eddy et al. 2018) to be 4% by anchoring to the MCID of the asthma control questionnaire (ACQ). This value suggests a sensitivity that is comparable to FEV1%predicted, and given the additional advantages of direct regional information and possible increased sensitivity with the denser ^{129}Xe gas, VDP seems well poised as a possible endpoint for clinical therapy trials in asthma.

The field in general lacks larger scale repeatability studies, which should be a major focus of future research efforts. There is also a lack of clarity concerning which techniques can be used for clinical application and in what settings. The ongoing dissemination of functional lung MRI methods beyond the specialized institutions where they have been developed will, in general, lead to a better characterization of the performance and relative strengths and weaknesses of the techniques presented in this chapter. In conclusion, advances in functional lung MRI have brought the field on the brink of dissemination of the most promising methods raising the potential for clinical relevance, particularly for improving therapy of pediatric lung diseases.

Glossary

ACQ	Asthma Control Questionnaire
CF	Cystic Fibrosis
CNR	Contrast-to-Noise Ratio
COPD	Chronic Obstructive Pulmonary Disease
CT	Computed Tomography
DIR	Deformable Image Registration
FD	Fourier Decomposition
FEV1	Forced Expiratory Volume in 1 second
FIO_2	Fractional Inhaled Oxygen
FRC	Functional Residual Capacity
FSE	Fast Spin Echo
FV	Fractional Ventilation
FVC	Forced Vital Capacity
FLASH	Fast Low-Angle Shot

Gd	Gadolinium
^{3}He	Helium-3 gas isotope
HP	Hyperpolarized
HASTE	Half-Acquisition with Short Echo Time
ICC	Intra-Class Correlation
IR	Inversion Recovery
MCID	Minimum Clinically Important Difference
MRI	Magnetic Resonance Imaging
OE	Oxygen Enhanced
OTF	Oxygen Transfer Function
PFT	Pulmonary Function Test
RT	Radiation Therapy
SNR	Signal-to-Noise Ratio
SV	Specific Ventilation
SPECT	Single Photon Emission Computed Tomography
SPGR	Spoiled Gradient Echo
SSFSE	Single-Shot Fast Spin Echo
T1	Longitudinal Recovery Time
T2*	Nonrecoverable Transverse Signal Decay Time
TE	Echo Time
TLC	Total Lung Capacity
UTE	Ultrashort Echo Time
VDP	Ventilation Defect Percentage
V_f	Volume of fresh air
V/Q	Ventilation-to-Perfusion ratio
V_r	Reference volume
VV	Ventilated Volume
^{129}Xe	Xenon-129 gas isotope

References

Ajraoui S, Parra-Robles J, Wild JM (2013) Incorporation of prior knowledge in compressed sensing for faster acquisition of hyperpolarized gas images. Magn Reson Med 69(2):360–369. https://doi.org/10.1002/mrm.24252

Altes TA, Gersbach JC, Mata JF, Mugler JPM III, Brookeman JR, Lange EE (2007) Evaluation of the safety of hyperpolarized helium-3 gas as an inhaled contrast agent for MRI. Proc Intl Soc Mag Reson Med 15:1305. Seattle, WA

Altes TA, Johnson M, Fidler M, Botfield M, Tustison NJ, Leiva-Salinas C, de Lange EE, Froh D, Mugler JP 3rd (2017a) Use of hyperpolarized helium-3 MRI to assess response to ivacaftor treatment in patients with cystic fibrosis. J Cyst Fibros 16(2):267–274. https://doi.org/10.1016/j.jcf.2016.12.004

Altes TA, Mata J, de Lange EE, Brookeman JR, Mugler JP 3rd (2006) Assessment of lung development using hyperpolarized helium-3 diffusion MR imaging. J Magn Reson Imaging 24(6):1277–1283. https://doi.org/10.1002/jmri.20723

Altes TA, Meyer CH, Mata JF, Froh DK, Paget-Brown A, Gerald Teague W, Fain SB, de Lange EE, Ruppert K, Botfield MC, Johnson MA, Mugler JP 3rd (2017b) Hyperpolarized helium-3 magnetic resonance lung imaging of non-sedated infants and young children: a proof-of-concept study. Clin Imaging 45:105–110. https://doi.org/10.1016/j.clinimag.2017.04.004

Altes TA, Mugler JP 3rd, Ruppert K, Tustison NJ, Gersbach J, Szentpetery S, Meyer CH, de Lange EE, Teague WG (2016) Clinical correlates of lung ventilation defects in asthmatic children. J Allergy Clin Immunol 137(3):789–796. e787. https://doi.org/10.1016/j.jaci.2015.08.045

Arai TJ, Horn FC, Sa RC, Rao MR, Collier GJ, Theilmann RJ, Prisk GK, Wild JM (2018) Comparison of quantitative multiple-breath specific ventilation imaging using colocalized 2D oxygen-enhanced MRI and hyperpolarized (3)He MRI. J Appl Physiol 125(5):1526–1535. https://doi.org/10.1152/japplphysiol.00500.2017

Arnold JF, Fidler F, Wang T, Pracht ED, Schmidt M, Jakob PM (2004) Imaging lung function using rapid dynamic acquisition of T1-maps during oxygen enhancement. MAGMA 16(5):246–253. https://doi.org/10.1007/s10334-004-0034-z

Bates EL, Bragg CM, Wild JM, Hatton MQ, Ireland RH (2009) Functional image-based radiotherapy planning for non-small cell lung cancer: A simulation study. Radiother Oncol 93(1):32–36. https://doi.org/10.1016/j.radonc.2009.05.018

Bauman G, Bieri O (2017) Matrix pencil decomposition of time-resolved proton MRI for robust and improved assessment of pulmonary ventilation and perfusion. Magn Reson Med 77(1):336–342. https://doi.org/10.1002/mrm.26096

Bauman G, Puderbach M, Deimling M, Jellus V, Chefd'hotel C, Dinkel J, Hintze C, Kauczor HU, Schad LR (2009) Non-contrast-enhanced perfusion and ventilation assessment of the human lung by means of fourier decomposition in proton MRI. Magn Reson Med 62(3):656–664. https://doi.org/10.1002/mrm.22031

Bauman G, Puderbach M, Heimann T, Kopp-Schneider A, Fritzsching E, Mall MA, Eichinger M (2013a) Validation of Fourier decomposition MRI with dynamic contrast-enhanced MRI using visual and automated scoring of pulmonary perfusion in young cystic fibrosis patients. Eur J Radiol 82(12):2371–2377. https://doi.org/10.1016/j.ejrad.2013.08.018

Bauman G, Pusterla O, Bieri O (2019) Functional lung imaging with transient spoiled gradient echo. Magn Reson Med 81(3):1915–1923. https://doi.org/10.1002/mrm.27535

Bauman G, Pusterla O, Santini F, Bieri O (2018) Dynamic and steady-state oxygen-dependent lung relaxometry using inversion recovery ultra-fast steady-state

free precession imaging at 1.5 T. Magn Reson Med 79(2):839–845. https://doi.org/10.1002/mrm.26739

Bauman G, Scholz A, Rivoire J, Terekhov M, Friedrich J, de Oliveira A, Semmler W, Schreiber LM, Puderbach M (2013b) Lung ventilation- and perfusion-weighted Fourier decomposition magnetic resonance imaging: in vivo validation with hyperpolarized 3He and dynamic contrast-enhanced MRI. Magn Reson Med 69(1):229–237. https://doi.org/10.1002/mrm.24236

Brennan D, Schubert L, Diot Q, Castillo R, Castillo E, Guerrero T, Martel MK, Linderman D, Gaspar LE, Miften M, Kavanagh BD, Vinogradskiy Y (2015) Clinical validation of 4-dimensional computed tomography ventilation with pulmonary function test data. Int J Radiat Oncol Biol Phys 92(2):423–429. https://doi.org/10.1016/j.ijrobp.2015.01.019

Cadman RV, Lemanske RF Jr, Evans MD, Jackson DJ, Gern JE, Sorkness RL, Fain SB (2013) Pulmonary 3He magnetic resonance imaging of childhood asthma. J Allergy Clin Immunol 131(2):369–376. e361–365. https://doi.org/10.1016/j.jaci.2012.10.032

Cai J, McLawhorn R, Altes TA, de Lange E, Read PW, Larner JM, Benedict SH, Sheng K (2011) Helical tomotherapy planning for lung cancer based on ventilation magnetic resonance imaging. Med Dosim 36(4):389–396. https://doi.org/10.1016/j.meddos.2010.09.008

Capaldi DP, Sheikh K, Guo F, Svenningsen S, Etemad-Rezai R, Coxson HO, Leipsic JA, McCormack DG, Parraga G (2015) Free-breathing pulmonary ^{1}H and hyperpolarized 3He MRI: comparison in COPD and bronchiectasis. Acad Radiol 22(3):320–329. https://doi.org/10.1016/j.acra.2014.10.003

Capaldi DP, Zha N, Guo F, Pike D, McCormack DG, Kirby M, Parraga G (2016) Pulmonary Imaging Biomarkers of Gas Trapping and Emphysema in COPD: (3)He MR Imaging and CT Parametric Response Maps. Radiology 279(2):597–608. https://doi.org/10.1148/radiol.2015151484

Capaldi DPI, Eddy RL, Svenningsen S, Guo F, Baxter JSH, McLeod AJ, Nair P, McCormack DG, Parraga G, Canadian Respiratory Research N (2018) Free-breathing pulmonary MR imaging to quantify regional ventilation. Radiology 287(2):693–704. https://doi.org/10.1148/radiol.2018171993

Castillo E, Castillo R, Vinogradskiy Y, Guerrero T (2017) The numerical stability of transformation-based CT ventilation. Int J Comput Assist Radiol Surg 12(4):569–580. https://doi.org/10.1007/s11548-016-1509-x

Chang YV, Conradi MS (2006) Relaxation and diffusion of perfluorocarbon gas mixtures with oxygen for lung MRI. J Magn Reson 181(2):191–198. https://doi.org/10.1016/j.jmr.2006.04.003

Chen Q, Jakob PM, Griswold MA, Levin DL, Hatabu H, Edelman RR (1998) Oxygen enhanced MR ventilation imaging of the lung. MAGMA 7(3):153–161

Chen Q, Levin DL, Kim D, David V, McNicholas M, Chen V, Jakob PM, Griswold MA, Goldfarb JW, Hatabu H, Edelman RR (1999) Pulmonary disorders: ventilation-perfusion MR imaging with animal models. Radiology 213(3):871–879. https://doi.org/10.1148/radiology.213.3.r99dc31871

Couch MJ, Ball IK, Li T, Fox MS, Littlefield SL, Biman B, Albert MS (2013) Pulmonary ultrashort echo time 19F MR imaging with inhaled fluorinated gas mixtures in healthy volunteers: feasibility. Radiology 269(3):903–909. https://doi.org/10.1148/radiol.13130609

Cox G, Thomson NC, Rubin AS, Niven RM, Corris PA, Siersted HC, Olivenstein R, Pavord ID, McCormack D, Chaudhuri R, Miller JD, Laviolette M, Group AIRTS (2007) Asthma control during the year after bronchial thermoplasty. N Engl J Med 356(13):1327–1337. https://doi.org/10.1056/NEJMoa064707

de Lange EE, Altes TA, Patrie JT, Battiston JJ, Juersivich AP, Mugler JP 3rd, Platts-Mills TA (2009) Changes in regional airflow obstruction over time in the lungs of patients with asthma: evaluation with 3He MR imaging. Radiology 250(2):567–575. https://doi.org/10.1148/radiol.2502080188

de Lange EE, Altes TA, Patrie JT, Gaare JD, Knake JJ, Mugler JP 3rd, Platts-Mills TA (2006) Evaluation of asthma with hyperpolarized helium-3 MRI: correlation with clinical severity and spirometry. Chest 130(4):1055–1062. https://doi.org/10.1378/chest.130.4.1055

de Lange EE, Mugler JP 3rd, Brookeman JR, Knight-Scott J, Truwit JD, Teates CD, Daniel TM, Bogorad PL, Cates GD (1999) Lung air spaces: MR imaging evaluation with hyperpolarized 3He gas. Radiology 210(3):851–857. https://doi.org/10.1148/radiology.210.3.r99fe08851

Dietrich O, Attenberger UI, Ingrisch M, Maxien D, Peller M, Nikolaou K, Reiser MF (2010) Analysis of signal dynamics in oxygen-enhanced magnetic resonance imaging. Investig Radiol 45(4):165–173. https://doi.org/10.1097/RLI.0b013e3181cd74e2

Dietrich O, Losert C, Attenberger U, Fasol U, Peller M, Nikolaou K, Reiser MF, Schoenberg SO (2005) Fast oxygen-enhanced multislice imaging of the lung using parallel acquisition techniques. Magn Reson Med 53(6):1317–1325. https://doi.org/10.1002/mrm.20495

Doganay O, Matin T, Chen M, Kim M, McIntyre A, McGowan DR, Bradley KM, Povey T, Gleeson FV (2018a) Time-series hyperpolarized xenon-129 MRI of lobar lung ventilation of COPD in comparison to V/Q-SPECT/CT and CT. Eur Radiol. https://doi.org/10.1007/s00330-018-5888-y

Doganay O, Matin TN, McIntyre A, Burns B, Schulte RF, Gleeson FV, Bulte D (2018b) Fast dynamic ventilation MRI of hyperpolarized (129) Xe using spiral imaging. Magn Reson Med 79(5):2597–2606. https://doi.org/10.1002/mrm.26912

Dregely I, Ruset IC, Wiggins G, Mareyam A, Mugler JP 3rd, Altes TA, Meyer C, Ruppert K, Wald LL, Hersman FW (2013) 32-channel phased-array receive with asymmetric birdcage transmit coil for hyperpolarized xenon-129 lung imaging. Magn Reson Med 70(2):576–583. https://doi.org/10.1002/mrm.24482

Driehuys B, Martinez-Jimenez S, Cleveland ZI, Metz GM, Beaver DM, Nouls JC, Kaushik SS, Firszt R, Willis C, Kelly KT, Wolber J, Kraft M, McAdams HP (2012) Chronic obstructive pulmonary disease: safety and tolerability of hyperpolarized 129Xe MR imaging in healthy volunteers and patients. Radiology 262(1):279–289. https://doi.org/10.1148/radiol.11102172

Dripps RD, Comroe JH (1947) The effect of inhalation of high and of low oxygen concentration upon human respiration and circulation. Am J Med Sci 213(2):248

Dunican EM, Elicker BM, Gierada DS, Nagle SK, Schiebler ML, Newell JD, Raymond WW, Lachowicz-Scroggins ME, Di Maio S, Hoffman EA, Castro M, Fain SB, Jarjour NN, Israel E, Levy BD, Erzurum SC, Wenzel SE, Meyers DA, Bleecker ER, Phillips BR, Mauger DT, Gordon ED, Woodruff PG, Peters MC, Fahy JV, National Heart L, Blood Institute Severe Asthma Research P (2018) Mucus plugs in patients with asthma linked to eosinophilia and airflow obstruction. J Clin Invest 128(3):997–1009. https://doi.org/10.1172/JCI95693

Ebner L, Kammerman J, Driehuys B, Schiebler ML, Cadman RV, Fain SB (2017) The role of hyperpolarized (129)xenon in MR imaging of pulmonary function. Eur J Radiol 86:343–352. https://doi.org/10.1016/j.ejrad.2016.09.015

Eddy RL, Svenningsen S, McCormack DG, Parraga G (2018) What is the minimal clinically important difference for helium-3 magnetic resonance imaging ventilation defects? Eur Respir J 51(6). https://doi.org/10.1183/13993003.00324-2018

Edelman RR, Hatabu H, Tadamura E, Li W, Prasad PV (1996) Noninvasive assessment of regional ventilation in the human lung using oxygen-enhanced magnetic resonance imaging. Nat Med 2(11):1236–1239

Emami K, Xu Y, Hamedani H, Profka H, Kadlecek S, Xin Y, Ishii M, Rizi RR (2013) Accelerated fractional ventilation imaging with hyperpolarized Gas MRI. Magn Reson Med. https://doi.org/10.1002/mrm.24582

Fain S, Schiebler ML, McCormack DG, Parraga G (2010) Imaging of lung function using hyperpolarized helium-3 magnetic resonance imaging: Review of current and emerging translational methods and applications. J Magn Reson Imaging 32(6):1398–1408. https://doi.org/10.1002/jmri.22375

Fain SB, Gonzalez-Fernandez G, Peterson ET, Evans MD, Sorkness RL, Jarjour NN, Busse WW, Kuhlman JE (2008) Evaluation of structure-function relationships in asthma using multidetector CT and hyperpolarized He-3 MRI. Acad Radiol 15(6):753–762. https://doi.org/10.1016/j.acra.2007.10.019

Fischer A, Weick S, Ritter CO, Beer M, Wirth C, Hebestreit H, Jakob PM, Hahn D, Bley T, Kostler H (2014) SElf-gated Non-Contrast-Enhanced FUnctional Lung imaging (SENCEFUL) using a quasi-random fast low-angle shot (FLASH) sequence and proton MRI. NMR Biomed 27(8):907–917. https://doi.org/10.1002/nbm.3134

Fischer MC, Spector ZZ, Ishii M, Yu J, Emami K, Itkin M, Rizi R (2004) Single-acquisition sequence for the measurement of oxygen partial pressure by hyperpolarized gas MRI. Magn Reson Med 52(4):766–773. https://doi.org/10.1002/mrm.20239

Freeman MS, Emami K, Driehuys B (2014) Characterizing and modeling the efficiency limits in large-scale production of hyperpolarized (129)Xe. Phys Rev A 90(2):023406

Glenny RW (2009) Determinants of regional ventilation and blood flow in the lung. Intensive Care Med 35(11):1833–1842. https://doi.org/10.1007/s00134-009-1649-3

Graeber SY, Dopfer C, Naehrlich L, Gyulumyan L, Scheuermann H, Hirtz S, Wege S, Mairbaurl H, Dorda M, Hyde R, Bagheri-Hanson A, Rueckes-Nilges C, Fischer S, Mall MA, Tummler B (2018) effects of lumacaftor-ivacaftor therapy on cystic fibrosis transmembrane conductance regulator function in Phe508del homozygous patients with cystic fibrosis. Am J Respir Crit Care Med 197(11):1433–1442. https://doi.org/10.1164/rccm.201710-1983OC

Gutberlet M, Kaireit TF, Voskrebenzev A, Kern AL, Obert A, Wacker F, Hohlfeld JM, Vogel-Claussen J (2019) Repeatability of regional lung ventilation quantification using fluorinated ((19)F) gas magnetic resonance imaging. Acad Radiol 26(3):395–403. https://doi.org/10.1016/j.acra.2018.10.021

Gutberlet M, Kaireit TF, Voskrebenzev A, Lasch F, Freise J, Welte T, Wacker F, Hohlfeld JM, Vogel-Claussen J (2018) Free-breathing dynamic (19)F gas MR imaging for mapping of regional lung ventilation in patients with COPD. Radiology 286(3):1040–1051. https://doi.org/10.1148/radiol.2017170591

Halaweish AF, Moon RE, Foster WM, Soher BJ, McAdams HP, MacFall JR, Ainslie MD, MacIntyre NR, Charles HC (2013) Perfluoropropane gas as a magnetic resonance lung imaging contrast agent in humans. Chest 144(4):1300–1310. https://doi.org/10.1378/chest.12-2597

Hatabu H, Tadamura E, Chen Q, Stock KW, Li W, Prasad PV, Edelman RR (2001) Pulmonary ventilation: dynamic MRI with inhalation of molecular oxygen. Eur J Radiol 37(3):172–178

He M, Driehuys B, Que LG, Huang YT (2016) Using hyperpolarized (129)Xe MRI to quantify the pulmonary ventilation distribution. Acad Radiol 23(12):1521–1531. https://doi.org/10.1016/j.acra.2016.07.014

He M, Zha W, Tan F, Rankine L, Fain S, Driehuys B (2018) A comparison of two hyperpolarized (129)Xe MRI ventilation quantification pipelines: the effect of signal to noise ratio. Acad Radiol. https://doi.org/10.1016/j.acra.2018.08.015

Heidelberger E, Lauterbur E (1982) PC gas phase 19F-NMR zeugmatography: a new approach to lung

ventilation imaging. In: Proceedings of the 1st Annual Meeting ISMRM, Boston, MA

Hersman FW, Ruset IC, Ketel S, Muradian I, Covrig SD, Distelbrink J, Porter W, Watt D, Ketel J, Brackett J, Hope A, Patz S (2008) Large production system for hyperpolarized 129Xe for human lung imaging studies. Acad Radiol 15(6):683–692. https://doi.org/10.1016/j.acra.2007.09.020

Hodge CW, Tome WA, Fain SB, Bentzen SM, Mehta MP (2010) On the use of hyperpolarized helium MRI for conformal avoidance lung radiotherapy. Med Dosim 35(4):297–303. https://doi.org/10.1016/j.meddos.2009.09.004

Holmes JH, O'Halloran RL, Brodsky EK, Bley TA, Francois CJ, Velikina JV, Sorkness RL, Busse WW, Fain SB (2009) Three-dimensional imaging of ventilation dynamics in asthmatics using multiecho projection acquisition with constrained reconstruction. Magn Reson Med 62(6):1543–1556. https://doi.org/10.1002/mrm.22150

Holmes JH, O'Halloran RL, Brodsky EK, Jung Y, Block WF, Fain SB (2008) 3D hyperpolarized He-3 MRI of ventilation using a multi-echo projection acquisition. Magn Reson Med 59(5):1062–1071. https://doi.org/10.1002/mrm.21437

Hopkins SR, Henderson AC, Levin DL, Yamada K, Arai T, Buxton RB, Prisk GK (2007) Vertical gradients in regional lung density and perfusion in the supine human lung: the Slinky effect. J Appl Physiol 103(1):240–248. https://doi.org/10.1152/japplphysiol.01289.2006

Horn FC, Deppe MH, Marshall H, Parra-Robles J, Wild JM (2014) Quantification of regional fractional ventilation in human subjects by measurement of hyperpolarized 3He washout with 2D and 3D MRI. J Appl Physiol 116(2):129–139. https://doi.org/10.1152/japplphysiol.00378.2013

Ireland RH, Bragg CM, McJury M, Woodhouse N, Fichele S, van Beek EJ, Wild JM, Hatton MQ (2007) Feasibility of image registration and intensity-modulated radiotherapy planning with hyperpolarized helium-3 magnetic resonance imaging for non-small-cell lung cancer. Int J Radiat Oncol Biol Phys 68(1):273–281. https://doi.org/10.1016/j.ijrobp.2006.12.068

Ireland RH, Woodhouse N, Hoggard N, Swinscoe JA, Foran BH, Hatton MQ, Wild JM (2008) An image acquisition and registration strategy for the fusion of hyperpolarized helium-3 MRI and x-ray CT images of the lung. Phys Med Biol 53(21):6055–6063. https://doi.org/10.1088/0031-9155/53/21/011

Jakob PM, Hillenbrand CM, Wang T, Schultz G, Hahn D, Haase A (2001) Rapid quantitative lung (1)H T(1) mapping. J Magn Reson Imaging 14(6):795–799. https://doi.org/10.1002/jmri.10024

Jakob PM, Wang T, Schultz G, Hebestreit H, Hebestreit A, Hahn D (2004) Assessment of human pulmonary function using oxygen-enhanced T(1) imaging in patients with cystic fibrosis. Magn Reson Med 51(5):1009–1016. https://doi.org/10.1002/mrm.20051

Johnson KM, Fain SB, Schiebler ML, Nagle S (2012) Optimized 3D ultrashort echo time pulmonary MRI. Magn Reson Med. https://doi.org/10.1002/mrm.24570

Kadlecek S, Hamedani H, Xu Y, Emami K, Xin Y, Ishii M, Rizi R (2013) Regional alveolar partial pressure of oxygen measurement with parallel accelerated hyperpolarized gas MRI. Acad Radiol 20(10):1224–1233. https://doi.org/10.1016/j.acra.2013.07.002

Kaireit TF, Gutberlet M, Voskrebenzev A, Freise J, Welte T, Hohlfeld JM, Wacker F, Vogel-Claussen J (2018) Comparison of quantitative regional ventilation-weighted fourier decomposition MRI with dynamic fluorinated gas washout MRI and lung function testing in COPD patients. J Magn Reson Imaging 47(6):1534–1541. https://doi.org/10.1002/jmri.25902

Kaireit TF, Sorrentino SA, Renne J, Schoenfeld C, Voskrebenzev A, Gutberlet M, Schulz A, Jakob PM, Hansen G, Wacker F, Welte T, Tummler B, Vogel-Claussen J (2017) Functional lung MRI for regional monitoring of patients with cystic fibrosis. PLoS One 12(12):e0187483. https://doi.org/10.1371/journal.pone.0187483

Kirby M, Eddy RL, Pike D, Svenningsen S, Coxson HO, Sin DD, McCormack DG, Parraga G, Canadian Respiratory Research N (2017) MRI ventilation abnormalities predict quality-of-life and lung function changes in mild-to-moderate COPD: longitudinal TINCan study. Thorax 72(5):475–477. https://doi.org/10.1136/thoraxjnl-2016-209770

Kirby M, Heydarian M, Svenningsen S, Wheatley A, McCormack DG, Etemad-Rezai R, Parraga G (2012) Hyperpolarized 3He magnetic resonance functional imaging semiautomated segmentation. Acad Radiol 19(2):141–152. https://doi.org/10.1016/j.acra.2011.10.007

Kirby M, Kanhere N, Etemad-Rezai R, McCormack DG, Parraga G (2013a) Hyperpolarized helium-3 magnetic resonance imaging of chronic obstructive pulmonary disease exacerbation. J Magn Reson Imaging 37(5):1223–1227. https://doi.org/10.1002/jmri.23896

Kirby M, Mathew L, Wheatley A, Santyr GE, McCormack DG, Parraga G (2010) Chronic obstructive pulmonary disease: longitudinal hyperpolarized (3)He MR imaging. Radiology 256(1):280–289. https://doi.org/10.1148/radiol.10091937

Kirby M, Parraga G (2013) Pulmonary functional imaging using hyperpolarized noble gas MRI: six years of start-up experience at a single site. Acad Radiol 20(11):1344–1356. https://doi.org/10.1016/j.acra.2013.02.020

Kirby M, Pike D, Coxson HO, McCormack DG, Parraga G (2014) Hyperpolarized (3)he ventilation defects used to predict pulmonary exacerbations in mild to moderate chronic obstructive pulmonary disease. Radiology 273(3):887–896. https://doi.org/10.1148/radiol.14140161

Kirby M, Svenningsen S, Ahmed H, Wheatley A, Etemad-Rezai R, Paterson NA, Parraga G (2011) Quantitative evaluation of hyperpolarized helium-3 magnetic

resonance imaging of lung function variability in cystic fibrosis. Acad Radiol 18(8):1006–1013. https://doi.org/10.1016/j.acra.2011.03.005

Kirby M, Svenningsen S, Kanhere N, Owrangi A, Wheatley A, Coxson HO, Santyr GE, Paterson NA, McCormack DG, Parraga G (2013b) Pulmonary ventilation visualized using hyperpolarized helium-3 and xenon-129 magnetic resonance imaging: differences in COPD and relationship to emphysema. J Appl Physiol 114(6):707–715. https://doi.org/10.1152/japplphysiol.01206.2012

Kruger SJ, Fain SB, Johnson KM, Cadman RV, Nagle SK (2014a) Oxygen-enhanced 3D radial ultrashort echo time magnetic resonance imaging in the healthy human lung. NMR Biomed. https://doi.org/10.1002/nbm.3158

Kruger SJ, Nagle SK, Couch MJ, Ohno Y, Albert M, Fain SB (2016) Functional imaging of the lungs with gas agents. J Magn Reson Imaging 43(2):295–315. https://doi.org/10.1002/jmri.25002

Kruger SJ, Niles DJ, Dardzinski B, Harman A, Jarjour NN, Ruddy M, Nagle SK, Francois CJ, Sorkness RL, Burton RM, Munoz del Rio A, Fain SB (2014b) Hyperpolarized Helium-3 MRI of exercise-induced bronchoconstriction during challenge and therapy. J Magn Reson Imaging 39(5):1230–1237. https://doi.org/10.1002/jmri.24272

Kuethe DO, Caprihan A, Fukushima E, Waggoner RA (1998) Imaging lungs using inert fluorinated gases. Magn Reson Med 39(1):85–88

Kuethe DO, Caprihan A, Gach HM, Lowe IJ, Fukushima E (2000) Imaging obstructed ventilation with NMR using inert fluorinated gases. J Appl Physiol 88(6):2279–2286

Kuo W, Ciet P, Tiddens HA, Zhang W, Guillerman RP, van Straten M (2014) Monitoring cystic fibrosis lung disease by computed tomography. Radiation risk in perspective. Am J Respir Crit Care Med 189(11):1328–1336. https://doi.org/10.1164/rccm.201311-2099CI

Laukemper-Ostendorf S, Scholz A, Burger K, Heussel CP, Schmittner M, Weiler N, Markstaller K, Eberle B, Kauxczor HU, Quintel M, Thelen M, Schreiber WG (2002) 19F-MRI of perflubron for measurement of oxygen partial pressure in porcine lungs during partial liquid ventilation. Magn Reson Med 47(1):82–89

Lee RF, Johnson G, Grossman RI, Stoeckel B, Trampel R, McGuinness G (2006) Advantages of parallel imaging in conjunction with hyperpolarized helium—a new approach to MRI of the lung. Magn Reson Med 55(5):1132–1141. https://doi.org/10.1002/mrm.20855

Lewis SM, Evans JW, Jalowayski AA (1978) Continuous distributions of specific ventilation recovered from inert gas washout. J Appl Physiol Respir Environ Exerc Physiol 44(3):416–423. https://doi.org/10.1152/jappl.1978.44.3.416

Liszewski MC, Hersman FW, Altes TA, Ohno Y, Ciet P, Warfield SK, Lee EY (2013) Magnetic resonance imaging of pediatric lung parenchyma, airways, vasculature, ventilation, and perfusion: state of the art. Radiol Clin N Am 51(4):555–582. https://doi.org/10.1016/j.rcl.2013.04.004

Loffler R, Muller CJ, Peller M, Penzkofer H, Deimling M, Schwaiblmair M, Scheidler J, Reiser M (2000) Optimization and evaluation of the signal intensity change in multisection oxygen-enhanced MR lung imaging. Magn Reson Med 43(6):860–866

Lutey BA, Lefrak SS, Woods JC, Tanoli T, Quirk JD, Bashir A, Yablonskiy DA, Conradi MS, Bartel ST, Pilgram TK, Cooper JD, Gierada DS (2008) Hyperpolarized 3He MR imaging: physiologic monitoring observations and safety considerations in 100 consecutive subjects. Radiology 248(2):655–661. https://doi.org/10.1148/radiol.2482071838

Mai VM, Tutton S, Prasad PV, Chen Q, Li W, Chen C, Liu B, Polzin J, Kurucay S, Edelman RR (2003) Computing oxygen-enhanced ventilation maps using correlation analysis. Magn Reson Med 49(3):591–594. https://doi.org/10.1002/mrm.10395

Martini K, Gygax CM, Benden C, Morgan AR, Parker GJM, Frauenfelder T (2018a) Correction to: Volumetric dynamic oxygen-enhanced MRI (OE-MRI): comparison with CT Brody score and lung function in cystic fibrosis patients. Eur Radiol 28(11):4922–4923. https://doi.org/10.1007/s00330-018-5549-1

Martini K, Gygax CM, Benden C, Morgan AR, Parker GJM, Frauenfelder T (2018b) Volumetric dynamic oxygen-enhanced MRI (OE-MRI): comparison with CT Brody score and lung function in cystic fibrosis patients. Eur Radiol 28(10):4037–4047. https://doi.org/10.1007/s00330-018-5383-5

Mata J, Altes T, Truwit J, Sylvester P, de Lange E, Shim Y, Vinayak A, Brookeman J, Mugler J 3rd (2011) Characterization and detection of physiologic lung changes before and after placement of bronchial valves using hyperpolarized helium-3 MR imaging: preliminary study. Acad Radiol 18(9):1195–1199. https://doi.org/10.1016/j.acra.2011.03.002

Mathew L, Kirby M, Farquhar D, Licskai C, Santyr G, Etemad-Rezai R, Parraga G, McCormack DG (2012a) Hyperpolarized 3He functional magnetic resonance imaging of bronchoscopic airway bypass in chronic obstructive pulmonary disease. Can Respir J 19(1):41–43

Mathew L, Vandyk J, Etemad-Rezai R, Rodrigues G, Parraga G (2012b) Hyperpolarized (3)He pulmonary functional magnetic resonance imaging prior to radiation therapy. Med Phys 39(7):4284–4290. https://doi.org/10.1118/1.4729713

Matin TN, Rahman N, Nickol AH, Chen M, Xu X, Stewart NJ, Doel T, Grau V, Wild JM, Gleeson FV (2017) Chronic obstructive pulmonary disease: lobar analysis with hyperpolarized (129)Xe MR imaging. Radiology 282(3):857–868. https://doi.org/10.1148/radiol.2016152299

Mentore K, Froh DK, de Lange EE, Brookeman JR, Paget-Brown AO, Altes TA (2005) Hyperpolarized HHe 3 MRI of the lung in cystic fibrosis: assessment at baseline and after bronchodilator and airway clearance

treatment. Acad Radiol 12(11):1423–1429. https://doi.org/10.1016/j.acra.2005.07.008

Miller GW, Mugler JP 3rd, Sa RC, Altes TA, Prisk GK, Hopkins SR (2014) Advances in functional and structural imaging of the human lung using proton MRI. NMR Biomed 27(12):1542–1556. https://doi.org/10.1002/nbm.3156

Molinari F, Eichinger M, Risse F, Plathow C, Puderbach M, Ley S, Herth F, Bonomo L, Kauczor HU, Fink C (2007) Navigator-triggered oxygen-enhanced MRI with simultaneous cardiac and respiratory synchronization for the assessment of interstitial lung disease. J Magn Reson Imaging 26(6):1523–1529. https://doi.org/10.1002/jmri.21043

Molinari F, Puderbach M, Eichinger M, Ley S, Fink C, Bonomo L, Kauczor HU, Bock M (2008) Oxygen-enhanced magnetic resonance imaging: influence of different gas delivery methods on the T1-changes of the lungs. Investig Radiol 43(6):427–432. https://doi.org/10.1097/RLI.0b013e318169012d

Mugler JP 3rd, Altes TA (2013) Hyperpolarized 129Xe MRI of the human lung. J Magn Reson Imaging 37(2):313–331. https://doi.org/10.1002/jmri.23844

Muller CJ, Schwaiblmair M, Scheidler J, Deimling M, Weber J, Loffler RB, Reiser MF (2002) Pulmonary diffusing capacity: assessment with oxygen-enhanced lung MR imaging preliminary findings. Radiology 222(2):499–506. https://doi.org/10.1148/radiol.2222000869

Mummy DG, Kruger SJ, Zha W, Sorkness RL, Jarjour NN, Schiebler ML, Denlinger LC, Evans MD, Fain SB (2018) Ventilation defect percent in helium-3 magnetic resonance imaging as a biomarker of severe outcomes in asthma. J Allergy Clin Immunol 141(3):1140–1141. e1144. https://doi.org/10.1016/j.jaci.2017.10.016

Naish JH, Parker GJ, Beatty PC, Jackson A, Young SS, Waterton JC, Taylor CJ (2005) Improved quantitative dynamic regional oxygen-enhanced pulmonary imaging using image registration. Magn Reson Med 54(2):464–469. https://doi.org/10.1002/mrm.20570

Nakagawa T, Sakuma H, Murashima S, Ishida N, Matsumura K, Takeda K (2001) Pulmonary ventilation-perfusion MR imaging in clinical patients. J Magn Reson Imaging 14(4):419–424

Newell JD Jr, Sieren J, Hoffman EA (2013) Development of quantitative computed tomography lung protocols. J Thorac Imaging 28(5):266–271. https://doi.org/10.1097/RTI.0b013e31829f6796

Nikolaou P, Coffey AM, Walkup LL, Gust BM, LaPierre CD, Koehnemann E, Barlow MJ, Rosen MS, Goodson BM, Chekmenev EY (2014) A 3D-printed high power nuclear spin polarizer. J Am Chem Soc 136(4):1636–1642. https://doi.org/10.1021/ja412093d

Nikolaou P, Coffey AM, Walkup LL, Gust BM, Whiting N, Newton H, Barcus S, Muradyan I, Dabaghyan M, Moroz GD, Rosen MS, Patz S, Barlow MJ, Chekmenev EY, Goodson BM (2013) Near-unity nuclear polarization with an open-source 129Xe hyperpolarizer for NMR and MRI. Proc Natl Acad Sci U S A 110(35):14150–14155. https://doi.org/10.1073/pnas.1306586110

Niles DJ, Kruger SJ, Dardzinski BJ, Harman A, Jarjour NN, Ruddy M, Nagle SK, Francois CJ, Fain SB (2013) Exercise-induced bronchoconstriction: reproducibility of hyperpolarized 3He MR imaging. Radiology 266(2):618–625. https://doi.org/10.1148/radiol.12111973

Nyilas S, Bauman G, Pusterla O, Ramsey K, Singer F, Stranzinger E, Yammine S, Casaulta C, Bieri O, Latzin P (2018) Ventilation and perfusion assessed by functional MRI in children with CF: reproducibility in comparison to lung function. J Cyst Fibros. https://doi.org/10.1016/j.jcf.2018.10.003

O'Halloran RL, Holmes JH, Wu YC, Alexander A, Fain SB (2010) Helium-3 MR q-space imaging with radial acquisition and iterative highly constrained back-projection. Magn Reson Med 63(1):41–50. https://doi.org/10.1002/mrm.22158

Ohno Y, Hatabu H (2007) Basics concepts and clinical applications of oxygen-enhanced MR imaging. Eur J Radiol 64(3):320–328. https://doi.org/10.1016/j.ejrad.2007.08.006

Ohno Y, Hatabu H, Higashino T, Nogami M, Takenaka D, Watanabe H, Van Cauteren M, Yoshimura M, Satouchi M, Nishimura Y, Sugimura K (2005) Oxygen-enhanced MR imaging: correlation with post-surgical lung function in patients with lung cancer. Radiology 236(2):704–711. https://doi.org/10.1148/radiol.2361040005

Ohno Y, Hatabu H, Takenaka D, Adachi S, Van Cauteren M, Sugimura K (2001) Oxygen-enhanced MR ventilation imaging of the lung: preliminary clinical experience in 25 subjects. AJR Am J Roentgenol 177(1):185–194. https://doi.org/10.2214/ajr.177.1.1770185

Ohno Y, Hatabu H, Takenaka D, Van Cauteren M, Fujii M, Sugimura K (2002) Dynamic oxygen-enhanced MRI reflects diffusing capacity of the lung. Magn Reson Med 47(6):1139–1144. https://doi.org/10.1002/mrm.10168

Ohno Y, Iwasawa T, Seo JB, Koyama H, Takahashi H, Oh YM, Nishimura Y, Sugimura K (2008a) Oxygen-enhanced magnetic resonance imaging versus computed tomography: multicenter study for clinical stage classification of smoking-related chronic obstructive pulmonary disease. Am J Respir Crit Care Med 177(10):1095–1102. https://doi.org/10.1164/rccm.200709-1322OC

Ohno Y, Koyama H, Matsumoto K, Onishi Y, Nogami M, Takenaka D, Matsumoto S, Sugimura K (2011) Oxygen-enhanced MRI vs. quantitatively assessed thin-section CT: pulmonary functional loss assessment and clinical stage classification of asthmatics. Eur J Radiol 77(1):85–91. https://doi.org/10.1016/j.ejrad.2009.06.027

Ohno Y, Koyama H, Nogami M, Takenaka D, Matsumoto S, Obara M, Sugimura K (2008b) Dynamic oxygen-enhanced MRI versus quantitative CT: pulmonary functional loss assessment and clinical stage

classification of smoking-related COPD. AJR Am J Roentgenol 190(2):W93–W99. https://doi.org/10.2214/AJR.07.2511

Ohno Y, Nishio M, Koyama H, Seki S, Yoshikawa T, Matsumoto S, Obara M, van Cauteren M, Sugimura K (2014) Asthma: comparison of dynamic oxygen-enhanced MR imaging and quantitative thin-section CT for evaluation of clinical treatment. Radiology:132660. https://doi.org/10.1148/radiol.14132660

Ohno Y, Nishio M, Koyama H, Yoshikawa T, Matsumoto S, Takenaka D, Sugimura K (2012) Oxygen-enhanced MRI, thin-section MDCT, and perfusion SPECT/CT: comparison of clinical implications to patient care for lung volume reduction surgery. AJR Am J Roentgenol 199(4):794–802. https://doi.org/10.2214/AJR.11.8250

O'Sullivan B, Couch M, Roche JP, Walvick R, Zheng S, Baker D, Johnson M, Botfield M, Albert MS (2014) Assessment of repeatability of hyperpolarized gas MR ventilation functional imaging in cystic fibrosis. Acad Radiol. https://doi.org/10.1016/j.acra.2014.07.008

Paulin GA, Svenningsen S, Jobse BN, Mohan S, Kirby M, Lewis JF, Parraga G (2014) Differences in hyperpolarized He ventilation imaging after 4 years in adults with cystic fibrosis. J Magn Reson Imaging. https://doi.org/10.1002/jmri.24744

Pennati F, Quirk JD, Yablonskiy DA, Castro M, Aliverti A, Woods JC (2014) Assessment of regional lung function with multivolume (1)H MR imaging in health and obstructive lung disease: comparison with (3)He MR imaging. Radiology 273(2):580–590. https://doi.org/10.1148/radiol.14132470

Pennati F, Roach DJ, Clancy JP, Brody AS, Fleck RJ, Aliverti A, Woods JC (2018) Assessment of pulmonary structure-function relationships in young children and adolescents with cystic fibrosis by multivolume proton-MRI and CT. J Magn Reson Imaging 48(2):531–542. https://doi.org/10.1002/jmri.25978

Pracht ED, Arnold JF, Wang T, Jakob PM (2005) Oxygen-enhanced proton imaging of the human lung using T2. Magn Reson Med 53(5):1193–1196. https://doi.org/10.1002/mrm.20448

Rayment JH, Couch MJ, McDonald N, Kanhere N, Manson D, Santyr G, Ratjen F (2019) Hyperpolarised (129)Xe MRI to monitor treatment response in children with cystic fibrosis. Eur Respir J. https://doi.org/10.1183/13993003.02188-2018

Reinhardt JM, Ding K, Cao K, Christensen GE, Hoffman EA, Bodas SV (2008) Registration-based estimates of local lung tissue expansion compared to xenon CT measures of specific ventilation. Med Image Anal 12(6):752–763. https://doi.org/10.1016/j.media.2008.03.007

Renne J, Hinrichs J, Schonfeld C, Gutberlet M, Winkler C, Faulenbach C, Jakob P, Schaumann F, Krug N, Wacker F, Hohlfeld JM, Vogel-Claussen J (2015a) Noninvasive quantification of airway inflammation following segmental allergen challenge with functional MR imaging: A proof of concept study. Radiology 274(1):267–275. https://doi.org/10.1148/radiol.14132607

Renne J, Lauermann P, Hinrichs J, Schonfeld C, Sorrentino S, Gutberlet M, Jakob P, Wacker F, Vogel-Claussen J (2015b) Clinical use of oxygen-enhanced T1 mapping MRI of the lung: reproducibility and impact of closed versus loose fit oxygen delivery system. J Magn Reson Imaging 41(1):60–66. https://doi.org/10.1002/jmri.24535

Ruiz-Cabello J, Barnett BP, Bottomley PA, Bulte JW (2011) Fluorine (19F) MRS and MRI in biomedicine. NMR Biomed 24(2):114–129. https://doi.org/10.1002/nbm.1570

Ruset IC, Ketel S, Hersman FW (2006) Optical pumping system design for large production of hyperpolarized. Phys Rev Lett 96(5):053002

Sa RC, Cronin MV, Henderson AC, Holverda S, Theilmann RJ, Arai TJ, Dubowitz DJ, Hopkins SR, Buxton RB, Prisk GK (2010) Vertical distribution of specific ventilation in normal supine humans measured by oxygen-enhanced proton MRI. J Appl Physiol 109(6):1950–1959. https://doi.org/10.1152/japplphysiol.00220.2010

Salerno M, Altes TA, Brookeman JR, de Lange EE, Mugler JP 3rd (2001) Dynamic spiral MRI of pulmonary gas flow using hyperpolarized (3)He: preliminary studies in healthy and diseased lungs. Magn Reson Med 46(4):667–677

Salerno M, de Lange EE, Altes TA, Truwit JD, Brookeman JR, Mugler JP 3rd (2002) Emphysema: hyperpolarized helium 3 diffusion MR imaging of the lungs compared with spirometric indexes--initial experience. Radiology 222(1):252–260

Samee S, Altes T, Powers P, de Lange EE, Knight-Scott J, Rakes G, Mugler JP 3rd, Ciambotti JM, Alford BA, Brookeman JR, Platts-Mills TA (2003) Imaging the lungs in asthmatic patients by using hyperpolarized helium-3 magnetic resonance: assessment of response to methacholine and exercise challenge. J Allergy Clin Immunol 111(6):1205–1211

Santyr G, Kanhere N, Morgado F, Rayment JH, Ratjen F, Couch MJ (2019) Hyperpolarized gas magnetic resonance imaging of pediatric cystic fibrosis lung disease. Acad Radiol 26(3):344–354. https://doi.org/10.1016/j.acra.2018.04.024

Sasaki T, Takahashi K, Obara M (2017) Viability of oxygen-enhanced ventilation imaging of the lungs using ultra-short echo time MRI. Magn Reson Med Sci 16(3):259–261. https://doi.org/10.2463/mrms.tn.2015-0074

Schreiber WG, Eberle B, Laukemper-Ostendorf S, Markstaller K, Weiler N, Scholz A, Burger K, Heussel CP, Thelen M, Kauczor HU (2001) Dynamic (19)F-MRI of pulmonary ventilation using sulfur hexafluoride (SF(6)) gas. Magn Reson Med 45(4):605–613

Snell GI, Holsworth L, Borrill ZL, Thomson KR, Kalff V, Smith JA, Williams TJ (2003) The potential for

bronchoscopic lung volume reduction using bronchial prostheses: a pilot study. Chest 124(3):1073–1080

Sotiras A, Davatzikos C, Paragios N (2013) Deformable medical image registration: a survey. IEEE Trans Med Imaging 32(7):1153–1190. https://doi.org/10.1109/TMI.2013.2265603

Stewart NJ, Chan HF, Hughes PJC, Horn FC, Norquay G, Rao M, Yates DP, Ireland RH, Hatton MQ, Tahir BA, Ford P, Swift AJ, Lawson R, Marshall H, Collier GJ, Wild JM (2018) Comparison of (3) He and (129) Xe MRI for evaluation of lung microstructure and ventilation at 1.5 T. J Magn Reson Imaging. https://doi.org/10.1002/jmri.25992

Stewart NJ, Norquay G, Griffiths PD, Wild JM (2015) Feasibility of human lung ventilation imaging using highly polarized naturally abundant xenon and optimized three-dimensional steady-state free precession. Magn Reson Med. https://doi.org/10.1002/mrm.25732

Stock KW, Chen Q, Morrin M, Hatabu H, Edelman RR (1999) Oxygen-enhanced magnetic resonance ventilation imaging of the human lung at 0.2 and 1.5 T. J Magn Reson Imaging 9(6):838–841

Svenningsen S, Eddy RL, Lim HF, Cox PG, Nair P, Parraga G (2018) Sputum eosinophilia and magnetic resonance imaging ventilation heterogeneity in severe asthma. Am J Respir Crit Care Med 197(7):876–884. https://doi.org/10.1164/rccm.201709-1948OC

Svenningsen S, Kirby M, Starr D, Coxson HO, Paterson NA, McCormack DG, Parraga G (2014) What are ventilation defects in asthma? Thorax 69(1):63–71. https://doi.org/10.1136/thoraxjnl-2013-203711

Svenningsen S, Kirby M, Starr D, Leary D, Wheatley A, Maksym GN, McCormack DG, Parraga G (2013) Hyperpolarized (3) He and (129) Xe MRI: differences in asthma before bronchodilation. J Magn Reson Imaging 38(6):1521–1530. https://doi.org/10.1002/jmri.24111

Svenningsen S, Nair P (2017) Asthma endotypes and an overview of targeted therapy for asthma. Front Med (Lausanne) 4:158. https://doi.org/10.3389/fmed.2017.00158

Tadamura E, Hatabu H, Li W, Prasad PV, Edelman RR (1997) Effect of oxygen inhalation on relaxation times in various tissues. J Magn Reson Imaging 7(1):220–225

Tahir BA, Hughes PJC, Robinson SD, Marshall H, Stewart NJ, Norquay G, Biancardi A, Chan HF, Collier GJ, Hart KA, Swinscoe JA, Hatton MQ, Wild JM, Ireland RH (2018) Spatial comparison of CT-based surrogates of lung ventilation with hyperpolarized Helium-3 and Xenon-129 Gas MRI in patients undergoing radiation therapy. Int J Radiat Oncol Biol Phys 102(4):1276–1286. https://doi.org/10.1016/j.ijrobp.2018.04.077

Tahir BA, Swift AJ, Marshall H, Parra-Robles J, Hatton MQ, Hartley R, Kay R, Brightling CE, Vos W, Wild JM, Ireland RH (2014) A method for quantitative analysis of regional lung ventilation using deformable image registration of CT and hybrid hyperpolarized gas/(1)H MRI. Phys Med Biol 59(23):7267–7277. https://doi.org/10.1088/0031-9155/59/23/7267

Teague WG, Tustison NJ, Altes TA (2014) Ventilation heterogeneity in asthma. J Asthma 51(7):677–684. https://doi.org/10.3109/02770903.2014.914535

Thomen RP, Sheshadri A, Quirk JD, Kozlowski J, Ellison HD, Szczesniak RD, Castro M, Woods JC (2015) Regional ventilation changes in severe asthma after bronchial thermoplasty with (3)He MR imaging and CT. Radiology 274(1):250–259. https://doi.org/10.1148/radiol.14140080

Thomen RP, Walkup LL, Roach DJ, Cleveland ZI, Clancy JP, Woods JC (2017) Hyperpolarized (129)Xe for investigation of mild cystic fibrosis lung disease in pediatric patients. J Cyst Fibros 16(2):275–282. https://doi.org/10.1016/j.jcf.2016.07.008

Togao O, Ohno Y, Dimitrov I, Hsia CC, Takahashi M (2011) Ventilation/perfusion imaging of the lung using ultra-short echo time (UTE) MRI in an animal model of pulmonary embolism. J Magn Reson Imaging 34(3):539–546. https://doi.org/10.1002/jmri.22645

Torres L, Kammerman J, Hahn AD, Zha W, Nagle SK, Johnson K, Sandbo N, Meyer K, Schiebler M, Fain SB (2019) Structure-function imaging of lung disease using ultrashort echo time MRI. Acad Radiol 26(3):431–441. https://doi.org/10.1016/j.acra.2018.12.007

Triphan SM, Jobst BJ, Anjorin A, Sedlaczek O, Wolf U, Terekhov M, Hoffmann C, Ley S, Duber C, Biederer J, Kauczor HU, Jakob PM, Wielputz MO (2017) Reproducibility and comparison of oxygen-enhanced T1 quantification in COPD and asthma patients. PLoS One 12(2):e0172479. https://doi.org/10.1371/journal.pone.0172479

Tustison NJ, Avants BB, Flors L, Altes TA, de Lange EE, Mugler JP 3rd, Gee JC (2011) Ventilation-based segmentation of the lungs using hyperpolarized (3)He MRI. J Magn Reson Imaging 34(4):831–841. https://doi.org/10.1002/jmri.22738

van Beek EJ, Dahmen AM, Stavngaard T, Gast KK, Heussel CP, Krummenauer F, Schmiedeskamp J, Wild JM, Sogaard LV, Morbach AE, Schreiber LM, Kauczor HU (2009) Hyperpolarised 3He MRI versus HRCT in COPD and normal volunteers: PHIL trial. Eur Respir J 34(6):1311–1321. https://doi.org/10.1183/09031936.00138508

Vaninbroukx J, Bosmans H, Sunaert S, Demedts M, Delcroix M, Marchal G, Verschakelen J (2003) The use of ECG and respiratory triggering to improve the sensitivity of oxygen-enhanced proton MRI of lung ventilation. Eur Radiol 13(6):1260–1265. https://doi.org/10.1007/s00330-002-1694-6

Virgincar RS, Cleveland ZI, Kaushik SS, Freeman MS, Nouls J, Cofer GP, Martinez-Jimenez S, He M, Kraft M, Wolber J, McAdams HP, Driehuys B (2013) Quantitative analysis of hyperpolarized 129Xe ventilation imaging in healthy volunteers and subjects with chronic obstructive pulmonary disease. NMR Biomed 26(4):424–435. https://doi.org/10.1002/nbm.2880

Voskrebenzev A, Gutberlet M, Kaireit TF, Wacker F, Vogel-Claussen J (2017) Low-pass imaging of dynamic acquisitions (LIDA) with a group-oriented

registration (GOREG) for proton MR imaging of lung ventilation. Magn Reson Med 78(4):1496–1505. https://doi.org/10.1002/mrm.26526

Voskrebenzev A, Gutberlet M, Klimes F, Kaireit TF, Schonfeld C, Rotarmel A, Wacker F, Vogel-Claussen J (2018) Feasibility of quantitative regional ventilation and perfusion mapping with phase-resolved functional lung (PREFUL) MRI in healthy volunteers and COPD, CTEPH, and CF patients. Magn Reson Med 79(4):2306–2314. https://doi.org/10.1002/mrm.26893

Wang C, Altes TA, Mugler JP 3rd, Miller GW, Ruppert K, Mata JF, Cates GD Jr, Borish L, de Lange EE (2008) Assessment of the lung microstructure in patients with asthma using hyperpolarized 3He diffusion MRI at two time scales: comparison with healthy subjects and patients with COPD. J Magn Reson Imaging 28(1):80–88. https://doi.org/10.1002/jmri.21408

Wielputz MO, Puderbach M, Kopp-Schneider A, Stahl M, Fritzsching E, Sommerburg O, Ley S, Sumkauskaite M, Biederer J, Kauczor HU, Eichinger M, Mall MA (2014) Magnetic resonance imaging detects changes in structure and perfusion, and response to therapy in early cystic fibrosis lung disease. Am J Respir Crit Care Med 189(8):956–965. https://doi.org/10.1164/rccm.201309-1659OC

Wild JM, Marshall H, Bock M, Schad LR, Jakob PM, Puderbach M, Molinari F, Van Beek EJ, Biederer J (2012) MRI of the lung (1/3): methods. Insights Imaging 3(4):345–353. https://doi.org/10.1007/s13244-012-0176-x

Wild JM, Paley MN, Kasuboski L, Swift A, Fichele S, Woodhouse N, Griffiths PD, van Beek EJ (2003) Dynamic radial projection MRI of inhaled hyperpolarized 3He gas. Magn Reson Med 49(6):991–997. https://doi.org/10.1002/mrm.10477

Wild JM, Paley MN, Viallon M, Schreiber WG, van Beek EJ, Griffiths PD (2002) k-space filtering in 2D gradient-echo breath-hold hyperpolarized 3He MRI: spatial resolution and signal-to-noise ratio considerations. Magn Reson Med 47(4):687–695

Wild JM, Teh K, Woodhouse N, Paley MN, Fichele S, de Zanche N, Kasuboski L (2006) Steady-state free precession with hyperpolarized 3He: experiments and theory. J Magn Reson 183(1):13–24. https://doi.org/10.1016/j.jmr.2006.07.015

Wild JM, Woodhouse N, Paley MN, Fichele S, Said Z, Kasuboski L, van Beek EJ (2004) Comparison between 2D and 3D gradient-echo sequences for MRI of human lung ventilation with hyperpolarized 3He. Magn Reson Med 52(3):673–678. https://doi.org/10.1002/mrm.20164

Woodhouse N, Wild JM, Paley MN, Fichele S, Said Z, Swift AJ, van Beek EJ (2005) Combined helium-3/proton magnetic resonance imaging measurement of ventilated lung volumes in smokers compared to never-smokers. J Magn Reson Imaging 21(4):365–369. https://doi.org/10.1002/jmri.20290

Zha W, Kruger SJ, Cadman RV, Mummy DG, Evans MD, Nagle SK, Denlinger LC, Jarjour NN, Sorkness RL, Fain SB (2018a) Regional heterogeneity of lobar ventilation in asthma using hyperpolarized Helium-3 MRI. Acad Radiol 25(2):169–178. https://doi.org/10.1016/j.acra.2017.09.014

Zha W, Kruger SJ, Johnson KM, Cadman RV, Bell LC, Liu F, Hahn AD, Evans MD, Nagle SK, Fain SB (2018b) Pulmonary ventilation imaging in asthma and cystic fibrosis using oxygen-enhanced 3D radial ultrashort echo time MRI. J Magn Reson Imaging 47(5):1287–1297. https://doi.org/10.1002/jmri.25877

Zha W, Nagle SK, Cadman RV, Schiebler ML, Fain SB (2019) Three-dimensional isotropic functional imaging of cystic fibrosis using oxygen-enhanced MRI: comparison with hyperpolarized (3) He MRI. Radiology 290(1):229–237. https://doi.org/10.1148/radiol.2018181148

Zhao L, Albert MS (1998) Biomedical imaging using hyperpolarized noble gas MRI: pulse sequence considerations. Nucl Instrum Methods Phys Res A 402:454–460

Principles and Clinical Applications of Respiratory Motion Assessment Using 4D Computed Tomography and Magnetic Resonance Imaging

Tae Iwasawa

Contents

1 **Introduction** 92
2 **Respiratory Motion Analysis Using MRI** 93
3 **Method of 4D Dynamic Ventilation MRI** 94
4 **Method of 4D Dynamic Ventilation CT** 96
5 **Clinical Application of 4DCT in Large Airways Disorders** 97
6 **Clinical Application of 4DCT in COPD Patients** 98
7 **Clinical Application of 4DCT in Patients with Lung Cancer** 101
8 **The Future of 4D Image Analysis** 102
9 **Conclusions** 103
References 103

Abstract

The motion of the chest wall (which includes the diaphragm) generates a periodic change in intrathoracic pressure, enabling the synchronous motion of each component, and an effective gas exchange. Four-dimensional (4D) magnetic resonance imaging (MRI) and 4D computed tomography (CT), which are continuous 3D images obtained during respiration, can directly demonstrate normal and abnormal respiratory motion.

Due to its lack of irradiation MRI is a suitable tool for respiratory motion analysis. Recently, ultrashort echo time (UTE) sequences have dramatically improved the signal-to-noise ratios of lung images. At the same time, the radial scan technique has increased time resolution. 4DMRI during free breathing using UTE and radial scan has been developed and applied to analyze the respiratory motion of the lung itself during tidal

Electronic supplementary material The online version of this chapter (https://doi.org/10.1007/978-3-030-43539-4_6) contains supplementary material, which is available to authorized users.

T. Iwasawa (✉)
Department of Radiology, Kanagawa Cardiovascular & Respiratory Center, Yokohama, Japan
e-mail: tae_i_md@wb3.so-net.ne.jp

© Springer Nature Switzerland AG 2021

Y. Ohno et al. (eds.), *Pulmonary Functional Imaging*, Medical Radiology Diagnostic Imaging,
https://doi.org/10.1007/978-3-030-43539-4_6

breathing. Furthermore, 4DMRI has been utilized in radiation therapy and in infants with tracheomalacia.

4DCT can be easily obtained using multidetector computed tomography (MDCT), and it can demonstrate displacement and/or deformation of the lung structures during respiratory cycles. Improvements in reconstruction algorithms such as iterative reconstruction can reduce the radiation dose to acceptable levels. Combining two or three 3D image sets has enabled the respiratory motion analysis of the whole lung. 4DCT analysis has been used in patients with large airway abnormalities such as tracheobronchomalacia, chronic obstructive lung disease, and pleural adhesion due to lung cancer as a preoperative assessment.

1 Introduction

The chest wall, consisting of the thoracic cage and the diaphragm, is a functional unit to change the intrapleural pressure and exchange gas in the lung. During inspiration, the contraction of the diaphragm moves the diaphragm downward, while the contraction of the intercostal muscles moves the ribs up- and outward. In the expiration phase, the respiratory muscles relax, and the intrapleural pressure becomes less negative with respect to atmospheric pressure. The elastic recoil of the lung tissue then compresses the alveolar gas and raises its pressure above that at the mouth. The chest wall motion results in lung volume changes and generates gas exchange (Troyer and Wilson 2016; Cotes et al. 2006). These physiological aspects support the hypothesis that motion analysis using imaging modalities could demonstrate not only chest wall motions but also respiratory functions of the lung itself if the modalities can demonstrate the lung structures with sufficient time and spatial resolution (Suga et al. 2000).

Figure 1 shows the respiratory motion trajectories of the large pulmonary vessels, which were obtained by continuous two-dimensional (2D) magnetic resonance imaging (MRI) during deep breathing (Shibata et al. 2012). The respiratory movement of the pulmonary vessels indi-

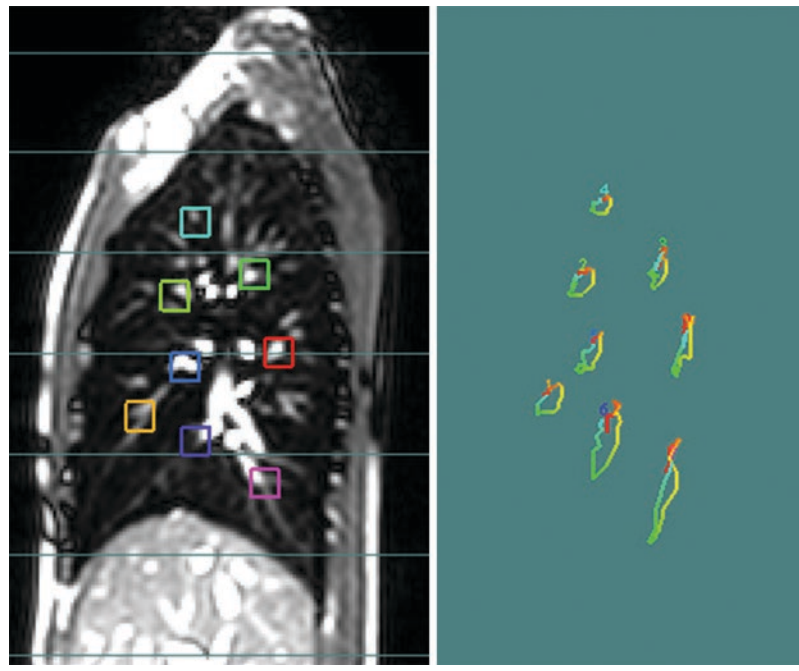


Fig. 1 Respiratory motion trajectories of the large pulmonary vessels in a healthy volunteer. The large pulmonary vessels are traced using continuous 2DMRI during deep breathing. The large vessels (left, *colored boxes*) move synchronously, and their trajectories (right, *line color corresponding to box color*) display an oval hysteresis loop

cates an oval trajectory, which means the lung structures move along different trajectories during the inspiratory and expiratory phase. This phenomenon is well known as "hysteresis," and it is caused by the compliance of the lung. In other words, static images obtained at end-inspiration and end-expiration are not enough to analyze the whole respiratory mechanism. Four-dimensional (4D) images, which are continuous 3D images obtained during respiration, are ideal for the analysis of the three-dimensional respiratory motion of the lung. In the past decade, 4D computed tomography (4DCT) and 4DMRI have been developed and utilized for respiratory motion analysis. I will describe the possibilities to generate 4D images and their applications in pulmonology Table 1.

2 Respiratory Motion Analysis Using MRI

Magnetic resonance imaging is a suitable approach for respiratory motion analysis because of its lack of irradiation. MRI can visualize the chest wall with high contrast, and continuous 2DMRI using gradient-recalled echo can easily demonstrate the chest wall motion directly (Gierada et al. 1995). Abnormal paradoxical motion has been observed in patients with severe chronic obstructive lung disease (COPD) (Suga et al. 2000; Iwasawa et al. 2002). Recently, Sekine et al. reported unilateral upper lung field pulmonary fibrosis radiologically consistent with pleuroparenchymal fibroelastosis after thoracotomy (Sekine et al. 2017). As shown in Fig. 2,

Table 1 Summarizes the comparison between 4DMRI and 4DCT

	4DMRI	4DCT
Irradiation	No invasiveness	Low invasiveness 1–3 mSv
Accessibility	Limited (research level)	Wide (possible using clinical equipment)
Spatial resolution	Depending on sequences Dynamic 3D MRI: not high UTE: high	High (equal to 3DCT)
Temporal resolution	Depending on sequences Dynamic 3D MRI: 1 s/phase UTE: high	Minimum 0.275 s/phase
Clinical application	Chest wall invasion of tumors Treatment planning for radiation therapy	Chest wall invasion of tumors Assessment of pleural adhesion before surgery Tracheobronchomalacia

4D four-dimensional, *MRI* magnetic resonance imaging, *CT* computed tomography, *3D* three-dimensional, *UTE* ultrashort echo time

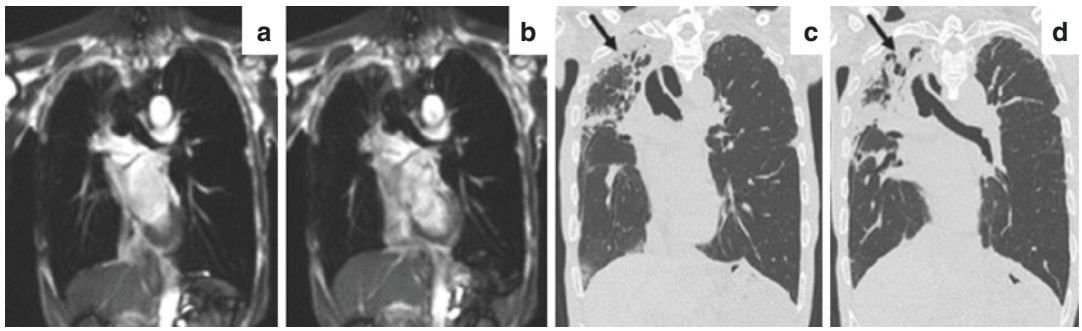


Fig.2 A 73-year-old male with unilateral pleuroparenchymal fibroelastosis-like apical fibrosis. **(a, b)** Inspiratory and expiratory phase of a 2DMRI obtained during deep breathing. **(c, d)** Coronal reformatted CTs obtained at the same time of this 2DMRI **(c)** and after 2 years **(d)**. The 2DMRI shows a smaller change in the area of the right lung between the deep inspiratory (**a**) and expiratory (**b**) phase. The coronal reformatted CTs show a progression of the apical fibrosis in the right upper lobe (**c, d**, *arrows*)

dynamic breathing chest MRIs could demonstrate the unilaterally impaired thoracic movements in these patients.

However, this 2DMRI method using gradient echo sequences is not adequate for assessing the respiratory motion of the lung parenchyma. These traditional MRI techniques cannot show the lung parenchyma due to the low proton density and high susceptibility. To demonstrate the whole respiratory motion of the lung and the chest wall, a 3D approach is necessary.

One solution to address this drawback is the use of hyperpolarized gas contrast agents including helium-3 (He-3) and xenon-129 (Xe-129) which generate sufficient signals in the pulmonary airspaces (Kruger et al. 2016). These hyperpolarized images can precisely visualize the gas distribution (Gast et al. 2002).

Holmes et al. proposed dynamic 3D imaging using hyperpolarized He-3 with isotropic high-spatiotemporal-resolution (1 s per 1 volume image) using hyperpolarized He-3 MRI. With this approach, they demonstrated local air trapping in asthmatic patients (Holmes et al. 2009). By combining hyperpolarized He-3 MRI with grid-tagging techniques, lung strain maps of the respiratory cycle can be obtained (Cai et al. 2007, 2009; Tustison et al. 2010). These hyperpolarized images are powerful tools for the evaluation of respiratory motion, but they need special equipment; therefore, they have not been widely used in clinical settings.

Dynamic 3D lung imaging has also been studied using proton MRI. Tokuda et al. obtained dynamic 3D lung imaging with frame rates of 0.62–0.76 frames/s to investigate dynamic changes in lung volume (Tokuda et al. 2009). Plathow et al. measured the volumes and rotations of pulmonary nodules during respiration by using three-dimensional fast low-angle shot dynamic MRI (1.5/0.6 [repetition time in ms/echo time in ms], 3.8 × 3.8 × 3.8-mm voxel size, imaging time per three-dimensional dataset of 1 s) (Plathow et al. 2006).

Tagging methods have also been utilized in proton MRIs to assess regional respiratory functions (Napadow et al. 2001; Voorhees et al. 2005). However, the T1 decay time of the lung parenchyma is much shorter than the duration of the respiratory cycle; thus, the tagging cannot assess the entire respiratory cycle. To solve this problem, Gee et al. developed methods to determine regional parenchymal deformations of the lung using the displacement of the pulmonary vasculature and parenchymal structures as natural sources of spatial markers (Gee et al. 2003; Kiryu et al. 2008).

3 Method of 4D Dynamic Ventilation MRI

In the past decade, ultrashort echo time (UTE) images have been introduced into chest MRI (Togao et al. 2010). Radial sampling can reduce echo time to less than 100 ms, which can minimize signal decay caused by short T2*. UTE images can produce an endogenous MR signal from the lung parenchyma which is usually unobservable by conventional proton MRI methods (Dournes et al. 2015; Lederlin and Cremillieux 2014; Delacoste et al. 2018).

Free-breathing UTE has achieved high spatial resolution (1.25 mm isotropic images) with reasonable imaging times of less than 5 min (Burris et al. 2016; Gai et al. 2016). UTE images have been utilized in a variety of clinical situations, e.g., pulmonary nodule detection and characterization (Burris et al. 2016; Wielpütz et al. 2018) or visualization of airway and parenchymal lung diseases in infants (Niwa et al. 2017; Hahn et al. 2017). In several recent studies, these UTE images have shown the potential to provide an image quality comparable to that of CT images. UTE images have also been applied for a variety of functional imaging, for example, evaluation of emphysema in COPD patients (Ohno et al. 2011; Roach et al. 2016), oxygen-enhanced UTE images (Triphan et al. 2015; Sasaki et al. 2017), and perfusion analysis (Bell et al. 2015).

In these high-quality 3DMRIs, respiratory gating based on signal changes is used to mini-



Fig. 3 Respiratory motion-resolved images. The *horizontal line* denotes the location of the diaphragm at end-expiration. (Reproduced from Jiang et al. (2018))

mize motion artifacts. Motion information can be extracted directly from the acquired k-space data as a self-navigator. A common approach is to use the k-space center, representing the average signal of the excitation volume, as a self-navigation signal. In other words, image-based self-navigation can measure the respiratory motion directly. Jiang et al. reported motion estimation with a high frame rate dynamic 3D self-navigator from a subset of acquired data with reconstruction that combines parallel imaging and compressed sensing with locally low-rank constraints (Jiang et al. 2018) (Fig. 3).

Bates et al. applied respiratory-gated UTE MRI to infants. They reconstructed inspiratory and expiratory images based on free-breathing 4D UTE-MRI datasets and could demonstrate with this method the dynamic tracheal collapse in neonates (tracheomalacia; Fig. 4) (Bates et al. 2018). Bronchoscopy is the clinical standard for diagnosing the presence and degree of airway collapse, but as mentioned in Sect. 5, 4DCT has been still utilized clinically to assess the airway narrowing. As a nonionizing imaging modality, MRI will be better diagnostic technique, in particular for infants and children. For this reason, I think 4DMRI should be widely utilized in clinical situations, especially in pediatric patients.

Respiratory-gated 4DMRI with UTE has achieved high temporal resolution and can demonstrate lung motion during tidal breathing. It will be meaningful, especially to visualize the lung structure at functional residual capacity (FRC). At the FRC level, respiratory muscles are relaxed, and the elastic recoil of the lung and thoracic cage are equal and opposite. An image at FRC cannot be obtained by the breath-holding method. UTE images will certainly provide us

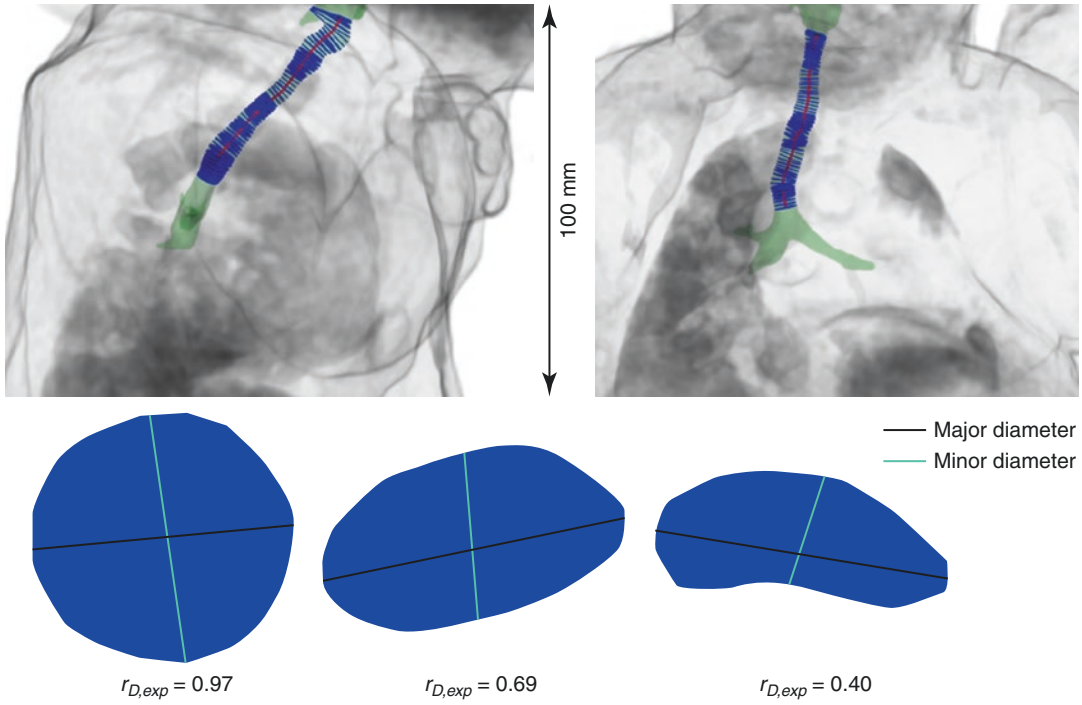


Fig.4 A neonatal airway surface rendering (*green*) shown within a body volume rendering (*gray*) from a neonatal UTE MRI scan, retrospectively respiratory-gated to end-inspiration. A centerline is defined along the trachea (*red*), with a series of luminal cross-sections (*blue*) bounded by the trachea and orthogonal to the centerline. Sagittal and coronal views are shown at left and right, respectively. Note that this subject's trachea is not aligned with any of the imaging planes, demonstrating the need to define a tracheal centerline for accurate cross-sections of the airway lumen. The major and minor diameters are shown in *black* and *cyan*, respectively. Three example luminal cross-sections are displayed below, demonstrating three different values of $r_{D,exp}$, which is the ratio of minor-to-major diameters at end-expiration. A perfectly round trachea would yield an $r_{D,exp}$ ratio of 1, with the value of $r_{D,exp}$ decreasing toward zero in less round tracheal sections. (Reproduced from Bates et al. (2018))

with new information about respiratory mechanics.

4DMRI during tidal breathing can also be utilized in radiation therapy. Accurate quantification and compensation of breathing-induced anatomical changes are key factors in radiation therapy of the thorax. Image acquisition and treatment under free-breathing conditions is an important goal for external beam radiotherapy. Several MR-guided treatment units have been developed already (Bainbridge et al. 2017). In its present state, 2DMRI is used to monitor the respiratory motion of tumors and organs at risk during exposure. By providing superior spatial resolution, 4DMRI has the potential to complement or even supersede 4DCT and 4D F-18-FDG PET.

4 Method of 4D Dynamic Ventilation CT

There are two types of 4DCTs: respiratory-gated 4DCT and dynamic scanning 4DCT. Respiratory-gated 4DCT needs special equipment for monitoring respiration; 3DCT data sets are obtained with respiratory gating and 4DCT data are retrospectively reconstructed along the respiratory cycle (Hurkmans et al. 2011). Respiratory-gated 4DCT needs regular breathing during data collection, and thus patients' cooperation is necessary. Respiratory-gated 4DCT allows multiple 3DCT data sets (usually 10% step of the respiratory cycle), which demonstrate the respiratory motion during the normal breathing cycle. Respiratory-gated 4DCT is mainly used in radia-

tion therapy planning and monitoring of tumor motion.

On the other hand, dynamic 4DCT scans could easily be obtained using multi-detector computed tomography (MDCT) (I have called 4DCT dynamic scanning as 4DCT in this chapter). Usually, CT images are obtained by X-ray exposure with table movement. In 4DCT, dynamic scanning is performed without table movement, resulting in fluoroscopic 3D images of a part of the body. Imaging parameters are as follows in 320-row MDCT (Aquilion One; Canon Medical Systems, Otawara, Tochigi, Japan): tube currents = 40 mA; tube voltage = 120 kVp; rotation time = 0.35 s; total scanning time = 4.0–6.5 s; collimation = 0.5 mm; slice thickness = 1 mm (without image interval or overlapping); reconstruction interval = 0.5 s/frame (total 8–13 frames); and reconstruction method = half reconstruction using an iterative reconstruction method (adaptive iterative dose reduction). In this setting, the total estimated radiation exposure varied from 3.7 to 6.1 mSv (mean 5.4 mSv) (Yamashiro et al. 2017). To decrease the radiation dose, 80 kVp can be also applicable (Wielputz et al. 2014), which will reduce the effective dose, e.g., to 1.7 mSv in pediatric patients (Greenberg 2012). Recent 320-row MDCT has achieved a rotation time of 0.275 s, and forward-projected model-based iterative reconstruction allows a further reduction of radiation dose while maintaining an acceptable contrast-to-noise ratio (Hassani et al. 2018). Figure 5 shows 4DCTs of normal volunteers. The movies of this 4DCT are shown in the online supplements Videos S1 and S2 (Table 1).

4DCT can be obtained during spontaneous breathing; therefore, it is a useful approach in pediatric patients (Greenberg 2012). However, since the rotation time of 0.275 s of 4DCT is slower compared with the time resolution of conventional fluoroscopy, deep slow breathing is necessary to detect fine structural abnormalities. For this purpose, several institutes use an audio indicator system and instruct adult patients to repeat deep breathing at a stable frequency (2 s inspiration and 2 s expiration) (Muramatsu et al. 2018). Stable respiration allows "whole-lung" 4DCTs, as shown in Fig. 5. Radiologic technologists monitor the patients' respiratory movements and ensure that the expiratory movement from the peak inspiratory phase to the peak expiratory phase is included during the scanning. In our experience, this forced breathing has no adverse effect on patients. But it is undeniable that forced breathing will induce dynamic hyperinflation in patients with severe COPD.

In 4DCT, the respiratory cycle is not monitored by a bellows belt or a spirometer as it can be determined by imaging analysis. For example, Yamashiro et al. demonstrated that the inspiratory and expiratory phase can be determined based on the change in mean lung density (Yamashiro et al. 2010) with density increases during expiration and decreases in inspiration. Thus, the respiratory phase can be determined based on the lung attenuation, even if the scan does not cover the whole lung.

5 Clinical Application of 4DCT in Large Airways Disorders

Tracheobronchomalacia is congenital or acquired condition, which is characterized by increased compliance and excessive collapsibility of the trachea and the bronchi due to a weakness of the airway wall or the supporting cartilage. The hallmark of tracheomalacia is an excessive expiratory collapse, generally defined by more than 50% reduction in the cross-sectional lumen of the trachea (Fig. 6). The utility of inspiratory and expiratory CT for tracheomalacia has already been reported using 64-raw MDCT (Lee and Boiselle 2009). Greenberg applied 320-row MDCT to 24 pediatric patients with persistent respiratory difficulty (Greenberg 2012). He observed tracheomalacia in five patients, all of whom also had both right and left bronchomalacia. A total of eight patients had left bronchomalacia, and twelve occurrences of lobar bronchomalacia were detected in eight children. According to this publication, 64-row MDCT scanners cover at most 4 cm, which is inadequate for evaluating lobar bronchial changes. In this study by Greenberg, all CT examinations were performed with 80 kVp energy. The mean effective dose for all patients

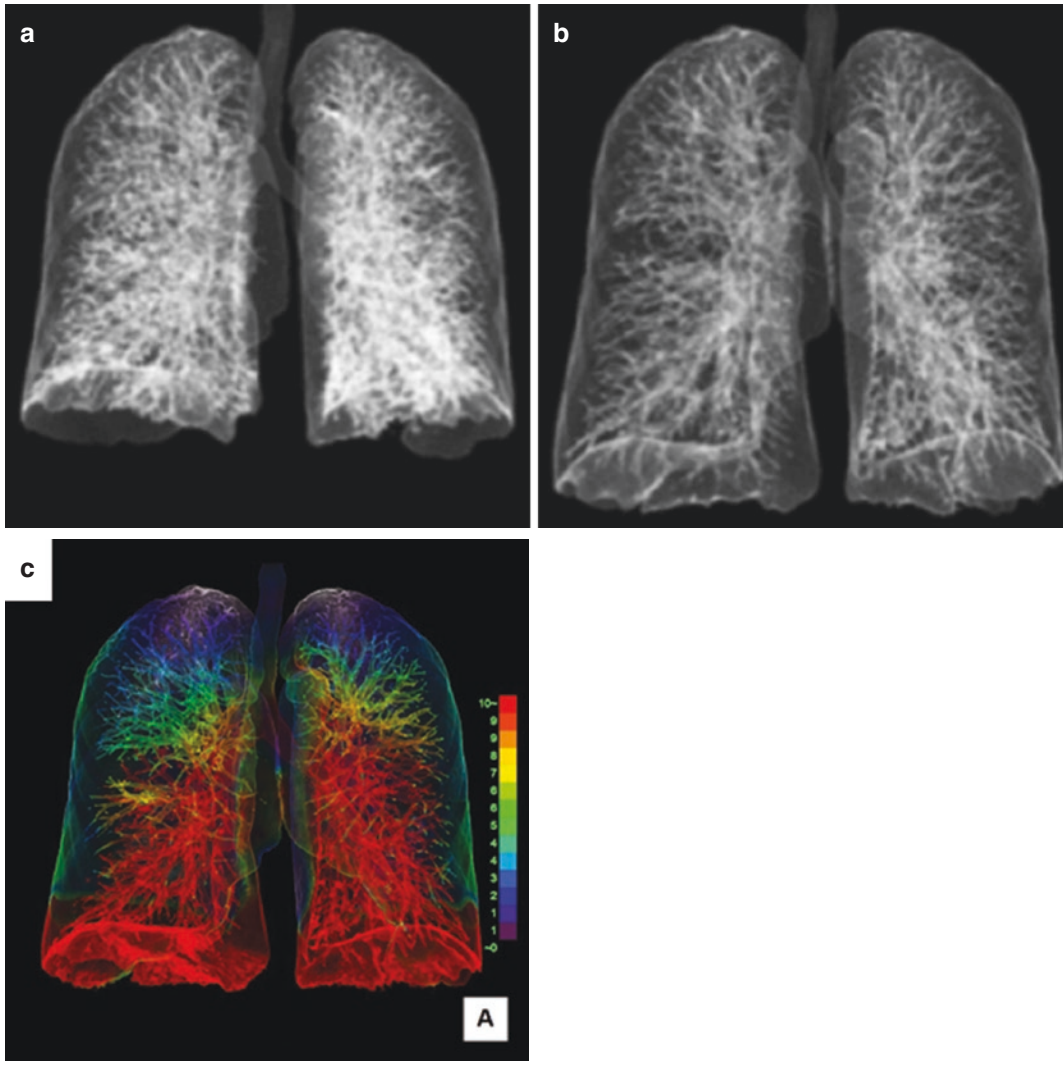


Fig. 5 4DCTs in a healthy volunteer. (**a**) Expiratory phase, (**b**) inspiratory phase, and (**c**) color map showing the displacement of each lung structure from the expiratory to the inspiratory phase. Using a 320-row multidetector CT, continuous images for the upper and lower parts of the lung were obtained separately, and they were connected in a workstation (Ziostation 2; Ziosoft, Tokyo, Japan). The displacement was measured using a commercially available software (Physiozio; Ziosoft). Note: *Red* color indicates large displacement. The displacement of the lower lobe is larger than that of the upper lobe. The time resolution is increased by image processing. Please also see the supplemental Videos S1 and S2

was 1.7 mSv (standard deviation 1.1 mSv). In infants and small children, invasive endoscopy is of limited applicability, while pulmonary function tests have limited validity in these patients and do not provide anatomical information. 4DCT using 320-row MDCT can demonstrate a more complete airway and pulmonary evaluation within acceptable radiation exposure limits.

6 Clinical Application of 4DCT in COPD Patients

COPD is a disease characterized by airflow limitation that is not fully reversible. It consists of small airway disease (obstructive bronchiolitis) and parenchymal destruction (emphysema), the relative contributions of which vary among

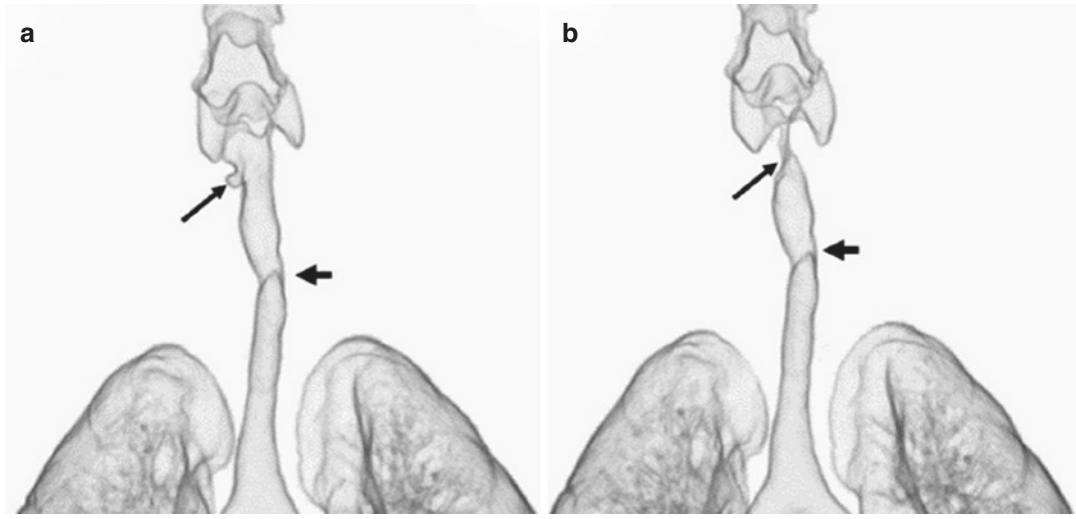


Fig. 6 4DCTs in an 11-year-old female with tracheomalacia. (**a**) Inspiratory and (**b**) expiratory phase of a 4DCT. These images were obtained with a 320-row multidetector CT (80 kVp, 40 mA) during free breathing. Abnormal closing of the trachea is observed in the expiratory phase (*arrows*). Web structure is also noted in the trachea (*bold arrows*). (Courtesy of Dr. Shoichiro Matsushita, St Marianna University School of Medicine)

patients (Global Initiative for Chronic Obstructive Lung Disease 2018). CT can well demonstrate emphysema, but airflow limitation evaluated by conventional pulmonary function tests does not have a good correlation with the severity of the emphysema on CT (Paoletti et al. 2015). Apparently, the small airway disease contributes more significantly to the airflow limitation in COPD patients. A recently developed CT-based technique allows for the noninvasive intraluminal evaluation of the peripheral airways in inspiratory 3DCTs (Hasegawa et al. 2006) and expiratory CT (Matsuoka et al. 2008).

Dynamic narrowing of the airways has already been visualized by high-speed electron-beam CT in COPD patients (Kurosawa and Kohzuki 2004). 4DCT can also demonstrate dynamic changes in the luminal areas during respiration (Fig. 7). Yamashiro et al. (2016) measured the mean lung density (MLD) of the scanned lung and the luminal areas (Ai) of fixed points in the trachea and the right proximal bronchi (main bronchus, upper bronchus, bronchus intermedius, and lower bronchus) in 4DCT using the commercially available software "4D airway analysis" (Canon Medical Systems). They showed that changes in bronchial Ai are closely correlated with MLD changes; the luminal area of bronchi decreased in expiration and increased during inspiration in healthy subjects (Fig. 8a). On the other hand, the changes in bronchial Ai are not perfectly correlated with changes in MLD in the patients with COPD (Fig. 8b). The cross-correlation coefficients between the airway Ai and MLD values were significantly correlated with the forced expiratory volume in 1 s/forced vital capacity (FEV1/FVC; $\rho = -0.56$ to -0.66, $P < 0.01$) (Yamashiro et al. 2016). This suggests that the synchrony between the airway and lung movement is lost in patients with severe airflow limitation. Abnormal heterogeneous ventilation in COPD patients has been demonstrated in several studies, for example, using conventional ventilation scintigraphy and hyperpolarized He-3 or Xe-129 MRI (Kirby et al. 2015). I expect that in the near future, 4DCT will be applied to analyze changes in more peripheral bronchi and/or lung parenchyma during respiration.

Another interesting result has been reported by Xu et al. (Fig. 9). They measured the cardiac cross-sectional area (CSA) in 4DCTs and showed that CSA at both inspiration and expiration was significantly smaller in COPD patients than in non-COPD smokers ($P < 0.05$). Moreover, the cross-correlation coefficient between cardiac CSA and MLD during expiration significantly

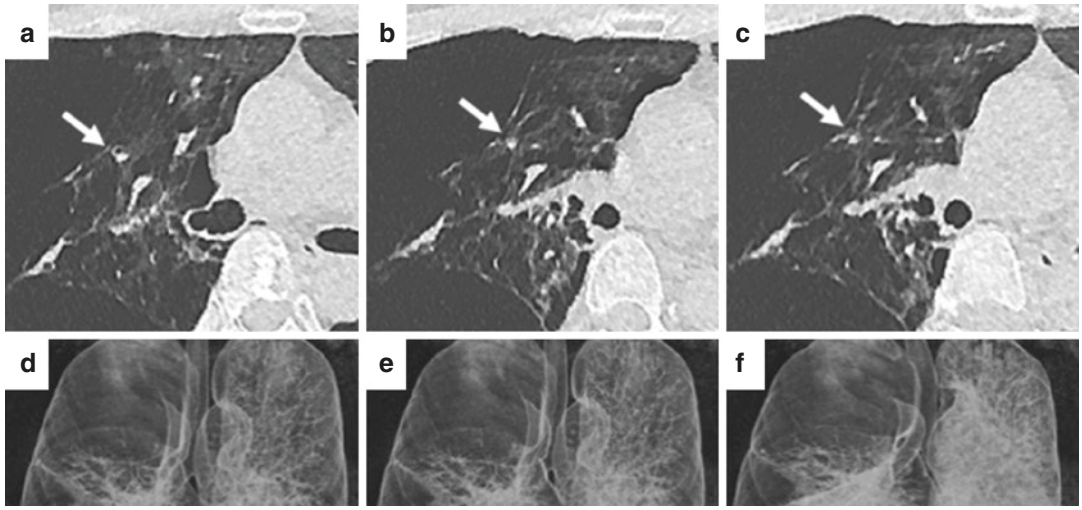


Fig. 7 4DCTs in a 48-year-old male with severe emphysema. (**a, d**) Deep inspiratory phase, (**b, e**) initial phase of expiration, (**c, f**) deep expiratory phase. Dynamic bronchial narrowing is observed in the initial phase of the expiration (*arrows*). The 3D images show marked air trapping of the right lung, and a mediastinal shift is noted in the deep expiratory phase

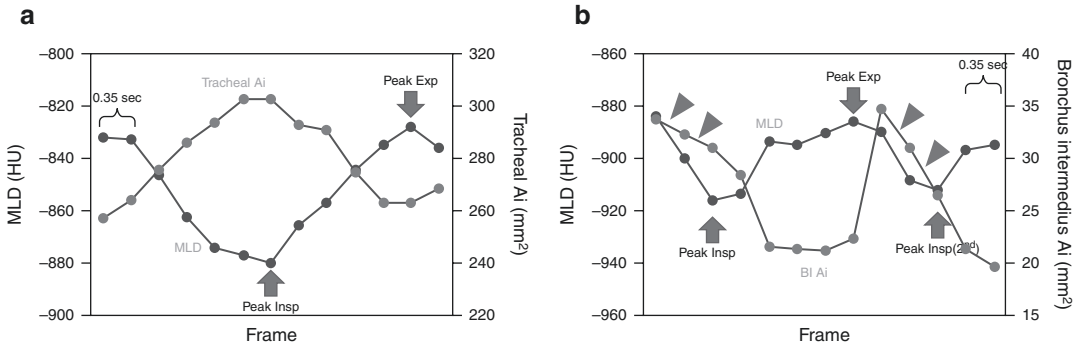


Fig.8 (**a**) Measurement of the cross-correlation coefficient between two curves representing the mean lung density and the airway luminal area over time. Notes: In this patient (a male smoker without COPD, FEV1/FVC = 0.81), the time curves for MLD and tracheal Ai move almost perfectly in the opposite direction, suggesting that tracheal dilation and lung inflation occurred simultaneously. The negative cross-correlation coefficient between these two time curves was with −0.98 large. (**b**) An example of a small cross-correlation between the mean lung density and airway luminal area in a female patient with COPD (FEV1/FVC = 0.53). Notes: The two time curves for MLD and bronchial Ai (bronchus intermedius) move in the opposite direction (cross-correlation coefficient = −0.21). Furthermore, it is repeatedly observed that the Ai of the bronchus intermedius unexpectedly decreases during inspiratory phases (*arrowheads*), suggesting the presence of paradoxical airway movements. Abbreviations: COPD, chronic obstructive lung disease; FEV1/FVC, forced expiratory volume in 1 s/forced vital capacity; MLD, mean lung density; Ai, luminal area; BI, bronchus intermedius. (Reproduced from Yamashiro et al. (2016))

correlated with FEV1/FVC ($\rho = 0.63$, $P < 0.001$), suggesting that the heart size decreases during expiration in COPD patients (Xu et al. 2017). Right-sided heart failure is an important complication in COPD patients, and its development is directly correlated with the patients' prognosis (Wells et al. 2012). As shown in Fig. 10 and its supplemental Video S3, 4DCT can demonstrate both respiratory motion and heartbeat. Heart-lung interaction got more attention than before

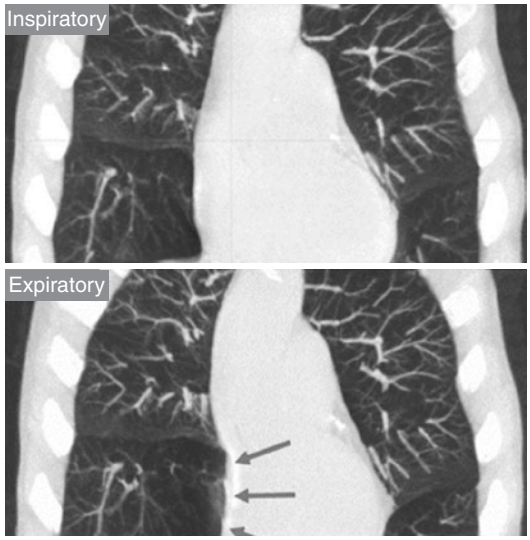


Fig. 9 4DCTs in a 70-year-old male with COPD. His FEV1/FVC was 0.55. The shape of the right atrium is normal during the inspiratory phase but is severely compressed (*arrows*) during the expiratory phase, probably due to the emphysematous right middle lobe. Abbreviations: 4DCT, four-dimensional computed tomography; COPD, chronic obstructive lung disease; FEV1/FVC, forced expiratory volume in 1 s/forced vital capacity. (Reproduced from Xu et al. (2017))

(Cheyne et al. 2016). 4DCT could add new perspectives regarding the dynamic interaction between the lung and the heart in the respiratory cycle.

7 Clinical Application of 4DCT in Patients with Lung Cancer

Lung cancer is the leading cause of cancer-related deaths in the United States. In preoperative patients, it is necessary to diagnose whether lung cancer invades the chest wall or large vessels directly. As shown in Fig. 10, 4DCT can determine tumor invasion into the chest wall and/or large vessels. Usually, local invasion of lung cancer has been evaluated using static CT and/or MRI, cine magnetic resonance imaging, or combined inspiratory and expiratory chest CT (Murata et al. 1994; Seo et al. 2005; Chang et al. 2015a, b). In static CT images, the length and the angle of the contact between the mass and adjacent structures, the obliteration of the fat plane, and adjacent pleural or pericardial thickening

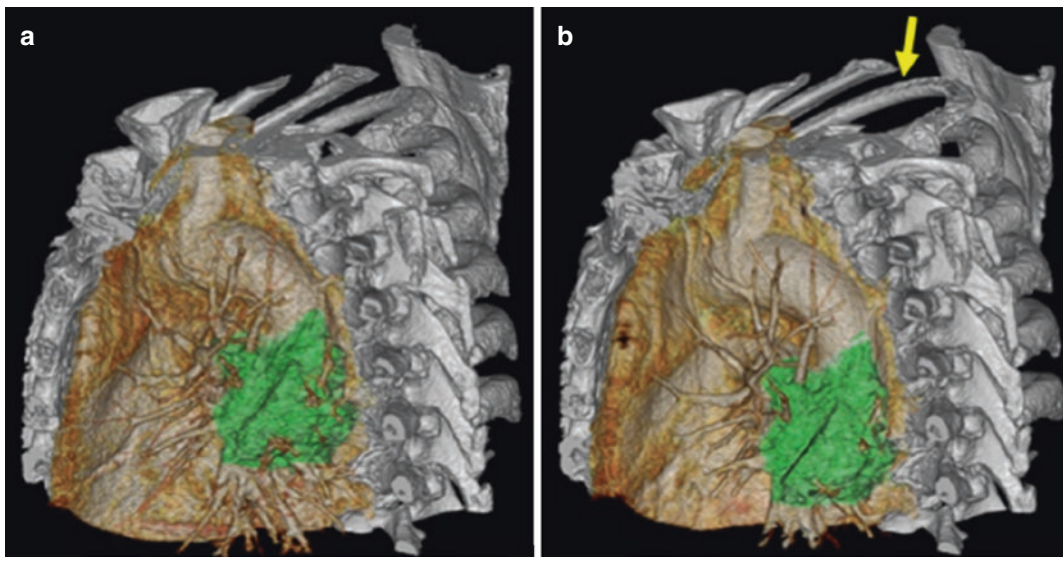


Fig.10 A 77-year-old male with lung cancer invading the aorta. (**a**) Expiratory and (**b**) inspiratory phase of the 4DCT. The tumor in the left lung moves with the aorta during respiration, which indicates the tumor infiltration of the aorta. Note: The ribs move upward during inspiration with a slight rotation, resulting in an increased distance between the ribs (*arrow*) and an expanded thoracic cage. Please also see the supplemental Video S3. (The time resolution is increased by image processing in a commercially available workstation [Ziostation 2; Ziosoft, Tokyo, Japan])

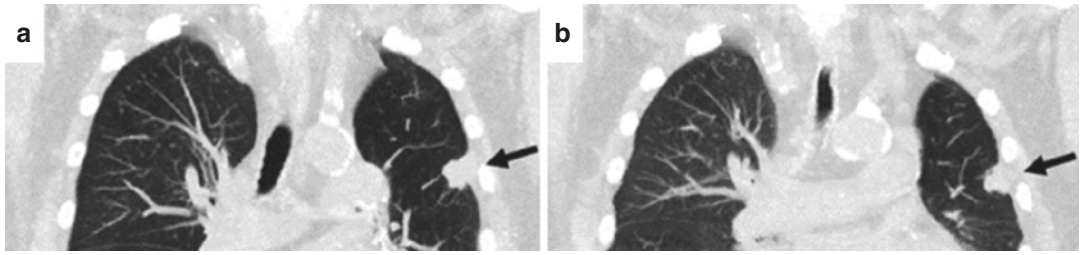


Fig. 11 4DCTs of a 70-year-old male with lung cancer in the inspiratory (**a**) and expiratory (**b**) phase. It was confirmed intraoperatively that the cancer in the left lung (*arrows*) did not invade the chest wall directly, but a total adhesion of the visceral and parietal pleura due to previous surgery was detected. On 4DCT, this adhesion was suspected based on the restricted mobility of the peripheral vessels during chest wall movements

have all been used as evidence for an invasion of the surrounding structure. However, it is difficult to determine the histological pleural invasion pl0 (without invasion) to pl3 (invasion to the parietal pleura) using only static CT images.

Recent studies showed the possibility that a quantitative analysis of 4DCT can demonstrate parietal pleural invasion and/or adhesion (Sakuma et al. 2017; Hashimoto et al. 2018) (Fig. 11). Sakuma et al. proposed three different approaches: (1) analysis of the distance moved from the inspiratory frame, (2) analysis of the total movement distance, and (3) vector analysis. They found several quantitative indices that can distinguish between patients with and without parietal pleural invasion/adhesion (Sakuma et al. 2017). Hashimoto et al. assessed local movement of several points on the pleura and the corresponding costal surface using automatic tracking functions on a dedicated workstation (4D Airway Analysis; Canon Medical Systems). The authors showed that the local movements were significantly different in patients with and without pleural adhesion (Hashimoto et al. 2018).

Thoracoscopic approaches in thoracic surgery have become extremely popular during the past decade. The pleural adhesions between the visceral and parietal pleura prevent the lung from collapsing, increase the risk of lung injury from the video telescope, and prevent in severe cases access to the pleural space, requiring conversion to an open thoracotomy. It is very difficult to evaluate adhesions between the visceral and parietal pleura, even when based on the pleural thickness on static CT images (Mason et al. 1999). Therefore, some surgeons use ultrasound before surgery (Sasaki et al. 2005; Tahiri et al. 2014). Ultrasound can demonstrate the sliding motion of the visceral pleura over the chest wall, but ultrasound from the body's surface cannot evaluate adhesion of the mediastinal aspect. Because 4DCT can precisely demonstrate the thoracic structures including hila and mediastinum, I expect the 4DCT analysis to possibly determine mediastinal pleural adhesion.

Respiratory-gated 4DCT is also used for radiation therapy planning as mentioned above. Radiation therapy is usually included as part of a multi-modality approach to treat locally advanced non-small-cell lung cancer (NSCLC) and is being increasingly used in patients with early-stage NSCLC receiving stereotactic body radiation therapy (SBRT). Identifying the complete extent of tumor motion and subsequently including all potential tumor locations as part of the treatment target are important for radiation planning, especially in SBRT. Chang et al. conducted a multicenter, randomized trial (Chang et al. 2015a, b) and reported that SBRT using respiratory-gated 4DCT-based radiation planning could be an option for treating operable stage I NSCLC.

8 The Future of 4D Image Analysis

Thanks to the continued development of analysis methods, 4DCT provides a lot of information about finer anatomical structures and their movements. Moriya et al. measured the lung volume at

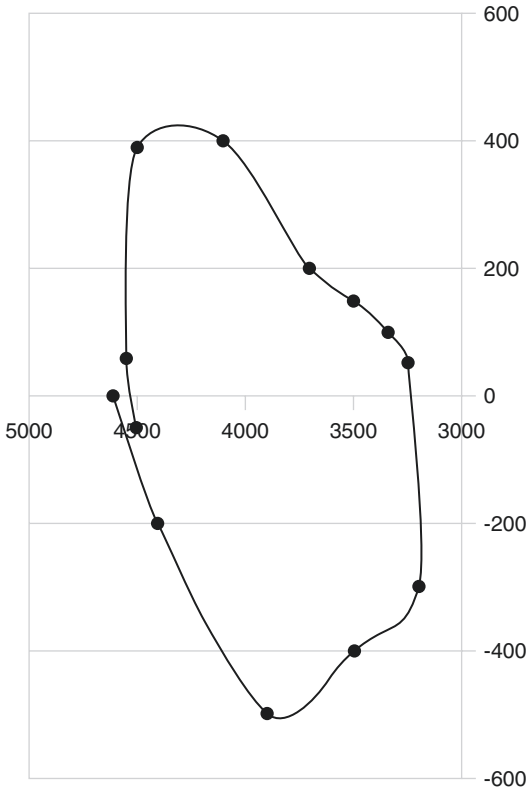


Fig. 12 CT flow-volume curves based on 4DCT in a healthy volunteer. The graphs show flow-volume loops of the whole lung. The volume changes of the lung are derived from sequential images and plotted as inspiratory and expiratory flow (on the *Y*-axis) against the CT lung volume (on the *X*-axis). The volumes of each phase were measured on 4DCT in a workstation (Ziostation 2; Ziosoft, Tokyo, Japan). (Courtesy of Dr. Hiroshi Moriya, Ohara General Hospital, Fukushima, Japan)

each respiratory phase on 4DCT and determined a "CT flow-volume curve" separately for the right and left lung (Fig. 12) (Moriya et al. 2018). This method could be applied to the motion analysis of each segment or subsegment. Moreover, displacement of the peripheral pulmonary structures between two sequential images can be measured with commercially available software, as shown in Fig. 5 and the supplemental Video S2. Of course, changes in CT lung volume and displacement of lung structures do not equal gas exchange; gas is compressible and easily changes volume as a result of changing pressure. The conventional flow-volume curve is a principle of pneumology, which the CT flow-volume curve cannot replace. The conventional flow-volume curve has been analyzed based on a simple model in which the lung parenchyma is a uniform isotropic material and uniformly inflates and deflates. However, the lung does not expand uniformly, the different lung regions will open and empty asynchronously (Capaldi et al. 2016). An improved quantitative analysis of 4DCTs will facilitate an understanding of the mechanics of the lung parenchyma.

9 Conclusions

Several methods of 4DMRI and 4DCT have already been developed and applied to patients in clinical situations such as radiation therapy planning and monitoring, preoperative assessment of pleural adhesion, and tracheobronchomalacia. These 4D images will provide new information about respiratory mechanics and heart-lung interactions, which will be beneficial for patient care. 4DMRI and 4DCT should be used in clinical routine. Due to the lack of irradiation, 4DMRI is especially suitable in infant and children.

References

Bainbridge H, Salem A, Tijssen RHN, Dubec M, Wetscherek A, Van ESC, Belderbos J, Faivre-Finn C, McDonald F (2017) Magnetic resonance imaging in precision radiation therapy for lung cancer. Transl Lung Cancer Res 6:689–707

Bates AJ, Higano NS, Hysinger EB, Fleck RJ, Hahn AD, Fain SB, Kingma PS, Woods JC (2018) Quantitative assessment of regional dynamic airway collapse in neonates via retrospectively respiratory-gated ^{1}H ultrashort echo time MRI. J Magn Reson Imaging. https://doi.org/10.1002/jmri.26296

Bell LC, Johnson KM, Fain SB, Wentland A, Drees R, Johnson RA, Bauman G, Francois CJ, Nagle SK (2015) Simultaneous MRI of lung structure and perfusion in a single breathhold. J Magn Reson Imaging 41:52–59

Burris NS, Johnson KM, Larson PE, Hope MD, Nagle SK, Behr SC, Hope TA (2016) Detection of small pulmonary nodules with ultrashort echo time sequences in oncology patients by using a PET/MR system. Radiology 278:239–246

Cai J, Miller GW, Altes TA, Read PW, Benedict SH, De Lange EE, Cates GD, Brookeman JR, Mugler JP 3rd,

Sheng K (2007) Direct measurement of lung motion using hyperpolarized helium-3 MR tagging. Int J Radiat Oncol Biol Phys 68:650–653

Cai J, Sheng K, Benedict SH, Read PW, Larner JM, Mugler JP 3rd, De Lange EE, Cates GD Jr, Miller GW (2009) Dynamic MRI of grid-tagged hyperpolarized helium-3 for the assessment of lung motion during breathing. Int J Radiat Oncol Biol Phys 75:276–284

Capaldi DP, Zha N, Guo F, Pike D, McCormack DG, Kirby M, Parraga G (2016) Pulmonary imaging biomarkers of gas trapping and emphysema in COPD: (3) He MR imaging and CT parametric response maps. Radiology 279:597–608

Chang JY, Senan S, Paul MA, Mehran RJ, Louie AV, Balter P, Groen HJ, McRae SE, Widder J, Feng L, Van Den Borne BE, Munsell MF, Hurkmans C, Berry DA, Van Werkhoven E, Kresl JJ, Dingemans AM, Dawood O, Haasbeek CJ, Carpenter LS, De Jaeger K, Komaki R, Slotman BJ, Smit EF, Roth JA (2015a) Stereotactic ablative radiotherapy versus lobectomy for operable stage I non-small-cell lung cancer: a pooled analysis of two randomised trials. Lancet Oncol 16(6):630–637

Chang S, Hong SR, Kim YJ, Hong YJ, Hur J, Choi BW, Lee HJ (2015b) Usefulness of thin-section single-shot turbo spin echo with half-Fourier acquisition in evaluation of local invasion of lung cancer. J Magn Reson Imaging 41:747–754

Cheyne WS, Williams AM, Harper MI, Eves ND (2016) Heart-lung interaction in a model of COPD: importance of lung volume and direct ventricular interaction. Am J Physiol Heart Circ Physiol 311:H1367–H1374

Cotes J, Chinn D, Miller M (eds) (2006) Lung function: physiology, measurement and application in medicine. Blackwell, London

Delacoste J, Chaptinel J, Beigelman-Aubry C, Piccini D, Sauty A, Stuber M (2018) A double echo ultra short echo time (UTE) acquisition for respiratory motion-suppressed high resolution imaging of the lung. Magn Reson Med 79:2297–2305

Dournes G, Grodzki D, Macey J, Girodet PO, Fayon M, Chateil JF, Montaudon M, Berger P, Laurent F (2015) Quiet submillimeter MR imaging of the lung is feasible with a PETRA sequence at 1.5 T. Radiology 276:258–265

Gai ND, Malayeri A, Agarwal H, Evers R, Bluemke D (2016) Evaluation of optimized breath-hold and free-breathing 3D ultrashort echo time contrast agent-free MRI of the human lung. J Magn Reson Imaging 43:1230–1238

Gast KK, Puderbach MU, Rodriguez I, Eberle B, Markstaller K, Hanke AT, Schmiedeskamp J, Weiler N, Lill J, Schreiber WG, Thelen M, Kauczor HU (2002) Dynamic ventilation (3)He-magnetic resonance imaging with lung motion correction: gas flow distribution analysis. Investig Radiol 37: 126–134

Gee J, Sundaram T, Hasegawa I, Uematsu H, Hatabu H (2003) Characterization of regional pulmonary mechanics from serial magnetic resonance imaging data. Acad Radiol 10:1147–1152

Gierada DS, Curtin JJ, Erickson SJ, Prost RW, Strandt JA, Goodman LR (1995) Diaphragmatic motion: fast gradient-recalled-echo MR imaging in healthy subjects. Radiology 194:879–884

Global Initiative For Chronic Obstructive Lung Disease. (2018) Global strategy for the diagnosis, management, and prevention of chronic obstructive lung disease. https://goldcopd.org/gold-reports/reportXYZ.pdf. Accessed 12 Dec 2018

Greenberg SB (2012) Dynamic pulmonary CT of children. AJR Am J Roentgenol 199:435–440

Hahn AD, Higano NS, Walkup LL, Thomen RP, Cao X, Merhar SL, Tkach JA, Woods JC, Fain SB (2017) Pulmonary MRI of neonates in the intensive care unit using 3D ultrashort echo time and a small footprint MRI system. J Magn Reson Imaging 45:463–471

Hasegawa M, Nasuhara Y, Onodera Y, Makita H, Nagai K, Fuke S, Ito Y, Betsuyaku T, Nishimura M (2006) Airflow limitation and airway dimensions in chronic obstructive pulmonary disease. Am J Respir Crit Care Med 173:1309–1315

Hashimoto M, Nagatani Y, Oshio Y, Nitta N, Yamashiro T, Tsukagoshi S, Ushio N, Mayumi M, Kimoto T, Igarashi T, Yoshigoe M, Iwai K, Tanaka K, Sato S, Sonoda A, Otani H, Murata K, Hanaoka J (2018) Preoperative assessment of pleural adhesion by Four-Dimensional Ultra-Low-Dose Computed Tomography (4D-ULDCT) with Adaptive Iterative Dose Reduction using Three-Dimensional processing (AIDR-3D). Eur J Radiol 98:179–186

Hassani C, Ronco A, Prosper AE, Dissanayake S, Cen SY, Lee C (2018) Forward-projected model-based iterative reconstruction in screening low-dose chest Ct: Comparison with adaptive iterative dose reduction 3D. AJR Am J Roentgenol 211:548–556

Holmes JH, O'halloran RL, Brodsky EK, Bley TA, Francois CJ, Velikina JV, Sorkness RL, Busse WW, Fain SB (2009) Three-dimensional imaging of ventilation dynamics in asthmatics using multiecho projection acquisition with constrained reconstruction. Magn Reson Med 62:1543–1556

Hurkmans CW, Van Lieshout M, Schuring D, Van Heumen MJ, Cuijpers JP, Lagerwaard FJ, Widder J, Van Der Heide UA, Senan S (2011) 2015. Quality assurance of 4D-CT scan techniques in multicenter phase III trial of surgery versus stereotactic radiotherapy (radiosurgery or surgery for operable early stage (stage 1A) non-small-cell lung cancer [ROSEL] study). Int J Radiat Oncol Biol Phys 80(3):918–927

Iwasawa T, Kagei S, Gotoh T, Yoshiike Y, Matsushita K, Kurihara H, Saito K, Matsubara S (2002) Magnetic resonance analysis of abnormal diaphragmatic motion in patients with emphysema. Eur Respir J 19: 225–231

Jiang W, Ong F, Johnson KM, Nagle SK, Hope TA, Lustig M, Larson PEZ (2018) Motion robust high resolution 3D free-breathing pulmonary MRI using dynamic 3D image self-navigator. Magn Reson Med 79:2954–2967

Kirby M, Pike D, Sin DD, Coxson HO, McCormack DG, Parraga G (2015) COPD: do imaging measurements of

emphysema and airway disease explain symptoms and exercise capacity? Radiology 277:872–880

Kiryu S, Sundaram T, Kubo S, Ohtomo K, Asakura T, Gee JC, Hatabu H, Takahashi M (2008) MRI assessment of lung parenchymal motion in normal mice and transgenic mice with sickle cell disease. J Magn Reson Imaging 27:49–56

Kruger SJ, Nagle SK, Couch MJ, Ohno Y, Albert M, Fain SB (2016) Functional imaging of the lungs with gas agents. J Magn Reson Imaging 43: 295–315

Kurosawa H, Kohzuki M (2004) Images in clinical medicine dynamic airway narrowing. N Engl J Med 350:1036

Lederlin M, Crémillieux Y (2014) Three-dimensional assessment of lung tissue density using a clinical ultrashort echo time at 3 Tesla: a feasibility study in healthy subjects. J Magn Reson Imaging 40:839–847

Lee EY, Boiselle PM (2009) Tracheobronchomalacia in infants and children: multidetector CT evaluation. Radiology 252:7–22

Mason AC, Miller BH, Krasna MJ, White CS (1999) Accuracy of CT for the detection of pleural adhesions: correlation with video-assisted thoracoscopic surgery. Chest 115:423–427

Matsuoka S, Kurihara Y, Yagihashi K, Hoshino M, Nakajima Y (2008) Airway dimensions at inspiratory and expiratory multisection CT in chronic obstructive pulmonary disease: correlation with airflow limitation. Radiology 248:1042–1049

Moriya H, Muramatsu S, Yamashiro T, Nagatani Y, Ushio S, Mekaru H, Tsukagoshi S (2018) The whole-lung dynamic respiratory CT: the novel respiratory function examination by dynamic wide volume scaning using 320-row ADCT. In: Proceeding of the 77th Annual meeting of the Japan Radiological Society, p S284

Muramatsu S, Moriya H, Tsukagoshi S, Yamada N (2018) Development of audio indicator system for respiratory dynamic CT imaging. Nihon Hoshasen Gijutsu Gakkai Zasshi 74:154–160

Murata K, Takahashi M, Mori M, Shimoyama K, Mishina A, Fujino S, Itoh H, Morita R (1994) Chest wall and mediastinal invasion by lung cancer: evaluation with multisection expiratory dynamic CT. Radiology 191:251–255

Napadow VJ, Mai V, Bankier A, Gilbert RJ, Edelman R, Chen Q (2001) Determination of regional pulmonary parenchymal strain during normal respiration using spin inversion tagged magnetization MRI. J Magn Reson Imaging 13:467–474

Niwa T, Nozawa K, Aida N (2017) Visualization of the airway in infants with MRI using pointwise encoding time reduction with radial acquisition (PETRA). J Magn Reson Imaging 45:839–844

Ohno Y, Koyama H, Yoshikawa T, Matsumoto K, Takahashi M, Van Cauteren M, Sugimura K (2011) T2* measurements of 3-T MRI with ultrashort TEs: capabilities of pulmonary function assessment and clinical stage classification in smokers. AJR Am J Roentgenol 197:W279–W285

Paoletti M, Cestelli L, Bigazzi F, Camiciottoli G, Pistolesi M (2015) Chronic obstructive pulmonary disease: pulmonary function and CT lung attenuation do not show linear correlation. Radiology 276:571–578

Plathow C, Schoebinger M, Fink C, Hof H, Debus J, Meinzer HP, Kauczor HU (2006) Quantification of lung tumor volume and rotation at 3D dynamic parallel MR imaging with view sharing: preliminary results. Radiology 240:537–545

Roach DJ, Crémillieux Y, Serai SD, Thomen RP, Wang H, Zou Y, Szczesniak RD, Benzaquen S, Woods JC (2016) Morphological and quantitative evaluation of emphysema in chronic obstructive pulmonary disease patients: a comparative study of MRI with CT. J Magn Reson Imaging 44:1656–1663

Sakuma K, Yamashiro T, Moriya H, Murayama S, Ito H (2017) Parietal pleural invasion/adhesion of subpleural lung cancer: quantitative 4-dimensional CT analysis using dynamic-ventilatory scanning. Eur J Radiol 87:36–44

Sasaki M, Kawabe M, Hirai S, Yamada N, Morioka K, Ihaya A, Tanaka K (2005) Preoperative detection of pleural adhesions by chest ultrasonography. Ann Thorac Surg 80:439–442

Sasaki T, Takahashi K, Obara M (2017) Viability of oxygen-enhanced ventilation imaging of the lungs using ultra-short echo time MRI. Magn Reson Med Sci 16:259–261

Sekine A, Satoh H, Iwasawa T, Matsui K, Ikeya E, Ikeda S, Yamakawa H, Okuda R, Kitamura H, Shinohara T, Baba T, Komatsu S, Kato T, Hagiwara E, Ogura T (2017) Unilateral upper lung field pulmonary fibrosis radiologically consistent with pleuroparenchymal fibroelastosis after thoracotomy: a new disease entity related to thoracotomy. Respiration 94:431–441

Seo JS, Kim YJ, Choi BW, Choe KO (2005) Usefulness of magnetic resonance imaging for evaluation of cardiovascular invasion: evaluation of sliding motion between thoracic mass and adjacent structures on cine MR images. J Magn Reson Imaging 22:234–241

Shibata H, Iwasawa T, Gotoh T, Kagei S, Shinohara T, Ogura T, Hagiwara H, Tateishi U, Inoue T (2012) Automatic tracking of the respiratory motion of lung parenchyma on dynamic magnetic resonance imaging: comparison with pulmonary function tests in patients with chronic obstructive pulmonary disease. J Thorac Imaging 27:387–392

Suga K, Tsukuda T, Awaya H, Matsunaga N, Sugi K, Esato K (2000) Interactions of regional respiratory mechanics and pulmonary ventilatory impairment in pulmonary emphysema: assessment with dynamic MRI and xenon-133 single-photon emission Ct. Chest 117:1646–1655

Tahiri M, Khereba M, Thiffault V, Ferraro P, Duranceau A, Martin J, Liberman M (2014) Preoperative assessment of chest wall invasion in non-small cell lung cancer using surgeon-performed ultrasound. Ann Thorac Surg 98:984–989

Togao O, Tsuji R, Ohno Y, Dimitrov I, Takahashi M (2010) Ultrashort echo time (UTE) MRI of the lung:

assessment of tissue density in the lung parenchyma. Magn Reson Med 64:1491–1498

Tokuda J, Schmitt M, Sun Y, Patz S, Tang Y, Mountford CE, Hata N, Wald LL, Hatabu H (2009) Lung motion and volume measurement by dynamic 3D MRI using a 128-channel receiver coil. Acad Radiol 16:22–27

Triphan SM, Breuer FA, Gensler D, Kauczor HU, Jakob PM (2015) Oxygen enhanced lung MRI by simultaneous measurement of T1 and T2 * during free breathing using ultrashort TE. J Magn Reson Imaging 41:1708–1714

Troyer AD, Wilson TA (2016) Action of the diaphragm on the rib cage. J Appl Physiol 121:391–400

Tustison NJ, Awate SP, Cai J, Altes TA, Miller GW, De Lange EE, Mugler JP 3rd, Gee JC (2010) Pulmonary kinematics from tagged hyperpolarized helium-3 MRI. J Magn Reson Imaging 31:1236–1241

Voorhees A, An J, Berger KI, Goldring RM, Chen Q (2005) Magnetic resonance imaging-based spirometry for regional assessment of pulmonary function. Magn Reson Med 54:1146–1154

Wells JM, Washko GR, Han MK, Abbas N, Nath H, Mamary AJ, Regan E, Bailey WC, Martinez FJ, Westfall E, Beaty TH, Curran-Everett D, Curtis JL, Hokanson JE, Lynch DA, Make BJ, Crapo JD, Silverman EK, Bowler RP, Dransfield MT (2012) Pulmonary arterial enlargement and acute exacerbations of COPD. N Engl J Med 367:913–921

Wielpütz MO, Eberhardt R, Puderbach M, Weinheimer O, Kauczor HU, Heussel CP (2014) Simultaneous assessment of airway instability and respiratory dynamics with low-dose 4D-CT in chronic obstructive pulmonary disease: a technical note. Respiration 87:294–300

Wielpütz MO, Lee HY, Koyama H, Yoshikawa T, Seki S, Kishida Y, Sakai Y, Kauczor HU, Sugimura K, Ohno Y (2018) Morphologic characterization of pulmonary nodules with ultrashort TE MRI at 3T. AJR Am J Roentgenol 210:1216–1225

Xu Y, Yamashiro T, Moriya H, Tsubakimoto M, Tsuchiya N, Nagatani Y, Matsuoka S, Murayama S (2017) Hyperinflated lungs compress the heart during expiration in COPD patients: a new finding on dynamic-ventilation computed tomography. Int J Chron Obstruct Pulmon Dis 12:3123–3131

Yamashiro T, Matsuoka S, Bartholmai BJ, San José Estépar R, Ross JC, Diaz A, Murayama S, Silverman EK, Hatabu H, Washko GR (2010) Collapsibility of lung volume by paired inspiratory and expiratory CT scans: correlations with lung function and mean lung density. Acad Radiol 17:489–495

Yamashiro T, Moriya H, Matsuoka S, Nagatani Y, Tsubakimoto M, Tsuchiya N, Murayama S (2017) Asynchrony in respiratory movements between the pulmonary lobes in patients with COPD: continuous measurement of lung density by 4-dimensional dynamic-ventilation CT. Int J Chron Obstruct Pulmon Dis 12:2101–2109

Yamashiro T, Moriya H, Tsubakimoto M, Matsuoka S, Murayama S (2016) Continuous quantitative measurement of the proximal airway dimensions and lung density on four-dimensional dynamic-ventilation CT in smokers. Int J Chron Obstruct Pulmon Dis 11:755–764

Pulmonary Functional Imaging, Basics and Clinical Application of Nuclear Medicine and Hybrid Imaging

Marika Bajc, Dinko Franceschi, and Ari Lindqvist

Contents

1 **Introduction** 108

2 **Principles of Measuring Pulmonary Function in Cardiopulmonary Diseases with V/P Spect** 109
2.1 Ventilation Scintigraphy 110
2.2 Perfusion Scintigraphy 111
2.3 How to Perform V/P SPECT 111
2.4 Radiation Doses 115

3 **Clinical Use of Hybrid V/P SPECT/CT** 116

4 **Additional Findings** 117
4.1 Chronic Obstructive Pulmonary Disease (COPD) 117
4.2 Pneumonia 118
4.3 Left Heart Failure 118
4.4 Preoperative Evaluation of Lung Function 118
4.5 PET and PET/CT or PET/MRI 119

5 **Conclusion** 121

References 122

Abstract

Ventilation/perfusion tomography (V/P SPECT) is recommended as the firsthand tool for diagnosis of pulmonary embolism (PE) based on standardized technology and new holistic interpretation criteria. Pre-test probability helps clinicians to choose the most appropriate objective test for diagnosis or exclusion of PE. Interpretation takes into account all ventilation and perfusion patterns allowing for diagnosis of other cardiopulmonary diseases than PE. In such contexts, V/P SPECT has both an excellent sensitivity and

M. Bajc (✉)
Department of Clinical Sciences, University Hospital Lund, Lund, Sweden
e-mail: marika.bajc@med.lu.se

D. Franceschi
Department of Radiology, Stony Brook Medicine, Stony Brook, NY, USA
e-mail: Dinko.Franceschi@stonybrookmedicine.edu

A. Lindqvist
Research Unit of Pulmonary Diseases, Clinical Research Institute HUCH, HUS Helsinki University Hospital, Helsinki, Finland

© Springer Nature Switzerland AG 2021

Y. Ohno et al. (eds.), *Pulmonary Functional Imaging*, Medical Radiology Diagnostic Imaging,
https://doi.org/10.1007/978-3-030-43539-4_7

an excellent specificity for detecting PE. V/P SPECT has no contraindication; it is noninvasive and radiation exposure is low. Moreover, acquisition time for V/P SPECT is only 20 min. It allows for quantification of PE extension, which has an impact on individual treatment. It is uniquely useful for a clinical follow-up and for research.

Hybrid SPECT/CT imaging is a novel technique primarily developed to improve sensitivity and specificity of oncological diseases. Hybrid SPECT/CT imaging is not recommended as the primary tool for PE diagnosis in all patients with suspected PE. SPECT/CT may be relevant in COPD patients in order to identify small lung tumors and to classify severity of COPD. This is currently under investigation.

PET and PET CT or PET MRI are additional imaging techniques that are used to asses and quantify lung function and metabolic changes. Usually most explored biomarker is F-FDG used to show activity of pulmonary inflammation in a variety of respiratory diseases.

1 Introduction

Lung scintigraphy is an essential method to study pulmonary function. The basic studies are designed to demonstrate patterns of ventilation and perfusion.

In a healthy individual there is a balance between regional perfusion and ventilation to achieve optimal gas exchange. Some pulmonary disease causes changes in both ventilation and perfusion; they are "matched." The other ones can only cause changes in perfusion or ventilation, i.e., leading to mismatch that implies imbalance between perfusion and ventilation. The single most important application of lung scintigraphy is the evaluation of patients with suspected pulmonary embolism (PE). The value of scintigraphy in the detection of PE was first demonstrated by Wagner in 1964, using ^{131}I human serum albumin (HSA) for perfusion scintigraphy and a rectilinear scanner for imaging (Wagner 1964).

Studies of pulmonary ventilation and perfusion were commonly based on planar imaging that was the primary noninvasive method for diagnosis of pulmonary embolism (PE). However, the technique suffered disrepute since the PIOPED I study showed that 65% of scans were nondiagnostic (PIOPED Investigators 1990). As will be reviewed below, results from later studies based upon modern imaging techniques and new holistic principles (combining clinical information, pre-test probability, results of chest radiograph, and pattern typical of PE or other diseases) reduce the number of nondiagnostic findings to 4% or less, while sensitivity and specificity are excellent (Kan et al. 2015).

Since the early 1980s, single photon emission computed tomography (SPECT) has signified a new era in nuclear medicine making planar imaging obsolete in several fields. When the issue is identification and quantification of focal or regional aberration of organ function, SPECT is the method of choice. Undeniable advantage of ventilation/perfusion tomography (V/P SPECT) over the planar technique has been shown in numerous studies (Bajc et al. 2008; Grunig et al. 2014; Gutte et al. 2009; Leblanc et al. 2007; Lemb and Pohlabeln 2001; Reinartz et al. 2004; Mahdavi et al. 2013). V/P SPECT is recommended as the firsthand method for diagnosis of PE by the European Association of Nuclear medicine and endorsed by the Canadian Association (Bajc et al. 2009b; Bajc et al. 2019). Estimation of the clinical probability for PE before performing imaging tests is an important issue elaborated upon in the European Guidelines for Lung Scintigraphy (Bajc et al. 2009b) and by Mamlouk et al. (2010). The Guidelines are updated and extended to show indication of V/P SPECT not only for PE but also for other respiratory diseases such as pneumonia, COPD, and left heart failure.

Advantages of V/P SPECT based on standardized technology and new holistic interpretation criteria are as follows:

1. Fast procedure
2. Low radiation dose
3. No contraindication
4. High diagnostic accuracy and few nondiagnostic reports

5. Utility for selection of treatment strategy
6. Suitability for follow-up and research

2 Principles of Measuring Pulmonary Function in Cardiopulmonary Diseases with V/P Spect

Ventilation/perfusion scintigraphy is based on the facts that emboli affecting individual pulmonary arteries cause characteristic lobar, segmental, or sub-segmental peripheral wedge-shaped perfusion defects due to the distinctive pulmonary arterial segmental anatomy. Within a segment or segments affected by PE, ventilation is usually preserved. This pattern of preserved ventilation and absent perfusion, known as V/P mismatch, provides the basis for PE diagnosis (Fig. 1).

The ventilation scan maps regional ventilation and helps define lung borders, thereby facilitating the recognition of peripheral perfusion defects. The ventilation scan may also provide additional information about cardiopulmonary disorders, other than PE. For example, in COPD, the distribution of ventilation is uneven and focal deposition is often observed in peripheral airways, and in severe disease in central airways, too. Pneumonias cause regional ventilation defects, usually more extensive than the associated perfusion defects. A combined ventilation and perfusion study increases the specificity for PE diagnosis and allows recognition of additional pathology. It is therefore recommended that in PE diagnosis, a combined one-day protocol is used (Figs. 1, 2, and 3) (Bajc et al. 2009b).

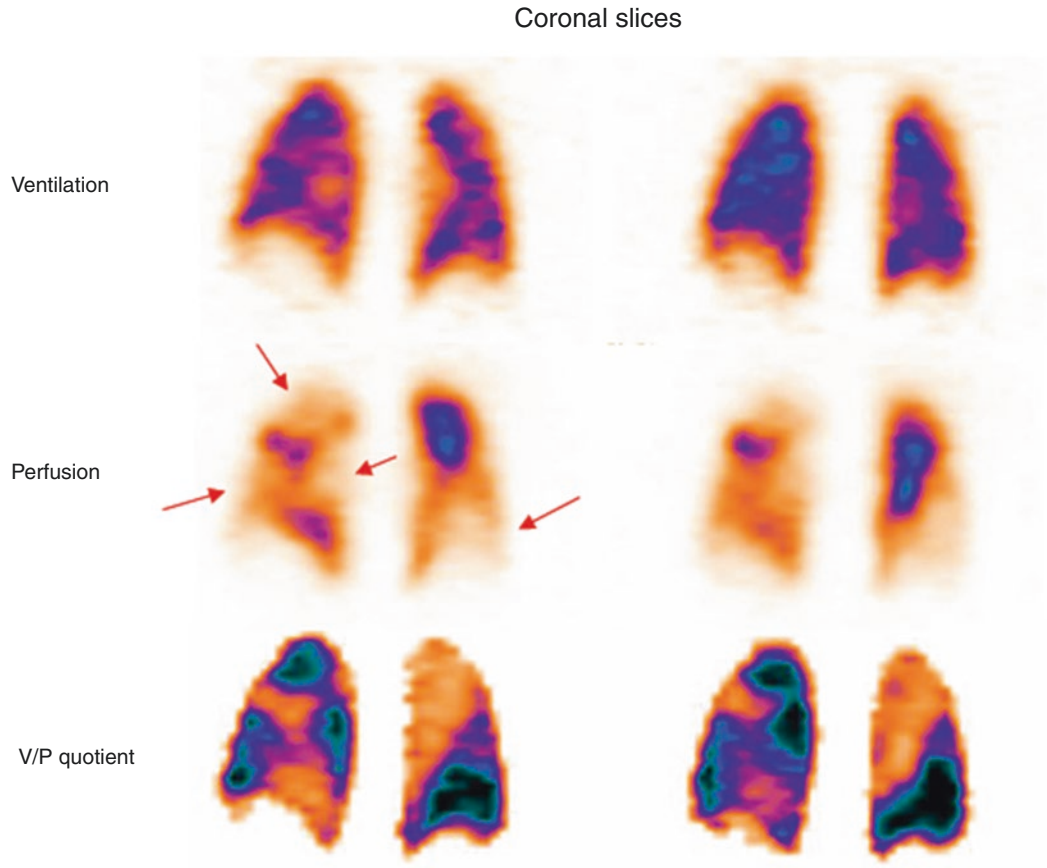


Fig. 1 Patient with PE. Coronal slices; segmental perfusion defects (PE, red arrows; in areas with preserved ventilation. V/P quotient images enlightened mismatches and facilitate interpretation

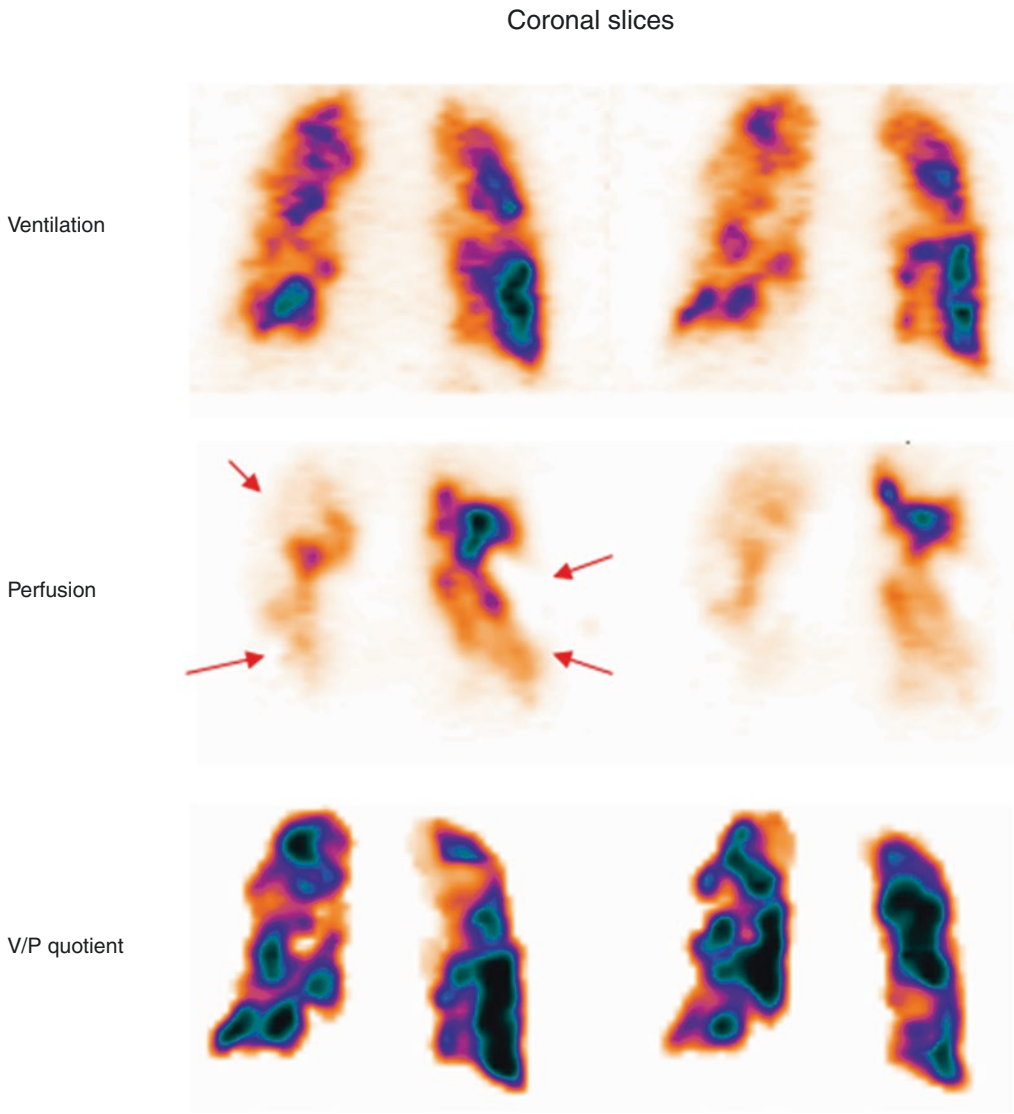


Fig. 2 Patient with severe COPD and massive PE. Coronal slices; uneven distribution of ventilation with central deposition of aerosols indicating severe degree of airway obstruction. Corresponding perfusion images (middle row) show multiple segmental and lobar perfusion defects in the ventilated areas (PE, red arrows) well delineated on V/P quotient image

2.1 Ventilation Scintigraphy

Ventilation can be performed with radioactive gases or labeled aerosols.

The ideal aerosol particles are in the range of 0.1–0.5 μm. Large particles (> 2 μm) are deposited mainly by impaction in large airways. Very fine particles, <1 μm, are mainly deposited in alveoli finally by diffusion. Radiolabeled liquid aerosols, such as diethylene triamine penta-acetate (DTPA) labeled, are hydro-soluble and have a tendency to grow in size during inhalation. Therefore, they may cause hot spots in images and deteriorate interpretation. High flow rates at forced breathing patterns and turbulent flow enhances particle deposition in airways and augments tendencies to hot spots in ventilation images, particularly in chronic obstructive pulmonary disease (COPD).

The 99mTc-labeled Technegas has hydrophobic particles with a constant size of 0.005–0.2μm. These penetrate to the alveolar level nearly as a gas. Technegas is advantageous, compared to other aerosols, particularly in patients with obstructive lung disease (Jogi et al. 2010). Technegas showed significantly improved outcomes with deposition of aerosol in central airway and better penetration to the periphery, which is important for patients with obstructive lung disease. Thus, it enables a correct diagnosis of PE even in obstructive patients and its use is generally recommended (Fig. 2).

2.2 Perfusion Scintigraphy

Perfusion scintigraphy is accomplished by micro embolization with radiolabeled particles injected in a peripheral vein. The commercially used particles are macro aggregate of human albumin (MAA), marked with ^{99m}Tc. The size is 15–100 μm and particles lodge in the pulmonary capillaries and precapillary arterioles. The particle distribution accurately illustrates regional perfusion. When performing the study, an important concern is the number of particles given. A minimum of 60,000 particles is required to obtain an even distribution of activity reflecting regional perfusion (Heck and Duley 1974). Normally, about 400,000 labeled particles are injected. Having in mind that there are over 280 billion pulmonary capillaries and 300 million precapillary arterioles, the routinely administered particles will result in obstruction of only a very small fraction of pulmonary vessels. However, a special preparation of 100,000–200,000 particles is usually given to patients with known pulmonary hypertension, right to left heart shunt, or after a single lung transplantation.

2.3 How to Perform V/P SPECT

2.3.1 Image Acquisition

Using a dual head camera, a fast and efficient clinical method for V/P SPECT was developed (Palmer et al. 2001). Doses of 25–30 MBq for ventilation studies and 120–140 MBq for perfusion studies were found optimal by using a general-purpose collimator and 64 × 64 matrix. A total acquisition time is about 20 min. During the examination, the supine patient carefully maintains the position between ventilation and perfusion acquisitions. Immobilization during the examination is usually well tolerated by patients and is comfortable even for most critically ill patients. It is also more convenient for the staff.

2.3.2 Reconstruction

Iterative reconstruction is performed using ordered subset expectation maximization (OSEM), e.g., with 8 subsets and 2 iterations. In processing the images the ventilation background is subtracted from the perfusion tomograms and a normalized V/P image set is calculated, V/P quotient (Palmer et al. 2001). V/P quotient images facilitate recognition of mismatch, particularly important in the middle lobe and lingula where mismatch may be overlooked if the lung is not accurately delineated by its ventilation images. Furthermore, quotient images facilitate the quantification of PE extension (Elf et al. 2015; Olsson et al. 2006). Volume rendered images, such as "Maximum Intensity Projection," are available with almost all SPECT systems, allowing rotating 3D views. This modality is another valuable option, particularly for quantification and follow-up of ventilation/perfusion changes.

2.3.3 Interpretation with Emphasis on PE

In PE, a perfusion defect is due to an embolus blocking blood flow. Because there is no corresponding blockage in the airways, ventilation remains normal causing a mismatch pattern. The distinction of whether a given perfusion defect is matched or mismatched is fundamental. The next step is to characterize the perfusion defects. Perfusion defects due to a blockage of a pulmonary artery should reflect the branching of the pulmonary circulation and its classical segmental anatomy. A segmental defect is wedge shaped with its base on the pleura (Figs. 1, 2, and 3).

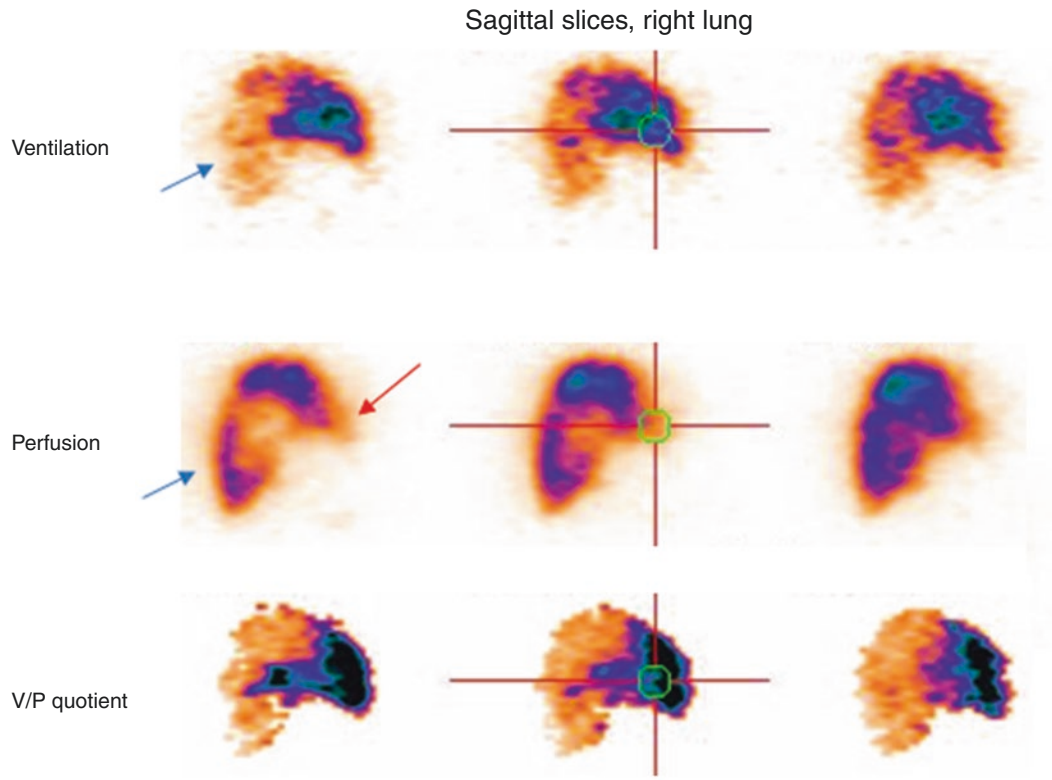


Fig. 3 Patient with PE and pneumonia. Sagittal slices; perfusion defect in the middle lobe (red arrow). Reduction in ventilation posteriorly (blue arrow) and stripe sign seen on perfusion image (pneumonia, blue arrow)

2.3.4 Recommended Criteria for Reading V/P SPECT with Respect to Acute PE

PE:

- V/P mismatch of at least one segment or two subsegments in keeping with the pulmonary vascular anatomy (wedge-shaped defects with the base projecting to the lung periphery).

No PE:

- Normal perfusion pattern in keeping with the anatomic boundaries of the lungs.
- Matched or reversed-mismatched V/P defects of any size, shape or number in the absence of mismatch.
- Mismatch that does not follow a lobar, segmental or subsegmental pattern.

Nondiagnostic for PE:

- Widespread V/P abnormalities not typical of specific diseases.

2.3.5 Quantification of PE Extent

An important step in the diagnostic procedure is to quantify the extent of embolism. V/P SPECT is particularly suitable for this because of its greater sensitivity compared to alternative planar scintigraphy and CTPA. The number of segments and sub-segments indicating PE typical mismatch are counted and expressed in percentage of the total lung parenchyma. Furthermore, areas with ventilation abnormalities were recognized and this allowed the degree of total lung malfunction to be estimated. The study showed that patients with PE engaging up 40% of the lung could be safely treated at home if ventilation abnormalities engaged not more than 20%

of the lung (Olsson et al. 2006). Outpatient management in hemodynamically stable patients with PE is safe, provided that the embolic burden, quantified using V/P SPECT, is included in the treatment decision algorithm (Elf et al. 2015). The extent of PE is an independent risk factor for PE recurrence (Alhadad et al. 2012; Couturaud and Kearon 2008; Couturaud et al. 2015; Couturaud 2016).

2.3.6 Follow-Up

Knowledge about the natural history of PE is limited. There is a need to study alternative strategies for PE therapy, with respect to therapy duration and choice of drugs in different categories of patients. The issue of small emboli is particularly important, particularly regarding the treatment. Figure 4 presents a patient with untreated small PE who developed chronic PE after 3 months follow-up.

Follow-up of PE using imaging is essential to:

- Assess the effect of therapy
- Differentiate between new and old PE when there is a suspicion of PE recurrence
- Explain physical incapacity after PE

Some patients have a tendency to develop recurrent episodes of PE (Fig. 5a). The patient had initially small segmental PE and was treated initially for 6 months with a low-molecular-weight heparin. Two years after discontinuing

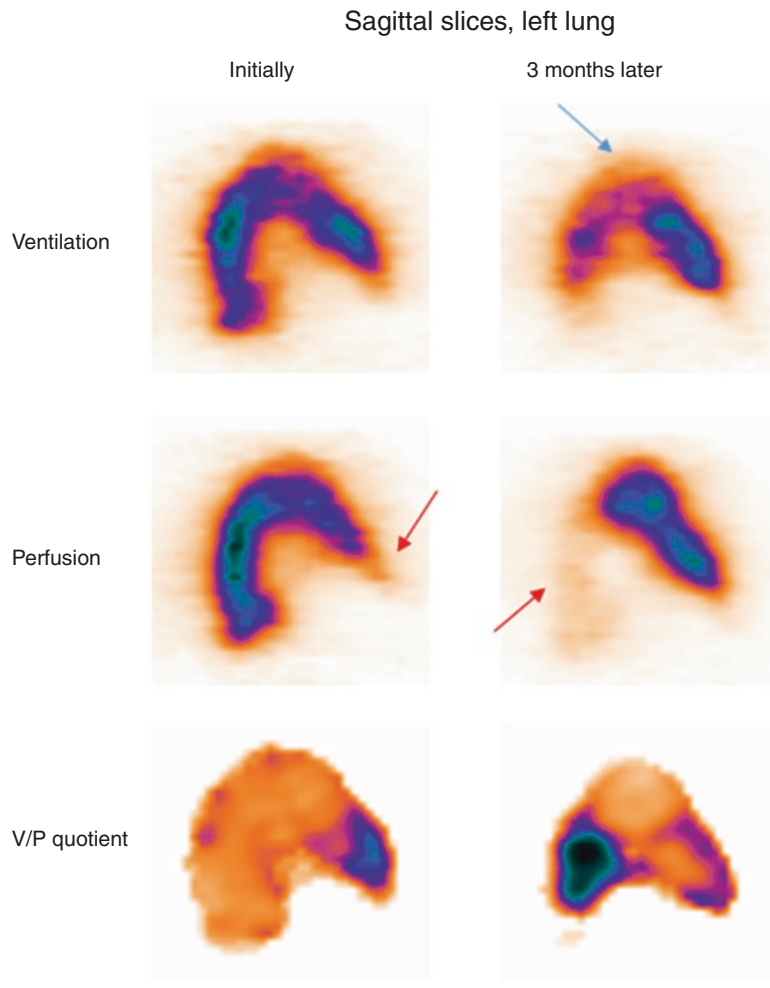


Fig. 4 Patient with small PE, not treated. Sagittal slice; the left lung showed initially a small perfusion defect in lingula (PE). This patient was not treated but was examined again 3 months later. On follow-up, the initial perfusion defect was more prominent and perfusion defects were extended into the whole lower lobe (red arrow). Moreover, patient develop pneumonia, seen as a reduction of ventilation in the upper lobe (blue arrow)

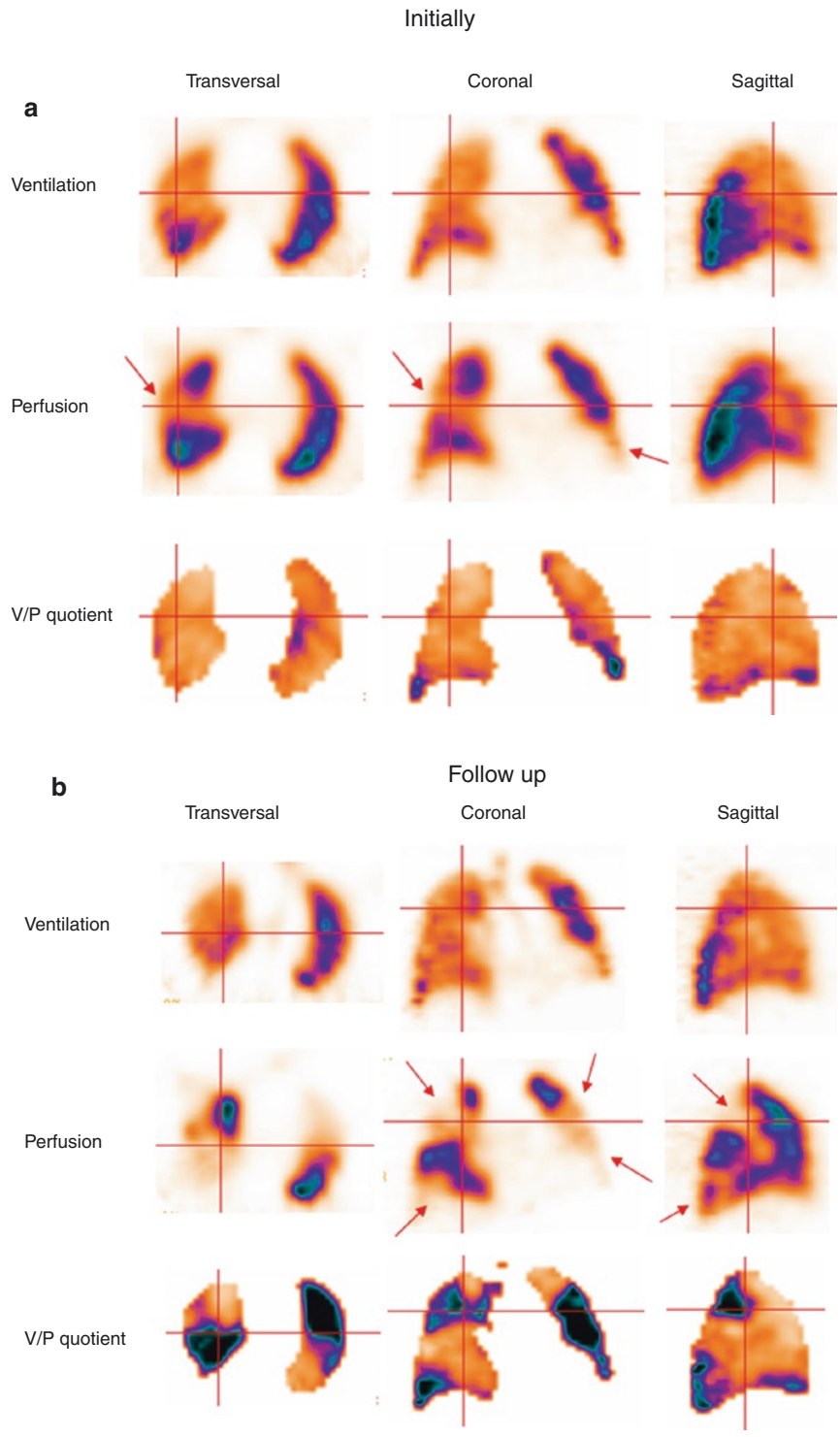


Fig. 5 Patient with recurrent PE. (**a**) Initially, segmental perfusion reductions were observed (PE, red arrows, marked on coronal and sagittal slices); (**b**) 2 years after discontinuing therapy patient experience new symptom. New, massive perfusion defects (red arrows on coronal slices) were observed in ventilated areas. Patient started treatment again; (**c**) follow-up scan, 5 months later (under treatment) showed partially improved perfusion defects (red arrows), mainly in the left lung. The patient continue with long life therapy

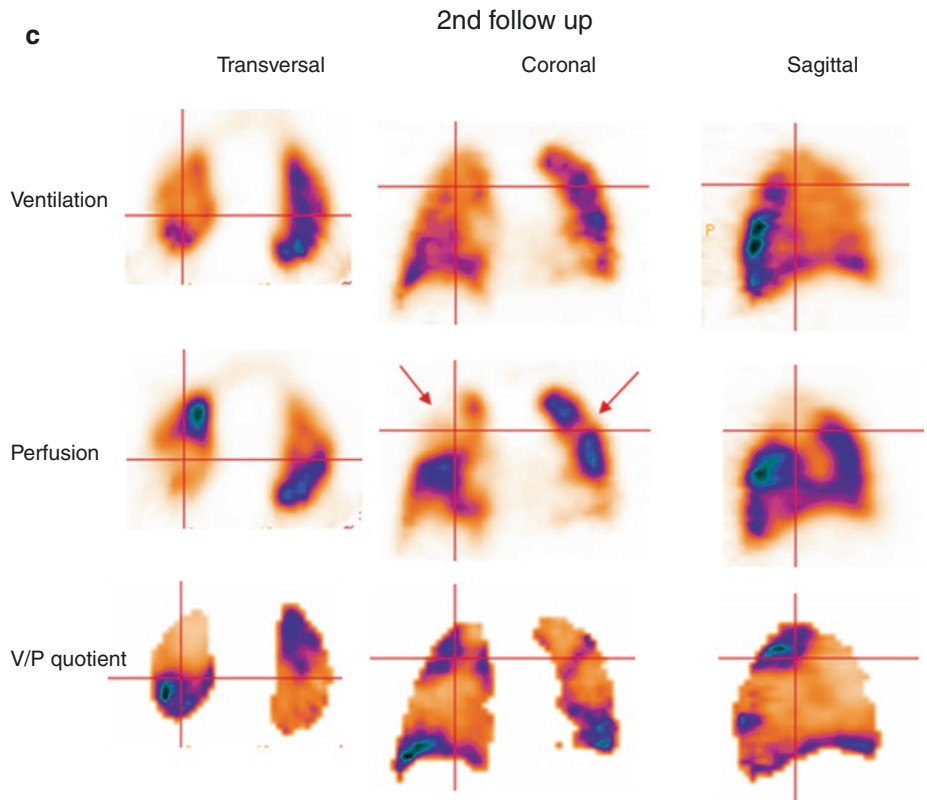


Fig. 5 (continued)

therapy patient experienced new symptoms. Multiple perfusion defects were observed in the follow-up scans bilaterally (Fig. 5b). The patient started treatment again. Five months later, during the treatment, control scan showed some reperfusion, mainly in the left lung (Fig. 5c). However, persistent perfusion defects, more than 30% of total lung function, demand further treatment and probably life-long treatment. Without the initial and follow-up images, it is often impossible to differentiate between old and new PE. Immediate imaging control gives objective information about the further therapy decisions. Symptomatic patients with a small emboli are diagnosed with sensitive methods, particularly V/P SPECT.

Requirements on a method used for follow-up are:

- Applicability to all patients
- Low radiation dose
- High sensitivity to allow estimation of resolution of even small emboli and occurrence of new ones

V/P SPECT seems ideally suited for use in the follow-up of PE because small and large emboli are recognized so that regression or progression of thrombotic disease can be studied in detail (Begic et al. 2011, 2015b; Olsson et al. 2006). Furthermore, the low radiation exposure enables repeated studies. Obviously, using the same method for diagnosis and follow-up is advantageous. Research in this area is particularly indicated.

2.4 Radiation Doses

Following the good clinical practice it is important to minimize radiation exposure without sacrificing image quality and diagnostic accuracy.

Based upon data from ICRP reports (ICRP 1988), the effective dose for V/P SPECT with the recommended protocol is 2 mSv. In a systematic review and meta-analysis of literature, radiation exposure was 2.12 mSv for V/P SPECT per correct diagnosis compared with 4.96 mSv for CTPA (Phillips et al. 2015). In clinical routine, radiation doses between 3.5 and 13.2 mSv have been reported for CTPA (Bucher et al. 2016; Elbakri 2014). In general, higher effective doses (>5 mSv) are reported from automatically collected data (Smith-Bindman et al. 2017; MacGregor et al. 2015). The most critical organ in CTPA is the female breast. Absorbed radiation doses to the female breast ranging from 8.6 mSv to 44 mSv have been reported (Astani et al. 2014; Isidoro et al. 2017; Sabarudin et al. 2014). Tube current modulation is able to decrease the breast dose from 51.5 mSv to 8.6 mSv (Sabarudin et al. 2014), while shielding is less effective (Revel et al. 2015). Absorbed radiation doses to the female breast from V/P SPECT is <1 mSv (Astani et al. 2014). Fetal-absorbed doses for V/P SPECT and CTPA are similar and so small that they are unlikely to be clinically significant (Astani et al. 2014; Isidoro et al. 2017; Gruning et al. 2016).

3 Clinical Use of Hybrid V/P SPECT/CT

The hybrid SPECT/CT system is a dual imaging modality technique. Its clinical application is particularly relevant in oncological diseases as it leads to improved sensitivity and specificity, combining co-registration of anatomical and functional data. It may lead to improved staging and treatment monitoring. Nuclear medicine procedures have the ability to visualize early functional changes sooner than structural changes occur. An additional CT procedure may improve correction for photon attenuation and allow co-registration of morphology and function. However, SPECT/CT acquisition of the chest constitutes a challenge due to respiratory movements, which can cause image artifacts and thus decrease diagnostic accuracy.

Some authors have recently recommended V/P SPECT/low-dose CT as a first-line procedure in patients with suspected PE. This was based on their prospective study performing V/P SPECT and low-dose CT and making head-to-head comparison with CTPA (Gutte et al. 2009). In a total of 81 simultaneous studies, 38% of patients had PE. They showed 97% sensitivity and 88% specificity when only V/P SPECT was used. However, adding low-dose CT the sensitivity was unchanged but specificity increased to 100%. Interestingly 18% of patients had false positive PE diagnosis when V/P SPECT alone was interpreted (Gutte et al. 2009). A reason for this may be that they were interpreting every mismatch as PE and not only mismatches that conform to segmental lung circulation as recommended by the European Guidelines (Bajc et al. 2009a, b; Bajc et al. 2019).

In our opinion, V/P SPECT is a primary tool in patients with suspected PE. Since 2003, more than 20,000 examinations have been performed. Based on our experience, we do not recommend hybrid V/P SPECT/CT as a first-line procedure for all patients with suspected PE. We recognize an ethical problem in advocating CT study in addition to V/P SPECT for every patient with suspected PE when prevalence of PE is about 30% in our experience and might be as low as 10% (Mamlouk et al. 2010). Following the good clinical practice recommendation to use a hybrid system for PE diagnosis is premature (Bajc et al. 2014). CT utilization has increased dramatically in the evaluation of patients with suspected PE without improving rate of PE or other clinically significant diagnoses (Coco and O'Gurek 2012). Therefore, it is important to validate the V/P SPECT/CT system and to assess the benefits and risks (Einstein et al. 2007).

We consider, however, that the dual modality will have impact in some groups of patients. SPECT/CT may provide added value to COPD patients showing morphological changes in addition to functional defects, particularly in visualizing small tumors. Figure 6 presents a patient with COPD and small tumor (Jogi et al. 2015).

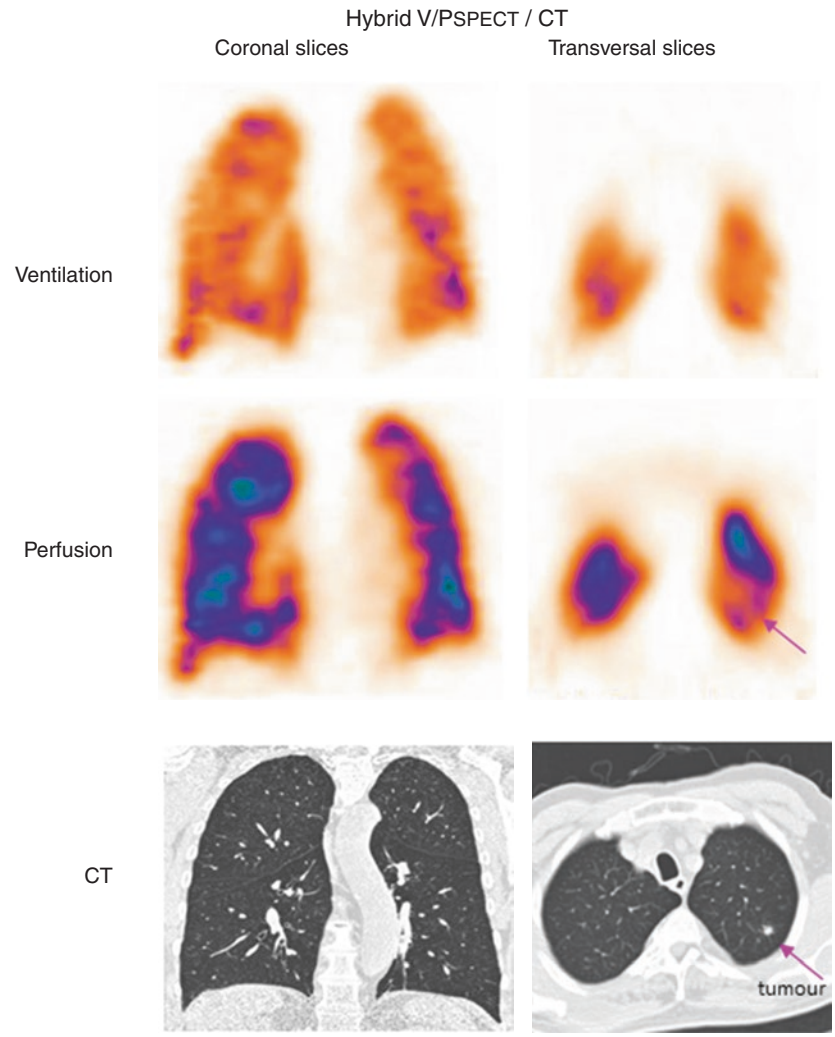


Fig. 6 Patient with COPD and small tumor, hybrid imaging. Coronal and transversal slices; ventilation and perfusion SPECT image. In the lower row corresponding CT images. Uneven distribution of ventilation with focal deposition of aerosols indicating airway obstruction in the smaller airways. On transversal CT image small tumor (1 cm) is visualized (purple arrow). Aligning both modalities small perfusion defect is observed in this area

4 Additional Findings

4.1 Chronic Obstructive Pulmonary Disease (COPD)

COPD is frequently observed in patients suspected for PE, because COPD patients are at high risk of PE (Bajc et al. 2008; Begic et al. 2015a; Nasr et al. 2017). The rate of PE in patients hospitalized for acute exacerbation of COPD may be as high as 25%. PE accounts for up to 10% of deaths in stable COPD patients. Different from PIOPED study, PE can be diagnosed even in the presence of COPD with V/P SPECT (Nasr et al. 2017) (Fig. 2).

The characteristic of COPD is a general unevenness of ventilation. Focal deposition of aerosol actually locates sites of airway obstruction (Jobse et al. 2012, 2013) (Figs. 2 and 6). The degree of unevenness of aerosol distribution correlates with lung function tests (Bajc et al. 2017, 2015a; Jogi et al. 2011; Norberg et al. 2014). In healthy subjects, even distribution of Technegas with good peripheral penetration and without accumulation in large or small airways is observed.

The grading of obstruction in ventilation SPECT has been standardized using Technegas V SPECT (Bajc et al. 2015a):

Grade 1: Mild airway obstruction, slightly uneven distribution with some deposition of

Technegas in small and intermediate airways. Only minor areas with reduced peripheral penetration are observed.

Grade 2: Moderate airway obstruction, deposition of Technegas in intermediate and large airways, diminished peripheral penetration with maximum accumulation in the central half of the lung.

Grade 3: Severe airway obstruction, central deposition in large airways with severely impaired penetration of Technegas and major areas with reduced or abolished function.

V/P SPECT has a high sensitivity to show an obstructive pattern in the lungs of many apparently healthy smokers (work in progress).

V/P SPECT gives the possibility to localize ventilation and perfusion impairment and estimate the total lung function (Bajc et al. 2017). It is noteworthy that there are no contraindications to V/P SPECT and that even very sick and breathless patients can be studied. Figure 2 shows coronal slices in a patient with a severe COPD and massive PE.

4.2 Pneumonia

Pneumonia is also a frequent finding in patients investigated for a suspected PE (Figs. 3 and 4). Pneumonia is here a general term for conditions of lung inflammation, often caused by a bacterial, viral, or fungal infection. Blood biomarkers are not sufficient for diagnosing pneumonia and unspecific clinical symptoms can lead to diagnostic problems (Scherer and Chen 2016; Ewig et al. 2009).

In pneumonia, V/P SPECT shows ventilation defects that usually exceed perfusion defects known as reverse mismatch (reversed V/P mismatch) (Carvalho and Lavender 1989; Li et al. 1994). Preserved perfusion along the pleural border peripheral to a central matched defect recognized as the "stripe sign" is a specific sign of pneumonia (Fig. 3) (Sostman and Gottschalk 1982). Figure 3 shows that this patient has beside a pneumonia in the posterior part of right lung also a PE in the middle lobe. PE could not have been identified without SPECT and ventilation images. The natural history and the value of treatment in this group of patients are rather unknown. Dyspnea was a common symptom in these patients. It can be caused by a pneumonia as well as by a PE or COPD. Pneumonia is frequently comorbid with a PE (Figs. 3 and 4). In a recent study, following patients with PE and pneumonia clinically and with V/P SPECT, reversed mismatched or matched V/P defects typical for pneumonia were confirmed (Begic et al. 2015a). In some patients, V/P defects typical for pneumonia reduce the total lung function in the absence of any morphological CT changes. In these clinical scenarios, PE is frequently missed by CT (Bajc 2005; Begic et al. 2015a). This is important information because in general, current clinical and nuclear medicine practices do not recognize nor use V/P SPECT as a potential imaging method to diagnose or manage pneumonia.

4.3 Left Heart Failure

Antigravitational perfusion distribution from posterior to anterior region indicates pulmonary congestion. The pattern was described already in 1966 (Friedman and Braunwald 1966) and studied later (Jogi et al. 2008, 2018; Pistolesi et al. 1988). As ventilation is usually less affected, the typical pattern is antigravitational redistribution of perfusion and V/P mismatch in dorsal regions of the lung. This V/P mismatch has a nonsegmental pattern (does not conform pulmonary vascular architecture) and should not be misinterpreted as pulmonary embolism (Fig. 7). The positive predictive value ≥88% for heart failure has been observed (Jogi et al. 2008). The power of V/P SPECT for diagnosis of heart failure was recently confirmed against right heart catheterization (Jogi et al. 2018).

4.4 Preoperative Evaluation of Lung Function

The assessment of lung function is essential for planning and predicting the outcomes of surgery

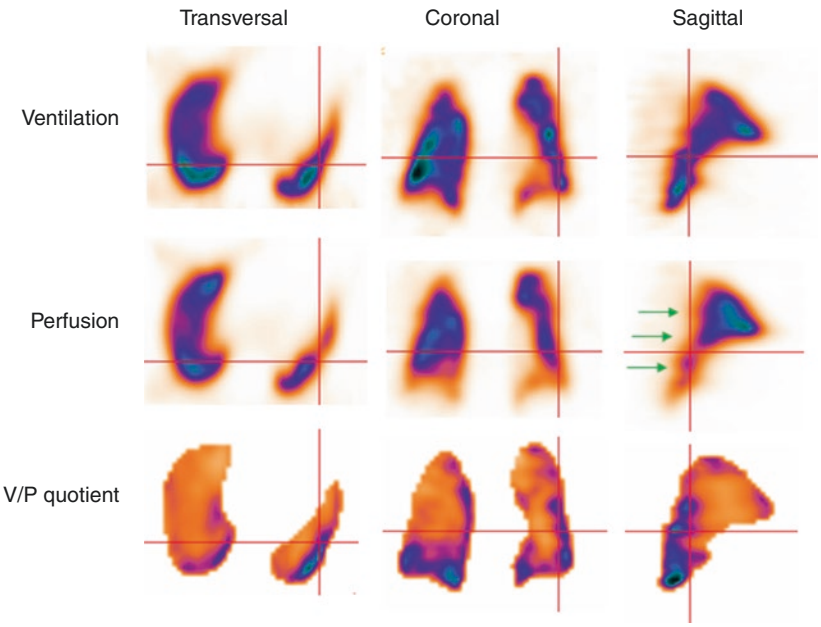


Fig. 7 Patient with left heart failure. On the sagittal slice of the left lung antigravitational redistribution of perfusion is seen (green arrows). Ventilation is less affected causing mismatch. Mind the pattern; it is not of segmental character

such as lung volume reduction surgery and in patients with lung tumor or lung transplantation.

Previously, planar lung scintigraphy was applied for this purpose measuring ventilation and perfusion from geometrical mean of anterior and posterior projection using the whole lung and upper middle and lower zone. Today, V/P SPECT is recommended because it allows quantitative measurement of ventilation and perfusion and thus evaluation of the regional lung function reserve. Planar and tomographic techniques allow comparable assessment of the whole lung function. However, V/P SPECT is significantly better than planar scintigraphy to assess lobar lung function (Wechalekar et al. 2019).

Combination of functional and morphological imaging by V/P SPECT and CT offers a better identification of malignancy and emphysema than using only one method (Jogi et al. 2015). The new hybrid V/P SPECT/CT imaging technique has shown advantages in predicting postoperative lung function in patients with non-small cell lung cancer (Ohno et al. 2011) as well the assessment of the outcome after chemotherapy (Ma et al. 2015). The area is challenging and more work needs to be done to further develop techniques.

4.5 PET and PET/CT or PET/MRI

Positron emission tomography (PET) is another powerful methodology that might use essentially unlimited number of biological compounds to be labeled with the positron emitting isotopes such as oxygen, carbon, and fluorine as a hydrogen substitute. Early studies were using PET focused on the inhalation of ^{11}CO (or $C^{15}O$) and ^{19}Ne gases and the intravenous injection of ^{13}N in saline and $H_2{}^{15}O$ for the measurement of relatively simple aspects of regional lung function, such as tissue, blood and gas volumes, blood flow, ventilation and ventilation/perfusion. More recent work has been directed towards the more challenging areas of regional endothelial permeability, carbohydrate utilization, enzyme and receptor binding assays, and in vivo pharmacokinetics. The short physical half-lives of the PET isotopes in the range from 17 s to 2 h and the noninvasive nature of PET allow for serial measurements to assess the effect of physiological and therapeutic interventions.

The availability of carbon-11 and fluorine-18 for radiochemical synthesis gives positron emitters a distinct chemical advantage over the single photon emitters, such as technetium-99 m. Furthermore, in general PET imaging is the

modality of choice for the in vivo quantification of various molecular targets and biochemical processes using the appropriate quantitative biomarkers. The quantification of lung molecular imaging data is challenging considering various tissue compartments. There is however an effort to investigate different quantification approaches that could possibly help in understanding of molecular changes and underlying mechanisms in the development of respiratory diseases (Chen et al. 2017).

Positron emission tomography (PET) using F-18 fluorodeoxyglucose (FDG) and combined with computed tomography (CT) or magnetic resonance imaging (MRI) is a widely adopted diagnostic modality that is considered as a method of choice in cancer imaging. In addition to structural details available on CT or MRI, this hybrid approach provides functional/metabolic information related to glucose utilization. Increased FDG uptake in the malignant tissues is related to increased glycolysis and overexpression of various glucose transporter receptors. Similarly, activated inflammatory cells demonstrate increased glucose utilization and that is a rationale for use of PET FDG in inflammatory and infectious processes including the various lung diseases. In particular, granulomatous inflammatory diseases involving the lung parenchyma, infectious and noninfectious, demonstrate very high uptake of FDG. PET FDG can be used to assess the extent and activity of tuberculosis and monitor response to therapy. In patients with sarcoidosis, granulomatous disease can affect essentially any organ, most frequently lung parenchyma with involvement of regional mediastinal and hilar lymph nodes. It is important to determine the level of inflammatory activity in order to define which patients need more aggressive therapy including the corticosteroids. It has been shown that PET FDG is more reliable than serological markers in evaluation of activity of the disease (Capitanio et al. 2016).

The functional evaluation of inflammatory and infectious lung diseases using the PET FDG imaging has been also documented in patients with pneumoconiosis, cystic fibrosis, Langerhans cell histiocytosis, and other conditions based on predominant inflammatory response. More recently, interstitial lung disease (ILD) has been studied using PET/FDG in order to quantify disease and assess prognostic value. It has been reported that SUV measurements correlate with clinical indicators and provide independent prognostic information that may help in monitoring and risk stratification of ILD patients (Nobashi et al. 2016).

Increasing use of immunotherapy in cancer treatment can cause serious side effects including inflammation of many different organs that is frequently seen on PET FDG scan performed to monitor the effects of therapy. In the lungs it can cause interstitial lung disease/pneumonitis or pneumonia (Fig. 8) (Akella et al. 2019).

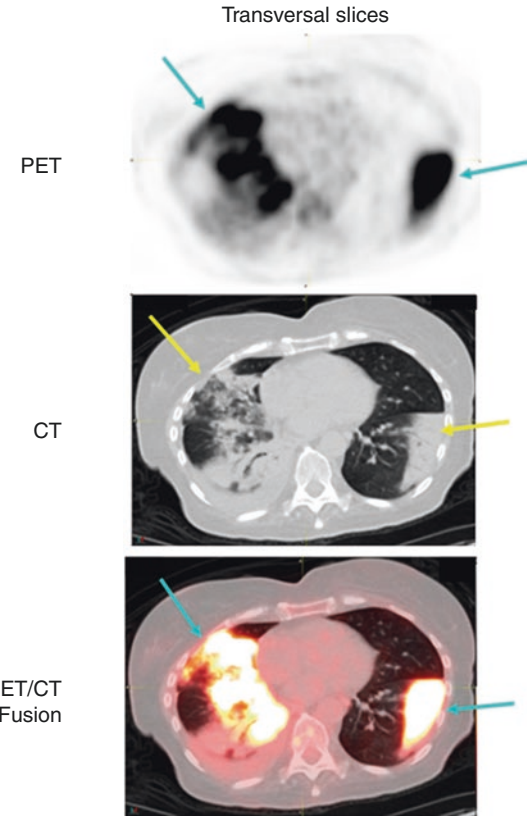


Fig. 8 Patient with pneumonia. On transversal PET slice (upper row) hypermetabolic activity is seen bilaterally, more on the right site (blue arrows). On CT, large areas of consolidation is seen in the same area (yellow arrows) as visualized on fusion PET/CT image. The finding is consistent with pneumonia related to immunotherapy

There are several new radiopharmaceuticals of interest that are used to evaluate inflammation. Tracers that target translocator protein (TSPO) found in the inflammatory cells are C-11 PK11195 and F-18 labeled FEPPA and FEDAC. They bind to benzodiazepine-like receptors abundant in macrophages. TSPO is considered as a reliable marker of inflammation and many studies are conducted to investigate TSPO expression in activated macrophages. In the human lungs there is multicellular high expression of TSPO, including the bronchial and bronchiole epithelium, submucosal glands in intrapulmonary bronchi, pneumocytes, and alveolar macrophages (Hatori et al. 2012). TSPO PET data revealed that tracer uptake was higher in COPD patients and asthmatics than in healthy volunteers, and cigarette smoke exposure, leading cause of COPD, altered directly TSPO expression. On the other hand, there was apparent TSPO downregulation in interstitial lung diseases indicating that TSPO expression is a dynamic process probably integrated in a time-dependent fashion, e.g., acute versus chronic injury (Largeau et al. 2017). Another approach is to use PET and develop novel tracers that are specific for infections. An example is F-18 PABA that appears to be highly selective for bacteria imaging in animal model of MRSA infection (Zhang et al. 2018). PET technology also can be used to perform a ventilation/perfusion (V/P) scan instead of conventional V/P SPECT. This can be performed using Ga-68 labeled carbon nanoparticles for ventilation images and Ga-68 labeled macroaggregated albumin (MAA) for perfusion images. The authors demonstrated faster acquisition with PET tracer and superior image quality, possibly providing more accurate diagnosis (Hofman et al. 2011). Ga-68 is a convenient PET radionuclide, generator produced and readily available with relatively short half-life of 68 min offering more flexible acquisition protocols for perfusion imaging in various pulmonary conditions. Although the role of Ga-68 V/P PET may be limited for acute applications from a logistical perspective, V/P PET/CT scan may overall improve diagnostic performance and may be relevant in clinical situations such as preoperative assessment of the lung cancer patients, radiotherapy planning, or presurgical evaluation of patients undergoing lung volume reduction surgery (Le Roux et al. 2019).

In the future, possibility of molecular imaging using PET could include studies of specific targets on cell surface and regional vascular and alveolar permeability.

5 Conclusion

Ventilation/perfusion (V/P SPECT) is the recommended scintigraphic technique for the diagnosis of PE and many other disorders that affect lung function. Moreover, according to European Association of Nuclear Medicine guidelines, it should be the preferred modality whenever possible for the diagnosis of PE because it has the highest sensitivity and accuracy and neither contraindications nor complications. It produces very few nondiagnostic reports, and radiation doses are low. This is particularly important for women in the reproductive period and during pregnancy (Bajc et al. 2015b). Furthermore, full use should be made of display options, which are integrated in modern camera systems. Holistic interpretation is the most important strategy for V/P SPECT, giving a clear report with respect to PE, its extension, as well as other diagnoses such as pneumonia, COPD, and left heart failure based on V/P patterns typical for various diseases. Interpretation is based upon all relevant clinical information about the patient and all V/P patterns. The abovementioned advantages of V/P SPECT are favoring the method as the most suitable technique both for diagnosing and for follow-up of patients with PE and other cardiopulmonary diseases and preoperative assessment of pulmonary function. V/P SPECT is an ideal technique for research regarding measurement of treatment effects as well as pathophysiology of the diseases.

SPECT/CT needs further validation but might have important role preoperatively as well; it may provide added value to COPD patients showing morphological changes in addition to functional defects, particularly in visualizing small tumors.

PET and PET/CT or PET/MRI are additional imaging techniques that are used to asses and quantify lung function and metabolic changes. Usually most explored biomarker is F-FDG used to show activity of pulmonary inflammation in a variety of respiratory diseases.

References

Akella P, Loganathan S, Jindal V, Akhtar J, Lal A (2019) Anti PD-1 immunotherapy related interstitial lung disease presenting as respiratory failure—a review with case series. Respir Med Case Rep 26:17–22. https://doi.org/10.1016/j.rmcr.2018.11.005

Alhadad A, Miniati M, Alhadad H, Gottsater A, Bajc M (2012) The value of tomographic ventilation/perfusion scintigraphy (V/PSPECT) for follow-up and prediction of recurrence in pulmonary embolism. Thromb Res 130(6):877–881. https://doi.org/10.1016/j.thromres.2012.09.002

Astani SA, Davis LC, Harkness BA, Supanich MP, Dalal I (2014) Detection of pulmonary embolism during pregnancy: comparing radiation doses of CTPA and pulmonary scintigraphy. Nucl Med Commun 35(7):704–711. https://doi.org/10.1097/MNM.0000000000000114

Bajc M (2005) Value of ventilation/perfusion SPECT detecting extensive pulmonary embolism in a patient with pneumonia. Thromb Haemost 93(5):993–994

Bajc M, Chen Y, Wang J, Li XY, Shen WM, Wang CZ et al (2017) Identifying the heterogeneity of COPD by V/P SPECT: a new tool for improving the diagnosis of parenchymal defects and grading the severity of small airways disease. Int J Chron Obstruct Pulmon Dis 12:1579–1587. https://doi.org/10.2147/COPD.S131847

Bajc M, Maffioli L, Miniati M (2014) Good clinical practice in pulmonary embolism diagnosis: where do we stand today? Eur J Nucl Med Mol Imaging 41(2):333–336. https://doi.org/10.1007/s00259-013-2612-7

Bajc M, Markstad H, Jarenback L, Tufvesson E, Bjermer L, Jogi J (2015a) Grading obstructive lung disease using tomographic pulmonary scintigraphy in patients with chronic obstructive pulmonary disease (COPD) and long-term smokers. Ann Nucl Med 29(1):91–99. https://doi.org/10.1007/s12149-014-0913-y

Bajc M, Neilly JB, Miniati M, Schuemichen C, Meignan M, Jonson B (2009a) EANM guidelines for ventilation/perfusion scintigraphy: Part 1. Pulmonary imaging with ventilation/perfusion single photon emission tomography. Eur J Nucl Med Mol Imaging 36(8):1356–1370. https://doi.org/10.1007/s00259-009-1170-5

Bajc M, Neilly JB, Miniati M, Schuemichen C, Meignan M, Jonson B (2009b) EANM guidelines for ventilation/perfusion scintigraphy: Part 2. Algorithms and clinical considerations for diagnosis of pulmonary emboli with V/P(SPECT) and MDCT. Eur J Nucl Med Mol Imaging 36(9):1528–1538. https://doi.org/10.1007/s00259-009-1169-y

Bajc M, Olsson B, Gottsater A, Hindorf C, Jogi J (2015b) V/P SPECT as a diagnostic tool for pregnant women with suspected pulmonary embolism. Eur J Nucl Med Mol Imaging 42(8):1325–1330. https://doi.org/10.1007/s00259-015-3056-z

Bajc M, Olsson B, Palmer J, Jonson B (2008) Ventilation/perfusion SPECT for diagnostics of pulmonary embolism in clinical practice. J Intern Med 264(4):379–387

Bajc M, Schümichen C, Grüning T, Lindqvist A, Le Roux PY, Alatri A, Bauer RW, Dilic M, Neilly B, Verberne HJ, Delgado Bolton RC, Jonson B (2019) EANM guideline for ventilation/perfusion single-photon emission computed tomography (SPECT) for diagnosis of pulmonary embolism and beyond. Eur J Nucl Med Mol Imaging 46(12):2429–2451

Begic A, Jogi J, Hadziredzepovic A, Kucukalic-Selimovic E, Begovic-Hadzimuratovic S, Bajc M (2011) Tomographic ventilation/perfusion lung scintigraphy in the monitoring of the effect of treatment in pulmonary embolism: serial follow-up over a 6-month period. Nucl Med Commun 32(6):508–514. https://doi.org/10.1097/MNM.0b013e328344dfd5

Begic A, Opankovic E, Cukic V, Lindqvist A, Miniati M, Bajc M (2015a) Ancillary findings assessed by ventilation/perfusion tomography. Impact and clinical outcome in patients with suspected pulmonary embolism. Nuklearmedizin 54(5):223–230. https://doi.org/10.3413/Nukmed-0748-15-06

Begic A, Opankovic E, Cukic V, Rustempasic M, Basic A, Miniati M et al (2015b) Impact of ventilation/perfusion single-photon emission computed tomography on treatment duration of pulmonary embolism. Nucl Med Commun 36(2):162–167. https://doi.org/10.1097/MNM.0000000000000224

Bucher AM, Kerl MJ, Albrecht MH, Beeres M, Ackermann H, Wichmann JL et al (2016) Systematic comparison of reduced tube current protocols for high-pitch and standard-pitch pulmonary CT angiography in a large single-center population. Acad Radiol 23(5):619–627. https://doi.org/10.1016/j.acra.2016.01.003

Capitanio S, Nordin AJ, Noraini AR, Rossetti C (2016) PET/CT in nononcological lung diseases: current applications and future perspectives. Eur Respir Rev 25(141):247–258. https://doi.org/10.1183/16000617.0051-2016

Carvalho P, Lavender JP (1989) The incidence and etiology of the ventilation/perfusion reverse mismatch defect. Clin Nucl Med 14(8):571–576

Chen DL, Cheriyan J, Chilvers ER, Choudhury G, Coello C, Connell M et al (2017) Quantification of lung PET images: challenges and opportunities. J Nucl Med 58(2):201–207. https://doi.org/10.2967/jnumed.116.184796

Coco AS, O'Gurek DT (2012) Increased emergency department computed tomography use for common chest symptoms without clear patient benefits. J Am

Board Fam Med 25(1):33–41. https://doi.org/10.3122/jabfm.2012.01.110039

Couturaud F (2016) Guided duration of anticoagulation after unprovoked venous thromboembolism using D-dimer testing. Eur Respir J 47(5):1313–1314. https://doi.org/10.1183/13993003.00212-2016

Couturaud F, Kearon C (2008) Optimum duration of anticoagulant treatment after an episode of venous thromboembolism. Rev Pneumol Clin 64(6):305–315. https://doi.org/10.1016/j.pneumo.2008.09.007

Couturaud F, Meyer G, Mottier D (2015) Thrombophilia and the risk of recurrent venous thromboembolism--reply. JAMA 314(18):1976. https://doi.org/10.1001/jama.2015.12610

Einstein AJ, Henzlova MJ, Rajagopalan S (2007) Estimating risk of cancer associated with radiation exposure from 64-slice computed tomography coronary angiography. JAMA 298(3):317–323. https://doi.org/10.1001/jama.298.3.317

Elbakri IA (2014) Estimation of dose-area product-to-effective dose conversion factors for neonatal radiography using PCXMC. Radiat Prot Dosim 158(1):43–50. https://doi.org/10.1093/rpd/nct192

Elf JE, Jogi J, Bajc M (2015) Home treatment of patients with small to medium sized acute pulmonary embolism. J Thromb Thrombolysis 39(2):166–172. https://doi.org/10.1007/s11239-014-1097-y

Ewig S, Birkner N, Strauss R, Schaefer E, Pauletzki J, Bischoff H et al (2009) New perspectives on community-acquired pneumonia in 388 406 patients. Results from a nationwide mandatory performance measurement programme in healthcare quality. Thorax 64(12):1062–1069. https://doi.org/10.1136/thx.2008.109785

Friedman WF, Braunwald E (1966) Alterations in regional pulmonary blood flow in mitral valve disease studied by radioisotope scanning. A simple nontraumatic technique for estimation of left atrial pressure. Circulation 34(3):363–376

Grunig E, Ehlken N, Hohenforst-Schmidt W, Kruger U, Kruger S, Lichtblau M et al (2014) Supportive therapy in pulmonary arterial hypertension. Dtsch Med Wochenschr 139(Suppl. 4):S136–S141. https://doi.org/10.1055/s-0034-1387453

Gruning T, Mingo RE, Gosling MG, Farrell SL, Drake BE, Loader RJ et al (2016) Diagnosing venous thromboembolism in pregnancy. Br J Radiol 89(1062):20160021. https://doi.org/10.1259/bjr.20160021

Gutte H, Mortensen J, Jensen CV, Johnbeck CB, von der Recke P, Petersen CL et al (2009) Detection of pulmonary embolism with combined ventilation-perfusion SPECT and low-dose CT: head-to-head comparison with multidetector CT angiography. J Nucl Med 50(12):1987–1992

Hatori A, Yui J, Yamasaki T, Xie L, Kumata K, Fujinaga M et al (2012) PET imaging of lung inflammation with [^{18}F]FEDAC, a radioligand for translocator protein (18 kDa). PLoS One 7(9):e45065. https://doi.org/10.1371/journal.pone.0045065

Heck LL, Duley JW Jr (1974) Statistical considerations in lung imaging with 99mTc albumin particles. Radiology 113(3):675–679

Hofman MS, Beauregard JM, Barber TW, Neels OC, Eu P, Hicks RJ (2011) ^{68}Ga PET/CT ventilation-perfusion imaging for pulmonary embolism: a pilot study with comparison to conventional scintigraphy. J Nucl Med 52(10):1513–1519. https://doi.org/10.2967/jnumed.111.093344

ICRP (1988) Radiation dose to patients from radiopharmaceuticals, publication 53. Oxford, NY, ICRP, p 121

PIOPED Investigators (1990) Value of the ventilation/perfusion scan in acute pulmonary embolism. Results of the prospective investigation of pulmonary embolism diagnosis (PIOPED). JAMA 263(20):2753–2759

Isidoro J, Gil P, Costa G, Pedroso de Lima J, Alves C, Ferreira NC (2017) Radiation dose comparison between V/P-SPECT and CT-angiography in the diagnosis of pulmonary embolism. Phys Med 41:93–96. https://doi.org/10.1016/j.ejmp.2017.04.026

Jobse BN, Rhem RG, McCurry CA, Wang IQ, Labiris NR (2012) Imaging lung function in mice using SPECT/CT and per-voxel analysis. PLoS One 7(8):e42187. https://doi.org/10.1371/journal.pone.0042187

Jobse BN, Rhem RG, Wang IQ, Counter WB, Stampfli MR, Labiris NR (2013) Detection of lung dysfunction using ventilation and perfusion SPECT in a mouse model of chronic cigarette smoke exposure. J Nucl Med 54(4):616–623. https://doi.org/10.2967/jnumed.112.111419

Jogi J, Al-Mashat M, Radegran G, Bajc M, Arheden H (2018) Diagnosing and grading heart failure with tomographic perfusion lung scintigraphy: validation with right heart catheterization. ESC Heart Fail. https://doi.org/10.1002/ehf2.12317

Jogi J, Ekberg M, Jonson B, Bozovic G, Bajc M (2011) Ventilation/perfusion SPECT in chronic obstructive pulmonary disease: an evaluation by reference to symptoms, spirometric lung function and emphysema, as assessed with HRCT. Eur J Nucl Med Mol Imaging 93:1344–1352. https://doi.org/10.1007/s00259-011-1757-5

Jogi J, Jonson B, Ekberg M, Bajc M (2010) Ventilation-perfusion SPECT with 99mTc-DTPA versus technegas: a head-to-head study in obstructive and nonobstructive disease. J Nucl Med. https://doi.org/10.2967/jnumed.109.073957

Jogi J, Markstad H, Tufvesson E, Bjermer L, Bajc M (2015) The added value of hybrid ventilation/perfusion SPECT/CT in patients with stable COPD or apparently healthy smokers. Cancer-suspected CT findings in the lungs are common when hybrid imaging is used. Int J Chron Obstruct Pulmon Dis 10:25–30. https://doi.org/10.2147/COPD.S73423

Jogi J, Palmer J, Jonson B, Bajc M (2008) Heart failure diagnostics based on ventilation/perfusion single photon emission computed tomography pattern and quantitative perfusion gradients. Nucl Med Commun 29(8):666–673

Kan Y, Yuan L, Meeks JK, Li C, Liu W, Yang J (2015) The accuracy of V/Q SPECT in the diagnosis of pulmonary embolism: a meta-analysis. Acta Radiol 56(5):565–572. https://doi.org/10.1177/0284185114533682

Largeau B, Dupont AC, Guilloteau D, Santiago-Ribeiro MJ, Arlicot N (2017) TSPO PET imaging: from microglial activation to peripheral sterile inflammatory diseases? Contrast Media Mol Imaging 2017:6592139. https://doi.org/10.1155/2017/6592139

Le Roux PY, Hicks RJ, Siva S, Hofman MS (2019) PET/CT Lung ventilation and perfusion scanning using galligas and Gallium-68-MAA. Semin Nucl Med 49(1):71–81. https://doi.org/10.1053/j.semnuclmed.2018.10.013

Leblanc M, Leveillee F, Turcotte E (2007) Prospective evaluation of the negative predictive value of V/Q SPECT using 99mTc-Technegas. Nucl Med Commun 28(8):667–672

Lemb M, Pohlabeln H (2001) Pulmonary thromboembolism: a retrospective study on the examination of 991 patients by ventilation/perfusion SPECT using Technegas. Nuklearmedizin 40(6):179–186. doi:01060179 [pii]

Li DJ, Stewart I, Miles KA, Wraight EP (1994) Scintigraphic appearances in patients with pulmonary infection and lung scintigrams of intermediate or low probability for pulmonary embolism. Clin Nucl Med 19(12):1091–1093

Ma Q, Min K, Wang T, Chen B, Wen Q, Wang F et al (2015) (99m)Tc-3PRGD 2 SPECT/CT predicts the outcome of advanced nonsquamous non-small cell lung cancer receiving chemoradiotherapy plus bevacizumab. Ann Nucl Med 29(6):519–527. https://doi.org/10.1007/s12149-015-0975-5

MacGregor K, Li I, Dowdell T, Gray BG (2015) Identifying institutional diagnostic reference levels for CT with radiation dose index monitoring software. Radiology 276(2):507–517. https://doi.org/10.1148/radiol.2015141520

Mahdavi R, Caronia J, Fayyaz J, Panagopoulos G, Lessnau KD, Scharf SC et al (2013) Agreement between SPECT V/Q scan and CT angiography in patients with high clinical suspicion of PE. Ann Nucl Med 27(9):834–838. https://doi.org/10.1007/s12149-013-0753-1

Mamlouk MD, vanSonnenberg E, Gosalia R, Drachman D, Gridley D, Zamora JG et al (2010) Pulmonary embolism at CT angiography: implications for appropriateness, cost, and radiation exposure in 2003 patients. Radiology 256(2):625–632. https://doi.org/10.1148/radiol.10091624

Nasr A, Lindqvist A, Bajc M (2017) Ventilation defect typical for COPD is frequent among patients suspected for pulmonary embolism but does not prevent the diagnosis of PE by V/P SPECT (research article). EC Pulmqnol Respir Med 4(3):85–91

Nobashi T, Kubo T, Nakamoto Y, Handa T, Koyasu S, Ishimori T et al (2016) 18F-FDG uptake in less affected lung field provides prognostic stratification in patients with interstitial lung disease. J Nucl Med 57(12):1899–1904. https://doi.org/10.2967/jnumed.116.174946

Norberg P, Persson HL, Schmekel B, Carlsson GA, Wahlin K, Sandborg M et al (2014) Does quantitative lung SPECT detect lung abnormalities earlier than lung function tests? Results of a pilot study. EJNMMI Res 4(1):39. https://doi.org/10.1186/s13550-014-0039-1

Ohno Y, Koyama H, Nogami M, Takenaka D, Onishi Y, Matsumoto K et al (2011) State-of-the-art radiological techniques improve the assessment of postoperative lung function in patients with non-small cell lung cancer. Eur J Radiol 77(1):97–104. https://doi.org/10.1016/j.ejrad.2009.07.024

Olsson CG, Bitzen U, Olsson B, Magnusson P, Carlsson MS, Jonson B et al (2006) Outpatient tinzaparin therapy in pulmonary embolism quantified with ventilation/perfusion scintigraphy. Med Sci Monit 12(2):PI9–P13

Palmer J, Bitzen U, Jonson B, Bajc M (2001) Comprehensive ventilation/perfusion SPECT. J Nucl Med 42(8):1288–1294

Phillips JJ, Straiton J, Staff RT (2015) Planar and SPECT ventilation/perfusion imaging and computed tomography for the diagnosis of pulmonary embolism: a systematic review and meta-analysis of the literature, and cost and dose comparison. Eur J Radiol 84(7):1392–1400. https://doi.org/10.1016/j.ejrad.2015.03.013

Pistolesi M, Miniati M, Bonsignore M, Andreotti F, Di Ricco G, Marini C et al (1988) Factors affecting regional pulmonary blood flow in chronic ischemic heart disease. J Thorac Imaging 3(3):65–72

Reinartz P, Wildberger JE, Schaefer W, Nowak B, Mahnken AH, Buell U (2004) Tomographic imaging in the diagnosis of pulmonary embolism: a comparison between V/Q lung scintigraphy in SPECT technique and multislice spiral CT. J Nucl Med 45(9):1501–1508

Revel MP, Fitton I, Audureau E, Benzakoun J, Lederlin M, Chabi ML et al (2015) Breast dose reduction options during thoracic CT: influence of breast thickness. AJR Am J Roentgenol 204(4):W421–W428. https://doi.org/10.2214/AJR.14.13255

Sabarudin A, Mustafa Z, Nassir KM, Hamid HA, Sun Z (2014) Radiation dose reduction in thoracic and abdomen-pelvic CT using tube current modulation: a phantom study. J Appl Clin Med Phys 16(1):5135. https://doi.org/10.1120/jacmp.v16i1.5135

Scherer PM, Chen DL (2016) Imaging pulmonary inflammation. J Nucl Med 57(11):1764–1770. https://doi.org/10.2967/jnumed.115.157438

Smith-Bindman R, Wang Y, Yellen-Nelson TR, Moghadassi M, Wilson N, Gould R et al (2017) Predictors of CT radiation dose and their effect on patient care: a comprehensive analysis using automated data. Radiology 282(1):182–193. https://doi.org/10.1148/radiol.2016151391

Sostman HD, Gottschalk A (1982) The stripe sign: a new sign for diagnosis of nonembolic defects on pulmonary perfusion scintigraphy. Radiology 142(3):737–741. https://doi.org/10.1148/radiology.142.3.7063693

Wagner HN Jr (1964) Pulmonary scanning. Northwest Med 63:857–864

Wechalekar K, Garner J, Gregg S (2019) Pre-surgical evaluation of lung function. Semin Nucl Med 49(1):22–30. https://doi.org/10.1053/j.semnuclmed.2018.10.011

Zhang Z, Ordonez AA, Wang H, Li Y, Gogarty KR, Weinstein EA et al (2018) Positron emission tomography imaging with 2-[(18)F]F-p-aminobenzoic acid detects Staphylococcus aureus infections and monitors drug response. ACS Infect Dis 4(11):1635–1644. https://doi.org/10.1021/acsinfecdis.8b00182

Functional Assessment of COPD

Hye Jeon Hwang, Sang Min Lee,
and Joon Beom Seo

Contents

1 **Introduction** 126

2 **Quantitative Imaging of COPD for Assessment of Pulmonary Function** 126
2.1 Emphysema Quantification 126
2.2 Large Airway Measurement: Direct Measurement 129
2.3 Small Airway Measurement: Air-Trapping Measurement 131
2.4 Other Comorbidities of COPD 132

3 **Evaluation of Parenchymal Perfusion and Ventilation** 135
3.1 Evaluation of Parenchymal Perfusion 136
3.2 Evaluation of Parenchymal Ventilation 139
3.3 Evaluation of Pulmonary Ventilation, Perfusion and Relationship of Ventilation and Perfusion 141

4 **Future Perspectives** 144

References 144

Abstract

Chronic obstructive pulmonary disease (COPD) is a heterogeneous condition with variable clinical and pathophysiologic features. Functional information of the lungs is important to understand the complex pathophysiology of COPD. With recent technical advances in the CT imaging and magnetic resonance imaging (MRI), various imaging techniques have been used for the evaluation of functional changes in COPD. The quantitative CT imaging can be used to objectively assess the severity of emphysema, airway wall changes, air trapping, and other comorbidities, which are correlated with functional aspect of

H. J. Hwang · S. M. Lee
Department of Radiology and Research Institute of Radiology, University of Ulsan College of Medicine, Seoul, South Korea

J. B. Seo (✉)
Department of Radiology and Research Institute of Radiology, University of Ulsan College of Medicine, Seoul, South Korea

Division of Cardiothoracic Radiology, Department of Radiology, University of Ulsan College of Medicine, Asan Medical Center, Seoul, South Korea
e-mail: seojb@amc.seoul.kr

© Springer Nature Switzerland AG 2021

Y. Ohno et al. (eds.), *Pulmonary Functional Imaging*, Medical Radiology Diagnostic Imaging,
https://doi.org/10.1007/978-3-030-43539-4_8

COPD. The dual-energy CT imaging and functional MRI can directly assess and visualize the functional changes such as ventilation, perfusion, and ventilation–perfusion relationship with anatomically matched structural information of the lung in COPD. In this chapter, we will review the current technical status of functional imaging briefly, and focus on its clinical applications, limitations, and some of the most recent works in COPD.

1 Introduction

Chronic obstructive pulmonary disease (COPD) is characterized by persistent airflow limitation which is caused by persistent airway inflammation and emphysematous alveolar destruction (Hogg et al. 1968, 2004; Mead et al. 1967; Yanai et al. 1992). Although image findings of COPD may vary from normal lung to severe emphysema, emphysematous parenchymal destruction and bronchial wall thickening are major CT findings of COPD. It also shows pulmonary vascular changes that are characterized by hypoxic vasoconstriction and endothelial dysfunction of the small pulmonary arteries, as well as a reduction in their number (Barbera et al. 1994; Hale et al. 1980; Peinado et al. 1998). Furthermore, cachexia or muscle wasting including respiratory muscle is accompanied. These characteristic changes impair lung function including alveolar gas exchange and blood flow, and the mismatch of alveolar ventilation and blood flow is the most important cause of arterial hypoxemia (with or without hypercapnia) in COPD patients (Barbera et al. 1997; Sandek et al. 2001). Therefore, it may be important to evaluate morphological changes of the lung, as well as functional changes in COPD patients.

Currently, pulmonary function test (PFT) is used to diagnose and classify the severity of COPD, and imaging of patient with COPD is not routinely recommended in clinical practice. However, using imaging methods, an evaluation of objectivity-based assessments in relationship between pulmonary structure and lung function and assessment of functional phenotypes are important to improve insight into disease pathology and pathophysiology. Chest CT is the modality of choice for the evaluation of the structural and pathophysiologic changes in COPD patients. In particular, thin-section volumetric CT with quantitative assessment has been accepted one of essential components of studies which includes correlation with pulmonary function in COPD patients. The MRI of the lung has difficulty such as small amount of tissues in lung which generate signal in MRI and fast decay of signal due to susceptibility artifact from air-tissue interfaces. With technical advance, several sequences of MRI can obtain morphologic and functional image of the lung (Ley-Zaporozhan et al. 2008). This chapter encompasses the conventional multi-detector CT (MDCT) in the evaluation of pulmonary function, including quantitative assessment of emphysema, airway wall thickening, and air trapping, and its clinical values in COPD patients. In addition, new emerging imaging methods, such as dual-energy CT (DECT) and MRI, to evaluate morphologic feature as well as functional aspects including direct visualization of ventilation, perfusion, and chest wall motion of lung in COPD patients will be introduced.

2 Quantitative Imaging of COPD for Assessment of Pulmonary Function

2.1 Emphysema Quantification

Pulmonary emphysema is defined as an abnormal permanent dilatation of the air spaces distal to the terminal bronchioles. Emphysema area is shown as decreased attenuation areas approaching air attenuation of −1000HU on CT, due to the increased air fraction in the lung (Hayhurst et al. 1984). CT is currently the method of choice for noninvasive detection of emphysema, and has been shown to correlate well with pathologic findings (Gevenois et al. 1996; Newell et al. 2004). Since the introduction of the “density mask

method" in 1988, emphysema on CT image can be objectively measured by calculating the voxels that are lower than a certain Hounsfield units (HU) threshold (Muller et al. 1988). The optimal HU threshold is estimated to be between −950 and −970 HU on the basis of comparisons with macroscopic and microscopic morphometry of pathologic specimens (Gevenois et al. 1995; Madani et al. 2006), and −950HU is most widely used. The term of the percentage of low attenuation areas less than −950 (%LAA_{-950}) or emphysema index (EI) for the relative area of lung less than −950 HU is used for such CT measurement. Many studies showed significant correlation between CT measurements of emphysema severity and airflow obstruction parameters of PFT in COPD patients. The range of correlation coefficients between %LAA_{-950} and percentage of predicted forced expiratory volume-one second (%FEV_1) was −0.43 to −0.67 and that between %LAA_{-950} and the ratio of forced expiratory volume-one second to forced vital capacity (FEV_1/FVC) was −0.49 to −0.76. (Akira et al. 2009; Bon et al. 2009; Dransfield et al. 2007; Hesselbacher et al. 2011; Iwasawa et al. 2011; Park et al. 2008; Schroeder et al. 2013; Lee et al. 2008). This method also has been shown to be associated with other disease parameters including exercise capacity (6-min walk distance, 6MWD) and the BODE index (a multicomponent parameter that includes BMI, FEV_1, dyspnea-score, and exercise capacity as measured with the 6MWD) (Lee et al. 2008). The association between these density-based CT measurements of emphysema severity and COPD mortality was reported, and the CT-quantified emphysema severity predicted respiratory and cardiovascular mortality as well as all-cause mortality (Haruna et al. 2010; Johannessen et al. 2013). Furthermore, CT measurements of emphysema were associated with deterioration of COPD and were independent predictors of frequent deterioration in patients with COPD (Han et al. 2011; Oh et al. 2014) (Fig. 1). Another method of emphysema quantification is "percentile index," which is using calculation of the lung parenchymal HU at a given percentile along the frequency histogram of lung parenchymal attenuation. The first percentile value is estimated optimal for correlation with pathologic specimens; however, because of concerns regarding artifacts from image noise and truncation effect, the 15th percentile threshold is most widely used (Heussel et al. 2009; Stolk et al. 2001). As compared with PFT parameters, correlation between 15 percentile index (Perc15) and %FEV_1 or FEV_1/FVC has been reported to be weak or moderate (r = 0.09–0.62 and r = 0.12–0.62, respectively) (Akira et al. 2009; Heussel et al. 2009; Shaker et al. 2005; Yamashiro et al. 2010a). However, this value has been reported to be more robust for longitudinal evaluation and less sensitive to lung volume changes (Dirksen 2008; Heussel et al. 2009). And patients with greater Perc15 were reported to be related to more rapid decline of PFT parameters (Mohamed Hoesein et al. 2011). The last method is to assess the mean of the whole lung attenuation (mean lung density, MLD). It is the simplest measurement which is utilized especially for pulmonary fibrosis, but also for estimation of emphysema extent. However, MLD is not a sensitive index and other histogram-based indexes are more commonly used for quantification with densitometry of emphysema. The correlation coefficients between MLD and %FEV_1 ranged from 0.44 to 0.69, and between MLD and FEV_1/FVC from 0.56 to 0.76 (Akira et al. 2009; Lee et al. 2008; Yamashiro et al. 2010a).

The inherent limitations of CT density-based measurements is that they do not take into account heterogeneous patterns of distribution, size, or clustering of models that can affect the evaluation of COPD patients. Since emphysema is a locally distributed disease, it may be important to assess the regional distribution of emphysema as well as quantify the total amount of emphysema involvement. For assessment of heterogeneous distribution of emphysema, the most available quantitative CT methods is to divide each lung into separate anatomical zones, upper, mid, and lower zones or inner and outer zone, and ratios of the extent of emphysema in different lung zones can be calculated. Basal distribution of emphysema was reported to have an association with greater impairment of FEV_1

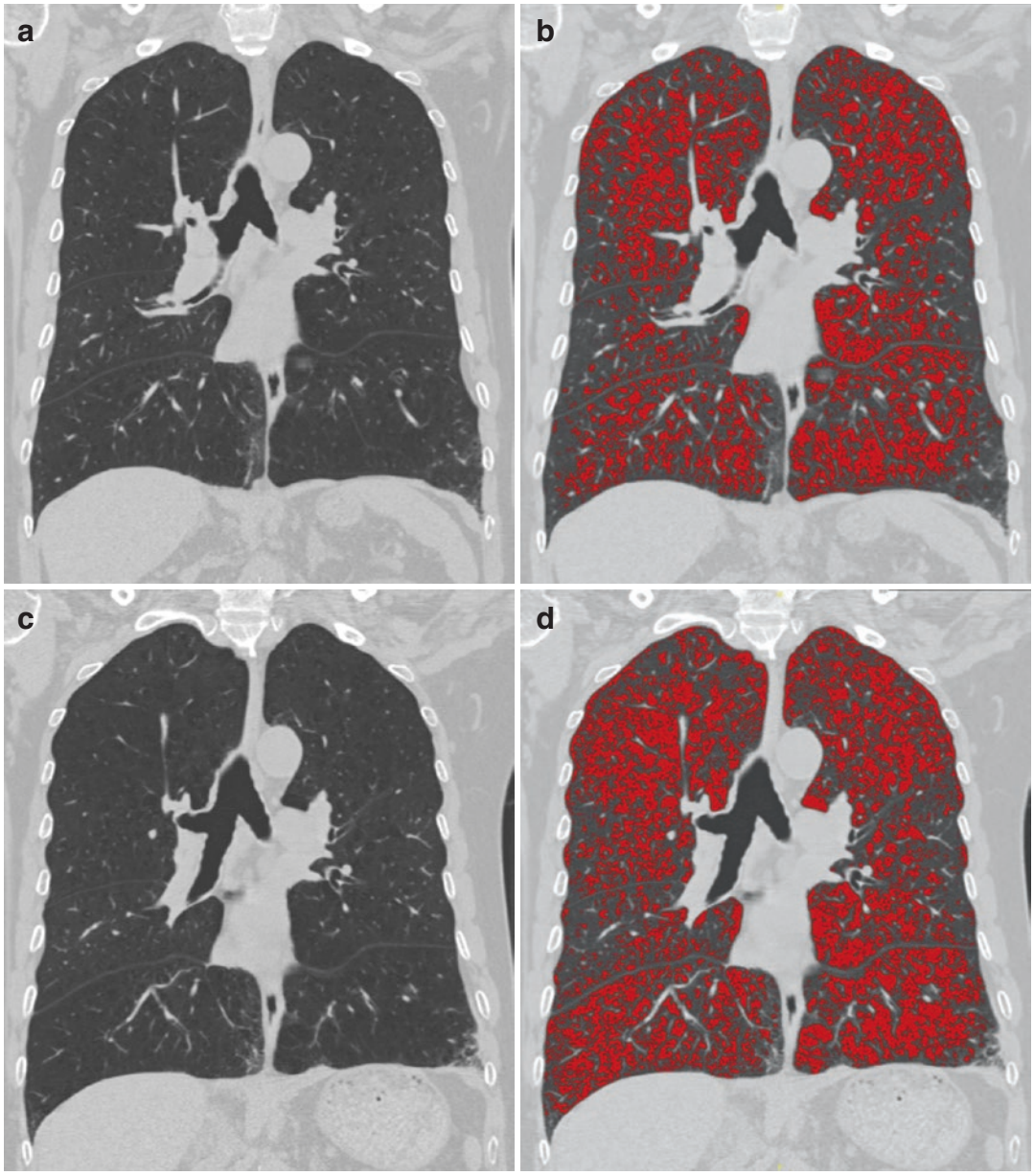


Fig. 1 CT measurement of emphysema severity with %LAA-950 and follow-up of %LAA-950 in the same subject. Initial %LAA-950 was measured to 26.4% on CT image (**a**) and matched color-coding image (**b**). After three years, %LAA-950 has increased and measured to 33.5% on CT image (**c**) and matched color-coding image (**d**). FEV_1 has aggravated from 1.29 to 0.69 L

than the apical distribution of emphysema, but less impairment of gas exchange (PaO_2) and alveolar-arterial oxygen gradient (Parr et al. 2004). Emphysema are more often found in the inner areas of the lung than in the outer areas, and the extent of emphysema in the inner segment of the lower lung on QCT showed much more clear correlation with airflow limitation than that of the outer segment (Nakano et al. 1999). Recently, the segmentation of each lobe to compute lobar volumes and the extent of emphysema objectively have become available.

There are also individual variabilities in size and shape of emphysema in COPD patients. In addition to quantification of emphysema extent, it may be necessary to assess the size of the emphysema cluster to account for disease progression. To assessing the size of emphysema cluster, the *D* value which represents the slope of the log-log plot of the cumulative frequency-size distributions of the $\%LAA_{-950}$ has been used. Mishima et al., found that smokers with normal %LAAs had lower D values compared with nonsmokers, suggesting that the *D* value could be a sensitive approach for detecting early emphysema (Mishima et al. 1999). However, the *D* value was not correlated with the macroscopic or microscopic indices of emphysema (Madani et al. 2008). Recently, new method to assess size of emphysema holes on CT was developed by using a modified length scale method (Oh et al. 2017). However, more works are required to identify the best way to measure the size of emphysema clusters or holes.

Emphysematous change of lung cannot be easily diagnosed by a loss of MR signal. The MR signal can be improved and emphysema can be quantified by using the balanced steady-state free precession (bSSFP), volumetric interpolated breath-hold examination (VIBE), half-Fourier-acquired single-shot turbo spin-echo (HASTE), and ultra-short echo time (UTE) (Rajaram et al. 2012; Ley-Zaporozhan et al. 2007b, 2010; Mayo et al. 1992). Using UTE pulse sequence, pulmonary emphysema can be estimated (Ohno et al. 2011; Takahashi et al. 2010). Recently with transverse T2-weighted sequence using the periodically rotated overlapping parallel lines with enhanced reconstruction (PROPELLER) technique, the presence and extent of emphysema can be assessed quantitatively with correlation to low dose chest CT (Meier-Schroers et al. 2018). Also, in patients with early cystic fibrosis lung disease, HASTE sequence reliably detects mosaic signal intensity (Leutz-Schmidt et al. 2018). The heterogeneous of emphysema distribution is one of key features of COPD patients. Using oxygen-enhanced MRI, the cranial-caudal heterogeneity of emphysema distribution can be evaluated (Fuseya et al. 2018).

2.2 Large Airway Measurement: Direct Measurement

Direct CT measurement of airway is most commonly used in large airways, which are segmental and sub-segmental airways by definition, because of limited resolution of current CT scanner. Although the changes of large airways are known to have a relatively small effect on airflow obstruction compared to small airways, the evaluation of large airways with CT may be helpful to correlate with symptomatic exacerbation and other symptoms, and to provide a window into changes in the small airways in COPD (Nakano et al. 2005).

The "full-width half-maximum (FWHM)" method is a most widely used method for quantitative airway measurements including absolute measures (bronchial luminal diameter or area, bronchial wall thickness or area, and total bronchial area) and relative measures (bronchial wall area %, WA%: 100 × (wall area)/(lumen + wall area)). Briefly, this calculates the CT attenuation values along the projecting linear rays placed from the airway center outwards in all direction, using an HU threshold for differentiating the airway wall from the surrounding lung parenchyma. The airway wall boundaries are assumed to be at the point where attenuation is halfway to the maximum on the lumen side and halfway to the minimum on the parenchymal side. This method is standardized and straightforward that has been incorporated into many commercially available software, but it systematically overestimates the airway wall area, especially in smaller airways (Kim et al. 2008). Several other algorithms have been developed to increase accuracy, including a threshold-based method that showed better correlation with PFT than the FWHM method (Cho et al. 2015). Another widely used CT airway parameter is the square root of wall area of a hypothetical bronchus having internal perimeter of 10 mm (Pi10) (Grydeland et al. 2009). Pi10 may provide the standardized airway measurements by avoiding the potential bias that may occur from the different distribution of airway sizes among subjects (Fig. 2). A variety of airway parameters are obtained from CT, including wall

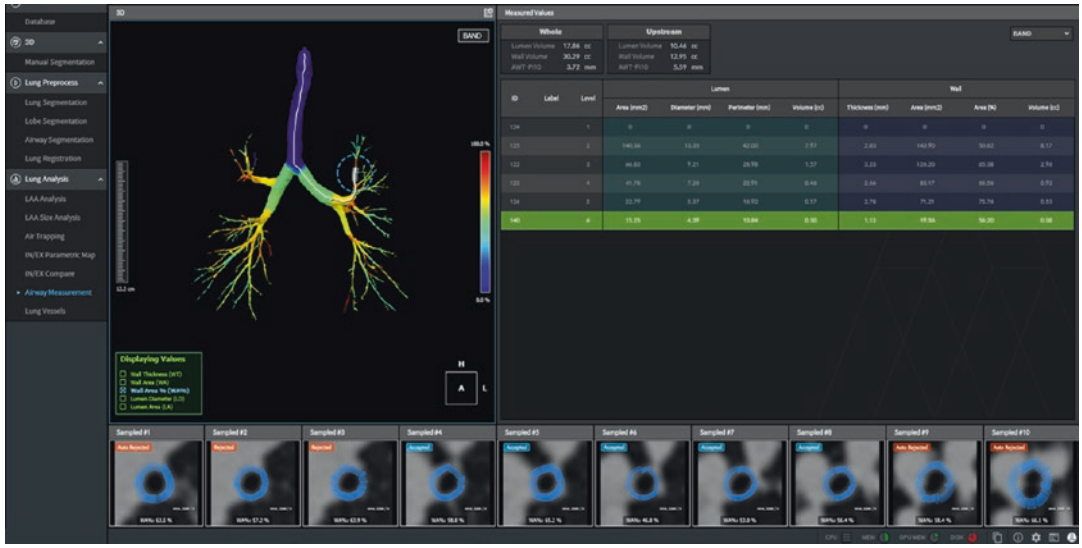


Fig. 2 Example of software providing automatic extractions of airways with three-dimensional volumetric reconstructions and automatic quantification of airway wall thickening. Once airways are extracted and target points of the airways are selected (blue dotted circle), several quantitative parameters of airway are automatically measured. The measured bronchial wall area % are shown in blue on lower part of figure

area percentage (WA%), airway wall thickness, wall area, lumen diameter, lumen area, and internal perimeter. The WA% is the most widely performed metric for clinical investigation and modestly correlated with lung physiologic impairment (Schroeder et al. 2013; Yamashiro et al. 2010a). The increase of WA% is reported to be correlated with a decrease of FEV_1, and this correlation is reported to be stronger in more peripheral airways ($r = -0.69$ to -0.47) (Cho et al. 2015; Hasegawa et al. 2006; Ohno et al. 2012; Yamashiro et al. 2010b). Furthermore, as compared with airway luminal areas measured on inspiratory CT, the correlation between airflow limitation and airway luminal areas of the third- to fifth-generation bronchi measured at expiratory CT were stronger (Matsuoka et al. 2008a). In recent report, QCT measured bronchial wall thickening as well as severity of emphysema are independently related with an increased frequency of exacerbation and increased mortality from exacerbations in COPD patients, and also could be used to define the predominating COPD phenotype (Han et al. 2011). Additionally, WA% and peak airway attenuation were reported to be independent predictors of $\%FEV_1$ on multivariate analysis (Yamashiro et al. 2010a).

More recently, CT image-based counting of airway segments with various methods have been tried and investigated to demonstrate relation between total airway count (TAC) and disease severity and lung function change in COPD patients. The massive destruction of terminal bronchioles, which precede the emphysematous destruction, has been well established in COPD (McDonough et al. 2011), and such changes in the small airways could be reflected in proximal airways and quantified using CT TAC. TAC measurements can be obtained by visually inspecting CT images, but they can also be obtained by automatically summing all of the airway segments in the divided airway tree in CT image using commercially available software. Diaz et al. found that CT image-based TAC of a subset of smokers was inversely related to CT density-based emphysema severity and was also a predictor of a high BODE index (Diaz et al. 2010). In a recent report, automatically quantified TAC in CT was significantly reduced in mild COPD patients compared with never

smokers and smokers with normal spirometry independent of emphysema. And reduced TAC was significantly and independently associated with lung function decline (Kirby et al. 2018). However, there are still many technical difficulties and uncertainties associated with airway measurements in COPD patients compared with emphysema quantification, and further researches are required.

MRI usually visualizes central and peripheral bronchiectasis and central bronchi, whereas poorly visualizes normal peripheral bronchi. Using 3D VIBE with high spatial resolution, the airway can be visualized (Biederer et al. 2003). T2-weighted sequences can visualize inflammation, mucus, edema, and fluid collections. Active inflammation can be represented by increased fluid, which shows high signal of the bronchial wall on T2-weighted sequences. Inflammatory activity has relation with contrast enhancement of thickened bronchial wall on contrast-enhanced T1-weighted sequence. Airway inflammation can be visualized without radiation by combination of T2-weighted and contrast-enhanced T1-weighted sequences (Beckmann et al. 2004). MRI can visualize well mucus plugging on peripheral bronchi due to high signal intensity of fluid content on T2-weighted sequence without contrast enhancement on T1-weighted sequence.

2.3 Small Airway Measurement: Air-Trapping Measurement

Small airway remodeling is an important factor in COPD, and is known as the strongest determinant of airflow limitation. Airways with a diameter less than 2 mm are the major sites of airflow obstruction, and small airway narrowing is known to occur in early stages of COPD, before major emphysematous changes occur. As the small airways cannot be directly visualized using current CT scanners, the presence of air trapping on expiratory phase CT scans can be used as an indirect functional estimate to evaluate small airways disease.

Several quantitative CT indices on expiratory phase CT, including LAA% and MLD, are used for the evaluation of the air trapping. One of the simplest ways to assess the presence of air trapping using chest CT is to evaluate %LAA with CT values lower than the threshold of −856 HU or −850 HU ($\%LAA_{exp\text{-}856}$ or $\%LAA_{exp\text{-}850}$) in expiration (Lee et al. 2008). The threshold is chosen because it is known to be the attenuation of normally inflated lung on inspiration, with the concept being that the attenuation should be higher than this value on expiration in a normal lung. With this method, several studies reported the relationship between expiratory CT and airflow limitation in cigarette smokers or COPD, and high correlations were noted between $\%LAA_{exp\text{-}850}$ or $\%LAA_{exp\text{-}856}$ and FEV_1/FVC and $\%FEV_1$ (Murphy et al. 2012; Schroeder et al. 2013). And in a study by Schroeder et al., correlation between $\%LAA_{exp\text{-}850}$ and FEV_1/FVC and $\%FEV_1$ ($r = -0.77$ and -0.84, respectively) was stronger than the correlation between $\%LAA_{-950}$ in inspiration CT and FEV_1 and FEV_1/FVC ($r = -0.67$ and -0.76, respectively). However, the drawback of this single-threshold method is that it does not separate trapped air due to small airway disease areas from air remaining in emphysematous areas; it combines air trapping and emphysema quantification into one measure. As an effort to overcome this limitation, the method that quantifies air trapping outside the emphysematous area is developed through the density-based quantification method (Matsuoka et al. 2007, 2008b). To exclude emphysema area, all voxels with attenuation lower than −950 HU were excluded from inspiration and expiration scans. Thus, the relative volume changes with attenuation value between −860 HU and −950HU were calculated on each inspiratory and expiratory CTs as follows: Relative volume change $_{< -860\ HU}$ (%) = expiratory relative volume $_{< -860\ HU}$ − inspiratory relative volume$_{< -860\ HU}$. This air-trapping measure revealed significant correlation with lung physiologic parameters ($r = 0.50$–0.80) (Matsuoka et al. 2008b). Other methods to measure air trapping are to quantify the ratio of lung volume in expiratory CT and inspiratory CT

($E/I\text{-}ratio_{LV}$) and the ratio of MLD in expiratory CT and inspiratory CT ($E/I\text{-}ratio_{MLD}$). E/I-ratioMLD correlated with clinical parameters of COPD such as BODEindex ($0.48 < r < 0.68$), and E/I-ratioLV showed a very strong correlation with E/I-ratioMLD ($r = 0.95$, $p < 0.001$) (Lee et al. 2008; Yamashiro et al. 2010a). The objective assessment of the heterogeneity of the lung field by measuring of kurtosis and skewness of the CT lung histogram also has been addressed. The expiratory kurtosis and skewness showed significant correlation with PFT results ($\%FEV_1$: $r = -0.581$ and $r = -0.584$, FEV_1/FVC: $r = -0.612$ and $r = -0.619$, residual volume (RV)/total lung capacity (TLC): $r = 0.613$ and $r = 0.585$), while the inspiratory kurtosis or skewness showed no significant correlations with PFT results (Yamashiro et al. 2011). Recently, the continuous measurements of lung density or airway dimensions on dynamic-ventilation CT during respiration also have been attempted for a better understanding of the airflow limitation in patients with COPD (Yamashiro et al. 2016).

However, these methods were limited because pixel-by-pixel matching of inspiration and expiration scans was not performed. To overcome this limitation, new approach, so-called parametric response mapping (PRM) has been developed using the deformation techniques to perform a pixel-by-pixel co-registration of inspiratory and expiratory CT scans (Galban et al. 2012). In a study by Galban et al., PRM classified lung areas by normal lung tissue, functional small airway disease or emphysema based on the assumption that voxels of lung less than −950 HU on inspiratory CT were emphysematous, while voxels that were greater than −950 HU on inspiration but less than −856 HU on expiration represented non-emphysematous functional small airways disease with providing insight of spatial information of disease area (Galban et al. 2012). Several studies have been reported on the association between PRM and clinical COPD parameters such as FEV_1 and FEV_1/FVC and lung function decline (Bhatt et al. 2016; Galban et al. 2012). Another method, called air-trapping index has been proposed (Kim et al. 2015; Lee et al. 2016). This method uses the HU difference of each voxel detected on co-registered inspiration and expiration CT images, and the areas with decreased density change can be defined as the area of air trapping. With this method, regional assessment of air trapping is possible in addition to the global assessment (Fig. 3). Until now, no comparison of published quantitative CT measurements for air trapping has been performed, and the optimal quantitative measures have not yet been identified.

Many studies has been showed that the significant correlation between the quantitatively measured lung density or airway and PFT results which indicate airflow limitation and air trapping on the inspiratory and expiratory static CTs.

2.4 Other Comorbidities of COPD

2.4.1 Pulmonary Vascular Change

Pulmonary vascular change is one of the characteristic features of COPD and the extent of emphysema, rather than airway obstruction, is known to be responsible for pulmonary endothelial dysfunction in COPD (Barr et al. 2007). With the usage of QCT measuring the cross-sectional area (CSA) of small pulmonary vessels (subsubsegmental level, CSA less than 5 mm^2), the total CSA showed strong correlation with the emphysema severity ($\%LAA_{-950}$), whereas weak correlation with air trapping in COPD patients (Matsuoka et al. 2010). Moreover, the percentage of the total CSA for the lung area is significantly lower in subjects with emphysema phenotype than in subjects with airway dominant phenotype in all COPD GOLD stage. Recently, using automatic segmentation of pulmonary vasculature and measurement of the total blood vessel volume in a volumetric CT scan, distal pruning of the small blood vessels (<5 mm^2) and a disproportionate loss of nonvascular tissue in regions of emphysema was suggested as an early change in smoking-related COPD (Estepar et al. 2013) (Fig. 4). The clinical significance of these results still need to be clarified and continued investigation is required. There are some studies about abnormal aortic stiffness and increased arterial stiffness in COPD (Maclay et al. 2009; McAllister

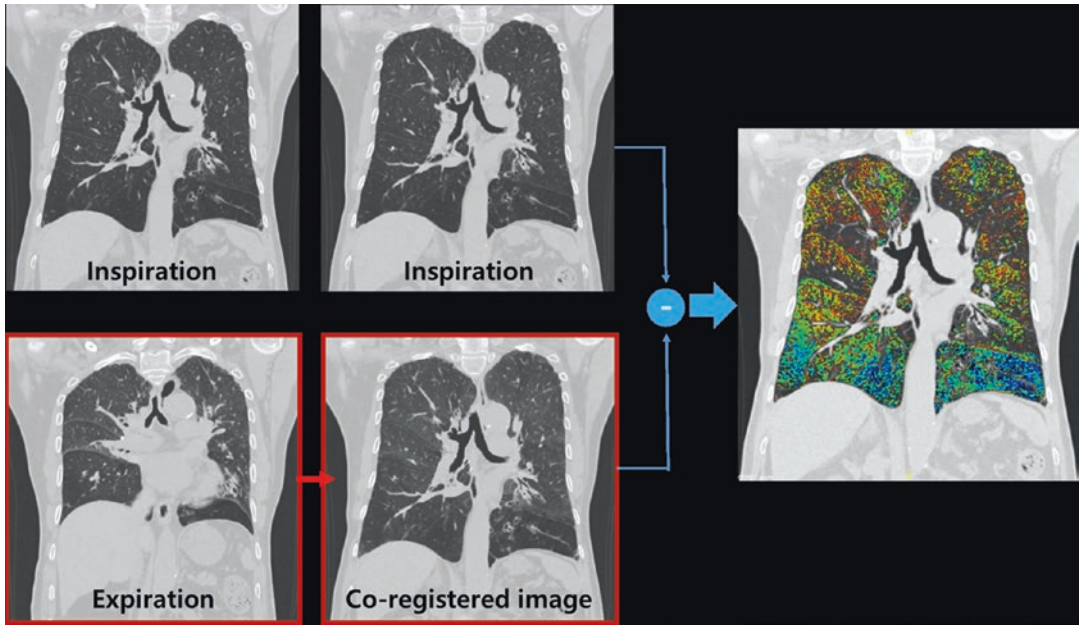


Fig. 3 Measurement of air trapping using a co-registration method. Using an image co-registration technique, expiratory CT images are registered to inspiratory CT images. After registration, voxel-by-voxel comparison and subtraction of attenuation changes between inspiration and expiration are obtained. Air trapping is defined as areas with less change in attenuation than the preset threshold, and the density changes of all of the voxels can be displayed on the color-coded map. Red colors represent air-trapping areas with voxels with a density change below a threshold of 50, green and yellow colors, voxels with a subtraction value between the threshold of 50 and 100, and blue colors, voxels with a subtraction value over a threshold of 100

et al. 2007). Stiffness of the pulmonary arteries using MRI is correlated with emphysema and COPD severity (Liu et al. 2018).

2.4.2 Osteoporosis

Osteoporosis should be considered as one of the important pathologies of COPD, because it often results in vertebral compression fractures, which can cause deterioration of FEV_1 and decrease in vital capacity. Actually, the reduction in vertebral bone mineral density on CT is closely related to the emphysema severity, because these two entities share many similar risk factors such as low BMI, decreased activity, systemic inflammation, and use of corticosteroids (Harrison et al. 2007; Lehouck et al. 2011; Ohara et al. 2008). The dual-energy X-ray absorptiometry of the lumbar spine and hip is currently the gold standard for osteoporosis diagnosis, but quantitative CT has recently emerged as a robust alternative for evaluating bone mineral density (BMD), using three-dimensional techniques to provide volumetric assessment of bone (Fig. 5). There has been reported that the decrease in thoracic vertebral BMD measured on chest CT is significantly associated with COPD exacerbations and baseline PaO_2. Indeed, osteoporosis progression should be checked in COPD patients, especially in those with a history of recurrent exacerbations (Kiyokawa et al. 2012).

2.4.3 Diaphragm and Respiratory Muscle

Respiratory muscle dysfunction is a cardinal feature of COPD. Hyperinflation in COPD makes diaphragm to be flatter and shorter. Although the diaphragm plays a major role in breathing, the act of breathing becomes gradually more dependent on the thoracic intercostal respiratory muscles as the progression of COPD. The thoracic respiratory muscles play an important role in alveolar ventilation, especially when ventilator needs are

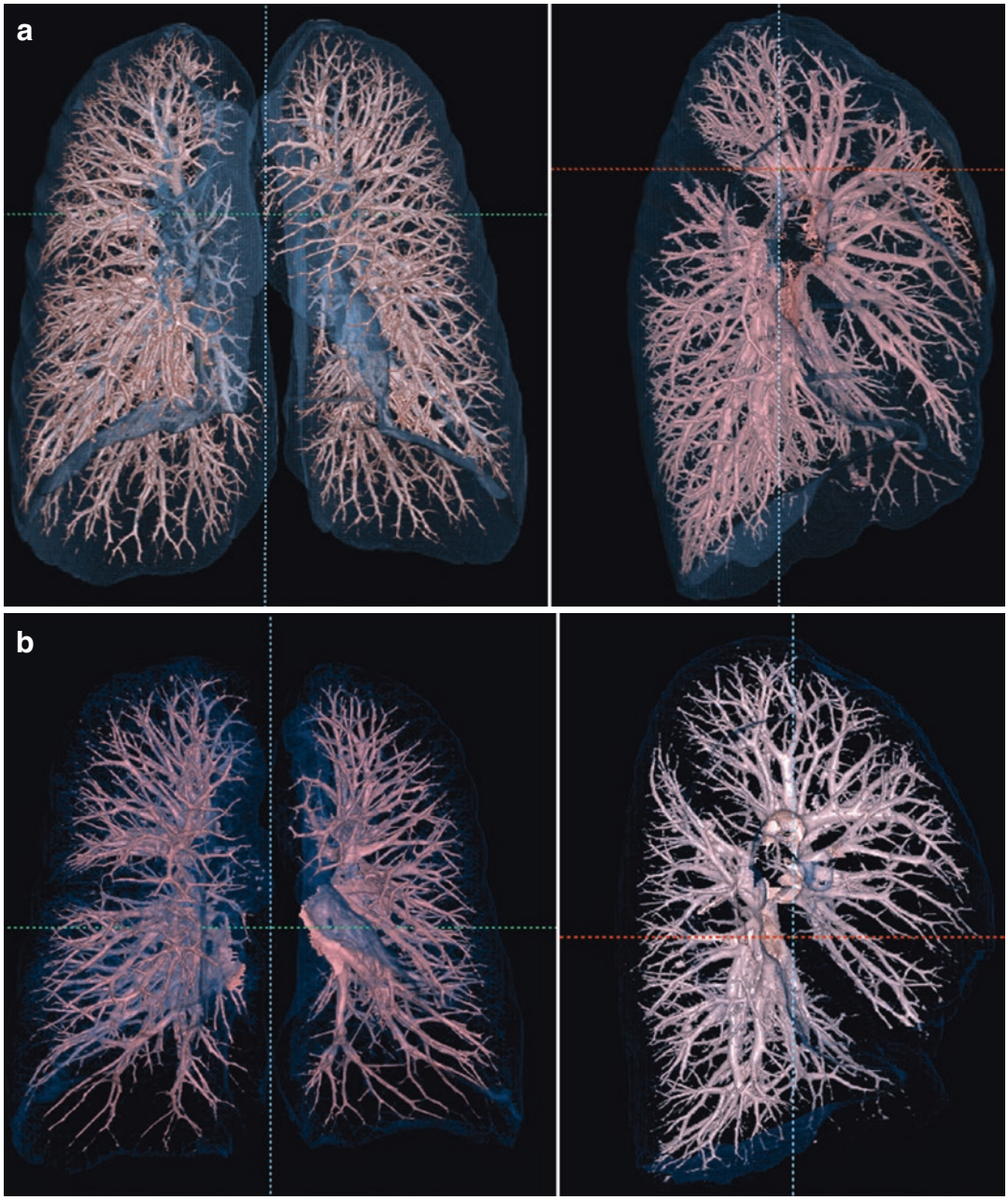


Fig. 4 Automatic segmentation of pulmonary vasculature in a volumetric CT scan. (**a**) As compared with pulmonary vasculature of a 50-year-old male patient with normal lung function (coronal image and 3D volume image, green: low attenuation area, red: pulmonary artery, blue: pulmonary vein), (**b**) distal pruning of the peripheral blood vessels and decreased number of pulmonary vessels are noted in a 67-year-old male patient with COPD (coronal image and 3D volume image, green: low attenuation area, red: pulmonary artery, blue: pulmonary vein)

increased. And respiratory muscle weakness results in dyspnea and respiratory failure associated with mortality in COPD patients. The intercostal mass and intercostal attenuation measured by QCT were reported to have significant correlation with FEV_1 and extent of emphysema of

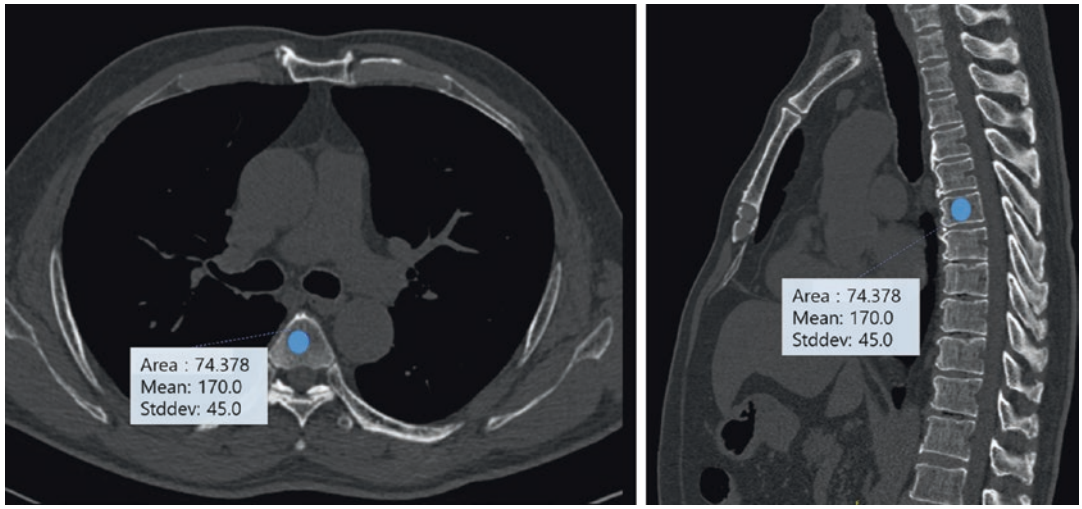


Fig. 5 Quantitative chest CT can provide bone marrow density measurement of thoracic spine. Vertebral bone mineral density on CT is closely related to the severity of emphysema

QCT measurement (Park et al. 2014a). Decreased thoracic muscle mass with increasing intercostal fat is associated with worsening of COPD. Using MR-fluoroscopy, diaphragmatic movement and treatment response in COPD patients can be evaluated with accurate measurement of diaphragmatic contractility (Etlik et al. 2004). Emphysema in lower lung shows significant correlation with diaphragmatic flattening, abnormal chest wall motion, and severe airflow limitation (Iwasawa et al. 2011). Although both normal and paradoxical diaphragmatic motion are restricted by severe hyperinflation, the paradoxical diaphragmatic motion shows significant correlation with hyperinflation (Iwasawa et al. 2000).

2.4.4 Atherosclerosis

Ischemic heart disease is a common comorbidity in COPD. Patients with COPD tend to have more frequent and more fatal myocardial infarctions, even after adjusting for common risk factors such as smoking status and old age (Stefan et al. 2012). And in COPD patients, decrease of FEV1 is known to be an increased risk factor for cardiovascular diseases and mortality (Sin et al. 2005). In other words, systemic inflammation in COPD patients can accelerate the incidence of cardiovascular disease, and degree or status of atherosclerosis may be associated with lung function impairment and emphysema in COPD patients. An attempt has been made to demonstrate the association of the total amount of calcification in coronary artery, thoracic aorta, mitral and aortic annuli, and the extent of emphysema on QCT and lung physiology (Chae et al. 2013). Calcium score as a measure of degree of systemic atherosclerosis showed weak but significant correlation with volume fraction of emphysema on QCT, FEV_1/FVC, and diffusion capacity, with these correlations being independent of age, body mass index (BMI), and amount of smoking. The severity of atherosclerosis may be associated with lung function impairment and emphysema extent.

3 Evaluation of Parenchymal Perfusion and Ventilation

Characteristic anatomic changes of COPD may influence alveolar gas exchange and pulmonary vascular change, and the uneven distribution of alveolar ventilation and pulmonary blood flow (V/Q mismatch) is the most important cause of arterial hypoxemia in COPD patients (Barbera et al. 1997; Sandek et al. 2001). Therefore, there has been an attempt to demonstrate the parenchymal ventilation or perfusion status as well as anatomical evaluation using various imaging

methods. Scintigraphy and single-photon emission computed tomography (SPECT) provide the pulmonary functional information in regarding ventilation and perfusion, with imaging of the distribution of radiotracer which is introduced into the body. There also have been attempts to evaluate a pulmonary function using MDCT. However MDCT has some limitations for the evaluation of parenchymal ventilation or perfusion, such as repeated CT scans and incorrect registration of lung images. Recently introduced dual-energy CT (DECT) can provide high-resolution anatomic information of the lung parenchyma coupled with an anatomically matched parenchymal ventilation and perfusion change with a single CT scan in COPD. Advantage of perfusion MRI in COPD is combination of perfusion and morphologic information about parenchymal destruction and cause of perfusion changes.

3.1 Evaluation of Parenchymal Perfusion

In COPD, the regional lung perfusion impairment occurs as a result of several processes: hypoxic vasoconstriction of the area with decreased ventilation, reduction of the pulmonary capillary by the chronic inflammation of pulmonary artery, and loss of capillary beds from emphysematous destruction (Barbera et al. 2003). Moreover, alveolar surface destruction is accompanied by the reduction of the pulmonary capillary bed. Thus, considerable attention has been paid to evaluate lung perfusion alterations in COPD patients, because the severity of parenchymal destruction and the alteration of lung perfusion determine the functional effect of emphysematous changes. Dynamic pulmonary perfusion imaging with MDCT can provide the regional parenchymal perfusion status. With this technique, it has been demonstrated that smokers with subtle centrilobular emphysema on CT and normal spirometry has increased regional heterogeneity of lung perfusion compared with never smoked subjects and smokers with normal CT image (Alford et al. 2010). However, this technique necessitates central venous catheter for high-pressure bolus of contrast material and repeated scanning of limited lung area during a cardiac-gated scan. With DECT technique, the anatomic information for evaluating the severity of parenchymal destruction with high-resolution CT image and the anatomically matched functional information of parenchymal perfusion can be obtained by single image scan (Fig. 6). Pansini et al. have firstly demonstrated that contrast-enhanced DECT could be used to assess regional alteration of pulmonary parenchymal perfusion, and local change of parenchymal perfusion matched with the structural destruction in 47 smokers with predominant emphysema (Pansini et al. 2009). Moreover, contrast-enhanced DECT can be used for density-based emphysema quantification as well as regional perfusion evaluation, simultaneously, without additional radiation (Lee et al. 2012). As described above, CT density-based quantification of emphysema severity such as the $LAA\%_{-950}$ from a non-enhanced CT image has been well established and correlated with PFT results (Akira et al. 2009; Dransfield et al. 2007; Hesselbacher et al. 2011; Iwasawa et al. 2011; Lee et al. 2008; Park et al. 2008; Schroeder et al. 2013). However, contrast-enhanced CT image cannot be used for density-based emphysema quantification because the CT density of contrast-enhanced CT image is the sum of native parenchymal density and iodine density. The DECT technique can divide the CT density of contrast-enhanced CT images by the native parenchymal density (virtual noncontrast (VNC) image) and the iodine density. Lee et al. demonstrated that the density-based quantified CT parameters for emphysema severity from VNC image of DECT showed moderate correlation with the airflow obstruction parameter ($\%LAA_{-950}$ and $\%FEV_1$: $r = -0.47$ and MeanVNC and $\%FEV_1$: $r = 0.41$) and quantified perfusion status, as determined from pulmonary blood volume (PBV) map of DECT ($\%LAA_{-950}$ and volume fraction of the low iodine area below 5 HU: $r = 0.48$, and MeanVNC and MeanIodine: $r = 0.47$), respectively (Lee et al. 2012). Meinel et al. used the automated quantified PBV value of contrast-enhanced DECT to evaluate pulmonary perfusion

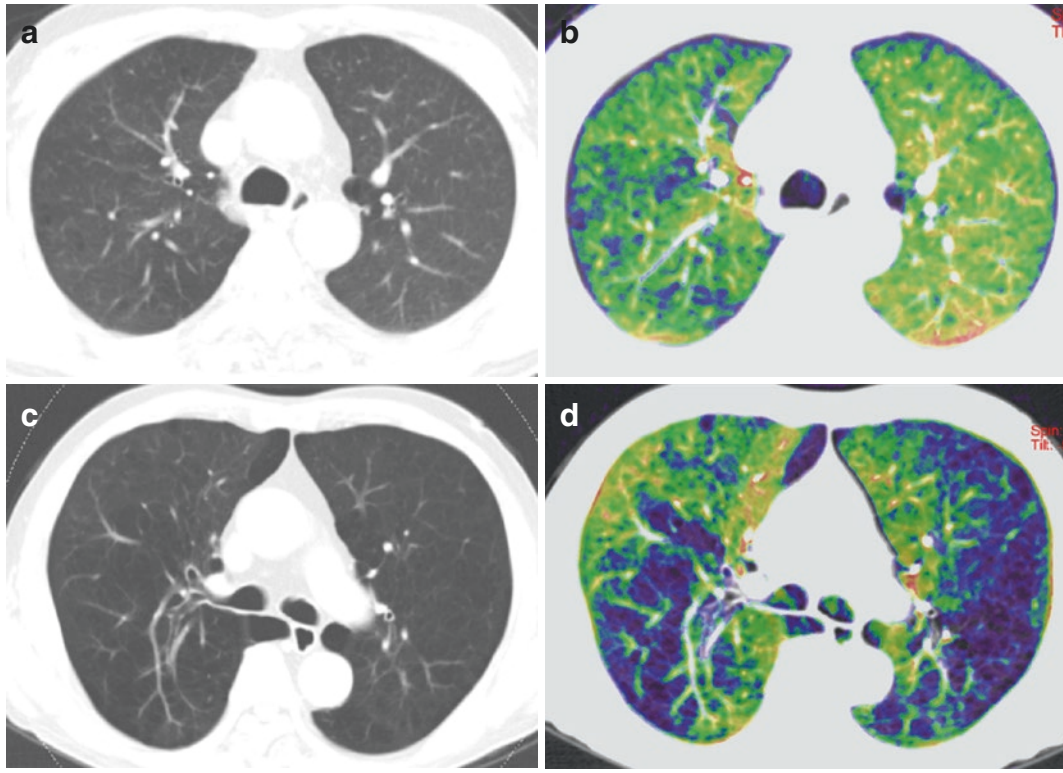


Fig. 6 Iodine perfusion DECTs in patients with COPD in 63-year-old male with mild emphysema (**a**, **b**) and 71-year-old male with moderate to severe emphysema (**c**, **d**). (**a**) Weighted conventional CT image shows mild centrilobular emphysema in both upper lobes. (**b**) Homogeneous parenchymal perfusion in left upper lobe, while patchy inhomogeneous parenchymal perfusion in right upper lobe are identified on perfusion map. (**c**) Axial conventional CT image shows severe emphysema. (**d**) On perfusion map, multifocal areas with decreased parenchymal perfusion are identified in both upper lobes

in the patients with emphysema. Quantified PBV values were correlated with clinical parameters (global PBV and %FEV1: $r = 0.67$, and global PBV and carbon monoxide diffusing capacity (DLCO): $r = 0.80$), and also with the visually or quantitatively assessed emphysema severities ($r = -0.46$ or -0.63) (Meinel et al. 2013). Assessing the distribution of pulmonary emphysema and anatomically matched perfusion status using DECT may be particularly applicable to target lobe selection in patients undergoing lung volume reduction surgery or bronchoscopic-lung volume reduction. According to National Emphysema Treatment Trial with more than 1000 patients who underwent lung volume reduction surgery, lung volume reduction surgery reduces mortality in patients with upper-lobe predominant emphysema only if there is low perfusion to the upper lobe on scintigraphy (Chandra et al. 2010). Park et al. used DECT instead of scintigraphy for target lobe selection of bronchoscopic lung volume reduction, and the most hyperinflated and least perfused lobe of emphysematous lung on DECT without collateral ventilation with other lobes on the Chartis® System (Pulmonx Inc.) was selected as the target lobe. Additionally, the fissure integrity of target lobe could be successfully assessed on high-resolution DECT image, and only patients having a complete fissure of the target lobe were eligible for bronchoscopic lung volume reduction in this study (Park et al. 2014b). DECT may be more useful than scintigraphy for the selection of target lobe for bronchoscopic lung volume reduction as it provides high-resolution information of emphysema, parenchymal inflation status and fissure

integrity as well as parenchymal perfusion status of the target lobe with single DECT scan.

Perfusion MRI shows high accuracy in detecting perfusion abnormalities in patients with emphysema (Sergiacomi et al. 2003; Molinari et al. 2006). The perfusion abnormalities in COPD usually show a low degree of inhomogeneous contrast enhancement, especially in the area of severe emphysema (Morino et al. 2006) and decreased peak signal intensity. In COPD patients with severe emphysema, visual assessment of perfusion using 3D perfusion MRI shows high agreement with parenchymal destruction (Ley-Zaporozhan et al. 2007a). With quantitative analysis, decreased perfusion parameters on MRI correlate with worsening of FEV_1/FVC and increased emphysema index on CT (Jang et al. 2008). Quantitative perfusion MRI in COPD shows decreased value and heterogeneous change in mean pulmonary blood flow (PBF), pulmonary blood volume (PBV), and mean transit time (MTT) than those in normal volunteer (Fig. 7) (Ohno et al. 2004). MR perfusion patterns correlated with CT phenotype in emphysema.

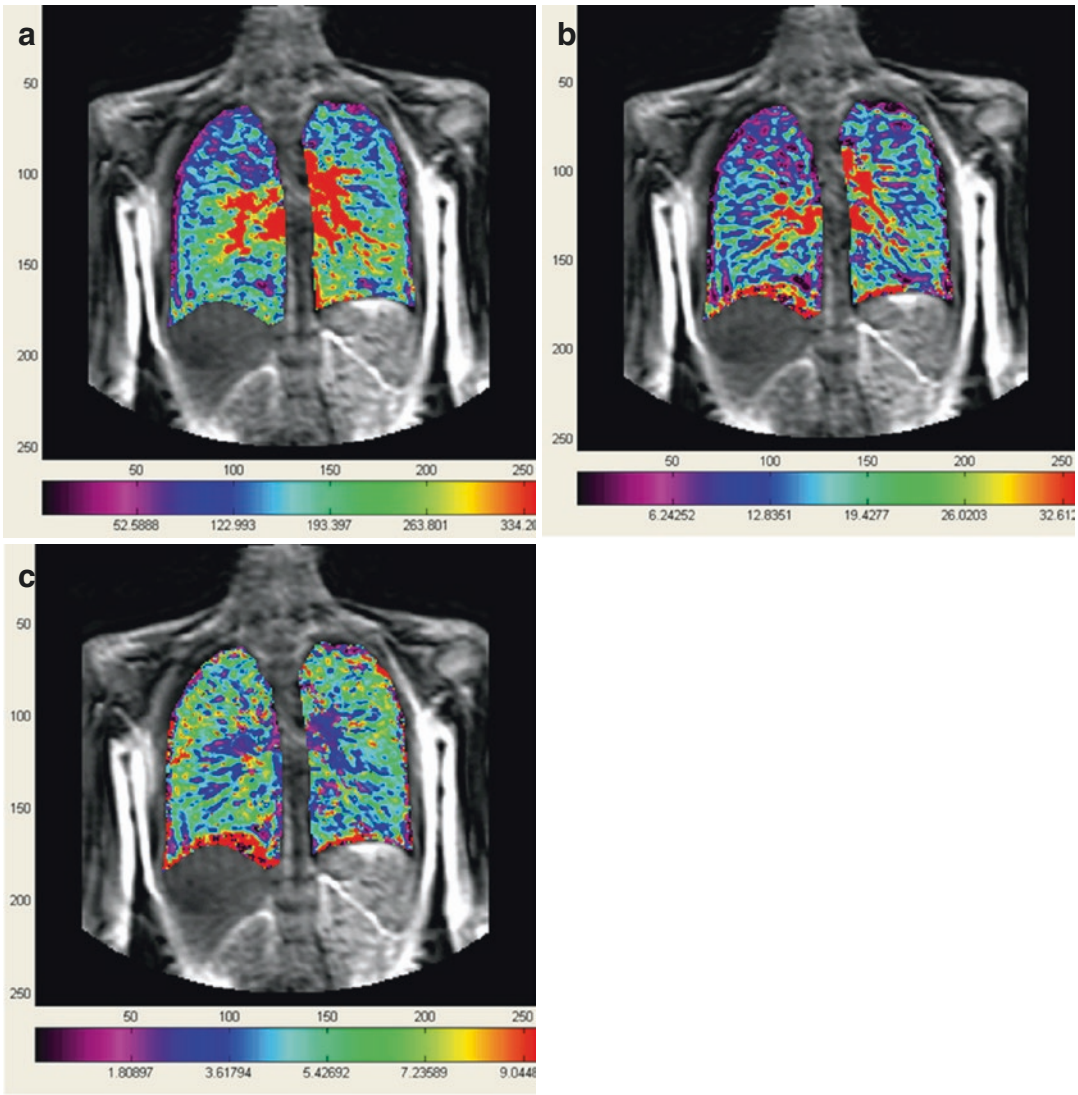


Fig. 7 Using perfusion MRI technique, PBF map (**a**), a PBV map (**b**), and an MTT map (**c**) are generated

Centrilobular emphysema shows heterogeneous perfusion reduction while panlobular emphysema shows loss of perfusion (Bryant et al. 2015). Recently, noncontrast-enhanced perfusion-weighted phase-resolved functional lung MRI with free breathing showed comparable results with dynamic gadolinium-enhanced perfusion MRI in COPD patients (Kaireit et al. 2018b).

Scintigraphy and SPECT also provide functional information for pulmonary perfusion. The perfusion SPECT has been shown to be more sensitive than HRCT for detection of mild physiologic changes of elastase-induced pulmonary emphysema in an animal study (Noma et al. 1992). Moreover, Suga et al. have been demonstrated that perfusion abnormalities on breath-hold SPECT-CT fusion image can demonstrate the pulmonary pathophysiology better than the emphysema index on CT image (Suga et al. 2008). As mentioned earlier, these techniques have been used for the target lobe selection for lung volume reduction surgery or bronchoscopic lung volume reduction. Chandra et al. have demonstrated that lung volume reduction surgery reduces mortality in patients with upper-lobe-predominant emphysema only if there is low perfusion to the upper lobe on perfusion scintigraphy (Chandra et al. 2010). And Argula et al. have demonstrated that perfusion scintigraphy is useful in selecting target lobe for endobronchial valve therapy in patients with advanced emphysema, and patients having heterogeneous emphysema with a low baseline target lobe perfusion benefited from endobronchial valve therapy (Argula et al. 2013). Scintigraphy and SPECT have some drawbacks, low spatial resolution and long image acquisition time; however they are widely applied due to their availability in many centers to date.

3.2 Evaluation of Parenchymal Ventilation

The evaluation of COPD severity is mostly based on the PFT results in clinical practice. Although clearly useful, PFT provides global measures of pulmonary function from that are inferred primary structural and functional alterations, and does not show the regional distribution of structural and functional abnormalities. Conventional CT scan is widely performed in COPD patients to assess the regional distribution of low attenuation areas, but when assessed as a single full inspiratory scan, it is limited because it provides only structural information. MDCT also can be used to depict lung ventilation with inhalation of radio-opaque gas (Gur et al. 1979; Herbert et al. 1982). Two stable gases, xenon and krypton, with high atomic numbers (54 for xenon and 36 for krypton) are eligible for CT ventilation imaging, and the concentrations of these gases in alveolar space can be measured based on the CT density change. However, MDCT requires repeated CT scans to depict the time course of CT density change in lung parenchyma, and the accurate measurement of lung ventilation function is limited because of the variability of baseline lung attenuation between images due to misregistration artifacts and different respiration levels. Recently, a 320-row MDCT with a subtraction technique has been proposed as another useful technique to perform xenon ventilation CT (Ohno et al. 2017).

Currently, DECT is most widely used CT imaging technique for the simultaneous evaluation of pulmonary parenchymal ventilation and anatomical changes (Fig. 8). Chae et al. reported the first clinical study with xenon ventilation imaging with DECT in eight healthy volunteers and four COPD patients. The authors have shown the direct visualization of the degree of xenon gas enhancement of the lung parenchyma with a color mapping on a conventional thin-section chest CT image by material decomposition (Chae et al. 2008). Park et al. performed two-phase (wash-in and wash-out phase) xenon ventilation imaging with DECT in 32 COPD patients. And regionally quantified value of xenon enhancement in low attenuating lung areas on wash-in and wash-out phases showed inverse correlation with PFT results, and the xenon value of low attenuating lung areas on wash-out phase showed a better correlation with FEV_1 than CT density-based quantification of emphysema severity (Park et al. 2010). The authors categorized the

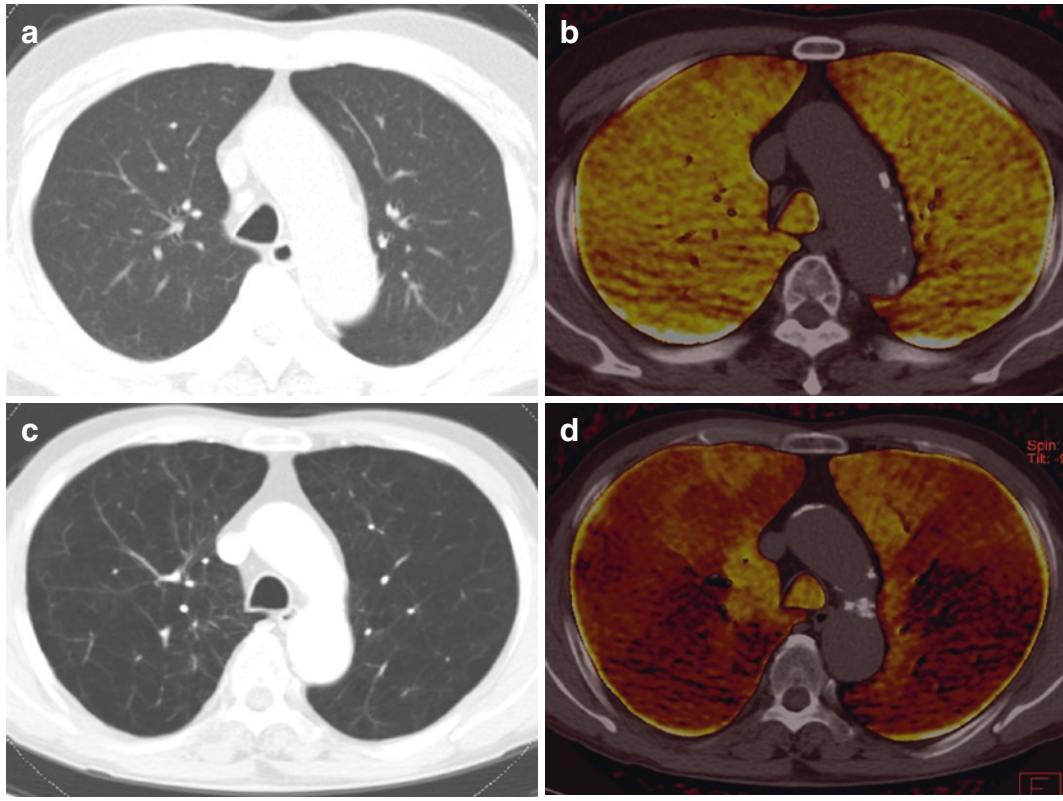


Fig. 8 Xenon ventilation DECTs in patients with COPD in 66-year-old male with mild emphysema (**a**, **b**) and 71-year-old male with moderate to severe emphysema (**c**, **d**). (**a**) DECT shows mild centrilobular emphysema on axial conventional CT image and (**b**) homogeneous xenon enhancement on xenon ventilation map in both upper lobes. (**c**) Axial conventional CT image shows severe emphysema. (**d**) On xenon ventilation map inhomogeneously decreased xenon enhancement is identified in both upper lobes, while xenon ventilation is relatively preserved in central areas of both upper lobes

lung ventilation abnormalities on two-phase xenon imaging into four patterns for visual analysis. Visual analysis showed the areas with emphysema exhibited iso-attenuation or high attenuation in both wash-in and the wash-out phase, while the areas with predominant airway disease showed low attenuation during the wash-in period and various attenuation during the wash-out period. Hachulla et al. have firstly reported the ventilation DECT imaging with krypton gas in COPD patients. The maximum level of krypton enhancement in the lung parenchyma was 18.5 HU, which is lower than that reported with xenon gas, with an average maximum degree of xenon enhancement of 23.78 HU. However, it is sufficient to detect ventilation abnormalities, with significant krypton attenuation differences between normal and emphysematous lung (Hachulla et al. 2012). Most of studies have used multiple breath-in method of xenon gas inhalation to obtain images with sufficient attenuation for the visual and quantitative analyses, but might possibly obscure mild degree ventilation defects that can be seen on ^{3}He MRI scans obtained using the single breath-in method. Recently, the xenon ventilation DECT imaging with a single vital capacity inhalation of xenon gas and single static scan has been tried (Honda et al. 2012). A few or single inhalation method may be more easily implementable for radiologists and patients, without side effects. However, different ventilation dynamics can be evaluated depending on the scanning method and gas inhalation method.

Several methods of MRI, such as hyperpolarized noble gas MRI, oxygen-enhanced MRI, and ventilation-weighted Fourier decomposition MRI, can be used for assessment of lung ventilation. Using hyperpolarized noble gas MRI with ^{3}He or ^{129}Xe gas, ventilation MRI can be acquired (Bauman and Eichinger 2012; Kirby et al. 2010; Kaushik et al. 2011) and the ^{3}He or ^{129}Xe gas in airway and airspaces can be visualized for regional mapping of airflow and assessment of diffusion in airspace (Altes and Salerno 2004; de Lange et al. 2006). In stage III COPD, ventilation defect volume was sensitive to minimal changes during short follow-up and percentage of ventilation volume was significantly different among healthy volunteers, healthy asymptomatic smokers, and COPD patients. COPD patients are separated from healthy subjects by apparent diffusion coefficient (ADC) map (van Beek et al. 2009). Using diffusion-weighted hyperpolarized ^{129}Xe MRI, ADC was significantly correlated with FEV_1, FEV_1/FVC, and DLco (Kaushik et al. 2011). Ventilation defect percentages in ^{3}He MRI show significant correlations with ventilation defect percentages in ^{129}Xe MRI and ventilation defect percentages show strong correlations with FEV_1 (Kirby et al. 2012). ADC can measure airspace size sensitively. In COPD, airspace dimensions are increased comparing to nonsmokers (Swift et al. 2005). ADCs in emphysema show regional variations and significantly larger than those of healthy volunteers, which is homogeneous (Salerno et al. 2002). Without expensive and limited hyperpolarized noble gases, oxygen-enhanced MRI is used to assess ventilation abnormalities in pulmonary emphysema (Ohno et al. 2002). Regional changes in ventilation on oxygen-enhanced MRI reflect the regional lung function (Ohno et al. 2001). In patients with severe COPD using dynamic oxygen-enhanced MRI, FEV_1 and DLco well correlate with slope of oxygen enhancement time-course curve and degree of oxygen enhancement (Fig. 9). Oxygen-enhanced MRI shows a correlation with CT in the evaluation of emphysema, measurements of airflow obstruction and diffusion capacity using standard pulmonary function testing (Ohno et al. 2008). Without radiation and contrast agent, ventilation-weighted Fourier decomposition MRI can quantitatively measure regional lung ventilation (Bauman et al. 2009). Native and oxygen-enhanced T1 mapping showed correlation with lung perfusion deficits of dynamic contrast-enhanced perfusion MRI and severity of COPD (Jobst et al. 2015). Fractional volume using MRI is decreased with increasing GOLD stage and correlates with FEV_1, RV/TLC, and FEV_1/FVC in COPD patients (Kaireit et al. 2018a).

Scintigraphy and SPECT are also used for the evaluation of pulmonary ventilation. Two types of inhalation radiotracers, gaseous radioisotopes or radiolabeled particulate aerosols, are used for ventilation scintigraphy and SPECT. 81 m Kr and 133 Xe as gaseous radioisotopes have been used, and several studies using these gaseous radioisotopes have demonstrated ventilation heterogeneity in patients with COPD (Stavngaard et al. 2005; Suga et al. 1996). And with technegas (99 m Tc-labeled, aerosolized ultrafine carbon particle, approximately 200 nm diameter) as a radiolabeled particulate aerosol, the inhomogeneities in ventilation on scintigraphy and SPECT in COPD patients have been visualized and quantified (Cukic and Begic 2014; Xu et al. 2001).

3.3 Evaluation of Pulmonary Ventilation, Perfusion and Relationship of Ventilation and Perfusion

The pulmonary parenchymal ventilation and perfusion are concurrently changed, and an imbalance between pulmonary ventilation and perfusion is the important feature which results in arterial hypoxemia in the COPD patients. Using DECT technique, pulmonary parenchymal ventilation and perfusion status and ventilation–perfusion relationship can be assessed. Investigating 10 patients with various disease from an anesthesiological intensive care unit, Thieme et al. have reported the potential of DECT to provide both pulmonary ventilation and perfusion imaging (Thieme et al. 2010). Hwang et al. have applied combined pulmonary ventilation and perfusion imaging with DECT for

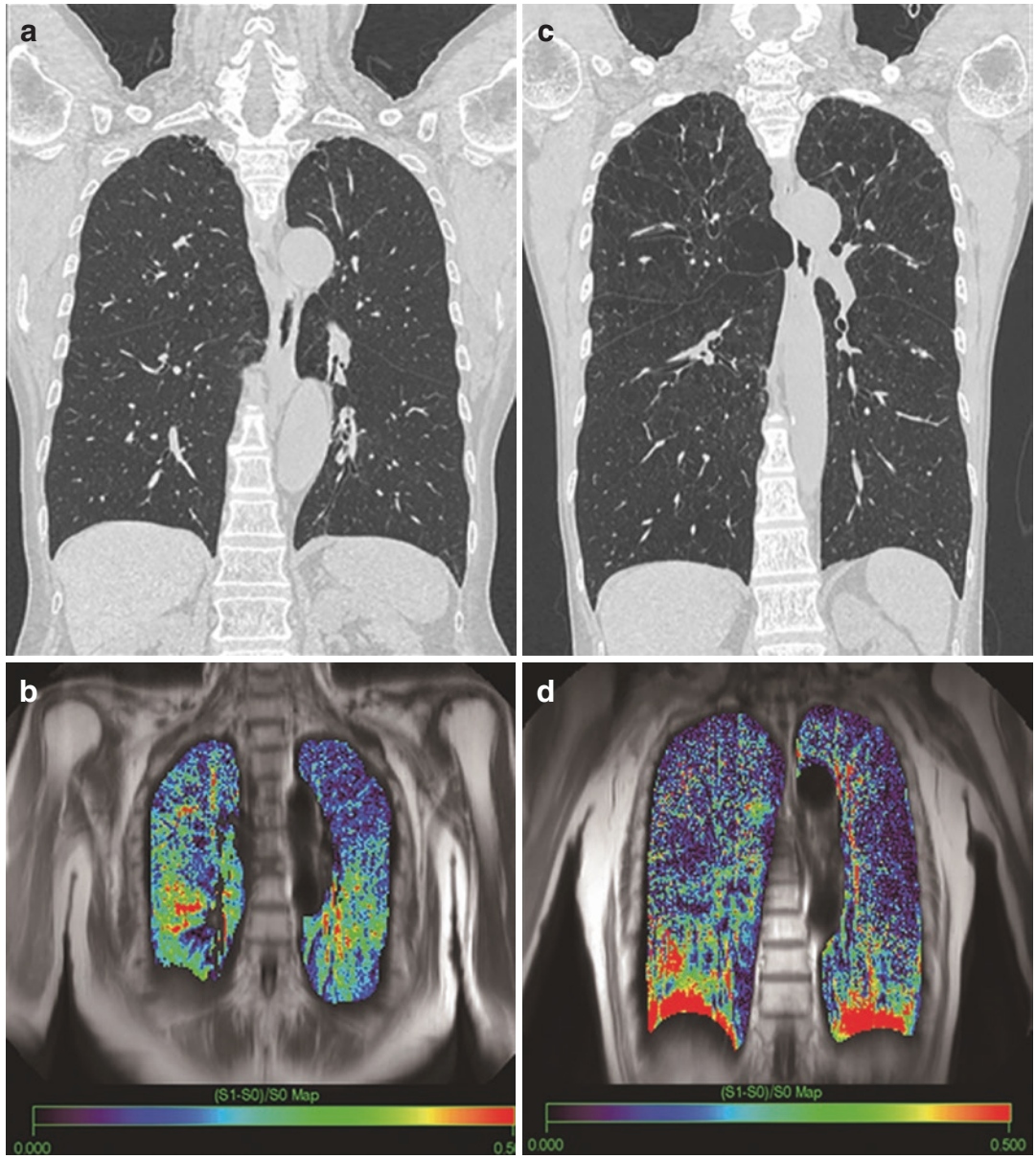


Fig. 9 (**a**, **b**) 75-year-old female smoker with mild COPD (**a**: thin-section coronal multiplanar reformatted (MPR) CT image shows centrilobular emphysema in the left upper lung field, **b**: relative enhancement (RER) map from oxygen O_2-enhanced MRI demonstrates heterogeneously decreased oxygen enhancement in both the lungs, especially left upper lung filed.) (**c**, **d**) 56-year-old female smoker with severe COPD (**c**: thin-section coronal MPR CT image demonstrates panlobular emphysema in bilateral upper and middle lung field. **d**: RER map from oxygen O_2-enhanced MRI demonstrates heterogeneously decreased oxygen enhancement in both the lungs, especially upper lung fields.) Image courtesy of Yoshiharu Ohno, Kobe University Graduate School of Medicine

comprehensive assessing of the regional ventilation, perfusion, and relationship of ventilation and perfusion in COPD (Hwang et al. 2016) (Fig. 10). The authors found that this image technique was useful for a visual assessment of regional ventilation, perfusion, and ventilation–perfusion relationships in addition to the evaluation of the morphologic parenchymal

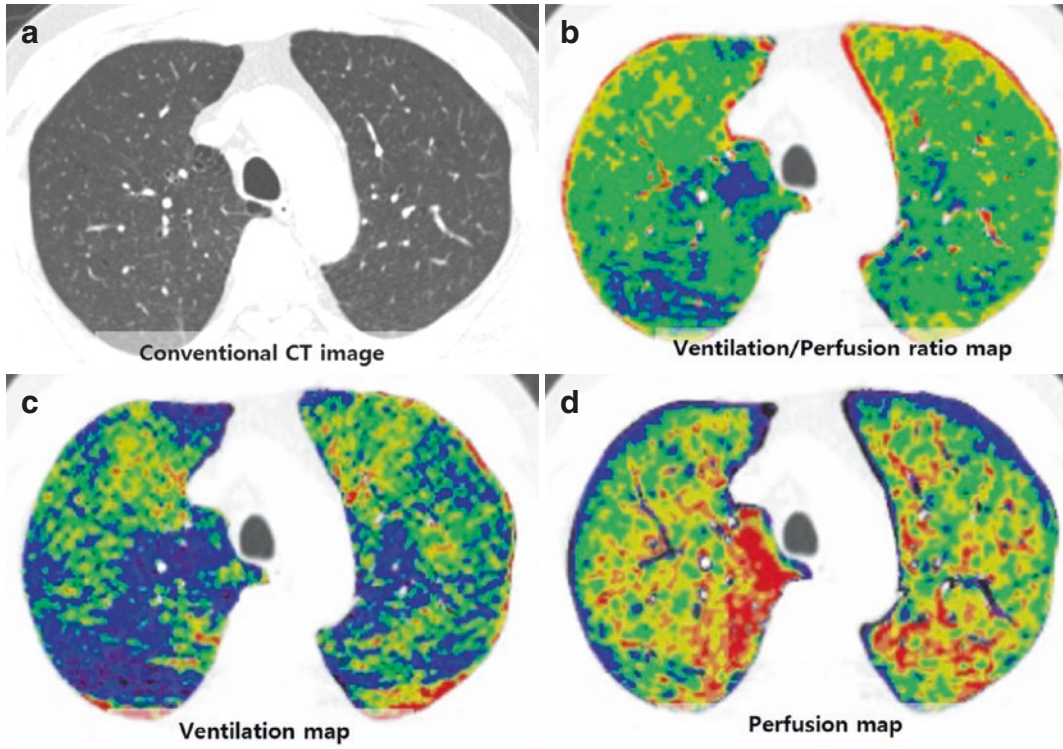


Fig. 10 Combined ventilation and perfusion DECT in a 63-year-old man with COPD. From combined xenon ventilation and iodine perfusion CT using DECT, (**a**) conventional CT image, (**b**) color-coded xenon ventilation/perfusion (pulmonary blood volume) map, (**c**) ventilation map, and (**d**) perfusion map are generated. Lung parenchymal ventilation, perfusion, and ventilation–perfusion imbalance with high-resolution anatomic CT information can be simultaneously evaluated with combined ventilation and perfusion DECT. (**a**) In upper lower lobes, although mild centrilobular emphysema with mild bronchial wall thickening is noted throughout the lung on conventional CT image, (**b**–**d**) variable ventilation and perfusion changes are evident. (**c**) Ventilation is decreased (blue color), while (**d**) perfusion is preserved (yellow and green color) in the posterior segment of the right upper lobe, (**b**) resulting in the mismatch of ventilation–perfusion relationship (blue color)

abnormalities in COPD patients. On visual analysis, in the normal appearing lung areas on conventional CT images, parenchymal perfusion and ventilation were usually preserved, resulting in a matched ventilation–perfusion relationship. However, in the areas of bronchial wall thickening, ventilation was frequently decreased while perfusion was preserved, resulting in a ventilation–perfusion mismatch (reversed mismatch). In areas with emphysema, there were no dominant ventilation or perfusion patterns. Furthermore, quantified CT parameters for ventilation, perfusion and ventilation–perfusion relationships in this combined DECT imaging are significantly correlated with PFT results. Using this combined DECT imaging, the functional and physiologic changes after bronchoscopic lung volume reduction COPD patients can be demonstrated. In a study with 30 COPD patients who underwent bronchoscopic lung volume reduction, DECT showed improved pulmonary ventilation and V/Q mismatch after bronchoscopic lung volume reduction (Lee et al. 2017).

Noncontrast-enhanced ventilation and perfusion MRI, known as Fourier decomposition MRI, uses a short echo dynamic SSFP acquisition with subsequent compensation for respiratory motion by using nonrigid image registration (Hermosillo et al. 2002; Bauman et al. 2009). Peaks at the respiratory and cardiac frequencies can be identified by spectral analysis of the image time series. Deformation of lung parenchyma and pulmonary

blood flow leads to regional proton density change, which is related to amplitude of these peaks (Suga et al. 2002). With image post-processing, ventilation- and perfusion-weighted maps are generated for regional assessment of lung function (Voskrebenzev et al. 2018).

The imbalance of ventilation and perfusion status also can be evaluated with ventilation/perfusion SPECT in the patients with COPD. Jogi et al. have demonstrated that the findings of ventilation/perfusion SPECT showed a significant correlation between spirometric lung function and emphysema severity on CT in patients with COPD (Jogi et al. 2011). Suga et al. have described that quantitative analysis of ventilation/perfusion distribution by SPECT was more sensitive for detecting emphysema compared with CT density mask on morphologic CT. And the standard deviation and kurtosis of the ventilation/perfusion profile could be an adequate indicator for the severity of ventilation–perfusion imbalance causing gas exchange impairment in patients with emphysema (Suga et al. 2008). Regional ventilation and perfusion also can be evaluated with positron emission tomography (PET) using isotope $^{13}N_2$ gas dissolved in saline solution. Brudin et al. have reported that high V/Q tended to be more common in the emphysema dominant subjects, whereas low V/Q was more common in the bronchial inflammation dominant subjects (Brudin et al. 1992). In previous study using $^{13}N_2$ saline PET, the regional heterogeneity in perfusion has been increased in patients with COPD compared to healthy controls, and Heterogeneity of ventilation–perfusion ratios was larger in COPD (Vidal Melo et al. 2010).

4 Future Perspectives

Although functional evaluation with CT or MRI in COPD patients has shown promising results in many studies, the present GOLD strategy does not recommend routine use of radiologic evaluation including CT or MRI scanning in COPD patients. This may be because of the relative lack of evidence that information collected from functional imaging can actually change the treatment plans, predict therapeutic response or prognosis, and ultimately alter the mortality of COPD patients. Numerous previous studies mostly have compared quantitative or functional image parameters with simple PFT results. However, it is important to prove the value of functional lung imaging through the studies on the prediction of therapeutic response or prognosis in COPD patients, and in recent years, studies on these issues using CT or MRI have been attempted (Loh et al. 2018; Han et al. 2011; Johannessen et al. 2013). However, still more studies will need to be performed to solidify the evidence regarding the value of functional imaging methods for improved prediction of treatment response and outcome assessment in COPD related to the alteration of lung function.

References

Akira M, Toyokawa K, Inoue Y, Arai T (2009) Quantitative CT in chronic obstructive pulmonary disease: inspiratory and expiratory assessment. AJR Am J Roentgenol 192(1):267–272. https://doi.org/10.2214/AJR.07.3953

Alford SK, van Beek EJ, McLennan G, Hoffman EA (2010) Heterogeneity of pulmonary perfusion as a mechanistic image-based phenotype in emphysema susceptible smokers. Proc Natl Acad Sci U S A 107(16):7485–7490. https://doi.org/10.1073/pnas.0913880107

Altes TA, Salerno M (2004) Hyperpolarized gas MR imaging of the lung. J Thorac Imaging 19(4):250–258

Argula RG, Strange C, Ramakrishnan V, Goldin J (2013) Baseline regional perfusion impacts exercise response to endobronchial valve therapy in advanced pulmonary emphysema. Chest 144(5):1578–1586. https://doi.org/10.1378/chest.12-2826

Barbera JA, Peinado VI, Santos S (2003) Pulmonary hypertension in chronic obstructive pulmonary disease. Eur Respir J 21(5):892–905

Barbera JA, Riverola A, Roca J, Ramirez J, Wagner PD, Ros D, Wiggs BR, Rodriguez-Roisin R (1994) Pulmonary vascular abnormalities and ventilation-perfusion relationships in mild chronic obstructive pulmonary disease. Am J Respir Crit Care Med 149(2 Pt 1):423–429. https://doi.org/10.1164/ajrccm.149.2.8306040

Barbera JA, Roca J, Ferrer A, Felez MA, Diaz O, Roger N, Rodriguez-Roisin R (1997) Mechanisms of worsening gas exchange during acute exacerbations of chronic obstructive pulmonary disease. Eur Respir J 10(6):1285–1291

Barr RG, Mesia-Vela S, Austin JH, Basner RC, Keller BM, Reeves AP, Shimbo D, Stevenson L (2007) Impaired flow-mediated dilation is associated with low pulmonary function and emphysema in ex-smokers: the Emphysema and Cancer Action Project (EMCAP) Study. Am J Respir Crit Care Med 176(12):1200–1207. https://doi.org/10.1164/rccm.200707-980OC

Bauman G, Eichinger M (2012) Ventilation and perfusion magnetic resonance imaging of the lung. Polish J Radiol 77(1):37–46

Bauman G, Puderbach M, Deimling M, Jellus V, Chefd'hotel C, Dinkel J, Hintze C, Kauczor HU, Schad LR (2009) Non-contrast-enhanced perfusion and ventilation assessment of the human lung by means of fourier decomposition in proton MRI. Magn Reson Med 62(3):656–664. https://doi.org/10.1002/mrm.22031

Beckmann N, Cannet C, Zurbruegg S, Rudin M, Tigani B (2004) Proton MRI of lung parenchyma reflects allergen-induced airway remodeling and endotoxin-aroused hyporesponsiveness: a step toward ventilation studies in spontaneously breathing rats. Magn Reson Med 52(2):258–268. https://doi.org/10.1002/mrm.20127

Bhatt SP, Terry NL, Nath H, Zach JA, Tschirren J, Bolding MS, Stinson DS, Wilson CG, Curran-Everett D, Lynch DA, Putcha N, Soler X, Wise RA, Washko GR, Hoffman EA, Foreman MG, Dransfield MT (2016) Genetic epidemiology of CI association between expiratory central airway collapse and respiratory outcomes among smokers. JAMA 315(5):498–505. https://doi.org/10.1001/jama.2015.19431

Biederer J, Both M, Graessner J, Liess C, Jakob P, Reuter M, Heller M (2003) Lung morphology: fast MR imaging assessment with a volumetric interpolated breath-hold technique: initial experience with patients. Radiology 226(1):242–249. https://doi.org/10.1148/radiol.2261011974

Bon JM, Leader JK, Weissfeld JL, Coxson HO, Zheng B, Branch RA, Kondragunta V, Lee JS, Zhang Y, Choi AM, Lokshin AE, Kaminski N, Gur D, Sciurba FC (2009) The influence of radiographic phenotype and smoking status on peripheral blood biomarker patterns in chronic obstructive pulmonary disease. PLoS One 4(8):e6865. https://doi.org/10.1371/journal.pone.0006865

Brudin LH, Rhodes CG, Valind SO, Buckingham PD, Jones T, Hughes JM (1992) Regional structure-function correlations in chronic obstructive lung disease measured with positron emission tomography. Thorax 47(11):914–921

Bryant M, Ley S, Eberhardt R, Menezes R, Herth F, Sedlaczek O, Kauczor HU, Ley-Zaporozhan J (2015) Assessment of the relationship between morphological emphysema phenotype and corresponding pulmonary perfusion pattern on a segmental level. Eur Radiol 25(1):72–80. https://doi.org/10.1007/s00330-014-3385-5

Chae EJ, Seo JB, Goo HW, Kim N, Song KS, Lee SD, Hong SJ, Krauss B (2008) Xenon ventilation CT with a dual-energy technique of dual-source CT: initial experience. Radiology 248(2):615–624. https://doi.org/10.1148/radiol.2482071482

Chae EJ, Seo JB, Oh YM, Lee JS, Jung Y, Lee SD (2013) Severity of systemic calcified atherosclerosis is associated with airflow limitation and emphysema. J Comput Assist Tomogr 37(5):743–749. https://doi.org/10.1097/RCT.0b013e318299f9e7

Chandra D, Lipson DA, Hoffman EA, Hansen-Flaschen J, Sciurba FC, Decamp MM, Reilly JJ, Washko GR, National Emphysema Treatment Trial Research G (2010) Perfusion scintigraphy and patient selection for lung volume reduction surgery. Am J Respir Crit Care Med 182(7):937–946. https://doi.org/10.1164/rccm.201001-0043OC

Cho YH, Seo JB, Kim N, Lee HJ, Hwang HJ, Kim EY, Oh SY (2015) Comparison of a new integral-based half-band method for CT measurement of peripheral airways in COPD with a conventional full-width half-maximum method using both phantom and clinical CT images. J Comput Assist Tomogr 39(3):428–436. https://doi.org/10.1097/RCT.0000000000000218

Cukic V, Begic A (2014) Potential role of lung ventilation scintigraphy in the assessment of COPD. Acta Informatica Med 22(3):170–173. https://doi.org/10.5455/aim.2014.22.170-173

de Lange EE, Altes TA, Patrie JT, Gaare JD, Knake JJ, Mugler JP 3rd, Platts-Mills TA (2006) Evaluation of asthma with hyperpolarized helium-3 MRI: correlation with clinical severity and spirometry. Chest 130(4):1055–1062. https://doi.org/10.1378/chest.130.4.1055

Diaz AA, Valim C, Yamashiro T, Estepar RS, Ross JC, Matsuoka S, Bartholmai B, Hatabu H, Silverman EK, Washko GR (2010) Airway count and emphysema assessed by chest CT imaging predicts clinical outcome in smokers. Chest 138(4):880–887. https://doi.org/10.1378/chest.10-0542

Dirksen A (2008) Monitoring the progress of emphysema by repeat computed tomography scans with focus on noise reduction. Proc Am Thorac Soc 5(9):925–928. https://doi.org/10.1513/pats.200804-033QC

Dransfield MT, Washko GR, Foreman MG, Estepar RS, Reilly J, Bailey WC (2007) Gender differences in the severity of CT emphysema in COPD. Chest 132(2):464–470. https://doi.org/10.1378/chest.07-0863

Estepar RS, Kinney GL, Black-Shinn JL, Bowler RP, Kindlmann GL, Ross JC, Kikinis R, Han MK, Come CE, Diaz AA, Cho MH, Hersh CP, Schroeder JD, Reilly JJ, Lynch DA, Crapo JD, Wells JM, Dransfield MT, Hokanson JE, Washko GR, Study CO (2013) Computed tomographic measures of pulmonary vascular morphology in smokers and their clinical implications. Am J Respir Crit Care Med 188(2):231–239. https://doi.org/10.1164/rccm.201301-0162OC

Etlik O, Sakarya ME, Uzun K, Harman M, Temizoz O, Durmus A (2004) Demonstrating the effect of theophylline treatment on diaphragmatic movement in chronic obstructive pulmonary disease patients by

MR-fluoroscopy. Eur J Radiol 51(2):150–154. https://doi.org/10.1016/S0720-048X(03)00210-9

Fuseya Y, Muro S, Sato S, Tanabe N, Sato A, Tanimura K, Hasegawa K, Uemasu K, Kubo T, Kido A, Fujimoto K, Fushimi Y, Kusahara H, Sakashita N, Ohno Y, Togashi K, Mishima M, Hirai T (2018) Complementary regional heterogeneity information from COPD patients obtained using oxygen-enhanced MRI and chest CT. PLoS One 13(8):e0203273. https://doi.org/10.1371/journal.pone.0203273

Galban CJ, Han MK, Boes JL, Chughtai KA, Meyer CR, Johnson TD, Galban S, Rehemtulla A, Kazerooni EA, Martinez FJ, Ross BD (2012) Computed tomography-based biomarker provides unique signature for diagnosis of COPD phenotypes and disease progression. Nat Med 18(11):1711–1715. https://doi.org/10.1038/nm.2971

Gevenois PA, de Maertelaer V, De Vuyst P, Zanen J, Yernault JC (1995) Comparison of computed density and macroscopic morphometry in pulmonary emphysema. Am J Respir Crit Care Med 152:653–657

Gevenois PA, De Vuyst P, de Maertelaer V, Zanen J, Jacobovitz D, Cosio MG, Yernault JC (1996) Comparison of computed density and microscopic morphometry in pulmonary emphysema. Am J Respir Crit Care Med 154(1):187–192. https://doi.org/10.1164/ajrccm.154.1.8680679

Grydeland TB, Dirksen A, Coxson HO, Pillai SG, Sharma S, Eide GE, Gulsvik A, Bakke PS (2009) Quantitative computed tomography: emphysema and airway wall thickness by sex, age and smoking. Eur Respir J 34(4):858–865. https://doi.org/10.1183/09031936.00167908

Gur D, Drayer BP, Borovetz HS, Griffith BP, Hardesty RL, Wolfson SK (1979) Dynamic computed tomography of the lung: regional ventilation measurements. J Comput Assist Tomogr 3(6):749–753

Hachulla AL, Pontana F, Wemeau-Stervinou L, Khung S, Faivre JB, Wallaert B, Cazaubon JF, Duhamel A, Perez T, Devos P, Remy J, Remy-Jardin M (2012) Krypton ventilation imaging using dual-energy CT in chronic obstructive pulmonary disease patients: initial experience. Radiology 263(1):253–259. https://doi.org/10.1148/radiol.12111211

Hale KA, Niewoehner DE, Cosio MG (1980) Morphologic changes in the muscular pulmonary arteries: relationship to cigarette smoking, airway disease, and emphysema. Am Rev Respir Dis 122(2):273–278. https://doi.org/10.1164/arrd.1980.122.2.273

Han MK, Kazerooni EA, Lynch DA, Liu LX, Murray S, Curtis JL, Criner GJ, Kim V, Bowler RP, Hanania NA, Anzueto AR, Make BJ, Hokanson JE, Crapo JD, Silverman EK, Martinez FJ, Washko GR, Investigators CO (2011) Chronic obstructive pulmonary disease exacerbations in the COPDGene study: associated radiologic phenotypes. Radiology 261(1):274–282. https://doi.org/10.1148/radiol.11110173

Harrison RA, Siminoski K, Vethanayagam D, Majumdar SR (2007) Osteoporosis-related kyphosis and impairments in pulmonary function: a systematic review. J Bone Miner Res 22(3):447–457. https://doi.org/10.1359/jbmr.061202

Haruna A, Muro S, Nakano Y, Ohara T, Hoshino Y, Ogawa E, Hirai T, Niimi A, Nishimura K, Chin K, Mishima M (2010) CT scan findings of emphysema predict mortality in COPD. Chest 138(3):635–640. https://doi.org/10.1378/chest.09-2836

Hasegawa M, Nasuhara Y, Onodera Y, Makita H, Nagai K, Fuke S, Ito Y, Betsuyaku T, Nishimura M (2006) Airflow limitation and airway dimensions in chronic obstructive pulmonary disease. Am J Respir Crit Care Med 173(12):1309–1315. https://doi.org/10.1164/rccm.200601-037OC

Hayhurst MD, MacNee W, Flenley DC, Wright D, McLean A, Lamb D, Wightman AJ, Best J (1984) Diagnosis of pulmonary emphysema by computerised tomography. Lancet 2(8398):320–322

Herbert DL, Gur D, Shabason L, Good WF, Rinaldo JE, Snyder JV, Borovetz HS, Mancici MC (1982) Mapping of human local pulmonary ventilation by xenon enhanced computed tomography. J Comput Assist Tomogr 6(6):1088–1093

Hermosillo G, Chefd'Hotel C, Faugeras O (2002) Variational methods for multimodal image matching. Int J Comput Vision 50(3):329–343. https://doi.org/10.1023/A:1020830525823

Hesselbacher SE, Ross R, Schabath MB, Smith EO, Perusich S, Barrow N, Smithwick P, Mammen MJ, Coxson H, Krowchuk N, Corry DB, Kheradmand F (2011) Cross-sectional analysis of the utility of pulmonary function tests in predicting emphysema in ever-smokers. Int J Environ Res Public Health 8(5):1324–1340. https://doi.org/10.3390/ijerph8051324

Heussel CP, Herth FJ, Kappes J, Hantusch R, Hartlieb S, Weinheimer O, Kauczor HU, Eberhardt R (2009) Fully automatic quantitative assessment of emphysema in computed tomography: comparison with pulmonary function testing and normal values. Eur Radiol 19(10):2391–2402. https://doi.org/10.1007/s00330-009-1437-z

Hogg JC, Chu F, Utokaparch S, Woods R, Elliott WM, Buzatu L, Cherniack RM, Rogers RM, Sciurba FC, Coxson HO, Pare PD (2004) The nature of small-airway obstruction in chronic obstructive pulmonary disease. N Engl J Med 350(26):2645–2653. https://doi.org/10.1056/NEJMoa032158

Hogg JC, Macklem PT, Thurlbeck WM (1968) Site and nature of airway obstruction in chronic obstructive lung disease. N Engl J Med 278(25):1355–1360. https://doi.org/10.1056/NEJM196806202782501

Honda N, Osada H, Watanabe W, Nakayama M, Nishimura K, Krauss B, Otani K (2012) Imaging of ventilation with dual-energy CT during breath hold after single vital-capacity inspiration of stable xenon. Radiology 262(1):262–268. https://doi.org/10.1148/radiol.11110569

Hwang HJ, Seo JB, Lee SM, Kim N, Oh SY, Lee JS, Lee SW, Oh YM (2016) Assessment of regional xenon ventilation, perfusion, and ventilation-perfusion

mismatch using dual-energy computed tomography in chronic obstructive pulmonary disease patients. Investig Radiol 51(5):306–315. https://doi.org/10.1097/RLI.0000000000000239

Iwasawa T, Takahashi H, Ogura T, Asakura A, Gotoh T, Shibata H, Inoue T (2011) Influence of the distribution of emphysema on diaphragmatic motion in patients with chronic obstructive pulmonary disease. Jpn J Radiol 29(4):256–264. https://doi.org/10.1007/s11604-010-0552-8

Iwasawa T, Yoshiike Y, Saito K, Kagei S, Gotoh T, Matsubara S (2000) Paradoxical motion of the hemidiaphragm in patients with emphysema. J Thorac Imaging 15(3):191–195

Jang YM, Oh YM, Seo JB, Kim N, Chae EJ, Lee YK, Lee SD (2008) Quantitatively assessed dynamic contrast-enhanced magnetic resonance imaging in patients with chronic obstructive pulmonary disease: correlation of perfusion parameters with pulmonary function test and quantitative computed tomography. Investig Radiol 43(6):403–410. https://doi.org/10.1097/RLI.0b013e31816901ab

Jobst BJ, Triphan SM, Sedlaczek O, Anjorin A, Kauczor HU, Biederer J, Ley-Zaporozhan J, Ley S, Wielputz MO (2015) Functional lung MRI in chronic obstructive pulmonary disease: comparison of T1 mapping, oxygen-enhanced T1 mapping and dynamic contrast enhanced perfusion. PLoS One 10(3):e0121520. https://doi.org/10.1371/journal.pone.0121520

Jogi J, Ekberg M, Jonson B, Bozovic G, Bajc M (2011) Ventilation/perfusion SPECT in chronic obstructive pulmonary disease: an evaluation by reference to symptoms, spirometric lung function and emphysema, as assessed with HRCT. Eur J Nucl Med Mol Imaging 38(7):1344–1352. https://doi.org/10.1007/s00259-011-1757-5

Johannessen A, Skorge TD, Bottai M, Grydeland TB, Nilsen RM, Coxson H, Dirksen A, Omenaas E, Gulsvik A, Bakke P (2013) Mortality by level of emphysema and airway wall thickness. Am J Respir Crit Care Med 187(6):602–608. https://doi.org/10.1164/rccm.201209-1722OC

Kaireit TF, Gutberlet M, Voskrebenzev A, Freise J, Welte T, Hohlfeld JM, Wacker F, Vogel-Claussen J (2018a) Comparison of quantitative regional ventilation-weighted fourier decomposition MRI with dynamic fluorinated gas washout MRI and lung function testing in COPD patients. J Magn Reson Imaging 47(6):1534–1541. https://doi.org/10.1002/jmri.25902

Kaireit TF, Voskrebenzev A, Gutberlet M, Freise J, Jobst B, Kauczor HU, Welte T, Wacker F, Vogel-Claussen J (2018b) Comparison of quantitative regional perfusion-weighted phase resolved functional lung (PREFUL) MRI with dynamic gadolinium-enhanced regional pulmonary perfusion MRI in COPD patients. J Magn Reson Imaging. https://doi.org/10.1002/jmri.26342

Kaushik SS, Cleveland ZI, Cofer GP, Metz G, Beaver D, Nouls J, Kraft M, Auffermann W, Wolber J, McAdams HP, Driehuys B (2011) Diffusion-weighted hyperpolarized ^{129}Xe MRI in healthy volunteers and subjects with chronic obstructive pulmonary disease. Magn Reson Med 65(4):1154–1165. https://doi.org/10.1002/mrm.22697

Kim EY, Seo JB, Lee HJ, Kim N, Lee E, Lee SM, Oh SY, Hwang HJ, Oh YM, Lee SD (2015) Detailed analysis of the density change on chest CT of COPD using non-rigid registration of inspiration/expiration CT scans. Eur Radiol 25(2):541–549. https://doi.org/10.1007/s00330-014-3418-0

Kim N, Seo JB, Song KS, Chae EJ, Kang SH (2008) Semi-automatic measurement of the airway dimension by computed tomography using the full-with-half-maximum method: a study of the measurement accuracy according to the orientation of an artificial airway. Korean J Radiol 9(3):236–242. https://doi.org/10.3348/kjr.2008.9.3.236

Kirby M, Mathew L, Wheatley A, Santyr GE, McCormack DG, Parraga G (2010) Chronic obstructive pulmonary disease: longitudinal hyperpolarized (3)He MR imaging. Radiology 256(1):280–289. https://doi.org/10.1148/radiol.10091937

Kirby M, Svenningsen S, Owrangi A, Wheatley A, Farag A, Ouriadov A, Santyr GE, Etemad-Rezai R, Coxson HO, McCormack DG, Parraga G (2012) Hyperpolarized ^{3}He and ^{129}Xe MR imaging in healthy volunteers and patients with chronic obstructive pulmonary disease. Radiology 265(2):600–610. https://doi.org/10.1148/radiol.12120485

Kirby M, Tanabe N, Tan WC, Zhou G, Obeidat M, Hague CJ, Leipsic J, Bourbeau J, Sin DD, Hogg JC, Coxson HO, Can CCRG, Canadian Respiratory Research N, CanCold Collaborative Research Group tCRRN (2018) Total airway count on computed tomography and the risk of chronic obstructive pulmonary disease progression. Findings from a population-based study. Am J Respir Crit Care Med 197(1):56–65. https://doi.org/10.1164/rccm.201704-0692OC

Kiyokawa H, Muro S, Oguma T, Sato S, Tanabe N, Takahashi T, Kudo M, Kinose D, Kondoh H, Kubo T, Hoshino Y, Ogawa E, Hirai T, Mishima M (2012) Impact of COPD exacerbations on osteoporosis assessed by chest CT scan. COPD 9(3):235–242. https://doi.org/10.3109/15412555.2011.650243

Lee CW, Seo JB, Lee Y, Chae EJ, Kim N, Lee HJ, Hwang HJ, Lim CH (2012) A pilot trial on pulmonary emphysema quantification and perfusion mapping in a single-step using contrast-enhanced dual-energy computed tomography. Investig Radiol 47(1):92–97. https://doi.org/10.1097/RLI.0b013e318228359a

Lee SM, Seo JB, Lee SM, Kim N, Oh SY, Oh YM (2016) Optimal threshold of subtraction method for quantification of air-trapping on coregistered CT in COPD patients. Eur Radiol 26(7):2184–2192. https://doi.org/10.1007/s00330-015-4070-z

Lee SW, Lee SM, Shin SY, Park TS, Oh SY, Kim N, Hong Y, Lee JS, Oh YM, Lee SD, Seo JB (2017) Improvement in ventilation-perfusion mismatch after bronchoscopic lung volume reduction: quantitative

image analysis. Radiology 285(1):250–260. https://doi.org/10.1148/radiol.2017162148

Lee YK, Oh YM, Lee JH, Kim EK, Lee JH, Kim N, Seo JB, Lee SD, Group KS (2008) Quantitative assessment of emphysema, air trapping, and airway thickening on computed tomography. Lung 186(3):157–165. https://doi.org/10.1007/s00408-008-9071-0

Lehouck A, Boonen S, Decramer M, Janssens W (2011) COPD, bone metabolism, and osteoporosis. Chest 139(3):648–657. https://doi.org/10.1378/chest.10-1427

Leutz-Schmidt P, Stahl M, Sommerburg O, Eichinger M, Puderbach MU, Schenk JP, Alrajab A, Triphan SMF, Kauczor HU, Mall MA, Wielputz MO (2018) Non-contrast enhanced magnetic resonance imaging detects mosaic signal intensity in early cystic fibrosis lung disease. Eur J Radiol 101:178–183. https://doi.org/10.1016/j.ejrad.2018.02.023

Ley-Zaporozhan J, Ley S, Eberhardt R, Kauczor HU, Heussel CP (2010) Visualization of morphological parenchymal changes in emphysema: comparison of different MRI sequences to 3D-HRCT. Eur J Radiol 73(1):43–49. https://doi.org/10.1016/j.ejrad.2008.09.029

Ley-Zaporozhan J, Ley S, Eberhardt R, Weinheimer O, Fink C, Puderbach M, Eichinger M, Herth F, Kauczor HU (2007a) Assessment of the relationship between lung parenchymal destruction and impaired pulmonary perfusion on a lobar level in patients with emphysema. Eur J Radiol 63(1):76–83. https://doi.org/10.1016/j.ejrad.2007.01.020

Ley-Zaporozhan J, Ley S, Kauczor HU (2007b) Proton MRI in COPD. COPD 4(1):55–65. https://doi.org/10.1080/15412550701198719

Ley-Zaporozhan J, Ley S, Kauczor HU (2008) Morphological and functional imaging in COPD with CT and MRI: present and future. Eur Radiol 18(3):510–521. https://doi.org/10.1007/s00330-007-0772-1

Liu CY, Parikh M, Bluemke DA, Balte P, Carr J, Dashnaw S, Poor HD, Gomes AS, Hoffman EA, Kawut SM, Lima JAC, McAllister DA, Prince MA, Vogel-Claussen J, Barr RG (2018) Pulmonary artery stiffness in chronic obstructive pulmonary disease (COPD) and emphysema: The Multi-Ethnic Study of Atherosclerosis (MESA) COPD Study. J Magn Reson Imaging 47(1):262–271. https://doi.org/10.1002/jmri.25753

Loh LC, Ong CK, Koo HJ, Lee SM, Lee JS, Oh YM, Seo JB, Lee SD (2018) A novel CT-emphysema index/FEV1 approach of phenotyping COPD to predict mortality. Int J Chron Obstruct Pulmon Dis 13:2543–2550. https://doi.org/10.2147/COPD.S165898

Maclay JD, McAllister DA, Mills NL, Paterson FP, Ludlam CA, Drost EM, Newby DE, Macnee W (2009) Vascular dysfunction in chronic obstructive pulmonary disease. Am J Respir Crit Care Med 180(6):513–520. https://doi.org/10.1164/rccm.200903-0414OC

Madani A, Van Muylem A, de Maertelaer V, Zanen J, Gevenois PA (2008) Pulmonary emphysema: size distribution of emphysematous spaces on multidetector CT images--comparison with macroscopic and microscopic morphometry. Radiology 248(3):1036–1041. https://doi.org/10.1148/radiol.2483071434

Madani A, Zanen J, de Maertelaer V, Gevenois PA (2006) Pulmonary emphysema: objective quantification at multi-detector row CT–comparison with macroscopic and microscopic morphometry. Radiology 238:1036–1043

Matsuoka S, Kurihara Y, Yagihashi K, Hoshino M, Nakajima Y (2008a) Airway dimensions at inspiratory and expiratory multisection CT in chronic obstructive pulmonary disease: correlation with airflow limitation. Radiology 248(3):1042–1049. https://doi.org/10.1148/radiol.2491071650

Matsuoka S, Kurihara Y, Yagihashi K, Hoshino M, Watanabe N, Nakajima Y (2008b) Quantitative assessment of air trapping in chronic obstructive pulmonary disease using inspiratory and expiratory volumetric MDCT. AJR Am J Roentgenol 190(3):762–769. https://doi.org/10.2214/AJR.07.2820

Matsuoka S, Kurihara Y, Yagihashi K, Nakajima Y (2007) Quantitative assessment of peripheral airway obstruction on paired expiratory/inspiratory thin-section computed tomography in chronic obstructive pulmonary disease with emphysema. J Comput Assist Tomogr 31(3):384–389. https://doi.org/10.1097/01.rct.0000243457.00437.10

Matsuoka S, Washko GR, Dransfield MT, Yamashiro T, San Jose Estepar R, Diaz A, Silverman EK, Patz S, Hatabu H (2010) Quantitative CT measurement of cross-sectional area of small pulmonary vessel in COPD: correlations with emphysema and airflow limitation. Acad Radiol 17(1):93–99. https://doi.org/10.1016/j.acra.2009.07.022

Mayo JR, MacKay A, Muller NL (1992) MR imaging of the lungs: value of short TE spin-echo pulse sequences. AJR Am J Roentgenol 159(5):951–956. https://doi.org/10.2214/ajr.159.5.1414805

McAllister DA, Maclay JD, Mills NL, Mair G, Miller J, Anderson D, Newby DE, Murchison JT, Macnee W (2007) Arterial stiffness is independently associated with emphysema severity in patients with chronic obstructive pulmonary disease. Am J Respir Crit Care Med 176(12):1208–1214. https://doi.org/10.1164/rccm.200707-1080OC

McDonough JE, Yuan R, Suzuki M, Seyednejad N, Elliott WM, Sanchez PG, Wright AC, Gefter WB, Litzky L, Coxson HO, Pare PD, Sin DD, Pierce RA, Woods JC, McWilliams AM, Mayo JR, Lam SC, Cooper JD, Hogg JC (2011) Small-airway obstruction and emphysema in chronic obstructive pulmonary disease. N Engl J Med 365(17):1567–1575. https://doi.org/10.1056/NEJMoa1106955

Mead J, Turner JM, Macklem PT, Little JB (1967) Significance of the relationship between lung recoil and maximum expiratory flow. J Appl Physiol 22(1):95–108. https://doi.org/10.1152/jappl.1967.22.1.95

Meier-Schroers M, Sprinkart AM, Becker M, Homsi R, Thomas D (2018) Quantitative and qualitative assessment of pulmonary emphysema with

T2-weighted PROPELLER MRI in a high-risk population compared to low-dose CT. Rofo 190(8):733–739. https://doi.org/10.1055/a-0577-5619

Meinel FG, Graef A, Thieme SF, Bamberg F, Schwarz F, Sommer WH, Helck AD, Neurohr C, Reiser MF, Johnson TR (2013) Assessing pulmonary perfusion in emphysema: automated quantification of perfused blood volume in dual-energy CTPA. Investig Radiol 48(2):79–85. https://doi.org/10.1097/RLI.0b013e3182778f07

Mishima M, Hirai T, Itoh H, Nakano Y, Sakai H, Muro S, Nishimura K, Oku Y, Chin K, Ohi M, Nakamura T, Bates JH, Alencar AM, Suki B (1999) Complexity of terminal airspace geometry assessed by lung computed tomography in normal subjects and patients with chronic obstructive pulmonary disease. Proc Natl Acad Sci U S A 96(16): 8829–8834

Mohamed Hoesein FA, de Hoop B, Zanen P, Gietema H, Kruitwagen CL, van Ginneken B, Isgum I, Mol C, van Klaveren RJ, Dijkstra AE, Groen HJ, Boezen HM, Postma DS, Prokop M, Lammers JW (2011) CT-quantified emphysema in male heavy smokers: association with lung function decline. Thorax 66(9):782–787. https://doi.org/10.1136/thx.2010.145995

Molinari F, Fink C, Risse F, Tuengerthal S, Bonomo L, Kauczor HU (2006) Assessment of differential pulmonary blood flow using perfusion magnetic resonance imaging: comparison with radionuclide perfusion scintigraphy. Investig Radiol 41(8):624–630. https://doi.org/10.1097/01.rli.0000225399.65609.45

Morino S, Toba T, Araki M, Azuma T, Tsutsumi S, Tao H, Nakamura T, Nagayasu T, Tagawa T (2006) Noninvasive assessment of pulmonary emphysema using dynamic contrast-enhanced magnetic resonance imaging. Exp Lung Res 32(1–2):55–67. https://doi.org/10.1080/01902140600691548

Muller NL, Staples CA, Miller RR, Abboud RT (1988) "Density mask". An objective method to quantitate emphysema using computed tomography. Chest 94(4):782–787

Murphy K, Pluim JP, van Rikxoort EM, de Jong PA, de Hoop B, Gietema HA, Mets O, de Bruijne M, Lo P, Prokop M, van Ginneken B (2012) Toward automatic regional analysis of pulmonary function using inspiration and expiration thoracic CT. Med Phys 39(3):1650–1662. https://doi.org/10.1118/1.3687891

Nakano Y, Sakai H, Muro S, Hirai T, Oku Y, Nishimura K, Mishima M (1999) Comparison of low attenuation areas on computed tomographic scans between inner and outer segments of the lung in patients with chronic obstructive pulmonary disease: incidence and contribution to lung function. Thorax 54(5): 384–389

Nakano Y, Wong JC, de Jong PA, Buzatu L, Nagao T, Coxson HO, Elliott WM, Hogg JC, Pare PD (2005) The prediction of small airway dimensions using computed tomography. Am J Respir Crit Care Med 171(2):142–146. https://doi.org/10.1164/rccm.200407-874OC

Newell JD Jr, Hogg JC, Snider GL (2004) Report of a workshop: quantitative computed tomography scanning in longitudinal studies of emphysema. Eur Respir J 23(5):769–775

Noma S, Moskowitz GW, Herman PG, Khan A, Rojas KA (1992) Pulmonary scintigraphy in elastase-induced emphysema in pigs. Correlation with high-resolution computed tomography and histology. Investig Radiol 27(6):429–435

Oh SY, Lee M, Seo JB, Kim N, Lee SM, Lee JS, Oh YM (2017) Size variation and collapse of emphysema holes at inspiration and expiration CT scan: evaluation with modified length scale method and image co-registration. Int J Chron Obstruct Pulmon Dis 12:2043–2057. https://doi.org/10.2147/COPD.S130081

Oh YM, Sheen SS, Park JH, Jin UR, Yoo JW, Seo JB, Yoo KH, Lee JH, Kim TH, Lim SY, Yoon HI, Lee JS, Lee SD (2014) Emphysematous phenotype is an independent predictor for frequent exacerbation of COPD. Int J Tuberc Lung Dis 18(12):1407–1414. https://doi.org/10.5588/ijtld.14.0205

Ohara T, Hirai T, Muro S, Haruna A, Terada K, Kinose D, Marumo S, Ogawa E, Hoshino Y, Niimi A, Chin K, Mishima M (2008) Relationship between pulmonary emphysema and osteoporosis assessed by CT in patients with COPD. Chest 134(6):1244–1249. https://doi.org/10.1378/chest.07-3054

Ohno Y, Hatabu H, Murase K, Higashino T, Kawamitsu H, Watanabe H, Takenaka D, Fujii M, Sugimura K (2004) Quantitative assessment of regional pulmonary perfusion in the entire lung using three-dimensional ultrafast dynamic contrast-enhanced magnetic resonance imaging: preliminary experience in 40 subjects. J Magn Reson Imaging 20(3):353–365. https://doi.org/10.1002/jmri.20137

Ohno Y, Hatabu H, Takenaka D, Adachi S, Van Cauteren M, Sugimura K (2001) Oxygen-enhanced MR ventilation imaging of the lung: preliminary clinical experience in 25 subjects. AJR Am J Roentgenol 177(1): 185–194. https://doi.org/10.2214/ajr.177.1.1770185

Ohno Y, Hatabu H, Takenaka D, Van Cauteren M, Fujii M, Sugimura K (2002) Dynamic oxygen-enhanced MRI reflects diffusing capacity of the lung. Magn Reson Med 47(6):1139–1144. https://doi.org/10.1002/mrm.10168

Ohno Y, Iwasawa T, Seo JB, Koyama H, Takahashi H, Oh YM, Nishimura Y, Sugimura K (2008) Oxygen-enhanced magnetic resonance imaging versus computed tomography: multicenter study for clinical stage classification of smoking-related chronic obstructive pulmonary disease. Am J Respir Crit Care Med 177(10):1095–1102. https://doi.org/10.1164/rccm.200709-1322OC

Ohno Y, Koyama H, Yoshikawa T, Matsumoto K, Aoyama N, Onishi Y, Takenaka D, Matsumoto S, Nishimura Y, Sugimura K (2012) Comparison of capability of dynamic O(2)-enhanced MRI and quantitative thin-section MDCT to assess COPD in smokers. Eur J Radiol 81(5):1068–1075. https://doi.org/10.1016/j.ejrad.2011.02.004

Ohno Y, Koyama H, Yoshikawa T, Matsumoto K, Takahashi M, Van Cauteren M, Sugimura K (2011) T2* measurements of 3-T MRI with ultrashort TEs: capabilities of pulmonary function assessment and clinical stage classification in smokers. AJR Am J Roentgenol 197(2):W279–W285. https://doi.org/10.2214/AJR.10.5350

Ohno Y, Yoshikawa T, Takenaka D, Fujisawa Y, Sugihara N, Kishida Y, Seki S, Koyama H, Sugimura K (2017) Xenon-enhanced CT using subtraction CT: basic and preliminary clinical studies for comparison of its efficacy with that of dual-energy CT and ventilation SPECT/CT to assess regional ventilation and pulmonary functional loss in smokers. Eur J Radiol 86:41–51. https://doi.org/10.1016/j.ejrad.2016.10.035

Pansini V, Remy-Jardin M, Faivre JB, Schmidt B, Dejardin-Bothelo A, Perez T, Delannoy V, Duhamel A, Remy J (2009) Assessment of lobar perfusion in smokers according to the presence and severity of emphysema: preliminary experience with dual-energy CT angiography. Eur Radiol 19(12):2834–2843. https://doi.org/10.1007/s00330-009-1475-6

Park EA, Goo JM, Park SJ, Lee HJ, Lee CH, Park CM, Yoo CG, Kim JH (2010) Chronic obstructive pulmonary disease: quantitative and visual ventilation pattern analysis at xenon ventilation CT performed by using a dual-energy technique. Radiology 256(3):985–997. https://doi.org/10.1148/radiol.10091502

Park MJ, Cho JM, Jeon KN, Bae KS, Kim HC, Choi DS, Na JB, Choi HC, Choi HY, Kim JE, Shin HS (2014a) Mass and fat infiltration of intercostal muscles measured by CT histogram analysis and their correlations with COPD severity. Acad Radiol 21(6):711–717. https://doi.org/10.1016/j.acra.2014.02.003

Park TS, Hong Y, Lee JS, Lee SM, Seo JB, Oh YM, Lee SD, Lee SW (2014b) Efficacy of bronchoscopic lung volume reduction by endobronchial valves in patients with heterogeneous emphysema: report on the first Asian cases. J Korean Med Sci 29(10):1404–1410. https://doi.org/10.3346/jkms.2014.29.10.1404

Park YS, Seo JB, Kim N, Chae EJ, Oh YM, Lee SD, Lee Y, Kang SH (2008) Texture-based quantification of pulmonary emphysema on high-resolution computed tomography: comparison with density-based quantification and correlation with pulmonary function test. Investig Radiol 43(6):395–402. https://doi.org/10.1097/RLI.0b013e31816901c7

Parr DG, Stoel BC, Stolk J, Stockley RA (2004) Pattern of emphysema distribution in alpha1-antitrypsin deficiency influences lung function impairment. Am J Respir Crit Care Med 170(11):1172–1178. https://doi.org/10.1164/rccm.200406-761OC

Peinado VI, Barbera JA, Ramirez J, Gomez FP, Roca J, Jover L, Gimferrer JM, Rodriguez-Roisin R (1998) Endothelial dysfunction in pulmonary arteries of patients with mild COPD. Am J Phys 274(6 Pt 1):L908–L913

Rajaram S, Swift AJ, Capener D, Telfer A, Davies C, Hill C, Condliffe R, Elliot C, Hurdman J, Kiely DG, Wild JM (2012) Lung morphology assessment with balanced steady-state free precession MR imaging compared with CT. Radiology 263(2):569–577. https://doi.org/10.1148/radiol.12110990

Salerno M, de Lange EE, Altes TA, Truwit JD, Brookeman JR, Mugler JP 3rd (2002) Emphysema: hyperpolarized helium 3 diffusion MR imaging of the lungs compared with spirometric indexes--initial experience. Radiology 222(1):252–260. https://doi.org/10.1148/radiol.2221001834

Sandek K, Bratel T, Hellstrom G, Lagerstrand L (2001) Ventilation-perfusion inequality and carbon dioxide sensitivity in hypoxaemic chronic obstructive pulmonary disease (COPD) and effects of 6 months of long-term oxygen treatment (LTOT). Clin Physiol 21(5):584–593

Schroeder JD, McKenzie AS, Zach JA, Wilson CG, Curran-Everett D, Stinson DS, Newell JD Jr, Lynch DA (2013) Relationships between airflow obstruction and quantitative CT measurements of emphysema, air trapping, and airways in subjects with and without chronic obstructive pulmonary disease. AJR Am J Roentgenol 201(3):W460–W470. https://doi.org/10.2214/AJR.12.10102

Sergiacomi G, Sodani G, Fabiano S, Manenti G, Spinelli A, Konda D, Di Roma M, Schillaci O, Simonetti G (2003) MRI lung perfusion 2D dynamic breath-hold technique in patients with severe emphysema. In Vivo 17(4):319–324

Shaker SB, Maltbaek N, Brand P, Haeussermann S, Dirksen A (2005) Quantitative computed tomography and aerosol morphometry in COPD and alpha1-antitrypsin deficiency. Eur Respir J 25(1):23–30. https://doi.org/10.1183/09031936.04.00075304

Sin DD, Wu L, Man SF (2005) The relationship between reduced lung function and cardiovascular mortality: a population-based study and a systematic review of the literature. Chest 127(6):1952–1959. https://doi.org/10.1378/chest.127.6.1952

Stavngaard T, Sogaard LV, Mortensen J, Hanson LG, Schmiedeskamp J, Berthelsen AK, Dirksen A (2005) Hyperpolarized ^{3}He MRI and 81mKr SPECT in chronic obstructive pulmonary disease. Eur J Nucl Med Mol Imaging 32(4):448–457. https://doi.org/10.1007/s00259-004-1691-x

Stefan MS, Bannuru RR, Lessard D, Gore JM, Lindenauer PK, Goldberg RJ (2012) The impact of COPD on management and outcomes of patients hospitalized with acute myocardial infarction: a 10-year retrospective observational study. Chest 141(6):1441–1448. https://doi.org/10.1378/chest.11-2032

Stolk J, Dirksen A, van der Lugt AA, Hutsebaut J, Mathieu J, de Ree J, Reiber JH, Stoel BC (2001) Repeatability of lung density measurements with low-dose computed tomography in subjects with alpha-1-antitrypsin deficiency-associated emphysema. Investig Radiol 36(11):648–651

Suga K, Kawakami Y, Iwanaga H, Hayashi N, Seto A, Matsunaga N (2008) Assessment of anatomic rela-

tion between pulmonary perfusion and morphology in pulmonary emphysema with breath-hold SPECT-CT fusion images. Ann Nucl Med 22(5):339–347. https://doi.org/10.1007/s12149-007-0137-5

Suga K, Nishigauchi K, Kume N, Koike S, Takano K, Tokuda O, Matsumoto T, Matsunaga N (1996) Dynamic pulmonary SPECT of xenon-133 gas washout. J Nucl Med 37(5):807–814

Suga K, Ogasawara N, Okada M, Tsukuda T, Matsunaga N, Miyazaki M (2002) Lung perfusion impairments in pulmonary embolic and airway obstruction with noncontrast MR imaging. J Appl Physiol 92(6):2439–2451. https://doi.org/10.1152/japplphysiol.00900.2001

Swift AJ, Wild JM, Fichele S, Woodhouse N, Fleming S, Waterhouse J, Lawson RA, Paley MN, Van Beek EJ (2005) Emphysematous changes and normal variation in smokers and COPD patients using diffusion ^{3}He MRI. Eur J Radiol 54(3):352–358. https://doi.org/10.1016/j.ejrad.2004.08.002

Takahashi M, Togao O, Obara M, van Cauteren M, Ohno Y, Doi S, Kuro-o M, Malloy C, Hsia CC, Dimitrov I (2010) Ultra-short echo time (UTE) MR imaging of the lung: comparison between normal and emphysematous lungs in mutant mice. J Magn Reson Imaging 32(2):326–333. https://doi.org/10.1002/jmri.22267

Thieme SF, Hoegl S, Nikolaou K, Fisahn J, Irlbeck M, Maxien D, Reiser MF, Becker CR, Johnson TR (2010) Pulmonary ventilation and perfusion imaging with dual-energy CT. Eur Radiol 20(12):2882–2889. https://doi.org/10.1007/s00330-010-1866-8

van Beek EJ, Dahmen AM, Stavngaard T, Gast KK, Heussel CP, Krummenauer F, Schmiedeskamp J, Wild JM, Sogaard LV, Morbach AE, Schreiber LM, Kauczor HU (2009) Hyperpolarised ^{3}He MRI versus HRCT in COPD and normal volunteers: PHIL trial. Eur Respir J 34(6):1311–1321. https://doi.org/10.1183/09031936.00138508

Vidal Melo MF, Winkler T, Harris RS, Musch G, Greene RE, Venegas JG (2010) Spatial heterogeneity of lung perfusion assessed with (13)N PET as a vascular biomarker in chronic obstructive pulmonary disease. J Nucl Med 51(1):57–65. https://doi.org/10.2967/jnumed.109.065185

Voskrebenzev A, Gutberlet M, Klimes F, Kaireit TF, Schonfeld C, Rotarmel A, Wacker F, Vogel-Claussen J (2018) Feasibility of quantitative regional ventilation and perfusion mapping with phase-resolved functional lung (PREFUL) MRI in healthy volunteers and COPD, CTEPH, and CF patients. Magn Reson Med 79(4):2306–2314. https://doi.org/10.1002/mrm.26893

Xu J, Moonen M, Johansson A, Gustafsson A, Bake B (2001) Quantitative analysis of inhomogeneity in ventilation SPET. Eur J Nucl Med 28(12):1795–1800. https://doi.org/10.1007/s002590100649

Yanai M, Sekizawa K, Ohrui T, Sasaki H, Takishima T (1992) Site of airway obstruction in pulmonary disease: direct measurement of intrabronchial pressure. J Appl Physiol (1985) 72(3):1016–1023. https://doi.org/10.1152/jappl.1992.72.3.1016

Yamashiro T, Matsuoka S, Bartholmai BJ, San Jose Estepar R, Ross JC, Diaz A, Murayama S, Silverman EK, Hatabu H, Washko GR (2010a) Collapsibility of lung volume by paired inspiratory and expiratory CT scans: correlations with lung function and mean lung density. Acad Radiol 17(4):489–495. https://doi.org/10.1016/j.acra.2009.11.004

Yamashiro T, Matsuoka S, Estepar RS, Bartholmai BJ, Diaz A, Ross JC, Murayama S, Silverman EK, Hatabu H, Washko GR (2011) Kurtosis and skewness of density histograms on inspiratory and expiratory CT scans in smokers. COPD 8(1):13–20. https://doi.org/10.3109/15412555.2010.541537

Yamashiro T, Matsuoka S, Estepar RS, Dransfield MT, Diaz A, Reilly JJ, Patz S, Murayama S, Silverman EK, Hatabu H, Washko GR (2010b) Quantitative assessment of bronchial wall attenuation with thin-section CT: an indicator of airflow limitation in chronic obstructive pulmonary disease. AJR Am J Roentgenol 195(2):363–369. https://doi.org/10.2214/AJR.09.3653

Yamashiro T, Moriya H, Tsubakimoto M, Matsuoka S, Murayama S (2016) Continuous quantitative measurement of the proximal airway dimensions and lung density on four-dimensional dynamic-ventilation CT in smokers. Int J Chron Obstruct Pulmon Dis 11:755–764. https://doi.org/10.2147/COPD.S100658

Structure-Function Imaging of Asthma: Airway and Ventilation Biomarkers

Andrea L. Barker, Rachel L. Eddy, Hannah Yaremko, Miranda Kirby, and Grace Parraga

Contents

1 **Introduction** 154

2 **Chest Radiography and X-Ray Computed Tomography** 154
2.1 Dual-Energy Xenon CT 157
2.2 Challenges 159

3 **Optical Coherence Tomography** 160
3.1 Challenges 161

4 **Positron Emission Tomography** 161
4.1 ^{18}F-FDG 161
4.2 iNOS 161
4.3 ^{13}NN 162
4.4 Challenges 162

5 **Magnetic Resonance Imaging** 162
5.1 Inhaled Noble Gas MRI 163
5.2 Inhaled Fluorine Gas MRI 164
5.3 Fourier Decomposition ^{1}H MRI (FDMRI) 164
5.4 O_2-Enhanced ^{1}H MRI 165
5.5 ^{1}H MRI Specific Ventilation 165
5.6 Challenges 167

6 **Future Opportunities** 168

References 168

A. L. Barker · R. L. Eddy · H. Yaremko
Robarts Research Institute, Western University, London, ON, Canada

M. Kirby
Department of Physics, Ryerson University, Toronto, ON, Canada

G. Parraga (✉)
Robarts Research Institute, Western University, London, ON, Canada

Division of Respirology, Department of Medicine, Western University, London, ON, Canada
e-mail: gparraga@robarts.ca

© Springer Nature Switzerland AG 2021

Y. Ohno et al. (eds.), *Pulmonary Functional Imaging*, Medical Radiology Diagnostic Imaging,
https://doi.org/10.1007/978-3-030-43539-4_9

Abstract

Asthma is a heterogeneous, chronic airway disease resulting from inflammation, airway hyperresponsiveness and remodeling as well as abnormal mucus secretions that obstruct airflow. Asthma patients report symptoms of debilitating and unpredictable dyspnea and wheeze that dramatically diminish quality of life and exercise capacity that increase healthcare resource utilization and lost work and school days. Due in part to the limitations of spirometry and despite decades of research, it remains difficult, if not impossible, to identify and measure the pathologies directly responsible for asthma symptoms, response to therapy, and chronic worsening. In vivo imaging offers the potential to measure asthma airway structure and function simultaneously, noninvasively and repeatedly; pulmonary structure-function imaging in particular provides a wide array of applications that have been developed and evaluated in the research setting to support patient phenotyping, treatment decisions, therapy response evaluations, and longitudinal monitoring. However, despite the potential to improve asthma outcomes, medical imaging methods have played very little, if not negligible, role in asthma patient clinical care. To bridge this knowledge and healthcare gap, we summarize the potential for anatomical and functional imaging methods in asthma patients. This chapter focuses on Xe-enhanced dual-energy CT, PET imaging using ^{18}F-FDG glucose, ^{13}NN, and ^{18}F-(±) iNOS, OCT, and a variety of MRI techniques including Fourier decomposition ^{1}H MRI, 4DMRI, and inhaled gas (O_2, ^{19}F, ^{3}He, ^{129}Xe) applications. The novel and clinically relevant information pulmonary imaging provides in asthma patients may now be considered in patients to personalize care and improve asthma patient outcomes while decreasing healthcare costs and resource utilization.

1 Introduction

Asthma is a chronic inflammatory airway disorder characterized by breathlessness, chest tightness, wheezing, and coughing. Importantly, although severe asthma is observed in ~5–10% of all asthma patients, it accounts for nearly 50% of all asthma-related healthcare costs (Global Initiative for Asthma (GINA) 2006; Bateman et al. 2008). To reduce the burden of asthma on patients and asthma-associated healthcare costs, new, more sensitive ways to measure and manage asthma, and in particular, severe asthma, are urgently needed. This chapter focuses on chest imaging applications in patients with asthma, as summarized in Table 1, and their current and potential role in phenotyping, measuring, and managing patients with asthma. Thoracic imaging methods and the measurements these provide may be used independently or in hybrid fashion to better understand asthma and personalize therapy to improve costs and outcomes that matter to patients. We also note that excellent, recent reviews of medical imaging methods and measurements in asthma patients (Castro et al. 2011; Teague et al. 2014; Trivedi et al. 2017; Ash and Diaz 2017; Eddy et al. 2017) provide relevant guidance on their potential utility, especially in severe asthma.

2 Chest Radiography and X-Ray Computed Tomography

Chest X-ray and X-ray computed tomography (CT) are the gold standard imaging techniques for evaluating patients with respiratory disease. In patients with asthma, chest radiography is infrequently used for the detection of structural abnormalities such as pneumothorax and pneumomediastinum (Scoggin et al. 1977; White et al. 1991; Afessa et al. 2001), and CT is generally indicated to rule out the diagnosis of any other complication that may be contributing to uncontrolled asthma symptoms (Chung et al. 2014),

Table 1 Summary of pulmonary imaging techniques and their biomarkers, advantages, disadvantages, and current applications

	Imaging modality		Biomarkers	Advantages	Disadvantages	Current applications
Structure	CT	Standard	Structural abnormalities: Airway wall thickness, wall area, lumen area, pneumothorax, air trapping	High spatial resolution images, highly available in the clinical setting, no need for special equipment or gas	Exposure to radiation bars frequent use, no functional information available	Gold standard of clinical lung imaging, rule out other conditions
		Xe	Ventilation defects	Can be used for dynamic or static acquisition	Exposure to radiation, risk of O_2 desaturation from breathing Xe gas	Research setting only
	OCT		Structural airway wall changes	Can be used monitoring patient over time, response to therapeutic intervention	Requires bronchoscopy, sensitive to movement	Research setting only
Function	PET	^{18}F-FDG	Neutrophils as a marker of inflammation	Already used in the clinical setting, noninvasive method of quantifying inflammation	Exposure to radiolabeled tracer, low-resolution images	Clinical setting for oncological imaging, research setting
		^{18}F(±) NOS	iNOS as a marker of inflammation	Noninvasive	Exposure to radiolabeled tracer	Research setting only
		^{13}NN	Nitrogen washout to measure pulmonary perfusion, ventilation defects, gas trapping	Information about ventilation and perfusion	Exposure to radiolabeled tracer, low-resolution images	Research setting only
Structure/ function	MRI	$_1$H	Neutrophils as a marker of inflammation	Already used in the clinical setting, noninvasive	Provides less structural information than CT, lower resolution, limited access	Clinical and research setting
		^{3}He	Ventilation defects	Currently the best method to evaluate ventilation defects	^{3}He is in limited supply on earth, specific equipment required	Research setting
		^{129}Xe	Ventilation defects	More detailed images due to better signal	Very expensive, polarizer required, displaces oxygen	Clinical and research setting
		^{19}F	Static ventilation, dynamic washout time	Dynamic assessment of ventilation, no need for polarizer	Expensive gas required	Research setting only
		FD ^{1}H	Ventilation defects	Can account for respiratory and cardiac rate allowing free-breathing acquisition, fast 3-D assessment	Lower resolution	Research setting only
		Specific ventilation ^{1}H	Lung perfusion and ventilation defects	No breath holds or manoeuvers required, no expensive specialized equipment	Lower resolution than HP gas MRI, special algorithms required	Research setting only

CT computed tomography, *Xe* xenon, O_2 oxygen, *OCT* optical coherence tomography, ^{18}F fluorine-18 (isotope), ^{18}F-*FDG* ^{18}F-labeled fluorodeoxyglucose, $^{18}F(\pm)NOS$ ^{18}F-labeled nitric oxide synthase, *iNOS* inducible nitric oxide synthase, ^{13}NN radiolabeled nitrogen (isotope), ^1H proton, ^3He helium-3 (isotope), ^{129}Xe xenon-129 (isotope), ^{19}F fluorine, *FD* fourier decomposition

including upper airway and laryngeal abnormalities. Continuous improvements in high resolution CT have provided new ways to describe and evaluate asthma airways, mainly in the research setting.

There is considerable potential for research assessments in asthma patients based on the fact that CT provides rapid, three-dimensional, high-resolution images of the lung parenchyma, vessels, and airways (Ambrose and Hounsfield 1973; Grenier et al. 1996; Goddard et al. 1982) with doses that are acceptable for patients (ranging from 1.5 to 10 mSv total dose). A number of commercially available software platforms have been developed for semi- and fully automated quantitative analysis of thoracic CT volumes, including Pulmonary Workstation^{R} and Apollo^{R} (VIDA Diagnostics Inc., Coralville, IA, USA), Thoracic VCAR (General Electric Healthcare, Milwaukee, WI, USA), Pulmo3D (Fraunhofer MEVIS, Bremen, Germany), Pulmonary module (Mimics Innovation Suite, Materialise, Leuven, Belgium), Chest Imaging Platform for SLICER (Brigham and Women's Hospital, Boston, MA, USA), Pulmonary Analysis Software Suite (University of Iowa), FLUIDDA (FLUIDDA nv, Kontich, Belgium), and Pulmonary Toolkit (available in a Github repository: https://github.com/tomdoel/pulmonarytoolkit), some of which have gained regulatory approval for research and clinical use (Apollo^{R} and VCAR).

Asthma is predominantly an airways disease and thoracic CT has been extensively used in research studies to evaluate airway morphology and structure in asthma patients. As shown in Fig. 1, the large airways can be segmented in three-dimensions to measure airway wall

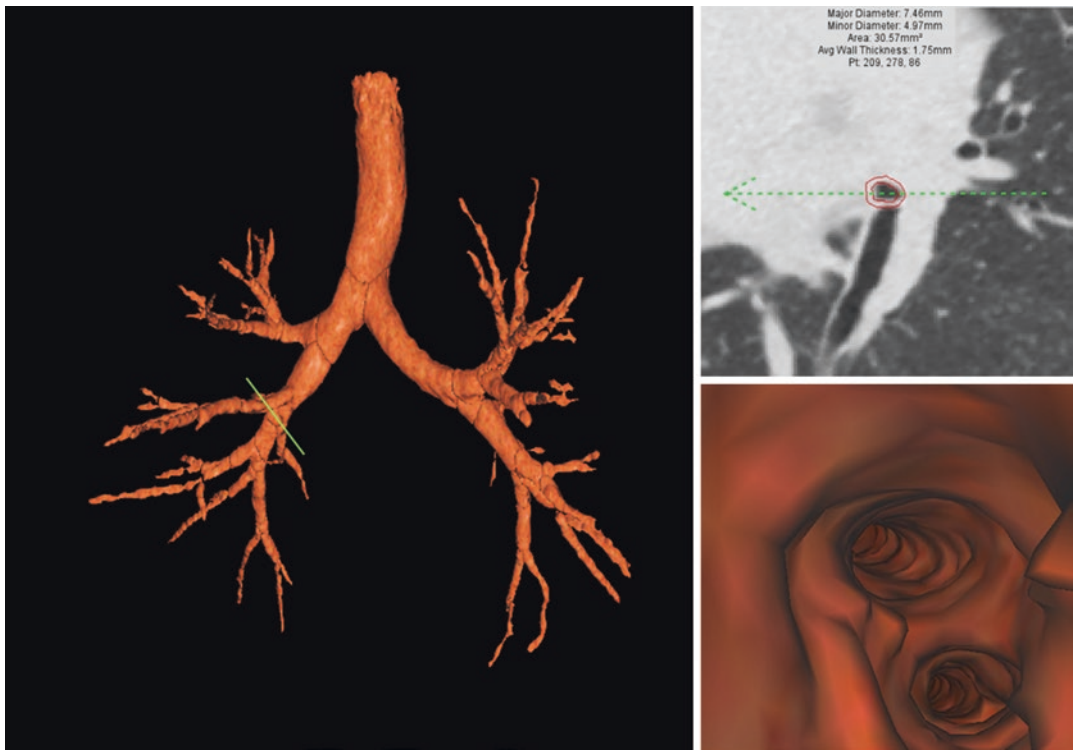


Fig. 1 CT-derived airway tree reconstruction with segmental airway wall thickness. Airway wall thickness and lumen area can be measured using CT and provide structural information about the airways and parenchyma. The images below show the airway tree, as well as airway wall thickness and the inner surface of a segmental airways RB 4 and 5

thickness, wall area, and lumen area; reliable quantification can typically be achieved for the first to sixth generation airways (Tschirren et al. 2005). Research studies using CT have shown that for the airways that can be measured, airway walls are thicker in patients with asthma compared to healthy controls (Grenier et al. 1996; Okazawa et al. 1996; Awadh et al. 1998; Niimi et al. 2000; Kasahara et al. 2002; Siddiqui et al. 2009; Gupta et al. 2010), and that CT airway wall dimensions are significantly correlated with asthma duration and severity (Niimi et al. 2000; Little et al. 2002; Aysola et al. 2008), airflow limitation (Niimi et al. 2000; Kasahara et al. 2002; Aysola et al. 2008; Gono et al. 2003; Gupta et al. 2010), airway hyperresponsiveness (Niimi et al. 2003; Aysola et al. 2008; Siddiqui et al. 2009), neutrophilic airway inflammation (Gupta et al. 2010), and airway epithelial thickness on biopsy (Aysola et al. 2008). CT airway measurements have also been shown to respond to intervention in asthmatics, including deep inspiration (Brown et al. 2001), methacholine (Okazawa et al. 1996), inhaled corticosteroids (Lee et al. 2004; Niimi et al. 2004; Kurashima et al. 2008), and anti-IL13 therapy (Brightling et al. 2016).

Although the larger central airways can be evaluated directly using CT, dose limitations in patients mean that for clinical CT, spatial resolution is limited to airways >2 mm in diameter, and this means the small airways cannot be directly measured. The functional effects of small airway obstruction can however be measured using expiratory images and evaluating lung regions with tissue density ≤856 Hounsfield units (HU), or "air trapping" (Newman et al. 1994). Figure 2 shows CT low attenuation clusters color-coded by lobe for three asthma patients and the ≤856HU and ≤950HU thresholds. The LAC_{850} representation shows air trapping that is also obvious on CT as expiratory lucency and these have been shown to be significantly greater in patients with asthma than healthy controls (Newman et al. 1994; Beigelman-Aubry et al. 2002), and correlate with asthma severity (Mitsunobu et al. 2001; Ueda et al. 2006), airflow limitation (Newman et al. 1994; Gono et al. 2003; Ueda et al. 2006; Busacker et al. 2009) and exacerbations (Tunon-de-Lara et al. 2007). CT air trapping has also been used to show response to therapy (Goldin et al. 1999; Zeidler et al. 2006; Tunon-de-Lara et al. 2007) and is associated with the need for treatment in the intensive care unit (Washko et al. 2012; Busacker et al. 2009; Tunon-de-Lara et al. 2007).

Beyond airways disease, asthma is also associated with changes in the pulmonary vasculature (Harkness et al. 2015). Investigation of the pulmonary vasculature in asthma has however been mostly limited to preclinical studies and small cohort studies without the use of imaging. A single study recently showed the loss of peripheral pulmonary vasculature quantified using CT in asthmatic patients and showed that this phenomenon is associated with disease severity and rate of exacerbations (Ash et al. 2018).

Overall, structural biomarkers of asthma from conventional CT may be used to not only noninvasively and sensitively describe disease characteristics but also to measure response to therapy and identify novel treatment targets (e.g., pulmonary vasculature). One particular study performed a cluster analysis using a number of CT biomarkers and identified four different CT-based patient clusters that are believed to represent distinct clinical phenotypes (Choi et al. 2017). Importantly, CT is widely available in the clinical setting and standard acquisition protocols can be completed in seconds to minutes; with the advent of automated image analysis platforms which are being improved to control for intersite and intersubject variability (Choi et al. 2014; Choi et al. 2015), CT provides a powerful tool for quantitative assessment of asthma.

2.1 Dual-Energy Xenon CT

Dual-energy CT (DECT) was first introduced in the 1970s (Chiro et al. 1979) but only recently has been applied for functional lung imaging (Ko et al. 2012; Lu et al. 2012) using inhaled xenon (Kong et al. 2014). Images at different tube voltages (high and low energy) are acquired simultaneously and a xenon gas distribution map is generated using material decomposition, which

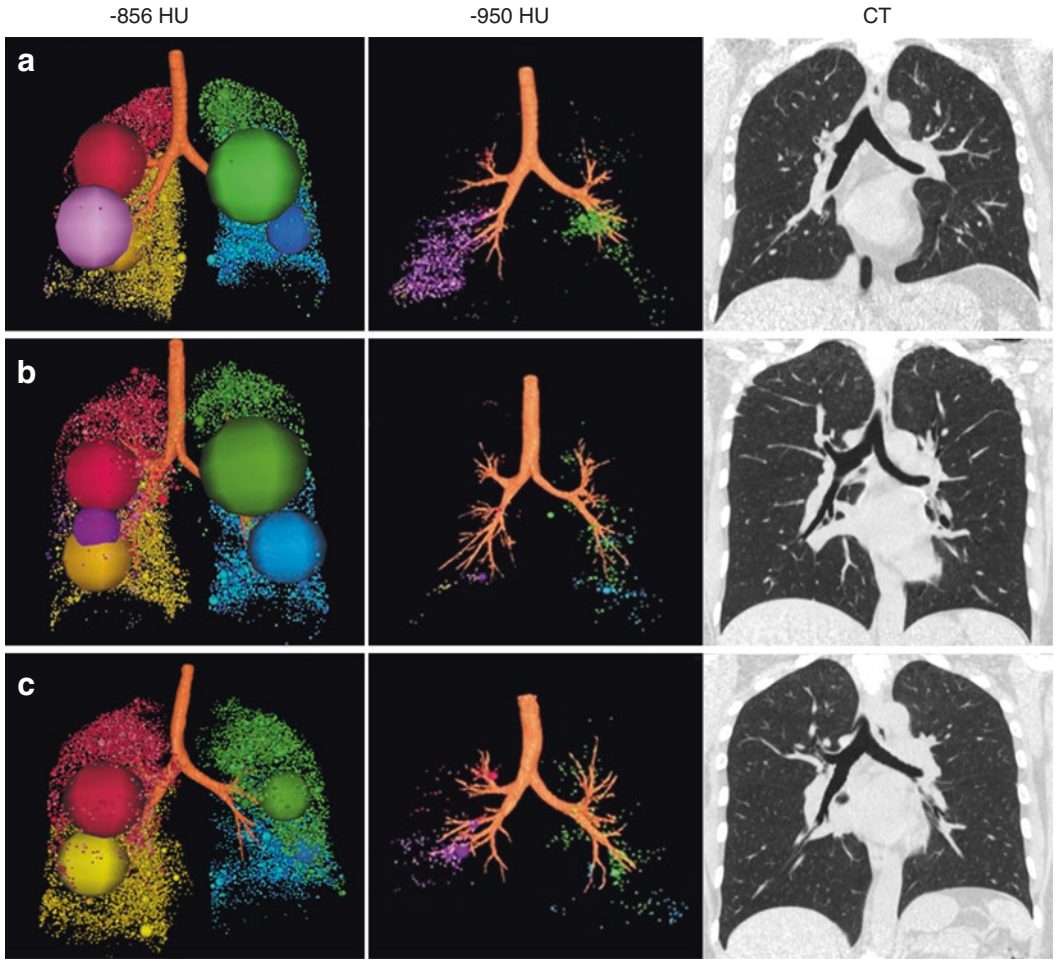


Fig. 2 CT-derived 3D LAC at −856 and −950 HU. These images represent low attenuating clusters (LAC) in three different asthma patients. The two thresholds (−856 and −950 HU) are validated in full expiratory (FRC) and full inspiratory (TLC), respectively, and the CT images are taken at FRC plus 1 L. This technique is used to quantify gas trapping from CT

allows for differentiation of xenon from the lung parenchyma and air. Static DECT images may be acquired during an inspiratory breath-hold following a wash-in period where patients breathe a mixture of xenon and oxygen for 2–3 min, while dynamic DECT images may be acquired during wash-in and wash-out phases (Tajik et al. 2002). Ventilation DECT has revealed ventilation defects in asthma patients using both static (Chae et al. 2010a) and dynamic (Jung et al. 2013) DECT protocols, which were correlated to pulmonary function tests (Chae et al. 2010b) and asthma control and symptoms (Jung et al. 2013; Park et al. 2014). Moreover, DECT ventilation defects were shown to respond to intervention with methacholine (Kim et al. 2012; Park et al. 2012) and bronchodilator (Goo and Yu 2011; Kim et al. 2012). Perfusion, as well as ventilation-perfusion mismatch, may also be quantified using DECT (Hwang et al. 2017); however this has not yet been investigated in asthma patients. Figure 3 shows porcine xenon-enhanced DECT ventilation images of the lungs and central and peripheral airways. The ability to acquire high-resolution static and dynamic images of the lungs provides a unique opportunity to study the relationships been

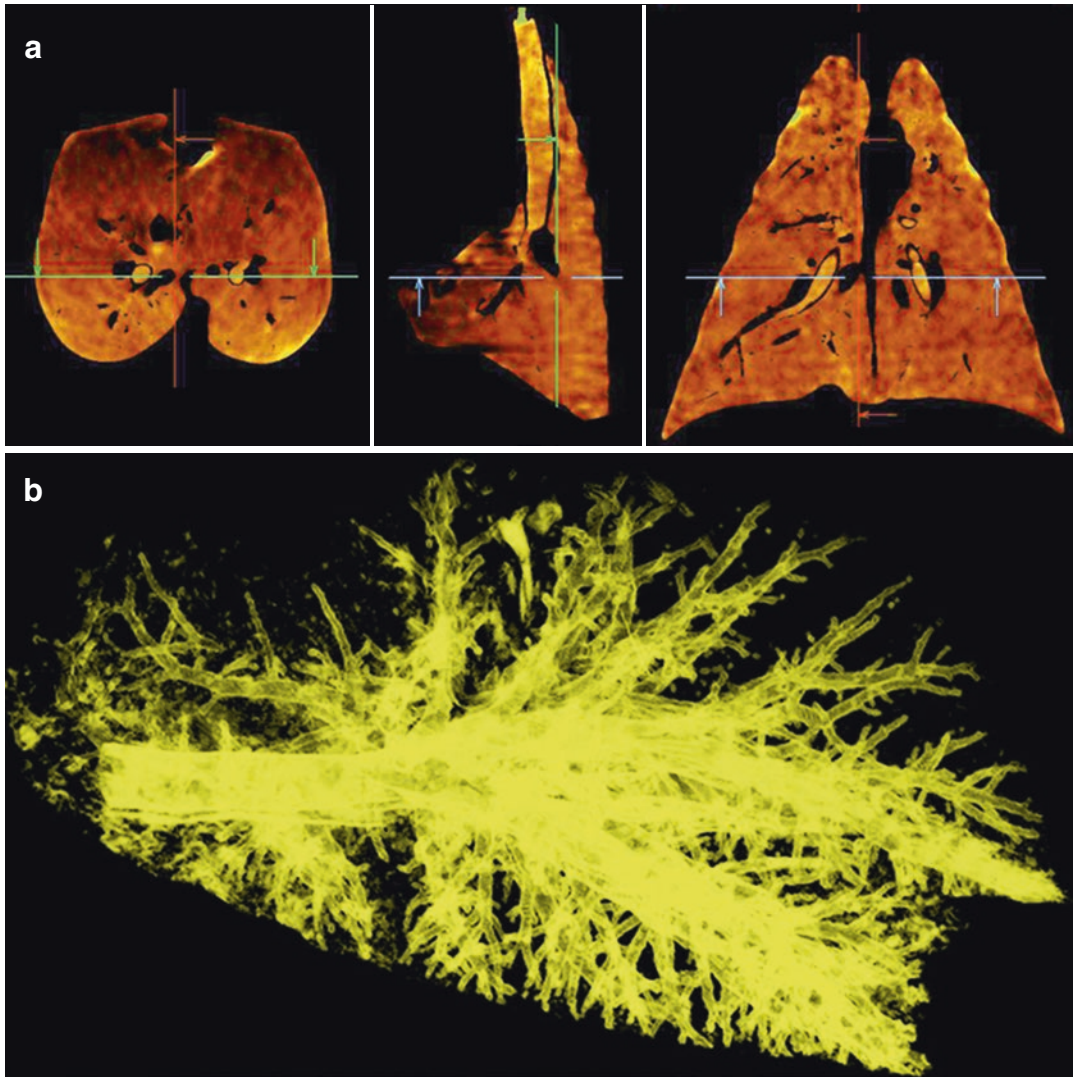


Fig. 3 Xenon-enhanced CT image of the lung. Xenon-enhanced CT images in the swine. (**a**) from left to right: axial, sagittal, and coronal views of the lungs, (**b**) central and peripheral airways to approximately 2 mm in diameter. Adapted with permission from Wolters Kluwer: Investigative Radiology, Matthew Fuld, Ahmed Halaweish, John Newell et al., Optimization of Dual-Energy Xenon-Computed Tomography for Quantitative Assessment of Regional Pulmonary Ventilation, 48(9): 629–637; https://doi.org/10.1097/RLI.0b013e31828ad647, 2013

local airway wall abnormalities and ventilation using a single imaging modality (Fuld et al. 2013).

2.2 Challenges

As briefly outlined in Table 1, radiation exposure limits the application of CT in general for longitudinal monitoring or assessment of treatment response in patients, particularly in pediatric populations. While conventional CT provides only structural information, DECT with inhaled xenon provides functional information. Though dynamic DECT may provide more physiologically relevant measurements of ventilation compared to static breath-holds, it is associated with a much higher radiation dose. A limitation of xenon-enhanced DECT in particular is the anes-

thetic properties of xenon and respiratory depression caused by its inhalation in the concentrations required to provide adequate contrast (Remy-Jardin et al. 2014; Park et al. 2010; Goo et al. 2010; Fuld et al. 2013). To circumvent this issue, oxygen gas may be inhaled before the test, and a 30/70 by volume Xe/O_2 mixture is typically inhaled during the procedure (Goo et al. 2011; Fuld et al. 2013). Xenon is not routinely available; krypton or a mixture of xenon and krypton have been suggested as its replacement for clinical use (Chon et al. 2007; Hachulla et al. 2012). Krypton DECT has not yet been prospectively evaluated in asthmatics; however krypton-81 m scintigraphy has been used to show treatment response in asthma exercise-induced bronchospasm in a case report only (Takahashi et al. 2000). Unfortunately, xenon-enhanced DECT is limited to specialized healthcare centers because of the complex acquisition procedure and computational methods required to generate clinically relevant information (Park et al. 2010; Fuld et al. 2013).

3 Optical Coherence Tomography

Optical coherence tomography (OCT) is a minimally invasive bronchoscopic imaging method that uses infrared light through a fiber-optic catheter and provides 3D, near histological resolution images of the airway wall at the airway surface (Hariri et al. 2013). Airways can be directly measured using OCT and this approach is limited only by the size of the OCT probe, and therefore images of the small airways (<2 mm in diameter) may obtained (Coxson and Lam 2009). In patients with asthma, OCT-measured airway lumens were decreased in size compared to healthy controls (Williamson et al. 2011), and in the same study, airway lumen measurements were acquired at different airway pressure to also extract functional measures of airway compliance. Another study not only demonstrated response to treatment with bronchial thermoplasty, but also demonstrated the opportunity to use OCT for pretreatment pheno-

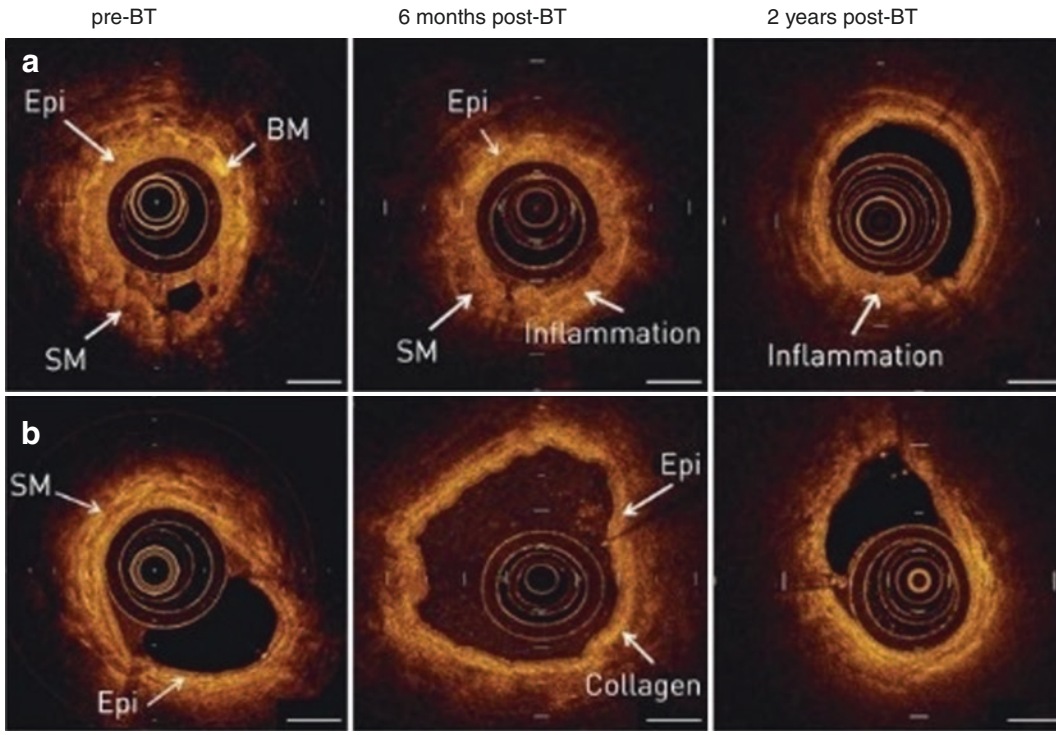


Fig. 4 OCT images of the airways pre- and post-bronchial thermoplasty in two asthma patients. This method can be used to assess the effectiveness of an intervention such as bronchial thermoplasty (BT) before and after treatment. Reproduced with permission of the © ERS 2018. European Respiratory Journal 46(3) 859–862; https://doi.org/10.1183/09031936.00016815 Published 31 August 2015

typing (Kirby et al. 2015). Figure 4 shows OCT images for two asthma patients pre-bronchial thermoplasty and at two time points post-procedure, and reveals the differences in response to treatment for two different airway phenotypes. The decrease in smooth muscle over time can be visualized over time in the patient that responded to bronchial thermoplasty (Patient B).

3.1 Challenges

The application of OCT in the assessment of asthma has been limited to a small number of studies. Though OCT airway imaging is a minimally invasive bronchoscopic method, it does require local anesthesia and conscious sedation; this limits its use in the routine evaluation of mild-moderate asthma.

4 Positron Emission Tomography

Positron emission tomography (PET) tracers may be used to identify the activity of a given metabolic or biochemical pathway (Bailey and Willowson 2014; Wolf and Fowler 1995; Harris and Schuster 2007) and has been used to investigate pulmonary perfusion and ventilation, as well as pulmonary inflammation (Schuster 2007).

4.1 ^{18}F-FDG

Fluorine-18-fluorodeoxyglucose (^{18}F-FDG) identifies metabolically active tissues and is the most commonly used PET tracer in clinical practice. FDG-PET has been suggested as a biomarker for pulmonary inflammation (Chen and Schuster 2006); the primary source of increased FDG signal in the lung is hypothesized to be due to neutrophils (Chen and Schuster 2006) while another study suggested that FDG was a biomarker of eosinophilic inflammation (Harris et al. 2011). FDG signal has also been shown to increase following bronchoscopic allergen challenge (Taylor et al. 1996; Harris et al. 2011). Future work in humans is required to elucidate the mechanisms of FDG uptake in asthmatics.

4.2 iNOS

Inducible nitric oxide synthase (iNOS) is another target for the tracking lung inflammation (Harris and Schuster 2007; Huang et al. 2015). iNOS is upregulated in response to cytokines and other pro-inflammatory cellular signaling molecules in the lung epithelium (Guo et al. 1995). Accordingly, ^{18}F(±)NOS may be used to identify the presence of iNOS (Huang et al. 2015) as shown in Fig. 5 whereby lung inflammation may

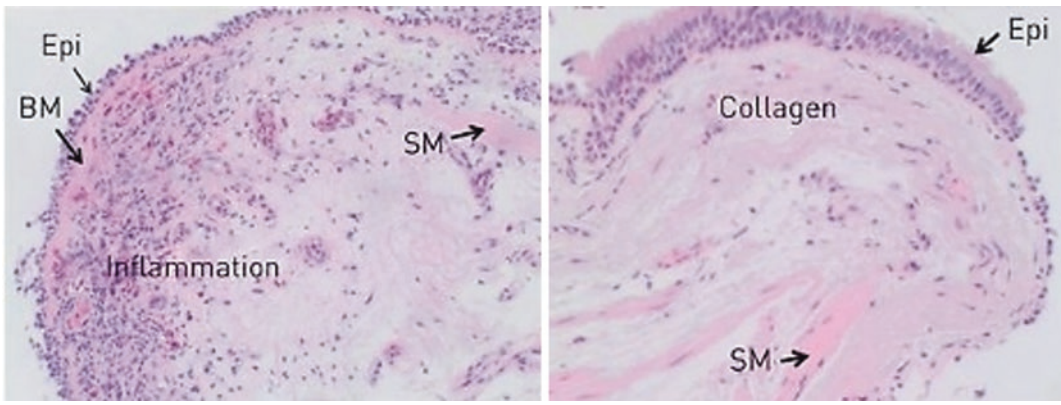


Fig. 5 Histological samples acquired via bronchial biopsy in two asthma patients. These images demonstrate the tissue organization of the airway wall of two asthma patients 6 months post-bronchial thermoplasty. *BM* basement membrane, *SM* smooth muscle, *WA* airway wall. Reproduced with permission of the © ERS 2018. European Respiratory Journal 46(3) 859–862; https://doi.org/10.1183/09031936.00016815 Published 31 August 2015

be investigated using this exogenous contrast agent which is not retained within edematous airways due to inflammation (Huang et al. 2015).

4.3 ^{13}NN

^{13}NN can be used to measure ventilation, perfusion, and ventilation-perfusion mismatch using either a bolus injection or inhalation of ^{13}NN. For a bolus injection, ^{13}NN crosses the alveolar membrane and is retained within unventilated lung regions or ventilation defects due to gas trapping whereas ^{13}NN is quickly washed out of ventilation lung regions. For inhalations, the tracer is unable to reach poor-ventilated regions. Using a bolus injection, regions of poor ventilation in asthmatics were identified after methacholine-induced bronchoconstriction (Venegas et al. 2005b), and this is shown in Fig. 6 in an asthma patient after washout and deep inhalations. Another study also used ^{13}NN to show that perfusion redistributes away from ventilation defects (Harris et al. 2006).

Molecular imaging using PET provides the opportunity to improve the management and treatment of asthma by allowing for the early detection of inflammatory phenotypes in its early stages, quantifying the activity of inflammatory pathways and evaluating the effectiveness of therapies aimed at attenuating the progression of inflammation and associated tissue damage. It can also be used to inform elucidation of asthma pathophysiology in order to refine animal models of the disease for preclinical studies (Venegas et al. 2005a; Schuster 2007).

4.4 Challenges

Although these are promising results, the clinical and research use of ^{13}NN, ^{18}F(±)NOS, and ^{18}F-FDG PET have been limited in part due to the limited availability of PET, somewhat limited spatial resolution, and because the exposure to radiation is nontrivial (Trivedi et al. 2017; Schuster 2007; Huang et al. 2015).

5 Magnetic Resonance Imaging

Conventional pulmonary ^{1}H magnetic resonance imaging (MRI) poses technological and methodological challenges, such as the low

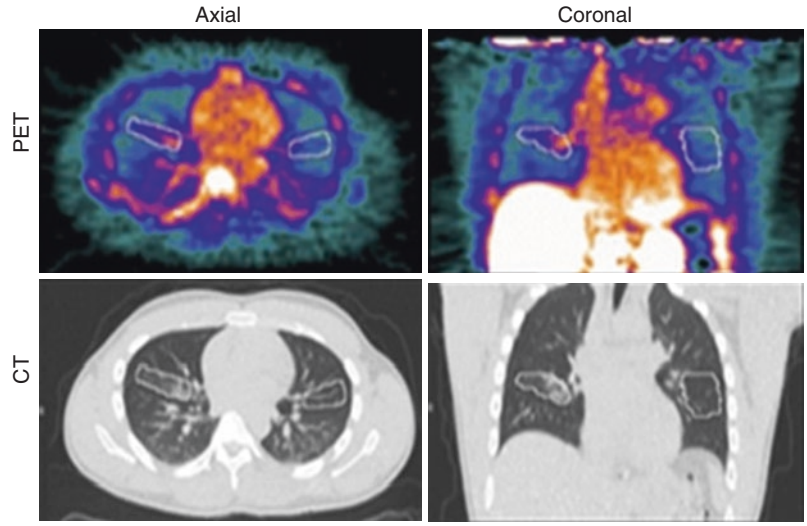


Fig. 6 PET image labeling iNOS expression in the lung using ^{18}F(±)NOS tracer. This tracer can be used to identify areas of inflammation in asthma in order to understand its distribution in the lungs and airways. Reprinted from European Journal of Radiology, 86, Delphine L Chen, Mark L Schiebler, Min Mo Goo, JR Van Beek, PET imaging approaches for inflammatory lung diseases: Current concepts and future directions, 371–76, Copyright (2017), with permission from Elsevier

proton density of the lungs and numerous air-tissue interfaces that create magnetic field inhomogeneities (Bergin et al. 1993). Innovations in the type and quality of information that can be acquired using MRI have emerged over the past 25 years since short echo time ^{1}H lung MRI was demonstrated by Mayo and Mueller over two decades ago (Mayo 1994). Some of these advances include pulmonary functional MRI using hyperpolarized ^{3}He and ^{129}Xe, inhaled ^{19}F MRI and ^{1}H based methods including Fourier decomposition (FDMRI), O_2-enhanced MRI and ^{1}H MRI for the measurement of specific ventilation.

5.1 Inhaled Noble Gas MRI

Hyperpolarized noble gas MRI was first described by a team of pioneers investigating ^{129}Xe polarization signals (Albert et al. 1994) and the first description of heterogeneous ventilation in asthma was in 2001 using inhaled ^{3}He (Altes et al. 2001). Since then, numerous studies using hyperpolarized gas MRI have shown that inhaled gas distribution is spatially heterogeneous in patients with asthma (Altes et al. 2001; de Lange et al. 2006; de Lange et al. 2007; de Lange et al. 2009; Tzeng et al. 2009; Samee et al. 2003; Fain et al. 2008; Ebner et al. 2017; Costella et al. 2012). Ventilation heterogeneity is now widely recognized as a key feature of asthma and the topic has been reviewed previously (Teague et al. 2014; Trivedi et al. 2017; Eddy et al. 2017). Ventilation defects are defined as regions of polarized gas signal void and are quantified as the ventilation defect percent (VDP), which is the volume of ventilation defects normalized to thoracic cavity volume (Kirby et al. 2012; He et al. 2014). Figure 7 demonstrates different patterns of ventilation defects in asthma patients as compared to a healthy control, and likely a result from varying influences of these various factors contributing to the disease between patients. VDP in asthmatics correlates with clinical features in asthmatics such as medication requirement, airway pathology, severity, symptom score, and atopic markers (Altes et al. 2001). As asthma control worsens, VDP tends to increase (Svenningsen et al. 2016). Focal ventilation defects are quantitatively and spatially related to thickened airway walls and narrowed lumens and are likely derived from remodeling or smooth muscle dysfunction and inflammation (Svenningsen et al. 2014b). VDP worsens with disease severity (de Lange et al. 2006), airflow limitation (de Lange et al. 2006; Samee et al. 2003; de Lange et al. 2007; Fain et al. 2008; Ebner et al. 2017), dyspnea (Costella et al. 2012), and airway resistance (Costella et al. 2012), is directly related to the severity of asthma (de Lange et al. 2006), and predictive of quality of life and disease control in adults (Svenningsen et al. 2016; Simon et al. 2012). Multiple MRI

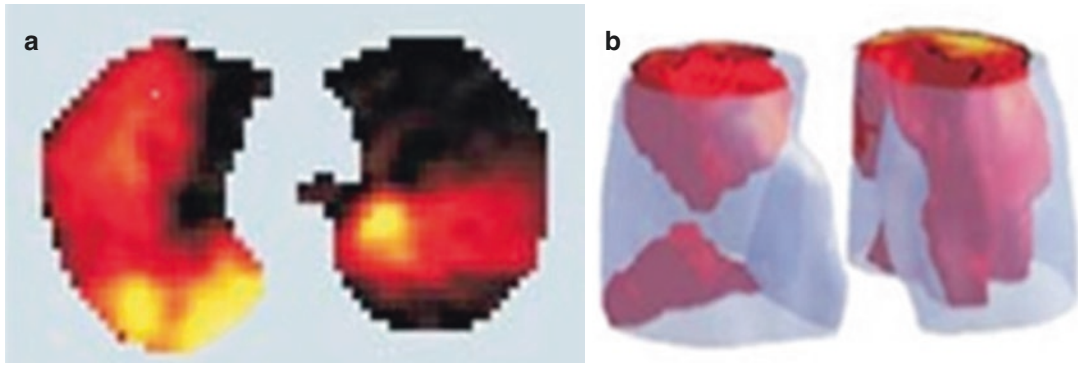


Fig. 7 PET image using a bolus injection of ^{13}NN tracer to measure nitrogen washout in asthma. An (**a**) axial and (**b**) 3D reconstruction of the lung showing the presence of the isotope after a washout period, indicative of low ventilation. Reprinted by permission from Springer Nature: Nature, Self-organized patchiness in asthma as a prelude to catastrophic shifts. Jose G. Venegas, Tilo Winkler, Guido Musch, Marcos F. Vidal Melo, Dominick Layfield et al., 434(7034):777–781; https://doi.org/10.1038/nature03490, Copyright 2005

time points may be used to quantify the interactions between space, time, and airway hyperresponsiveness. Persistent ventilation defects are likely a result of remodeled, collapsed, or narrowed airways, and temporal-spatial pulmonary maps can be used to identify targets for asthma therapy (Svenningsen et al. 2014a). Similar to ventilation defects identified using other modalities, MRI ventilation defects respond to methacholine (Samee et al. 2003; de Lange et al. 2007; Costella et al. 2012) and exercise challenge (Niles et al. 2013; Kruger et al. 2014), as well as therapy using bronchodilators (Altes et al. 2001; Svenningsen et al. 2013), oral montelukast (Kruger et al. 2014), and even bronchial thermoplasty (Thomen et al. 2015). Hyperpolarized gas MRI could help identify patients at a higher risk of exacerbation in the future, to elucidate phenotypes based on the distribution of ventilation defects, to guide treatment and serve as intermediate end points in trials of new treatments, and should therefore be investigated and improved.

5.2 Inhaled Fluorine Gas MRI

Inert ^{19}F gas can be also be used as an inhaled MRI contrast agent to quantify static and dynamic ventilation (Halaweish and Charles 2014; Halaweish et al. 2013; Gutberlet et al. 2018; Couch et al. 2014); variations of ^{19}F gas for inhalation include tetrafluoromethane (CF_4), sulfur hexafluoride (SF_6), hexafluoroethane (C_2F_6), and perfluoropropane (C_3F_8 or PFP). ^{19}F is considerably less expensive than ^{3}He and ^{129}Xe and does not require polarization. Moreover, resident lung and inhaled O_2 does not have a large effect on the T_1 of fluorinated gases (compared to hyperpolarized gases); thus, fluorinated contrast gases can be mixed with O_2 to improve patient safety. This is important because current imaging protocols require 5–7 breaths of a fluorinated gas mixture to reach an approximate steady state of gas concentration in the lung followed by a breath-hold maneuver of 1 L of the same gas mixture during image acquisition (Halaweish et al. 2013; Couch et al. 2013). A recent study has applied ^{19}F MRI in asthma and demonstrated increased heterogeneity in gas distribution compared to healthy controls (Couch et al. 2013).

The majority of hyperpolarized noble gas work in asthma to date has been limited to ^{3}He gas. ^{3}He gas is available in limited quantities (Shea and Morgan 2010) and is therefore very expensive which completely halts its widespread clinical application. ^{129}Xe gas on the other hand is much more abundant and therefore can overcome these limitations. While ^{129}Xe gas has historically only been approved for investigational use, it was recently approved for use in the UK, which may aid in the translation of hyperpolarized gas MRI in clinical practice. Nonetheless, hyperpolarized gas MRI requires specialized equipment that is limited to a small number of specialized centers worldwide. Finally, the breath-hold maneuver used to create MRI images requires patients to hold their breath for up to 20 s, which can be difficult for severe asthmatics and pediatric patients (Cadman et al. 2013). ^{19}F can overcome these challenges, but is still limited itself by complex acquisition protocols. These limitations must be addressed before MRI ventilation imaging can be applied in clinical practice for the management and treatment of asthma.

In an effort to bypass some of the limitations of the application of hyperpolarized gas MRI in the clinical setting, free-breathing ^{1}H MRI has recently been developed. Free-breathing techniques such as Fourier decomposition (FD), O_2-enhanced, and specific ventilation MRI provide unique information about lung perfusion and ventilation in vivo and without the use of rare and expensive contrast agents or breath-hold protocols.

5.3 Fourier Decomposition ^{1}H MRI (FDMRI)

In 2009, FDMRI was developed as a non-contrast method for assessing pulmonary ventilation and perfusion using fast proton MRI (Bauman et al. 2009). FDMRI acquires a time series of images during free breathing which are deformably registered to generate ventilation and/or perfusion maps. Fast Fourier transforms are

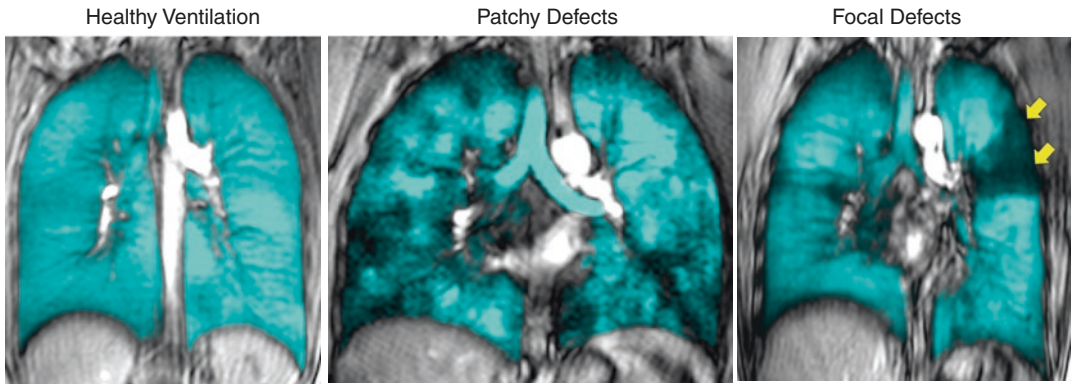


Fig. 8 Ventilation distribution using ^{3}He MRI. Ventilation maps in a healthy participant (left) and two asthma patients demonstrating different functional ventilation defect phenotypes: patchy (middle) or focal (right)

performed on a voxel-wise basis on the signal intensity oscillations, which are caused by the expansion and contraction of lung parenchyma during breathing. Ventilation- and perfusion-weighted images can be generated by mapping the signal at the frequency of the respiratory and cardiac rates, respectively. Figure 8 shows the spatial relationship between FDMRI ventilation-weighted images and inhaled ^{3}He MRI, demonstrating the similarity of functional information provided by the two techniques. In asthmatics, FD MRI is also sensitive to changes in ventilation induced by methacholine and bronchodilator (Capaldi et al. 2017). This approach can be used to identify regions of low proton intensity that lack tissue (Gutberlet et al. 2018) and regions of high proton intensity that may be related to edema or fluid infiltrates (Kaireit et al. 2018; Fain et al. 2010). Future studies will focus on strengthening the clinical applications of this technique and reducing the time required to perform a 3D assessment of perfusion and ventilation (Bauman et al. 2009).

5.4 O_2-Enhanced ^{1}H MRI

O_2-enhanced ^{1}H MRI provides another way to assess pulmonary function that has been used to describe the regional ventilation in patients (Edelman et al. 1996) and relies on the paramagnetic properties of O_2 to generate ventilation images. Different concentrations of O_2 in the lung cause changes in the longitudinal relaxation time (T_1) of protons in the lung tissue, which is measured while breathing pure O_2 and directly compared with T_1-weighted ^{1}H images acquired during free breathing of room air. The advantage of O_2-enhanced MRI is ease of access to O_2 as a contrast agent in the clinical setting. Studies employing O_2-enhanced MRI in patients with asthma have shown that the O_2-enhancement ratio was related to pulmonary function tests and disease severity (Ohno et al. 2011; Ohno et al. 2014). Moreover, the potential for evaluation of therapeutic outcome using O_2-enhanced MRI has also been demonstrated (Ohno et al. 2014). O_2-enhanced MRI can also be used to measure specific ventilation (Sa et al. 2010; Sa et al. 2014; Geier et al. 2018); however this technique has not yet been applied in asthmatics.

5.5 ^{1}H MRI Specific Ventilation

Recently, specific ventilation has been derived from free-breathing ^{1}H MRI to quantify whole-lung pulmonary function. Free-breathing images are sorted by respiratory phase and interpolated to classify these as belonging to inspiration or expiration, and specific ventilation maps may be generated without exogenous contrast (such as pioneered using ^{1}H MRI with O_2 enhancement discussed above) on a voxel-wise basis after co-registration of inspiratory and expiratory volumes based on signal intensity variations within a voxel. This

technique was compared to ^{3}He MRI in healthy and asthmatic subjects (Capaldi et al. 2018) which demonstrated the spatial and quantitative relationship between the two techniques, worse specific ventilation in asthmatics compared to healthy controls and strong correlations between MRI- and plethysmography-measured specific ventilation; these observations are shown in Figs. 9, 10.

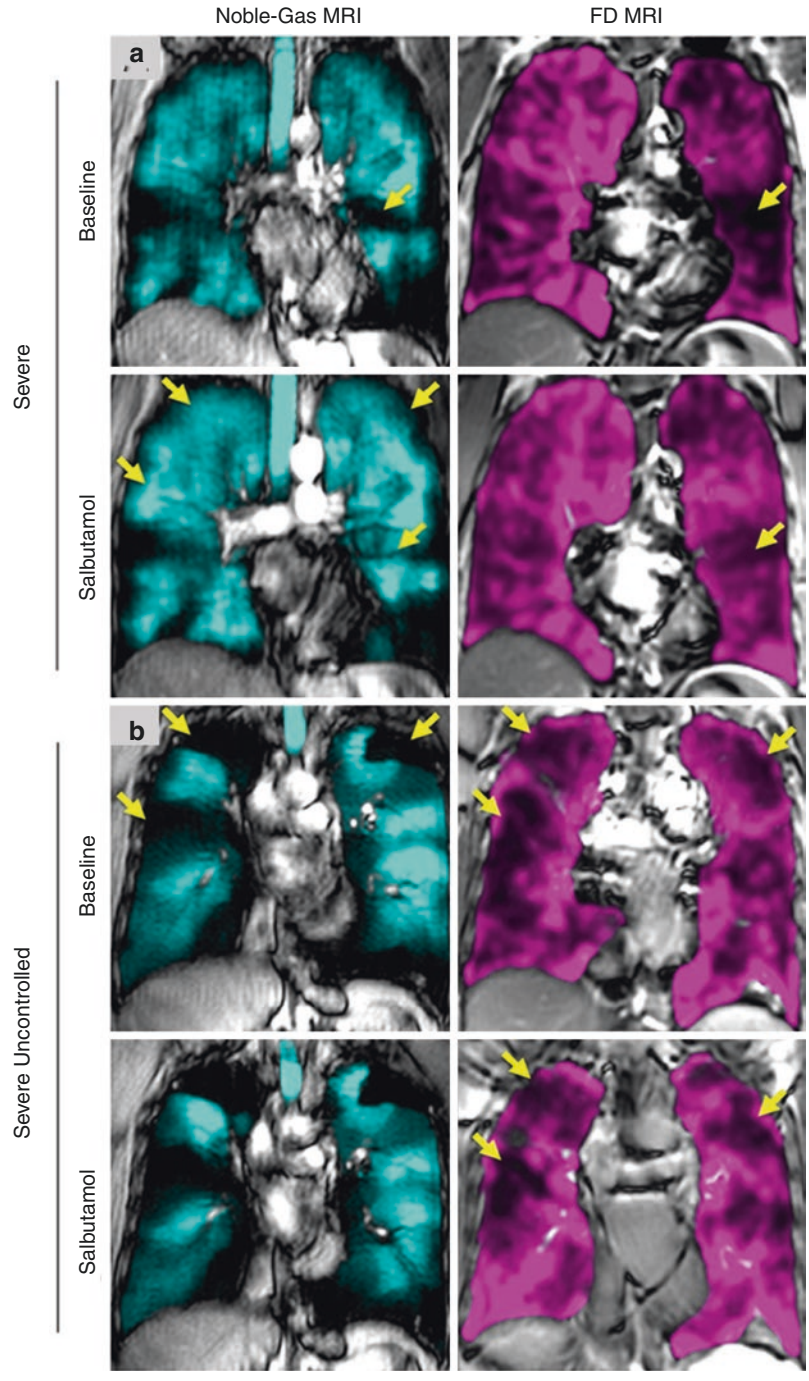


Fig. 9 Fourier decomposition pulmonary ^{1}H MRI compared to hyperpolarized gas MRI. The figure below compares images acquired using hyperpolarized MRI and FD MRI pre- and post-bronchodilator in two patients with severe and severe uncontrolled asthma, respectively

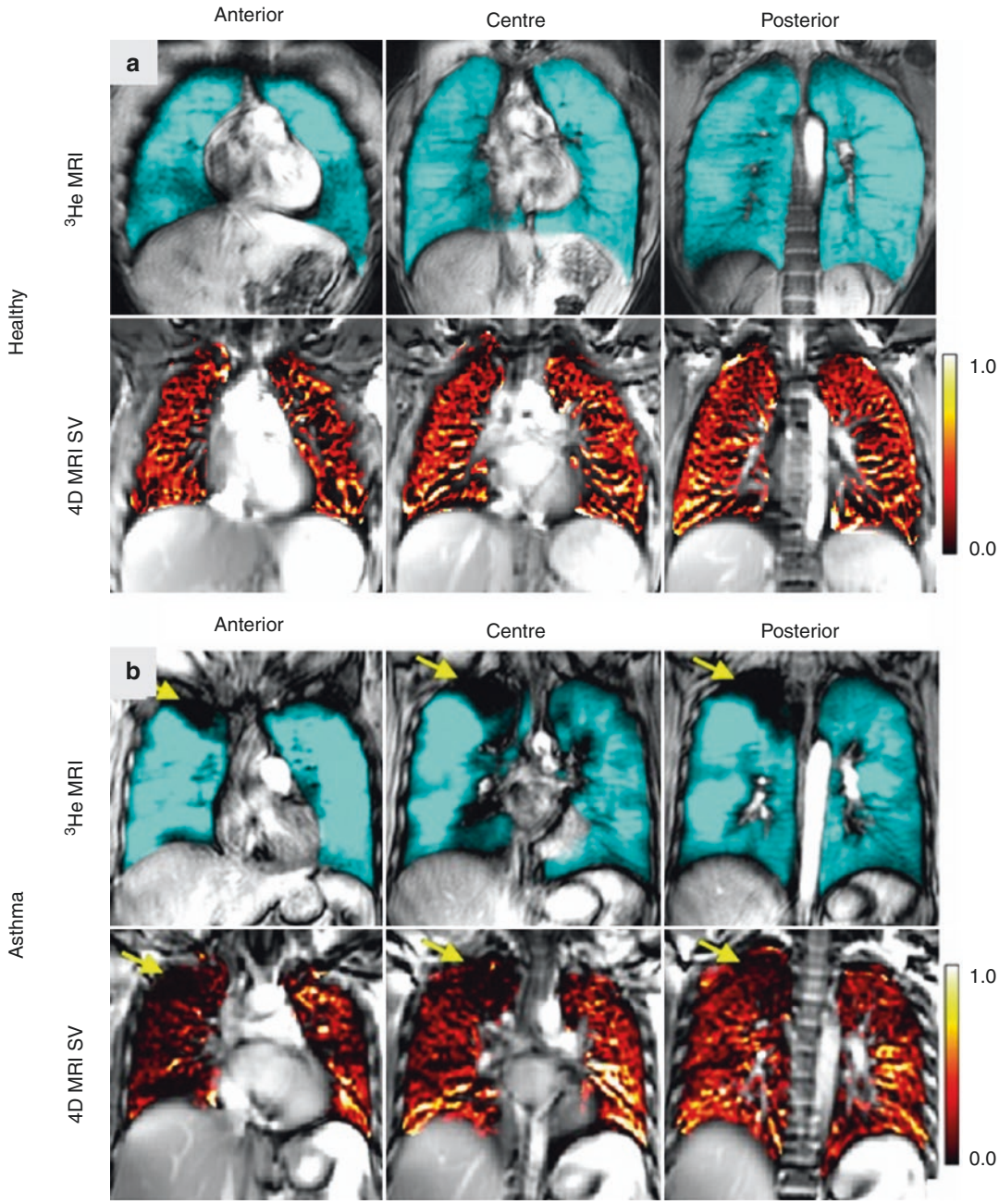


Fig. 10 ^{1}H free-breathing specific ventilation and ^{3}He MR images in a healthy (top) and asthmatic (bottom) lungs. The ability to develop a free-breathing ^{1}H MRI sequence capable of quantifying specific ventilation in the lungs is an important step in making functional lung imaging available in the clinical setting

5.6 Challenges

Despite the promise of FD, O_2-enhanced and specific ventilation MRI as noninvasive, free-breathing imaging techniques, all are limited by the complexity of post-processing required to generate the functional information (Capaldi et al. 2017; Bauman et al. 2009; Kaireit et al.

2018). Automated, commercially available image-processing pipelines and packages are required for integration of these techniques in clinical workflow.

6 Future Opportunities

Although pulmonary imaging provides measurements of minimally and noninvasive regional structural and functional pulmonary abnormalities, these methods and measurements currently only play a minor role in the clinical management of asthma. The possibilities and potential that dedicated asthma imaging methods and measurements may provide in asthma drug development strategies (Castro et al. 2011; Ash and Diaz 2017) is now clear but not realized. The use of CT and MRI in combination, for example, may help elucidate the relationship between airway morphology and functional abnormalities (Schuster 2007; Fain et al. 2008; Svenningsen et al. 2014a), measurements that may serve helpful in clinical trials of new therapies or in individual patients. Moreover, studies investigating computational lung models alongside in vivo imaging measurements may also help drive a better understanding of the complex nature of airway narrowing, airflow obstruction, and lung biomechanics in asthma (Venegas et al. 2005b; Tgavalekos et al. 2003; Tgavalekos et al. 2005; Tgavalekos et al. 2007; Campana et al. 2009).

Biomarkers that relate to patient outcomes may be used as intermediate endpoints in clinical trials of new therapies, and this has certainly focused and accelerated the development of static breath-hold and free-breathing lung imaging methods and measurements. Hybrid modality investigations in particular using CT and MRI have identified the relationships between abnormal airway structure and function and opened the door to developing imaging "signatures" (a combination of imaging biomarkers specific to the disease and patient) which could be used to define phenotypes for asthma patients (Schuster 2007; Trivedi et al. 2017)(Schuster 2007; Trivedi et al. 2017)(Schuster 2007; Trivedi et al. 2017). The prospectively planned and tactical use of imaging in asthma patients is now dependent on the strategic development, application, and optimization of these methods for routine clinical and clinical research use. Only then will the potential of medical imaging measurements be realized and the novel and clinically relevant information used to personalize care and improve asthma patient outcomes.

References

Afessa B, Morales I, Cury JD (2001) Clinical course and outcome of patients admitted to an ICU for status asthmaticus. Chest 120(5):1616–1621

Albert MS, Cates GD, Driehuys B, Happer W, Saam B, Springer CS Jr, Wishnia A (1994) Biological magnetic resonance imaging using laser-polarized 129Xe. Nature 370(6486):199–201. https://doi.org/10.1038/370199a0

Altes TA, Powers PL, Knight-Scott J, Rakes G, Platts-Mills TA, de Lange EE, Alford BA, Mugler JP 3rd, Brookeman JR (2001) Hyperpolarized 3He MR lung ventilation imaging in asthmatics: preliminary findings. J Magn Reson Imaging 13(3):378–384

Ambrose J, Hounsfield G (1973) Computerized transverse axial tomography. Br J Radiol 46(542):148–149

Ash SY, Diaz AA (2017) The role of imaging in the assessment of severe asthma. Curr Opin Pulm Med 23(1):97–102. https://doi.org/10.1097/mcp.0000000000000341

Ash SY, Rahaghi FN, Come CE, Ross JC, Colon AG, Cardet-Guisasola JC, Dunican EM, Bleecker ER, Castro M, Fahy JV, Fain SB, Gaston BM, Hoffman EA, Jarjour NN, Mauger DT, Wenzel SE, Levy BD, San Jose Estepar R, Israel E, Washko GR (2018) Pruning of the pulmonary vasculature in asthma. The severe asthma research program (SARP) cohort. Am J Respir Crit Care Med 198(1):39–50. https://doi.org/10.1164/rccm.201712-2426OC

Awadh N, Muller NL, Park CS, Abboud RT, FitzGerald JM (1998) Airway wall thickness in patients with near fatal asthma and control groups: assessment with high resolution computed tomographic scanning. Thorax 53(4):248–253

Aysola RS, Hoffman EA, Gierada D, Wenzel S, Cook-Granroth J, Tarsi J, Zheng J, Schechtman KB, Ramkumar TP, Cochran R, Xueping E, Christie C, Newell J, Fain S, Altes TA, Castro M (2008) Airway remodeling measured by multidetector CT is increased in severe asthma and correlates with pathology. Chest 134(6):1183–1191. https://doi.org/10.1378/chest.07-2779

Bailey DL, Willowson KP (2014) Quantitative SPECT/CT: SPECT joins PET as a quantitative imaging modality. Eur J Nucl Med Mol Imaging 41(Suppl 1):S17–S25. https://doi.org/10.1007/s00259-013-2542-4

Bateman ED, Hurd SS, Barnes PJ, Bousquet J, Drazen JM, FitzGerald JM, Gibson P, Ohta K, O'Byrne P, Pedersen SE, Pizzichini E, Sullivan SD, Wenzel SE, Zar HJ (2008) Global strategy for asthma management and prevention: GINA executive summary. Eur Respir J 31(1):143–178. https://doi.org/10.1183/09031936.00138707

Bauman G, Puderbach M, Deimling M, Jellus V, Chefd'hotel C, Dinkel J, Hintze C, Kauczor HU, Schad LR (2009) Non-contrast-enhanced perfusion and ventilation assessment of the human lung by means of fourier decomposition in proton MRI. Magn Reson Med 62(3):656–664. https://doi.org/10.1002/mrm.22031

Beigelman-Aubry C, Capderou A, Grenier PA, Straus C, Becquemin MH, Similowski T, Zelter M (2002) Mild intermittent asthma: CT assessment of bronchial cross-sectional area and lung attenuation at controlled lung volume. Radiology 223(1):181–187. https://doi.org/10.1148/radiol.2231010779

Bergin CJ, Glover GM, Pauly J (1993) Magnetic resonance imaging of lung parenchyma. J Thorac Imaging 8(1):12–17

Brightling CE, Nordenmark LH, Jain M, Piper E, She D, Braddock M, Colice G, Tornling G (2016) Effect of anti-IL-13 treatment on airway dimensions in severe asthma. Am J Respir Crit Care Med 194(1):118–120. https://doi.org/10.1164/rccm.201511-2224LE

Brown RH, Scichilone N, Mudge B, Diemer FB, Permutt S, Togias A (2001) High-resolution computed tomographic evaluation of airway distensibility and the effects of lung inflation on airway caliber in healthy subjects and individuals with asthma. Am J Respir Crit Care Med 163(4):994–1001. https://doi.org/10.1164/ajrccm.163.4.2007119

Busacker A, Newell JD Jr, Keefe T, Hoffman EA, Granroth JC, Castro M, Fain S, Wenzel S (2009) A multivariate analysis of risk factors for the air-trapping asthmatic phenotype as measured by quantitative CT analysis. Chest 135(1):48–56. https://doi.org/10.1378/chest.08-0049

Cadman RV, Lemanske RF Jr, Evans MD, Jackson DJ, Gern JE, Sorkness RL, Fain SB (2013) Pulmonary 3He magnetic resonance imaging of childhood asthma. J Allergy Clin Immunol 131(2):369–376 e361-365. https://doi.org/10.1016/j.jaci.2012.10.032

Campana L, Kenyon J, Zhalehdoust-Sani S, Tzeng YS, Sun Y, Albert M, Lutchen KR (2009) Probing airway conditions governing ventilation defects in asthma via hyperpolarized MRI image functional modeling. J Appl Physiol (Bethesda, Md : 1985) 106(4):1293–1300. https://doi.org/10.1152/japplphysiol.91428.2008

Capaldi DPI, Sheikh K, Eddy RL, Guo F, Svenningsen S, Nair P, McCormack DG, Parraga G (2017) Free-breathing functional pulmonary MRI: response to bronchodilator and Bronchoprovocation in severe asthma. Acad Radiol 24:1268. https://doi.org/10.1016/j.acra.2017.04.012

Capaldi DPI, Eddy RL, Svenningsen S, Guo F, Baxter JSH, McLeod AJ, Nair P, McCormack DG, Parraga G (2018) Free-breathing pulmonary MR imaging to quantify regional ventilation. Radiology 287(2):693–704. https://doi.org/10.1148/radiol.2018171993

Castro M, Fain SB, Hoffman EA, Gierada DS, Erzurum SC, Wenzel S (2011) Lung imaging in asthmatic patients: the picture is clearer. J Allergy Clin Immunol 128(3):467–478. https://doi.org/10.1016/j.jaci.2011.04.051

Chae EJ, Seo JB, Lee J (2010a) Xenon ventilation imaging using dual-energy computed tomography in asthmatics: initial experience. Investig Radiol 45:354

Chae EJ, Seo JB, Lee J, Kim N, Goo HW, Lee HJ, Lee CW, Ra SW, Oh YM, Cho YS (2010b) Xenon ventilation imaging using dual-energy computed tomography in asthmatics: initial experience. Investig Radiol 45(6):354–361. https://doi.org/10.1097/RLI.0b013e3181dfdae0

Chen DL, Schuster DP (2006) Imaging pulmonary inflammation with positron emission tomography: a biomarker for drug development. Mol Pharm 3(5):488–495. https://doi.org/10.1021/mp060050w

Chiro GD, Brooks RA, Kessler RM, Johnston GS, Jones AE, Herdt JR, Sheridan WT (1979) Tissue signatures with dual-energy computed tomography. Radiology 131(2):521–523. https://doi.org/10.1148/131.2.521

Choi S, Hoffman EA, Wenzel SE, Castro M, Lin CL (2014) Improved CT-based estimate of pulmonary gas trapping accounting for scanner and lung-volume variations in a multicenter asthmatic study. J Appl Physiol (Bethesda, Md : 1985) 117(6):593–603. https://doi.org/10.1152/japplphysiol.00280.2014

Choi S, Hoffman EA, Wenzel SE, Castro M, Fain SB, Jarjour NN, Schiebler ML, Chen K, Lin CL (2015) Quantitative assessment of multiscale structural and functional alterations in asthmatic populations. J Appl Physiol (Bethesda, Md : 1985) 118(10):1286–1298. https://doi.org/10.1152/japplphysiol.01094.2014

Choi S, Hoffman EA, Wenzel SE, Castro M, Fain S, Jarjour N, Schiebler ML, Chen K, Lin CL, National Heart L, Blood Institute's Severe Asthma Research P (2017) Quantitative computed tomographic imaging-based clustering differentiates asthmatic subgroups with distinctive clinical phenotypes. J Allergy Clin Immunol 140:690. https://doi.org/10.1016/j.jaci.2016.11.053

Chon D, Beck KC, Simon BA, Shikata H, Saba OI, Hoffman EA (2007) Effect of low-xenon and krypton supplementation on signal/noise of regional CT-based ventilation measurements. J Appl Physiol (Bethesda, Md : 1985) 102(4):1535–1544. https://doi.org/10.1152/japplphysiol.01235.2005

Chung KF, Wenzel SE, Brozek JL, Bush A, Castro M, Sterk PJ, Adcock IM, Bateman ED, Bel EH, Bleecker ER, Boulet LP, Brightling C, Chanez P, Dahlen SE, Djukanovic R, Frey U, Gaga M, Gibson P, Hamid Q, Jajour NN, Mauad T, Sorkness RL, Teague WG (2014) International ERS/ATS guidelines on definition, evaluation and treatment of severe asthma. Eur Respir J 43(2):343–373. https://doi.org/10.1183/09031936.00202013

Costella S, Kirby M, Maksym GN, McCormack DG, Paterson NA, Parraga G (2012) Regional pulmonary response to a methacholine challenge using hyperpolarized (3)He magnetic resonance imaging. Respirology (Carlton, Vic) 17(8):1237–1246. https://doi.org/10.1111/j.1440-1843.2012.02250.x

Couch MJ, Ball IK, Li T, Fox MS, Littlefield SL, Biman B, Albert MS (2013) Pulmonary ultrashort echo time 19F MR imaging with inhaled fluorinated gas mixtures in healthy volunteers: feasibility. Radiology 269(3):903–909. https://doi.org/10.1148/radiol.13130609

Couch MJ, Ball IK, Li T, Fox MS, Ouriadov AV, Biman B, Albert MS (2014) Inert fluorinated gas MRI: a new pulmonary imaging modality. NMR Biomed 27(12):1525–1534. https://doi.org/10.1002/nbm.3165

Coxson HO, Lam S (2009) Quantitative assessment of the airway wall using computed tomography and optical coherence tomography. Proc Am Thorac Soc 6(5):439–443. https://doi.org/10.1513/pats.200904-015AW

Ebner L, He M, Virgincar RS, Heacock T, Kaushik SS, Freemann MS, McAdams HP, Kraft M, Driehuys B (2017) Hyperpolarized 129Xenon magnetic resonance imaging to quantify regional ventilation differences in mild to moderate asthma: a prospective comparison between semiautomated ventilation defect percentage calculation and pulmonary function tests. Investig Radiol 52(2):120–127. https://doi.org/10.1097/rli.0000000000000322

Eddy RL, Svenningsen S, Kassay A, McCormack DG, Nair P, Parraga G (2017) This is what asthma looks like: review of new and emerging functional imaging methods and results. Can J Respir Crit Care Sleep Med 2:1–14. https://doi.org/10.1080/24745332.2017.1393637

Edelman RR, Hatabu H, Tadamura E, Li W, Prasad PV (1996) Noninvasive assessment of regional ventilation in the human lung using oxygen-enhanced magnetic resonance imaging. Nat Med 2(11):1236–1239

Fain SB, Gonzalez-Fernandez G, Peterson ET, Evans MD, Sorkness RL, Jarjour NN, Busse WW, Kuhlman JE (2008) Evaluation of structure-function relationships in asthma using multidetector CT and hyperpolarized He-3 MRI. Acad Radiol 15(6):753–762. https://doi.org/10.1016/j.acra.2007.10.019

Fain S, Schiebler ML, McCormack DG, Parraga G (2010) Imaging of lung function using hyperpolarized helium-3 magnetic resonance imaging: review of current and emerging translational methods and applications. J Magn Reson Imaging 32(6):1398–1408. https://doi.org/10.1002/jmri.22375

Fuld MK, Halaweish AF, Newell JD Jr, Krauss B, Hoffman EA (2013) Optimization of dual-energy xenon-computed tomography for quantitative assessment of regional pulmonary ventilation. Investig Radiol 48(9):629–637. https://doi.org/10.1097/RLI.0b013e31828ad647

Geier ET, Neuhart I, Theilmann RJ, Prisk GK, Sa RC (2018) Spatial persistence of reduced specific ventilation following methacholine challenge in the healthy human lung. J Appl Physiol (Bethesda, Md : 1985) 124(5):1222–1232. https://doi.org/10.1152/japplphysiol.01032.2017

Global Initiative for Asthma (GINA) (2006) Global Strategy for Asthma Management and Prevention: Revised 2006

Goddard PR, Nicholson EM, Laszlo G, Watt I (1982) Computed tomography in pulmonary emphysema. Clin Radiol 33(4):379–387

Goldin JG, Tashkin DP, Kleerup EC, Greaser LE, Haywood UM, Sayre JW, Simmons MD, Suttorp M, Colice GL, Vanden Burgt JA, Aberle DR (1999) Comparative effects of hydrofluoroalkane and chlorofluorocarbon beclomethasone dipropionate inhalation on small airways: assessment with functional helical thin-section computed tomography. J Allergy Clin Immunol 104(6):S258–S267

Gono H, Fujimoto K, Kawakami S, Kubo K (2003) Evaluation of airway wall thickness and air trapping by HRCT in asymptomatic asthma. Eur Respir J 22(6):965–971

Goo HW, Yu J (2011) Redistributed regional ventilation after the administration of a bronchodilator demonstrated on xenon-inhaled dual-energy CT in a patient with asthma. Korean J Radiol 12(3):386–389. https://doi.org/10.3348/kjr.2011.12.3.386

Goo HW, Yang DH, Hong SJ, Yu J, Kim BJ, Seo JB, Chae EJ, Lee J, Krauss B (2010) Xenon ventilation CT using dual-source and dual-energy technique in children with bronchiolitis obliterans: correlation of xenon and CT density values with pulmonary function test results. Pediatr Radiol 40(9):1490–1497. https://doi.org/10.1007/s00247-010-1645-3

Goo HW, Yang DH, Kim N, Park SI, Kim DK, Kim EA (2011) Collateral ventilation to congenital hyperlucent lung lesions assessed on xenon-enhanced dynamic dual-energy CT: an initial experience. Korean J Radiol 12(1):25–33. https://doi.org/10.3348/kjr.2011.12.1.25

Grenier P, Mourey-Gerosa I, Benali K, Brauner MW, Leung AN, Lenoir S, Cordeau MP, Mazoyer B (1996) Abnormalities of the airways and lung parenchyma in asthmatics: CT observations in 50 patients and inter- and intraobserver variability. Eur Radiol 6(2):199–206

Guo FH, De Raeve HR, Rice TW, Stuehr DJ, Thunnissen FB, Erzurum SC (1995) Continuous nitric oxide synthesis by inducible nitric oxide synthase in normal human airway epithelium in vivo. Proc Natl Acad Sci U S A 92(17):7809–7813

Gupta S, Siddiqui S, Haldar P, Entwisle JJ, Mawby D, Wardlaw AJ, Bradding P, Pavord ID, Green RH, Brightling CE (2010) Quantitative analysis of high-resolution computed tomography scans in severe asthma subphenotypes. Thorax 65(9):775–781. https://doi.org/10.1136/thx.2010.136374

Gutberlet M, Kaireit TF, Voskrebenzev A, Lasch F, Freise J, Welte T, Wacker F, Hohlfeld JM, Vogel-Claussen J (2018) Free-breathing dynamic (19)F gas MR imaging for mapping of regional lung ventilation in patients with COPD. Radiology 286(3):1040–1051. https://doi.org/10.1148/radiol.2017170591

Hachulla AL, Pontana F, Wemeau-Stervinou L, Khung S, Faivre JB, Wallaert B, Cazaubon JF, Duhamel A, Perez T, Devos P, Remy J, Remy-Jardin M (2012) Krypton ventilation imaging using dual-energy CT in chronic obstructive pulmonary disease patients: initial experience. Radiology 263(1):253–259. https://doi.org/10.1148/radiol.12111211

Halaweish AF, Charles HC (2014) Physiorack: an integrated MRI safe/conditional, gas delivery, respiratory gating, and subject monitoring solution for structural and functional assessments of pulmonary function. J Magn Reson Imaging 39(3):735–741. https://doi.org/10.1002/jmri.24219

Halaweish AF, Moon RE, Foster WM, Soher BJ, McAdams HP, MacFall JR, Ainslie MD, MacIntyre NR, Charles HC (2013) Perfluoropropane gas as a magnetic resonance lung imaging contrast agent in humans. Chest 144(4):1300–1310. https://doi.org/10.1378/chest.12-2597

Hariri LP, Applegate MB, Mino-Kenudson M, Mark EJ, Medoff BD, Luster AD, Bouma BE, Tearney GJ, Suter MJ (2013) Volumetric optical frequency domain imaging of pulmonary pathology with precise correlation to histopathology. Chest 143(1):64–74. https://doi.org/10.1378/chest.11-2797

Harkness LM, Ashton AW, Burgess JK (2015) Asthma is not only an airway disease, but also a vascular disease. Pharmacol Ther 148:17–33. https://doi.org/10.1016/j.pharmthera.2014.11.010

Harris RS, Schuster DP (2007) Visualizing lung function with positron emission tomography. J Appl Physiol (Bethesda, Md : 1985) 102(1):448–458. https://doi.org/10.1152/japplphysiol.00763.2006

Harris RS, Winkler T, Tgavalekos N, Musch G, Melo MF, Schroeder T, Chang Y, Venegas JG (2006) Regional pulmonary perfusion, inflation, and ventilation defects in bronchoconstricted patients with asthma. Am J Respir Crit Care Med 174(3):245–253. https://doi.org/10.1164/rccm.200510-1634OC

Harris RS, Venegas JG, Wongviriyawong C, Winkler T, Kone M, Musch G, Vidal Melo MF, de Prost N, Hamilos DL, Afshar R, Cho J, Luster AD, Medoff BD (2011) 18F-FDG uptake rate is a biomarker of eosinophilic inflammation and airway response in asthma. J Nucl Med 52(11):1713–1720. https://doi.org/10.2967/jnumed.110.086355

He M, Kaushik SS, Robertson SH, Freeman MS, Virgincar RS, McAdams HP, Driehuys B (2014) Extending semiautomatic ventilation defect analysis for hyperpolarized (129)Xe ventilation MRI. Acad Radiol 21(12):1530–1541. https://doi.org/10.1016/j.acra.2014.07.017

Huang HJ, Isakow W, Byers DE, Engle JT, Griffin EA, Kemp D, Brody SL, Gropler RJ, Miller JP, Chu W, Zhou D, Pierce RA, Castro M, Mach RH, Chen DL (2015) Imaging pulmonary inducible nitric oxide synthase expression with PET. J Nucl Med 56(1):76–81. https://doi.org/10.2967/jnumed.114.146381

Hwang HJ, Hoffman EA, Lee CH, Goo JM, Levin DL, Kauczor HU, Seo JB (2017) The role of dual-energy computed tomography in the assessment of pulmonary function. Eur J Radiol 86:320–334. https://doi.org/10.1016/j.ejrad.2016.11.010

Jung JW, Kwon JW, Kim TW, Lee SH, Kim KM, Kang HR, Park HW, Lee CH, Goo JM, Min KU, Cho SH (2013) New insight into the assessment of asthma using xenon ventilation computed tomography. Ann Allergy Asthma Immunol 111(2):90–95. e92. https://doi.org/10.1016/j.anai.2013.04.019

Kaireit TF, Gutberlet M, Voskrebenzev A, Freise J, Welte T, Hohlfeld JM, Wacker F, Vogel-Claussen J (2018) Comparison of quantitative regional ventilation-weighted fourier decomposition MRI with dynamic fluorinated gas washout MRI and lung function testing in COPD patients. J Magn Reson Imaging 47(6):1534–1541. https://doi.org/10.1002/jmri.25902

Kasahara K, Shiba K, Ozawa T, Okuda K, Adachi M (2002) Correlation between the bronchial subepithelial layer and whole airway wall thickness in patients with asthma. Thorax 57(3):242–246

Kim WW, Lee CH, Goo JM, Park SJ, Kim JH, Park EA, Cho SH (2012) Xenon-enhanced dual-energy CT of patients with asthma: dynamic ventilation changes after methacholine and salbutamol inhalation. AJR Am J Roentgenol 199(5):975–981. https://doi.org/10.2214/ajr.11.7624

Kirby M, Heydarian M, Svenningsen S, Wheatley A, McCormack DG, Etemad-Rezai R, Parraga G (2012) Hyperpolarized 3He magnetic resonance functional imaging semiautomated segmentation. Acad Radiol 19(2):141–152. https://doi.org/10.1016/j.acra.2011.10.007

Kirby M, Ohtani K, Lopez Lisbona RM, Lee AM, Zhang W, Lane P, Varfolomeva N, Hui L, Ionescu D, Coxson HO, MacAulay C, FitzGerald JM, Lam S (2015) Bronchial thermoplasty in asthma: 2-year follow-up using optical coherence tomography. Eur Respir J 46(3):859–862. https://doi.org/10.1183/09031936.00016815

Ko JP, Brandman S, Stember J, Naidich DP (2012) Dual-energy computed tomography: concepts, performance, and thoracic applications. J Thorac Imaging 27(1):7–22. https://doi.org/10.1097/RTI.0b013e31823fe0e9

Kong X, Sheng HX, Lu GM, Meinel FG, Dyer KT, Schoepf UJ, Zhang LJ (2014) Xenon-enhanced dual-energy CT lung ventilation imaging: techniques and clinical applications. AJR Am J Roentgenol 202(2):309–317. https://doi.org/10.2214/ajr.13.11191

Kruger SJ, Niles DJ, Dardzinski B, Harman A, Jarjour NN, Ruddy M, Nagle SK, Francois CJ, Sorkness RL, Burton RM, Munoz del Rio A, Fain SB (2014) Hyperpolarized Helium-3 MRI of exercise-induced bronchoconstriction during challenge and therapy. J Magn Reson Imaging 39(5):1230–1237. https://doi.org/10.1002/jmri.24272

Kurashima K, Kanauchi T, Hoshi T, Takaku Y, Ishiguro T, Takayanagi N, Ubukata M, Sugita Y (2008) Effect of early versus late intervention with inhaled corticosteroids on airway wall thickness in patients with asthma. Respirology (Carlton, Vic) 13(7):1008–1013. https://doi.org/10.1111/j.1440-1843.2008.01384.x

de Lange EE, Altes TA, Patrie JT, Gaare JD, Knake JJ, Mugler JP 3rd, Platts-Mills TA (2006) Evaluation of asthma with hyperpolarized helium-3 MRI: correlation with clinical severity and spirometry. Chest 130(4):1055–1062. https://doi.org/10.1378/chest.130.4.1055

de Lange EE, Altes TA, Patrie JT, Parmar J, Brookeman JR, Mugler JP 3rd, Platts-Mills TA (2007) The variability of regional airflow obstruction within the lungs of patients with asthma: assessment with hyperpolarized helium-3 magnetic resonance imaging. J Allergy Clin Immunol 119(5):1072–1078. https://doi.org/10.1016/j.jaci.2006.12.659

de Lange EE, Altes TA, Patrie JT, Battiston JJ, Juersivich AP, Mugler JP 3rd, Platts-Mills TA (2009) Changes in regional airflow obstruction over time in the lungs of patients with asthma: evaluation with 3He MR imaging. Radiology 250(2):567–575. https://doi.org/10.1148/radiol.2502080188

Lee YM, Park JS, Hwang JH, Park SW, Uh ST, Kim YH, Park CS (2004) High-resolution CT findings in patients with near-fatal asthma: comparison of patients with mild-to-severe asthma and normal control subjects and changes in airway abnormalities following steroid treatment. Chest 126(6):1840–1848. https://doi.org/10.1378/chest.126.6.1840

Little SA, Sproule MW, Cowan MD, Macleod KJ, Robertson M, Love JG, Chalmers GW, McSharry CP, Thomson NC (2002) High resolution computed tomographic assessment of airway wall thickness in chronic asthma: reproducibility and relationship with lung function and severity. Thorax 57(3):247–253

Lu GM, Zhao Y, Zhang LJ, Schoepf UJ (2012) Dual-energy CT of the lung. AJR 199:S40

Mayo JR (1994) Magnetic resonance imaging of the chest. Where we stand. Radiol Clin N Am 32(4): 795–809

Mitsunobu F, Mifune T, Ashida K, Hosaki Y, Tsugeno H, Okamoto M, Harada S, Takata S, Tanizaki Y (2001) Influence of age and disease severity on high resolution CT lung densitometry in asthma. Thorax 56(11):851–856

Newman KB, Lynch DA, Newman LS, Ellegood D, Newell JD Jr (1994) Quantitative computed tomography detects air trapping due to asthma. Chest 106(1):105–109

Niimi A, Matsumoto H, Amitani R, Nakano Y, Mishima M, Minakuchi M, Nishimura K, Itoh H, Izumi T (2000) Airway wall thickness in asthma assessed by computed tomography. Relation to clinical indices. Am J Respir Crit Care Med 162(4 Pt 1):1518–1523. https://doi.org/10.1164/ajrccm.162.4.9909044

Niimi A, Matsumoto H, Takemura M, Ueda T, Chin K, Mishima M (2003) Relationship of airway wall thickness to airway sensitivity and airway reactivity in asthma. Am J Respir Crit Care Med 168(8):983–988. https://doi.org/10.1164/rccm.200211-1268OC

Niimi A, Matsumoto H, Amitani R, Nakano Y, Sakai H, Takemura M, Ueda T, Chin K, Itoh H, Ingenito EP, Mishima M (2004) Effect of short-term treatment with inhaled corticosteroid on airway wall thickening in asthma. Am J Med 116(11):725–731. https://doi.org/10.1016/j.amjmed.2003.11.026

Niles DJ, Kruger SJ, Dardzinski BJ, Harman A, Jarjour NN, Ruddy M, Nagle SK, Francois CJ, Fain SB (2013) Exercise-induced bronchoconstriction: reproducibility of hyperpolarized 3He MR imaging. Radiology 266(2):618–625. https://doi.org/10.1148/radiol.12111973

Ohno Y, Koyama H, Matsumoto K, Onishi Y, Nogami M, Takenaka D, Matsumoto S, Sugimura K (2011) Oxygen-enhanced MRI vs. quantitatively assessed thin-section CT: pulmonary functional loss assessment and clinical stage classification of asthmatics. Eur J Radiol 77(1):85–91. https://doi.org/10.1016/j.ejrad.2009.06.027

Ohno Y, Nishio M, Koyama H, Seki S, Yoshikawa T, Matsumoto S, Obara M, van Cauteren M, Sugimura K (2014) Asthma: comparison of dynamic oxygen-enhanced MR imaging and quantitative thin-section CT for evaluation of clinical treatment. Radiology 273(3):907–916. https://doi.org/10.1148/radiol.14132660

Okazawa M, Muller N, McNamara AE, Child S, Verburgt L, Pare PD (1996) Human airway narrowing measured using high resolution computed tomography. Am J Respir Crit Care Med 154(5):1557–1562. https://doi.org/10.1164/ajrccm.154.5.8912780

Park EA, Goo JM, Park SJ, Lee HJ, Lee CH, Park CM, Yoo CG, Kim JH (2010) Chronic obstructive pulmonary disease: quantitative and visual ventilation pattern analysis at xenon ventilation CT performed by using a dual-energy technique. Radiology 256(3):985–997. https://doi.org/10.1148/radiol.10091502

Park SJ, Lee CH, Goo JM, Kim JH, Park EA, Jung JW, Park HW, Cho SH (2012) Quantitative analysis of dynamic airway changes after methacholine and salbutamol inhalation on xenon-enhanced chest CT. Eur Radiol 22(11):2441–2450. https://doi.org/10.1007/s00330-012-2516-0

Park HW, Jung JW, Kim KM, Kim TW, Lee SH, Lee CH, Goo JM, Min KU, Cho SH (2014) Xenon ventilation computed tomography and the management of asthma in the elderly. Respirology (Carlton, Vic) 19(3):389–395. https://doi.org/10.1111/resp.12242

Remy-Jardin M, Faivre JB, Pontana F, Molinari F, Tacelli N, Remy J (2014) Thoracic applications of dual energy. Semin Respir Crit Care Med 35(1):64–73. https://doi.org/10.1055/s-0033-1363452

Sa RC, Cronin MV, Henderson AC, Holverda S, Theilmann RJ, Arai TJ, Dubowitz DJ, Hopkins SR, Buxton RB, Prisk GK (2010) Vertical distribution of specific ventilation in normal supine humans measured by oxygen-enhanced proton MRI. J Appl Physiol (Bethesda, Md : 1985) 109(6):1950–1959. https://doi.org/10.1152/japplphysiol.00220.2010

Sa RC, Asadi AK, Theilmann RJ, Hopkins SR, Prisk GK, Darquenne C (2014) Validating the distribution of specific ventilation in healthy humans measured using proton MR imaging. J Appl Physiol (Bethesda, Md

: 1985) 116(8):1048–1056. https://doi.org/10.1152/japplphysiol.00982.2013

Samee S, Altes T, Powers P, de Lange EE, Knight-Scott J, Rakes G, Mugler JP 3rd, Ciambotti JM, Alford BA, Brookeman JR, Platts-Mills TA (2003) Imaging the lungs in asthmatic patients by using hyperpolarized helium-3 magnetic resonance: assessment of response to methacholine and exercise challenge. J Allergy Clin Immunol 111(6):1205–1211

Schuster DP (2007) The opportunities and challenges of developing imaging biomarkers to study lung function and disease. Am J Respir Crit Care Med 176(3):224–230. https://doi.org/10.1164/rccm.200703-462PP

Scoggin CH, Sahn SA, Petty TL (1977) Status asthmaticus. A nine-year experience. JAMA 238(11):1158–1162

Shea DA, Morgan D (2010) The helium-3 shortage: Supply, demand, and options for congress. Congressional Research Service, Library of Congress

Siddiqui S, Gupta S, Cruse G, Haldar P, Entwisle J, McDonald S, Whithers PJ, Hainsworth SV, Coxson HO, Brightling C (2009) Airway wall geometry in asthma and nonasthmatic eosinophilic bronchitis. Allergy 64(6):951–958. https://doi.org/10.1111/j.1398-9995.2009.01951.x

Simon BA, Kaczka DW, Bankier AA, Parraga G (2012) What can computed tomography and magnetic resonance imaging tell us about ventilation? J Appl Physiol (Bethesda, MD: 1985) 113(4):647–657. https://doi.org/10.1152/japplphysiol.00353.2012

Svenningsen S, Kirby M, Starr D, Leary D, Wheatley A, Maksym GN, McCormack DG, Parraga G (2013) Hyperpolarized (3) He and (129) Xe MRI: differences in asthma before bronchodilation. J Magn Reson Imaging 38(6):1521–1530. https://doi.org/10.1002/jmri.24111

Svenningsen S, Guo F, Kirby M, Choy S, Wheatley A, McCormack DG, Parraga G (2014a) Pulmonary functional magnetic resonance imaging: asthma temporal-spatial maps. Acad Radiol 21(11):1402–1410. https://doi.org/10.1016/j.acra.2014.08.002

Svenningsen S, Kirby M, Starr D, Coxson HO, Paterson NA, McCormack DG, Parraga G (2014b) What are ventilation defects in asthma? Thorax 69(1):63–71. https://doi.org/10.1136/thoraxjnl-2013-203711

Svenningsen S, Nair P, Guo F, McCormack DG, Parraga G (2016) Is ventilation heterogeneity related to asthma control? Eur Respir J 48(2):370–379. https://doi.org/10.1183/13993003.00393-2016

Tajik JK, Chon D, Won C, Tran BQ, Hoffman EA (2002) Subsecond multisection CT of regional pulmonary ventilation. Acad Radiol 9(2):130–146

Takahashi N, Ishibashi Y, Murakami Y, Shimizu H, Ohta Y, Asanuma T, Katoh H, Sano K, Shimada T (2000) Beneficial effect of combination therapy with ozagrel and pranlukast in exercise-induced asthma demonstrated by krypton-81 m ventilation scintigraphy--a case report. Ann Acad Med Singap 29(6):766–769

Taylor IK, Hill AA, Hayes M, Rhodes CG, O'Shaughnessy KM, O'Connor BJ, Jones HA, Hughes JM, Jones T, Pride NB, Fuller RW (1996) Imaging allergen-invoked airway inflammation in atopic asthma with [18F]-fluorodeoxyglucose and positron emission tomography. Lancet (London, England) 347(9006):937–940

Teague WG, Tustison NJ, Altes TA (2014) Ventilation heterogeneity in asthma. J Asthma 51(7):677–684. https://doi.org/10.3109/02770903.2014.914535

Tgavalekos NT, Venegas JG, Suki B, Lutchen KR (2003) Relation between structure, function, and imaging in a three-dimensional model of the lung. Ann Biomed Eng 31(4):363–373

Tgavalekos NT, Tawhai M, Harris RS, Musch G, Vidal-Melo M, Venegas JG, Lutchen KR (2005) Identifying airways responsible for heterogeneous ventilation and mechanical dysfunction in asthma: an image functional modeling approach. J Appl Physiol (Bethesda, Md : 1985) 99(6):2388–2397. https://doi.org/10.1152/japplphysiol.00391.2005

Tgavalekos NT, Musch G, Harris RS, Vidal Melo MF, Winkler T, Schroeder T, Callahan R, Lutchen KR, Venegas JG (2007) Relationship between airway narrowing, patchy ventilation and lung mechanics in asthmatics. Eur Respir J 29(6):1174–1181. https://doi.org/10.1183/09031936.00113606

Thomen RP, Sheshadri A, Quirk JD, Kozlowski J, Ellison HD, Szczesniak RD, Castro M, Woods JC (2015) Regional ventilation changes in severe asthma after bronchial thermoplasty with (3)He MR imaging and CT. Radiology 274(1):250–259. https://doi.org/10.1148/radiol.14140080

Trivedi A, Hall C, Hoffman EA, Woods JC, Gierada DS, Castro M (2017) Using imaging as a biomarker for asthma. J Allergy Clin Immunol 139(1):1–10. https://doi.org/10.1016/j.jaci.2016.11.009

Tschirren J, Hoffman EA, McLennan G, Sonka M (2005) Intrathoracic airway trees: segmentation and airway morphology analysis from low-dose CT scans. IEEE Trans Med Imaging 24(12):1529–1539

Tunon-de-Lara JM, Laurent F, Giraud V, Perez T, Aguilaniu B, Meziane H, Basset-Merle A, Chanez P (2007) Air trapping in mild and moderate asthma: effect of inhaled corticosteroids. J Allergy Clin Immunol 119(3):583–590. https://doi.org/10.1016/j.jaci.2006.11.005

Tzeng YS, Lutchen K, Albert M (2009) The difference in ventilation heterogeneity between asthmatic and healthy subjects quantified using hyperpolarized 3He MRI. J Appl Physiol (Bethesda, Md : 1985) 106(3):813–822. https://doi.org/10.1152/japplphysiol.01133.2007

Ueda T, Niimi A, Matsumoto H, Takemura M, Hirai T, Yamaguchi M, Matsuoka H, Jinnai M, Muro S, Chin K, Mishima M (2006) Role of small airways in asthma: investigation using high-resolution computed tomography. J Allergy Clin Immunol 118(5):1019–1025

Venegas JG, Schroeder T, Harris S, Winkler RT, Melo MF (2005a) The distribution of ventilation during bronchoconstriction is patchy and bimodal: a PET imaging study. Respir Physiol Neurobiol 148(1–2):57–64. https://doi.org/10.1016/j.resp.2005.05.023

Venegas JG, Winkler T, Musch G, Vidal Melo MF, Layfield D, Tgavalekos N, Fischman AJ, Callahan RJ, Bellani G, Harris RS (2005b) Self-organized patchiness in asthma as a prelude to catastrophic shifts. Nature 434(7034):777–782. https://doi.org/10.1038/nature03490

Washko GR, Parraga G, Coxson HO (2012) Quantitative pulmonary imaging using computed tomography and magnetic resonance imaging. Respirology (Carlton, Vic) 17(3):432–444. https://doi.org/10.1111/j.1440-1843.2011.02117.x

White CS, Cole RP, Lubetsky HW, Austin JH (1991) Acute asthma. Admission chest radiography in hospitalized adult patients. Chest 100(1):14–16

Williamson JP, McLaughlin RA, Noffsinger WJ, James AL, Baker VA, Curatolo A, Armstrong JJ, Regli A, Shepherd KL, Marks GB, Sampson DD, Hillman DR, Eastwood PR (2011) Elastic properties of the central airways in obstructive lung diseases measured using anatomical optical coherence tomography. Am J Respir Crit Care Med 183(5):612–619. https://doi.org/10.1164/rccm.201002-0178OC

Wolf AP, Fowler JS (1995) Positron emission tomography. Biomedical research and clinical application. Neuroimaging Clin N Am 5(1):87–101

Zeidler MR, Kleerup EC, Goldin JG, Kim HJ, Truong DA, Simmons MD, Sayre JW, Liu W, Elashoff R, Tashkin DP (2006) Montelukast improves regional air-trapping due to small airways obstruction in asthma. Eur Respir J 27(2):307–315. https://doi.org/10.1183/09031936.06.00005605

Functional Assessment of Cystic Fibrosis Lung Disease

Mark O. Wielpütz

Contents

1 **Introduction** 176

2 **Computed Tomography** 177
2.1 Quantification of Airway Changes 177
2.2 Imaging of Ventilation and Perfusion with CT 182
2.3 CT as an Endpoint in Clinical Trials 187

3 **Magnetic Resonance Imaging** 187
3.1 Quantification of Airway Changes 187
3.2 Imaging of Ventilation and Perfusion with MRI 188
3.3 MRI as an Endpoint in Clinical Trials 198

4 **Conclusion** 200

References 200

Abstract

Cystic fibrosis is the most common early lethal genetic disorder in white populations. Defective epithelial ion transport results in highly viscous airway secretions, which provide the basis for chronic inflammation from birth. Newborn screening is implemented in most Western countries, allowing for early treatment in subclinical stage. Imaging plays an increasing role in disease monitoring, when lung function using spirometry is normal. Initially, scoring systems have been used to quantify the heterogeneous structural lung changes in CF, now being supplemented by functional techniques, based on lung pathophysiology. Functional techniques using

M. O. Wielpütz (✉)
Department of Diagnostic and Interventional Radiology, Subdivision of Pulmonary Imaging, University Hospital of Heidelberg, Heidelberg, Germany

Translational Lung Research Center Heidelberg (TLRC), German Lung Research Center (DZL), Heidelberg, Germany

Department of Diagnostic and Interventional Radiology with Nuclear Medicine, Thoraxklinik at the University Hospital of Heidelberg, Heidelberg, Germany
e-mail: mark.wielpuetz@med.uni-heidelberg.de

© Springer Nature Switzerland AG 2021

Y. Ohno et al. (eds.), *Pulmonary Functional Imaging*, Medical Radiology Diagnostic Imaging,
https://doi.org/10.1007/978-3-030-43539-4_10

computed tomography (CT) and magnetic resonance imaging (MRI) can be subdivided into non-contrast and contrast-dependent techniques. The earlier use physiological changes in lung signal to compute images of lung ventilation and perfusion. The latter exploit exogenous injectable and volatile contrast materials in order to induce signal changes related to lung function. Several functional techniques such as paired inspiratory-expiratory CT and 4D perfusion MRI have proven clinically meaningful and robust, and are being developed into imaging endpoint for noninvasive monitoring of disease activity. Initial data available documents their sensitivity to disease progression despite stable lung function and to detect therapy response in small prospective cohorts.

1 Introduction

Cystic fibrosis (CF) is the most common early lethal hereditary disease in whites, which follows an autosomal-recessive pattern (Mall and Hartl 2014; Kerem et al. 1989). Due to a defect of an epithelial chloride channel, the cystic fibrosis transmembrane conductance regulator *CFTR*, an imbalance of the electrolyte and subsequent fluid homeostasis of conducting airways, sweat and gastrointestinal glands results in highly viscous secretions (Mall and Boucher 2014; Mall 2008). Besides abdominal manifestations, pulmonary morbidity and mortality dominate the course of the disease and require intensive medical attention (Mall and Boucher 2006; Dodge et al. 2007; Kerem et al. 1992). Specifically, mucus plugs along the whole tracheobronchial tree obstruct the air in- and outflow, sometimes to a different degree, and lay the basis for recurrent infections and chronic inflammation of the airways and lung parenchyma (Mall and Hartl 2014).

Two major developments have changed the situation of patients to the better, and at the same time have increased the demand for imaging of the course of lung disease. First, extensive improvements in routine care have extended the life span of CF patients beyond the age of 50 in Western countries (Dodge et al. 2007; Stern et al. 2008). Importantly, a completely new class of drugs has been introduced into the medical field very recently, which modify residual activity of the *CFTR* and can, in some *CFTR* genotypes, restore a channel conductance close to normal (Davies et al. 2013; Graeber et al. 2015; Ratjen et al. 2017). Second, screening programs in most Western countries have been established as part of the routine newborn screening, which aim at preventing or at least delaying irreversible lung destruction by starting therapy as early as possible (Sommerburg et al. 2010, 2015; Mall et al. 2016; Ramsey et al. 2012). In consequence, the life span in which CF patients require medical attention is extended in both directions, towards infancy as well as towards seniority. Due to improved care, many CF patients now retain a normal FEV1 through a longer period of time. Together with the early diagnosis in infancy this means that spirometry is not a sufficient marker for disease activity and therapy efficacy anymore, as it has been in the past decades (Kerem et al. 1992), and that imaging is becoming more and more important in order to grade disease severity in presymptomatic infants as well as in adults with conserved lung function.

As laid out in Chap. 1, of this compendium, airway obstruction results in vascular constriction through the mechanism of hypoxic pulmonary vasoconstriction (HPV, Euler-Liljestrand reflex) (Hopkins et al. 2012). Together with localized hyperinflation in case of partial airway obstruction (so-called air trapping), which blocks mainly air outflow, the regional decrease in blood volume induces distinct changes in lung tissue composition, which can be captured by cross-sectional imaging, and are enhanced by respiratory maneuvers as well as gaseous or injectable contrast materials during image data acquisition. In addition to direct ventilation imaging, the HPV is thus the most important basis for using perfusion imaging in airways disease, because perfusion imaging can act as a mirror for ventilation imaging.

One important aspect of CF needs to be introduced, because many imaging studies reported below have used this condition as a model to test sensitivity of imaging for therapy-induced changes. CF patients often experience abrupt declines of their clinical condition due to acute pulmonary infection. Although there is no exact definition of these pulmonary exacerbations, which may occur several times per year and may drive rapid disease progression, a practical definition can be derived from previous studies. Major criteria are change in sputum (amount, color), hemoptysis (new/more), new/increased dyspnea, fever, malaise, fatigue, or lethargy, decrease in pulmonary function by 10% or more from a previously recorded value, and radiographic changes indicative of pulmonary infection (consolidation) (Rosenfeld et al. 2012; Fuchs et al. 1994).

This chapter aims at explaining the most important functional imaging techniques in CT and MRI that have been used in patients with CF. The multiple functional techniques available may in general be differentiated into techniques that require the administration of exogenous contrast material (inhalative, injectable) to generate a signal representative of lung function, and those techniques that directly infer such signal from the physiological respiratory and cardiac cycle by elaborate acquisition and post-processing techniques. Some of these techniques have left the field of feasibility studies and entered the arena of pathophysiological and clinical studies, and sometimes even made their way into routine patient care. For CT, this obviously refers to paired inspiratory-expiratory CT. For MRI, contrast-enhanced perfusion MRI and hyperpolarized gas MRI are the most robust and widely used techniques. After having read this chapter the reader should acknowledge that besides highly resolved structural imaging, CF specifically benefits from functional imaging techniques in clinical routine and research. For a review of CF with emphasis on structural imaging, the reader may also refer to other dedicated work and book chapters (Wielpütz et al. 2016; Nagle et al. 2017).

2 Computed Tomography

CT techniques discussed in this chapter are mostly non-contrast dependent. So far, dual-energy techniques obtaining iodine perfusion CT and also Xe-ventilation CT have not been used considerably to functionally assess the cystic fibrosis lung disease.

2.1 Quantification of Airway Changes

2.1.1 Scoring

In the past decade, some authors have suggested to use limited slice sampling to reduce radiation exposure especially in young children with CF (Sly et al. 2009; O'connor et al. 2010). However, volumetric multidetector CT with reconstructed overlapping slice thicknesses of $\leq$1.5 mm has the highest sensitivity for morphological changes. Further, software-based post-processing with segmentation of airways, vasculature, and lung lobes depends on high volumetric resolution. Thus, isotropic helical CT should be preferred to incremental CT for functional assessment, even though no valid clinical guidelines exist (Kauczor et al. 2011; Mott et al. 2013). These datasets not only allow for exact comparison of follow-up exams, multiplanar reformats, and maximum intensity projections (MIP) for better identification of airway changes, but also enable dedicated post-processing with advanced software tools (Kauczor et al. 2011; Wielpütz et al. 2013b, 2016).

Main structural changes to be captured by scoring systems are airway wall thickening bronchiectasis, mucus plugging, consolidations as well as mosaicism, air trapping and emphysema (Hansell et al. 2008). Scoring systems for X-ray, CT, and also MRI seek to differentially capture these changes, which are heterogeneously distributed among individuals as well as in a single lung affected by CF with a numeric value, which represents the amount of abnormalities present, as well as an indicator of the location. Numeric values are assigned to the different airway and

parenchyma pathologies found in CF, in order to quantify the regional prevalence and extent of different abnormalities in the CF lung. It is intended that the higher a sum of these numeric values (sum score, composite score), the more severely a patient's lung is affected. To give these scoring systems prognostic value, they are usually cross-validated against lung function testing, which is still the main prognosticator in CF, as discussed later in this chapter. Some changes are considered potentially reversible, because they can react to mobilization of mucus and reduction of inflammation by adequate therapy, which are airway wall thickening, mucus plugging, consolidations, or air trapping. Other findings such as (extensive) bronchiectasis or emphysema and destroyed lobes as well as dilated bronchial arteries are thought to be signs of irreversible lung destruction and function loss (Table 1).

Initially, visual scoring systems have been developed for chest X-ray (e.g., Chrispin-Norman Score, Brasfield Score, Wisconsin Score) (Chrispin and Norman 1974; Brasfield et al. 1979; Weatherly et al. 1993; Benden et al. 2005), then for CT (e.g., Bhalla Score, Helbich Score, Brody Score) (Bhalla et al. 1991; Helbich et al. 1999; Brody et al. 2005a), and more recently for MRI (Eichinger Score) (Eichinger et al. 2012). Such scores allow for a semiquantitative statistical evaluation and may facilitate follow-up and therapy monitoring. A more advanced approach uses a grid overlay on selected CT slices and allows a reader to assign a pathology to each lung-containing square, which results into a semiautomatic score of disease severity (PRAGMA-CF system) (Rosenow et al. 2015). CT correlates better with lung function tests than chest X-ray, indicating that cross-sectional imaging provides a more precise grading (Demirkazik et al. 2001). However, the main finding using scoring was that CT scoring proved to be superior over pulmonary function testing in detecting subtle disease progression (De Jong et al. 2006; Brody et al. 2005b). Obviously, the different abnormalities in the CF lung have a very heterogeneous distribution within one patient, and between patients, and resulting abnormalities in spirometry (mainly percent predicted forced expiratory volume in 1 s, FEV1%) only reflect an overall marker of disease severity. Because relatively normal lung can compensate for diseased lung during early disease, such regional changes over time can thus go unnoticed until more severe destruction has occurred. This is the basis for using cross-sectional imaging as a tool to grade disease activity in CF, which is the main lesson to be learned from correlative studies with imaging vs. spirometry.

Table 1 Imaging hallmarks in cystic fibrosis

Potentially reversible	Irreversible
Mucus plugging	Bronchiectasis
Airway wall thickening	Emphysema
Consolidation	Dilated bronchial arteries
Mosaicism	Destroyed lobe
Air trapping	

2.1.2 Initial Steps of Software-Based Quantification

Because visual scoring is somewhat cumbersome and subject to inter- and intra-reader variability (Terheggen-Lagro et al. 2003; Brody et al. 2006; Eichinger et al. 2012), a fully automatic computational approach seems desirable to allow for a more precise, reproducible, and objective quantification of image information (Kauczor et al. 2011; Wielpütz et al. 2016). As a form of software-supported scoring, the PRAGMA-CF system has been developed, which uses a grid overlay on slice samples in order to provide a basis for spatial distribution and quantification of airway changes (Rosenow et al. 2015). High potential lies in the direct quantification of airway changes by generation- and lobe-based quantitative post-processing of non-enhanced thin-slice CT datasets (Fig. 1). Putative imaging biomarkers such as wall thickness or airway diameter, air trapping, and emphysema may be derived (Wielpütz et al. 2013b, c), but a high amount of automation is necessary to avoid any user interaction and bias (Wielpütz et al. 2013b).

Several steps are part of the process of quantification of imaging data, and isotropic high-resolution CT is a prerequisite up front. Initially, so-called segmentation is required, which basically means that anatomical structures are

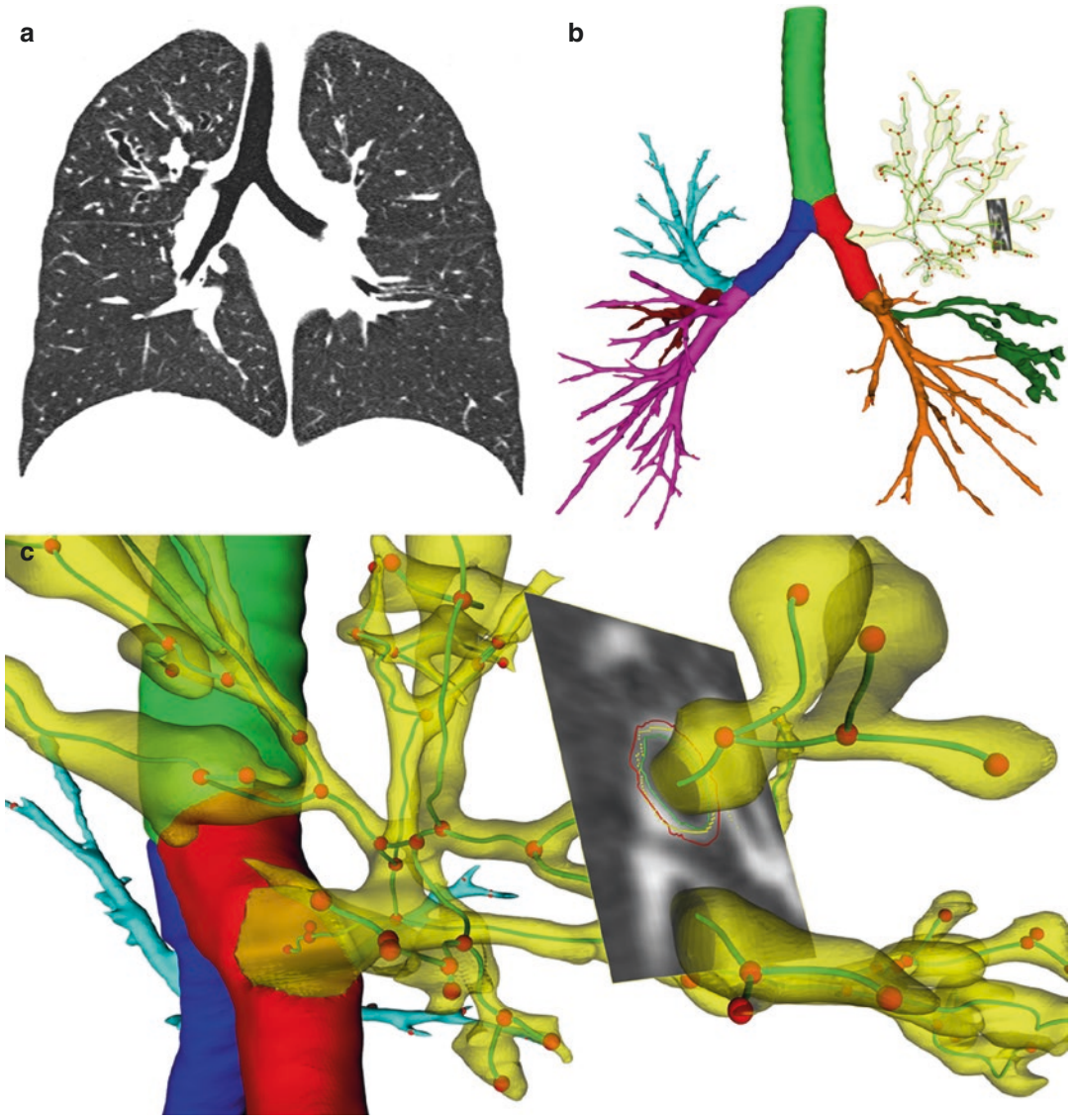


Fig. 1 Airway segmentation. (**a**) Coronal view of a CT from a school-age CF patient with mild disease. Note bronchiectasis in the right upper lobe. (**b**) Airways are segmented by a region-growing algorithm based on voxel density, reaching out from an automatically detected starting point in the tracheal lumen. After successful segmentation, which on average encompasses all airways down to the 8th–tenth generation, the airway tree is skeletonized and a centerline is calculated, which runs exactly in the center of the airway lumen and thus represents the airway axis. (**c**) Magnified view demonstrating the course of the centerlines of each airway segment. Branching points are highlighted. These separate subsequent airway generations. As a secondary reconstruction, an image plane perpendicular to the centerline is generated. These hold the basis for detection and measurement of airway wall geometry. The segmented outer and inner circumference of the airway wall are highlighted in red and green, respectively. Note the grape-like appearance of bronchiectatic airway segments. Figure provided by O. Weinheimer, Heidelberg University, and Terry E. Robinson, Stanford University Palo Alto

spatially recognized and annotated as precisely as possible (Fig. 1). In some cases, the process of registration will be employed subsequently in order to spatially align several CT datasets from the same patient to the same anatomic frame for a direct comparison of voxel information which

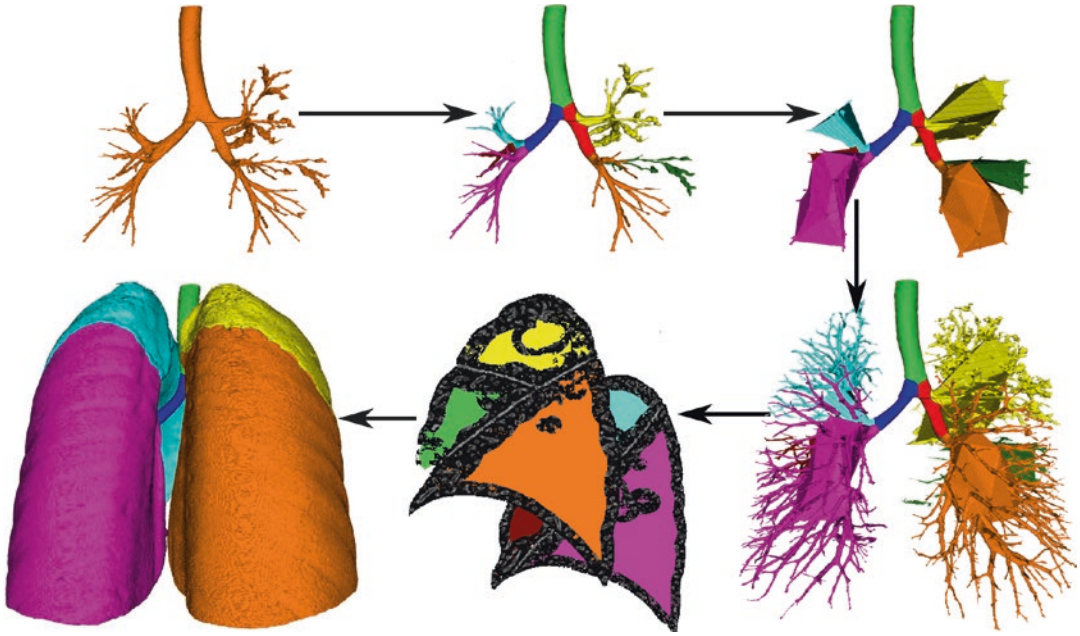


Fig. 2 Lobe segmentation. After segmentation of the tracheobronchial tree, each lobar bronchus is annotated and subsequent segmental and subsegmental airways as labelled. Then, convex hulls are formed according to the subsegmental airways. The vasculature of each lobe is segmented and added subsequently to the hulls in an iterative process. Fissures are detected and added to the lobe information derived from the peripheral vasculature. By a watershed transformation, the lobe segmentation is finalized. From: Konietzke et al. PLoS One 2018 13(4):e0194557

refer to the same anatomical position, e.g., inspiratory and expiratory CT or longitudinal studies (Weinheimer et al. 2018) (Fig. 2). Artificial intelligence-based algorithms may assist with these processes, and the author advises to refer to separate literature elsewhere for this complex topic. Aim of these computational steps is to separate coherent lung anatomy from the image in order to perform quantitative measurements on size, form, density, and inferred variables such as kurtosis of the density histogram, etc. After the initial step of segmenting the lung, potentially lung lobes, and the airway tree lumen, the airway walls need to be derived. For this, a centerline is calculated which runs exactly in the center of the segmented airway lumen (Fig. 1). Subsequent reconstructions use such centerlines to derive secondary reconstructions perpendicular to and along the airway axis between branching points. On these novel image planes, centrifugal rays are cast from the centerline, on which a voxel density profile is generated. These density profiles are the basis for detecting the airway wall whose margins are somewhat blurry, traditionally by the full-width at half maximum (FWHM) approach, or by modern parameter-free integral-based methods (pfIBM) (Weinheimer et al. 2008, 2009, 2011, 2017). Weinheimer et al. demonstrated that with advanced algorithms, airways smaller than 2 mm in diameter can be measured with acceptable error rates below approx. 5% (Weinheimer et al. 2008, 2009). When the inner and outer airway wall margins are carved out of the image data, quantitative airway metrics may be derived. For the airways, plenty of literature exists on quantitative airway measurements which often use overlapping but mostly not identical variables such as airway wall thickness, airway diameter, airway lumen area or luminal diameter, relative wall thickness, wall density, etc. Such measurements can be carried out separately by airway generation, which inevitably leads to a multitude of measurements of the airway tree making correlations with clinical data, disease

severity or therapy outcome rather complex. Some authors suggested the use of so-called pi10, which mostly means that the airway wall thickness is averaged across several generations measured and normalized to a "virtual" airway of 10 mm inner diameter (Grydeland et al. 2009), but which has little been used in CF. In a similar fashion, lobes are separated from the segmented lung (Fig. 2). The addition of lobe information might enhance the value of quantitative airway metrics, as this allows for a more regional differentiation of processes and correlative analyses with parenchymal findings (see below) (Konietzke et al. 2018).

Quantification of airway dimensions has some limitations, partially overlapping those of air-trapping quantification (see below). These can be separated into limitations due to CT acquisition and reconstruction techniques, intra-patient variation, and inter-software variations. Clearly, only airways visible on clinical CT scans can be routinely quantified by post-processing. Achieved CT resolution is essential for the precision of airway measurements (Zach et al. 2012), which is strongly influenced by selecting an appropriate field-of-view for lung reconstructions and slice thickness, obviously. With modern CT scanners, the influence of radiation dose and also iterative reconstruction on quantitative airway metrics is minimal using the identical scanner (Mets et al. 2012; Leutz-Schmidt et al. 2017). On the other hand, variance between different scanner types and manufacturers is significant, especially for lung density measurements required for emphysema and air-trapping analysis (Zach et al. 2012). This is critical also because each institution uses its own scanning protocols, often also different scanners for same patients in follow-up studies, which in total is detrimental for a stringent standardization and reproducibility of quantitative metrics (Kuo et al. 2016). At present, it is advisable to use the same scanner and protocol for intra- and inter-individual comparisons (Kauczor et al. 2011).

To reduce the influence of respiratory effort and degree of inflation, Robinson et al. and other groups suggested to use real-time spirometry in order to trigger the scan at the optimal level of inflation (Robinson et al. 2001, 2003; Salamon et al. 2017). Of note, spirometer-triggering is possible with MRI also, using dedicated MRI-compatible spirometers (Eichinger et al. 2007; Tetzlaff et al. 2008; Ciet et al. 2014). Another approach is to normalize airway metrics to lung volume, thus taking subtle differences in inspiration depth into account. Normalization, however, might also reduce the influence of actual disease, thus counteracting the intention to quantify disease severity, as different levels of disease severity may change lung volumes and hyperinflation.

In an effort to calibrate the CT scanner, Robinson et al. and other groups performed phantom measurements with simulated airways of precisely known dimensions. Scans of such a phantom can be used as a standard to gauge measurements by quantitative software (Robinson et al. 2009). Guo et al. designed a small-size phantom, which can be scanned with each patient and contains tubes and sponges calibrated to a specific diameter, thickness, and density, acting as an internal standard for post-processing (personal communication). Such steps are required to standardize quantitative CT—similar to quality assurance in laboratory medicine—in order to derive imaging biomarkers on which prognosis and therapy decision can be substantiated. Of note, the RSNA "QIBA" initiative as an international consortium is collectively working on this aim (Sieren et al. 2016; Chen-Mayer et al. 2017). Finally, it needs to be mentioned that without standardization of algorithms, variance between software quantifying the same parameter is a major factor contributing to measurement variability (Lim et al. 2016; Wielpütz et al. 2014a), and thus the identical software needs to be employed for quantitative CT at present.

2.1.3 Use of Quantitative Airway Metrics in CF and Correlation with Pulmonary Function Testing

Algorithms to quantify airway dimensions were mostly validated in phantom studies (Weinheimer et al. 2008, 2017), and for some, histological validation in porcine lungs exist as well (Achenbach et al. 2012). Subsequently, studies in other

chronic obstructive lung diseases such as COPD and asthma preceded those in CF. Quantitative CT wall thickening correlated with spirometry (Hasegawa et al. 2006; Niimi et al. 2000; Achenbach et al. 2008), and also with the wall thickness measured histologically in patients (Aysola et al. 2008), further broadening the basis for validation of airway metrics as quantitative and reproducible biomarkers. In COPD and asthma, a significant effect of corticoids and bronchodilators on quantified airway dimensions could be demonstrated as well (Niimi et al. 2004; Hasegawa et al. 2009).

In CF, Montaudon et al. measured bronchial wall and luminal area on CTs of 16 patients (mean age 27.4 years, range 21–44 years) semi-automatically on a limited number of putatively representative airways, using a "Laplacian of Gaussian"-algorithm. The group found a good correlation with visual scoring systems and also spirometry (Montaudon et al. 2007a, b). However, a fully automatic approach is more desirable, in order to quantify the whole visible airway tree and to reduce user-interaction for faster throughput and avoidance of inter-reader variation. Using such an automated approach, Wielpütz et al. segmented up to the 11th airway generation in CF and described significantly increased airway diameters and thickened airway walls throughout all airway generations in 14 school-age and 23 adult CF patients compared to a healthy control group (11 children and 22 adults). The total airway diameter correlated with FEV1% at $r = -0.86$ for the fifth airway generation in adult CF but not in school-age children with CF, nor in the healthy control group (Wielpütz et al. 2013b). More recently, Kuo et al. used an approach in comparison to neighboring pulmonary arteries to classify airways as bronchiectatic, the latter acting as a form of internal standard (Kuo et al. 2017a), reflecting the Fleischner terminology (Hansell et al. 2008). The group could show that the mean airway to artery ratios are increased in 12 scans from young children with CF (mean age 2.9 years, range 0–5 years) from the ARREST-CF cohort compared to a control group (Kuo et al. 2017b). However, such an approach introduces another factor of potential variability into the calculation of airway dimensions, as the vasculature itself may show substantial intra-individual variability (e.g., inflation level, hypoxic vasoconstriction, hydration) (Kuo et al. 2017a), and segmentation of the vasculature is by itself subject to variability independent of airway segmentation as well. Also, one needs to keep in mind that the Fleischner terminology is somewhat arbitrary in defining bronchiectasis and primarily directed at clinical use for visual diagnosis. Another approach is a taper or bronchiectasis index, taking the normally continuous reduction in caliber of an airway from trachea to the periphery into account. Weinheimer et al. could show that a bronchiectasis index correlates moderately with the visual Brody bronchiectasis score with r^2 of 0.25–0.41 in 144 CT scans from 36 school-age children with mild CF (Weinheimer et al. 2017). As a novel approach, fully segmented datasets may also be used as templates for 3D-printing, thus deriving lung models from actual patients, for example, for teaching or training purposes (Mirza et al. 2018).

2.2 Imaging of Ventilation and Perfusion with CT

2.2.1 Non-Contrast-Dependent Techniques

2.2.1.1 Mosaicism

Probably the most common observation of functional changes in the lung, which can be seen without specific acquisition techniques at CT, is mosaic attenuation (Stern et al. 1995; Hansell 2001; Hansell et al. 2008). The impression of a mosaic results from multiple often sharply delineated areas of black lung side-by-side with a ground-glass opacity (GGO). Often, the secondary lobule is the smallest unit of such areas, which can be considered the smallest functional unit in the lung (Fig. 3) (Webb et al. 1988). This is important to appreciate, as this also relates to the spatial resolution required to capture functional changes in the lung. It has a diameter of approx. 10–25 mm (Kauczor and Wielpütz 2018). It is important to note that mosaicism and GGO themselves are also

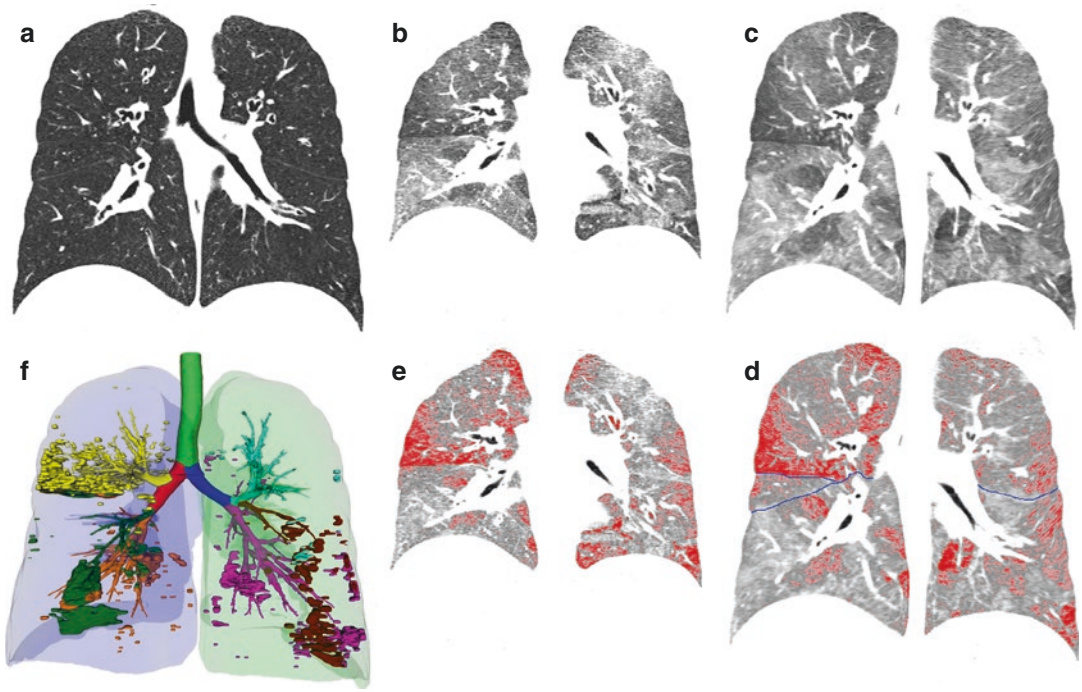


Fig. 3 Registration for air-trapping quantification. (**a**) and (**b**) show a paired inspiratory-expiratory CT from a school-age CF patient with relatively mild disease in coronal plane. (**c**) Registration deforms the expiratory pixel-values into the spatial framework of the inspiratory dataset but maintains pixel density information. Air trapping can be quantified by comparison of registered expiratory to the inspiratory pixel density based on variable thresholds and displayed as an overlay on the registered (**d**) and unregistered (**e**) expiratory map. Fissures are highlighted in (**d**), indicating lobe segmentation used for volume rendering image of air trapping in (**f**). Figure provided by O. Weinheimer, Heidelberg University, Craig J. Galbán, Michigan University Ann Arbor, and Terry E. Robinson, Stanford University Palo Alto

just a result of the limited resolution of clinical CT, because a given lung voxel at CT represents a mixture of airspace, interstitium (incl. Alveolar walls, lymphatic tissue, connective tissue), and blood, and a change of one of these components will invariably change the attenuation of the voxel as a whole. The specificity of mosaicism is limited however, as the abovementioned components may all be affected in pathologic conditions, and mosaicism can thus have multiple causes (Stern et al. 1995). The GGO part of the pattern may actually represent disease, that partially replaces the air from a given voxel, e.g., by interstitial pneumonias and fibrosis, or by partial filling of the alveolar lumen, e.g., by pulmonary hemorrhage. In case mosaic attenuation is a result of functional changes, the "black" bits actually represent the diseased lung due to a removal of blood and an increase in air content of the voxel. Here, primary vascular changes, e.g., pulmonary embolism or chronic-thromboembolic pulmonary hypertension (chapters "Functional Assessment of Pulmonary Venous Thromboembolism" and "Multimodality Imaging of Pulmonary Hypertension: Prognostication of Therapeutic Outcomes"), need to be differentiated from secondary, HPV-induced hypoperfusion with hyperinflation in case of air trapping, which is the case in cystic fibrosis and is what we are actually after in this chapter. Apart from hyperlucencies due to hyperinflation and HPV, irreversible emphysema similar to COPD can be present in CF patients also, and need to be differentiated functionally from potentially reversible air trapping (Esterly and Oppenheimer 1968; Wielpütz et al. 2013c; Mets et al. 2015). In order to differentiate these causes, a CT acquisition in inspiratory and expiratory breath hold has been established.

2.2.1.2 Paired Inspiratory-Expiratory Breath-Hold CT

CT attenuation of a voxel, is, as mentioned above, an average of several compartments which cannot be resolved separately by clinical CT. Partial or complete removal of air from the lung will subsequently increase the density of a voxel towards opacification (consolidation). As long as parts of air are conserved inside such a voxel, it will show (in larger groups) a GGO attenuation. This mechanism is exploited by the additional acquisition of expiratory CT, which can then be compared against the inspiratory CT acquisition. Because regionally trapped air cannot be exhaled, such diseased lung areas will not increase in density on expiratory CT, unlike normal lung. In consequence, non-contrast-enhanced paired inspiratory-expiratory CT is recommended to differentiate mosaic attenuation due to airways disease from other causes like vascular disease or interstitial lung disease (Stern et al. 1995), and is thus part of functional CT protocols in CF. In young children unable to cooperate, CT scanning may require sedation, or a scanner with a high-pitch mode delivering near artifact-free images even in free-breathing children. To acquire paired inspiratory and expiratory scans in uncooperative children however, usually anesthesia, intubation, and controlled ventilation are necessary (Sly et al. 2013), which is restricting such examinations to the research setting. Mosaic attenuation and air trapping is also part of some CT scoring systems (e.g., Helbich and Brody Score, and the PRAGMA-CF scoring system) (Helbich et al. 1999; Brody et al. 2005a; Rosenow et al. 2015), although the Helbich score even allows to score mosaicism on inspiratory CT.

Several factors influence detection of air trapping on expiratory CT

1. Deepness and stability of expiratory breath hold (Ley-Zaporozhan et al. 2017; Wielpütz et al. 2014b). The position of the posterior membrane of the trachea is considered a handy visual marker. If it is bowed anteriorly, the patient exhaled. Is it bowed posteriorly, the patient very likely performs a Valsalva's maneuver. Kongstad et al. showed that spirometer control during acquisition of paired inspiratory-expiratory CT scans yields a larger difference in mean lung density, and thus improves conspicuity of air trapping (Kongstad et al. 2013).
2. Slice thickness. Thin-slice multidetector CT is recommended, e.g., ≤1.5 mm reconstructed slice thickness, whereas thick slices obscure mosaicism (Kauczor et al. 2011). Minimum intensity projections, e.g., 5–10 mm thick, are helpful to delineate mosaic attenuation, because airways and vessels are suppressed and lung parenchyma attenuation can be observed more clearly. Again, volumetric datasets are required for quantitative post-processing.
3. Radiation dose. CT density in Hounsfield units of lung tissue is clearly dependent on applied dose settings, well examined in studies on pulmonary emphysema in COPD (Zaporozhan et al. 2006; Yuan et al. 2007; Zach et al. 2012). However, previous work also showed that low-dose CT is not detrimental for the detection of air trapping (Bankier et al. 2007, 2008; Kauczor et al. 2011). In consequence, it is our recommendation that both inspiratory and expiratory acquisitions apply the same exposure and reconstruction settings, which can be low-dose, incl. Choice of iterative reconstruction, especially if quantitative software-based post-processing is planned.

2.2.2 Quantitative Post-Processing of Air Trapping

For software-based quantification of air trapping by lung densitometry (Fig. 3), similar conditions and limitations apply as mentioned for quantification of airway metrics (see above). Incorrect scanner calibration and inter-vendor variability due to different design of X-ray tube, detector or image reconstruction algorithms can also affect densitometry (Coxson 2013). Besides, biological variations such as body mass index (BMI) or lung volume are known to influence lung densitometry (Zach et al. 2012; Coxson 2013). If applicable, the smoking status at the time of imaging also needs to be considered (Zach et al.

2012, 2016; Jobst et al. 2018). Further, software itself shows a great variability between algorithms for emphysema and airway analysis (Wielpütz et al. 2014a; Lim et al. 2016). Although reported differences resulting from aforementioned factors along the chain of generating quantitative information from image data are rather subtle, they often are within the same order of magnitude as reported longitudinal changes for emphysema or clinically meaningful variations in airway wall metrics.

Segmentation of lung tissue and potentially lung lobes is performed before the density of the lung can be measured. Usually, large airways and vasculature are excluded from the segmented lung, which can be subject to great inter-software variability. Densitometry has first been used to quantify emphysema in COPD, for which a threshold of −950 Hounsfield Units (HU) has been defined based on histopathological correlations (Gevenois et al. 1996; Coxson et al. 2009). Voxels below this threshold are considered emphysematous, whereas for air trapping the definition is less clear. Different indices have been postulated to best represent trapped air, mostly derived from COPD studies, which rely on the difference in lung attenuation between inspiratory and expiratory CT, or on the ratio of relative volumes of lung between −950 and − 856 HU in both respiratory states (Matsuoka et al. 2007, 2008). Also, dynamic adjustments of such thresholds depending on expiration depth have been postulated (Goris et al. 2003).

2.2.3 Clinical Relevance of Air Trapping

Air trapping is considered among the first CF manifestations in the lung detectable by imaging. Sly et al. documented visual air trapping on expiratory CT in 40 of 57 (66.7%) mechanically ventilated CF infants (mean age 3.6 months) diagnosed by newborn screening in Australia (Sly et al. 2009). In this population it was even more prevalent than bronchial dilatation (18.6%) or bronchial wall thickening (45%). At preschool age, Ramsey et al. report a high prevalence of air trapping in 85% of patients, and even up to 94% at school age (Ramsey et al. 2016).

2.2.4 Variability of Air Trapping

Little is known about the variability of quantitative air trapping over time. As opposed to bronchiectasis, it may be considered a potentially reversible abnormality. Using visual scoring, the group of Sly et al. reported in a study adjunct to the abovementioned one that in 127 infants the overall prevalence of gas trapping was 68.0% at initial CT at the age of three months and was relatively stable in annual follow-up CTs until the age of three years (69.2%) (Sly et al. 2013). The mean extent score increased slightly from 2.59 ± 2.68 to 3.35 ± 3.32 during that period. Very similar results were reported by Mott et al. in 143 preschool children with CF (mean age at initial CT 2.00 years, range 0.97–3.24 years) (Mott et al. 2012).

In summary, studies have shown that air trapping is present already very early in the course of the disease after birth, and that its high prevalence persists in children and school-age patients. However, these studies did not specifically analyze the regional changes in distribution and severity of air trapping but only report whole-lung data. More recently, in a study using in-house software applying deformable registration Loeve et al. assessed areas of trapped air in 30 school-age children with CF (mean age 11.9 years, range 5–17 years), and quantified areas of stable, resolved, and newly developed air trapping on CT scans 2 years apart (Loeve et al. 2015). The authors found that mean air trapping did not change in this group (approx. 9% of lung area overall), but on an individual basis it is very variable. Reported median area of stable air trapping was 3.0%, whereas median area of dissolved air trapping was 5.0%, and median area of newly developed air trapping was 7.0%, documenting high spontaneous variability. As such, the spontaneous regional variability of quantitative air trapping at CT needs further investigation, and also needs consideration, for example, as a control group when air trapping is used as an endpoint. Importantly, few studies could demonstrate a reduction of regional air trapping after antibiotic therapy for pulmonary exacerbation, again supporting the hypothesis of partial reversibility (Davis et al. 2007; Sheikh et al. 2015a).

2.2.5 Correlation with Lung Function Testing

Air trapping contributes significantly to airflow limitation in CF. This has been confirmed by correlation with different lung function tests across all age groups. In infants and uncooperative young children, tracer gas washout approaches (multiple breath washout, MBW) have been established recently, resulting in the calculation of a lung clearance index (LCI). In short, a tracer gas is washed in over a tight mouthpiece or face mask over several tidal breaths. In steady state, the inflow is stopped, and the time until complete removal of the gas from exhaled air is measured. Regions of air trapping thus lead to a prolonged washout and higher LCI (Subbarao et al. 2013; Stahl et al. 2014, 2018a). Using this approach, Ramsey et al. studied the correlation of LCI with chest CT scores (PRAGMA-CF) in 42 infants (ages 0–2 years), 39 preschool children (3–6 years), and 38 school-age children (7–16 years) in comparison to 72 healthy controls (Ramsey et al. 2016). Interestingly, in these three groups the prevalence of air trapping increased from 58% over 85–94%. The concordance with an abnormal LCI declined with increasing prevalence and was 65%, 60%, and 56%, respectively. An agreement with $\kappa = 0.30$ was only found for infants, but not in preschool or school-age children. Thus, the predictive value of air trapping for an abnormal LCI was low at older ages, which may have several reasons. The prevalence of air trapping is very high already from birth (thus limiting correlative analyses if most patients are positive for air trapping), and more structural changes such as bronchiectasis may accumulate with age, then with dominating effects on lung function decline. Another theory suggests that totally occluded airways do not contribute to LCI increase at all, because no tracer gas can be washed in in the first place.

2.2.6 Correlation with Structural Lung Disease

Little is known about the actual correlation of air trapping with changes of the larger, visible airways at CT. One may speculate, that more severe air trapping may indicate more intense inflammation in a given lung region, which might also result in more extensive dilation and wall thickening of the visible airways. However, this has not been studied on a regional basis. Sly et al. only reported that air trapping is a risk factor (among many others, such as meconium ileus, respiratory symptoms, etc.) for developing bronchiectasis at follow-up CT in infants diagnosed by newborn screening, however without taking the regional component into consideration. Further studies are required to analyze the spatial and especially the temporal correlation of small airways disease (air trapping) with changes of the large airways (bronchiectasis, wall thickening).

2.2.7 Differentiation of Air Trapping from Emphysema

Quantitative post-processing may also identify emphysema within lung areas of low attenuation (Gevenois et al. 1996), using a threshold of usually −950 HU on inspiratory CT by convention, mostly derived from studies on chronic obstructive pulmonary disease COPD (Coxson et al. 2009; Jobst et al. 2018; Heussel et al. 2009). Histologically, emphysema has been found in some studies on CF (Esterly and Oppenheimer 1968; Bedrossian et al. 1976; Sobonya and Taussig 1986), but was given little attention on imaging studies. It is included in the Helbich scoring system (Helbich et al. 1999), but its overall contribution to disease severity is unclear. More recently, Wielpütz et al. reported that emphysema is progressively prevalent in school-age children with CF, and can be detected from the age of approx. 13 years (Wielpütz et al. 2013c). In this study, the authors could also show that the emphysema index correlates inversely with FEV1% (correlation coefficient $r = -0.66$, $p < 0.05$). These findings were later confirmed by Mets et al. who correlated quantitative CT with histopathology in the explants from CF patients undergoing lung transplantation, reporting good correlations of the emphysema index with patient age ($r = 0.45$, $p = 0.045$) and histological scoring ($r = 0.49$, $p = 0.03$) (Mets et al. 2015).

2.2.7.1 Other Dynamic Techniques

In COPD, chronic bronchitis is known to cause dynamic instability of the large airways, resulting in collapse of the trachea and main stem bronchi on exhalation (tracheobronchomalacia), which can go undiagnosed by spirometry and static CT examinations, but is revealed by bronchoscopy and dynamic CT techniques (Boiselle and Ernst 2003; Baroni et al. 2005; Wielpütz et al. 2014b). By analogy, dynamic instability due to cartilaginous malacia can be suspected in CF as well. The only study actually assessing tracheal lumen by two-dimensional cine-CT (2D + t) in CF was exerted by McDermott et al., who confirmed a high prevalence of tracheobronchomalacia in 24 (69%) out of 40 adults with CF (mean age 28 years, range 18–54 years) examined, based on a lumen reduction of more than 50% in forced expiration (Mcdermott et al. 2009). However, there was no correlation with FEV1% or Bhalla CT scores. Thus, clinical relevance remains unclear.

2.3 CT as an Endpoint in Clinical Trials

When CT is used as a measure of therapeutic effects, changes in air trapping are usually graded in conjunction with structural changes using scoring systems. Few initial studies used antibiotic therapy for pulmonary exacerbation as a model to test CT's sensitivity, usually with a timeframe of one month. Interestingly, Shah et al. described a reduction of mucus plugging and wall thickening but did not detect reversibility of mosaicism on inspiratory CT in this setting as early as 1997 (Shah et al. 1997). Brody et al. used incremental 1 mm slices with 10 mm gaps to score for hyperinflation on inspiratory CT in 8 children (mean age 12.7 years, range 5–16 years) with altogether 15 admissions for antibiotic therapy for pulmonary exacerbation. Although overall Brody score showed a significant decrease hyperinflation (mosaicism in this case) did not improve (Brody et al. 1999). Robinson et al. used spirometer control to scan in inspiration and in two different levels of expiration in 17 subjects (17.3 ± 7.2 years) before and after antibiotic therapy (15 days period). Especially mucus plugging was found to be reversible, but air trapping showed only small effect (Robinson et al. 2001). Davis et al. only scanned three selected slices in expiration together with volumetric inspiratory CT, and reported an average decrease of a hyperinflation score, among the other items of the Brody score, by 3.9 ($p < 0.01$) in 13 preschool children (mean age 17 months, range 2–44 months) with pulmonary exacerbation (Davis et al. 2007). The first study to use CT to assess efficacy of ivacaftor as a novel therapeutic in ten adults (20.9 years, range 10–4 years) showed an overall improvement of Brody CT scores after one year of treatment, but authors unfortunately did not use scores for mosaicism or air trapping (Sheikh et al. 2015b). The only study using quantitative post-processing to assess therapy-related changes so far is that by Robinson et al. in 2005, quantifying air trapping on spirometer-controlled inspiratory and expiratory CT by custom software before and after inhalative rhDNase therapy over one year in 25 school-age children and adolescents (age range 6–18 years). The prospective double-blinded and placebo-controlled study could detect a decrease of several air-trapping indices after three and twelve months in the therapy group in comparison to an increase in air trapping in the placebo group (Robinson et al. 2005).

3 Magnetic Resonance Imaging

3.1 Quantification of Airway Changes

MRI using conventional pulse sequences may depict structural lung disease in CF (bronchiectasis, wall thickening, mucus plugging, consolidation, etc.) to a similar degree as CT. Vendor-independent protocols have been published (Puderbach et al. 2007b; Biederer et al. 2012a, b), and multicenter-standardization of a

chest MRI protocol designed for infants and preschool children with CF could be achieved recently (Wielpütz et al. 2018b), extended by phantom-based approaches in adults (Triphan et al. 2018). MRI even has the advantage of higher tissue contrast using combinations of T1- and T2-weighted sequences, which, with the addition of i.v. contrast, may differentiate inflammatory wall thickening from mucus filling of an airway lumen, for example (Wielpütz et al. 2013a, 2016; Nagle et al. 2017). This is not possible with CT (Wielpütz et al. 2013b, 2016). However, the signal-to-noise ratio and resolution of MRI is somewhat lower than in CT. In consequence, automated quantitative post-processing of the structural changes in the CF lung has not been successfully accomplished yet, as has been done for multidetector CT, partially because MRI protocols in CF usually consist of a multitude of 2D sequences with overlapping but distinct signal properties and resolution. To date, automatic whole-lung segmentation from MRI datasets has been achieved (Kohlmann et al. 2015), but not of the larger airways or of parenchymal abnormalities.

The improved resolution of novel sequence techniques employing ultra-short echo times may hold further potential for the quantification of structural lung disease by automated software tools, which remains to be elucidated in the future (Dournes et al. 2015, 2016; Wielpütz et al. 2018a; Roach et al. 2016). Currently, structural abnormalities of the CF lung are most often quantified using a dedicated MRI scoring system published in 2012, which also includes a scoring item for perfusion abnormalities as discussed below (Eichinger et al. 2012; Wielpütz et al. 2014c; Wielpütz and Mall 2015, 2017; Stahl et al. 2017; Renz et al. 2015). The score employs a 3-point scale to rate disease manifestations based on lobes (lingula treated as separate lobe), comparable to scores in CT. Importantly, the basic proton protocol incl. The chest MRI score has been validated against chest X-ray (Puderbach et al. 2007b; Wielpütz et al. 2014c), CT (Puderbach et al. 2007a, b), and LCI (Stahl et al. 2017), and was also used in a multicenter setting (Wielpütz et al. 2018b).

3.2 Imaging of Ventilation and Perfusion with MRI

3.2.1 Non-contrast-Dependent Techniques

3.2.1.1 Mosaicism

As in CT, a mosaic pattern can also be observed with 1.5 T MRI on respiratory-gated T2-weighted sequences (e.g., T2 HASTE, Siemens scanners), which correlates moderately with contrast-enhanced perfusion imaging (κ = 0.58) in 50 infants and preschool children with CF (mean age 3.5 ± 1.4 years, range 0–6 years) (Leutz-Schmidt et al. 2018) (Fig. 4). In another study in an older population (median age 21 years, range 6–56 years) using heavily T2-weighted PROPELLER MRI (T2 BLADE, Siemens scanners), the authors did not find a good correlation of MRI air trapping with CT air trapping (Ciet et al. 2015). This very likely results from the limited parenchymal signal derived by this sequence type, as well as the older population. Potentially, mosaicism could also be enhanced by the acquisition of paired inspiratory and expiratory MRI, because MRI signal also increases on expiration (Bankier et al. 2004), but which has not been published in CF yet.

3.2.1.2 Fourier Decomposition MRI and Closely Related Approaches

Importantly, other methods have arisen from this basic principle that the respiratory cycle and pulsatile cardiac inflow induce subtle but periodical signal changes to the lung parenchyma. Using fast steady-state free precession sequences (SSFP) at a high temporal resolution (116 ms^{-1}), an acquisition of less than 1 min per slice can generate a dataset with sufficient information to perform image registration and subsequently a Fourier Decomposition in order to extract voxel-wise signal peaks at the frequencies of respiration and heart rate, which has been introduced first by Bauman and colleagues (Bauman et al. 2009). Ventilation- and perfusion-weighted maps can be composed (Fig. 5), which have already been validated against the gold standards hyperpolarized ^{3}He-MRI ventilation and gadolinium-based 4D

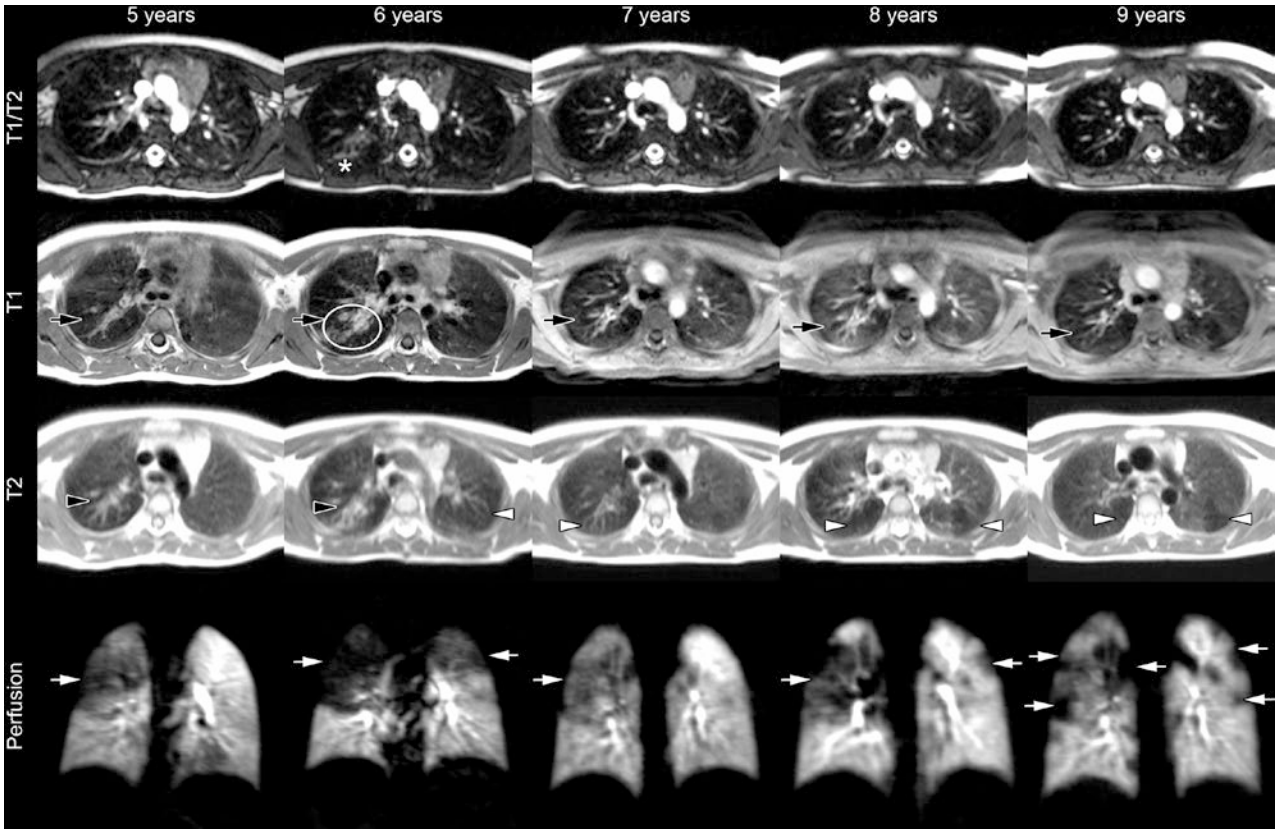


Fig. 4 Variability of perfusion abnormalities in annual surveillance MRI. This female patient with CF participates in our surveillance imaging program with annual routine follow-up. Irreversible bronchiectasis (black arrow) could be identified in the right superior lobe from age 5. These airways showed mucus plugging (black arrowhead) at age 5 and 6, which was reversible thereafter. Around this area as well as in the left superior lobe reduced parenchymal signal on T2 (white arrowhead) similar to mosaic perfusion on CT was present, with different severity over time. Perfusion abnormalities (white arrow) were detected at all ages, but with significantly different severity. Note that perfusion abnormalities also correlate with the areas of reduced signal on T2. At age 6, the subject had a pulmonary exacerbation, which was evidenced on imaging by the presence of a right superior lobe consolidation (circle) with adjacent pleural reaction (asterisk) and more severe perfusion abnormalities. One year later (therapy was enacted immediately), mucus plugging, consolidation, and perfusion abnormalities were alleviated. Note the following variability of perfusion abnormalities over time. Reprinted with permission from Thieme. Copyright © 2016 Georg Thieme Verlag. From Wielpütz M. O. et al. Rofo. 2016 Sep;188(9):834–45

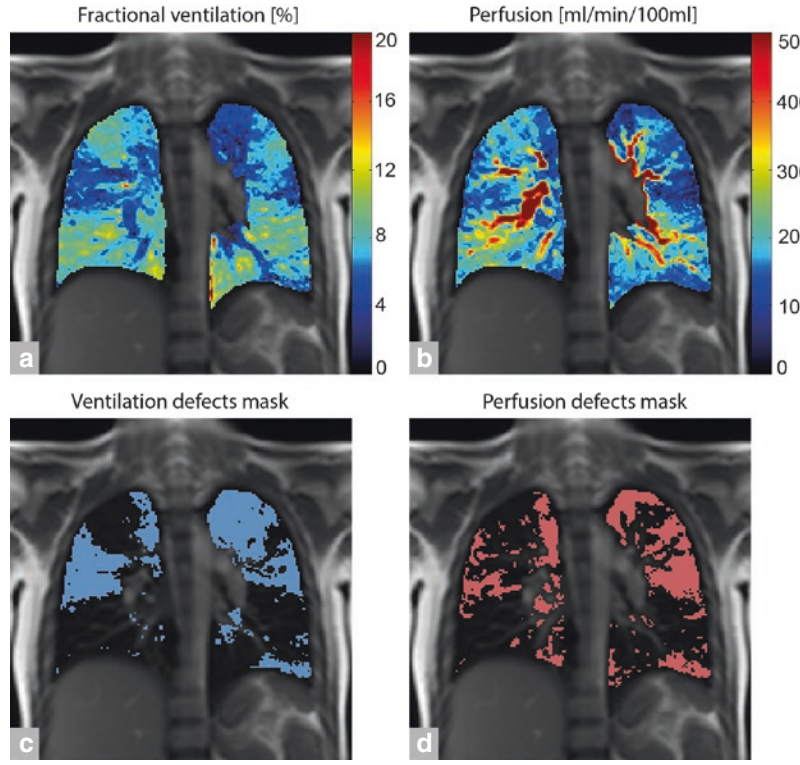


Fig. 5 Example of functional matrix pencil decomposition MRI in a 16-year-old girl with cystic fibrosis. Fractional ventilation (**a**) and perfusion (**b**) maps show several regions with decreased signal values in both lungs. Regions with impaired fractional ventilation (**c**) and perfusion (**d**) as presented as masks overlaid on morphological images. Figure provided by Grzegorz Bauman, University of Basel Hospital, Basel, Switzerland and Philipp Latzin, Inselspital, Bern, Switzerland

perfusion MRI in a porcine model (Bauman et al. 2013b), and a good reproducibility was confirmed in healthy volunteers (Lederlin et al. 2013). Visual and automated quantification of the segmented perfusion maps was also validated against 4D perfusion MRI in 34 CF patients (median age 4 years, range 0–30 years) (Bauman et al. 2013a). Importantly, this technique can be used in free breathing, respiratory maneuvers are not required.

Using an ultra-fast SSFP (ufSSFP), acquisition time could be shortened, volume extended to whole-lung coverage, and signal improved for reduction of repetitions (Bieri 2013). From five voluntary breath holds, ventilation-weighted maps based on pixel-wise signal differences between the respiratory states are computed even from the low-proton lungs of emphysema patients (Pusterla et al. 2016). As a drawback, perfusion information is lost with this approach. So far, data in CF is pending.

Matrix pencil decomposition, a modification of Fourier decomposition, based on ufSSP has been applied in a larger population of 40 school-age CF patients (median age 12 years, range 6–18 years) and 12 healthy controls together with lung function testing by N2 multiple breath washout (see above). The group of Nyilas et al. could demonstrate an excellent correlation of the LCI with fractional ventilation (r = 0.76) and perfusion abnormalities (r = 0.85) in this population. Also, correlation with the MRI morphology score was as high as r = 0.81 (Nyilas et al. 2017; Bauman and Bieri 2017). Of note, the method also allows for the calculation of blood arrival time. If this data can be confirmed also in infants and preschool children, it opens a perspective for non-contrast-dependent comprehensive morphological and function MRI solely based on proton imaging. As a side note, this method has already been applied with similar success in primary cilia dyskinesia as well (Nyilas et al. 2018). Phase resolved functional lung imaging (PREFUL) MRI is based on spoiled gradient echo sequences instead of SSFP at a temporal resolution of 288–324 ms. It aims at reconstruction a full respiratory and cardiac cycle (Voskrebenzev et al. 2018). So far, application in CF cohorts is pending as well.

3.2.1.3 Arterial Spin Labelling

Arterial spin labelling (ASL) has been introduced for imaging of brain perfusion, and has subsequently been transferred to the lung. It is based on the inflow of "labelled" protons from outside the imaging plane into a slice of the lung in which the signal from blood has been saturated before (Mai and Berr 1999). Its application in CF is very limited so far. Initial results have been reported by Schraml et al. in (2012), who found that the intrinsically quantitative ALS technique correlated well with a FEV1% decline in 33 pediatric CF patients (age 13 ± 5 years) with $r = 0.84$ (Schraml et al. 2012).

3.2.1.4 Phase-Contrast MRI

Another method that has scarcely been used in the past decade is phase-contrast MRI for the quantification of hemodynamics in the central thoracic vasculature in CF patients. Due to chronic inflammation with persistent hypoxic vasoconstriction as well as tissue loss, the blood pressure in the pulmonary vascular system may increase in CF patients, and pulmonary hypertension can occur. In 2009, Wolf et al. measured mean flow and acceleration time with phase-contrast MRI in a group of 48 CF patients (median age 16 years, range 10–45 years) in comparison to healthy volunteers, and found a reduction in mean flow and acceleration time in the CF group (Wolf et al. 2009). Although the authors did not perform invasive correlative measurements, reduction of the flow seemed to be more pronounced in CF patients with radiologically more severe disease, supporting the hypothesis that pulmonary hypertension develops in CF. However, this study neglected another potentially more important aspect of increasing collateral flow through systemic bronchial arteries to the lungs, which are dilated in advanced CF lung disease, and prone to life-threatening pulmonary hemorrhage. In this case one would expect decreased flow in the pulmonary arteries but increased flow in the systemic arteries. Ley et al. studied such hemodynamics in ten CF patients (mean age 29 ± 6 years), and also observed a reduced flow in the pulmonary trunk overall. The mean flow in the ascending aorta tended to be increased (Ley et al. 2005). Importantly, the shunt volume, i.e., the difference between pulmonary and systemic flow, measured with MRI was significantly increased even in this relatively small group of CF patients at 1.3 ± 1.7 L/min compared to 0.1 ± 0.4 L/min.

3.2.2 Contrast-Dependent Techniques

3.2.2.1 Gadolinium-Enhanced 4D Perfusion MRI

The most robust and often used MRI technique for functional imaging of the lung is gadolinium-enhanced four-dimensional (4D) perfusion MRI (Fig. 4) (Risse and Bauman 2016). For this, a spoiled gradient echo keyhole sequence with view sharing and parallel imaging is used, which achieves a temporal resolution of up to 1.5 s^{-1} for the acquisition of the whole lung in coronal plane at a spatial resolution of 1.2 × 1.7 mm in plane and 5 mm slice thickness, for example (Ley et al. 2004; Fink et al. 2005b; Eichinger et al. 2006, 2012; Risse et al. 2011; Wielpütz et al. 2014c, 2018b, 2019; Stahl et al. 2017). Gd-based contrast material is administered via a power injector at rates of 1.5–5 mL/s, followed by a saline chaser, depending on patient age. Dosing is dependent on patient weight as per prescribing information, but usually in adults 2 mL of Gd-contrast material is sufficient for perfusion imaging. It is important to note that a series of sequence acquisitions is started approx. 5 s prior to commencing contrast injection, and that approx. 35 whole-lung acquisitions should be performed in total. By this approach, the technique has sufficient time to measure the underlying anatomy before contrast arrival, which is then propagated through the following acquisitions. Key to this sequence type is that from acquisition to acquisition, mostly the k-space center is re-sampled (contrast), whereas little measurement time is used for re-sampling of the periphery (anatomy, resolution) (Griswold et al. 2002; Fink et al. 2005a). Two physiological factors support this approach. First, the size of the smallest functional unit of the lung, the secondary lobule, is sufficiently larger than the spatial resolution of

the sequence used, ensuring that small perfusion changes can be observed. Second, only contrast material-related changes are to be expected during the series of acquisitions, which are preferably detected by the keyhole approach. The temporal resolution and measurement time are sufficient to monitor the first (and also second) pass of the contrast bolus through the lung and large vasculature. Bolus length is usually long enough to achieve at least one series of homogeneous maximum enhancement of the lung tissue, and at the same time short enough to observe temporal changes related to pulmonary perfusion dynamics (see "Quantification of Perfusion MRI"). As the basic post-processing technique for an easy visualization, the signal-time-course in healthy lung tissue should be followed, and the series before contrast arrival should be subtracted from the series with the highest lung signal. Gray-scale coding is usually considered sufficient for routine imaging. These subtracted perfusion maps allow for an easy identification and visual semi-quantification of perfusion abnormalities, because the anatomical background is suppressed and contrast-enhancement is pronounced (Wielpütz et al. 2016).

By applying this technique, the lungs of healthy individuals usually display a completely homogeneous enhancement of the whole lung tissue from infancy to adulthood (Wielpütz et al. 2014c; Ley et al. 2004; Ley-Zaporozhan et al. 2011). Typically, a ventro-to-dorsal increase in enhancement can be observed, which is due to the physiologically higher perfusion of the gravity-dependent areas of the lung in supine position (Fig. 6) (Hopkins et al. 2007, 2012). In cystic fibrosis, small mottled or larger wedge-shaped perfusion abnormalities can occur as mild changes, and confluent larger areas of up to whole lobes may show as more advanced perfusion abnormalities (Eichinger et al. 2012; Wielpütz et al. 2013a, 2014c, 2016, 2018b; Stahl et al. 2017). In case of lobar atelectasis or infiltrates, perfusion may also be relatively increased due to inflammation. This technique was also used in a multicenter setting, which has not been achieved for other functional techniques in CF (Wielpütz et al. 2018b).

3.2.2.2 Quantification of 4D Perfusion MRI

Up to now, perfusion abnormalities are semi-quantified using the dedicated MRI scoring system published by Eichinger et al. in (2012). Subtracted perfusion maps, however, have the disadvantage that the temporal component of perfusion abnormalities is completely neglected. Risse et al., for example, using dedicated post-processing, identified not only areas of overall reduced perfusion in CF, but also showed that some lung areas will show a delayed peak of the perfusion signal (Risse et al. 2011). This finding is especially intriguing in the context of dilated bronchial arteries, which frequently occur with advanced CF lung disease, often directed at lung regions which suffer from a sustained extensive perfusion deficit (in the pulmonary arterial phase). One might speculate that this delay of the peak signal is due to an increased supply from the bronchial arteries (and thus from the systemic circulation), and inflammatory processes may also contribute to an increase in permeability of

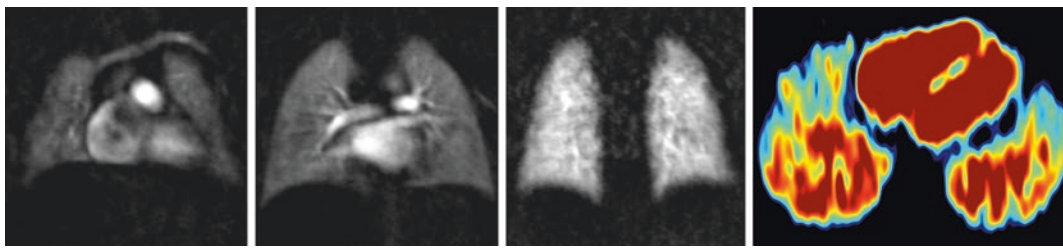


Fig. 6 Subtracted perfusion map of normal lung perfusion in a patient with cystic fibrosis. In supine position perfusion typically exhibits a ventro-to-dorsal increase following gravity. The axial reconstruction with color-coding (jet) at the level of the heart also clearly demonstrates this gradient

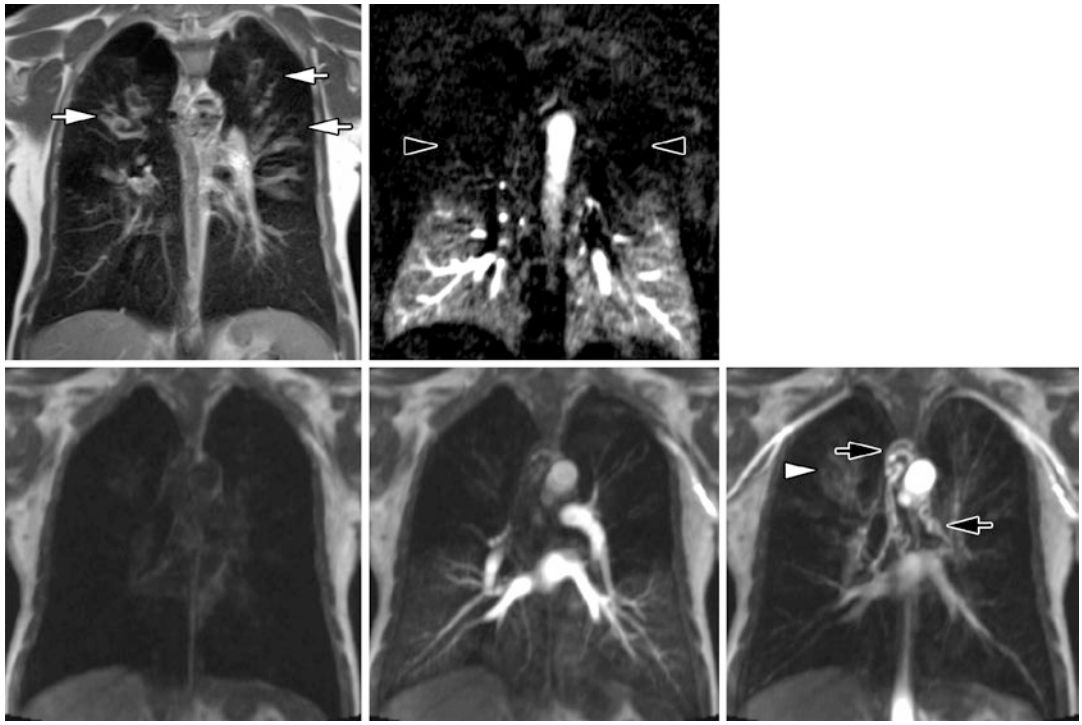


Fig. 7 Dynamic lung signal changes in perfusion MRI identify areas of delayed perfusion. In this male CF patient with extensive bronchoceles (white arrow) pronounced in the superior lobes the subtracted perfusion map shows complete perfusion loss in the superior lobes in the pulmonary arterial phase (black arrowhead). The dynamic perfusion series shows an area of delayed enhancement in the right superior lobe during the systemic arterial phase (white arrowhead). Note the presence of dilated bronchial arteries (black arrow)

the pulmonary vasculature for Gd. Thus, further studies are necessary to support this hypothesis (Fig. 7).

Based on the indicator dilution theory, the temporal changes during perfusion MRI can be used to calculate the mean transit time (MTT) as well as pulmonary blood flow (PBF) per ml of lung volume (Roberts 1997; Nikolaou et al. 2004; Ley-Zaporozhan et al. 2011; Kohlmann et al. 2015; Ter-Karapetyan et al. 2018), and pulmonary blood volume (PBV) can be derived as PBV = PBF/MTT. These measures are potentially highly valuable in assessing lung function, but are unfortunately affected by some limitations, which have so far hindered a broader application in airways disease. First, the dose–signal relationship of Gd-based contrast material is not linear, unlike the situation in CT—and thus the measurements of the signal in the pulmonary trunk required for the linear input function may be false, which then translates into faulty perfusion values in the lung (Puderbach et al. 2008). The short-term repeatability of lung perfusion measurements within 24 h was established in healthy volunteers. However, in COPD patients repeatability was much lower and obviously impaired by residual intravascular contrast even 24 h after the first injection, and potentially by residual contrast material in inflamed lung areas (Ley-Zaporozhan et al. 2011; Ter-Karapetyan et al. 2018). Thus far, scoring of perfusion MRI exams represents the basis for disease quantification (Eichinger et al. 2012).

3.2.2.3 Variability of Perfusion Abnormalities

Independent studies in preschool children and adolescents showed that perfusion abnormalities are more prevalent and more extensive in CF patients with acute pulmonary exacerbation than

in clinically stable situation (Wielpütz et al. 2014c; Stahl et al. 2017). For example, in 10 preschool children the perfusion score in exacerbation was 6.0 ± 1.0 in comparison to 40 clinically stable children with 3.5 ± 2.3 ($p < 0.01$). Moreover, antibiotic therapy reduced the perfusion score to a mean of 2.0 ± 1.0 ($p < 0.05$) (Wielpütz et al. 2014c). The latter finding is especially important, as this supports the hypothesis that perfusion abnormalities as a functional deficit in the CF lung are reversible under effective therapy (Fig. 8) (Wielpütz et al. 2014c; Stahl et al. 2017). Thus, it is conceivable that perfusion abnormalities will show some variability with disease progression and repeat therapy as usually performed in CF routine care (Wielpütz et al. 2016) (Fig. 4). To date, little is known about the spontaneous intra-individual variation of these changes over time, and further studies are warranted to specifically scrutinize this phenomenon in CF. At least for COPD it has been shown that perfusion abnormalities are reproducible within 24 h (Jobst et al. 2015b). More recently, it was shown that perfusion MRI is reproducible within one month in a group of 15 clinically stable adult CF patients (Wielpütz et al. 2019).

3.2.2.4 Correlation with Structural Lung Disease

In a study with 50 infants and preschool children with stable lung disease, perfusion abnormalities were correlated with the different structural abnormalities in the CF lung. Here, only approx. 20% of the detected perfusion abnormalities were associated with structural disease in the same lung lobe, which indicates that perfusion MRI has additional value for the detection of small airways disease (Wielpütz et al. 2014c). This relationship is probably similar to the use of expiratory CT for the detection of small airway obstruction, even though both methods have not been compared directly in CF.

3.2.2.5 Correlation with Pulmonary Function Testing

So far, only limited data exist on the correlation of proton MRI incl. Perfusion MRI with spirometry. The focus in the recent past has been on early CF, at which stage lung function testing with spirometry is often normal whereas imaging can display significant disease. In analogy to aforementioned CT studies, perfusion MRI has been studied together with LCI measurements in a group of 97 clinically stable infants to school-age children (age range 0.2–21.1 years) (Stahl et al. 2017). In this study, the authors demonstrate that perfusion MRI correlates moderately with age ($r = 0.35$), and moderately to well with the LCI ($r = 0.45$ and $r = 0.74$). Also, MRI scores were worse in patients with pulmonary exacerbation and in case of chronic *P. aeruginosa* infection, which indicates more advanced disease severity.

3.2.2.6 Gadolinium-Enhanced MR Angiography

Multiphasic MR angiography is an established method to study the thoracic vasculature with regard to the aorta and pulmonary vessels (Tsuchiya et al. 2018). It may also be used to directly display dilated bronchial arteries (Fig. 7) (Hopkins et al. 2012), but the clinical standard is still CT angiography for planning of emergency procedures (Wielpütz et al. 2016; Remy-Jardin et al. 2004).

3.2.2.7 Oxygen-Enhanced Ventilation MRI and T1-Mapping

The direct measurement of T1 relaxation times, so-called T1 mapping per se is not dependent on the application of exogenous contrast materials. Tissue T1 has been regarded as a constant, which could be measured independently of scanner vendors and is intrinsically quantitative. Interestingly however, a lung voxel contains different compositions of protons from air, lung tissue, and blood, each influenced by the immediate environment. Triphan et al. could show by using ultra-short echo time sequences that measuring T1 at different echo times will deliver different results, and seemingly echo-time-dependent acquisitions can deliver "lung tissue-weighted" or more "blood-weighted" T1 (Fig. 9) (Triphan et al. 2015). So far, it has been shown in COPD that T1 mapping may correlate with lung perfusion using visual scoring (Jobst et al. 2015a), which is supporting

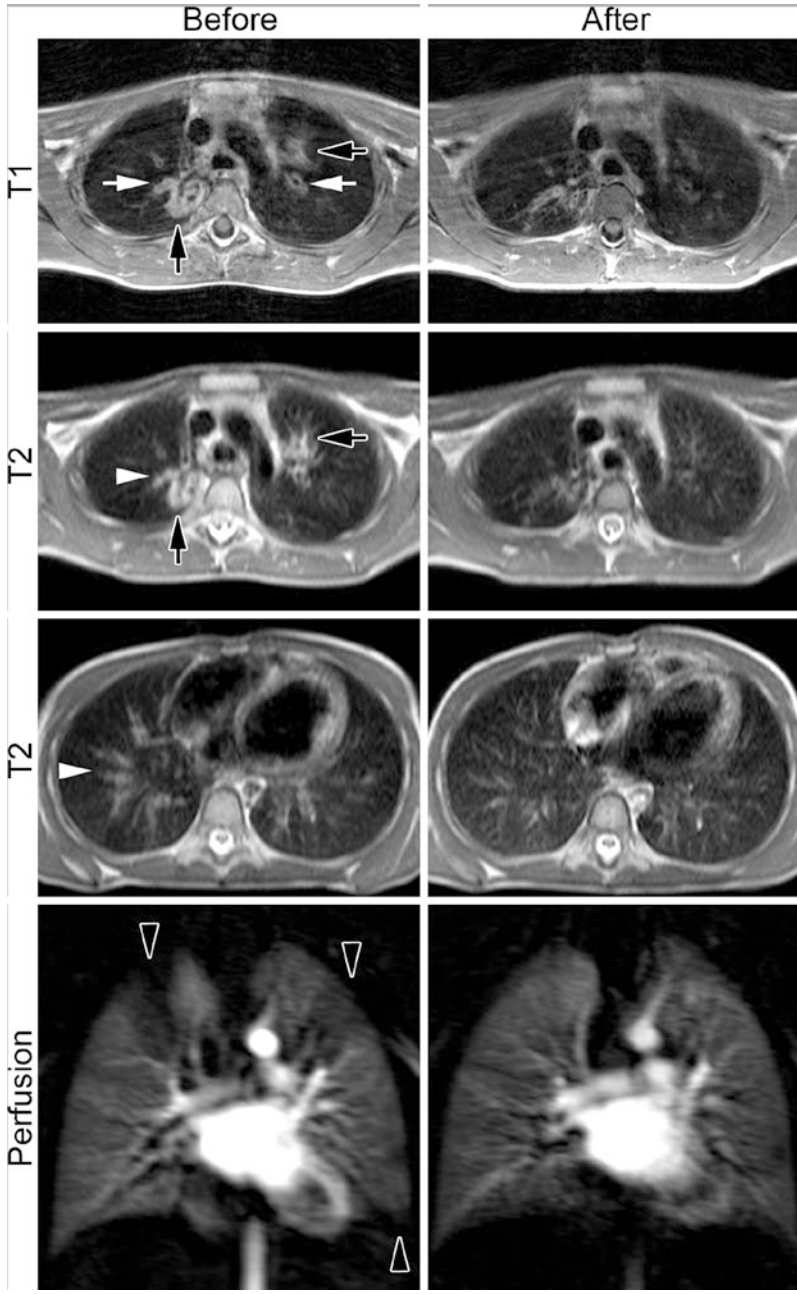


Fig. 8 MRI of acute exacerbations in early cystic fibrosis lung disease before and after antibiotic therapy. Representative MRI studies of a 6-year-old cystic fibrosis patient at the time of acute pulmonary exacerbation and one month after i.v. antibiotic therapy. The initial MRI study before treatment revealed extensive contrast-enhancing airway wall thickening (white arrows) and mucus plugging with high signal intensity on T2-weighted sequences (white arrowheads) of upper and lower lung lobes. Consolidations were present in both upper lobes (black arrows). Wedge-shaped perfusion abnormalities were identified on the subtracted perfusion map (black arrowheads). After antibiotic therapy, airway wall thickening and enhancement, mucus plugging and consolidations were substantially reduced. Most perfusion defects resolved and a more homogeneous perfusion was restored. Reprinted with permission of the American Thoracic Society. Reprinted with permission of the American Thoracic Society. Copyright © 2019 American Thoracic Society. Cite: Wielpütz M. O. et al. Am J Respir Crit Care Med 2014 189(8):956–65. The American Journal of Respiratory and Critical Care Medicine is an official journal of the American Thoracic Society

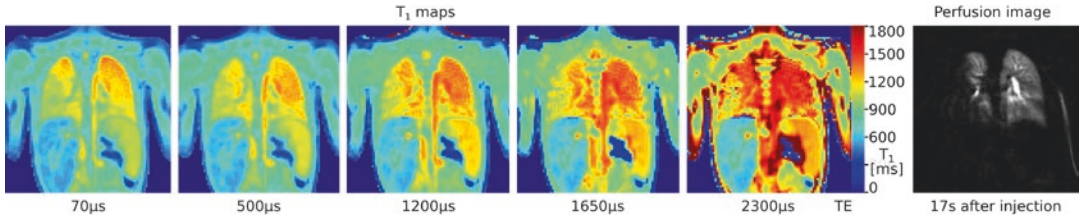


Fig. 9 T1 mapping using ultra-short echo times. T1 maps and subtracted perfusion image of a 13-year-old male CF patient. T1 maps were calculated from an inversion recovery multi-echo 2D UTE measurement at 5 echo times using a pixel-wise parameter fit. The perfusion image was generated using a keyhole sequence with 1.5 s^{-1} temporal resolution and shows the subtraction of one image after contrast agent injection from the baseline image. Note that areas of perfusion abnormalities nicely match areas of reduced T1. Figure provided by Simon M. F. Triphan, University of Heidelberg

the hypothesis that part of T1 is driven by pulmonary blood content. In CF, Donnola et al. studied the correlation of T1 at relatively long echo times of 0.84 ms (more "blood weighted") with perfusion MRI in eight adult CF patients in comparison to six healthy volunteers. In a grossly regional analysis T1 correlated moderately with FEV1% ($r = 0.46–0.68$, $p = 0.1–0.008$) and with quantitative perfusion MRI ($r = 0.56–0.71$, 0.05–0.005) in CF patients.

T1 mapping is often employed in conjunction with oxygen enhancement, mostly using snapshot FLASH sequences. Because of its paramagnetic capabilities, the presence of oxygen—probably in dissolved phase in lung tissue and veins—leads to regional T1 shortening in its close vicinity, laying the basis for oxygen-enhanced MRI. It is best captured by direct measurements of the T1 relaxation time, rather than using T1-weighted imaging (Kauczor and Wielpütz 2018), and inhalation of pure oxygen via a face mask over at least 5 min is recommended to achieve a maximal effect in ventilated lung regions. Even though application of this method seems reasonably easy to use, little data has been obtained in CF patients, mostly because hyperpolarized gas MRI and other contrast-dependent techniques seem to deliver a stronger signal of disease. In 2004, Jakob et al. described an inhomogeneous T1 distribution in the lungs of five CF patients (age range 13–34 years) at baseline (room air), and calculated an oxygen transfer function based on T1 measurements at different concentrations of inhaled oxygen, which was also reduced in more diseased lung areas (Jakob et al. 2004). T1 reduction at baseline and after O_2 seemed to match the perfusion deficit detected by Gd-based perfusion MRI. Stadler et al. studied T1 in inspiration and expiration, and also observed a significantly diminished T1 reduction after oxygen inhalation in diseased CF lungs (Stadler et al. 2007). As described also in COPD, it seems that areas with reduced T1 at room air also show a low response to inhaled oxygen, probably reflecting that reduced perfusion to obstructed lung areas is driving T1 reduction and thus limiting oxygen enhancement. Since these pioneering studies, little work has been published on O_2-enhanced MRI. Only very recently, Zha et al. from the Wisconsin group demonstrated that—using ultra-short echo times—oxygen-enhanced proton MRI delivers information similar to the more challenging ^{3}He ventilation MRI in 25 CF patients (age range 10–55 years). The authors report that VDP with oxygen was 5% lower on average than on ^{3}He MRI, and that these measures were highly correlated with $r = 0.79$ (Zha et al. 2019). As another acquisition technique, oxygen-enhancement has also been studied in conjunction with ufSSFP in healthy volunteers, but CF data is pending (Pusterla et al. 2018).

3.2.2.8 Hyperpolarized Gas Ventilation MRI

Noble gas MRI is probably the most often used technique for ventilation MRI in CF, even though the additional hardware required is costly

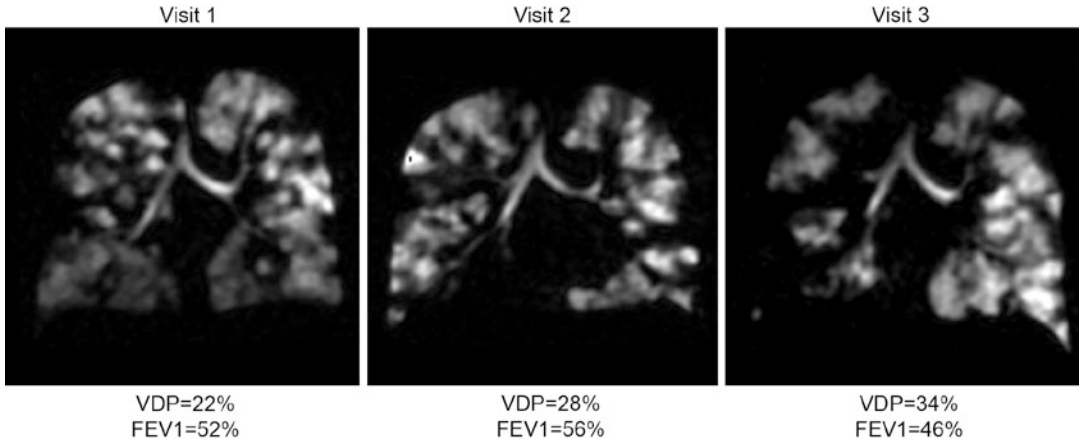


Fig. 10 Longitudinal ^{3}He-MRI. Annual hyperpolarized ^{3}He-MRI of an adult CF patient with impaired spirometry. The ventilation defect percent (VDP), derived from the segmented lung volume using signal value thresholds to quantify lung regions with impaired ventilation, decreased with each MRI exam. Note that the FEV1 slightly increased on visit 2 despite visual and quantitative deterioration of ventilation. Figure provided by J. Wild, University of Sheffield

(chapter "Basics and Clinical Application of MR Assessment of Ventilation") (Donnelly et al. 1999). Current standard for the quantification of ventilation abnormalities is the calculation of ventilation defect percent (VDP), which is threshold-based and requires prior segmentation of the lung from the anatomical background (Fig. 10). Apart from VDP calculations from static breath-hold acquisitions, dynamic techniques have also been described to measure a delay in wash-in and washout, but which received little attention in CF cohorts (Horn et al. 2014).

Donnelly et al. studied ventilation abnormalities on ^{3}He MRI in four CF patients together with rudimentary proton images of the lung already in 1999 (Donnelly et al. 1999). Subsequent work on ^{3}He MRI sought to correlate its findings against established radiological measures of lung disease in CF. In 2006, McMahon visually scored and validated ^{3}He MRI from eight adults and clinically stable CF patients against CT (Bhalla scoring system) and spirometry (Mcmahon et al. 2006). Morphological abnormalities such as bronchiectasis, wall thickening, mucus plugging, bullae, and consolidations correlated individually (univariate model) with ventilation abnormalities on ^{3}He MRI ($r = -0.80$ to -0.95), whereas mosaicism (inspiratory CT only) did not ($r = r = 0.37$) (Mcmahon et al. 2006). Subsequently, van Beek et al. demonstrated only a mild correlation of ^{3}He MRI scores with two different chest X-ray scores in 18 CF patients (age range 5–7 years), indicating that chest X-ray may not be sensitive enough to capture subtle disease which is evident on MRI (Van Beek et al. 2007). Both authors found a moderate correlation with FEV1% of $r = 0.86$ and $r = -0.41$, respectively (Mcmahon et al. 2006; Van Beek et al. 2007).

Two studies used ^{3}He MRI to monitor efficacy of established CF therapy. Woodhouse et al. first assessed immediate reproducibility of ^{3}He MRI within 30 min in five CF patients (age range 6–15 years) (Woodhouse et al. 2009). Subsequently, the authors measured ventilation abnormalities in nine CF patients (age range 5–15 years) before and after a course of chest physiotherapy and detected a trend towards an increase in ventilated lung volume. Bannier et al. similarly performed ^{3}He ventilation MRI before and after 20 min of chest physical therapy in ten CF patients (age range 8–16 years), also detecting ventilation impairment despite normal lung function. However, they were also unable to display significant therapy response by ^{3}He MRI (Bannier et al. 2010). Of note, therapy effects in this model are probably too small to be captured

in such small populations. Bronchodilator therapy but not physiotherapy led to a small but significant reduction in the amount of ventilation defects in CF in another study (Mentore et al. 2005). More obvious changes could be expected in pulmonary exacerbation, which has been studied with ^{129}Xe (see below).

To assess mid-term repeatability, five CF patients underwent weekly ^{3}He MRI four times, demonstrating a good concordance of detected ventilation defects (O'sullivan et al. 2014). Paulin et al. followed a group of five patients over four years using ^{3}He MRI, and described a tendency towards worsening VDP at relatively stable FEV1 (Paulin et al. 2014). The first longitudinal study employing ^{3}He MRI in a larger group has been published recently by the Sheffield group in 14 children with CF (mean age at baseline 10.3 ± 2.3 years). Within an interval of 1.3–2.0 years, mean VDP increased significantly from 4.37 ± 1.89% to 10.8 ± 4.62% (Smith et al. 2018) (Fig. 10). Of note, FEV1% remained stable and LCI increased slightly but significantly in this cohort.

One major criticism against 3He MRI has been the need for patient cooperativity and breath-holding, which seemingly precluded its use in young children, i.e., early CF lung disease where it may be most useful for detecting preclinical lung manifestations. For this purpose, Altes et al. performed ^{3}He MRI in seven non-sedated children ≤4 years (three CF), demonstrating the feasibility of the method and sufficient image quality in this challenging age group (Altes et al. 2017b). Still, ^{3}He MRI suffers from small patient cohorts recruited as well as limited multicenter availability.

Because ^{3}Helium gas is expensive, ^{129}Xenon is increasingly being used as an alternative (Fig. 11). Initial studies show that its anesthetic potential is controllable in a group of school-age children (Walkup et al. 2016), and also that it delivers image information probably equivalent to static ^{3}He MRI (Stewart et al. 2018). In eleven patients with mild CF (age range 8–16 years, FEV1% > 70%) ^{129}Xe demonstrated ventilation defects, and even in a subgroup with normal FEV1% mean VDP was 15.4% (Thomen et al. 2017). Thus, it may be feasible as an endpoint in early CF lung disease when FEV1% does not detect significant disease. This is further supported by Kanhere et al., who could demonstrate a strong correlation of VDP with LCI in 18 participants (age range 8–17 years, 10 CF patients) at R^2 = 0.88, but only a weak correlation with FEV1% at R^2 = 0.31 (Kanhere et al. 2017). Rayment and colleagues recently studied treatment response to antibiotics in 15 CF patients (age range 8–18 years) with pulmonary exacerbation using ^{129}Xe MRI and state that compared to FEV1% and LCI, VDP showed the largest relative improvement with 42.1% on average (Rayment et al. 2019). Without paralleling morphological imaging however, the reason of this increase, either being due to mucus plugging, atelectasis, or infiltrates, and subsequently the additional value provided by ^{129}Xe remain unclear. The added potential of dissolved-phase ^{129}Xe MRI for measuring lung diffusion capacity has not been utilized in CF so far.

As an alternative to hyperpolarized gas MRI, fluorinated gases may be used as inhalative contrast materials. Especially SF6 is particularly interesting (Schreiber et al. 2001; Gutberlet et al. 2018) because it is also a tracer gas used for LCI measurements, but application in CF is pending.

3.3 MRI as an Endpoint in Clinical Trials

As already mentioned above, 4D perfusion MRI as well as ^{129}Xe MRI could detect response to antibiotic therapy in acute pulmonary exacerbation in preschool children as well as in adolescents (Wielpütz et al. 2014c; Stahl et al. 2017; Rayment et al. 2019). This may be considered a relatively strong physiological signal to detect, and FEV1, for example, is also able to monitor therapy-related changes in this clinical condition. The more challenging situation is thus characterized by little short-term therapeutic effect and early lung disease, which only has limited structural and functional damage from baseline. On the other hand, this may reinforce the great strengths of imaging, because with diagnosis at early lung disease and new therapies, FEV1 usually remains normal for a long period of time in

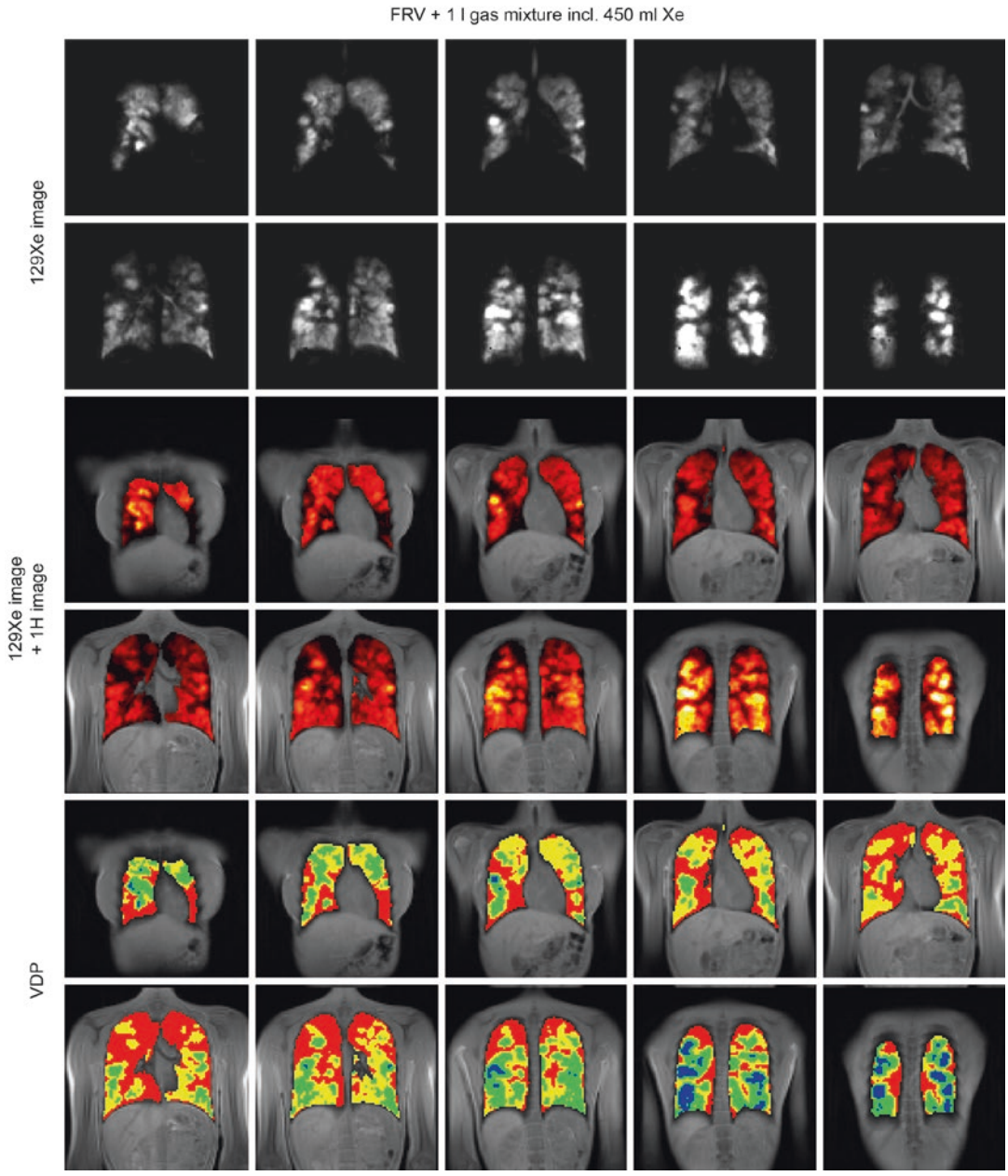


Fig. 11 Hyperpolarized ^{129}Xe-MRI in a 17-year-old female with CF. FEV1% was normal at 100%, but residual volume increased with 196%. Images were acquired after forced exhalation and then inhalation of 1 l of a gas mixture including 450 mL ^{129}Xe. Color-coded ^{129}Xe-MRI with ^{1}H-MRI overlay for anatomic background (top row) and ventilation defect percentage (VDP) maps (bottom row) are shown. The latter indicates ventilation defects in red, mild hypoventilation in yellow, normal ventilation in green, and hyperventilation in blue. Figure provided by J. Vogel-Claussen and A. Kern, Hannover Medical School

CF and is thus insensitive to therapeutic modulation.

The only MRI technique validated in a multicenter setting so far is 4D perfusion MRI (Wielpütz et al. 2018b; Triphan et al. 2018). The same centers of this preparatory study have then participated in the first study using morphological MRI as a primary endpoint.

Because of prescription regulations of Gd-contrast agents for infants, perfusion MRI was not included in the MRI protocol at that time, and morphological MRI alone could not should a difference between the inhalation of isotonic and hypertonic saline as a preventive treatment in infants diagnosed by newborn screening (Stahl et al. 2018b).

Hyperpolarized ^{3}He-MRI has recently been used to assess response to ivacaftor in single-center Phase 2 study in a small population of adolescents and adults with a G551D *CFTR* mutation (Altes et al. 2017a; Wielpütz and Mall 2017). Depending on the method of quantification, the total ventilation deficit at ^{3}He-MRI was reduced in eight CF patients from baseline by 12.8% ($p = 0.008$) after four weeks of treatment (Altes et al. 2017a). In a long-term treatment arm over 48 weeks, the reduction in total ventilation deficit in eight patients who completed the study was insignificant with 9.0%. After treatment was stopped, ventilation deficits returned to baseline levels. Unfortunately, controls were not included with this pioneering study.

4 Conclusion

During the next decade, radiology will be confronted with an increasing number of very young CF patients detected by newborn screening, who will—thanks to novel therapy regimes—retain normal lung function through a longer period of their extended life span. Thus, new imaging strategies are required to repetitively monitor disease activity noninvasively when spirometry is of little use anymore. Cross-sectional imaging with CT and MRI has demonstrated great value in detecting early and subclinical CF lung disease from infancy. Further, functional CT and MRI techniques have shown promising results in initial therapy studies using antibiotics and other strongly acting agents. Of all the functional techniques, 4D perfusion MRI is the most widely used and robust technique to date. It is to be expected that novel non-contrast-dependent techniques will enter the clinical arena, avoiding the need for Gd injection. The next few years will show which techniques are most useful as endpoints in monitoring therapy efficacy especially for subtle long-term disease modification, thus replacing lung function testing.

References

Achenbach T, Weinheimer O, Biedermann A et al (2008) MDCT assessment of airway wall thickness in COPD patients using a new method: correlations with pulmonary function tests. Eur Radiol 18: 2731–2738

Achenbach T, Weinheimer O, Brochhausen C et al (2012) Accuracy of automatic airway morphometry in computed tomography-correlation of radiological-pathological findings. Eur J Radiol 81:183–188

Altes TA, Johnson M, Fidler M et al (2017a) Use of hyperpolarized helium-3 MRI to assess response to ivacaftor treatment in patients with cystic fibrosis. J Cyst Fibros 16:267–274

Altes TA, Meyer CH, Mata JF et al (2017b) Hyperpolarized helium-3 magnetic resonance lung imaging of non-sedated infants and young children: a proof-of-concept study. Clin Imaging 45:105–110

Aysola RS, Hoffman EA, Gierada D et al (2008) Airway remodeling measured by multidetector CT is increased in severe asthma and correlates with pathology. Chest 134:1183–1191

Bankier AA, O'donnell CR, Boiselle PM (2008) Quality initiatives. Respiratory instructions for CT examinations of the lungs: a hands-on guide. Radiographics 28:919–931

Bankier AA, O'donnell CR, Mai VM et al (2004) Impact of lung volume on MR signal intensity changes of the lung parenchyma. J Magn Reson Imaging 20:961–966

Bankier AA, Schaefer-Prokop C, De Maertelaer V et al (2007) Air trapping: comparison of standard-dose and simulated low-dose thin-section CT techniques. Radiology 242:898–906

Bannier E, Cieslar K, Mosbah K et al (2010) Hyperpolarized 3He MR for sensitive imaging of ventilation function and treatment efficiency in young cystic fibrosis patients with normal lung function. Radiology 255:225–232

Baroni RH, Feller-Kopman D, Nishino M et al (2005) Tracheobronchomalacia: comparison between end-expiratory and dynamic expiratory CT for evaluation of central airway collapse. Radiology 235:635–641

Bauman G, Bieri O (2017) Matrix pencil decomposition of time-resolved proton MRI for robust and improved assessment of pulmonary ventilation and perfusion. Magn Reson Med 77:336–342

Bauman G, Puderbach M, Deimling M et al (2009) Non-contrast-enhanced perfusion and ventilation assessment of the human lung by means of fourier decomposition in proton MRI. Magn Reson Med 62:656–664

Bauman G, Puderbach M, Heimann T et al (2013a) Validation of Fourier decomposition MRI with dynamic contrast-enhanced MRI using visual and automated scoring of pulmonary perfusion in young cystic fibrosis patients. Eur J Radiol 82:2371–2377

Bauman G, Scholz A, Rivoire J et al (2013b) Lung ventilation- and perfusion-weighted Fourier decomposition magnetic resonance imaging: in vivo validation with hyperpolarized ^{3}He and dynamic contrast-enhanced MRI. Magn Reson Med 69:229–237

Bedrossian CW, Greenberg SD, Singer DB et al (1976) The lung in cystic fibrosis. A quantitative study including prevalence of pathologic findings among different age groups. Hum Pathol 7:195–204

Benden C, Wallis C, Owens CM et al (2005) The Chrispin-Norman score in cystic fibrosis: doing away with the lateral view. Eur Respir J 26:894–897

Bhalla M, Turcios N, Aponte V et al (1991) Cystic fibrosis: scoring system with thin-section CT. Radiology 179:783–788

Biederer J, Beer M, Hirsch W et al (2012a) MRI of the lung (2/3). Why ... when ... how? Insights Imaging 3:355–371

Biederer J, Mirsadraee S, Beer M et al (2012b) MRI of the lung (3/3)-current applications and future perspectives. Insights Imaging 3:373–386

Bieri O (2013) Ultra-fast steady state free precession and its application to in vivo H morphological and functional lung imaging at 1.5 T. Magn Reson Med 70(3):657–663

Boiselle PM, Ernst A (2003) State-of-the-art imaging of the central airways. Respiration 70:383–394

Brasfield D, Hicks G, Soong S et al (1979) The chest roentgenogram in cystic fibrosis: a new scoring system. Pediatrics 63:24–29

Brody AS, Kosorok MR, Li Z et al (2006) Reproducibility of a scoring system for computed tomography scanning in cystic fibrosis. J Thorac Imaging 21:14–21

Brody AS, Molina PL, Klein JS et al (1999) High-resolution computed tomography of the chest in children with cystic fibrosis: support for use as an outcome surrogate. Pediatr Radiol 29:731–735

Brody AS, Sucharew H, Campbell JD et al (2005a) Computed tomography correlates with pulmonary exacerbations in children with cystic fibrosis. Am J Respir Crit Care Med 172:1128–1132

Brody AS, Tiddens HA, Castile RG et al (2005b) Computed tomography in the evaluation of cystic fibrosis lung disease. Am J Respir Crit Care Med 172:1246–1252

Chen-Mayer HH, Fuld MK, Hoppel B et al (2017) Standardizing CT lung density measure across scanner manufacturers. Med Phys 44:974–985

Chrispin AR, Norman AP (1974) The systematic evaluation of the chest radiograph in cystic fibrosis. Pediatr Radiol 2:101–105

Ciet P, Serra G, Bertolo S et al (2015) Assessment of CF lung disease using motion corrected PROPELLER MRI: a comparison with CT. Eur Radiol 26(3): 780–787

Ciet P, Wielopolski P, Manniesing R et al (2014) Spirometer-controlled cine magnetic resonance imaging used to diagnose tracheobronchomalacia in paediatric patients. Eur Respir J 43:115–124

Coxson HO (2013) Sources of variation in quantitative computed tomography of the lung. J Thorac Imaging 28:272–279

Coxson HO, Mayo J, Lam S et al (2009) New and current clinical imaging techniques to study chronic obstructive pulmonary disease. Am J Respir Crit Care Med 180:588–597

Davies JC, Wainwright CE, Canny GJ et al (2013) Efficacy and safety of ivacaftor in patients aged 6–11 years with cystic fibrosis with a G551D mutation. Am J Respir Crit Care Med 187:1219–1225

Davis SD, Fordham LA, Brody AS et al (2007) Computed tomography reflects lower airway inflammation and tracks changes in early cystic fibrosis. Am J Respir Crit Care Med 175:943–950

De Jong PA, Lindblad A, Rubin L et al (2006) Progression of lung disease on computed tomography and pulmonary function tests in children and adults with cystic fibrosis. Thorax 61:80–85

Demirkazik FB, Ariyurek OM, Ozcelik U et al (2001) High resolution CT in children with cystic fibrosis: correlation with pulmonary functions and radiographic scores. Eur J Radiol 37:54–59

Dodge JA, Lewis PA, Stanton M et al (2007) Cystic fibrosis mortality and survival in the UK: 1947–2003. Eur Respir J 29:522–526

Donnelly LF, Macfall JR, Mcadams HP et al (1999) Cystic fibrosis: combined hyperpolarized 3He-enhanced and conventional proton MR imaging in the lung--preliminary observations. Radiology 212:885–889

Dournes G, Grodzki D, Macey J et al (2015) Quiet Ssubmillimeter MR imaging of the lung is feasible with a PETRA sequence at 1.5 T. Radiology 276(1):258–265

Dournes G, Menut F, Macey J et al (2016) Lung morphology assessment of cystic fibrosis using MRI with ultra-short echo time at submillimeter spatial resolution. Eur Radiol 26(11):3811–3820

Eichinger M, Optazaite D-E, Kopp-Schneider A et al (2012) Morphologic and functional scoring of cystic fibrosis lung disease using MRI. Eur J Radiol 81:1321–1329

Eichinger M, Puderbach M, Fink C et al (2006) Contrast-enhanced 3D MRI of lung perfusion in children with cystic fibrosis--initial results. Eur Radiol 16:2147–2152

Eichinger M, Puderbach M, Smith HJ et al (2007) Magnetic resonance-compatible-spirometry: principle, technical evaluation and application. Eur Respir J 30:972–979

Esterly JR, Oppenheimer EH (1968) Cystic fibrosis of the pancreas: structural changes in peripheral airways. Thorax 23:670–675

Fink C, Ley S, Kroeker R et al (2005a) Time-resolved contrast-enhanced three-dimensional magnetic resonance angiography of the chest: combination of

parallel imaging with view sharing (TREAT). Investig Radiol 40:40–48

Fink C, Ley S, Risse F et al (2005b) Effect of inspiratory and expiratory breathhold on pulmonary perfusion: assessment by pulmonary perfusion magnetic resonance imaging. Investig Radiol 40:72–79

Fuchs HJ, Borowitz DS, Christiansen DH et al (1994) Effect of aerosolized recombinant human DNase on exacerbations of respiratory symptoms and on pulmonary function in patients with cystic fibrosis. The Pulmozyme Study Group. N Engl J Med 331:637–642

Gevenois PA, De Vuyst P, De Maertelaer V et al (1996) Comparison of computed density and microscopic morphometry in pulmonary emphysema. Am J Respir Crit Care Med 154:187–192

Goris ML, Zhu HJ, Blankenberg F et al (2003) An automated approach to quantitative air trapping measurements in mild cystic fibrosis. Chest 123:1655–1663

Graeber SY, Hug MJ, Sommerburg O et al (2015) Intestinal current measurements detect activation of mutant CFTR in patients with cystic fibrosis with the G551D mutation treated with ivacaftor. Am J Respir Crit Care Med 192:1252–1255

Griswold MA, Jakob PM, Heidemann RM et al (2002) Generalized autocalibrating partially parallel acquisitions (GRAPPA). Magn Reson Med 47:1202–1210

Grydeland TB, Dirksen A, Coxson HO et al (2009) Quantitative computed tomography: emphysema and airway wall thickness by sex, age and smoking. Eur Respir J 34:858–865

Gutberlet M, Kaireit TF, Voskrebenzev A et al (2018) Free-breathing dynamic (19)F gas MR imaging for mapping of regional lung ventilation in patients with COPD. Radiology 286:1040–1051

Hansell DM (2001) Small airways diseases: detection and insights with computed tomography. Eur Respir J 17:1294–1313

Hansell DM, Bankier AA, Macmahon H et al (2008) Fleischner society: glossary of terms for thoracic imaging. Radiology 246:697–722

Hasegawa M, Makita H, Nasuhara Y et al (2009) Relationship between improved airflow limitation and changes in airway calibre induced by inhaled anticholinergic agents in COPD. Thorax 64:332–338

Hasegawa M, Nasuhara Y, Onodera Y et al (2006) Airflow limitation and airway dimensions in chronic obstructive pulmonary disease. Am J Respir Crit Care Med 173:1309–1315

Helbich TH, Heinz-Peer G, Eichler I et al (1999) Cystic fibrosis: CT assessment of lung involvement in children and adults. Radiology 213:537–544

Heussel CP, Herth FJ, Kappes J et al (2009) Fully automatic quantitative assessment of emphysema in computed tomography: comparison with pulmonary function testing and normal values. Eur Radiol 19:2391–2402

Hopkins SR, Henderson AC, Levin DL et al (2007) Vertical gradients in regional lung density and perfusion in the supine human lung: the Slinky effect. J Appl Physiol 103:240–248

Hopkins SR, Wielpütz MO, Kauczor H-U (2012) Imaging lung perfusion. J Appl Physiol 113:328–339

Horn FC, Deppe MH, Marshall H et al (2014) Quantification of regional fractional ventilation in human subjects by measurement of hyperpolarized ^{3}He washout with 2D and 3D MRI. J Appl Physiol 116:129–139

Jakob PM, Wang T, Schultz G et al (2004) Assessment of human pulmonary function using oxygen-enhanced T(1) imaging in patients with cystic fibrosis. Magn Reson Med 51:1009–1016

Jobst BJ, Triphan SM, Sedlaczek O et al (2015a) Functional lung MRI in chronic obstructive pulmonary disease: comparison of T1 mapping, oxygen-enhanced T1 mapping and dynamic contrast enhanced perfusion. PLoS One 10:e0121520

Jobst BJ, Weinheimer O, Trauth M et al (2018) Effect of smoking cessation on quantitative computed tomography in smokers at risk in a lung cancer screening population. Eur Radiol 28(2):807–815

Jobst BJ, Wielpütz MO, Triphan SMF et al (2015b) Morpho-functional ^{1}H-MRI of the lung in COPD: short-term test-retest reliability. PLoS One 10:e0137282

Kanhere N, Couch MJ, Kowalik K et al (2017) Correlation of lung clearance index with hyperpolarized (129) Xe magnetic resonance imaging in pediatric subjects with cystic fibrosis. Am J Respir Crit Care Med 196:1073–1075

Kauczor H-U, Wielpütz MO (2018) MRI of the lung. Springer, Berlin, Heidelberg

Kauczor HU, Wielpütz MO, Owsijewitsch M et al (2011) Computed tomographic imaging of the airways in COPD and asthma. J Thorac Imaging 26:290–300

Kerem B, Rommens JM, Buchanan JA et al (1989) Identification of the cystic fibrosis gene: genetic analysis. Science 245:1073–1080

Kerem E, Reisman J, Corey M et al (1992) Prediction of mortality in patients with cystic fibrosis. N Engl J Med 326:1187–1191

Kohlmann P, Strehlow J, Jobst B et al (2015) Automatic lung segmentation method for MRI-based lung perfusion studies of patients with chronic obstructive pulmonary disease. Int J Comput Assist Radiol Surg 10:403–417

Kongstad T, Buchvald FF, Green K et al (2013) Improved air trapping evaluation in chest computed tomography in children with cystic fibrosis using real-time spirometric monitoring and biofeedback. J Cyst Fibros 12:559–566

Konietzke P, Weinheimer O, Wielpütz MO et al (2018) Validation of automated lobe segmentation on paired inspiratory-expiratory chest CT in 8-14 year-old children with cystic fibrosis. PLoS One 13:e0194557

Kuo W, De Bruijne M, Petersen J et al (2017a) Diagnosis of bronchiectasis and airway wall thickening in children with cystic fibrosis: objective airway-artery quantification. Eur Radiol 27:4680–4689

Kuo W, Kemner-Van De Corput MP, Perez-Rovira A et al (2016) Multicentre chest computed tomogra-

phy standardisation in children and adolescents with cystic fibrosis: the way forward. Eur Respir J 47: 1706–1717

Kuo W, Soffers T, Andrinopoulou ER et al (2017b) Quantitative assessment of airway dimensions in young children with cystic fibrosis lung disease using chest computed tomography. Pediatr Pulmonol 52:1414–1423

Lederlin M, Bauman G, Eichinger M et al (2013) Functional MRI using Fourier decomposition of lung signal: reproducibility of ventilation- and perfusion-weighted imaging in healthy volunteers. Eur J Radiol 82:1015–1022

Leutz-Schmidt P, Stahl M, Sommerburg O et al (2018) Non-contrast enhanced magnetic resonance imaging detects mosaic signal intensity in early cystic fibrosis lung disease. Eur J Radiol 101:178–183

Leutz-Schmidt P, Weinheimer O, Jobst BJ et al (2017) Influence of exposure parameters and iterative reconstruction on automatic airway segmentation and analysis on MDCT-An ex vivo phantom study. PLoS One 12:e0182268

Ley S, Fink C, Puderbach M et al (2004) Contrast-enhanced 3D MR perfusion of the lung: application of parallel imaging technique in healthy subjects. Rofo 176:330–334

Ley S, Puderbach M, Fink C et al (2005) Assessment of hemodynamic changes in the systemic and pulmonary arterial circulation in patients with cystic fibrosis using phase-contrast MRI. Eur Radiol 15:1575–1580

Ley-Zaporozhan J, Ley S, Mews J et al (2017) Changes of emphysema parameters over the respiratory cycle during free breathing: preliminary results using respiratory gated 4D-CT. COPD 14:597–602

Ley-Zaporozhan J, Molinari F, Risse F et al (2011) Repeatability and reproducibility of quantitative whole-lung perfusion magnetic resonance imaging. J Thorac Imaging 26:230–239

Lim HJ, Weinheimer O, Wielpütz MO et al (2016) Fully automated pulmonary lobar segmentation: influence of different prototype software programs onto quantitative evaluation of chronic obstructive lung disease. PLoS One 11:e0151498

Loeve M, Rosenow T, Gorbunova V et al (2015) Reversibility of trapped air on chest computed tomography in cystic fibrosis patients. Eur J Radiol 84:1184–1190

Mai VM, Berr SS (1999) MR perfusion imaging of pulmonary parenchyma using pulsed arterial spin labeling techniques: FAIRER and FAIR. J Magn Reson Imaging 9:483–487

Mall M, Boucher RC (2006) Pathogenesis of pulmonary disease in cystic fibrosis. In: Bush A, Alton EWFW, Davies JC, Griesenbach U, Jaffe A (eds) Cystic fibrosis in the 21st century. Karger, Basel, pp 116–121

Mall MA (2008) Role of cilia, mucus, and airway surface liquid in mucociliary dysfunction: lessons from mouse models. J Aerosol Med Pulm Drug Deliv 21:13–24

Mall MA, Boucher RC (2014) Pathophysiology of cystic fibrosis lung disease. In: Mall MA, Elborn S (eds) Cystic fibrosis. European Respiratory Society, Sheffield, pp 1–13

Mall MA, Hartl D (2014) CFTR: cystic fibrosis and beyond. Eur Respir J 44:1042–1054

Mall MA, Stahl M, Graeber SY et al (2016) Early detection and sensitive monitoring of CF lung disease: prospects of improved and safer imaging. Pediatr Pulmonol 51:S49–S60

Matsuoka S, Kurihara Y, Yagihashi K et al (2008) Quantitative assessment of air trapping in chronic obstructive pulmonary disease using inspiratory and expiratory volumetric MDCT. AJR Am J Roentgenol 190:762–769

Matsuoka S, Kurihara Y, Yagihashi K et al (2007) Quantitative assessment of peripheral airway obstruction on paired expiratory/inspiratory thin-section computed tomography in chronic obstructive pulmonary disease with emphysema. J Comput Assist Tomogr 31:384–389

Mcdermott S, Barry SC, Judge EP et al (2009) Tracheomalacia in adults with cystic fibrosis: determination of prevalence and severity with dynamic cine CT. Radiology 252:577–586

Mcmahon CJ, Dodd JD, Hill C et al (2006) Hyperpolarized 3helium magnetic resonance ventilation imaging of the lung in cystic fibrosis: comparison with high resolution CT and spirometry. Eur Radiol 16: 2483–2490

Mentore K, Froh DK, De Lange EE et al (2005) Hyperpolarized HHe 3 MRI of the lung in cystic fibrosis: assessment at baseline and after bronchodilator and airway clearance treatment. Acad Radiol 12:1423–1429

Mets OM, Roothaan SM, Bronsveld I et al (2015) Emphysema is common in lungs of cystic fibrosis lung transplantation patients: a histopathological and computed tomography study. PLoS One 10:e0128062

Mets OM, Willemink MJ, De Kort FP et al (2012) The effect of iterative reconstruction on computed tomography assessment of emphysema, air trapping and airway dimensions. Eur Radiol 22:2103–2109

Mirza AA, Robinson TE, Gifford K et al (2018) 3D Printing and the cystic fibrosis lung. J Cyst Fibros 17:153–178

Montaudon M, Berger P, Cangini-Sacher A et al (2007a) Bronchial measurement with three-dimensional quantitative thin-section CT in patients with cystic fibrosis. Radiology 242:573–581

Montaudon M, Berger P, De Dietrich G et al (2007b) Assessment of airways with three-dimensional quantitative thin-section CT: in vitro and in vivo validation. Radiology 242:563–572

Mott LS, Park J, Gangell CL et al (2013) Distribution of early structural lung changes due to cystic fibrosis detected with chest computed tomography. J Pediatr 163(243–248):e241–e243

Mott LS, Park J, Murray CP et al (2012) Progression of early structural lung disease in young children with cystic fibrosis assessed using CT. Thorax 67: 509–516

Nagle SK, Puderbach M, Eichinger M et al (2017) Magnetic resonance imaging of the lung: cystic fibrosis. In: Kauczor H, Wielpütz M (eds) MRI of the lung, 2nd edn. Springer, New York

Niimi A, Matsumoto H, Amitani R et al (2000) Airway wall thickness in asthma assessed by computed tomography. Relation to clinical indices. Am J Respir Crit Care Med 162:1518–1523

Niimi A, Matsumoto H, Amitani R et al (2004) Effect of short-term treatment with inhaled corticosteroid on airway wall thickening in asthma. Am J Med 116:725–731

Nikolaou K, Schoenberg SO, Brix G et al (2004) Quantification of pulmonary blood flow and volume in healthy volunteers by dynamic contrast-enhanced magnetic resonance imaging using a parallel imaging technique. Investig Radiol 39:537–545

Nyilas S, Bauman G, Pusterla O et al (2018) Structural and functional lung impairment in primary ciliary dyskinesia. Assessment with magnetic resonance imaging and multiple breath washout in comparison to spirometry. Ann Am Thorac Soc 15:1434–1442

Nyilas S, Bauman G, Sommer G et al (2017) Novel magnetic resonance technique for functional imaging of cystic fibrosis lung disease. Eur Respir J 50:1701464

O'connor OJ, Vandeleur M, Mcgarrigle AM et al (2010) Development of low-dose protocols for thin-section CT assessment of cystic fibrosis in pediatric patients. Radiology 257:820–829

O'sullivan B, Couch M, Roche JP et al (2014) Assessment of repeatability of hyperpolarized gas MR ventilation functional imaging in cystic fibrosis. Acad Radiol 21:1524–1529

Paulin GA, Svenningsen S, Jobse BN et al (2014) Differences in hyperpolarized He ventilation imaging after 4 years in adults with cystic fibrosis. J Magn Reson Imaging 273:887À96

Puderbach M, Eichinger M, Gahr J et al (2007a) Proton MRI appearance of cystic fibrosis: comparison to CT. Eur Radiol 17:716–724

Puderbach M, Eichinger M, Haeselbarth J et al (2007b) Assessment of morphological MRI for pulmonary changes in cystic fibrosis (CF) patients: comparison to thin-section CT and chest x-ray. Investig Radiol 42:715–724

Puderbach M, Risse F, Biederer J et al (2008) In vivo Gd-DTPA concentration for MR lung perfusion measurements: assessment with computed tomography in a porcine model. Eur Radiol 18: 2102–2107

Pusterla O, Bauman G, Bieri O (2018) Three-dimensional oxygen-enhanced MRI of the human lung at 1.5T with ultra-fast balanced steady-state free precession. Magn Reson Med 79:246–255

Pusterla O, Bauman G, Wielputz MO et al (2016) Rapid 3D in vivo 1H human lung respiratory imaging at 1.5 T using ultra-fast balanced steady-state free precession. Magn Reson Med 78(3):1059–1069

Ramsey BW, Banks-Schlegel S, Accurso FJ et al (2012) Future directions in early cystic fibrosis lung disease research: an NHLBI workshop report. Am J Respir Crit Care Med 185:887–892

Ramsey KA, Rosenow T, Turkovic L et al (2016) Lung clearance index and structural lung disease on computed tomography in early cystic fibrosis. Am J Respir Crit Care Med 193:60–67

Ratjen F, Hug C, Marigowda G et al (2017) Efficacy and safety of lumacaftor and ivacaftor in patients aged 6-11 years with cystic fibrosis homozygous for F508del-CFTR: a randomised, placebo-controlled phase 3 trial. Lancet Respir Med 5:557–567

Rayment JH, Couch MJ, Mcdonald N et al (2019) Hyperpolarised (129)Xe MRI to monitor treatment response in children with cystic fibrosis. Eur Respir J 53(5):1802188

Remy-Jardin M, Bouaziz N, Dumont P et al (2004) Bronchial and nonbronchial systemic arteries at multidetector row CT angiography: comparison with conventional angiography. Radiology 233:741–749

Renz DM, Scholz O, Bottcher J et al (2015) Comparison between magnetic resonance imaging and computed tomography of the lung in patients with cystic fibrosis with regard to clinical, laboratory, and pulmonary functional parameters. Investig Radiol 50:733–742

Risse F, Bauman G (2016) MR Perfusion in the lung. In: Kauczor H-U, Wielpütz MO (eds) MRI of the lung, 2nd edn. Springer, Heidelberg

Risse F, Eichinger M, Kauczor HU et al (2011) Improved visualization of delayed perfusion in lung MRI. Eur J Radiol 77:105–110

Roach DJ, Cremillieux Y, Fleck RJ et al (2016) Ultrashort echo-time magnetic resonance imaging is a sensitive method for the evaluation of early cystic fibrosis lung disease. Ann Am Thorac Soc 13:1923–1931

Roberts TP (1997) Physiologic measurements by contrast-enhanced MR imaging: expectations and limitations. J Magn Reson Imaging 7:82–90

Robinson TE, Goris ML, Zhu HJ et al (2005) Dornase alfa reduces air trapping in children with mild cystic fibrosis lung disease: a quantitative analysis. Chest 128:2327–2335

Robinson TE, Leung AN, Northway WH et al (2001) Spirometer-triggered high-resolution computed tomography and pulmonary function measurements during an acute exacerbation in patients with cystic fibrosis. J Pediatr 138:553–559

Robinson TE, Leung AN, Northway WH et al (2003) Composite spirometric-computed tomography outcome measure in early cystic fibrosis lung disease. Am J Respir Crit Care Med 168:588–593

Robinson TE, Long FR, Raman P et al (2009) An airway phantom to standardize CT acquisition in multicenter clinical trials. Acad Radiol 16:1134–1141

Rosenfeld M, Ratjen F, Brumback L et al (2012) Inhaled hypertonic saline in infants and children younger than 6 years with cystic fibrosis: the ISIS randomized controlled trial. JAMA 307:2269–2277

Rosenow T, Oudraad MC, Murray CP et al (2015) PRAGMA-CF. A quantitative structural lung disease computed tomography outcome in young children

with cystic fibrosis. Am J Respir Crit Care Med 191:1158–1165

Salamon E, Lever S, Kuo W et al (2017) Spirometer guided chest imaging in children: It is worth the effort! Pediatr Pulmonol 52:48–56

Schraml C, Schwenzer NF, Martirosian P et al (2012) Non-invasive pulmonary perfusion assessment in young patients with cystic fibrosis using an arterial spin labeling MR technique at 1.5 T. MAGMA 25:155–162

Schreiber WG, Eberle B, Laukemper-Ostendorf S et al (2001) Dynamic (19)F-MRI of pulmonary ventilation using sulfur hexafluoride (SF(6)) gas. Magn Reson Med 45:605–613

Shah RM, Sexauer W, Ostrum BJ et al (1997) High-resolution CT in the acute exacerbation of cystic fibrosis: evaluation of acute findings, reversibility of those findings, and clinical correlation. AJR Am J Roentgenol 169:375–380

Sheikh SI, Long FR, Flucke R et al (2015a) Changes in pulmonary function and controlled ventilation-high resolution CT of chest after antibiotic therapy in infants and young children with cystic fibrosis. Lung 193:421–428

Sheikh SI, Long FR, Mccoy KS et al (2015b) Computed tomography correlates with improvement with ivacaftor in cystic fibrosis patients with G551D mutation. J Cyst Fibros 14:84–89

Sieren JP, Newell JD Jr, Barr RG et al (2016) SPIROMICS protocol for multicenter quantitative computed tomography to phenotype the lungs. Am J Respir Crit Care Med 194:794–806

Sly PD, Brennan S, Gangell C et al (2009) Lung disease at diagnosis in infants with cystic fibrosis detected by newborn screening. Am J Respir Crit Care Med 180:146–152

Sly PD, Gangell CL, Chen L et al (2013) Risk factors for bronchiectasis in children with cystic fibrosis. N Engl J Med 368:1963–1970

Smith L, Marshall H, Aldag I et al (2018) Longitudinal assessment of children with mild cystic fibrosis using hyperpolarized gas lung magnetic resonance imaging and lung clearance index. Am J Respir Crit Care Med 197:397–400

Sobonya RE, Taussig LM (1986) Quantitative aspects of lung pathology in cystic fibrosis. Am Rev Respir Dis 134:290–295

Sommerburg O, Hammermann J, Lindner M et al (2015) Five years of experience with biochemical cystic fibrosis newborn screening based on IRT/PAP in Germany. Pediatr Pulmonol 50:655–664

Sommerburg O, Lindner M, Muckenthaler M et al (2010) Initial evaluation of a biochemical cystic fibrosis newborn screening by sequential analysis of immunoreactive trypsinogen and pancreatitis-associated protein (IRT/PAP) as a strategy that does not involve DNA testing in a Northern European population. J Inherit Metab Dis 33:S263–S271

Stadler A, Stiebellehner L, Jakob PM et al (2007) Quantitative and o(2) enhanced MRI of the pathologic lung: findings in emphysema, fibrosis, and cystic fibrosis. Int J Biomed Imaging 2007:23624

Stahl M, Graeber SY, Joachim C et al (2018a) Three-center feasibility of lung clearance index in infants and preschool children with cystic fibrosis and other lung diseases. J Cyst Fibros 17:249–255

Stahl M, Joachim C, Blessing K et al (2014) Multiple breath washout is feasible in the clinical setting and detects abnormal lung function in infants and young children with cystic fibrosis. Respiration 87: 357–363

Stahl M, Wielpütz MO, Graeber SY et al (2017) Comparison of lung clearance index and magnetic resonance imaging for assessment of lung disease in children with cystic fibrosis. Am J Respir Crit Care Med 195:349–359

Stahl M, Wielputz MO, Ricklefs I et al (2018b) Preventive inhalation of hypertonic saline in infants with cystic fibrosis (PRESIS): a randomized, double-blind, controlled study. Am J Respir Crit Care Med

Stern EJ, Müller NL, Swensen SJ et al (1995) CT mosaic pattern of lung attenuation: etiologies and terminology. J Thorac Imaging 10:294–297

Stern M, Wiedemann B, Wenzlaff P (2008) From registry to quality management: the German Cystic Fibrosis Quality Assessment project 1995–2006. Eur Respir J 31:29–35

Stewart NJ, Chan HF, Hughes PJC et al (2018) Comparison of (3) He and (129) Xe MRI for evaluation of lung microstructure and ventilation at 1.5T. J Magn Reson Imaging 8:632–642

Subbarao P, Stanojevic S, Brown M et al (2013) Lung clearance index as an outcome measure for clinical trials in young children with cystic fibrosis. A pilot study using inhaled hypertonic saline. Am J Respir Crit Care Med 188:456–460

Ter-Karapetyan A, Triphan SMF, Jobst BJ et al (2018) Towards quantitative perfusion MRI of the lung in COPD: the problem of short-term repeatability. PLoS One 13:e0208587

Terheggen-Lagro S, Truijens N, Van Poppel N et al (2003) Correlation of six different cystic fibrosis chest radiograph scoring systems with clinical parameters. Pediatr Pulmonol 35:441–445

Tetzlaff R, Eichinger M, Schobinger M et al (2008) Semiautomatic assessment of respiratory motion in dynamic MRI--comparison with simultaneously acquired spirometry. Rofo 180:961–967

Thomen RP, Walkup LL, Roach DJ et al (2017) Hyperpolarized 129Xe for investigation of mild cystic fibrosis lung disease in pediatric patients. J Cyst Fibros 16:275–282

Triphan SMF, Biederer J, Burmester K et al (2018) Design and application of an MR reference phantom for multicentre lung imaging trials. PLoS One 13

Triphan SMF, Jobst BJ, Breuer FA et al (2015) Echo time dependence of observed T1 in the human lung. J Magn Reson Imaging 42:610–616

Tsuchiya N, Van Beek EJ, Ohno Y et al (2018) Magnetic resonance angiography for the primary diagnosis of

pulmonary embolism: a review from the international workshop for pulmonary functional imaging. World J Radiol 10:52–64

Van Beek EJ, Hill C, Woodhouse N et al (2007) Assessment of lung disease in children with cystic fibrosis using hyperpolarized 3-Helium MRI: comparison with Shwachman score, Chrispin-Norman score and spirometry. Eur Radiol 17:1018–1024

Voskrebenzev A, Gutberlet M, Klimes F et al (2018) Feasibility of quantitative regional ventilation and perfusion mapping with phase-resolved functional lung (PREFUL) MRI in healthy volunteers and COPD, CTEPH, and CF patients. Magn Reson Med 79:2306–2314

Walkup LL, Thomen RP, Akinyi TG et al (2016) Feasibility, tolerability and safety of pediatric hyperpolarized (129)Xe magnetic resonance imaging in healthy volunteers and children with cystic fibrosis. Pediatr Radiol 46:1651–1662

Weatherly MR, Palmer CG, Peters ME et al (1993) Wisconsin cystic fibrosis chest radiograph scoring system. Pediatrics 91:488–495

Webb WR, Stein MG, Finkbeiner WE et al (1988) Normal and diseased isolated lungs: high-resolution CT. Radiology 166:81–87

Weinheimer O, Achenbach T, Bletz C et al (2008) About objective 3-d analysis of airway geometry in computerized tomography. IEEE Trans Med Imaging 27:64–74

Weinheimer O, Achenbach T, Düber C (2009) Fully automated extraction of airways from CT scans based on self-adapting region growing. In: Brown M, De Bruijne B, Van Ginneken B, Kiraly AP, Kuhnigk JM, Lorenz C, Mcclelland JR, Mori K, Reeves AP, Reinhardt J (eds) Proceedings of Second International Workshop on Pulmonary Image Analysis (in conjunction with MICCAI) 2009

Weinheimer O, Achenbach T, Heussel CP et al (2011) Automatic lung segmentation in MDCT images. Fourth Int Workshop Pulmon Image Analysis 2011:241–255

Weinheimer O, Hoff BA, Fortuna AB et al (2018) Influence of inspiratory/expiratory CT registration on quantitative air trapping. Acad Radiol

Weinheimer O, Wielpütz MO, Konietzke P, et al. 2017. Fully automated lobe-based airway taper index calculation in a low dose MDCT CF study over 4 timepoints. *Medical Imaging 2017: Image Processing*

Wielpütz MO, Bardarova D, Weinheimer O et al (2014a) Variation of densitometry on computed tomography in COPD--influence of different software tools. PLoS One 9:e112898

Wielpütz MO, Eberhardt R, Puderbach M et al (2014b) Simultaneous assessment of airway instability and respiratory dynamics with low-dose 4D-CT in chronic obstructive pulmonary disease: a technical note. Respiration 87:294–300

Wielpütz MO, Eichinger M, Biederer J et al (2016) Imaging of cystic fibrosis lung disease and clinical interpretation. Rofo 188:834–845

Wielpütz MO, Eichinger M, Puderbach M (2013a) Magnetic resonance imaging of cystic fibrosis lung disease. J Thorac Imaging 28:151–159

Wielpütz MO, Eichinger M, Wege S et al (2019) Mid-term reproducibility of chest MRI in adults with clinically stable cystic fibrosis and chronic obstructive pulmonary disease. Am J Respir Crit Care Med 200(1):103–107

Wielpütz MO, Eichinger M, Weinheimer O et al (2013b) Automatic airway analysis on multidetector computed tomography in cystic fibrosis: correlation with pulmonary function testing. J Thorac Imaging 28:104–113

Wielpütz MO, Mall MA (2015) Imaging modalities in cystic fibrosis: emerging role of MRI. Curr Opin Pulm Med 21:609–616

Wielpütz MO, Mall MA (2017) MRI accelerating progress in functional assessment of cystic fibrosis lung disease. J Cyst Fibros 16:165–167

Wielpütz MO, Puderbach M, Kopp-Schneider A et al (2014c) Magnetic resonance imaging detects changes in structure and perfusion, and response to therapy in early cystic fibrosis lung disease. Am J Respir Crit Care Med 189:956–965

Wielpütz MO, Triphan SMF, Ohno Y et al (2018a) Outracing lung signal decay - potential of ultrashort echo time MRI. Rofo 191:415–423

Wielpütz MO, Von Stackelberg O, Stahl M et al (2018b) Multicentre standardisation of chest MRI as radiation-free outcome measure of lung disease in young children with cystic fibrosis. J Cyst Fibros 17: 518–527

Wielpütz MO, Weinheimer O, Eichinger M et al (2013c) Pulmonary emphysema in cystic fibrosis detected by densitometry on chest multidetector computed tomography. PLoS One 8:e73142

Wolf T, Anjorin A, Posselt H et al (2009) MRI-based flow measurements in the main pulmonary artery to detect pulmonary arterial hypertension in patients with cystic fibrosis. Rofo 181:139–146

Woodhouse N, Wild JM, Van Beek EJ et al (2009) Assessment of hyperpolarized 3He lung MRI for regional evaluation of interventional therapy: a pilot study in pediatric cystic fibrosis. J Magn Reson Imaging 30:981–988

Yuan R, Mayo JR, Hogg JC et al (2007) The effects of radiation dose and CT manufacturer on measurements of lung densitometry. Chest 132:617–623

Zach JA, Newell JD Jr, Schroeder J et al (2012) Quantitative computed tomography of the lungs and airways in healthy nonsmoking adults. Investig Radiol 47:596–602

Zach JA, Williams A, Jou SS et al (2016) Current smoking status is associated with lower quantitative CT measures of emphysema and gas trapping. J Thorac Imaging 31:29–36

Zaporozhan J, Ley S, Weinheimer O et al (2006) Multidetector CT of the chest: influence of dose onto quantitative evaluation of severe emphysema: a simulation study. J Comput Assist Tomogr 30:460–468

Zha W, Nagle SK, Cadman RV et al (2019) Three-dimensional isotropic functional imaging of cystic fibrosis using oxygen-enhanced MRI: comparison with hyperpolarized (3)He MRI. Radiology 290: 229–237

Functional Assessment of Pulmonary Venous Thromboembolism

Edwin J. R. van Beek and Andrew J. Swift

Contents

1 **Introduction** 208

2 **Diagnosis of Pulmonary Thromboembolism** 208

3 **Assessment of Effects of Acute Pulmonary Thromboembolism** 209
3.1 Lung Scintigraphy 209
3.2 Computed Tomography (CT) 210
3.3 Magnetic Resonance Imaging (MRI) 215

4 **Diagnosis of Chronic Pulmonary Thromboembolism** 216
4.1 CT Assessment of Chronic Thromboembolic Disease 217
4.2 MR Imaging of Chronic Thromboembolic Disease 218

5 **Conclusions** 219

References 220

Abstract

Pulmonary venous thromboembolism remains one of the most common, potentially lethal, disorders in clinical medicine with an estimated 7 per 10,000 population cases diagnosed annually. Most patients who reach hospital will ultimately survive the episode, although they will remain at risk of recurrent disease, acute complications such as pulmonary infarction and secondary infection, while the treatment modalities carry risks of haemorrhage.

Although morphologic assessment is key to diagnose the disease, it is equally important to stratify patients into groups with or without haemodynamic compromise, as this will affect therapeutic management. Thus, functional assessment of the effects of pulmonary venous thromboembolism on the pulmonary circulation and the heart are increasingly recognized as important steps to improving initial and long-term outcomes.

E. J. R. van Beek (✉)
Edinburgh Imaging, University of Edinburgh, Edinburgh, UK

Department of Radiology, Royal Infirmary of Edinburgh, Edinburgh, UK
e-mail: Edwin-vanbeek@ed.ac.uk

A. J. Swift
Academic Unit of Radiology, University of Sheffield, Sheffield, UK

© Springer Nature Switzerland AG 2021

Y. Ohno et al. (eds.), *Pulmonary Functional Imaging*, Medical Radiology Diagnostic Imaging,
https://doi.org/10.1007/978-3-030-43539-4_11

This chapter will focus on the opportunities to diagnose pulmonary venous thromboembolism, with a focus on the ability to link morphological assessment with functional classification of disease severity.

1 Introduction

The diagnosis of pulmonary venous thromboembolism (PE) is commonly contemplated, requiring significant numbers of patients to undergo testing. This need for testing is dominated by the potential fatal complications of acute PE (in up to 30% of patients following an acute initial event), the risks of treatment (with up to 7% haemorrhagic complications per year of anticoagulant therapy) and the risk of recurrent disease leading to more advanced pulmonary vascular disease, including chronic thromboembolic pulmonary hypertension (in up to 5% of patients). It has been estimated that PE is the third leading cause of cardiovascular mortality after stroke and myocardial infarction.

Pulmonary venous thromboembolism is frequently associated with underlying morbidities, which increase the risk for thrombotic disorders. Some of these are temporary risks, such as patients recovering from trauma or surgery, whereas others may be life-long, such as patients with malignancy or with underlying thrombophilia. These factors often determine the level of clinical suspicion, may influence the diagnostic pathway, and also impact on therapeutic options and outcomes. In all situations, the accurate diagnosis or exclusion of PE is paramount.

More recently, it has become increasingly apparent that merely making the diagnosis may not be sufficient for allocating the appropriate therapy for patients. Since a number of years, the haemodynamic response to an acute event of PE has been shown to have a direct impact on outcome, and therefore those with haemodynamic instability warrant more aggressive thrombolytic treatment compared to those where the haemodynamics are maintained. It is important to realize that cardiopulmonary reserve plays a significant role, and younger, healthier patients are more likely to survive more severe PE compared to older, frailer patients. Furthermore, the more severely affected patients are more likely to have incomplete PE resolution with treatment, placing them at an increased risk for developing pulmonary hypertension. Thus, not only do we need information regarding the morphological distribution of PE, we also require insights into the impact the PE has on the individual patient.

This chapter will describe the diagnostic abilities of imaging tests for PE, and will go into some detail as to how the severity and functional impact of PE can be assessed. The focus will be on lung scintigraphy, computed tomography (CT) and magnetic resonance imaging (MRI).

2 Diagnosis of Pulmonary Thromboembolism

The diagnosis of pulmonary embolism is often cumbersome, and requires a combination of clinical assessment (including history, electrocardiography and chest radiography), blood tests (e.g. plasma D-dimer), and various diagnostic imaging methods (ranging from echocardiography and leg vein ultrasound to computed tomography (CT), magnetic resonance imaging (MRI) and rarely invasive pulmonary angiography) (Konstantinides et al. 2014). The overriding need is to make an accurate diagnosis quickly in order to start appropriate treatment, or alternatively rule out the disease with sufficient certainty that anticoagulants (with their potential haemorrhagic side effects) may be withheld.

For the exclusion of pulmonary thromboembolism, a low clinical suspicion with a normal plasma D-dimer level is considered sufficient (Konstantinides et al. 2014). Other methods to exclude the disease include normal perfusion scintigraphy, normal CT pulmonary angiography and normal invasive catheter pulmonary angiography.

For the diagnosis of pulmonary thromboembolism, direct visualization of the emboli with the aid of echocardiography, CT, MRI or angiography is mandatory. Secondary findings, such as deep vein thrombosis on leg ultrasound, may be used to support the diagnosis.

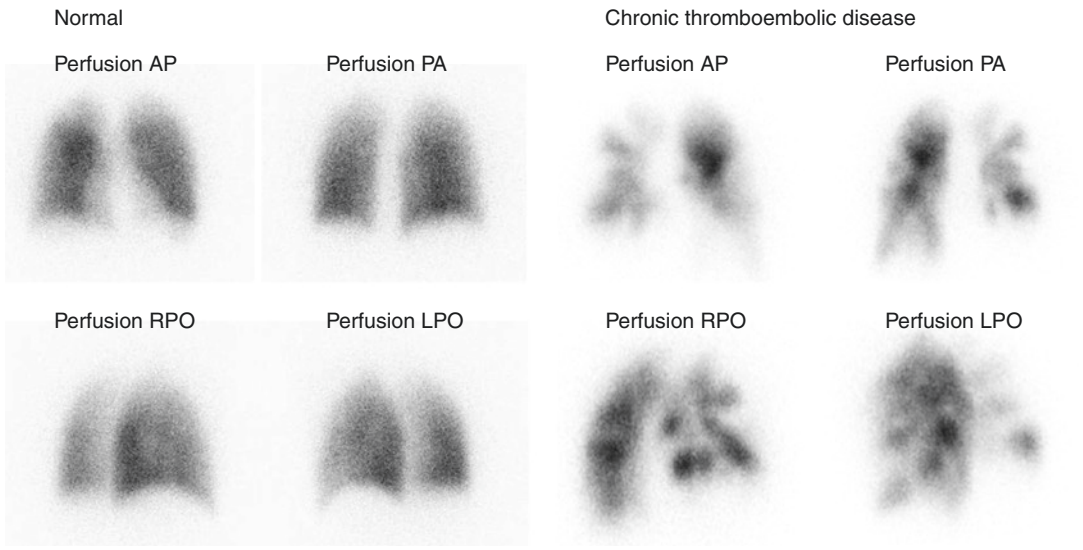


Fig. 1 99 m-Technetium perfusion and 81 m-Krypton ventilation scintigraphy in 6 planes, normal study

Lung scintigraphy was traditionally applied for the assessment of suspected pulmonary thromboembolism (van Beek et al. 1993). The ability to exclude clinically significant pulmonary embolism was shown (Fig. 1). The positive predictive value was less well developed, with up to 50% of patients requiring additional diagnostic testing. The application of higher resolution camera systems with incorporation of CT for anatomical correlation has slightly improved the diagnostic accuracy. Nevertheless, in most hospitals, lung scintigraphy is no longer the first-line test of choice due to lack of 24 h availability and the additional value of CT pulmonary angiography for the detection of alternative diagnoses.

The use of CT pulmonary angiography has increased significantly over the past few decades, leading to a gradual decrease in overall positive findings, and a greater number of smaller (possibly clinically insignificant) pulmonary emboli being diagnosed. Computer-aided diagnosis for CT pulmonary angiography has been developed, to avoid interobserver variation (Hochhegger et al. 2014) and to aid in the detection of smaller pulmonary emboli in particular. Several of these systems have made it into the clinical domain (Maizlin et al. 2007; Schoepf et al. 2007; Dewailly et al. 2010; Kligerman et al. 2014).

The impact of various technical conditions of CT pulmonary angiograms, including ECG gating or non-gating, the use of dual energy imaging and image quality should not be underestimated in clinical practice. One study demonstrated that a CAD system was less sensitive to these influences, with 97% peripheral emboli accurately detected (Dewailly et al. 2010).

Magnetic resonance angiography (MRA) has also shown promising results. Following the initial testing, which already showed high diagnostic accuracy in central and lobar embolism (Meaney et al. 1997; Oudkerk et al. 2002), the more recent application of faster MR methods has demonstrated the feasibility of using this as the first-line test (Nagle et al. 2016). Furthermore, it has allowed more functional assessment using MR perfusion, which have shown potential use in both acute and chronic pulmonary embolism assessment (Johns et al. 2017a, b).

3 Assessment of Effects of Acute Pulmonary Thromboembolism

3.1 Lung Scintigraphy

Lung scintigraphy has been established as a method to determine both pulmonary perfusion and ventilation using infusion of ^{99m}Technetium labelled macro-aggregates of albumin and

various inhaled gasses (^{131}Xe, ^{133}Xe, ^{81m}Kr) or particulates (^{99m}Tc-Carbon) (van Beek et al. 1993), Fig. 1. It continues to play a role in the diagnostic workup of patients with suspected acute pulmonary embolism despite the rise of CTPA as the workhorse in this disease area (Koukouraki et al. 2018). It is well established that SPECT imaging is superior to planar imaging in terms of diagnostic accuracy and radiation dose, and is the reference standard for perfusion assessment (Gutte et al. 2010; Kan et al. 2015; Phillips et al. 2015). From a systematic review and meta-analysis, V/Q SPECT was shown to have excellent diagnostic utility 96% sensitivity and 87% specificity for the diagnosis of pulmonary embolism (Kan et al. 2015). The original multicentre study, namely Prospective Investigation of Pulmonary Embolism Diagnosis (PIOPED) study classified V/Q scans as follows: high-probability, intermediate-probability, low-probability and indeterminate (Webber et al. 1990). The modified PIOPED II criteria classifies studies as follows: high probability, very low probability, normal and non-diagnostic. The modified PIOPED II and prospective investigative study of acute pulmonary embolism diagnosis (PISAPED) criteria have been shown to have fewer non-diagnostic examinations compared to previous approaches (Sostman et al. 2008; Parker et al. 2012).

In practice, typically SPECT is reserved as a second-line investigation in the case of indeterminate findings or for patients where CT pulmonary angiography is contraindicated. A hybrid approach has been proposed, SPECT/CT which has been suggested to be a promising approach with excellent diagnostic accuracy and economic value with lowest misdiagnosis or underdiagnosis (Toney et al. 2017). In pregnancy, if both CT pulmonary angiography and SPECT are available, then SPECT may be the preferred approach given the lower dose to breast tissue and similar foetal dose, but this would rely on only perfusion scintigraphy being performed in the presence of a normal chest radiograph.

3.1.1 Positron Emission Tomography

The use of ^{15}O-water positron emission tomography (^{15}O-H_2O PET) is regarded as the reference standard for assessment of tissue flow, as it can be precisely quantitatively assessed as ml/lung volume (Schuster et al. 1995). More recently, this method has been refined by compensating the tissue density of the lung within the measurements, allowing for better correlation of actual regional blood flow through the lungs (Matsunaga et al. 2017). The latest research suggests that the blood flow is more uniform than previously thought, and has potential implications for pulmonary blood flow assessment by non-invasive means.

To date, this method is not widely available, nor advocated due to radiation. However, it could be a useful method to test the hypothesis that non-invasive measurements, such as CT- or MR-based lung perfusion, should be validated against this technique.

3.2 Computed Tomography (CT)

CT pulmonary angiography is an excellent tool for the identification and exclusion of acute pulmonary embolism. CT pulmonary angiography is widely utilized for this purpose and is typically the first-line diagnostic imaging methodology in patients attending with suspected acute pulmonary embolism. CT pulmonary angiography is widely available, cost effective and well established in the clinical workup of these patients. Radiation dose is an important consideration and efforts should be made to optimize dose, modern scanners and the use of iterative reconstruction have vastly reduced radiation dose in recent years (Table 1) (Pontana et al. 2015).

Acute pulmonary emboli are seen as filling defects on CTPA allowing an assessment of the severity of the clots, and an assessment of their distribution (Mastora et al. 2003). In addition, review of the lungs may reveal lung parenchymal features such as a mosaic perfusion or pulmonary infarction which have prognostic significance (Atasoy et al. 2015).

Table 1 CT protocol suggestions for CT pulmonary angiography and CT perfusion

	CT pulmonary angiogram	CT pulmonary perfusion
	64 MDCT	320 MDCT
Breath-hold	Yes	Yes
Rotation time	0.5 s	0.5 s
Collimation	64 × 1.25	320 × 0.5 mm
Pitch	3	16 cm *z*-axis coverage
Slice thickness	0.6 mm	0.5 mm
kVp	100	100
mA	70	100 (50 mAs)
Iterative reconstruction	Yes	Yes
Matrix	512 × 512	512 × 512
Contrast	100 ml 320 mgI/ml	70 ml 400 mfI/ml
Injection rate	4 ml/s	9 ml/s
Scan delay	Automated	3 s
Repeated scans	No	11 at 1.5 s interval
Dose-length product	270 mGy.cm	540 mGy.cm
Effective dose ($k = 0.014$)	<3.0 mSv	7.56 mSv

Dual-energy CT (DECT) uses two energy levels to create data sets from two distinct X-ray spectra. DECT imaging is a novel approach to assess lung perfusion by mapping iodine distribution within lung parenchyma (Thieme et al. 2010). Compared with conventional CT pulmonary angiography, CT pulmonary angiography based on DE imaging not only displays the emboli and related morphologic information but also simultaneously provides function information associated with pulmonary perfusion on the iodine maps (Thieme et al. 2012). However, a recent study in 1144 CT studies in 1035 patients revealed PE in 147 studies (12.8%) (Weidman et al. 2018). The incremental value of DECT over standard CTPA was shown to detect an additional 27 emboli in 11 of 1144 studies, or an extra 1% of patients. Thus, the incremental value was small, although the technique is capable of better demonstrating occlusive from non-occlusive emboli.

The diagnostic potential of CT has been further studied using (semi-) automated computer-assisted diagnosis systems. A study aimed to link a fully automatic CAD detected severity/extent of pulmonary emboli and the development of right heart failure in 557 patients with proven pulmonary embolism and without underlying cardiopulmonary disease (Li et al. 2017). The study compared to overall burden of emboli with the ratio of the right ventricle over the left ventricle (as a parameter of right heart strain), and demonstrated a significant correlation. The reporting time for radiologists decreased from 15 to less than 5 min.

More recently, it has been suggested that machine learning may be applied to accurately predict the presence of pulmonary embolism without any need for imaging (Rucco et al. 2015). In this study of 1427 patients at risk of pulmonary embolism, they extracted 28 diagnostic features, which were incorporated in a neural hypernetwork, which was able to predict those going on to develop pulmonary embolism in 94% of cases. Although this may be helpful to better identify patients at risk of developing pulmonary embolism, it will not aid in the diagnostic process of pulmonary embolism.

Although several clinical CAD systems exist for the identification of pulmonary embolism, they have been fairly limited in gaining access to routine clinical workloads. This may in part be due to the excellent diagnostic quality of CT pulmonary angiograms with later CT systems or the utility of easier visualization of emboli, for instance through iodine mapping. It is important to recognize the various influences on the performance of these CAD systems, such as type of CT scanner, slice thickness and implementation by radiologists of different experience levels. The role for machine learning approaches to

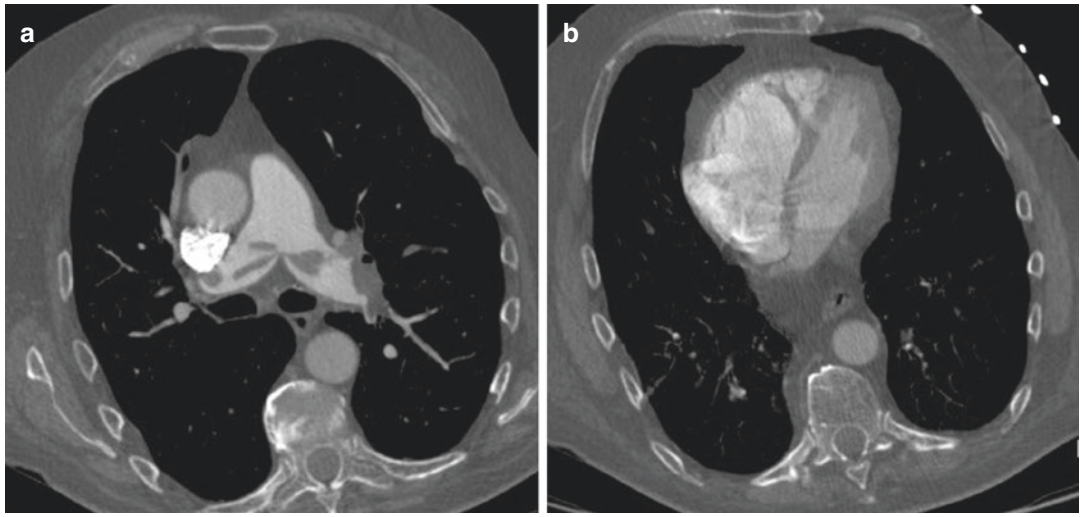


Fig. 2 CT pulmonary angiography demonstrating large central emboli (**a**) with evidence of increased right cardiac pressure with right ventricular enlargement (**b**)

pulmonary embolism is not clear at present, but this should be a promising area of research.

3.2.1 Cardiac Assessment and Right Heart Strain

Signs of right ventricular strain can be identified on CT (Fig. 2). The most commonly utilized measurement is the right ventricular to left ventricular diameter ratio (RV:LV); this parameter is consistently a strong predictor of early mortality following acute pulmonary embolism (Ghaye et al. 2006). The RV:LV ratio is a simple, practical and reproducible approach to assess right heart strain after simple instruction (Ende-Verhaar et al. 2017); in addition, it is consistently shown that the measuring RV strain is of more prognostic value than measures of pulmonary arterial clot load (Osman and Abdeldayem 2018). It has been shown that normal RV:LV ratio combined with standard clinical predictors can confidently exclude right heart strain and PE-related short-term mortality (Kumamaru et al. 2016a, b). In addition, a multimodality approach considering CT pulmonary angiography, echocardiography and serology in this case, Troponin may improve the prognostic assessment in acute pulmonary embolism (Carroll et al. 2018). Automatic calculation of RV:LV ratio has been trialled and may save reporters time making the measurements, though still does require manual adjustment in many cases (Kumamaru et al. 2016a, b). A different approach was used in a study that aimed to correlate automatically segmented cardiac chamber volume to the outcome of patients with pulmonary embolism (Aviram et al. 2016). Thus, although this software tool did not directly aim to visualize pulmonary embolism, it was applied as a predictor for mortality. Of 756 consecutive patients, segmentation was successful to determine cardiac chamber volumes in 636 patients (84% success rate) and was correlated with mortality (84 patients died within 30 days with a diagnosis of pulmonary embolism). The most predictive marker was decreased left atrial volume of 62 ml or less, which increased the mortality risk 2.4-fold. It is postulated that the smaller left atrium is due to vascular obstruction and high pulmonary vascular resistance and decreased left heart preload/filling (Aviram et al. 2016).

3.2.2 Pulmonary Perfusion

Until recently, the use of CT perfusion for assessment of the pulmonary vasculature was not recommended due to radiation dose constraints. However, since the introduction of faster CT systems, that could cover a larger volume and used dose reduction measures, such as iterative

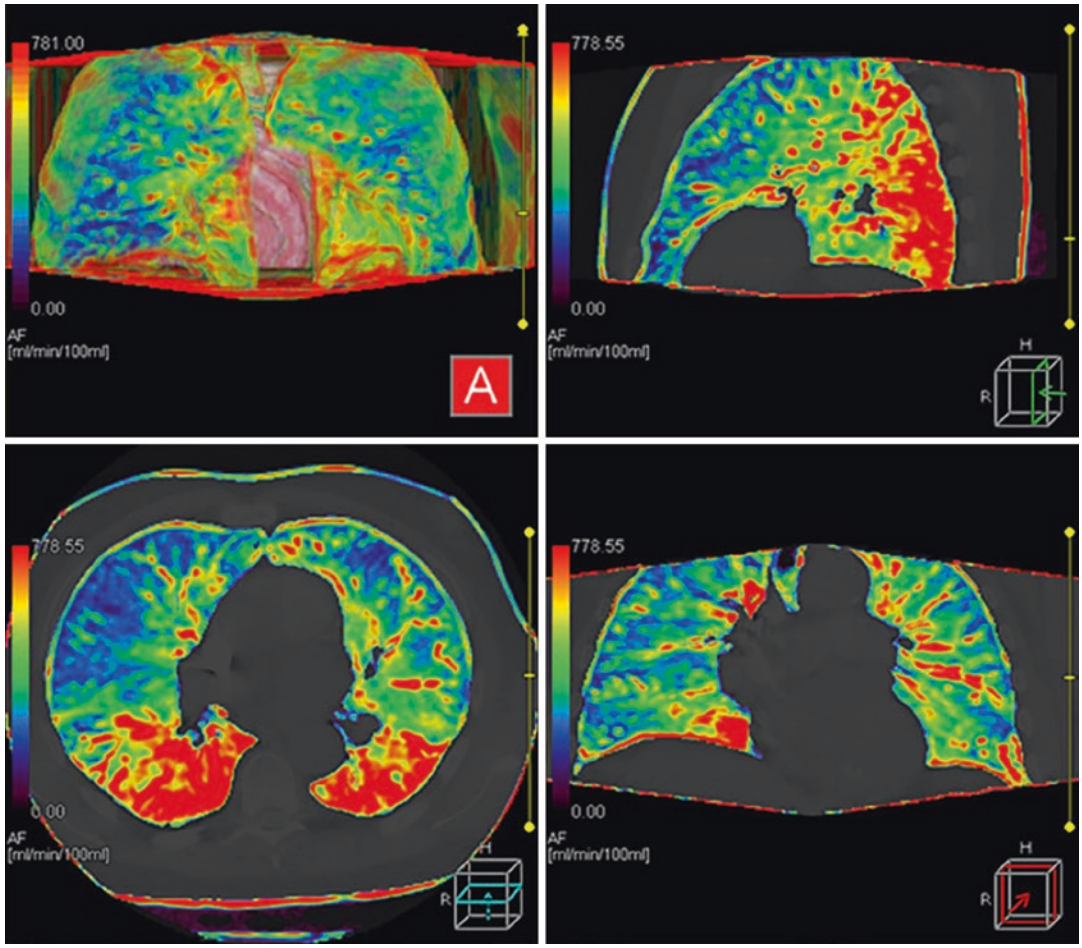


Fig. 3 CT perfusion study demonstrating normal gravity-dependent perfusion in a patient following 6 months treatment for an acute CT proven episode of pulmonary embolism

reconstruction, CT perfusion protocols have been developed and successfully tested in research studies (Fig. 3) (Mirsadraee et al. 2015). A study in 26 patients, who were imaged after 3–6 months of anticoagulant treatment for acute PE, demonstrated significant perfusion abnormalities in 17 patients, even in the absence of CT angiography demonstrated emboli (Fig. 4) (Mirsadraee et al. 2016). Furthermore, time courses of contrast attenuation demonstrated systemic circulation had replaced pulmonary circulation, thus allowing for continued viability of the affected lung. None of the patients demonstrated right ventricular dilation at follow-up imaging (Mirsadraee et al. 2016).

An alternative approach has been to use multi-energy (and more recently, spectral) CT to detect so-called perfusion abnormalities. It should be pointed out that this is not perfusion in the strictest sense, but rather refers to blood volume measurements. Nevertheless, the application of iodine mapping in DECT has proven useful for quantification of absent contrast enhancement and has shown to be of prognostic significance for the outcome of patients with both acute and chronic PE (Meinel et al. 2013; Masy et al. 2018). A direct correlation was demonstrated between DECT severity assessment of pulmonary embolism, a score of pulmonary arterial clot load (Mastora), blood oxygenation and right ventricular failure in 63 patients with acute PE (Thieme et al. 2012). Thus, this method may assist in the stratification of risk for significant adverse events

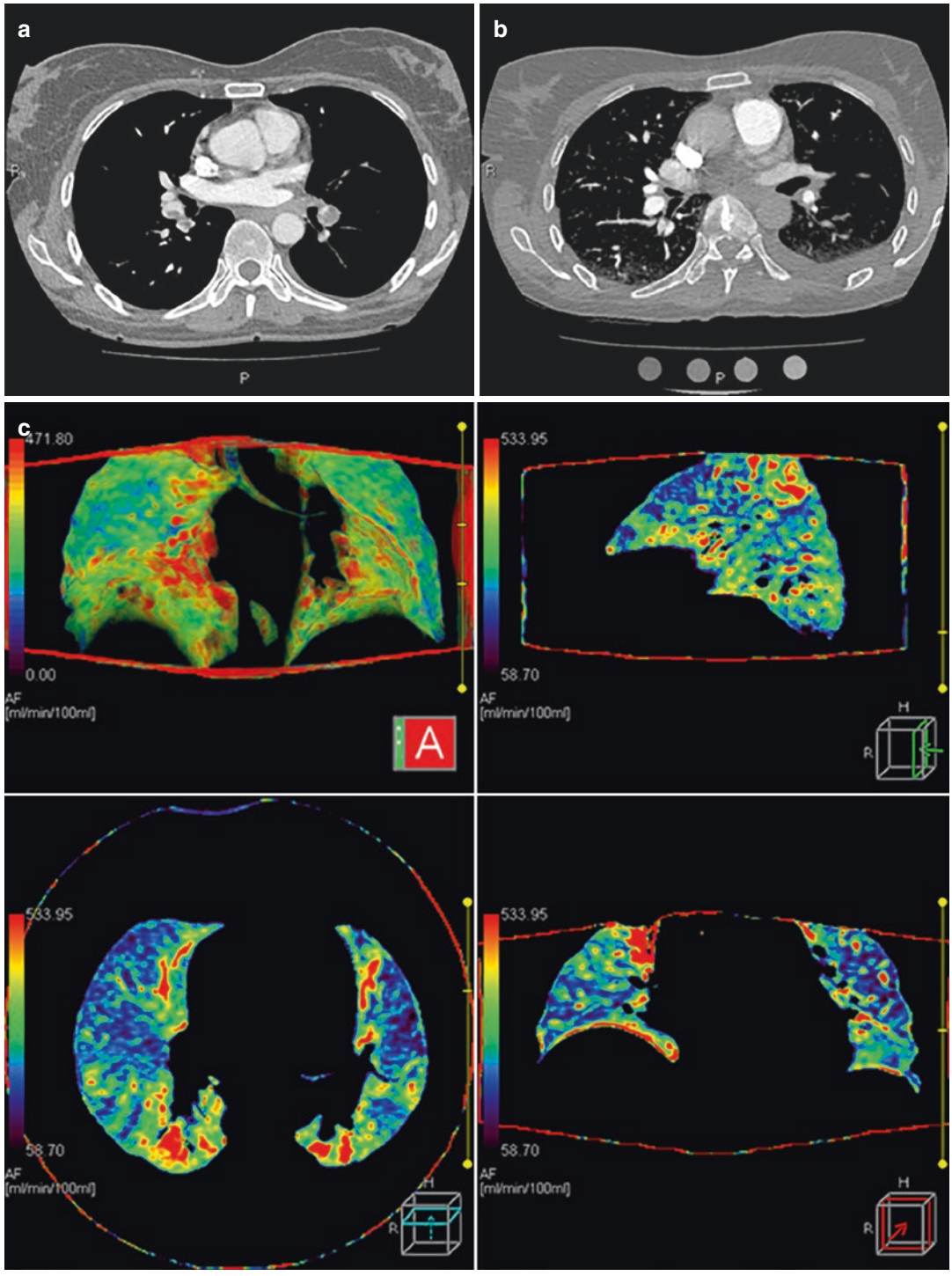


Fig. 4 (**a**) Pre-treatment CT pulmonary angiogram with multiple lobar pulmonary emboli. (**b**) Post-treatment CT pulmonary angiogram with resolution of lobar pulmonary emboli. (**c**) Post-treatment CT perfusion demonstrating multiple perfusion defects following 6 months of anticoagulant therapy

and help determine treatment requirements and necessity for more aggressive thrombolytic therapy (Meinel et al. 2013). However, a recent retrospective study in 172 patients with acute PE could not demonstrate a prognostic value of the extent of perfusion defects over right ventricular dilatation for 30-day mortality (Im et al. 2017).

3.3 Magnetic Resonance Imaging (MRI)

Magnetic resonance imaging (MRI) has the potential to assess the pulmonary arteries using MR pulmonary angiography. The great advantage of MRI is the lack of ionizing radiation and multitude of functional information that can be attained (Fig. 5). MR angiography has been shown to be diagnostic of pulmonary embolism, most accurate for proximal pulmonary emboli. The PIOPED III study showed that MR angiography was limited by a high rate of technically inadequate studies (Sostman et al. 2012). The key factors resulting in lower accuracy are poor vascular opacification and motion, typically breathing artefact; in addition, there are clear differences in imaging quality between centres. More recently, with protocol refinements, higher consistency and accuracy has been achieved (Table 2) (Schiebler et al. 2013), though this may

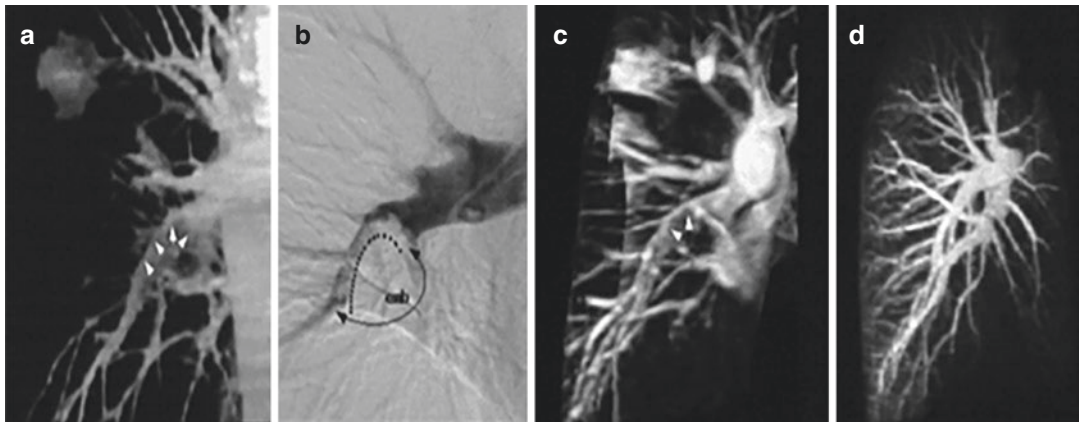


Fig. 5 Comparison of CT angiogram (**a**), invasive angiogram (**b**) and MR angiogram (**c**) in a patient with lobar pulmonary embolism. A follow-up MR angiogram demonstrates complete resolution (**d**). Reproduced from reference Oudkerk et al. (2002)

Table 2 Suggested protocol for MRA and MR perfusion imaging

	3D MR perfusion imaging	Time resolved contrast kinetic imaging	Magnetic resonance angiography
TE (ms)	0.7	103	1
TR (ms)	2.1	2.8	2.8
Flip angle (degrees)	30	30	30
Band width (Hz)	125	128	125
FOV (mm)	48	48	48
Slice thickness (mm)	10	8	3
PHASE	120	256	320
FREQ	80	160	200
NEX	1	1	1
Temporal phases	48	48	
Temporal resolution	0.5 s	1 s	
Asset	2	2	2
ZIP		2	
K-space filling	Centric	Centric	Centric

still not be adequate for widespread clinical implementation (Li et al. 2016). Access to MRI, costs and technical expertise are further potential hurdles to clinical implementation.

3.3.1 Cardiac Assessment and Right Heart Strain

MRI is highly capable of performing cardiac functional assessment in combination with performing pulmonary vascular diagnostic procedures. Thus, both morphological measurements, such as chamber size and myocardial hypertrophy, and functional characteristics, such as myocardial viability and motion/contractiblity, can be performed in a single setting. Thus, MRI may offer a very comprehensive assessment of right heart strain in the context of acute PE.

However, overall assessment will likely be limited due to time constraints as well as the acute situation of patients. Table time should be limited, and therefore will focus mainly on the pulmonary vasculature itself to determine whether acute PE is present or not. Simple assessment of right ventricular/left ventricular ratio and a cine evaluation of the right ventricle may be feasible within this limited period of time.

3.3.2 Pulmonary Perfusion

Three-dimensional contrast-enhanced lung perfusion MRI allows evaluation of lung parenchyma perfusion and can thus detect lung perfusion defects due to pulmonary embolism. A combined approach using MR angiography and 3D contrast-enhanced lung perfusion MRI may increase diagnostic accuracy of acute pulmonary embolism. Though the IRM-EP study showed that with current MRI technology high specificity and high sensitivity for proximal pulmonary embolism can be achieved, but still demonstrated limited sensitivity for distal pulmonary emboli and a high inconclusive rate (Revel et al. 2012). The functional sensitivity of MRI is an advantage and further study of the effectiveness of new approaches such as non-contrast ECG-gated Fourier decomposition MRI, an approach that allows lung perfusion to be assessed by detecting the pulsation of blood in the lung parenchyma. The clinical utility of this method in acute pulmonary embolism remains unclear. In addition, approaches to counter breathing artefact, such as free breathing approaches to MR lung perfusion, may reduce the inadequate study rates (Ingrisch et al. 2016).[4]

4 Diagnosis of Chronic Pulmonary Thromboembolism

Non-fatal pulmonary thromboembolism usually resolves completely, with no residual disease remaining and normal pulmonary artery pressures being restored within 10–21 days (Dalen et al. 1969). In a small percentage of cases (1–7% of all acute events), vascular remodelling occurs due to the thrombus which leads to chronic elevation of pulmonary arterial pressure (Moser and Bloor 1993; Auger et al. 2007); this condition is known as chronic thromboembolic pulmonary hypertension (CTEPH). The true prevalence of CTEPH in the general population is thought to be significantly underestimated with studies indicating that up to 4% of patients with acute symptomatic pulmonary thromboembolism will develop CTEPH (Pengo et al. 2004).

Imaging plays a key role in the assessment of patients with suspected CTEPH. Patients with CTEPH are divided based on CT imaging into either surgically accessible or surgically non-accessible; this is important as it guides further management. Surgically accessible CTEPH is treatable with endarterectomy; removal of the obstructing clots leads to a reduction in RV afterload and improved RV function. Studies have shown improvements in patient symptoms (van der Plas et al. 2010), pulmonary haemodynamics and reduced mortality (Condliffe et al. 2008). Pulmonary endarterectomy, despite being an effective therapy (Lang 2009), has drawbacks: some patients are considered unsuitable for surgery due to co-morbidities or technical difficulties relating to patient anatomy and the location of the thromboembolic disease, while some patients choose for non-surgical options (Quadery et al. 2018). Non-accessible CTEPH is

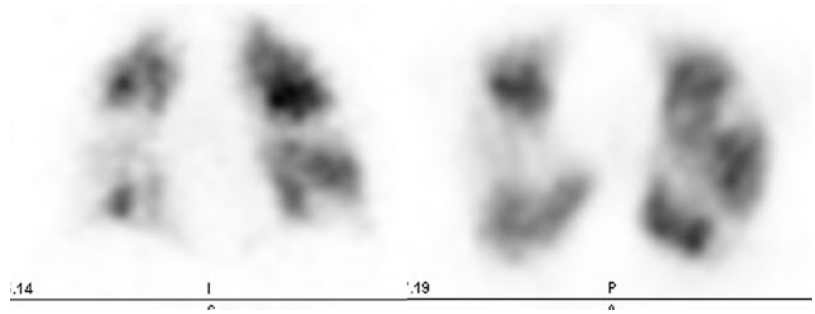


Fig. 6 SPECT slices in a patient with chronic thromboembolic disease. Bilateral segmental 'wedge-shaped' lung perfusion defects are shown

considered inoperable, and thus treatment is restricted to pharmacological therapies (Suntharalingam et al. 2007). From an imaging perspective, non-accessible or distal CTEPH represents thromboembolic disease situated predominantly at the subsegmental pulmonary arterial level or beyond (Suntharalingam et al. 2007).

Chest radiographs may suggest the diagnosis of chronic thromboembolic disease. Features include cardiomegaly, asymmetrical pulmonary artery enlargement / pruning of the vasculature and subpleural scarring—however, they are not diagnostic, and the chest radiograph is commonly normal. Traditionally decisions on diagnosis and surgical management were traditionally based on V/Q scintigraphy, conventional pulmonary angiography with right heart catheterization. The current ESC/ERS guidelines indicate that V/Q scintigraphy should be performed as routine in patients with suspected chronic thromboembolic disease (Fig. 6) (Tunariu et al. 2007; Fang et al. 2008; Soler et al. 2011). CTPA has been shown to have lower sensitivity for the detection of chronic thromboembolic disease than V/Q scintigraphy. However CT and MRI methods are emerging with great potential.

The recent pulmonary vascular research institute imaging algorithm for patients with suspected pulmonary hypertension places computed tomography more centrally for identification of chronic emboli (Kiely et al. 2019). It is recommended that all patients with intermediate or high probability of PH on echocardiography undergo CTPA with referral to a PH centre in the presence of chronic emboli. If patients have a negative CTPA, dedicated perfusion imaging is recommended (Lakens 2013).

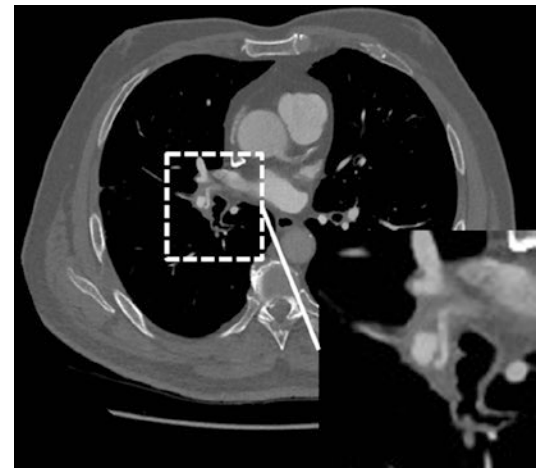


Fig. 7 Illustration of a right lower lobe pulmonary arterial web in a patient with chronic thromboembolic disease

4.1 CT Assessment of Chronic Thromboembolic Disease

Rapid developments in CT technology, have led to marked improvement in CTEPH detection and characterization. In experienced centres, recent studies demonstrate that CTPA has high diagnostic accuracy similar to V/Q (Rajaram et al. 2012). The main findings include detection of vessel wall adherent thrombus, webs seen as fine bands in the pulmonary arteries, stenosis/post-stenotic dilatation and occlusions (Fig. 7). Bronchial artery dilatation is also commonly seen (Shimizu et al. 2008).

A mosaic perfusion pattern in the lungs is seen in the vast majority of patients with chronic thromboembolic disease (Kasai et al. 2017). The main differential is air trapping, which typically

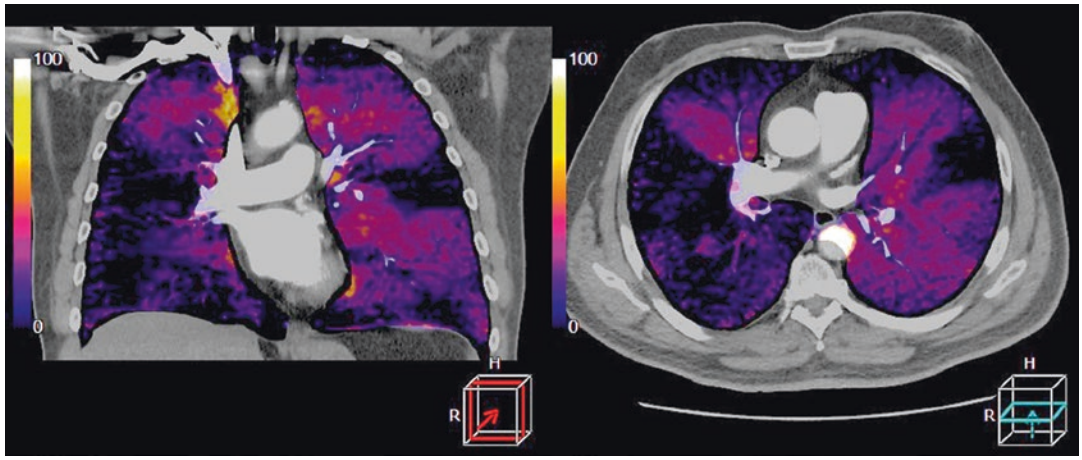


Fig. 8 Iodine subtraction map in a patient with chronic thromboembolic disease (same patient as Fig. 6). Bilateral segmental 'wedge-shaped' lung perfusion defects are clearly shown

has a lobular distribution rather than the larger geographical areas that are more frequently seen in the lung periphery in chronic thromboembolic disease. Expiratory CT may be helpful in the differentiation of mosaic perfusion from air trapping. Sub-pleural scarring as a feature of an established infarct may also be seen in chronic thromboembolic disease (Harris et al. 2008).

Dual-energy CT imaging allows for the generation of maps of regional iodine density in the lung tissue. This may further improve the evaluation of suspected CTEPH by better demonstrating regions of decreased or absent blood flow and also has the potential for quantification of the affected vascular bed (Hoey et al. 2011; Dournes et al. 2014; Koike et al. 2016; Le Faivre et al. 2016; Takagi et al. 2016). CTPA with iodine mapping is an alternative technique, which generates a lung perfusion map by subtracting a low-dose unenhanced CT scan from the CTPA (Fig. 8) (Tamura et al. 2017). In contrast to dual energy CT, it does not require specialized hardware but involves subtraction of unenhanced images from the contrast-enhanced study, the disadvantage is that the low-dose unenhanced CT require spatial co-registration, which may lead to inaccuracy in some cases. The major advantage of including perfusion imaging is an increased detection rate of chronic thromboembolic disease, particularly more distal or subtle disease (Tamura et al. 2017).

By providing an assessment of the lung parenchyma and the mediastinum CT can be helpful in identifying the presence of diffuse lung diseases and emphysema, an advantage over a perfusion assessment alone as with lung scintigraphy. CTPA has largely replaced invasive catheter-based angiography for the assessment of pulmonary thromboembolic disease. However, catheter-based angiography may still have a role in the evaluation of chronic thromboembolic disease in selected cases. Recently, balloon pulmonary angioplasty has emerged as a useful tool in selected patients with CTEPH with promising results (Lang et al. 2017; Zhai et al. 2018). To plan for this procedure a detailed evaluation of the segmental and subsegmental pulmonary arteries is required and catheter-based techniques are mainly utilized.

4.2 MR Imaging of Chronic Thromboembolic Disease

MR imaging can provide an evaluation of the pulmonary vasculature and lung perfusion and is increasingly being used in select centres for the evaluation of known or suspected chronic thromboembolic disease. The pulmonary arterial tree on MR angiography (MRA) can be visualized down to the subsegmental level. In contrast to

data in acute pulmonary embolism, higher diagnostic accuracy for detection of chronic thromboembolic disease using MRA has been shown (Rajaram et al. 2012); however the accuracy is relatively limited if the disease is confined to vessels at the segmental/subsegmental level. The higher diagnostic accuracy in the context of chronic PE may be due to on average more severe disease in the presence of chronic thromboembolism. The addition of an unenhanced white blood proton MR imaging of the pulmonary arteries can add diagnostic accuracy for detection of wall adherent clot (Rajaram et al. 2012).

3D MR perfusion imaging has proven highly accurate for the detection of chronic thromboembolic disease when compared to planar perfusion scintigraphy (Rajaram et al. 2013) and compared to lung perfusion SPECT (Johns et al. 2017a, b). A further advantage of the 3D perfusion dataset is the haemodynamic information generated from the passage of the contrast bolus through the cardiopulmonary system. Transit time parameters such as the pulmonary transit time, or the full-width half maximum of the pulmonary artery have shown a close correlation with pulmonary vascular resistance, cardiac index and mixed venous oxygen saturations (Skrok et al. 2012; Swift et al. 2014).

5 Conclusions

Imaging plays a crucial role in the diagnosis of acute and chronic pulmonary embolism (Table 3). Computed tomography pulmonary angiography is widely accepted as the first-line investigation of acute pulmonary embolism with high diagnostic accuracy. SPECT is superior to planar lung scintigraphy and still plays an important role, particularly in indeterminate CT pulmonary angiography cases and in pregnant women or where contraindications for CTPA exist. MRI requires further technical development and further study to determine a future role in the diagnosis of acute pulmonary emboli.

SPECT is recommended in the screening of chronic pulmonary embolism; however spectral CT is a viable alternative with advantages of evaluation of lung perfusion and the pulmonary vasculature in a single investigation. MRI is also a useful tool for suspected chronic thromboembolic disease with high accuracy in specialist centres.

Table 3 Diagnostic accuracy of CT, SPECT and nuclear medicine for suspected chronic embolic disease

	Method	Diagnostic accuracy	Strengths	Weaknesses
CT pulmonary angiography	CT scan with iodine contrast injection timed to the pulmonary arteries	High diagnostic accuracy for proximal central disease Distal disease may be missed	Widely available Other lung, cardiac or mediastinal pathology may be diagnosed	Distal embolic disease can be missed particularly at non-specialist centres
DECT or CT-LSIM	CT pulmonary angiogram and perfusion imaging of the lungs	High diagnostic accuracy for pulmonary thromboembolic disease	Available at many centres and availability is increasing Higher diagnostic accuracy for distal embolic disease compared to CTPA Other lung, cardiac or mediastinal pathology may be diagnosed	
SPECT scintigraphy	Nuclear medicine tomographic imaging technique	High diagnostic accuracy for pulmonary thromboembolic disease	Widely available Easy to interpret by non-radiologists	Only lung perfusion is assessed

CT computed tomography, *DECT* dual energy computed tomography, *CT-LSIM* computed tomography-lung subtraction imaging, *SPECT* single photon emission computed tomography

References

Atasoy MM, Sariman N, Levent E, Cubuk R, Celik O, Saygi A, Atasoy I, Sahin S (2015) Nonsevere acute pulmonary embolism: prognostic CT pulmonary angiography findings. J Comput Assist Tomogr 39(2):166–170

Auger WR, Kim NH, Kerr KM, Test VJ, Fedullo PF (2007) Chronic thromboembolic pulmonary hypertension. Clin Chest Med 28(1):255–269. x

Aviram G, Soikher E, Bendet A, Shmueli H, Ziv-Baran T, Amitai Y, Friedensohn L, Berliner S, Meilik A, Topilsky Y (2016) Prediction of mortality in pulmonary embolism based on left atrial volume measured on CT pulmonary angiography. Chest 149(3): 667–675

van Beek EJ, Tiel-van Buul MM, Buller HR, van Royen EA, ten Cate JW (1993) The value of lung scintigraphy in the diagnosis of pulmonary embolism. Eur J Nucl Med 20(2):173–181

Carroll BJ, Heidinger BH, Dabreo DC, Matos JD, Mohebali D, Feldman SA, McCormick I, Litmanovich D, Manning WJ (2018) Multimodality assessment of right ventricular strain in patients with acute pulmonary embolism. Am J Cardiol 122(1):175–181

Condliffe R, Kiely DG, Gibbs JS, Corris PA, Peacock AJ, Jenkins DP, Hodgkins D, Goldsmith K, Hughes RJ, Sheares K, Tsui SS, Armstrong IJ, Torpy C, Crackett R, Carlin CM, Das C, Coghlan JG, Pepke-Zaba J (2008) Improved outcomes in medically and surgically treated chronic thromboembolic pulmonary hypertension. Am J Respir Crit Care Med 177(10):1122–1127

Dalen JE, Banas JS Jr, Brooks HL, Evans GL, Paraskos JA, Dexter L (1969) Resolution rate of acute pulmonary embolism in man. N Engl J Med 280(22):1194–1199

Dewailly M, Remy-Jardin M, Duhamel A, Faivre JB, Pontana F, Deken V, Bakai AM, Remy J (2010) Computer-aided detection of acute pulmonary embolism with 64-slice multi-detector row computed tomography: impact of the scanning conditions and overall image quality in the detection of peripheral clots. J Comput Assist Tomogr 34(1):23–30

Dournes G, Verdier D, Montaudon M, Bullier E, Riviere A, Dromer C, Picard F, Billes MA, Corneloup O, Laurent F, Lederlin M (2014) Dual-energy CT perfusion and angiography in chronic thromboembolic pulmonary hypertension: diagnostic accuracy and concordance with radionuclide scintigraphy. Eur Radiol 24(1):42–51

Ende-Verhaar YM, Kroft LJM, Mos ICM, Huisman MV, Klok FA (2017) Accuracy and reproducibility of CT right-to-left ventricular diameter measurement in patients with acute pulmonary embolism. PLoS One 12(11):e0188862

Fang W, Ni XH, He JG, Liu ZH, Xiong CM, He ZX (2008) Value of radionuclide lung scintigraphy in the diagnosis and quantitative analysis of chronic thromboembolic pulmonary hypertension. Zhonghua Xin Xue Guan Bing Za Zhi 36(1):7–10

Ghaye B, Ghuysen A, Willems V, Lambermont B, Gerard P, D'Orio V, Gevenois PA, Dondelinger RF (2006) Severe pulmonary embolism:pulmonary artery clot load scores and cardiovascular parameters as predictors of mortality. Radiology 239(3):884–891

Gutte H, Mortensen J, Jensen CV, von der Recke P, Petersen CL, Kristoffersen US, Kjaer A (2010) Comparison of V/Q SPECT and planar V/Q lung scintigraphy in diagnosing acute pulmonary embolism. Nucl Med Commun 31(1):82–86

Harris H, Barraclough R, Davies C, Armstrong I, Kiely DG, van Beek E Jr (2008) Cavitating lung lesions in chronic thromboembolic pulmonary hypertension. J Radiol Case Rep 2(3):11–21

Hochhegger B, Alves GRT, Chaves M, Moreira AL, Kist R, Watte G, Moreira JS, Irion KL, Marchiori E (2014) Interobserver agreement between radiologists and radiology residents and emergency physicians in the detection of PE using CTPA. Clin Imaging 38(4):445–447

Hoey ET, Mirsadraee S, Pepke-Zaba J, Jenkins DP, Gopalan D, Screaton NJ (2011) Dual-energy CT angiography for assessment of regional pulmonary perfusion in patients with chronic thromboembolic pulmonary hypertension: initial experience. AJR Am J Roentgenol 196(3):524–532

Im DJ, Hur J, Han KH, Lee HJ, Kim YJ, Kwon W, Choi BW (2017) Acute pulmonary embolism: retrospective cohort study of the predictive value of perfusion defect volume measured with dual-energy CT. AJR Am J Roentgenol 209(5):1015–1022

Ingrisch M, Maxien D, Meinel FG, Reiser MF, Nikolaou K, Dietrich O (2016) Detection of pulmonary embolism with free-breathing dynamic contrast-enhanced MRI. J Magn Reson Imaging 43(4):887–893

Johns CS, Swift AJ, Hughes PJC, Ohno Y, Schiebler M, Wild JM (2017a) Pulmonary MR angiography and perfusion imaging-A review of methods and applications. Eur J Radiol 86:361–370

Johns CS, Swift AJ, Rajaram S, Hughes PJC, Capener DJ, Kiely DG, Wild JM (2017b) Lung perfusion: MRI vs. SPECT for screening in suspected chronic thromboembolic pulmonary hypertension. J Magn Reson Imaging 46(6):1693–1697

Kan Y, Yuan L, Meeks JK, Li C, Liu W, Yang J (2015) The accuracy of V/Q SPECT in the diagnosis of pulmonary embolism: a meta-analysis. Acta Radiol 56(5):565–572

Kasai H, Tanabe N, Fujimoto K, Hoshi H, Naito J, Suzuki R, Matsumura A, Sugiura T, Sakao S, Tatsumi K (2017) Mosaic attenuation pattern in non-contrast computed tomography for the assessment of pulmonary perfusion in chronic thromboembolic pulmonary hypertension. Respir Investig 55(5):300–307

Kiely DG, Levin D, Hassoun P, Ivy DD, Jone PN, Bwika J, Kawut SM, Lordan J, Lungu A, Mazurek J, Moledina S, Olschewski H, Peacock A, Puri GD, Rahaghi F, Schafer M, Schiebler M, Screaton N, Tawhai M, Van Beek EJ, Vonk-Noordegraaf A, Vanderpool RR, Wort J, Zhao L, Wild J, Vogel-Claussen J, Swift AJ (2019)

EXPRESS: statement on imaging and pulmonary hypertension from the pulmonary vascular research institute (PVRI). Pulm Circ 9(3):2045894019841990

Kligerman SJ, Lahiji K, Galvin JR, Stokum C, White CS (2014) Missed pulmonary emboli on CT angiography: assessment with pulmonary embolism-computer-aided detection. AJR Am J Roentgenol 202(1):65–73

Koike H, Sueyoshi E, Sakamoto I, Uetani M, Nakata T, Maemura K (2016) Quantification of lung perfusion blood volume (lung PBV) by dual-energy CT in patients with chronic thromboembolic pulmonary hypertension (CTEPH) before and after balloon pulmonary angioplasty (BPA): preliminary results. Eur J Radiol 85(9):1607–1612

Konstantinides SV, Torbicki A, Agnelli G, Danchin N, Fitzmaurice D, Galie N, Gibbs JS, Huisman MV, Humbert M, Kucher N, Lang I, Lankeit M, Lekakis J, Maack C, Mayer E, Meneveau N, Perrier A, Pruszczyk P, Rasmussen LH, Schindler TH, Svitil P, Vonk Noordegraaf A, Zamorano JL, Zompatori M, DTask Force for the Diagnosis and Management of Acute Pulmonary Embolism of the European Society of Cardiology (ESC) (2014) 2014 ESC guidelines on the diagnosis and management of acute pulmonary embolism. Eur Heart J 35(43):3033–3069, 3069a-3069k

Koukouraki SI, Hatzidakis AA, Mitrouska I, Stathaki MI, Perisinakis K (2018) Does lung perfusion scintigraphy continue to have a role in the clinical management of patients suspected of pulmonary embolism in the CT pulmonary angiography era? Ann Nucl Med 32(10):709–714

Kumamaru KK, George E, Aghayev A, Saboo SS, Khandelwal A, Rodriguez-Lopez S, Cai T, Jimenez-Carretero D, Estepar RS, Ledesma-Carbayo MJ, Gonzalez G, Rybicki FJ (2016a) Implementation and performance of automated software for computing right-to-left ventricular diameter ratio from computed tomography pulmonary angiography images. J Comput Assist Tomogr 40(3):387–392

Kumamaru KK, George E, Ghosh N, Quesada CG, Wake N, Gerhard-Herman M, Rybicki FJ (2016b) Normal ventricular diameter ratio on CT provides adequate assessment for critical right ventricular strain among patients with acute pulmonary embolism. Int J Cardiovasc Imaging 32(7):1153–1161

Lakens D (2013) Calculating and reporting effect sizes to facilitate cumulative science: a practical primer for t-tests and ANOVAs. Front Psychol 4:863

Lang I (2009) Managing chronic thromboembolic pulmonary hypertension: pharmacological treatment options. Eur Respir Rev 18(111):24–28

Lang I, Meyer BC, Ogo T, Matsubara H, Kurzyna M, Ghofrani HA, Mayer E, Brenot P (2017) Balloon pulmonary angioplasty in chronic thromboembolic pulmonary hypertension. Eur Respir Rev 26(143):160119

Le Faivre J, Duhamel A, Khung S, Faivre JB, Lamblin N, Remy J, Remy-Jardin M (2016) Impact of CT perfusion imaging on the assessment of peripheral chronic pulmonary thromboembolism: clinical experience in 62 patients. Eur Radiol 26(11):4011–4020

Li J, Feng L, Li J, Tang J (2016) Diagnostic accuracy of magnetic resonance angiography for acute pulmonary embolism - a systematic review and meta-analysis. Vasa 45(2):149–154

Li Y, Dai Y, Deng L, Yu N, Guo Y (2017) Computer-aided detection for the automated evaluation of pulmonary embolism. Technol Health Care 25(S1):135–142

Maizlin ZV, Vos PM, Godoy MC, Cooperberg PL (2007) Computer-aided detection of pulmonary embolism on CT angiography: initial experience. J Thorac Imaging 22(4):324–329

Mastora I, Remy-Jardin M, Masson P, Galland E, Delannoy V, Bauchart JJ, Remy J (2003) Severity of acute pulmonary embolism: evaluation of a new spiral CT angiographic score in correlation with echocardiographic data. Eur Radiol 13(1):29–35

Masy M, Giordano J, Petyt G, Hossein-Foucher C, Duhamel A, Kyheng M, De Groote P, Fertin M, Lamblin N, Bervar JF, Remy J, Remy-Jardin M (2018) Dual-energy CT (DECT) lung perfusion in pulmonary hypertension: concordance rate with V/Q scintigraphy in diagnosing chronic thromboembolic pulmonary hypertension (CTEPH). Eur Radiol 28(12):5100–5110

Matsunaga K, Yanagawa M, Otsuka T, Hirata H, Kijima T, Kumanogoh A, Tomiyama N, Shimosegawa E, Hatazawa J (2017) Quantitative pulmonary blood flow measurement using (15)O-H2O PET with and without tissue fraction correction: a comparison study. EJNMMI Res 7(1):102

Meaney JF, Weg JG, Chenevert TL, Stafford-Johnson D, Hamilton BH, Prince MR (1997) Diagnosis of pulmonary embolism with magnetic resonance angiography. N Engl J Med 336(20):1422–1427

Meinel FG, Graef A, Bamberg F, Thieme SF, Schwarz F, Sommer WH, Neurohr C, Kupatt C, Reiser MF, Johnson TR (2013) Effectiveness of automated quantification of pulmonary perfused blood volume using dual-energy CTPA for the severity assessment of acute pulmonary embolism. Investig Radiol 48(8):563–569

Mirsadraee S, Weir NW, Connolly S, Murchison JT, Reid JH, Hirani N, Connell M, van Beek EJ (2015) Feasibility of radiation dose reduction using AIDR-3D in dynamic pulmonary CT perfusion. Clin Radiol 70(8):844–851

Mirsadraee S, Reid JH, Connell M, MacNee W, Hirani N, Murchison JT, van Beek EJ (2016) Dynamic (4D) CT perfusion offers simultaneous functional and anatomical insights into pulmonary embolism resolution. Eur J Radiol 85(10):1883–1890

Moser KM, Bloor CM (1993) Pulmonary vascular lesions occurring in patients with chronic major vessel thromboembolic pulmonary hypertension. Chest 103(3):685–692

Nagle SK, Schiebler ML, Repplinger MD, Francois CJ, Vigen KK, Yarlagadda R, Grist TM, Reeder SB (2016) Contrast enhanced pulmonary magnetic resonance angiography for pulmonary embolism: building a successful program. Eur J Radiol 85(3):553–563

Osman AM, Abdeldayem EH (2018) Value of CT pulmonary angiography to predict short-term outcome in patient with pulmonary embolism. Int J Cardiovasc Imaging 34(6):975–983

Oudkerk M, van Beek EJ, Wielopolski P, van Ooijen PM, Brouwers-Kuyper EM, Bongaerts AH, Berghout A (2002) Comparison of contrast-enhanced magnetic resonance angiography and conventional pulmonary angiography for the diagnosis of pulmonary embolism: a prospective study. Lancet 359(9318):1643–1647

Parker JA, Coleman RE, Grady E, Royal HD, Siegel BA, Stabin MG, Sostman HD, Hilson AJ, Society of Nuclear Medicine (2012) SNM practice guideline for lung scintigraphy 4.0. J Nucl Med Technol 40(1):57–65

Pengo V, Lensing AWA, Prins MH, Marchiori A, Davidson BL, Tiozzo F, Albanese P, Biasiolo A, Pegoraro C, Iliceto S, Prandoni P, Thromboembolic Pulmonary Hypertension Study Group (2004) Incidence of chronic thromboembolic pulmonary hypertension after pulmonary embolism. N Engl J Med 350(22): 2257–2264

Phillips JJ, Straiton J, R. T. Staff (2015) Planar and SPECT ventilation/perfusion imaging and computed tomography for the diagnosis of pulmonary embolism: a systematic review and meta-analysis of the literature, and cost and dose comparison. Eur J Radiol 84(7):1392–1400

van der Plas MN, Reesink HJ, Roos CM, van Steenwijk RP, Kloek JJ, Bresser P (2010) Pulmonary endarterectomy improves dyspnea by the relief of dead space ventilation. Ann Thorac Surg 89(2):347–352

Pontana F, Henry S, Duhamel A, Faivre JB, Tacelli N, Pagniez J, Remy J, Remy-Jardin M (2015) Impact of iterative reconstruction on the diagnosis of acute pulmonary embolism (PE) on reduced-dose chest CT angiograms. Eur Radiol 25(4):1182–1189

Quadery SR, Swift AJ, Billings CG, Thompson AAR, Elliot CA, Hurdman J, Charalampopoulos A, Sabroe I, Armstrong IJ, Hamilton N, Sephton P, Garrad S, Pepke-Zaba J, Jenkins DP, Screaton N, Rothman AM, Lawrie A, Cleveland T, Thomas S, Rajaram S, Hill C, Davies C, Johns CS, Wild JM, Condliffe R, Kiely DG (2018) The impact of patient choice on survival in chronic thromboembolic pulmonary hypertension. Eur Respir J 52(3):1800589

Rajaram S, Swift AJ, Capener D, Telfer A, Davies C, Hill C, Condliffe R, Elliot C, Hurdman J, Kiely DG, Wild JM (2012) Diagnostic accuracy of contrast-enhanced MR angiography and unenhanced proton MR imaging compared with CT pulmonary angiography in chronic thromboembolic pulmonary hypertension. Eur Radiol 22(2):310–317

Rajaram S, Swift AJ, Telfer A, Hurdman J, Marshall H, Lorenz E, Capener D, Davies C, Hill C, Elliot C, Condliffe R, Wild JM, Kiely DG (2013) 3D contrast-enhanced lung perfusion MRI is an effective screening tool for chronic thromboembolic pulmonary hypertension: results from the ASPIRE registry. Thorax 68(7):677–678

Revel MP, Sanchez O, Couchon S, Planquette B, Hernigou A, Niarra R, Meyer G, Chatellier G (2012) Diagnostic accuracy of magnetic resonance imaging for an acute pulmonary embolism: results of the 'IRM-EP' study. J Thromb Haemost 10(5):743–750

Rucco M, Sousa-Rodrigues D, Merelli E, Johnson JH, Falsetti L, Nitti C, Salvi A (2015) Neural hypernetwork approach for pulmonary embolism diagnosis. BMC Res Notes 8:617

Schiebler ML, Nagle SK, Francois CJ, Repplinger MD, Hamedani AG, Vigen KK, Yarlagadda R, Grist TM, Reeder SB (2013) Effectiveness of MR angiography for the primary diagnosis of acute pulmonary embolism: clinical outcomes at 3 months and 1 year. J Magn Reson Imaging 38(4):914–925

Schoepf UJ, Schneider AC, Das M, Wood SA, Cheema JI, Costello P (2007) Pulmonary embolism: computer-aided detection at multidetector row spiral computed tomography. J Thorac Imaging 22(4):319–323

Schuster DP, Kaplan JD, Gauvain K, Welch MJ, Markham J (1995) Measurement of regional pulmonary blood flow with PET. J Nucl Med 36(3):371–377

Shimizu H, Tanabe N, Terada J, Masuda M, Sakao S, Kasahara Y, Takiguchi Y, Tatsumi K, Kuriyama T (2008) Dilatation of bronchial arteries correlates with extent of central disease in patients with chronic thromboembolic pulmonary hypertension. Circ J 72(7):1136–1141

Skrok J, Shehata ML, Mathai S, Girgis RE, Zaiman A, Mudd JO, Boyce D, Lechtzin N, Lima JA, Bluemke DA, Hassoun PM, Vogel-Claussen J (2012) Pulmonary arterial hypertension: MR imaging-derived first-pass bolus kinetic parameters are biomarkers for pulmonary hemodynamics, cardiac function, and ventricular remodeling. Radiology 263(3):678–687

Soler X, Hoh CK, Test VJ, Kerr KM, Marsh JJ, Morris TA (2011) Single photon emission computed tomography in chronic thromboembolic pulmonary hypertension. Respirology 16(1):131–137

Sostman HD, Miniati M, Gottschalk A, Matta F, Stein PD, Pistolesi M (2008) Sensitivity and specificity of perfusion scintigraphy combined with chest radiography for acute pulmonary embolism in PIOPED II. J Nucl Med 49(11):1741–1748

Sostman HD, Jablonski KA, Woodard PK, Stein PD, Naidich DP, Chenevert TL, Weg JG, Hales CA, Hull RD, Goodman LR, Tapson VF (2012) Factors in the technical quality of gadolinium enhanced magnetic resonance angiography for pulmonary embolism in PIOPED III. Int J Cardiovasc Imaging 28(2): 303–312

Suntharalingam J, Machado RD, Sharples LD, Toshner MR, Sheares KK, Hughes RJ, Jenkins DP, Trembath RC, Morrell NW, Pepke-Zaba J (2007) Demographic features, BMPR2 status and outcomes in distal chronic thromboembolic pulmonary hypertension. Thorax 62(7):617–622

Swift AJ, Telfer A, Rajaram S, Condliffe R, Marshall H, Capener D, Hurdman J, Elliot C, Kiely DG, Wild JM (2014) Dynamic contrast-enhanced magnetic

resonance imaging in patients with pulmonary arterial hypertension. Pulm Circ 4(1):61–70

Takagi H, Ota H, Sugimura K, Otani K, Tominaga J, Aoki T, Tatebe S, Miura M, Yamamoto S, Sato H, Yaoita N, Suzuki H, Shimokawa H, Takase K (2016) Dual-energy CT to estimate clinical severity of chronic thromboembolic pulmonary hypertension: comparison with invasive right heart catheterization. Eur J Radiol 85(9):1574–1580

Tamura M, Yamada Y, Kawakami T, Kataoka M, Iwabuchi Y, Sugiura H, Hashimoto M, Nakahara T, Okuda S, Nakatsuka S, Sano F, Abe T, Maekawa Y, Fukuda K, Jinzaki M (2017) Diagnostic accuracy of lung subtraction iodine mapping CT for the evaluation of pulmonary perfusion in patients with chronic thromboembolic pulmonary hypertension: correlation with perfusion SPECT/CT. Int J Cardiol 243: 538–543

Thieme SF, Johnson TR, Reiser MF, Nikolaou K (2010) Dual-energy lung perfusion computed tomography: a novel pulmonary functional imaging method. Semin Ultrasound CT MR 31(4):301–308

Thieme SF, Ashoori N, Bamberg F, Sommer WH, Johnson TR, Leuchte H, Becker A, Maxien D, Helck AD, Behr J, Reiser MF, Nikolaou K (2012) Severity assessment of pulmonary embolism using dual energy CT - correlation of a pulmonary perfusion defect score with clinical and morphological parameters of blood oxygenation and right ventricular failure. Eur Radiol 22(2):269–278

Toney LK, Kim RD, Palli SR (2017) The economic value of hybrid single-photon emission computed tomography with computed tomography imaging in pulmonary embolism diagnosis. Acad Emerg Med 24(9):1110–1123

Tunariu N, Gibbs SJ, Win Z, Gin-Sing W, Graham A, Gishen P, Al-Nahhas A (2007) Ventilation-perfusion scintigraphy is more sensitive than multidetector CTPA in detecting chronic thromboembolic pulmonary disease as a treatable cause of pulmonary hypertension. J Nucl Med 48(5):680–684

Webber MM, Gomes AS, Roe D, La Fontaine RL, Hawkins RA (1990) Comparison of Biello, McNeil, and PIOPED criteria for the diagnosis of pulmonary emboli on lung scans. AJR Am J Roentgenol 154(5):975–981

Weidman EK, Plodkowski AJ, Halpenny DF, Hayes SA, Perez-Johnston R, Zheng J, Moskowitz C, Ginsberg MS (2018) Dual-energy CT angiography for detection of pulmonary emboli: incremental benefit of iodine maps. Radiology 289(2):546–553

Zhai Z, Ota H, Staring M, Stolk J, Sugimura K, Takase K, Stoel BC (2018) Treatment effect of balloon pulmonary angioplasty in chronic thromboembolic pulmonary hypertension quantified by automatic comparative imaging in computed tomography pulmonary angiography. Investig Radiol 53(5): 286–292

Multimodality Imaging of Pulmonary Hypertension: Prognostication of Therapeutic Outcomes

Lindsay Griffin, Andrew J. Swift, Nanae Tsuchiya, Christopher François, Marc Humbert, Gideon Cohen, and Mark L. Schiebler

Contents

1 **Introduction** 227

2 **Cardiovascular Consequences of Pulmonary Hypertension** 230

3 **Evaluation of the Right Ventricle** 234
3.1 Non-contrast Computed Tomography 234
3.2 Contrast-Enhanced Computed Tomography 234
3.3 Cardiac-Gated Computed Tomographic Angiography 235

4 **MRI** 235

5 **Evaluation of the Interventricular Septum** 236

6 **Evaluation of Additional Cardiac Chambers** 237

7 **Evaluation of the Vasculature** 237

8 **Ratio of the Pulmonary to Systemic Blood Flow** 242

9 **Pulmonary and Tricuspid Valve Regurgitation and Jet Velocity** 243

L. Griffin
Department of Radiology, Lurie Children's Hospital, Northwestern University School of Medicine, Chicago, IL, USA

A. J. Swift
Department of Infection, Immunity and Cardiovascular Disease, University of Sheffield, Sheffield, UK

N. Tsuchiya
Department of Radiology, Graduate School of Medical Science, University of the Ryukyus, Okinawa, Japan

Department of Radiology, School of Medicine and Public Health, University of Wisconsin-Madison, Madison, WI, USA

C. François · M. L. Schiebler (✉)
Department of Radiology, School of Medicine and Public Health, University of Wisconsin-Madison, Madison, WI, USA
e-mail: mschiebler@uwhealth.org

M. Humbert
Department of Pulmonary Medicine, National Referral Center for Pulmonary Hypertension, Hospital Bicêtre, Université Paris-Sud, Le Kremlin-Bicêtre, France

G. Cohen
Department of Emergency Medicine, Beth Israel Deaconess Medical Center, Boston, MA, USA

© Springer Nature Switzerland AG 2021

Y. Ohno et al. (eds.), *Pulmonary Functional Imaging*, Medical Radiology Diagnostic Imaging,
https://doi.org/10.1007/978-3-030-43539-4_12

10 Mediastinal Diseases 243
11 Diseases of the Left Heart 244
12 Diastolic Dysfunction 244
13 Mitral Valve Disease 245
14 Aortic Valve Disease 246
15 Left Main Coronary artery Compression by the Pulmonary Artery 246
16 Four-Dimensional Phase-Contrast Flow-Encoded Magnetic Resonance Angiography (4D Flow MRI) 247
17 Lung Parenchymal Disease 247
18 Liver Disease 247
19 Obstructive Sleep Apnea 248
20 Synergy of Diseases 248
21 Modeling the Severity of Pulmonary Hypertension Using MRI Parameters 249
22 Prediction of Outcomes After Therapy for Pulmonary Hypertension 249
23 Noninvasive Imaging Costs 250
24 Conclusion 250
References 250

Abstract

There are many causes of pulmonary hypertension (PH). The new clinical classification system for PH relies on grouping the causes of this disorder by treatment paradigm. In the western world, PH is most commonly related to left heart disease/ischemic heart disease or due to chronic lung diseases. Pulmonary arterial hypertension (PAH) is a rare condition characterized by remodeling of the distal pulmonary vasculature. Commonly patients with PAH present late in their disease course after severe damage to the distal vasculature has occurred and the current treatment of PAH depends on the use of pulmonary vasodilators. Chronic thromboembolic pulmonary hypertension (CTEPH), which occurs in 1–3% of patients following acute pulmonary embolism, are treated with pulmonary endarterectomy and/or balloon pulmonary angioplasty provided the disease is accessible; patients with inaccessible disease require pulmonary vasodilators. For most causes of PH, the onset of right ventricular failure is rapid with death occurring within 5 years of diagnosis. Herein, we review the ability of ultrasound, nuclear medicine, and MRI for the diagnosis and follow up this group of diseases. Transthoracic ultrasound is the main tool to diagnose PH due to its portability, access, familiarity of use, and its ability to estimate mean pulmonary artery pressure from the velocity of the tricuspid regurgitation jet using the modified Bernoulli equation. For nuclear medicine, SPECT ventilation with ^{133}Xe gas and ^{99m}Tc-MAA perfusion imaging is quite useful for the diagnosis of CTEPH. The key cardiovascular MRI metrics found to relate to right ventricular volume and function along with pulmonary arterial pulsatility. While there are a number of noninvasive methods for the diagnosis and follow-up of PH and PAH, there is no current replacement for the intra-arterial pressure measurements of right heart catheterization.

Abbreviations

4D flow	Four-dimensional phase-contrast flow-encoded magnetic resonance angiography
BSA	Body surface area
bSSFP	Balanced steady-state free procession MRI pulse sequence for cine CMR
CE-MRA	Contrast-enhanced magnetic resonance angiography
CMR	Cardiac magnetic resonance imaging
CT	Computed tomography
CTEPH	Chronic thromboembolic pulmonary hypertension
FWHM	Full width half maximum of the transit time of the contrast material peak from the pulmonary artery to the aorta
GCSR	Global right ventricular circumferential strain rate
GLS	Global right ventricular longitudinal strain
GLSR	Global right ventricular longitudinal strain rate
HR	Hazard ratio
ISWT	Incremental shuttle walk test
LGE	Late gadolinium enhancement
LV	Left ventricle
LVEDVI	Left ventricular end-diastolic volume index
LVEF	Left ventricular ejection fraction
LVESVI	Left ventricular end-systolic volume index
LVSV	Left ventricle stroke volume
MPA	Main pulmonary artery
mPAP	Mean pulmonary artery pressure
MRA	Magnetic resonance angiography
MRI	Magnetic resonance imaging
NC-MRA	Non-contrast magnetic resonance angiography
PA RAC	Pulmonary artery relative area change
PAP	Pulmonary artery pressure
PTT	Pulmonary transit time
PVR	Pulmonary vascular resistance
Qp/Qs	Ratio of the pulmonary to systemic blood flow
RAC	Relative area change
RHC	Right heart catheterization
RV	Right ventricle
RVEDV	Right ventricular end-diastolic volume
RVEDVI	Right ventricular end-diastolic volume indexed to body surface area
RVEF	Right ventricular ejection fraction
RVESV	Right ventricular end-systolic volume
RVESVI	Right ventricular end-systolic volume indexed to body surface area
RVSV	Right ventricle stroke volume
SVI	Stroke volume Index = Cardiac output/heart rate (beats per minute)/BSA (m^2)
WHO FC	World Health Organization Functional Class (exercise capacity testing)

1 Introduction

Pulmonary hypertension (PH) is a condition of elevated pressure in the pulmonary arteries and is defined by having a mean pulmonary artery pressure (mPAP) > 25 mmHg at right heart catheterization (Galie et al. 2016). Several conditions lead to the development of PH with unique challenges in diagnosis and treatment. In the United States, the estimated rate for PH as contributing cause of the death was 6.5 deaths per 100,000 people in 2010 (George et al. 2014). During 1980–2002, the total number of deaths attributed to pulmonary arterial hypertension (PAH) increased from 10,922 to 15,668 (Hyduk et al. 2005). In 2002, the age-standardized death rate for pulmonary (arterial) hypertension was 5.3/100,000 for Caucasian-Americans, 7.3/100,000 for African-Americans, and 2.2/100,000 for Asian-Americans (Hyduk et al. 2005). This figure likely ignores the contribution of left heart disease to the cause of death in their examined population (Hyduk et al. 2005). PAH is characterized by disease of the small distal

Table 1 Simplified version of the 2019 classification system for pulmonary arterial and pulmonary hypertension (Galie et al. 2019)

1. Pulmonary arterial hypertension (PAH)
• Idiopathic PAH
• Heritable PAH
• Drug and toxin induced
• PAH associated with
– Connective tissue disease
– HIV infection
– Portal hypertension
– Congenital heart disease
– Schistosomiasis
• PAH associated with long-term responders to calcium channel blockers
• PAH with overt features of pulmonary veno-occlusive disease/capillary hemangiomatosis
• Persistent PH of the newborn
2. Pulmonary hypertension (PH) due to left heart disease
• PH due to left heart failure with preserved left ventricular ejection fraction
• PH due to left heart failure with reduced left ventricular ejection fraction
• Valvular heart disease
• Congenital or acquired cardiovascular lesions leading to post capillary PH
3. Pulmonary hypertension to lung diseases and or hypoxia.
• Obstructive lung disease
• Restrictive lung disease
• Other lung disease with mixed restrictive/obstructive pattern
• Hypoxia without lung disease
• Developmental lung disorders
4. PH due to pulmonary artery obstructions
• Chronic thromboembolic pulmonary arterial hypertension
• Other pulmonary artery obstructions
5. PH with unclear and/or multifactorial mechanisms
• Hematological disorders
• Systemic and metabolic disorders
• Others
• Complex congenital heart disease

pulmonary arteries. PAH is difficult to recognize, especially early on, as patients present with vague symptoms of dyspnea and fatigue. They can also present with chest pain, peripheral edema, and palpitations. When left untreated, there is progressive right ventricular failure. PH develops due to increases in pulmonary vascular resistance, pulmonary blood flow, pulmonary venous pressure, and/or a combination of those factors. The normal mean pulmonary artery pressure (mPAP) is 14 ± 3 mmHg. While a value above 20 mmHg is abnormal, the most recent European guidelines still define PH as mPAP greater than or equal to 25 mmHg at rest at right heart catheterization. As the understanding of the physiologic mechanisms of PH/PAH have progressed, so has the classification of disease types. Currently, the classification system groups patients by mechanism of disease and treatment paradigm (Goldberg et al. 2017). Table 1 provides a brief overview of the 2013 World Health Organization classification system, epidemiology, physiology, treatment strategies, and prognosis (Simonneau et al. 2013; Haeck and Vliegen 2015; Goldberg et al. 2017). Figure 1 is a schematic representation of the circulatory system that further outlines causes of PH/PAH and their effect on the pulmonary vascular bed. A careful history often reveals clues as to the underlying cause(s) of PH in each patient. The role of comorbid diseases having an additive

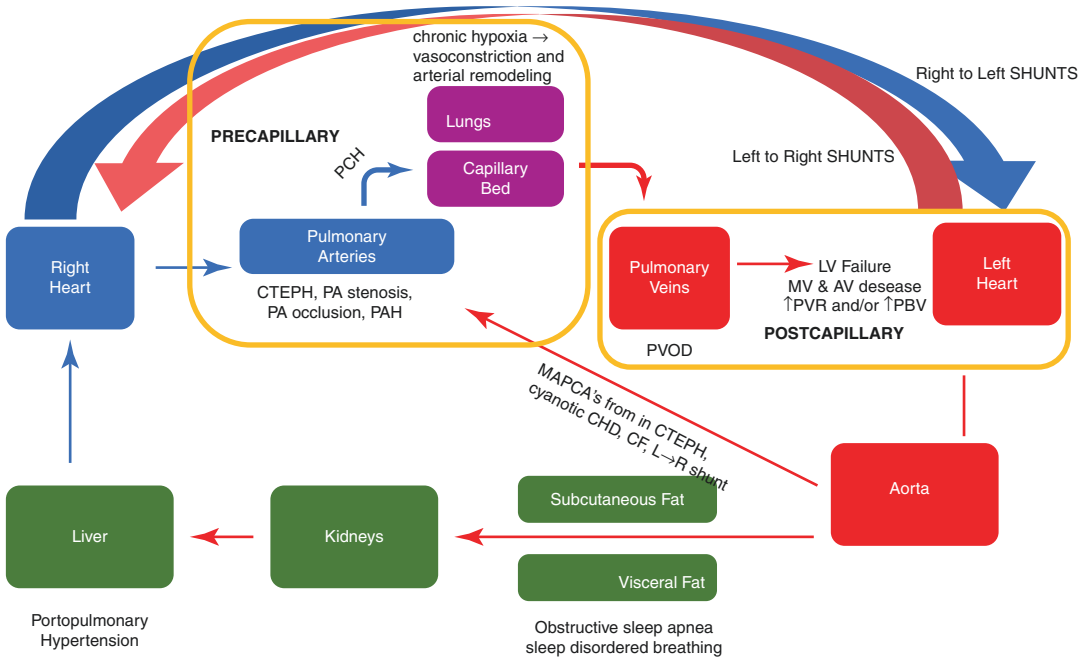


Fig. 1 Schematic of circulatory conditions that give rise to pulmonary arterial hypertension and pulmonary hypertension. *Eisenmenger syndrome occurs in setting of long-standing $L \rightarrow R$ shunt with increased pulmonary vascular resistance secondary to pulmonary arterial remodeling in setting of pulmonary overcirculation. Eventually, pulmonary hypertension reverses shunt, creating a $R \rightarrow L$ shunt, resulting in aortic and peripheral arterial cyanosis. Note the pathways in green represent complex systemic physiology contributing to pulmonary hypertension which is beyond the scope of this chapter. Abbreviations: *ASD* atrial septal defect, *VSD* ventricular septal defect, *PAPVR* partial anomalous pulmonary venous return, *PBV* pulmonary blood volume, *PVR* pulmonary vascular resistance, *PVP* pulmonary venous pressure; *LV* left ventricle, *MV* mitral valve, *AV* aortic valve, *MAPCA* major aortopulmonary collateral arteries, *HTN* hypertension, *CTEPH* chronic thromboembolic pulmonary HTN, *PA* pulmonary artery, *PAH* pulmonary arterial HTN, *PCH* pulmonary capillary hemangiomatosis, *PVOD* pulmonary veno-occlusive disease

or even synergetic effect on PH/PAH needs to be considered, as patients often have more than one potential cause of their elevated mPAP (e.g., obstructive sleep apnea, emphysema, and left ventricular diastolic dysfunction).

The diagnostic paradigm for workup of this disorder includes a clinical exam with designation of a New York Heart Association/World Health Organization Functional Class (MYHA/WHO FC), exercise capacity testing (6-min walk test), blood tests, right heart catheterization (RHC) for the determination of mean pulmonary artery pressure (mPAP), oxygenation and shunt fraction measurements, and pulmonary function testing (Galie et al. 2016). Common imaging modalities include chest radiography, echocardiography, nuclear medicine ventilation and perfusion scans, computed tomography (CT), and cardiac magnetic resonance imaging (CMR). The recent PVRI Statement on imaging in pulmonary hypertension sets the stage for the current paradigm for the workup of the many complex diseases that can give rise to this disease (Fig. 2) (Kiely et al. 2019). This chapter will provide a brief overview of the complementary roles of CT, CTA, echocardiography, and cardiovascular magnetic resonance imaging (CMR) for the diagnosis of PH and PAH. The organization and presentation of the materials roughly follows the circulation of blood (fluid mechanics) in the body. This will help to provide a heuristic device for the reader to understand the complexities of the many disease processes that can lead to an elevation in pulmonary artery pressure. We also

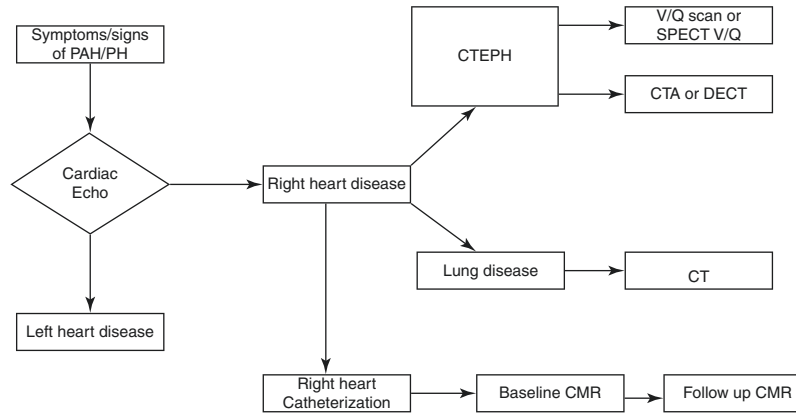


Fig. 2 Simplified triage diagram from the 2019 PVRI statement on the workup of suspected pulmonary hypertension (Kiely et al. 2019).

more fully discuss the role of CMR for the functional assessment, longitudinal follow-up, and prognosis of these patients.

2 Cardiovascular Consequences of Pulmonary Hypertension

A clear understanding of the changes that occur in the right ventricle (RV) and the pulmonary vascular system as PH worsens informs the parameters measurable by MRI (Vonk-Noordegraaf et al. 2013, 2017). The RV can increase contractility by 4- to five-fold to maintain stroke volume (SV) both through increased contractility and increasing muscle mass (right ventricular hypertrophy). This adaptive remodeling occurs with preserved systolic and diastolic function. Eventually, maladaptive remodeling takes over and the RV begins to dilate. The heart rate increases to maintain the right ventricle SV (RVSV). As wall tension and RV pressures continue increase, RV contraction is prolonged and leftward interventricular septal bowing develops. There is delayed closure of the pulmonary valve during RV systole and ventricular uncoupling with RV contraction continuing while the LV has transitioned to an early diastolic phase. On cardiac auscultation, this results in a split S2 sound on expiration. The tricuspid valve annulus is stretched by the volume overloaded RV and tricuspid valve regurgitation (TR) develops (Haddad et al. 2014; Marcus et al. 2008). The pulmonic valve closes while the RV is still contracting. Thus, this is pathophysiology behind the finding of tricuspid regurgitation in the setting of PH. Ventricular interdependency with leftward septal bowing both hampers LV filling and decreases RVSV, thereby further decreasing LV filling. These changes are illustrated in Fig. 3. In addition, the left ventricular stroke volume (LVSV) is decreased because LV cavity is reduced in size and the interventricular septum no longer contributes to left ventricular contraction. In many ways, this cardiac physiology is analogous to Tetralogy of Fallot before surgery, with the increased RV pressure, due to the stenotic RV outflow tract, causing right ventricular hypertrophy and a "D" shaped interventricular septum on the short axis electrocardiogram (ECG)-gated balanced steady-state free precession (bSSFP) cine images (Figs. 3, 4, 5 and 6) (Durongpisitkul et al. 2008).

Ventriculoarterial coupling, how the RV changes in response to afterload, describes the relationship between ventricular and arterial contractility. The pulmonary circulation differs from systemic circulation in key ways. The pulmonary vascular resistance (PVR) includes resistance in the arteries and arterioles as well as the capillaries and veins and may increase by a factor of 4 or more, which is many times more than what can be seen in the systemic circulation (London et al. 1987). The vascular load is constant with an inverse relationship between PVR and total arterial compliance (TAC) (Lankhaar et al. 2008). As PVR increases, TAC decreases. In early PH,

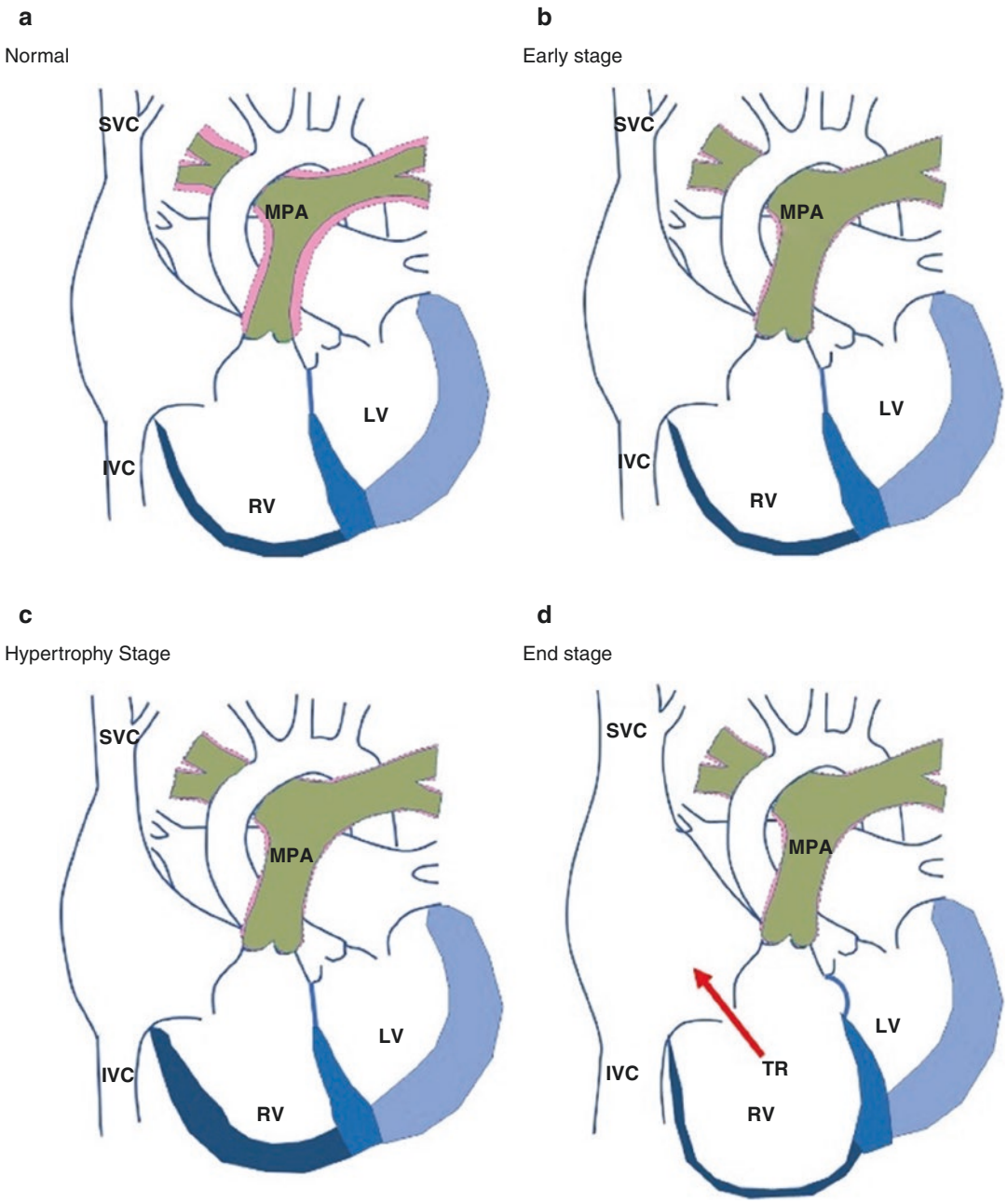


Fig. 3 Schematic drawing showing the adaption of the right ventricle (RV) to elevated pulmonary arterial pressure and volume. First, the pulmonary vascular bed will lose compliance and dilate to maintain normal pulmonary vascular resistance (MPA); but, eventually, it cannot compensate and PVR will rise. The right ventricle (RV) compensates through increase in contractility and wall thickening (right ventricular hypertrophy). Later, there is maladaptive dilatation of the RV with leftward bowing of the interventricular septum from chronic volume and pressure overload. This decreases filling of the left ventricle (LV) and LV stroke volume as the interventricular septum is no longer functional for LV contraction. In addition, RV contraction is prolonged with delayed closure of the pulmonary valve during RV systole and ventricular uncoupling with RV contraction while LV is in early diastole. The tricuspid valve (TV) annulus is stretched by the volume overloaded RV and TV regurgitation (TR) develops. The velocity of the TR jet is proportional to the mean pulmonary arterial pressure. Abbreviations: *SVC* superior vena cava, *IVC* inferior vena cava, *MPA* main pulmonary artery, *LV* left ventricle, *RV* right ventricle, *TR* tricuspid regurgitation

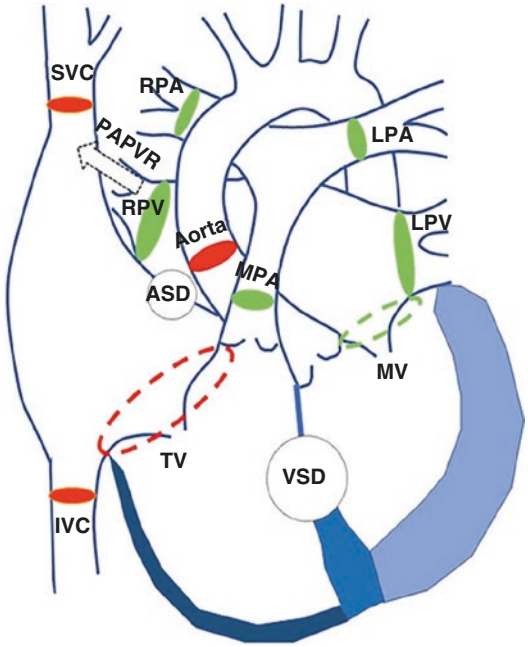


Fig. 4 Flow analysis with 4D flow or 2D phase-contrast MRI. Circles indicate the locations of analysis planes used for measuring flow volume. These are examples of $L \rightarrow R$ shunts for calculation of shunt fraction (Qp/Qs), with Qp representing flow in the pulmonary circulation and Qs systemic flow. Qp/Qs > 1 in these patients. If pulmonary vascular pressure remains lower than systemic circulation, blood will shunt $L \rightarrow R$ through the defects noted (PAPVR, ASD, VSD) and blood flow in the pulmonary circulation will be larger than systemic. Abbreviations: *SVC* superior vena cava, *IVC* inferior vena cava, *MPA* main pulmonary artery, *RPA* right pulmonary artery. *LPA* left pulmonary artery, *TV* tricuspid valve, *MV* mitral valve, *ASD* atrial septal defect, *VSD* ventricular septal defect, *PAPVR* partial anomalous venous return, *RPV* right pulmonary vein(s), *LPV* left pulmonary vein(s)

when PVR is still relatively low, TAC is the most variable component. Measuring pulmonary arterial compliance, pulmonary flow, pulmonary regurgitation and aortic flows and velocities is possible with either 2D phase-contrast MRI or 4D flow (Fig. 4). At high PVR, compliance changes little. Therefore, decreases in TAC may be a sensitive, early marker of increasing PVR and PH (Swift et al. 2012a; Sanz et al. 2009). Additional factors can affect the afterload the RV experiences. Afterload can be decreased through an alternative, less resistive path, such as tricuspid regurgitation and right-to-left shunting (e.g., through a patent foramen ovale). Elevated pulmonary capillary wedge pressure, as seen in left heart failure, decreases the resistance-compliance constant, which means changes in arterial compliance have a greater impact (Tedford et al. 2012). We next discuss how to evaluate the cardiopulmonary unit using CMR. Table 2 shows the typical CMR pulse sequences used for the characterization of PH.

These changes can also be easily found at echocardiography. While the quantification is the strength of CMR, ease of use, bedside access, and availability are the strengths of transthoracic echocardiography. The use of echocardiography is well accepted and its metrics are familiar and understood by clinicians. Assessment of IVC compliance helps to determine the presence of elevated central venous pressures (Stein et al. 1997). Commonly a collapse of the IVC of greater than or equal to 50% is commonly associated with normal central venous pressures (<5 mmHg), while failure of the IVC to collapse by half with respiratory variation is indicative of elevated central venous pressures (<15 mmHg). These are estimates however and there is variability that can be dependent on hydration of the patient. Other echocardiographic metrics that are used in the setting of acute pressure overload, e.g., pulmonary embolism, are: (a) the right ventricular end-diastolic volume (RVED)/left ventricular end-diastolic volume (LVED) from the parasternal long axis view or four-chamber view with a cutoff value of 0.6 determined to be abnormal (Mansencal et al. 2003). Please note that this is not the volume of either ventricle as found in CMR and that these values are not indexed to the body surface area of the patient; (b) continuous-wave Doppler of the peak velocity of the tricuspid regurgitant jet to get the gradient using the modified Bernoulli equation which in turn is correlated to the peak systolic pulmonary arterial pressure (sPAP) (Yock and Popp 1984). The velocity of the jet of tricuspid regurgitation provides a good estimation of the peak systolic pressure of the right ventricle and is thus a good proxy for the peak sPAP if there is no pulmonic outflow tract obstruction or pulmonary valve stenosis (Spiropoulos et al. 1999;

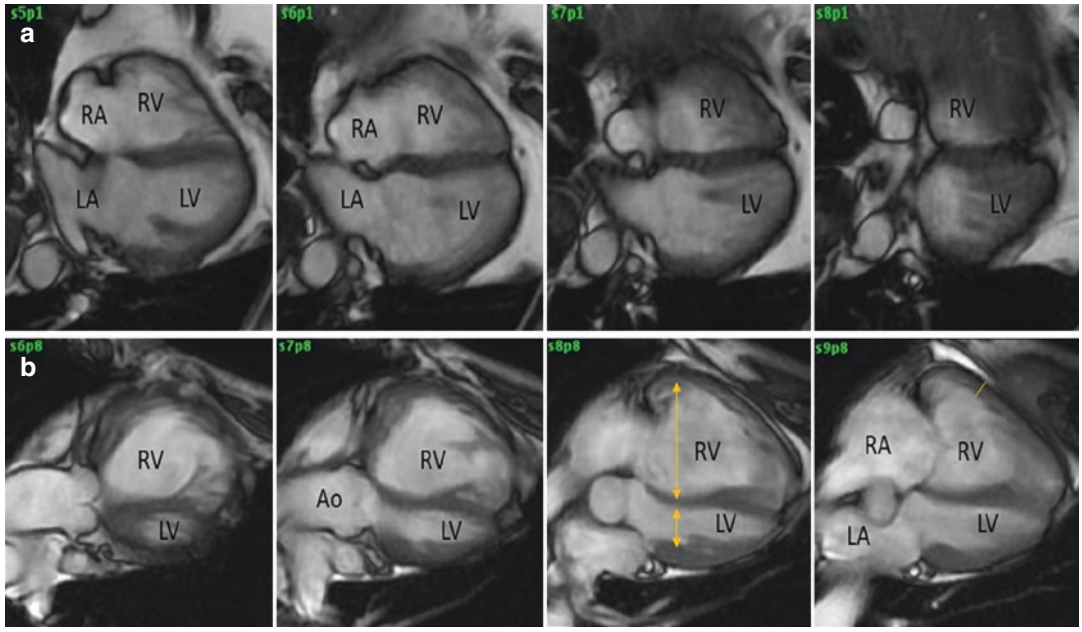


Fig. 5 Four-chamber stack of cine bSSFP images through mid-right ventricle showing right ventricular and interventricular septal changes in pulmonary arterial hypertension. (**a**) Normal right ventricle size and wall thickness. Interventricular septum is flat to slightly convex to the right. (**b**) Enlarged RV, including RV width > LV width. The interventricular septum bows into the left ventricle (better appreciated on short axis imaging). Given degree of dilation, the RV wall is likely thick

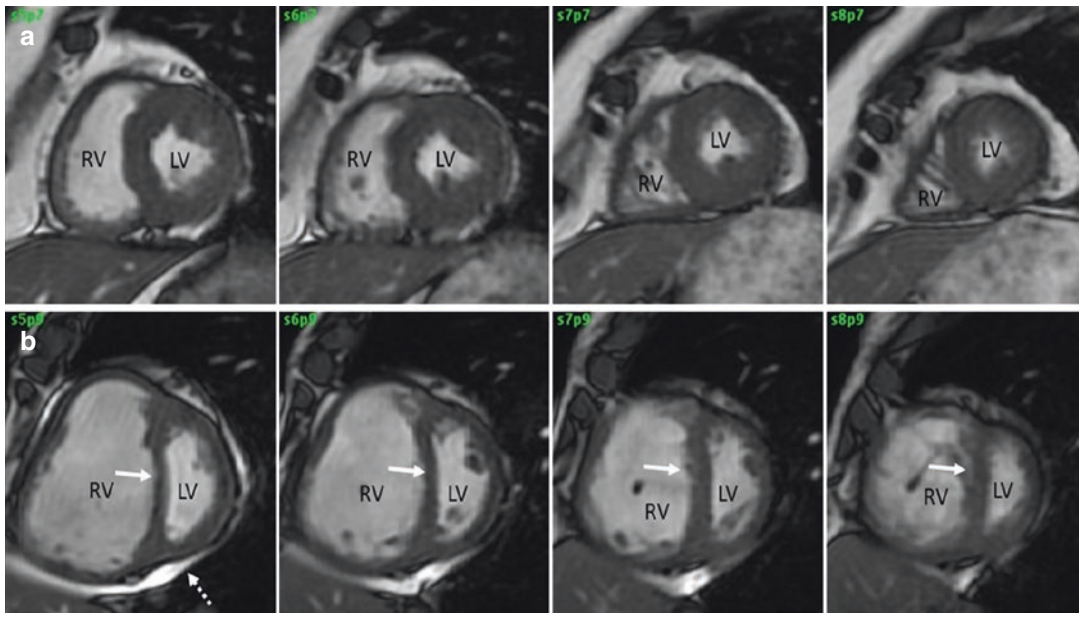


Fig. 6 Short axis stack of cine bSSFP images through mid-right ventricle showing right ventricular and interventricular septal changes in pulmonary arterial hypertension. (**a**) Normal right ventricle size and wall thickness. Interventricular septum configuration is normal, convex to the right. (**b**) Right ventricle is enlarged. The interventricular septum bows into the left ventricle (solid arrow). There is a small pericardial effusion (dotted arrow)

Table 2 Sequences used in MRI evaluation of pulmonary hypertension

Sequence	
Cine BSSFP	LV and RV dimensions, mass, function, volumes Interventricular septum changes
Black blood double IR T1 weighted	Anatomy
Contrast enhanced MRA, Including time resolved and/or perfusion	Vascular anatomy
	Lobar and segmental defects
	Lung and cardiac perfusion
Phase contrast (2D, 4D)	Shunt calculation
	Cardiac output
	PA flow profile, stiffness and pulsatility
	Pressure, hemodynamics
	Valvular regurgitation
Mapping T1, T2	Ventricular myocardial fibrosis, edema
Late Gadolinium	Ventricular myocardial fibrosis
Strain	Regional myocardial function

Current methods available using magnetic resonance imaging that can be applied to the initial diagnosis and follow-up of patients with pulmonary arterial hypertension

Yock and Popp 1984). In the acute setting of right ventricular pressure overload, the apex of the right ventricle has a characteristic change called the "apical wink," which is secondary to the bulging right ventricular apex in this situation.

3 Evaluation of the Right Ventricle

3.1 Non-contrast Computed Tomography

Non-contrast computed tomography of the chest is frequently performed for the evaluation of pulmonary diseases. While often overlooked, there is a great deal of information available about the heart as well. The relative size of the short axis of the right ventricle can be estimated on non-contrast computed tomography (Schlett et al. 2019). This is of importance because one of the key findings of elevated pulmonary artery pressures is the enlargement of the right ventricular volume, which in turn increases its minor axis and major axis. The outline of the wall of the ventricle is observable in patients with anemia (Title et al. 2005; Zhou et al. 2018). In 102 subjects Title et al. showed that using a Hounsfield unit threshold of 35, the sensitivity for anemia on non-contrast thoracic CT was 76% and specificity was 81%. Zhou et al. studied 317 participants and found that the difference between the HU density of the interventricular septum and the left ventricular cavity was more than 13.5 HU, the sensitivity/specificity was 95%/84% in males and 82%/85% in females for diagnosing severe anemia (Zhou et al. 2018).

3.2 Contrast-Enhanced Computed Tomography

Recently Kumamaru and colleagues have automated the calculation of the right to left ventricular diameter ratio from routine pulmonary computed tomographic angiography exams (Kumamaru et al. 2016). The right ventricle/left ventricle short axis ratio is >1.0 with acute and chronic elevations in pulmonary artery pressure. In the setting of acute of pulmonary embolism, this simple variable is associated with increased mortality. Henzler et al. showed that the right ventricle/left ventricle ratio (LV/RV) can be derived form routine CTA exams the RV/LV ratio (axial) 1.69 ± 0.84(Areas under the curve (AUC) = 0.84), RV/LV ratio (4-chamber) 1.52 ± 0.45 (AUC = 0.87) and RV volume/LV volume 1.97 ± 0.53 (AUC = 0.93)were predictive metrics for right ventricular dysfunction (Henzler et al. 2012).

3.3 Cardiac-Gated Computed Tomographic Angiography

The use of retrospectively gated cardiac computed tomographic angiography exams has declined due to the amount of medical radiation of these studies (Raff et al. 2009). Instead, prospective cardiac-gated exams are used clinically (Stocker et al. 2018). They were able to calculate the end-diastolic right ventricular wall mass index from these studies, but the ejection fraction cannot be determined without the end-systolic volumes. Takx et al. have shown that a dual-step method of gated dual source cardiac-gated computed tomography (DSCT) is able to obtain the systolic and diastolic phases of the heart for calculation of the right and left ventricular volumes and masses with a low overall dose to the subject (Mean radiation dose = 6.2 ± 1.8 mSv) (Takx et al. 2012). Using this DSCT method in twenty participants they found good correlation with CMR: left end-diastolic volume $r = 0.885$, right end-diastolic volume $r = 0.801$, left end-systolic volume $r = 0.947$, right end-systolic volume $r = 0.879$, left ventricular end-systolic volume $r = 0.62$, right ventricular stroke volume $r = 0.697$, left end-systolic volume $r = 0.869$, right ventricular ejection fraction $r = 0.751$, left myocardial mass $r = 0.959$, and right ventricular myocardial mass $r = 0.702$ (Takx et al. 2012; Raff et al. 2009). Thus, cardiac-gated CTA methods can be used to derive morphological changes in the ventricular cavities over the course of the cardiac cycle in health and disease. The primary limitation is the amount of medical radiation required for this exam.

4 MRI

Use of ECG-gated bSSFP cine imaging is well established for the assessment of ventricular function and size (Figs. 5 and 6). There is now normative data for all CMR-derived indices for adults and children (Grothues et al. 2004; Kawel-Boehm et al. 2015). CMR using ECG-gated bSSFP cine imaging can measure RV and LV volume, muscle mass, right and left ventricular SV, and the right and left ventricular ejection fractions (RVEF and LVEF). Numbers can be indexed to sex, age, and body surface area allowing more precise baseline assessments. The noninvasive, medical radiation free, assessment of the changes in the RV over time is a strength of MRI. Evaluation of the RV in healthy volunteers is most reproducible in the transaxial plane (Jauhiainen et al. 2002); however, the optimal approach in patients with PH remains to be determined. Early remodeling in PAH/PH will increase RV mass. Late, maladaptive remodeling causes an increase in RV volume. With disease progression, RVSV will decrease as the RV fails. RV hypertrophy is defined as wall thickness greater than 4 mm, based on early echocardiography studies (Prakash 1978). RV dilatation can be diagnosed on axial 4-chamber bSSFP cine images when the LV:RV ratio is greater than one. The ratio of RV to LV mass can also be calculated, referred to as the ventricular mass index, with ratio > 0.6 indicative of elevated RV mass (Goerne et al. 2018). Both RV mass and RV mass index have been found to be increased in PAH and are correlated with PAP in patients with PAH (Hagger et al. 2009; Ascha et al. 2017; Pena et al. 2012). The ratio of RV mass to RV volume has been proposed as an early marker for maladaptive RV remodeling (Badagliacca et al. 2016). A meta-analysis of 539 patients found RVEF to be the strongest predictor of mortality in PAH (pooled Hazard Ratio (HR) 1.23, 95% C.I. 1.07–1.41, p value = 0.003), with the LV end-diastolic volume index LVEDI also significant (pooled HR 1.16, 95% C.I. 1.0–1.34, p value = 0.05) (Baggen et al. 2016). In that study, RV mass did not provide mortality predictive information (Baggen et al. 2016).

Strain imaging utilizing feature- or tissue-tracking on bSSFP images is an emerging tool to identify early, subtle, regional wall motion abnormalities and is useful in measuring interventricular dependency by measuring time to peak strain in the RV versus the LV. In addition, an advantage of strain imaging is assessment of systolic and diastolic wall motion. Stain imaging has shown regional abnormalities using other methods such as tagging or strain-encoding (SENC) (Shehata et al. 2013; Mauritz et al. 2012b).

The most common pattern of late gadolinium enhancement (LGE) in PH is as at anterior and inferior RV septal insertion (hinge) points (Fig. 7).

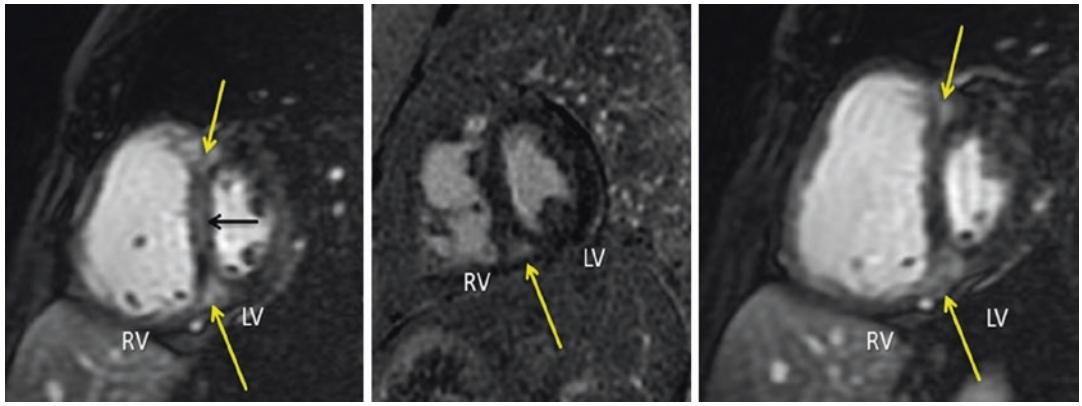


Fig. 7 Short axis delayed gadolinium enhancement images through the mid ventricles in three patients with pulmonary hypertension showing enhancement at the insertion point of the RV into the interventricular septum. While associated with pulmonary hypertension, the clinical significance remains uncertain. The black arrow points to midwall enhancement in the interventricular septum, seen in severe pulmonary hypertension

The etiology of this phenomenon is unclear; however, the evidence suggests enlargement of the extracellular space and without fibrosis (Bradlow et al. 2010). This may occur secondary to the dynamic movement occurring in the interventricular septum throughout the cardiac cycle causing stress-related change in the myocytes (Sato et al. 2013a; Blyth et al. 2005). Some patients develop extension of LGE in a band within the interventricular septum, a feature seen in more severe PH (Swift et al. 2014b); however, the prognostic value and clinical significance of this feature remains unclear (Fig. 7) (Freed et al. 2012; Swift et al. 2014b). The amount of LGE correlates with RV volume, RV mass, and interventricular septum position (Bradlow et al. 2010).

T1 mapping is emerging as a technique to evaluate for expanded extracellular space and/or fibrosis without the need for contrast (Kawel-Boehm et al. 2014). This may detect early interstitial abnormalities or diffuse fibrosis in the RV wall. In addition, T1 mapping values at the RV insertion points correlate with indices of RV dysfunction (Garcia-Alvarez et al. 2015). T2 mapping is used to evaluate the RV insertion points. Increased hinge point T2 relaxation times is associated with LGE in preliminary studies (Wang et al. 2018). Again, the clinical significance of the myocardial changes in T1 and T2 relaxation times in PH remains unclear.

5 Evaluation of the Interventricular Septum

Cine imaging with bSSFP, including free-breathing imaging, can show the physiologic ability of the RV to handle volume overload by assessing changes in the interventricular septum's response to an increased preload after a deep inspiration. Inspiration lowers intrathoracic pressure, thereby increasing venous return to the heart (Figs. 5, 6 and 7) (Alunni et al. 2010; Roeleveld et al. 2005). Mechanical asynchrony from prolonged RV contraction may be seen in these disorders (Roeleveld et al. 2005; Alunni et al. 2010; Sciancalepore et al. 2012). The position of the interventricular septum can be easily quantified by the curvature or the angle of the mid-point of the septum in relation to the RV insertion points. In systole, the degree of septal deviation, likely relating to the instantaneous pressure differential between the ventricles, correlates well with RV and PAP (Dellegrottaglie et al. 2007; Roeleveld et al. 2005; Swift et al. 2013). The position of the interventricular septum may also be useful for identifying patients with severe PH in left heart disease who may warrant PH referral and consideration of trials of new therapies (Johns et al. 2018b).

6 Evaluation of Additional Cardiac Chambers

In PH related to congestive heart failure, the left ventricle (LV) may be enlarged, hypertrophied, or both (Schiebler et al. 2013). This will impact RV measurements indexed to the LV. Left atrial volume has been proposed as a factor to distinguish PAH from PH in LV failure with preserved ejection fraction (Crawley et al. 2013). The ratio of the left to right atrial size has also been assessed to discriminate between preserved ejection fraction heart failure patients and idiopathic PAH patients (Huis In 'T Veld et al. 2016).

Evaluation of the right atrium has focused on three basic functions, as reservoir, conduit, and contractor, with measurements of reservoir and SV used to calculate ejection fraction. While increase in RA size has been associated with PH, functional changes in the right atrium are less straightforward, with increased ejection fraction in mild to moderate disease but decreased systolic function in severe disease (Sato et al. 2013b). A recent longitudinal study has shown that RA volume and its reservoir function, in combination with RVEF, can be used to predict some outcomes in precapillary PH (Sato et al. 2015; Bredfelt et al. 2018).

7 Evaluation of the Vasculature

In our discussion of the many causes of PH/PAH, perhaps no other disease is as iconic as chronic thromboembolic pulmonary hypertension (CTEPH) (Fig. 8). The reasons for this are that the findings are quite unique and easily visible using computed tomographic angiography (CTA) (Table 3). These features include the following

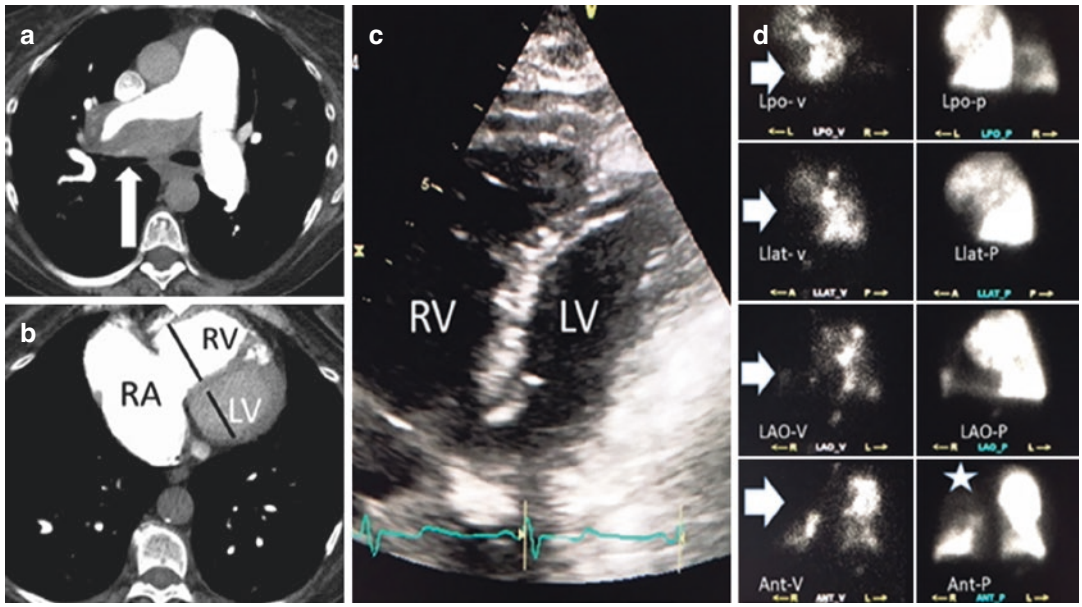


Fig. 8 Chronic thromboembolic pulmonary hypertension (CTEPH) complicated by emphysema: (**a**) shows a computed tomographic angiogram (CTA) with fibrin sheath of CTEPH in the left main pulmonary artery and calcification of the artery as well (arrow); (**b**) CTA of same subject showing a larger short axis for the right ventricle than the left ventricle, right ventricular hypertrophy, a delayed circulation time (little contrast in the left ventricle) and a very enlarged right atrium (RA); (**c**) transthoracic echocardiogram showing a massively enlarged right ventricle (RV) and a smaller left ventricle on this left ventricular outflow tract view; (**d**) nuclear medicine ventilation perfusion lung scan with the ventilation images on the left panels and the complementary perfusion images on the right-sided panels. There are multiple ventilation defects seen (arrows) and scattered large perfusion defects appreciated as well (anterior perfusion defect is marked with a star) in this patient with both CTEPH and emphysema

Table 3 Comparative analysis of transthoracic ultrasound and magnetic resonance imaging for the diagnosis and follow-up of cardiovascular indices relevant for pulmonary hypertension shows that MRI yields much more information and in the USA these studies are of similar cost

Variable	Transthoracic ultrasound	Non-contrast HRCT	Computed tomographic angiography	Magnetic resonance imaging
2018 CMS procedure code(s)	93,309	71,250	71,275	75,561,75,565
CMS reimbursement amount[a]	$204.42	$215.20	$370.78	$477.93
Time to perform	30–60 min	1 min	1 min	60 min
Able to perform at bedside	yes	no	no	no
SVI	No	No	No	Yes
mPAP	No	No	No	No
Estimated mPAP	Yes	No	No	Yes
Qp/Qs	No	No	No	Yes
FWHM	No	No	No	Yes
PTT	No	No	No	Yes
RVSV	No	No	No	Yes
RVSVI	No	No	No	Yes
RVEF	No	No	No	Yes
RVEDV	No	No	No	Yes
REVDVI	No	No	No	Yes
RVESV	No	No	No	Yes
RVESVI	No	No	No	Yes
RV mass	No	No	No	Yes
RV mass index	No	No	No	Yes
LV mass	No	No	No	Yes
LV mass index	No	No	No	Yes
LVSV	No	No	No	Yes
LVSVI	No	No	No	Yes
LVEF	Estimated	No	No	Yes
LVEDV	No	No	No	Yes
LEVDVI	No	No	No	Yes
LVESV	No	No	No	Yes
LVESVI	No	No	No	Yes
LVSV	No	No	No	Yes
PA RAC	No	No	No	Yes
GLS	No	No	No	Yes
GLSR	No	No	No	Yes
GCSR	No	No	No	Yes
Pulmonary artery PWV	No	No	No	Yes
Pulmonary artery WSS	No	No	No	Yes
Right atrial volume	No	Yes	Yes	Yes
Right atrial volume index	No	Yes	Yes	Yes
IVC size	Yes	Yes	Yes	Yes
IVC Flow	No	No	No	Yes
SVC size	Yes	Yes	Yes	Yes
SVC Flow	No	No	No	Yes
TAPSE	Yes	No	No	Yes
TV regurgitation jet velocity	Yes	No	No	Yes
TV regurgitation volume	No	No	No	Yes
PV regurgitation jet velocity	Yes	No	No	Yes
PV regurgitation volume	No	No	No	Yes
Pulmonary vein velocity	Yes	No	No	Yes
Pulmonary vein Flow	No	No	No	Yes
Left atrial volume	Partially	Yes	Yes	Yes
Left atrial volume index	No	Yes	Yes	Yes

Table 3 (continued)

Variable	Transthoracic ultrasound	Non-contrast HRCT	Computed tomographic angiography	Magnetic resonance imaging
MVR jet velocity	Yes	No	No	Yes
MVR volume	No	No	No	Yes
AV regurgitation velocity	Yes	No	No	Yes
AV jet volume	No	No	No	Yes
Aortic PWV	No	No	No	Yes
Aortic WSS	No	No	No	Yes
RV T1 mapping	No	No	No	Yes
RV T2 mapping	No	No	No	Yes
LV T1 mapping	No	No	No	Yes
LV T2 mapping	No	No	No	Yes
DCE of septal insertions	No	No	No	Yes
Acute pulmonary emboli	No	Yes	Yes	Yes
Chronic pulmonary emboli	No	Yes	Yes	Yes
CTEPH	No	Sometimes	Yes	Yes
PA Fractal dimension	No	No	Yes	Yes
Anomalous coronary arteries	Sometimes	Yes	Yes	Yes
Pulmonary artery compression of LAD coronary artery	Sometimes	Sometimes	Yes	Sometimes
ASD	Yes	No	Sometimes	Yes
PAPVR	Sometimes	Yes	Yes	Yes
PDA	Sometimes	Yes	Yes	Yes
VSD	Yes	No	Sometimes	Yes
PA Size	Yes	Yes	Yes	Yes
Lung masses	No	Yes	Yes	Yes
Mediastinal masses	No	Yes	Yes	Yes
Pulmonary veno-occlusive disease	No	Yes	Yes	No
Pulmonary capillary hemangiomatosis	No	Yes	Yes	No
Quantification of Emphysema	No	Yes	No	Yes
Fibrosing mediastinitis	No	Yes	Yes	Yes
hepatopulmonary syndrome	No	Yes	Yes	Yes
Portopulmonary hypertension	Yes	Sometimes	Sometimes	Yes
Tracheobronchomalacia	No	Yes	Yes	Yes
Obstructive sleep apnea	No	No	No	No
Liver cirrhosis	Yes	Yes	Yes	Yes
Quantification of liver fibrosis	Research	No	No	Yes

This table shows why MRI is a much better test for the initial workup and follow-up of patients with pulmonary arterial hypertension

Abbreviations: *AS*D atrial septal defect, *CMS* Center for Medicare and Medicaid Services 2018 Fee Schedule codes and reimbursement, *DCE* delayed contrast enhancement of the interventricular septal insertions, *FWHM* full width half maximum of the transit time of the contrast material peak from the pulmonary artery to the aorta, *GLS* global right ventricular longitudinal strain, *GLSR* global right ventricular longitudinal strain rate, *GCSR* global right ventricular circumferential strain rate, *LVEF* left ventricular ejection fraction, *LVSV* left ventricle stroke volume, *LVEDVI* left ventricular end-diastolic volume index, *LVESVI* left ventricular end-systolic volume index, *LV T1* mapping- Longitudinal relaxation time of the left ventricle, *LV T2* mapping- transverse relaxation time of the left ventricle, *PAPVR* partial anomalous pulmonary venous return, *mPAP* mean pulmonary artery pressure, *PA size* pulmonary artery transverse diameter, *PA RAC* pulmonary artery relative area change, *PDA* patent ductus arteriosus, *PTT* pulmonary transit time, *PWV* pulse wave velocity, *PA RAC* relative area change of the pulmonary trunk, *Qp/Qs* ratio of the pulmonary arterial flow to aortic flow, *RVEDV* right ventricular end-diastolic volume, *RVEDVI* right ventricular end-diastolic volume indexed to body surface area, *RVSV* right ventricle stroke volume, *RVEF* right ventricular ejection fraction, *RVESV* right ventricular end-systolic volume, *RVESVI* right ventricular end-systolic volume indexed to body surface area, *RV T1* mapping- Longitudinal relaxation time of the right ventricle, *RV T2* mapping- transverse relaxation time of the right ventricle; *SVI* stroke volume index = cardiac output/heart rate (beats per minute)/BSA (m_2), *VSD* ventricular septal defect, *WSS* wall sheer stress

[a]CMS reimbursement varies by location in the USA

associated imaging observations: (a) right ventricular hypertrophy; (b) main pulmonary artery enlargement; (c) lamellar and relatively concentric fibrin deposition in the right and left main pulmonary arteries, occasionally primary pulmonary artery sarcoma can present with similar findings in these vessels; (d) simplification of the branching of the pulmonary arteries (i.e., pruning of the arterial tree); (e) mosaic perfusion pattern that normalizes at expiration, unlike air-trapping; (f) intermittent visualization of the webs of resolving chronic pulmonary emboli; (g) septal flattening; (h) enlargement of the right atrium from chronic tricuspid regurgitation. Sometimes, there will also be calcification of the media of the right and left pulmonary arteries due to the long exposure to elevated pulmonary arterial pressures; however this can also be seen in the late stages of large left to right shunts that have developed Eisenmenger physiology; (i) there is also a larger right ventricle than left ventricle that can be shown easily by a right ventricle/left ventricle short axis ratio of >1.0 derived from a simple measurement using the non-angled axial images.

On MRI there are a number of methods that can be used to evaluate the pulmonary circulation. The simplest are black blood imaging and bSSFP images which can be used to obtain information about pulmonary artery size (Fig. 9). In addition, black blood imaging can show turbulent or slow-flow phenomenon in PH. This feature has high diagnostic accuracy when compared to standard cardiac volumetric parameters (Swift et al. 2012b). Further work is required to understand the significance of the black blood flow phenomenon and 4D flow may be a useful tool for this purpose. MR-angiography (MRA) can show characteristic vessel patterns in subtypes of PH, including tortuosity in idiopathic PAH, pruning, webs, bands, pouching defects due to post-embolic sequelae in CTEPH, and splayed vessels in COPD/emphysema (Fig. 10) (Swift et al. 2014d).

Time-resolved MRA or dynamic contrast-enhanced (DCE) MRI can be used to measure passage of contrast bolus through heart and lungs to assess pulmonary perfusion (Skrok et al. 2012; Ley et al. 2007). This can be used to measure mean transit time, time to peak, and blood volume (Ohno et al. 2007; Reiter et al. 2008; Swift et al. 2014c; Francois et al. 2003).

Phase-contrast imaging can further characterize flow in the cardiopulmonary unit. Pulmonary arterial and aortic compliance and flow analysis provides a second measurement of cardiac output beyond SV, which is altered by valvular disease (Fig. 11). In addition, pulmonary arterial average velocity may be useful diagnostic marker (Sanz et al. 2007). Phase-contrast imaging (or 4D flow) at two separate locations is used to calculate the pulse wave velocity, which can be used to infer vessel compliance (Bradlow et al. 2007; Stevens

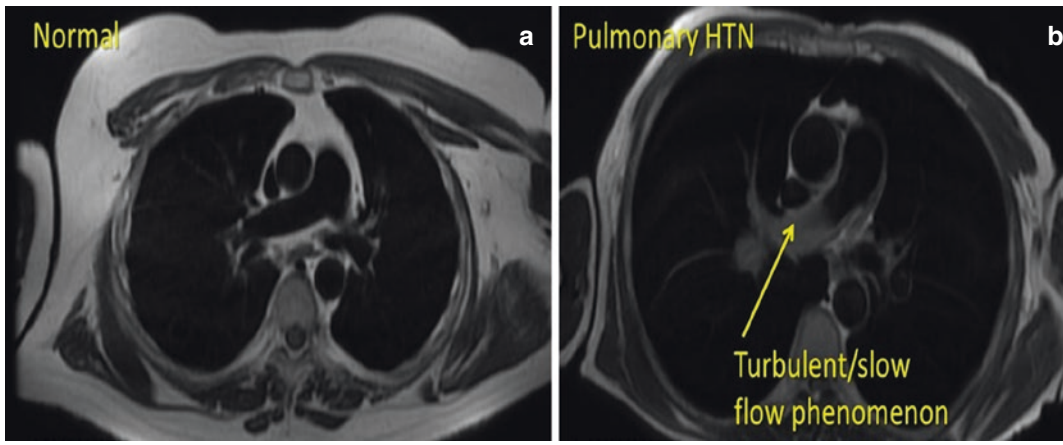


Fig. 9 Black blood image in a normal patient (**a**) and patient with pulmonary hypertension (**b**). Image B shows artifact in the right pulmonary artery (gray) indicative of abnormal flow

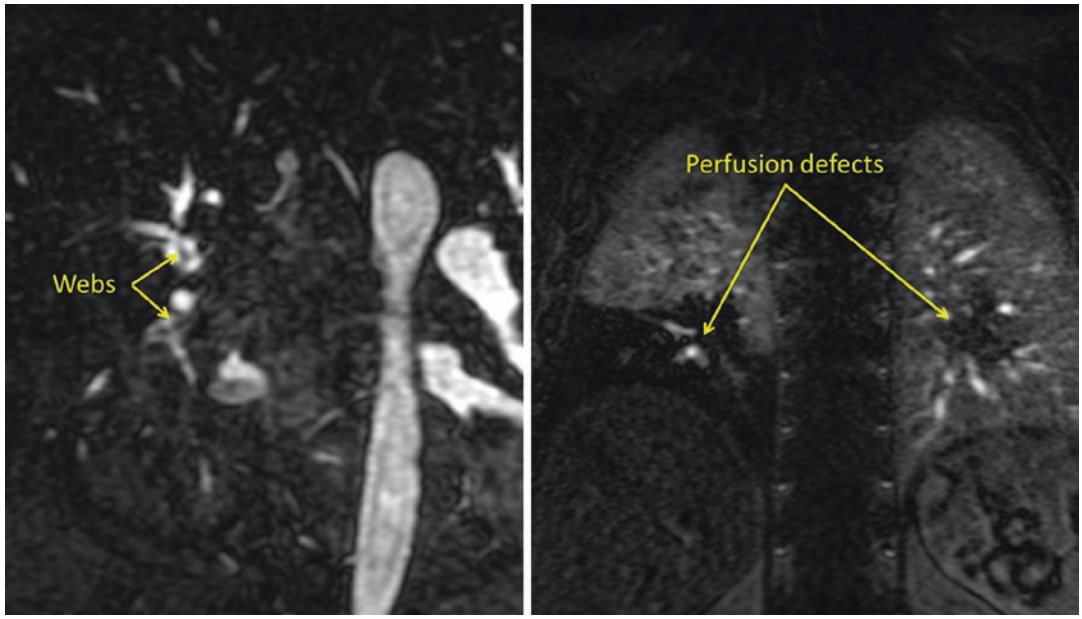


Fig. 10 Coronal images of contrast-enhanced MRA in two patients with chronic thromboembolic pulmonary hypertension. Image on the left shows webs. Image on the right shows perfusion defects as black areas, in this case, affecting nearly the entire right lower lobe

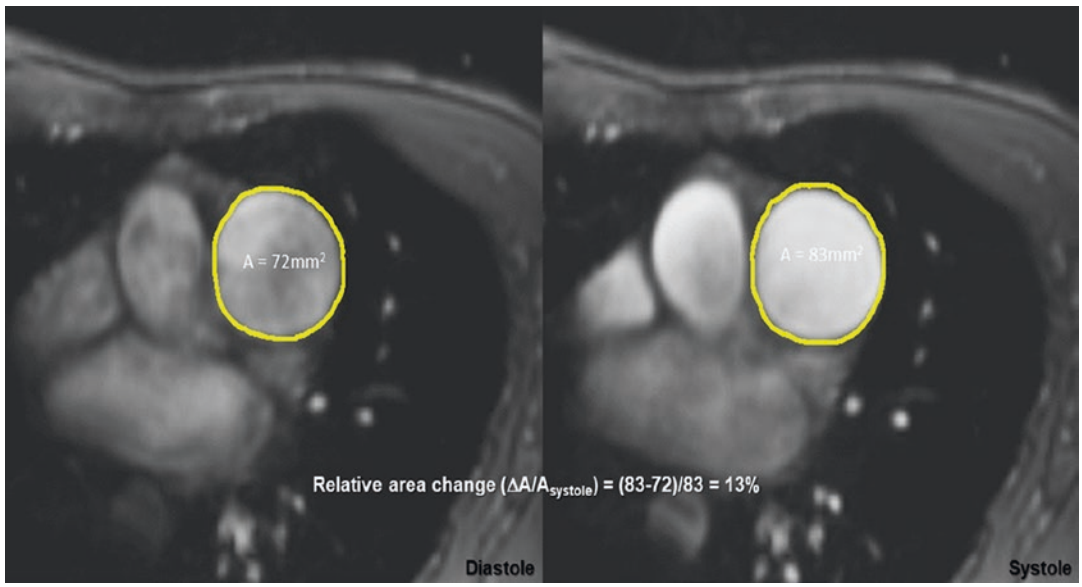


Fig. 11 Phase-contrast images during systole and diastole used to calculate the relative area change which is a measure of vessel distensibility

et al. 2012). When there is loss of compliance, the pulse wave velocity increases. The pulmonary artery relative area change (RAC) is measured with phase-contrast MRI as an index of pulmonary artery stiffness (Fig. 11). Pulmonary artery relative area change is calculated from the change in cross-sectional area of the main pulmonary artery (MPA) between systole and

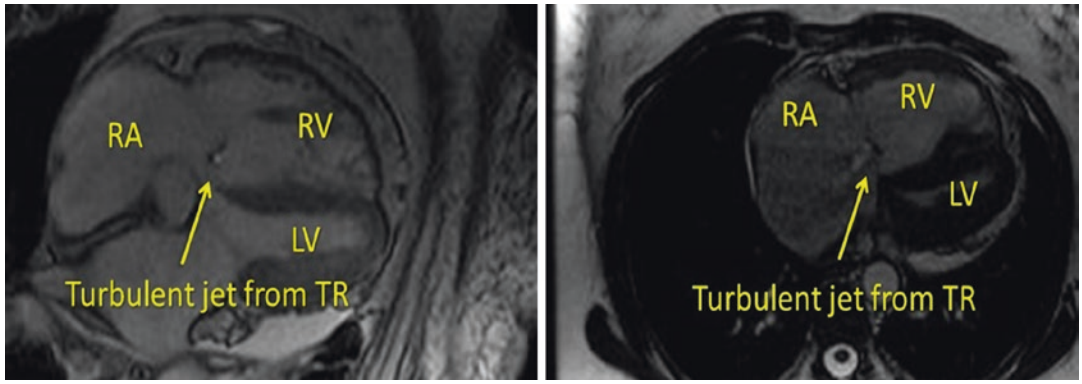


Fig. 12 Four-chamber bSSFP images through the mid-RV show artifact from tricuspid regurgitation (arrow). The right atrium is enlarged. Additional findings of pulmonary hypertension include marked enlargement of the RV and leftward bowing of the interventricular septum

diastole: diastolic cross-sectional area (maximum size area)—systolic cross-sectional area (minimum size area)/diastolic cross-sectional area (Swift et al. 2017). Decreased RAC indicates increased MPA stiffness, or decreased MPA compliance. Changes in MPA compliance are observed earlier than changes in pulmonary vascular resistance. Recently, Swift et al. showed that a decrease in pulmonary artery RAC is associated with a poor prognosis in these patients (Multivariate HR 0.76, 95% CI. 0.623–0.932, p value = 0.008) (Swift et al. 2017) (Fig. 12).

Treatment of CTEPH by pulmonary endarterectomy (PEA) or balloon pulmonary artery angioplasty (BPA) is very helpful and improves longevity in these patients (Taboada et al. 2014; Scholzel et al. 2014; Darocha et al. 2017). When the pulmonary arterial compliance is restored, there is improvement in performance of the right ventricle as the amount of pressure it sees at end systole is decreased. Condliffe et al. showed that the 3-year survival after CTEPH diagnosis was 70% for patients with nonsurgical disease and 76% for those treated surgically (P = 0.023). They also found functional and hemodynamic improvements in surgically treated patients: (a) increased 6-min-walk distance at 3 months of 105 m ($P < 0.001$) and (b) for the 35% of patients who survived to 3 months with persistent pulmonary hypertension, the 5-year survival was 94% (Condliffe et al. 2008).

8 Ratio of the Pulmonary to Systemic Blood Flow

In a normal cardiopulmonary unit, the systemic blood flow (Qs) is approximately equal to the pulmonary blood flow (Qp), yielding a Qp/Qs ratio of 1 (Figs. 4 and 11). However, these flows are influenced by respiration with the difference between the Qs and Qp larger in inspiratory breath-hold and smaller in expiratory breath-hold or free breathing; however this rarely, if ever, represents a diagnostic challenge and should not be mistaken for a hemodynamically significant shunt (Ley et al. 2006). When there is a significant cardiopulmonary shunt, such as ventricular septal defect (VSD), atrial septal defect (ASD), or partial anomalous pulmonary venous return (PAPVR), the Qp/Qs is not 1 (Fig. 4). Phase-contrast MRI or 4D flow provides blood flow volume in any vessel of interest by setting a cross-sectional area and post processing the data on a dedicated workstation. Qs is traditionally measured as the blood flow in the ascending aorta. Qp is traditionally measured as blood flow in the MPA but can also be measured as total flow in the right and left pulmonary arteries. Blood flow in the MPA is slightly larger than in the ascending aorta because a portion of the blood flow in the aorta immediately goes into the coronary arteries. Normal Qp/Qs is reported as 1.05 ± 0.07 (Chernobelsky et al.

2007). A Qp/Qs > 1.05 indicates the existence of a left-to-right shunt and a Qp/Qs < 1 means a right-to-left shunt. Qp/Qs is an index of severity of shunt and is important to making clinical decisions. When the Qp/Qs exceeds 1.5, this indicates a large shunt, for which surgical or percutaneous intervention needs to be considered by the multidisciplinary treatment team (Driscoll et al. 1994). The most severe condition of PAH, due to congenital heart disease, is Eisenmenger's syndrome which is the result of a long-standing, uncorrected left-to-right cardiac shunt. Over time, PVR rises so much there is eventual reversal of the shunt to a right-to-left cardiac shunt (Fig. 2).

9 Pulmonary and Tricuspid Valve Regurgitation and Jet Velocity

The most commonly used test for the diagnosis of PH/PAH is transthoracic ultrasound. This widely available test is helpful for quantitative assessment of the velocity of the tricuspid valve regurgitation jet. The TR velocity is proportional to the mean pulmonary arterial pressure.

The pulmonary and tricuspid valves are of interest in PH, as they can help define preload and afterload on the RV (Fig. 11). The regurgitant volume and flow velocity at a valve can be calculated using 2D phase-contrast MRI. For the pulmonary valve, these images are typically acquired approximately 1 cm above the pulmonary valve orthogonal to the MPA. PH causes pulmonic regurgitation, which further contributes to right heart failure. PH due to long-term valve deterioration tends to accelerate. Pulmonary regurgitant volume is measured as the retrograde flow in the MPA during the diastole. The pulmonary regurgitation fraction is calculated as the ratio between retrograde volume and forward volume. The grades of pulmonary regurgitation fraction are defined as insignificant or mild (<25%), moderate (25–40%), and severe (≥40%) (Gorter et al. 2015). The change in PR can be assessed longitudinally with CMR.

Tricuspid regurgitation occurs secondary to enlargement of the tricuspid annulus. The annulus enlarges as the RV dilates. The RV dilates from failing to keep up with rising pulmonary pressures and increased RVEDV from pulmonary valve insufficiency. The TR acts as a pressure pop off for the RV, which is not able to generate enough pressure to keep the pulmonary valve open for all of systole. Evaluation of the tricuspid valve is challenging given its complex geometry and motion throughout the cardiac cycle. Although 2D phase contrast can be used, it is limited for assessment of the atrioventricular valves given the large degree of through-plane motion. While TR can be indirectly calculated from RVSV minus flow volume in the pulmonary artery, 4D flow techniques using valve tracking software are more accurate (Driessen et al. 2018). Estimated pulmonary arterial pressure (PAP) can be obtained from the maximal regurgitant velocity at tricuspid valve (Vmax) by applying the modified Bernoulli equation and is commonly calculated in echocardiography. A mean right atrial pressure (RAP) of 10 mmHg is used in this MR-based estimation of pulmonary arterial pressure and Vmax is of the regurgitant jet at the tricuspid valve. The equation is as follows: Estimated PAP = 4 × Vmax + RAP (Nogami et al. 2009).

10 Mediastinal Diseases

Fibrosing mediastinitis is the most common cause of PH related to extrinsic pulmonary vein compression/stenosis at the level of the left atrium (Mallin et al. 1993). These mediastinal lymph nodes are usually calcified. While a rare event, when it does occur, histoplasmosis is often the cause of this disorder (Patel et al. 2015). Other benign causes of mediastinal lymph node enlargement, such as sarcoidosis, can also compress the pulmonary veins leading to PH (Toonkel et al. 2010; Diaz-Guzman et al. 2008). It is very uncommon for advanced lung cancer to cause enough fibrosing mediastinitis to raise pulmonary arterial pressure.

11 Diseases of the Left Heart

The scope of this chapter does not lend itself to a thorough discussion of left ventricular and left heart valvular disease that can lead to pulmonary hypertension. Probably the best way to think about this is to imagine a single oxygenated red blood cell's return to the left atrium and all of the adventures that it could possibly encounter on its way to the aorta. The changes in pressure required to move this cell can be modified by disease at any one of a number of structures. The possible structures that may affect a change in pressure for transit of this cell in the left heard includes the following: pulmonary venules, pulmonary veins, left atrium venous orifice, left atrial appendage, interatrial septum, left atrium, mitral valve, mitral valve annulus, left ventricle, left ventricular outflow tract, aortic valve, and the aortic valve annulus.

12 Diastolic Dysfunction

As the left ventricle stiffens with age, the left ventricular end-diastolic filling pressures elevate and the left atrium enlarges. This stiffening is measurable by US and MRI. On ultrasound the proxy used to gauge relaxation of the left ventricle is the mitral annular tissue Doppler velocity.

The prevalence of diastolic dysfunction increases with age. As measured by transthoracic echocardiographic criteria, more than 40% the US population over age 50 have some degree of diastolic dysfunction (Table 4) (Kuznetsova et al. 2009). In their transthoracic echocardiographic study of a randomly recruited population sample of 539 adults (50.5% women; mean age, 52.5 years), they measured the following: (a) early and late diastolic peak velocities of mitral inflow (E and A) (Group 1 diastolic dysfunction), (b) pulmonary vein flow by pulsed-wave Doppler (Group 2 diastolic dysfunction), and (c) the mitral valve annular tissue plane velocities (Ea and Aa) at 4 sites by tissue Doppler imaging (Group 3 diastolic dysfunction) (Kuznetsova et al. 2009). They established age-specific cutoff limits for normal E/A and E/Ea ratios and the differences in duration between the mitral A and the reverse pulmonary vein flows during atrial systole (ΔAd−ARdCMR ac) from a healthy subsample of 239 subjects (mean age, 43.7 years). They found that for their randomly recruited

Table 4 Increasing left ventricular diastolic dysfunction prevalence with age in an adult population in the United States

Age [Number in cohort]	Normal function	Impaired LV function Group 1	Elevated LVEDP Group 2	Combined dysfunction Group 3	% Nl [Nl/total]
<30 years [55]	13% [52]	6% [3]			96% [52/55]
30–39 years [49]	12% [47]	2% [1]	1% [1]		96% [47/49]
40–40 years [131]	31% [120]	13% [7]	4% [3]	4% [1]	92% [120/131]
50–59 years [131]	27% [104]	32%[17]	11% [8]	11% [2]	79% [104/131]
60–69 years [99]	13% [52]	25% [13]	36% [27]	39% [7]	53% [52/99]
70 years [74]	4% [17]	23% [12]	49% [37]	44% [8]	23% [17/74]
≥ 50 years [304]	**57% [173/304]**	**14% [42/304]**	**24% [72/304]**	**5% [17/304]**	**57% [173/304]**
Total [539]	73% [392/539]	10% [53/539]	14% [76/539]	3% [18/539]	73% [392/539]

Data modified from Table 6 in Kuznetsova et al. (Kuznetsova et al. 2009). Group 1- Impaired relaxation = low E/A and normal E/Ea, Group 2- elevated end-diastolic pressure = normal E/A and high E/Ea and Group 3- combined dysfunction = low E/A and high E/Ea

Abbreviations: *LVEDP* left ventricular end-diastolic pressure, *Nl* normal diastolic function at echocardiography, *Abnl* any abnormal measure of diastolic function at echocardiography

subject population 14% had group 1, 24% had group 2, while only 5% had group 3 diastolic dysfunction (Table 4) (Kuznetsova et al. 2009).

CMR can be used to quantify diastolic dysfunction as well (Caudron et al. 2011). The use of 4D flow can quantify the volume and velocity of the pulmonary veins (Lantz et al. 2018, 2019). All of the transthoracic echocardiographic components that comprise the criteria for diastolic dysfunction are measurable with CMR (Westenberg 2011; Gouda et al. 2014). Also, individuals with diastolic dysfunction and borderline PH have a higher risk of mortality and hospitalization (Table 5) (Maron et al. 2018).

The other way that PAH/PH can affect left ventricular filling pressures is by septal bowing from significant PAH (precapillary pulmonary hypertension) deforming the left ventricular cavity. The size of the RV with septal bowing into the LV cavity enhances interventricular dependence (Agrawal et al. 2019).

13 Mitral Valve Disease

The mitral valve is an important source of pulmonary hypertension in the developing world because of rheumatic mitral valve stenosis

Table 6 Comparative analysis of the prognostic significance of cardiovascular magnetic resonance imaging findings in the setting of pulmonary hypertension

Author	Size (n)	CMR metric	Hazard ratio	Hazard ratio 95% C.I.	*P* value	Analysis	Cutoff (Kaplan-Meier)
Gan et al. (2007)	70	PA RAC	0.87	0.79–0.96	0.006	uni	16%>
van Wolferen et al. (2007)	64	SVI	0.764		<0.001	multi	25 mL/m2>
		RVEDVI	1.61		<0.001		84 mL/m2<
		LVEDVI	0.705		0.002		40 mL/ms>
van de Veerdonk et al. (2011)	110	RVESVI	1.014	1.001–1.027	0.048	uni	
		RVEF	0.938	0.902–0.975	0.001		35%>
		LVEDVI	0.962	0.931–0.994	0.019		
		LVESVI	0.942	0.888–0.998	0.045		
		SVI	0.945	0.899–0.993	0.025		
Freed et al. (2012)	58	RVEF	0.91	0.83–0.99	0.036	multi	39%>
Yamada (2012)	41	RVEDVI	1.03	1.00–1.05	0.02	multi	
Swift et al. (2014a, b, c, d))	80	RVESV	1.551	1.152–2.087	0.004	multi	290%predicted<
		LVSV	0.631	0.400–0.995	0.048		57%predicted>
Swift et al. (2014a, b, c, d)	79	FWHM	1.08	1.01–1.16	0.034	uni	8 s<
		PTT	1.1	1.03–1.18	0.01		6.5 s<
Baggen et al. (2016)		RVEF	1.23	1.07–1.41	0.003	meta	
	539	RVEDVI	1.06	1.00–1.12	0.049		
		RVESVI	1.05	1.01–1.09	0.013		
		LVEDVI	1.16	1.00–1.34	0.045		
de Siqueira (2016)	110	GLS	1.06	1–1.12	0.026	multi	
		RVEF	0.97	0.94–0.99	0.03		
		GLSR	2.52	1.03–6.1	0.04		
		GCSR	4.5	1.3–15.6	0.01		-0.8S-1
Swift et al. (2017)	576	RVESV	1.217	1.061–1.539	0.005	multi	180%>
		PARAC	0.762	0.623–0.932	0.008		

Abbreviations: *PA RAC* pulmonary artery relative area change, *SVI* stroke volume index = cardiac output/heart rate (beats per minute)/BSA (m_2), *BSA* body surface area, *RVEDV* right ventricular end-diastolic volume, *RVEDVI* right ventricular end-diastolic volume index, *LVEDVI* left ventricular end-diastolic volume index, *RVEF* right ventricular ejection fraction, *LVESVI* left ventricular end-diastolic volume index, *LVSV* left ventricular stroke volume, *FWHM* full width half maximum of the transit time of the contrast material peak from the pulmonary artery to the aorta, *PTT* pulmonary transit time, *GLS* global right ventricular longitudinal strain, *GLSR* global right ventricular longitudinal strain rate, *GCSR* global right ventricular circumferential strain rate

Table 5 Comparative assessment of cardiovascular magnetic resonance criteria to transthoracic echocardiography for the determination of diastolic dysfunction for variables that had a *p* values of <0.05 (adapted from Wu et al. Table 2 and Fig. 3 (Wu et al. 2014)

Paired variables	CMR normal	CMR DD	TTE normal	TTE DD	*R* value (*p* value)
PSRe/PSRa	1.82 ± 0.69	0.9 ± 0.44			0.76 (<0.001)
TDI septal e'/a'			1.3 ± 0.4	0.75 ± 0.34	
PSRe/PSRa	1.82 ± 0.69	0.9 ± 0.44			0.80 (<0.001)
TDI lateral e'/a'			1.7 ± 0.7	0.89 ± 0.44	
PSRe/PSRa	1.82 ± 0.69	0.9 ± 0.44			0.83 (<0.001)
TDI ave. e'/a'			N/A	N/A	

(Pande et al. 2009). In the antibiotic era this terrible disease has for the most part been eradicated in the first world. At its end stage, rheumatic mitral valve stenosis can be associated with pulmonary ossification (Lakhdhar et al. 2009).

Mitral valve regurgitation is the most common valvular disorder and is the second most common reason for surgical repair of a valve (Patel et al. 2014). In the United States of America, it is estimated that over 2.5 million persons have this disease (Nkomo et al. 2006). It is an important cause of pulmonary hypertension and is much more common than mitral valve stenosis (Patel et al. 2014; Parker et al. 2010). The development of PH is one of the indications for mitral valve replacement surgery (American College of et al. 2006).

14 Aortic Valve Disease

It is not very hard to image why aortic stenosis would be an important risk factor for pulmonary hypertension (Ahn et al. 2014). Recently, Alushi et al. (2019) have studied subjects with PH that underwent trans aortic valve replacement (TAVR) surgery. They found some intriguing results after this procedure: (a) PH regressed in 46% of these patients, and (b) in those post TAVR subjects that did not have PH regression, the long-term all-cause mortality was increased (Hazard ratio 2.5, 95% CI: 1.7–3.5, *p*, 0.001). Independent predictors of pulmonary artery systolic pressure (PASP) improvement included: (a) left ventricular ejection fraction >40% (odds ratio [OR]: 3.6, 95% CI: 2.2–5.7; $p < 0.001$), (b) baseline PASP ≥46 mm Hg (OR: 3.26, 95% CI: 2.1–5.12; $p < 0.001$), and (c) absence of moderate or severe tricuspid regurgitation (TR) (OR: 0.5, 95% CI: 0.3–0.8; $p < 0.001$) (Alushi et al. 2019).

Aortic valve regurgitation is a less common cause of pulmonary hypertension than aortic stenosis. One of the goals with determining when to intervene for a leaky aortic valve is to prevent the development of left ventricular fibrosis and irreversible pulmonary hypertension (Bonow 2013). More research in this area is need to develop evidence-based criteria of when to intervene in this disorder.

15 Left Main Coronary artery Compression by the Pulmonary Artery

The enlarged and non-compliant pulmonary artery may compress the left main (LM) coronary artery (Galie et al. 2015). This may become symptomatic and require intervention. Patients with this diagnosis frequently have chest pain (angina like) symptoms (Galie et al. 2017). In their study of over seven hundred patients with PAH, 16% (121/765) had angina or angina-like symptoms, 12% (94/765) had an abnormal coronary artery computed tomographic angiogram (cCTA), with 6% (48/765) of the total group having stenosis of >50% (Galie et al. 2017). With stenting of the LM coronary artery 91% (41/45) had relief of their symptoms. They found that the best predictor of LM coronary artery stenosis was a pulmonary artery size >4 cm (Galie et al. 2017).

16 Four-Dimensional Phase-Contrast Flow-Encoded Magnetic Resonance Angiography (4D Flow MRI)

Recently, 4D flow MRI (time-resolved 3D phase-contrast MRI with three-directional velocity encoding) has emerged as a technique to evaluate vessel and valvular flow by providing noninvasive measurements of complex 3D hemodynamic changes with full volumetric coverage of the entire heart, proximal pulmonary arteries, and aorta. With this method, multiple flow assessments are obtained in a single scan (Francois et al. 2012). Additionally, 4D flow MRI is capable of measuring RV and LV function and estimating PVR (Roldan-Alzate et al. 2014). In qualitatively assessing flow patterns in the MPA, the vortex of blood flow is observed as an abnormal boundary layer along the wall of MPA. This helical flow found on the 4D flow pathlines images is characteristic of PAH. The duration of vortical/helical blood flow has been shown to correlate with mPAP; however, this feature warrants further investigation (Reiter et al. 2008). In addition, using quantitative assessment techniques, the wall shear stress, which regulates endothelial cell function and vascular remodeling, is quantifiable using 4D flow (Barker et al. 2015). Wall shear stress is lower in PAH patients than in healthy controls and correlates to disease status (Barker et al. 2015). The noninvasive, functional assessment of pulmonary arteries has the potential to give earlier diagnosis. Beyond the evaluation of standard parameters of right ventricular function, 4D flow MRI offers energy analysis of the RV based on kinetic energy (Han et al. 2015; Jeong et al. 2015).

17 Lung Parenchymal Disease

One of the most common causes of PAH is lung disease. The role of nicotine addiction/dependence on lung destruction and emphysema is well known. What is under appreciated is the fact that there is a concomitant destruction of the pulmonary vascular system as well which will lead to elevation of the pulmonary arterial pressures. The quantification of emphysema by CT and ventilation MRI using oxygen, fluorinated compounds, or hyperpolarized Nobel gasses is beyond the scope of this chapter. Suffice it to say that the ventilation defect percentage for the lungs is closely related to the loss of pulmonary function found at pulmonary function testing and the diffusion capacity of carbon monoxide (DLCO).

CT provides an important role in the diagnosis of two rare causes of PAH, pulmonary veno-occlusive disease (PVOD) and pulmonary capillary hemangiomatosis (PCH). In the first case, the finding of septal lines in a patient with elevated pulmonary artery pressures and a normal left ventricle function with a normal left atrial size should raise suspicion for PVOD (Gunther et al. 2012; Resten et al. 2004). In the second case, finding small ground glass centrilobular nodularity in the lung bases is a feature that can be associated with PCH (Xie et al. 2012; Miura et al. 2013).

18 Liver Disease

It is very interesting that diseases of the liver affect pulmonary function. With liver fibrosis there is a loss of metabolic integrity to the liver, and for unknown reasons two important changes in the lung vasculature can occur, hepatopulmonary syndrome and portopulmonary hypertension (Hoeper et al. 2004).

The hepatopulmonary syndrome (HPS) is characterized by intrapulmonary shunting between the pulmonary arteries and veins that results in peripheral desaturation (Koksal et al. 2006). On CT/CTA or MRA this disorder manifests as non-tapering pulmonary arteries and veins that extend out to the lung periphery. CTA may also show multiple pulmonary arteriovenous malformations (Chawla et al. 2015). A commonly used test for this right to left shunting is the nuclear medicine 99mTc-MAA perfusion exam. Under normal circumstances this small particle lodges in the small alveoli of the functional secondary lobules. In the setting of an intracardiac shunt or peripheral arteriovenous

shunting in the lung, the radiopharmaceutical will bypass the lungs and lodge in the systemic vasculature of other organs (e.g., brain, liver, and kidneys). Chen et al. have shown that CTA is not that efficacious for the diagnosis of HPS (Chen et al. 2016). In their series of 23 patients with HPS and 29 patients with other liver diseases, they found that those patients with liver disease of any kind had lower arterial bronchial ratios (ABRs) than controls, but HPS had the same ABRs as the other liver diseases (Liver disease ABR = 1.20 ± 0.19, versus normal controls ABR = 0.98 ± 0.10, $p < 0.01$) (Chen et al. 2016).

Portopulmonary hypertension (PoPH) is more difficult to diagnose (Savale et al. 2017; Devaraj et al. 2014). The exact cause of PoPH is not known, perhaps this is related to the lack of detoxification of vasoactive molecules from the blood stream, which in turn cause pulmonary vasoconstriction and increased pulmonary vascular resistance (Cosardereliogl u et al. 2016). For anesthesia, perioperative assessment of right ventricular dysfunction is critical for patient management during surgery (Kuo et al. 1999). The imaging features are one of association rather than direct effect. The imager needs to assess both for the presence of liver disease/cirrhosis and enlargement of the pulmonary trunk. The imager may be the first diagnostician to raise the possibility for PoPH. Where this often comes into play is in cases of workup for liver transplantation (Bozbas and Bozbas 2016). Liver transplant recipients with portopulmonary hypertension have more perioperative mortality and lower survival rates than those that do not. In their recent study of 223 liver transplant patients, there were 6% (14/223) with PoPH and 57% (8/14) of these died after liver transplant (median survival = 11 months) (Li et al. 2018). Most of their PoPH patients died of respiratory infections, possibly due to low cardiopulmonary reserve (Li et al. 2018).

19 Obstructive Sleep Apnea

While the definitive diagnosis of obstructive sleep apnea (OSA) depends on a sleep study, the possibility for this diagnosis is recognizable from some commonly seen imaging findings on non-contrast chest CT (Nattenmuller et al. 2019; Schlett et al. 2019). Imaging findings that can be associated with OSA include: (a) low density thyroid gland (low thyroid iodine stores/hypothyroidism), (b) tracheobronchomalacia, (c) pulmonary artery enlargement (>3.0 cm), and (d) an increased visceral fat/subcutaneous fat ratio. Haponik et al. 1983 showed that the cross-sectional areas of the airways of the head and neck were smaller in OSA patients ($p < 0.05$) than their control population. Recently, in their study of the tongue during sleep using MRI, Wang et al. showed that the size of the tongue significantly differs between OSA patients and normal controls and that the tongue of OSA subjects tends to move downward (Wang et al. 2014). The deleterious effects of nocturnal hypoxia on pulmonary arterial vasoconstriction and an increase in free radical formation enhancing lung parenchymal destruction may lead to the progression of PAH in these patients.

20 Synergy of Diseases

Patients can have as many diseases as they damn well please.

Hickam's dictum

The cardiopulmonary system is a very tightly coordinated system that in the normal individual has a large amount of redundancy in the air exchange capacity of the lungs and cardiac reserve. For example, in pregnancy the cardiac output normally increases by 3–4 times. This is due to an increase in circulating blood volume and the ability of the heart to improve stroke volume by moving farther out on the Starling curve. With more circulating blood volume, more capillary networks are opened in the lungs. What we observe in patients with pulmonary hypertension is a breakdown in one or more of the parts of this highly linked hydraulic and gas exchange system (Fig. 1). These patients often have more than one disease process and the additive and/or synergetic effect of the various physiological choke points in this system can be very debilitating and hard to manage. While it is comforting to try to place PAH/PH patients into one major treatment

category using the current guidelines, it remains important to understand that more often than not there may be more than one underlying diseases to treat to best establish optimal patient therapy.

21 Modeling the Severity of Pulmonary Hypertension Using MRI Parameters

The majority of studies using MRI in PH reports the diagnostic utility of individual CMR parameters. Several studies have attempted to identify empirical models by combining measurements in regression models for measurements of mPAP (Swift et al. 2013; Johns et al. 2018a; Zhang et al. 2017; Moral et al. 2012) and PVR (GARCIA-Alvarez et al. 2013; Swift et al. 2013; Zhang et al. 2017). Such approaches do not necessarily reflect the underlying pathophysiology, but these models do have high clinical value for the noninvasive detection of disease. Physiological modeling of pulmonary arterial flow to derive quantitative physiological parameters has proven of value for the estimation of pulmonary hemodynamics (Laffon et al. 2004). In addition, utilizing the pulmonary artery area change (compliance) over time as a surrogate of pulmonary pressure has also proven to be useful (Swift et al. 2012a). Swift et al. found that the relative area change of the pulmonary artery is an important metric for the prediction of mortality (HR- 0.85 [0.74–0.98]; $P = 0.03$) (Swift et al. 2012a). Simultaneous measurements of pulmonary artery flow have been interpreted by 0D and 1D mathematical models and been proven useful for stratification of PH (Lungu et al. 2014, 2016).

The reason for this high degree of correspondence between pulmonary arterial compliance and death is very interesting physiologically. This is due to the beneficial "windkessel" effect whereby the end-systolic pressure on the RV is dampened by the compliant (elastic) pulmonary artery, which then in diastole is able to contract and act as a secondary pump for pulmonary arterial and aortic flows (Nichols and Edwards 2001). This effect serves to dampen the pulse wave velocity. Stiff pulmonary or systemic arteries are problematic as they are no longer able to serve as reservoirs for the storage of energy from the pressure/volume bolus related to each ventricular contraction. A stiff pulmonary artery means that the RV must pump against the full pulmonary arterial resistance, hence the higher likelihood for premature RV failure in these cases. This is why pulmonary endarterectomy is so successful in the setting of CTEPH. The pulmonary arterial system has its compliance restored after the removal of the fibrin sheaths lining the pulmonary arteries and the oxidative stress on the RV is decreased with the reduction in afterload (less pulmonary artery pressure). This surgery can be lifesaving for CTEPH patients.

22 Prediction of Outcomes After Therapy for Pulmonary Hypertension

As CMR methodologies emerge as the gold standard noninvasive tool for risk stratification and treatment response in patients with PH/PAH, qualitative and quantitative MRI findings must relate to patient outcomes. Table 6 outlines the CMR metrics that are correlated with prognosis. The relative merits of using MRI for the diagnosis and follow-up of patients with PAH/PH is shown in Table 6. Important predictors of mortality include RV end-diastolic volume (RVEDV) and RV ejection fraction (RVEF). At baseline, RVEDV may be the strongest RV volumetric parameter for assessing mortality. These measures should also be indexed to body surface area and corrected for age and sex (Swift et al. 2014a). In the evaluation of vessel compliance, reduced relative area change of the MPA has been shown to predict mortality (Gan et al. 2007). This is a proxy for the loss of the "windkessel" effect. In a derivation and validation cohort, it has been shown that both RVEDV and pulmonary artery RAC are independent predictors of mortality and a composite model including these two parameters as well as demographic and diagnostic classification data has high prognostic accuracy, particularly in idiopathic pulmonary fibrosis (Swift et al. 2017). Improvement in RVEF at follow-up has been shown to associate with better outcomes, independent of invasive hemodynamic

parameters changes, notably PVR (van de Veerdonk et al. 2011). Changes in CMR metrics are also sensitive to treatment failure (Mauritz et al. 2012a; Swift et al. 2014a; van Wolferen et al. 2007). The presence of LGE has been associated with worse outcomes, though the independent prognostic value has not been shown (Bradlow et al. 2010). Transit time measurements have also shown prognostic significance (Skrok et al. 2012; Francois et al. 2003). The reason for this is that transit times are inversely related to PVR and compliance product measured at RHC (Hadinnapola et al. 2015; Bradlow et al. 2007).

23 Noninvasive Imaging Costs

There are many choices available to the clinician for the follow-up of patients with PH/PAH. Referral patterns will vary depending on familiarity with the various options that are available at each institution, the local expertise, and the patient's clinical status. The use of CMR is of similar cost to transthoracic ultrasound (Table 4) and offers more quantitative metrics that have higher precision and repeatability than transthoracic ultrasound measurements. Both tests are commonly used for the longitudinal follow-up of these complex patients, which helps to decrease the need for multiple right heart catheterizations.

24 Conclusion

The high reproducibility, precision, and prognostic value of the many ventricular, valvular, and arterial quantitative indices obtained by CMR suggests that the continued use of echocardiography in the *routine* follow-up of patients with PAH and PH may no longer be indicated in centers with easy access to MRI. The only missing piece of data needed for the diagnosis and follow-up of these patients is pressure and oxygenation levels in the right heart and pulmonary artery. These metrics should be forthcoming in the near future with the introduction of MRI-compatible catheters.

References

Agrawal V, Byrd BF 3rd, Brittain EL (2019) Echocardiographic evaluation of diastolic function in the setting of pulmonary hypertension. Pulm Circ 9:2045894019826043

Ahn HS, Chang SA, Kim HK, Kim SJ, Lee SP, Park SJ, Kim YJ, Cho GY, Sohn DW, Oh JK (2014) Determinants of pulmonary hypertension development in moderate or severe aortic stenosis. Int J Cardiovasc Imaging 30:1519–1528

Alunni JP, Degano B, Arnaud C, Tetu L, Blot-Souletie N, Didier A, Otal P, Rousseau H, Chabbert V (2010) Cardiac MRI in pulmonary artery hypertension: correlations between morphological and functional parameters and invasive measurements. Eur Radiol 20:1149–1159

Alushi B, Beckhoff F, Leistner D, Franz M, Reinthaler M, Stahli BE, Morguet A, Figulla HR, Doenst T, Maisano F, Falk V, Landmesser U, Lauten A (2019) Pulmonary hypertension in patients with severe aortic stenosis: prognostic impact after transcatheter aortic valve replacement: pulmonary hypertension in patients undergoing TAVR. JACC Cardiovasc Imaging 12:591–601

American College of Cardiology/American Heart Association Task Force on Practice Guidelines; Society of Cardiovascular Anesthesiologists; Society for Cardiovascular Angiography and Interventions; Society of Thoracic Surgeons, Bonow, R. O., Carabello, B. A., Chatterjee, K., De Leon, A. C., Jr., Faxon, D. P., Freed, M. D., Gaasch, W. H., Lytle, B. W., Nishimura, R. A., O'Gara, P. T., O'Rourke, R. A., Otto, C. M., Shah, P. M., Shanewise, J. S., Smith, S. C., Jr., Jacobs, A. K., Adams, C. D., Anderson, J. L., Antman, E. M., Fuster, V., Halperin, J. L., Hiratzka, L. F., Hunt, S. A., Lytle, B. W., Nishimura, R., Page, R. L. & Riegel, B. (2006) ACC/AHA 2006 guidelines for the management of patients with valvular heart disease: a report of the American College of Cardiology/American Heart Association Task Force on Practice Guidelines (writing Committee to Revise the 1998 guidelines for the management of patients with valvular heart disease) developed in collaboration with the Society of Cardiovascular Anesthesiologists endorsed by the Society for Cardiovascular Angiography and Interventions and the Society of Thoracic Surgeons. J Am Coll Cardiol 48:e1–e148

Ascha M, Renapurkar RD, Tonelli AR (2017) A review of imaging modalities in pulmonary hypertension. Ann Thorac Med 12:61–73

Badagliacca R, Poscia R, Pezzuto B, Papa S, Pesce F, Manzi G, Giannetta E, Raineri C, Schina M, Sciomer S, Parola D, Francone M, Carbone I, Fedele F, Vizza CD (2016) Right ventricular concentric hypertrophy and clinical worsening in idiopathic pulmonary arterial hypertension. J Heart Lung Transplant 35:1321–1329

Baggen VJ, Leiner T, Post MC, van Dijk AP, Roos-Hesselink JW, Boersma E, Habets J, Sieswerda GT

(2016) Cardiac magnetic resonance findings predicting mortality in patients with pulmonary arterial hypertension: a systematic review and meta-analysis. Eur Radiol 26:3771–3780

Barker AJ, Roldan-Alzate A, Entezari P, Shah SJ, Chesler NC, Wieben O, Markl M, Francois CJ (2015) Four-dimensional flow assessment of pulmonary artery flow and wall shear stress in adult pulmonary arterial hypertension: results from two institutions. Magn Reson Med 73:1904–1913

Blyth KG, Groenning BA, Martin TN, Foster JE, Mark PB, Dargie HJ, Peacock AJ (2005) Contrast enhanced-cardiovascular magnetic resonance imaging in patients with pulmonary hypertension. Eur Heart J 26:1993–1999

Bonow RO (2013) Chronic mitral regurgitation and aortic regurgitation: have indications for surgery changed? J Am Coll Cardiol 61:693–701

Bozbas SS, Bozbas H (2016) Portopulmonary hypertension in liver transplant candidates. World J Gastroenterol 22:2024–2029

Bradlow WM, Assomull R, Kilner PJ, Gibbs JS, Sheppard MN, Mohiaddin RH (2010) Understanding late gadolinium enhancement in pulmonary hypertension. Circ Cardiovasc Imaging 3:501–503

Bradlow WM, Gatehouse PD, Hughes RL, O'brien AB, Gibbs JS, Firmin DN, Mohiaddin RH (2007) Assessing normal pulse wave velocity in the proximal pulmonary arteries using transit time: a feasibility, repeatability, and observer reproducibility study by cardiovascular magnetic resonance. J Magn Reson Imaging 25:974–981

Bredfelt A, Radegran G, Hesselstrand R, Arheden H, Ostenfeld E (2018) Increased right atrial volume measured with cardiac magnetic resonance is associated with worse clinical outcome in patients with pre-capillary pulmonary hypertension. ESC Heart Fail 5(5):864–875

Caudron J, Fares J, Bauer F, Dacher JN (2011) Evaluation of left ventricular diastolic function with cardiac MR imaging. Radiographics 31:239–259

Chawla A, Gaikwad V, Dubey N, Bosco J (2015) CT pulmonary angiography features of a hepatopulmonary syndrome. Korean J Radiol 16:951–952

Chen YA, Prabhudesai V, Castel H, Gupta S (2016) CT scan does not differentiate patients with hepatopulmonary syndrome from other patients with liver disease. PLoS One 11:e0158637

Chernobelsky A, Shubayev O, Comeau CR, Wolff SD (2007) Baseline correction of phase contrast images improves quantification of blood flow in the great vessels. J Cardiovasc Magn Reson 9:681–685

Condliffe R, Kiely DG, Gibbs JS, Corris PA, Peacock AJ, Jenkins DP, Hodgkins D, Goldsmith K, Hughes RJ, Sheares K, Tsui SS, Armstrong IJ, Torpy C, Crackett R, Carlin CM, Das C, Coghlan JG, Pepke-Zaba J (2008) Improved outcomes in medically and surgically treated chronic thromboembolic pulmonary hypertension. Am J Respir Crit Care Med 177:1122–1127

Cosardereliogl C, Cosar AM, Gurakar M, Pustavoitau A, Russell SD, Dagher NN, Gurakar A (2016) Portopulmonary hypertension and liver transplant: recent review of the literature. Exp Clin Transplant 14:113–120

Crawley SF, Johnson MK, Dargie HJ, Peacock AJ (2013) LA volume by CMR distinguishes idiopathic from pulmonary hypertension due to HFpEF. JACC Cardiovasc Imaging 6:1120–1121

Darocha S, Pietura R, Pietrasik A, Norwa J, Dobosiewicz A, Pilka M, Florczyk M, Biederman A, Torbicki A, Kurzyna M (2017) Improvement in quality of life and hemodynamics in chronic thromboembolic pulmonary hypertension treated with balloon pulmonary angioplasty. Circ J 81:552–557

Dellegrottaglie S, Sanz J, Poon M, Viles-Gonzalez JF, Sulica R, Goyenechea M, Macaluso F, Fuster V, Rajagopalan S (2007) Pulmonary hypertension: accuracy of detection with left ventricular septal-to-free wall curvature ratio measured at cardiac MR. Radiology 243:63–69

Devaraj A, Loveridge R, Bosanac D, Stefanidis K, Bernal W, Willars C, Wendon JA, Auzinger G, Desai SR (2014) Portopulmonary hypertension: improved detection using CT and echocardiography in combination. Eur Radiol 24:2385–2393

Diaz-Guzman E, Farver C, Parambil J, Culver DA (2008) Pulmonary hypertension caused by sarcoidosis. Clin Chest Med 29:549–563, x

Driessen MMP, Schings MA, Sieswerda GT, Doevendans PA, Hulzebos EH, Post MC, Snijder RJ, Westenberg JJM, van Dijk APJ, Meijboom FJ, Leiner T (2018) Tricuspid flow and regurgitation in congenital heart disease and pulmonary hypertension: comparison of 4D flow cardiovascular magnetic resonance and echocardiography. J Cardiovasc Magn Reson 20:5

Driscoll D, Allen HD, Atkins DL, Brenner J, Dunnigan A, Franklin W, Gutgesell HP, Herndon P, Shaddy RE, Taubert KA et al (1994) Guidelines for evaluation and management of common congenital cardiac problems in infants, children, and adolescents. A statement for healthcare professionals from the Committee on Congenital Cardiac Defects of the Council on Cardiovascular Disease in the Young, American Heart Association. Circulation 90:2180–2188

Durongpisitkul K, Saiviroonporn P, Soongswang J, Laohaprasitiporn D, Chanthong P, Nana A (2008) Preoperative evaluation with magnetic resonance imaging in tetralogy of fallot and pulmonary atresia with ventricular septal defect. J Med Assoc Thail 91:350–355

Francois CJ, Shors SM, Bonow RO, Finn JP (2003) Analysis of cardiopulmonary transit times at contrast material-enhanced MR imaging in patients with heart disease. Radiology 227:447–452

Francois CJ, Srinivasan S, Schiebler ML, Reeder SB, Niespodzany E, Landgraf BR, Wieben O, Frydrychowicz A (2012) 4D cardiovascular magnetic resonance velocity mapping of alterations of right heart flow patterns and main pulmonary artery

hemodynamics in tetralogy of Fallot. J Cardiovasc Magn Reson 14:16

Freed BH, Gomberg-Maitland M, Chandra S, Mor-Avi V, Rich S, Archer SL, Jamison EB Jr, Lang RM, Patel AR (2012) Late gadolinium enhancement cardiovascular magnetic resonance predicts clinical worsening in patients with pulmonary hypertension. J Cardiovasc Magn Reson 14:11

Galie N, Humbert M, Vachiery JL, Gibbs S, Lang I, Torbicki A, Simonneau G, Peacock A, Vonk Noordegraaf A, Beghetti M, Ghofrani A, Gomez Sanchez MA, Hansmann G, Klepetko W, Lancellotti P, Matucci M, Mcdonagh T, Pierard LA, Trindade PT, Zompatori M, Hoeper M, ESC Scientific Document Group (2016) 2015 ESC/ERS Guidelines for the diagnosis and treatment of pulmonary hypertension: The Joint Task Force for the Diagnosis and Treatment of Pulmonary Hypertension of the European Society of Cardiology (ESC) and the European Respiratory Society (ERS): Endorsed by: Association for European Paediatric and Congenital Cardiology (AEPC), International Society for Heart and Lung Transplantation (ISHLT). Eur Heart J 37:67–119

Galie N, Mclaughlin VV, Rubin LJ, Simonneau G (2019) An overview of the 6th World Symposium on Pulmonary Hypertension. Eur Respir J 53

Galie N, Saia F, Manes A, Dall'ara G, Monti E, Palazzini M, Marrozzini C, Russo V, Zompatori M, Marzocchi A (2015) Left main coronary artery extrinsic compression by enlarged pulmonary artery in patients with pulmonary arterial hypertension. Eur Heart J 36:966–967

Galie N, Saia F, Palazzini M, Manes A, Russo V, Bacchi Reggiani ML, Dall'ara G, Monti E, Dardi F, Albini A, Rinaldi A, Gotti E, Taglieri N, Marrozzini C, Lovato L, Zompatori M, Marzocchi A (2017) Left main coronary artery compression in patients with pulmonary arterial hypertension and angina. J Am Coll Cardiol 69:2808–2817

Gan CT, Lankhaar JW, Westerhof N, Marcus JT, Becker A, Twisk JW, Boonstra A, Postmus PE, Vonk-Noordegraaf A (2007) Noninvasively assessed pulmonary artery stiffness predicts mortality in pulmonary arterial hypertension. Chest 132:1906–1912

GARCIA-Alvarez A, Fernandez-Friera L, Garcia-Ruiz JM, Nuno-Ayala M, Pereda D, Fernandez-Jimenez R, Guzman G, Sanchez-Quintana D, Alberich-Bayarri A, Pastor-Escuredo D, Sanz-Rosa D, Garcia-Prieto J, Gonzalez-Mirelis JG, Pizarro G, Jimenez-Borreguero LJ, Fuster V, Sanz J, Ibanez B (2013) Noninvasive monitoring of serial changes in pulmonary vascular resistance and acute vasodilator testing using cardiac magnetic resonance. J Am Coll Cardiol 62:1621–1631

Garcia-Alvarez A, Garcia-Lunar I, Pereda D, Fernandez-Jimenez R, Sanchez-Gonzalez J, Mirelis JG, Nuno-Ayala M, Sanchez-Quintana D, Fernandez-Friera L, Garcia-Ruiz JM, Pizarro G, Aguero J, Campelos P, Castella M, Sabate M, Fuster V, Sanz J, Ibanez B (2015) Association of myocardial T1-mapping CMR with hemodynamics and RV performance in pulmonary hypertension. JACC Cardiovasc Imaging 8:76–82

George MG, Schieb LJ, Ayala C, Talwalkar A, Levant S (2014) Pulmonary hypertension surveillance: United States, 2001 to 2010. Chest 146:476–495

Goerne H, Batra K, Rajiah P (2018) Imaging of pulmonary hypertension: an update. Cardiovasc Diagn Ther 8:279–296

Goldberg AB, Mazur W, Kalra DK (2017) Pulmonary hypertension: diagnosis, imaging techniques, and novel therapies. Cardiovasc Diagn Ther 7:405–417

Gorter TM, van Melle JP, Freling HG, Ebels T, Bartelds B, Pieper PG, Berger RM, van Veldhuisen DJ, Willems TP (2015) Pulmonary regurgitant volume is superior to fraction using background-corrected phase contrast MRI in determining the severity of regurgitation in repaired tetralogy of Fallot. Int J Cardiovasc Imaging 31:1169–1177

Gouda AM, Abdelazeem AH, Arafa El SA, Abdellatif KR (2014) Design, synthesis and pharmacological evaluation of novel pyrrolizine derivatives as potential anticancer agents. Bioorg Chem 53:1–7

Grothues F, Moon JC, Bellenger NG, Smith GS, Klein HU, Pennell DJ (2004) Interstudy reproducibility of right ventricular volumes, function, and mass with cardiovascular magnetic resonance. Am Heart J 147:218–223

Gunther S, Jais X, Maitre S, Berezne A, Dorfmuller P, Seferian A, Savale L, Mercier O, Fadel E, Sitbon O, Mouthon L, Simonneau G, Humbert M, Montani D (2012) Computed tomography findings of pulmonary venoocclusive disease in scleroderma patients presenting with precapillary pulmonary hypertension. Arthrit Rheum 64:2995–3005

Haddad F, Guihaire J, Skhiri M, Denault AY, Mercier O, AL-Halabi S, Vrtovec B, Fadel E, Zamanian RT, Schnittger I (2014) Septal curvature is marker of hemodynamic, anatomical, and electromechanical ventricular interdependence in patients with pulmonary arterial hypertension. Echocardiography 31:699–707

Hadinnapola C, Li Q, Su L, Pepke-Zaba J, Toshner M (2015) The resistance-compliance product of the pulmonary circulation varies in health and pulmonary vascular disease. Physiol Rep 3:e12363

Haeck ML, Vliegen HW (2015) Diagnosis and treatment of pulmonary hypertension. Heart 101:311–319

Hagger D, Condliffe R, Woodhouse N, Elliot CA, Armstrong IJ, Davies C, Hill C, Akil M, Wild JM, Kiely DG (2009) Ventricular mass index correlates with pulmonary artery pressure and predicts survival in suspected systemic sclerosis-associated pulmonary arterial hypertension. Rheumatology (Oxford) 48:1137–1142

Han QJ, Witschey WR, Fang-Yen CM, Arkles JS, Barker AJ, Forfia PR, Han Y (2015) Altered right ventricular kinetic energy work density and viscous energy dissipation in patients with pulmonary arterial hypertension: a pilot study using 4D flow MRI. PLoS One 10:e0138365

Haponik EF, Smith PL, Bohlman ME, Allen RP, Goldman SM, Bleecker ER (1983) Computerized tomography

in obstructive sleep apnea. Correlation of airway size with physiology during sleep and wakefulness. Am Rev Respir Dis 127:221–226

Henzler T, Roeger S, Meyer M, Schoepf UJ, Nance JW Jr, Haghi D, Kaminski WE, Neumaier M, Schoenberg SO, Fink C (2012) Pulmonary embolism: CT signs and cardiac biomarkers for predicting right ventricular dysfunction. Eur Respir J 39:919–926

Hoeper MM, Krowka MJ, Strassburg CP (2004) Portopulmonary hypertension and hepatopulmonary syndrome. Lancet 363:1461–1468

Huis In 'T Veld AE, Van Vliet AG, Spruijt OA, Handoko ML, Marcus JT, Vonk-Noordegraaf A, Bogaard HJ (2016) CTA-derived left to right atrial size ratio distinguishes between pulmonary hypertension due to heart failure and idiopathic pulmonary arterial hypertension. Int J Cardiol 223:723–728

Hyduk A, Croft JB, Ayala C, Zheng K, Zheng ZJ, Mensah GA (2005) Pulmonary hypertension surveillance--United States, 1980-2002. MMWR Surveill Summ 54:1–28

Jauhiainen T, Jarvinen VM, Hekali PE (2002) Evaluation of methods for MR imaging of human right ventricular heart volumes and mass. Acta Radiol 43: 587–592

Jeong D, Anagnostopoulos PV, Roldan-Alzate A, Srinivasan S, Schiebler ML, Wieben O, Francois CJ (2015) Ventricular kinetic energy may provide a novel noninvasive way to assess ventricular performance in patients with repaired tetralogy of Fallot. J Thorac Cardiovasc Surg 149:1339–1347

Johns CS, Rajaram S, Capener DA, Oram C, Elliot C, Condliffe R, Kiely DG, Wild JM, Swift AJ (2018a) Non-invasive methods for estimating mPAP in COPD using cardiovascular magnetic resonance imaging. Eur Radiol 28:1438–1448

Johns CS, Wild JM, Rajaram S, Tubman E, Capener D, Elliot C, Condliffe R, Charalampopoulos A, Kiely DG, Swift AJ (2018b) Identifying at-risk patients with combined pre- and postcapillary pulmonary hypertension using interventricular septal angle at cardiac MRI. Radiology:180120

Kawel-Boehm N, Dellas Buser T, Greiser A, Bieri O, Bremerich J, Santini F (2014) In-vivo assessment of normal T1 values of the right-ventricular myocardium by cardiac MRI. Int J Cardiovasc Imaging 30:323–328

Kawel-Boehm N, Maceira A, Valsangiacomo-Buechel ER, Vogel-Claussen J, Turkbey EB, Williams R, Plein S, Tee M, Eng J, Bluemke DA (2015) Normal values for cardiovascular magnetic resonance in adults and children. J Cardiovasc Magn Reson 17:29

Kiely D, Levin D, Hassoun P, Ivy DD, Jone PN, Bwika J, Kawut SM, Lordan J, Lungu A, Mazurek J, Moledina S, Olschewski H, Peacock A, Puri GD, Rahaghi F, Schafer M, Schiebler M, Screaton N, Tawhai M, Van Beek EJ, Vonk-Noordegraaf A, Vanderpool RR, Wort J, Zhao L, Wild J, Vogel-Claussen J, Swift A (2019) Express: statement on imaging and pulmonary hypertension from the Pulmonary Vascular Research Institute (PVRI). Pulm Circ 9(3):2045894019841990

Koksal D, Kacar S, Koksal AS, Tufekcioglu O, Kucukay F, Okten S, Sasmaz N, Arda K, Sahin B (2006) Evaluation of intrapulmonary vascular dilatations with high-resolution computed thorax tomography in patients with hepatopulmonary syndrome. J Clin Gastroenterol 40:77–83

Kumamaru KK, George E, Aghayev A, Saboo SS, Khandelwal A, Rodriguez-Lopez S, Cai T, Jimenez-Carretero D, Estepar RS, Ledesma-Carbayo MJ, Gonzalez G, Rybicki FJ (2016) Implementation and Performance of Automated Software for Computing Right-to-Left Ventricular Diameter Ratio From Computed Tomography Pulmonary Angiography Images. J Comput Assist Tomogr 40:387–392

Kuo PC, Plotkin JS, Gaine S, Schroeder RA, Rustgi VK, Rubin LJ, Johnson LB (1999) Portopulmonary hypertension and the liver transplant candidate. Transplantation 67:1087–1093

Kuznetsova T, Herbots L, Lopez B, Jin Y, Richart T, Thijs L, Gonzalez A, Herregods MC, Fagard RH, Diez J, Staessen JA (2009) Prevalence of left ventricular diastolic dysfunction in a general population. Circ Heart Fail 2:105–112

Laffon E, Vallet C, Bernard V, Montaudon M, Ducassou D, Laurent F, Marthan R (2004) A computed method for noninvasive MRI assessment of pulmonary arterial hypertension. J Appl Physiol (1985) 96: 463–468

Lakhdhar R, Berrais A, Drissa MA, Cheour M, Essefi N, Drissa H (2009) Mitral stenosis a rare antology of diffuse pulmonary ossification. Tunis Med 87:82–85

Lankhaar JW, Westerhof N, Faes TJ, Gan CT, Marques KM, Boonstra A, van den Berg FG, Postmus PE, Vonk-Noordegraaf A (2008) Pulmonary vascular resistance and compliance stay inversely related during treatment of pulmonary hypertension. Eur Heart J 29:1688–1695

Lantz J, Gupta V, Henriksson L, Karlsson M, Persson A, Carlhall CJ, Ebbers T (2018) Intracardiac Flow at 4D CT: Comparison with 4D Flow MRI. Radiology 289:51–58

Lantz J, Gupta V, Henriksson L, Karlsson M, Persson A, Carlhall CJ, Ebbers T (2019) Impact of Pulmonary Venous Inflow on Cardiac Flow Simulations: Comparison with In Vivo 4D Flow MRI. Ann Biomed Eng 47:413–424

Ley S, Fink C, Puderbach M, Zaporozhan J, Plathow C, Eichinger M, Hosch W, Kreitner KF, Kauczor HU (2006) MRI Measurement of the hemodynamics of the pulmonary and systemic arterial circulation: influence of breathing maneuvers. AJR Am J Roentgenol 187:439–444

Ley S, Mereles D, Risse F, Grunig E, Ley-Zaporozhan J, Tecer Z, Puderbach M, Fink C, Kauczor HU (2007) Quantitative 3D pulmonary MR-perfusion in patients with pulmonary arterial hypertension: correlation with invasive pressure measurements. Eur J Radiol 61:251–255

Li J, Zhuang Q, Zhang X, Zheng Y, Qiao Z, Zhang J, Shen X, Shen J (2018) Prevalence and prognosis of

portopulmonary hypertension in 223 liver transplant recipients. Can Respir J 2018:9629570

London GM, Weiss YA, Pannier BP, Laurent SL, Safar ME (1987) Tilt test in essential hypertension. Differential responses in heart rate and vascular resistance. Hypertension 10:29–34

Lungu A, Swift AJ, Capener D, Kiely D, Hose R, Wild JM (2016) Diagnosis of pulmonary hypertension from magnetic resonance imaging-based computational models and decision tree analysis. Pulm Circ 6:181–190

Lungu A, Wild JM, Capener D, Kiely DG, Swift AJ, Hose DR (2014) MRI model-based non-invasive differential diagnosis in pulmonary hypertension. J Biomech 47:2941–2947

Mallin WH, Silberstein EB, Shipley RT, Vu DN, Alspaugh JP, Moulton JS (1993) Fibrosing mediastinitis causing nonvisualization of one lung on pulmonary scintigraphy. Clin Nucl Med 18:594–596

Mansencal N, Joseph T, Vieillard-Baron A, Qanadli SD, Jondeau G, Lacombe P, Jardin F, Dubourg O (2003) Comparison of different echocardiographic indexes secondary to right ventricular obstruction in acute pulmonary embolism. Am J Cardiol 92:116–119

Marcus JT, Gan CT, Zwanenburg JJ, Boonstra A, Allaart CP, Gotte MJ, Vonk-Noordegraaf A (2008) Interventricular mechanical asynchrony in pulmonary arterial hypertension: left-to-right delay in peak shortening is related to right ventricular overload and left ventricular underfilling. J Am Coll Cardiol 51:750–757

Maron BA, Brittain EL, Choudhary G, Gladwin MT (2018) Redefining pulmonary hypertension. Lancet Respir Med 6:168–170

Mauritz GJ, Kind T, Marcus JT, Bogaard HJ, van de Veerdonk M, Postmus PE, Boonstra A, Westerhof N, Vonk-Noordegraaf A (2012a) Progressive changes in right ventricular geometric shortening and long-term survival in pulmonary arterial hypertension. Chest 141:935–943

Mauritz GJ, Vonk-Noordegraaf A, Kind T, Surie S, Kloek JJ, Bresser P, Saouti N, Bosboom J, Westerhof N, Marcus JT (2012b) Pulmonary endarterectomy normalizes interventricular dyssynchrony and right ventricular systolic wall stress. J Cardiovasc Magn Reson 14:5

Miura A, Akagi S, Nakamura K, Ohta-Ogo K, Hashimoto K, Nagase S, Kohno K, Kusano K, Ogawa A, Matsubara H, Toyooka S, Oto T, Ohtsuka A, Ohe T, Ito H (2013) Different sizes of centrilobular ground-glass opacities in chest high-resolution computed tomography of patients with pulmonary veno-occlusive disease and patients with pulmonary capillary hemangiomatosis. Cardiovasc Pathol 22:287–293

Moral S, Fernandez-Friera L, Stevens G, Guzman G, Garcia-alvarez A, Nair A, Evangelista A, Fuster V, Garcia MJ, Sanz J (2012) New index alpha improves detection of pulmonary hypertension in comparison with other cardiac magnetic resonance indices. Int J Cardiol 161:25–30

Nattenmuller J, Schlett CL, Tsuchiya N, Reeder SB, Pickhardt PJ, Kramer H, Kauczor HU, Wielputz MO, Seo JB, Hatabu H, van Beek E Jr, Schiebler ML, Representing the International Workshop for Pulmonary Functional, I (2019) Noncontrast chest computed tomographic imaging of obesity and the metabolic syndrome: part II noncardiovascular findings. J Thorac Imaging 34:126–135

Nichols WW, Edwards DG (2001) Arterial elastance and wave reflection augmentation of systolic blood pressure: deleterious effects and implications for therapy. J Cardiovasc Pharmacol Ther 6:5–21

Nkomo VT, Gardin JM, Skelton TN, Gottdiener JS, Scott CG, Enriquez-Sarano M (2006) Burden of valvular heart diseases: a population-based study. Lancet 368:1005–1011

Nogami M, Ohno Y, Koyama H, Kono A, Takenaka D, Kataoka T, Kawai H, Kawamitsu H, Onishi Y, Matsumoto K, Matsumoto S, Sugimura K (2009) Utility of phase contrast MR imaging for assessment of pulmonary flow and pressure estimation in patients with pulmonary hypertension: comparison with right heart catheterization and echocardiography. J Magn Reson Imaging 30:973–980

Ohno Y, Hatabu H, Murase K, Higashino T, Nogami M, Yoshikawa T, Sugimura K (2007) Primary pulmonary hypertension: 3D dynamic perfusion MRI for quantitative analysis of regional pulmonary perfusion. AJR Am J Roentgenol 188:48–56

Pande S, Agarwal SK, Dhir U, Chaudhary A, Kumar S, Agarwal V (2009) Pulmonary arterial hypertension in rheumatic mitral stenosis: does it affect right ventricular function and outcome after mitral valve replacement? Interact Cardiovasc Thorac Surg 9:421–425

Parker MW, Mittleman MA, Waksmonski CA, Sanders G, Riley MF, Douglas PS, Manning WJ (2010) Pulmonary hypertension and long-term mortality in aortic and mitral regurgitation. Am J Med 123:1043–1048

Patel H, Desai M, Tuzcu EM, Griffin B, Kapadia S (2014) Pulmonary hypertension in mitral regurgitation. J Am Heart Assoc 3

Patel M, Lu F, Hannaway M, Hochman K (2015) Fibrosing mediastinitis: a rare complication of histoplasmosis. BMJ Case Rep 2015:bcr2015212774

Pena E, Dennie C, Veinot J, Muniz SH (2012) Pulmonary hypertension: how the radiologist can help. Radiographics 32:9–32

Prakash R (1978) Determination of right ventricular wall thickness in systole and diastole. Echocardiographic and necropsy correlation in 32 patients. Br Heart J 40:1257–1261

Raff GL, Chinnaiyan KM, Share DA, Goraya TY, Kazerooni EA, Moscucci M, Gentry RE, Abidov A, Advanced Cardiovascular IMAGING Consortium, C.-I (2009) Radiation dose from cardiac computed tomography before and after implementation of radiation dose-reduction techniques. JAMA 301:2340–2348

Reiter G, Reiter U, Kovacs G, Kainz B, Schmidt K, Maier R, Olschewski H, Rienmueller R (2008) Magnetic resonance-derived 3-dimensional blood flow patterns

in the main pulmonary artery as a marker of pulmonary hypertension and a measure of elevated mean pulmonary arterial pressure. Circ Cardiovasc Imaging 1:23–30

Resten A, Maitre S, Humbert M, Rabiller A, Sitbon O, Capron F, Simonneau G, Musset D (2004) Pulmonary hypertension: CT of the chest in pulmonary venoocclusive disease. AJR Am J Roentgenol 183:65–70

Roeleveld RJ, Marcus JT, Faes TJ, Gan TJ, Boonstra A, Postmus PE, Vonk-Noordegraaf A (2005) Interventricular septal configuration at mr imaging and pulmonary arterial pressure in pulmonary hypertension. Radiology 234:710–717

Roldan-Alzate A, Frydrychowicz A, Johnson KM, Kellihan H, Chesler NC, Wieben O, Francois CJ (2014) Non-invasive assessment of cardiac function and pulmonary vascular resistance in an canine model of acute thromboembolic pulmonary hypertension using 4D flow cardiovascular magnetic resonance. J Cardiovasc Magn Reson 16:23

Sanz J, Kariisa M, Dellegrottaglie S, Prat-Gonzalez S, Garcia MJ, Fuster V, Rajagopalan S (2009) Evaluation of pulmonary artery stiffness in pulmonary hypertension with cardiac magnetic resonance. JACC Cardiovasc Imaging 2:286–295

Sanz J, Kuschnir P, Rius T, Salguero R, Sulica R, Einstein AJ, Dellegrottaglie S, Fuster V, Rajagopalan S, Poon M (2007) Pulmonary arterial hypertension: noninvasive detection with phase-contrast MR imaging. Radiology 243:70–79

Sato T, Tsujino I, Ohira H, Oyama-Manabe N, Ito YM, Noguchi T, Yamada A, Ikeda D, Watanabe T, Nishimura M (2013a) Paradoxical interventricular septal motion as a major determinant of late gadolinium enhancement in ventricular insertion points in pulmonary hypertension. PLoS One 8:e66724

Sato T, Tsujino I, Ohira H, Oyama-Manabe N, Ito YM, Yamada A, Ikeda D, Watanabe T, Nishimura M (2015) Right atrial volume and reservoir function are novel independent predictors of clinical worsening in patients with pulmonary hypertension. J Heart Lung Transplant 34:414–423

Sato T, Tsujino I, Oyama-Manabe N, Ohira H, Ito YM, Yamada A, Ikeda D, Watanabe T, Nishimura M (2013b) Right atrial volume and phasic function in pulmonary hypertension. Int J Cardiol 168:420–426

Savale L, Watherald J, Sitbon O (2017) Portopulmonary Hypertension. Semin Respir Crit Care Med 38:651–661

Schiebler ML, Bhalla S, Runo J, Jarjour N, Roldan A, Chesler N, Francois CJ (2013) Magnetic resonance and computed tomography imaging of the structural and functional changes of pulmonary arterial hypertension. J Thorac Imaging 28:178–193

Schlett CL, Nattenmuller J, Tsuchiya N, Vogel-Claussen J, Kauczor HU, Levin D, Hatabu H, Estepar JR, Wu MT, van Beek E Jr, Schiebler ML, Representing the International Workshop for Pulmonary functional, I (2019) Noncontrast chest computed tomographic imaging of obesity and the metabolic syndrome: part I cardiovascular findings. J Thorac Imaging 34(2):126–135

Scholzel BE, Post MC, van de Bruaene A, Dymarkowski S, Wuyts W, Meyns B, Budts W, Delcroix M (2014) Prediction of hemodynamic improvement after pulmonary endarterectomy in chronic thromboembolic pulmonary hypertension using non-invasive imaging. Int J Cardiovasc Imaging 31: 143–150

Sciancalepore MA, Maffessanti F, Patel AR, Gomberg-Maitland M, Chandra S, Freed BH, Caiani EG, Lang RM, Mor-Avi V (2012) Three-dimensional analysis of interventricular septal curvature from cardiac magnetic resonance images for the evaluation of patients with pulmonary hypertension. Int J Cardiovasc Imaging 28:1073–1085

Shehata ML, Harouni AA, Skrok J, Basha TA, Boyce D, Lechtzin N, Mathai SC, Girgis R, Osman NF, Lima JA, Bluemke DA, Hassoun PM, Vogel-Claussen J (2013) Regional and global biventricular function in pulmonary arterial hypertension: a cardiac MR imaging study. Radiology 266:114–122

Simonneau G, Gatzoulis MA, Adatia I, Celermajer D, Denton C, Ghofrani A, Gomez Sanchez MA, Krishna Kumar R, Landzberg M, Machado RF, Olschewski H, Robbins IM, Souza R (2013) Updated clinical classification of pulmonary hypertension. J Am Coll Cardiol 62:D34–D41

de Siqueira ME, Pozo E, Fernandes VR, et al (2016) Characterization and clinical significance of right ventricular mechanics in pulmonary hypertension evaluated with cardiovascular magnetic resonance feature tracking. J Cardiovasc Magn Reson 18:39

Skrok J, Shehata ML, Mathai S, Girgis RE, Zaiman A, Mudd JO, Boyce D, Lechtzin N, Lima JA, Bluemke DA, Hassoun PM, Vogel-Claussen J (2012) Pulmonary arterial hypertension: MR imaging-derived first-pass bolus kinetic parameters are biomarkers for pulmonary hemodynamics, cardiac function, and ventricular remodeling. Radiology 263:678–687

Spiropoulos K, Charokopos N, Petsas T, Trakada G, Dougenis D, Mazarakis A, Christodoulou J, Peristerakis A, Ginopoulos P, Mastronikolis N, Alexopoulos D (1999) Non-invasive estimation of pulmonary arterial hypertension in chronic obstructive pulmonary disease. Lung 177:65–75

Stein JH, Neumann A, Marcus RH (1997) Comparison of estimates of right atrial pressure by physical examination and echocardiography in patients with congestive heart failure and reasons for discrepancies. Am J Cardiol 80:1615–1618

Stevens GR, Garcia-Alvarez A, Sahni S, Garcia MJ, Fuster V, Sanz J (2012) RV dysfunction in pulmonary hypertension is independently related to pulmonary artery stiffness. JACC Cardiovasc Imaging 5:378–387

Stocker TJ, Deseive S, Leipsic J, Hadamitzky M, Chen MY, Rubinshtein R, Heckner M, Bax JJ, Fang XM, Grove EL, Lesser J, Maurovich-Horvat P, Otton J, Shin S, Pontone G, Marques H, Chow B, Nomura CH, Tabbalat R, Schmermund A, Kang JW, Naoum

C, Atkins M, Martuscelli E, Massberg S, Hausleiter J, Investigators PV (2018) Reduction in radiation exposure in cardiovascular computed tomography imaging: results from the PROspective multicenter registry on radiaTion dose Estimates of cardiac CT angiography in daily practice in 2017 (Protection VI). Eur Heart J 39:3715–3723

Swift AJ, Capener D, Johns C, Hamilton N, Rothman A, Elliot C, Condliffe R, Charalampopoulos A, Rajaram S, Lawrie A, Campbell MJ, Wild JM, Kiely DG (2017) Magnetic resonance imaging in the prognostic evaluation of patients with pulmonary arterial hypertension. Am J Respir Crit Care Med 196:228–239

Swift AJ, Rajaram S, Campbell MJ, Hurdman J, Thomas S, Capener D, Elliot C, Condliffe R, Wild JM, Kiely DG (2014a) Prognostic value of cardiovascular magnetic resonance imaging measurements corrected for age and sex in idiopathic pulmonary arterial hypertension. Circ Cardiovasc Imaging 7:100–106

Swift AJ, Rajaram S, Capener D, Elliot C, Condliffe R, Wild JM, Kiely DG (2014b) LGE patterns in pulmonary hypertension do not impact overall mortality. JACC Cardiovasc Imaging 7:1209–1217

Swift AJ, Rajaram S, Condliffe R, Capener D, Hurdman J, Elliot C, Kiely DG, Wild JM (2012a) Pulmonary artery relative area change detects mild elevations in pulmonary vascular resistance and predicts adverse outcome in pulmonary hypertension. Investig Radiol 47:571–577

Swift AJ, Rajaram S, Hurdman J, Hill C, Davies C, Sproson TW, Morton AC, Capener D, Elliot C, Condliffe R, Wild JM, Kiely DG (2013) Noninvasive estimation of PA pressure, flow, and resistance with CMR imaging: derivation and prospective validation study from the ASPIRE registry. JACC Cardiovasc Imaging 6:1036–1047

Swift AJ, Rajaram S, Marshall H, Condliffe R, Capener D, Hill C, Davies C, Hurdman J, Elliot CA, Wild JM, Kiely DG (2012b) Black blood MRI has diagnostic and prognostic value in the assessment of patients with pulmonary hypertension. Eur Radiol 22:695–702

Swift AJ, Telfer A, Rajaram S, Condliffe R, Marshall H, Capener D, Hurdman J, Elliot C, Kiely DG, Wild JM (2014c) Dynamic contrast-enhanced magnetic resonance imaging in patients with pulmonary arterial hypertension. Pulm Circ 4:61–70

Swift AJ, Wild JM, Nagle SK, Roldán-Alzate A, François CJ, Fain S, Johnson K, Capener D, van Beek EJ, Kiely DG, Wang K, Schiebler ML (2014d) Quantitative magnetic resonance imaging of pulmonary hypertension: a practical approach to the current state of the art. J Thorac Imaging 29:68–79

Taboada D, Pepke-Zaba J, Jenkins DP, Berman M, Treacy CM, Cannon JE, Toshner M, Dunning JJ, Ng C, Tsui SS, Sheares KK (2014) Outcome of pulmonary endarterectomy in symptomatic chronic thromboembolic disease. Eur Respir J 44:1635–1645

Takx RA, Moscariello A, Schoepf UJ, Barraza JM Jr, Nance JW Jr, Bastarrika G, Das M, Meyer M, Wildberger JE, Schoenberg SO, Fink C, Henzler T (2012) Quantification of left and right ventricular function and myocardial mass: comparison of low-radiation dose 2nd generation dual-source CT and cardiac MRI. Eur J Radiol 81:e598–e604

Tedford RJ, Hassoun PM, Mathai SC, Girgis RE, Russell SD, Thiemann DR, Cingolani OH, Mudd JO, Borlaug BA, Redfield MM, Lederer DJ, Kass DA (2012) Pulmonary capillary wedge pressure augments right ventricular pulsatile loading. Circulation 125: 289–297

Title RS, Harper K, Nelson E, Evans T, Tello R (2005) Observer performance in assessing anemia on thoracic CT. AJR Am J Roentgenol 185:1240–1244

Toonkel RL, Borczuk AC, Pearson GD, Horn EM, Thomashow BM (2010) Sarcoidosis-associated fibrosing mediastinitis with resultant pulmonary hypertension: a case report and review of the literature. Respiration 79:341–345

van de Veerdonk MC, Kind T, Marcus JT, Mauritz GJ, Heymans MW, Bogaard HJ, Boonstra A, Marques KM, Westerhof N, Vonk-Noordegraaf A (2011) Progressive right ventricular dysfunction in patients with pulmonary arterial hypertension responding to therapy. J Am Coll Cardiol 58:2511–2519

van Wolferen SA, Marcus JT, Boonstra A, Marques KM, Bronzwaer JG, Spreeuwenberg MD, Postmus PE, Vonk-Noordegraaf A (2007) Prognostic value of right ventricular mass, volume, and function in idiopathic pulmonary arterial hypertension. Eur Heart J 28:1250–1257

Vonk-Noordegraaf A, Haddad F, Chin KM, Forfia PR, Kawut SM, Lumens J, Naeije R, Newman J, Oudiz RJ, Provencher S, Torbicki A, Voelkel NF, Hassoun PM (2013) Right heart adaptation to pulmonary arterial hypertension: physiology and pathobiology. J Am Coll Cardiol 62:D22–D33

Vonk Noordegraaf A, Westerhof BE, Westerhof N (2017) The relationship between the right ventricle and its load in pulmonary hypertension. J Am Coll Cardiol 69:236–243

Wang J, Zhao H, Wang Y, Herrmann HC, Witschey WRT, Han Y (2018) Native T1 and T2 mapping by cardiovascular magnetic resonance imaging in pressure overloaded left and right heart diseases. J Thorac Dis 10:2968–2975

Wang Y, Mcdonald JP, Liu Y, Pan K, Zhang X, Hu R (2014) Dynamic alterations of the tongue in obstructive sleep apnea-hypopnea syndrome during sleep: analysis using ultrafast MRI. Genet Mol Res 13: 4552–4563

Westenberg JJ (2011) CMR for Assessment of Diastolic Function. Curr Cardiovasc Imaging Rep 4: 149–158

Wu V, Chyou JY, Chung S, Bhagavatula S, Axel L (2014) Evaluation of diastolic function by three-dimensional volume tracking of the mitral annulus with cardiovascular magnetic resonance: comparison with tissue Doppler imaging. J Cardiovasc Magn Reson 16:71

Xie WM, Dai HP, Jin ML, Wang Z, Yang YH, Zhai ZG, Wang C (2012) Clinical features and imaging findings in pulmonary capillary hemangiomatosis: report of two cases and a pooled analysis. Chin Med J 125:3069–3073

Yamada Y, Okuda S, Kataoka M, et al (2012) Prognostic value of cardiac magnetic resonance imaging for idiopathic pulmonary arterial hypertension before initiating intravenous prostacyclin therapy. Circulation Journal 76:1737–1743

Yock PG, Popp RL (1984) Noninvasive estimation of right ventricular systolic pressure by Doppler ultrasound in patients with tricuspid regurgitation. Circulation 70:657–662

Zhang Z, Wang M, Yang Z, Yang F, Li D, Yu T, Zhang N (2017) Noninvasive prediction of pulmonary artery pressure and vascular resistance by using cardiac magnetic resonance indices. Int J Cardiol 227:915–922

Zhou QQ, Yu YS, Chen YC, Ding BB, Fang SY, Yang X, Zhang B, Zhang H (2018) Optimal threshold for the diagnosis of anemia severity on unenhanced thoracic CT: a preliminary study. Eur J Radiol 108:236–241

Functional Assessment of Lung Cancer and Nodules

Yoshiharu Ohno, Hisanobu Koyama,
Kazuhiro Murayama, and Takeshi Yoshikawa

Contents

1 **Introduction** 260

2 **Prediction of Postoperative Lung Function of Lung Cancer Candidates for Surgical Treatment** 261
2.1 Current Guideline-Based Radiological Examination for Prediction of Postoperative Lung Function of Lung Cancer Candidates for Surgical Resection 261
2.2 Prediction of Postoperative Lung Function Using SPECT and SPECT/CT 263
2.3 Prediction of Postoperative Lung Function Using MR Imaging with Different Methods 264
2.4 Prediction of Postoperative Lung Function Using Dual-Energy CT with Perfusion and Ventilation Assessments 269

3 **Pulmonary Functional Imaging for Differentiating Malignant from Benign Lesions** 275
3.1 Background for Contrast Enhancement 275
3.2 Dynamic CE-CT and Dynamic CE-MR Imaging Without Ultra-Short TE 279
3.3 3D Dynamic First-Pass Contrast-Enhanced MR Imaging with Ultra-Short TE Equal to or Less Than 2.0 ms 281
3.4 Dynamic First-Pass CE-Perfusion CT Using Multidetector-Row and Area-Detector CT Systems 282

Y. Ohno (✉)
Department of Radiology, Fujita Health University School of Medicine, Toyoake, Aichi, Japan

Joint Research Laboratory of Advanced Medical Imaging, Fujita Health University School of Medicine, Toyoake, Aichi, Japan
e-mail: yohno@fujita-hu.ac.jp

H. Koyama
Department of Radiology, Osaka Police Hospital, Osaka, Japan

K. Murayama
Joint Research Laboratory of Advanced Medical Imaging, Fujita Health University School of Medicine, Toyoake, Aichi, Japan

T. Yoshikawa
Department of Diagnostic Radiology, Hyogo Cancer Center, Akashi, Japan

© Springer Nature Switzerland AG 2021

Y. Ohno et al. (eds.), *Pulmonary Functional Imaging*, Medical Radiology Diagnostic Imaging,
https://doi.org/10.1007/978-3-030-43539-4_13

4 **Prediction of Treatment Outcome and Recurrence for Lung Cancer Patients Treated with Conservative Therapy** 285
4.1 Dynamic CE-MR Imaging with Ultra-Short TE Equal to or Less Than 2.0 ms 286
4.2 Dynamic First-Pass CE-Perfusion CT and ADCT 286
5 **Conclusion** 291
References 291

Abstract

Pulmonary nodules are a common finding of chest radiography and computed tomography (CT) examinations not only in routine clinical practice but also in lung cancer screening with low-dose CT. Then, the main target for radiological examination for the detection of pulmonary nodules and lung cancer is differentiation of malignant from benign nodules and determination of accurate TNM staging based on morphological, metabolic, and relaxation time-dependent information obtained from CT and nuclear medicine studies including positron emission tomography (PET) or PET combined with CT (PET/CT) and magnetic resonance (MR) imaging. In addition, a limitation of the application of functional imaging has been its ability to prediction of postoperative lung function, and is therefore mainly used for perfusion scanning, perfusion single-photon emission tomography (SPECT) or SPECT/CT as well as CT, which is also used for prediction by means of the anatomical method, and is limited to non-small cell lung cancer (NSCLC) candidates for surgical resection. Moreover, some functional imaging methods have been suggested as having the capability for therapeutic effect prediction in advanced NSCLC patients. Therefore, pulmonary functional imaging is currently available for answering all above-mentioned clinical questions and applicable in routine clinical practice.

This chapter describes state-of-the-art pulmonary functional imaging with its clinical potentials for (1) prediction of postoperative lung function for lung cancer candidates for surgical treatment, (2) differentiation of malignant from benign lesions, and (3) prediction of treatment outcomes and recurrence for lung cancer patients treated with conservative therapy.

1 Introduction

Pulmonary nodules are a common finding of chest radiography and computed tomography (CT) examinations not only in routine clinical practice, but also in lung cancer screening with low-dose CT, which was found by the National Lung Screening Trial for Reducing Lung Cancer Mortality (National Lung Screening Trial Research Team 2011) to reduce lung cancer-specific mortality. Several additional trials addressing the same research question and verifying this finding have been performed worldwide (National Lung Screening Trial Research Team 2011; Nawa et al. 2012; Saghir et al. 2012; Horeweg et al. 2014; Infante et al. 2015; Walter et al. 2016). In addition, the recommendation by the Fleischner Society as well as the findings reported by the Lung Cancer Screening Committee for the American College of Radiology (ACR) Lung Imaging Reporting and Data Systems (Lung-RADS) suggest that nodule type and size assessments are effective biomarkers for nodule management to reduce lung cancer-specific mortality (MacMahon et al. 2005, 2017; Naidich et al. 2013; Kazerooni et al. 2015, 2016). For these reasons, clinicians are frequently asked to differentiate malignant from benign nodules.

While lung cancer is the leading cause of cancer death for both men and women world-

wide, non-small cell lung cancer (NSCLC), which accounts for 80% of all lung cancers, can be cured surgically if detected at an early stage. Small cell carcinoma (SCLC), on the other hand, which accounts for the remaining 20% of all lung cancers, entails more aggressive tumors. Clinicians are therefore frequently required to perform accurate tumor, lymph node, and metastasis (TNM) staging for NSCLC as well as SCLC patients in routine clinical practice. Moreover, to determine the appropriate treatment strategies for SCLC patients, clinicians are also required to use another SCLC staging system proposed by the Veterans Administration Lung Cancer Study Group (VALSG) (Micke et al. 2002).

In view of the aforementioned clinical requirements, the main target for radiological examination for the detection of pulmonary nodules and lung cancer is differentiation of malignant from benign nodules and determination of accurate TNM staging based on morphological, metabolic, and relaxation time-dependent information obtained from computed tomography (CT) and nuclear medicine studies including positron emission tomography (PET) or PET combined with CT (PET/CT) and magnetic resonance (MR) imaging (Silvestri et al. 2007; Jett et al. 2013; Koyama et al. 2013; Kozower et al. 2013; Ohno 2014; Ohno et al. 2015a, 2016a; Kim et al. 2015; Ciliberto et al. 2018). In addition, a limitation of the application of functional imaging has been its ability to predict postoperative lung function, and is therefore mainly used for perfusion scanning, perfusion single-photon emission tomography (SPECT) or SPECT/CT as well as CT, which is also used for prediction by means of the anatomical method, and is limited to NSCLC candidates for surgical resection (British Thoracic Society 2001; Beckles et al. 2003; Sudoh et al. 2006; Colice et al. 2007; Ohno et al. 2007a; Charloux et al. 2009; Yoshimoto et al. 2009; David and Marshall 2012; Brunelli et al. 2009, 2013).

Since the early 2000s, state-of-the-art pulmonary functional imaging has been introduced as having the potential for more accurate clinical prediction of postoperative lung function for lung cancer patients, and functional evaluation of pulmonary nodules or lymph nodes for diagnosis of malignancy and prediction of treatment outcome or recurrence in lung cancer patients treated with conservative therapy (Ohno et al. 2002, 2004a, b, c, 2005a, b, 2007a, b, c, d, 2008, 2011a, b, 2013, 2014, 2015a, b, c, 2016a, b; Schaefer et al. 2004; Sieren et al. 2010; Bohlsen et al. 2016; Yabuuchi et al. 2018). Almost all of these methods were directly compared with traditional methods or currently applied methods in accordance with certain guidelines and their clinical relevance was demonstrated (Ohno et al. 2002, 2004a, b, c, 2005a, b, 2007a, b, c, d, 2008, 2011a, b, 2013, 2002, 2004a, b, c, 2005a, b, 2007a, b, c, d, 2008, 2011a, b, 2013, 2018a, b).

This chapter describes state-of-the-art pulmonary functional imaging with its clinical potentials for (1) prediction of postoperative lung function for lung cancer candidates for surgical treatment, (2) differentiation of malignant from benign lesions, and (3) prediction of treatment outcomes and recurrence for lung cancer patients treated with conservative therapy.

2 Prediction of Postoperative Lung Function of Lung Cancer Candidates for Surgical Treatment

2.1 Current Guideline-Based Radiological Examination for Prediction of Postoperative Lung Function of Lung Cancer Candidates for Surgical Resection

Surgery is currently considered to be the best curative option for stage I, II, or IIIA non-small cell lung cancer (NSCLC) patients, although the risks of this procedure for NSCLC patients with chronic obstructive pulmonary disease (COPD) as well as interstitial lung disease (ILD) have been well established (Howington et al. 2013; Ramnath et al. 2013; Socinski et al. 2013). For

these reasons, clinicians are frequently asked to evaluate the risks and feasibility of lung resection, and guidelines have been introduced and certain algorithms recommended for the prediction of postoperative lung function of NSCLC patients considered to be candidates for surgical treatment and with poor pulmonary function (Pierce et al. 1994; Bolliger et al. 1995, 1996, 2002; Wyser et al. 1999; British Thoracic Society. 2001; Beckles, et al. 2003; Colice, et al. 2007; Charloux, et al. 2009; Brunelli, et al. 2009, 2013).

Several guidelines published since the 1990s (British Thoracic Society. 2001; Beckles, et al. 2003; Colice, et al. 2007; Charloux, et al. 2009; Brunelli, et al. 2009, 2013) have recommended that both forced expiratory volume in 1 second (FEV_1) and diffusing capacity for carbon monoxide (DL_{CO}) be measured for all patients and that both predicted postoperative FEV_1 ($ppoFEV_1$) and predicted postoperative DL_{CO} ($ppoDL_{CO}$) be calculated for patients with lung cancer being considered for surgery.

The risk of operative complications has been linked to predicted postoperative lung function. Different formulas are used to estimate this function for patients undergoing pneumonectomy and lobectomy. The predicted postoperative values can be converted into percentages by using standard equations. For illustrative purposes, the formulas below are used for the estimation of $ppoFEV_1$, but the same equations can be used for $ppoDL_{CO}$. In a few guidelines (Beckles, et al. 2003; Colice, et al. 2007; Brunelli et al. 2013), postoperative FEV1 of candidates for pneumonectomy are predicted on the basis of the perfusion method used with the following formula:

$$ppoFEV_1 = \text{preoperative } FEV_1 \times (1\text{-fraction of total perfusion for the resected lung})$$

The preoperative FEV_1 is obtained as the optimal measured post-bronchodilator value. A quantitative radionuclide perfusion scan is then performed to measure this value as a fraction of total perfusion for the resected lung. Standards for the perfusion scan have been published by the American College of Radiology (available at http://www.acr.org/~/media/ACR/Documents/PGTS/guidelines/Pulmonary_Scintigraphy.pdf).

On the other hand, postoperative values for candidates undergoing lobectomy are predicted with the anatomic method used with the following formula:

$$ppoFEV_1 = \text{preoperative } FEV_1 \times (1\text{-x/y})$$

The preoperative FEV_1 is obtained as the optimal measured post-bronchodilator value. The number of functional or unobstructed lung segments to be removed is termed x and the total number of functional segments is termed y (Bolliger et al. 1995, 1996, 2002; Beckles, et al. 2003; Colice, et al. 2007; Brunelli, et al. 2009, 2013). The total number of segments for both lungs is 19 (10 in the right lung [three in the upper, two in the middle, five in the lower] and nine in the left lung [five in the upper and four in the lower]) (Bolliger et al. 1995, 1996, 2002; Beckles, et al. 2003; Colice, et al. 2007; Brunelli, et al. 2009, 2013).

When these predictions are applied to specific cases, different management procedures have been suggested (Bolliger et al. 1995, 1996, 2002; Beckles, et al. 2003; Colice, et al. 2007; Brunelli, et al. 2009, 2013). In the case of patients with lung cancer being considered for surgery, if 60% is predicted for both $ppoFEV_1$ and $ppoDL_{CO}$, no further tests are recommended because these values indicate a low risk of perioperative death and cardiopulmonary complications following resection including pneumonectomy (Brunelli et al. 2013). If 60% is predicted for either $ppoFEV_1$ or $ppoDL_{CO}$ and more than 30% for both, it is recommended that a low technology exercise test (stair climb or shuttle walk test) be performed. If 30% or less is predicted for either $ppoFEV_1$ or $ppoDL_{CO}$, a formal cardiopulmonary exercise test with measurement of maximal oxygen consumption is recommended (Brunelli et al. 2013). This means that predictions of $ppoFEV_1$ and $ppoDL_{CO}$ are fundamental requirements for lung cancer candidates for not both pneumonectomy and lobectomy, and the methods used for this purpose, including ventilation scan (Markos et al.

1989; Sudoh et al. 2006; Ohno et al. 2007a), perfusion scans (Pierce et al. 1994; Bolliger et al. 1995, 1996, 2002; Giordano et al. 1997; Beckles, et al. 2003; Colice, et al. 2007; Brunelli, et al. 2009, 2013; Ohno et al. 2004a, 2005a, 2007a, b, 2011b, 2015c), quantitative CT scans (Wu et al. 1994, 2002; Bolliger et al. 2002; Ohno et al. 2004a, 2005a, 2007b, 2011b, 2015c), and anatomic estimation, which is based on counting the number of segments to be removed (Pierce et al. 1994; Bolliger et al. 1995, 1996, 2002; Giordano et al. 1997; Beckles, et al. 2003; Ohno et al. 2004a, b, c, 2005a, b, 2007b, 2011b, 2015c; Colice, et al. 2007; Brunelli, et al. 2009, 2013), all seem to provide similar quantitative estimates of prediction of postoperative lung function. However, the radionuclide perfusion scan method is preferable for estimating ppoFEV_1 and ppoDL_{CO} after pneumonectomy because the anatomic method tends to underestimate actual postoperative FEV_1 values (Smulders et al. 2004). The anatomic method, on the other hand, is recommended for estimating lung function after a lobectomy (British Thoracic Society. 2001; Beckles, et al. 2003; Colice, et al. 2007; Charloux, et al. 2009; Brunelli, et al. 2009, 2013). However, there are also possible advantages to using quantitative CT scan methods, which use the percentage of low-attenuation area within the total lung, determined by employing the threshold value for assessing pulmonary emphysema (Brunelli, et al. 2009, 2013). Because this imaging procedure is routinely used for staging purposes, estimating the amount of lung tissue to be lost at surgery from these images may eliminate the need for additional testing (e.g., perfusion scans) to predict postoperative lung function (Pierce et al. 1994; Bolliger et al. 1995, 1996, 2002; Giordano et al. 1997; Wu et al. 2002; Beckles, et al. 2003; Colice, et al. 2007; Brunelli, et al. 2009, 2013; Ohno et al. 2004a, 2005a, 2007a, 2007b, 2011b, 2015c,). Quantitative CT scans may also prove to be a more sensitive indicator of diffuse parenchymal lung disease, either emphysema or interstitial lung disease, than the combination of FEV_1 and DLco (Wu et al. 1994, 2002; Bolliger et al. 2002; Ohno et al. 2004a, 2005a, 2007b, 2011b, 2015c; Ueda et al. 2005). For the various abovementioned situations, other techniques such as nuclear medicine perfusion and ventilation studies using SPECT and SPECT/CT, as well as new CT techniques such as dual-energy CT and MR imaging with different methods, have been developed, tested, and proved for their clinical potential and usefulness for prediction of postoperative lung function.

2.2 Prediction of Postoperative Lung Function Using SPECT and SPECT/CT

The effectiveness of prediction of postoperative lung function by means of nuclear medicine studies has been mainly demonstrated in the form of perfusion scanning with technetium-99 m-labeled macroaggregated albumin (99mTc-MAA) (Pierce et al. 1994; Bolliger et al. 1995, 1996, 2002; Giordano et al. 1997; Beckles, et al. 2003; Colice, et al. 2007; Brunelli, et al. 2009, 2013; Ohno et al. 2004a, 2005a, 2007a, 2007b, 2011b, 2015c), while a few investigators have tested the capability of ventilation scan with krypton-81 m (^{81m}Kr) (Markos et al. 1989; Sudoh et al. 2006; Ohno et al. 2007a).

Since the beginning of the clinical application of ventilation and perfusion scans in the 1970s, both methods have been demonstrated to be useful by the use of descriptive statistics in this setting, although the application of ventilation scan has been more limited than that of perfusion scan (Kristersson et al. 1972; Olsen et al. 1974; Lipscomb and Pride 1977; Markos et al. 1989; Ryo 1990; Pierce et al. 1994; Bolliger et al. 1995, 1996, 2002; Giordano et al. 1997; Beckles, et al. 2003; Sudoh et al. 2006; Colice, et al. 2007; Brunelli, et al. 2009, 2013; Ohno et al. 2004a, 2005a, 2007a, 2007b, 2011b, 2015c). Moreover, since the 1990s results of statistical analyses have demonstrated the capability of perfusion scans for prediction of postoperative lung function (Pierce et al. 1994; Bolliger et al. 1995, 1996, 2002; Giordano et al. 1997; Beckles, et al. 2003; Sudoh et al. 2006; Colice, et al. 2007; Brunelli,

et al. 2009, 2013; Ohno et al. 2004a, 2005a, 2007a, 2007b, 2011b, 2015c). One of these studies found that radionuclide-based calculations of postoperative maximal O_2 uptake are predictive of operative morbidity and mortality, with a predicted postoperative maximal O_2 uptake of <10 mL/kg/min possibly an indication of inoperability (Bolliger et al. 1995). This study further demonstrated the accurate predictive capability of ppoFEV$_1$ for short-term postoperative performance and postoperative maximal O_2 uptake, but also found that long-term function after lobectomy is underestimated (Bolliger et al. 1995). Another study evaluated the prediction of capability of perfusion scan for candidates for pneumonectomy and lobectomy (Giordano et al. 1997). The findings of linear regression analyses performed in this study showed significant correlations between the predicted and observed values of FVC and FEV$_1$ (R^2 = 0.607 and 0.749, respectively). Moreover, the estimates of both FVC and FEV$_1$ were significantly better for right lung lobectomies than for left lung lobectomies. The authors concluded that the scintigraphic prediction of post-lobectomy residual function is easily implemented but with a greater margin of uncertainty than that of post-pneumonectomy, especially for left lobectomies. However, they maintain that the use of some safety thresholds for predicted values of FEV$_1$ guarantees a safe clinical use of the test (Giordano et al. 1997). In view of these findings, various guidelines have suggested perfusion scan is useful for management of NSCLC candidates for surgical treatment (British Thoracic Society 2001; Beckles et al. 2003; Colice et al. 2007; Charloux et al. 2009; Brunelli et al. 2009, 2013).

Since then, however, it has been suggested that SPECT or SPECT/CT is more useful than perfusion scans because of improved evaluation of regional radioisotope uptake within individual segments. Hirose et al. (1993) demonstrated that close relationships existed between actual FVC and ppoFVC (r = 0.87, $p < 0.001$), and between actual FEV$_1$ and ppoFEV$_1$ (r = 0.90, $p < 0.001$). This showed that accurate prediction of pulmonary function after lobectomy could be achieved by means of lung perfusion SPECT.

Another study prospectively assessed the capability of SPECT/CT using ^{81m}Kr and ^{99m}Tc-MAA for prediction of postoperative lung function of NSCLC patients compared with the capability of SPECT and planar imaging (Ohno et al. 2007a). This study found that the reproducibility coefficients of SPECT/CT (^{81m}Kr: 5.1%, ^{99m}Tc-MAA: 5.2%) were smaller than those of SPECT and planar imaging using ^{81m}Kr (SPECT: 7.4%, planar imaging: 12.1%) and ^{99m}Tc-MAA (SPECT: 7.2%, planar imaging: 11.8%). In addition, ppoFEV$_1$ values obtained with any of these methods demonstrated significantly strong correlation with those for actual FEV$_1$ ($p < 0.0001$). Further, the limits of agreement for SPCT/CT (^{81m}Kr: 3.3 ± 10.5%, ^{99m}Tc-MAA: 5.4 ± 11.0%) were smaller than those for SPECT (^{81m}Kr: 5.7 ± 10.8%, ^{99m}Tc-MAA: 6.8 ± 11.1%) and planar imaging (^{81m}Kr: 7.1 ± 12.1%, ^{99m}Tc-MAA: 8.8 ± 11.4%) and small enough for clinical purposes. The authors therefore concluded that SPECT/CT using ^{81m}Kr and ^{99m}Tc-MAA could predict postoperative lung function with greater reproducibility and accuracy than could SPECT and planar imaging.

Table 1 shows the capabilities of these methods for prediction of postoperative lung function of patients with lung cancer. In view of the above-mentioned nuclear medicine study results, it seems that the use of SPECT and SPECT/CT with not only ^{99m}Tc-MAA but also ^{81m}Kr would be more effective than planar imaging for prediction of postoperative lung function of lung cancer patients (Fig. 1).

2.3 Prediction of Postoperative Lung Function Using MR Imaging with Different Methods

Since the mid-1990s, pulmonary functional MR imaging has been developed and tested for various pulmonary diseases. In addition, the

Table 1 Prediction of postoperative lung function using nuclear medicine examination with and without quantitatively and qualitatively assessed CT for non-small cell lung cancer

Source	No. of cases	Methods	Correlation coefficient for actual and predicted lung function (r)	Limits of agreement between actual and predicted lung function (%)
Bolliger et al. (1995)	22	Perfusion scan	0.81 vs. 0.84 (FEV_1 at 3 months vs. 6 months)	N/A
			0.74 vs. 0.74 (DL_{CO} at 3 months vs. 6 months)	
Bolliger et al. (2002)	44	Perfusion scan	0.92	N/A
		Quantitative CT	0.91	
		Anatomical CT method	0.88	
Wu et al. (2002)	44	Perfusion scan	0.86 vs. 0.80 (Pneumonectomy vs. Lobectomy)	N/A
		Quantitative CT	0.88 vs. 0.90 (Pneumonectomy vs. Lobectomy)	
Sudoh et al. (2006)	22	Perfusion SPECT/CT	0.91	N/A
		Anatomical CT method	0.91	
Ohno et al. (2007a)	60	Ventilation scan	0.89	3.3 ± 10.5
		Perfusion scan	0.9	5.4 ± 11.0
		Ventilation SPECT	0.93	5.7 ± 10.8
		Perfusion SPECT/CT	0.92	6.8 ± 11.1
		Ventilation SPECT/CT	0.93	7.1 ± 12.1
		Perfusion SPECT/CT	0.92	8.8 ± 11.4

predictive capability of postoperative lung function with this method has been evaluated for NSCLC patients with three approaches for using pulmonary functional imaging in this setting: contrast-enhanced (CE-) perfusion MR imaging (Iwasawa et al. 2002; Ohno et al. 2004a, 2007b, 2011b, 2015c), oxygen (O_2)-enhanced MR imaging (Ohno et al. 2005a), and non-contrast-enhanced (non-CE-) perfusion MR imaging (Ohno et al. 2015c).

In comparison with the predictive capability for NSCLC patients of quantitative and/or qualitative CT, perfusion scan, perfusion SPECT, and/or perfusion SPECT combined with CT (SPECT/CT), that of quantitatively assessed 3D dynamic CE-perfusion MR imaging was found to be better than that of qualitative CT, perfusion scan, and perfusion SPECT, and almost similar to that of quantitative CT and perfusion SPECT/CT (Ohno et al. 2004a, 2007b, 2011b). In addition, the limit of agreement between actual postoperative lung function and predicted with the aid of 3D CE-perfusion MR imaging is reportedly less than 10% and therefore small enough for clinical purposes (Ohno et al. 2004a, 2007b, 2011b). Since this technique can thus utilize the same dataset as employed for dynamic CE-MR imaging with an ultra-short echo time (TE) and can also be used as dynamic MR imaging for pulmonary nodule and mass assessment, while it is not time consuming in routine clinical practice, it may replace perfusion scan, SPECT, and SPECT/CT in routine clinical practice.

In contrast to the numerous data reported for 3D dynamic CE-perfusion MR imaging, only one report has presented the findings of a comparative study of the predictive capability for postoperative lung function of O_2-enhanced MR imaging, quantitative and qualitative CT, and perfusion scan (Ohno et al. 2005a) (Fig. 2). This study found that postoperative lung function predicted by means of O_2-enhanced MR imaging

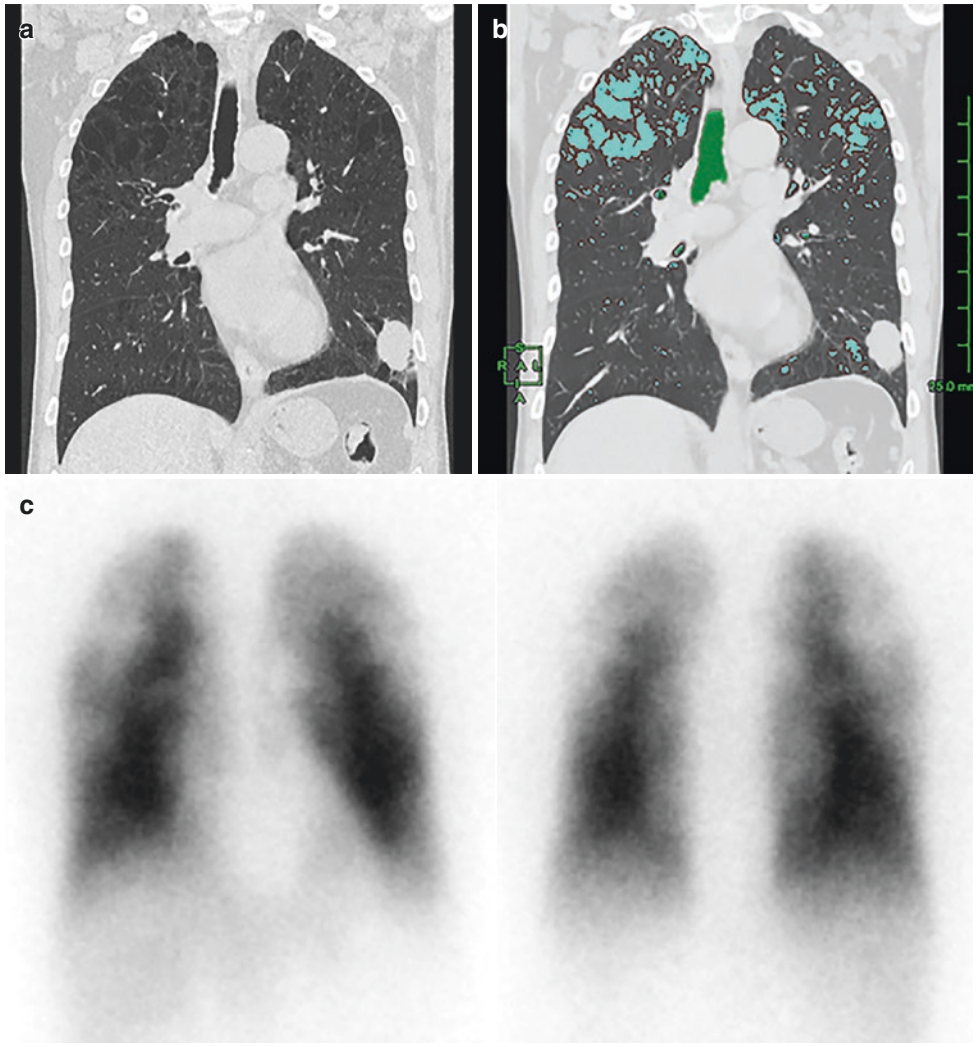


Fig. 1 A 68-yesr-old male patient with invasive adenocarcinoma in the left lower lobe. (**a**) Thin-section multiplanar reformatted (MPR) image at coronal plane demonstrates lung cancer in the left lower lobe. Pulmonary emphysema heterogeneously distributed, and it is determined as upper lobe predominance, especially right upper lobe. (**b**) On quantitatively assessed thin-section MPR image, pulmonary emphysema is determined as sky blue pixels, whose CT numbers are equal to or less than -950HU. (**c**) Perfusion scan (*L* to *R*: anterior to posterior) shows heterogeneous uptakes of ^{99m}Tc-MAA within both lungs, especially both upper lung field, due to pulmonary emphysema. (**d**) Ventilation scan (*L* to *R*: anterior to posterior) demonstrates slightly heterogeneous uptakes of ^{81m}Krypton (^{81m}Kr) within both lungs. (**e**) Perfusion SPECT at coronal plane matched with thin-section MPR image shows heterogeneous uptakes of ^{99m}Tc-MAA within both lungs, especially both upper lung field, due to pulmonary emphysema. In addition, uptake within left lower lung field is reduced due to lung cancer. (**f**) Ventilation SPECT at coronal plane matched with thin-section MPR image shows heterogeneous uptakes of ^{81m}Kr within both lungs, especially both upper lung field, due to pulmonary emphysema. In addition, uptake within left lower lung field is decreased due to lung cancer. (**g**) Perfusion SPECT/CT at coronal plane matched with thin-section MPR image shows heterogeneous uptakes of ^{99m}Tc-MAA within both lungs, especially both upper lung field, due to pulmonary emphysema. In addition, uptake within left lower lung field is due to lung cancer. (**h**) Ventilation SPECT/CT at coronal plane matched with thin-section MPR image shows heterogeneous uptakes of ^{81m}Kr within both lungs, especially both upper lung field, due to pulmonary emphysema. In addition, uptake within left lower lung field is due to lung cancer

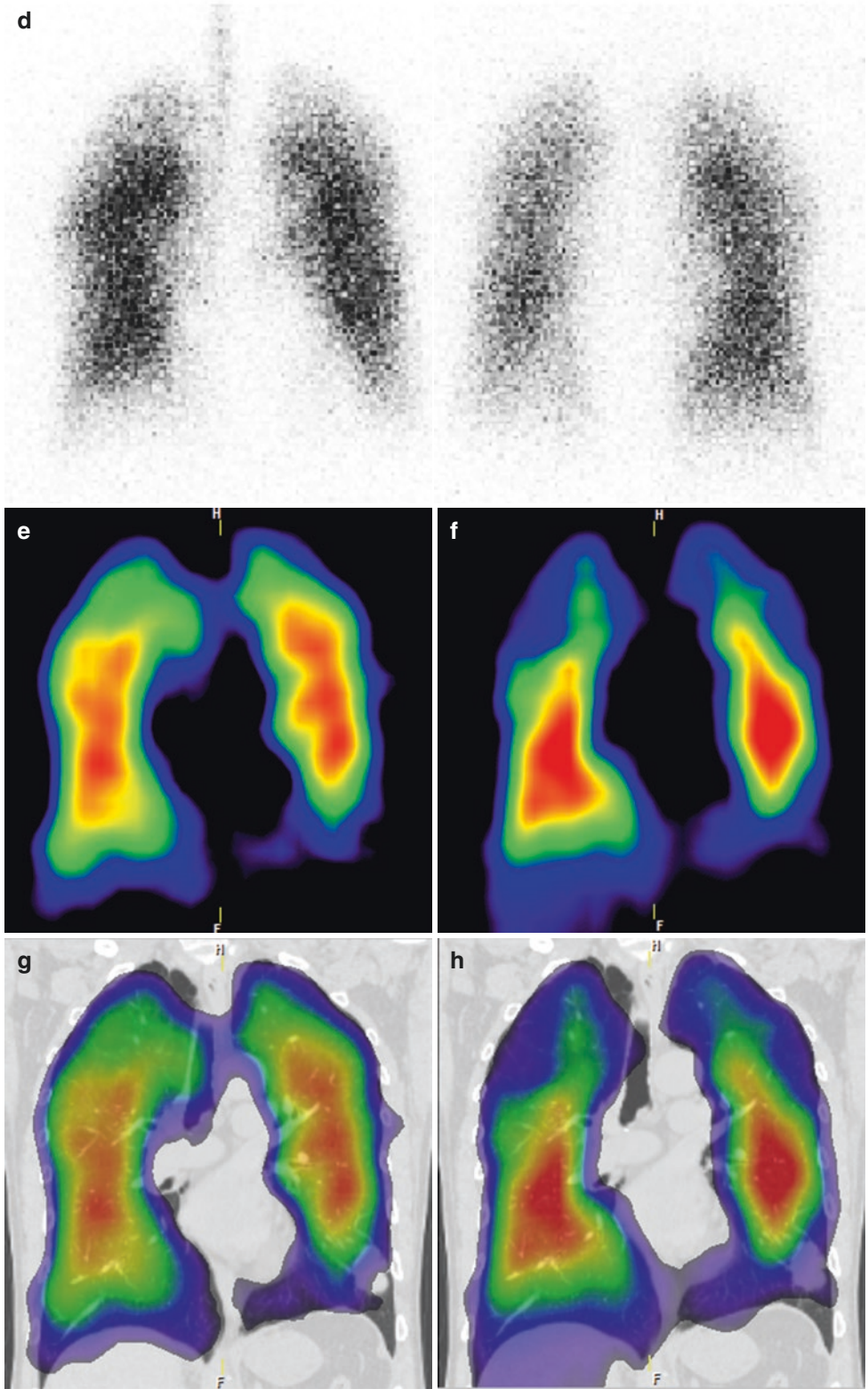


Fig. 1 (continued)

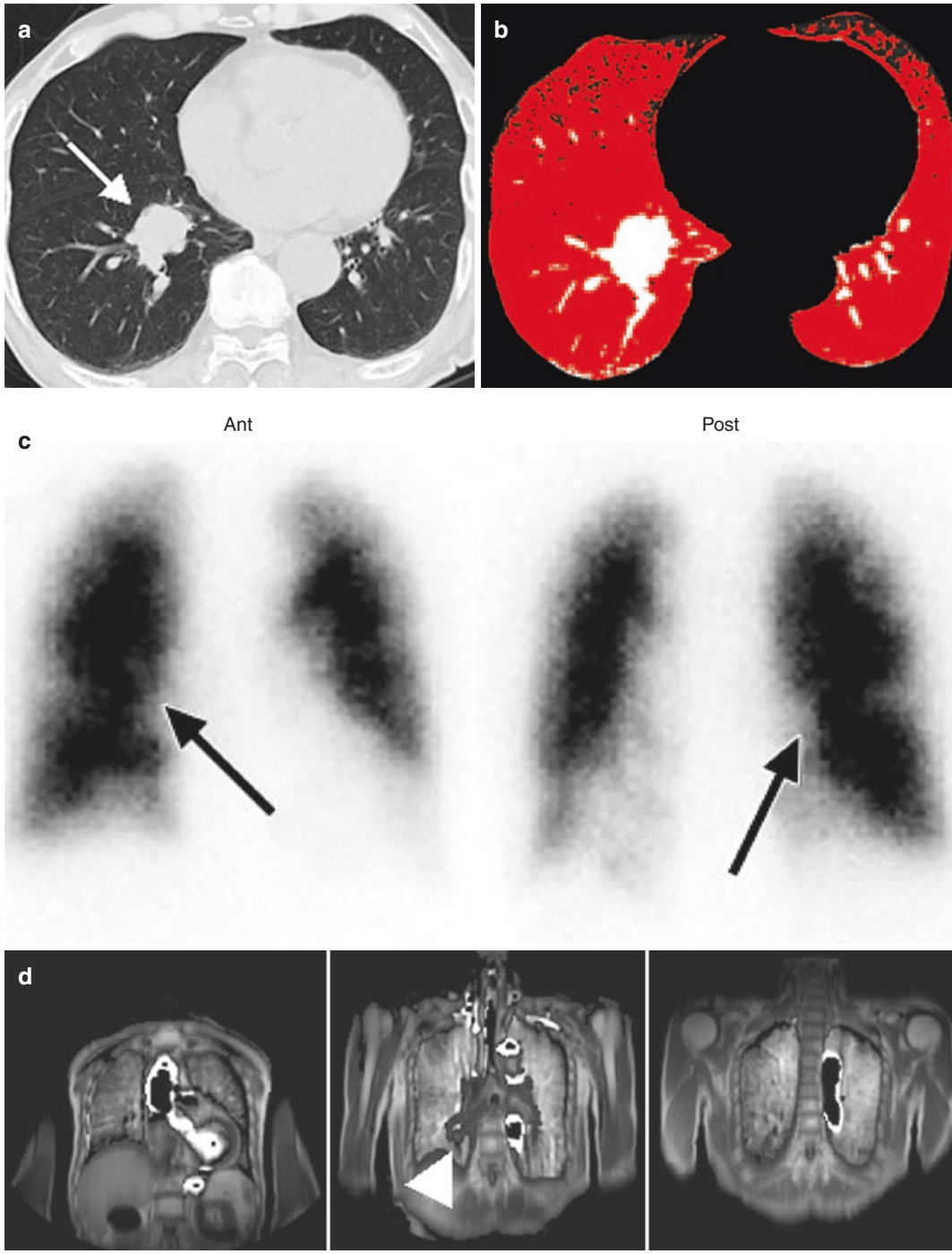


Fig. 2 Images in a 69-year-old patient with adenocarcinoma in the right lower lobe and subtle pulmonary emphysema. (Permission obtained from Ohno et al. 2005a). (**a**) Routine transverse CT image reveals no low-attenuation areas in either lung; the mass is seen (arrow). (**b**) At quantitative CT, the functional lung is expressed as red, pulmonary emphysema is expressed as gray, and lung cancer and fibrosis are expressed as white. (**c**) Perfusion scintigraphic images (anterior [Ant] and posterior [Post] views) demonstrate heterogeneous uptake, excluding the lung cancer (arrow). (**d**) Oxygen-enhanced MR images (from anterior to posterior, left to right) show heterogeneous oxygen enhancement in both lungs, excluding the lung cancer (arrowhead)

and quantitative CT (both methods: $r = 0.90$, $p < 0.0001$) showed significant and better correlations between actual FEV_1 and $ppoFEV_1$ than those for qualitatively assessed thin-section CT ($r = 0.87$, $p < 0.0001$) and perfusion scan ($r = 0.88$, $p < 0.0001$). In addition, the limits of agreement for the difference between actual FEV_1 (percentage predicted) and $ppoFEV_1$ (percentage predicted) when O_2-enhanced MR imaging was used was reportedly less than 10%, almost equal to that for the use of quantitative CT, smaller than that for qualitative CT and perfusion scan, and small enough for clinical purposes (Ohno et al. 2005a, b). This MR technique is therefore currently regarded as a promising predictive modality to be included in the guidelines for presurgical examination of NSCLC patients (Ohno et al. 2005a).

A study conducted in 2015 reported on the results of a comparison of the predictive capability of non-CE-perfusion MR imaging for postoperative lung function of NSCLC patients with that of non-CE- and dynamic CE-perfusion MR imaging, quantitative and qualitative CT, and perfusion scan (Ohno et al. 2015c) (Fig. 3). This study demonstrated that the prediction of postoperative lung function by non-CE-perfusion MR imaging for each $ppoFEV_1$ showed significant and positive correlation with the actual FEV_1 ($0.73 \leq r \leq 0.93$, $p < 0.0001$) (Ohno et al. 2015c). In addition, limits of agreement between FEV_1 obtained with non-CE-perfusion MR imaging ($0.3 \pm 10.0\%$), dynamic CE-perfusion MR imaging ($1.0 \pm 10.8\%$), quantitative CT ($1.2 \pm 9.0\%$), and qualitative CT ($1.5 \pm 10.2\%$) were similar and smaller than that of perfusion scan ($2.2 \pm 14.1\%$) (Ohno et al. 2015c).

Table 2 shows the capabilities of these methods for prediction of postoperative lung function of patients with NSCLC patients. Although further investigations are warranted to determine the clinical relevance of all MR methods, it is expected that in the near future pulmonary functional MR imaging will be able to function as a substitute for nuclear medicine studies as well as quantitative CT for quantitative prediction of postoperative lung function of NSCLC patients.

2.4 Prediction of Postoperative Lung Function Using Dual-Energy CT with Perfusion and Ventilation Assessments

Dual-energy CT (DE-CT) techniques using dual X-ray sources, dual-layer detectors, or fast kilovoltage-switching methods were introduced in the 1970s (Genant and Boyd 1977; Chiro et al. 1979; Millner et al. 1979) and have been clinically applied since 2008 (Flohr et al. 2006; Chae et al. 2008, 2010, 2013; Ko et al. 2012; Lu et al. 2012). Although their CT systems and data acquisition methods are different, all these techniques make it possible to display iodine distribution maps within the lungs as perfusion-weighted images as well as xenon distribution maps as ventilation-weighted images for lung cancer patients who are considered potential candidates for surgical treatment (Chae et al. 2013; Yanagita et al. 2013).

As for prediction of postoperative lung function derived from regional perfusion assessment on DE-CT, one study (Chae et al. 2013) reported that the limits of agreement between the actual postoperative FEV_1 (percentage predicted) and $ppoFEV_1$ (the percentage predicted) were − 29.3% and 26.9% for perfusion scintigraphy and − 28.9% and 17.3% for DE-CT. In addition, the coefficient for correlation between the actual postoperative FEV_1 and $ppoFEV_1$ obtained with DE-CT was significantly better than that for perfusion scintigraphy (DE-CT vs. perfusion scintigraphy: $r = 0.66$, $p < 0.0001$ vs. $r = 0.52$, $p = 0.0001$). It was therefore suggested that DE-CT had better potential for prediction of postoperative lung function based on regional perfusion evaluation of lung cancer patients.

In addition to prediction derived from perfusion assessment, another study demonstrated the capability of DE-CT with xenon (Xe) for prediction of postoperative lung function of patients with lung cancer (Yanagita et al. 2013). In this study, the capability of DE-CT with Xe for prediction of lung function (vital capacity [VC], forced vital capacity [FVC], and FEV_1) was compared with that of quantitative CT, perfusion SPECT, and anatomical method. Comparison of

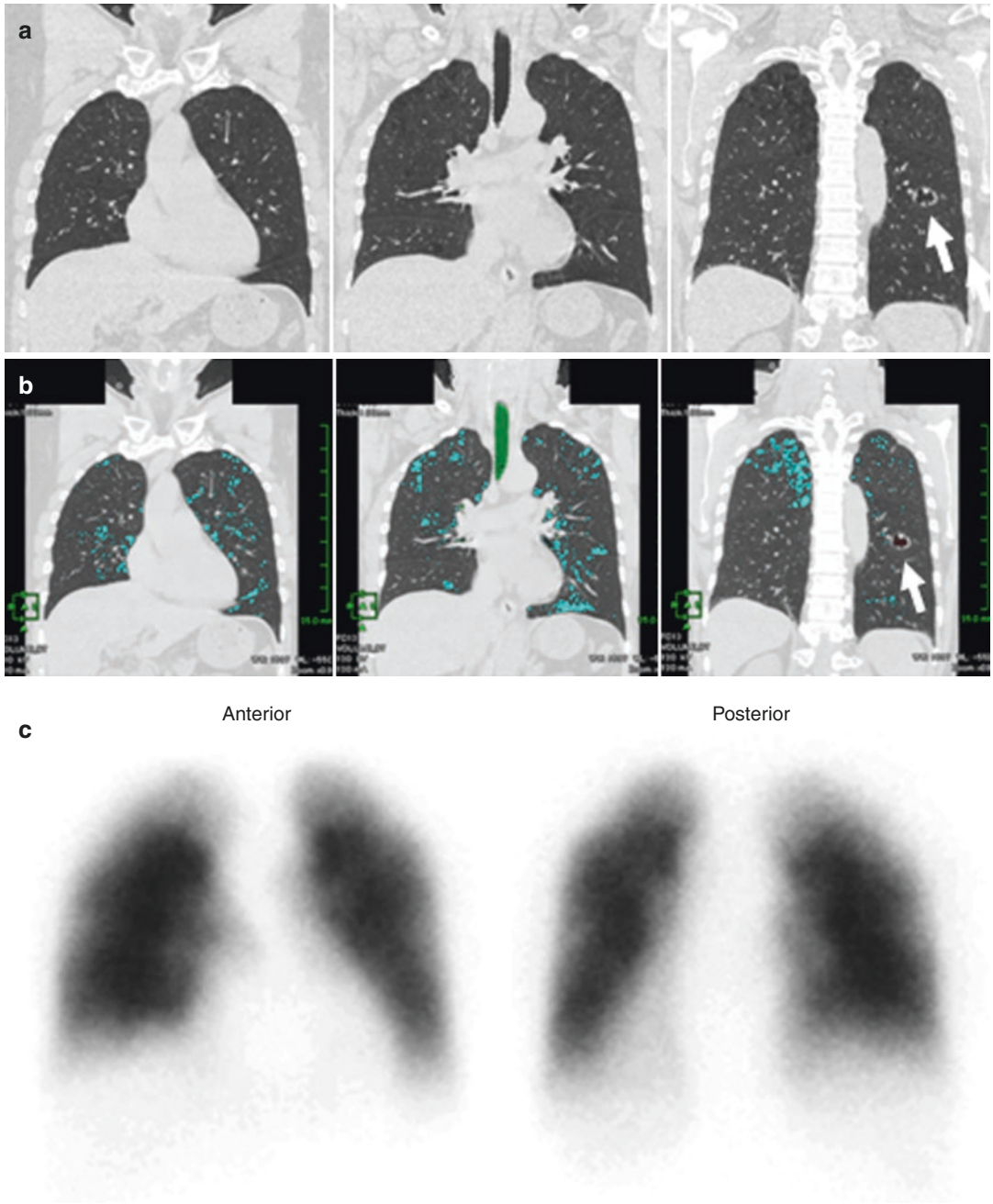


Fig. 3 A 63-year-old male patient with squamous cell carcinoma in the left lower lobe (Permission obtained from Ohno et al. 2015c). (**a**) (*L* to *R*, ventral to dorsal) Thin-section MPR image with lung window setting shows a nodule with cavity in the left lower lobe (arrow), and emphysema in both lungs. This nodule was diagnosed as squamous cell carcinoma. (**b**) (*L* to *R*, ventral to dorsal) On quantitative CT, pulmonary emphysema, shown in sky blue, has a CT value of less than -960HU. The lung cancer is also seen in the left lower lobe (arrow). (**c**) (*L* to *R*, anterior to posterior) Perfusion scan shows slightly and heterogeneously reduced uptake in both lungs. (**d**) (*L* to *R*, ventral to dorsal) Dynamic CE-perfusion MR images at 13.5 s show heterogeneously enhanced lung parenchyma due to emphysema and a thin-rimmed area enhanced due to lung cancer (arrow). (**e**) (*L* to *R*, original image at systolic phase, original image at diastolic phase, and non-CE-perfusion MRI generated as subtraction images between two phases; upper, middle, and lower line, ventral to dorsal) Non-CE-perfusion MR images show heterogeneously high signal intensity within both lungs due to emphysema and lung cancer (arrow)

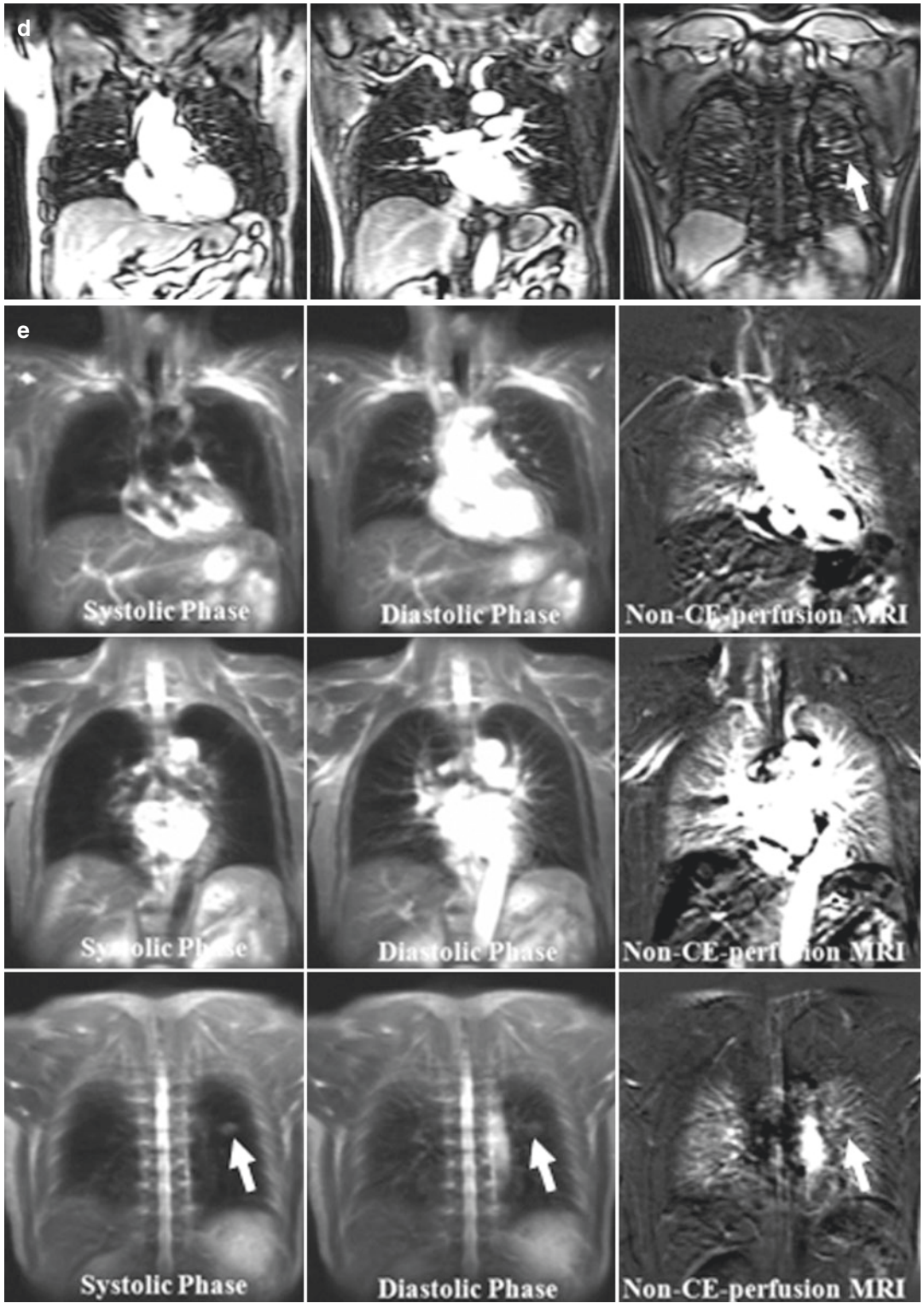


Fig. 3 (continued)

Table 2 Prediction of postoperative lung function using mr examination with and without quantitatively and qualitatively assessed CT and nuclear medicine examination for non-small cell lung cancer

Source	No. of cases	Methods	Correlation coefficient for actual and predicted lung function (r)	Limits of agreement between actual and predicted lung function (%)
Iwasawa et al. (2002)	20	Perfusion scan	0.66	N/A
		CE-perfusion MRI	0.68	
Ohno et al. (2004a)	60	Perfusion scan	0.89	2.1 ± 13.2
		CE-perfusion MRI	0.93	0.9 ± 10.4
Ohno et al. (2005a)	30	Perfusion scan	0.88	−0.5 ± 11.4
		Quantitative CT	0.90	0.7 ± 10.0
		Anatomical CT method	0.87	1.1 ± 11.8
		O_2-enhanced MRI	0.90	0.5 ± 10.4
Ohno et al. (2007b)	150	Perfusion SPECT	0.83	5.1 ± 14.0
		Quantitative CT	0.88	5.0 ± 11.6
		Anatomical CT method	0.83	6.8 ± 14.4
		CE-perfusion MRI	0.87	5.3 ± 11.8
Ohno et al. (2011b)	229	Perfusion scan	0.83	5.8 ± 18.2
		Perfusion SPECT	0.85	5.5 ± 16.8
		Perfusion SPECT/CT	0.88	5.1 ± 14.7
		Quantitative CT	0.88	4.7 ± 14.2
		Anatomical CT method	0.85	6.0 ± 17.4
		CE-perfusion MRI	0.88	4.4 ± 14.2
Ohno et al. (2015c)	60	Perfusion scan	0.87	2.2 ± 14.1
		Quantitative CT	0.93	1.2 ± 9.0
		Anatomical CT method	0.73	1.5 ± 10.2
		CE-perfusion MRI	0.92	1.0 ± 10.8
		Non-CE-perfusion MRI	0.93	0.3 ± 10.0

coefficients of determination (R^2) for VC, FVC, and FEV_1 obtained with DE-CT with Xe (VC: $R^2 = 0.76$, $p < 0.001$; FVC: $R^2 = 0.77$, $p < 0.001$; FEV_1: $R^2 = 0.70$, $p < 0.001$) and quantitative CT (VC: $R^2 = 0.76$, $p < 0.001$; FVC: $R^2 = 0.77$, $p < 0.001$; FEV_1: $R^2 = 0.70$, $p < 0.001$) showed that they were better than those obtained with perfusion SPECT (VC: $R^2 = 0.63$, $p < 0.001$; FVC: $R^2 = 0.67$, $p < 0.001$; FEV_1: $R^2 = 0.61$, $p < 0.001$) and the anatomical method (VC: $R^2 = 0.56$, $p < 0.001$; FVC: $R^2 = 0.63$, $p < 0.001$; FEV_1: $R^2 = 0.61$, $p < 0.001$). Although applications of DE-CT in this setting are currently limited, clinical installation of a new CT system, which is available for DE-CT examination, will demonstrate the utility of this technique for prediction of postoperative lung function of NSCLC patients.

It has recently been suggested that xenon-enhanced CT (Xe-CT) can be used not only for DE-CT but also for subtraction CT methods (Ohno et al. 2017c, 2018b). In addition, the subtraction CT method for visualization of Xe enhancement is potentially superior to the DE-CT method, and can more clearly demonstrate regional Xe ventilation on Xe-CT as well as be effectively matched with ^{81m}Kr SPECT/CT (Ohno et al. 2017c, 2018b) (Fig. 4). The subtraction CT method requires well-organized nonrigid registration software for visualization of Xe *on* unenhanced and contrast-enhanced CT with Xe, but does not need specific equipment such as dual-source X-ray tube, fast tube voltage switching, and dual-layer detector systems. Although further investigation is required, it is expected that Xe-CT using both methods as well as the iodine map derived from DE-CT with iodine contrast media will be used in the near future for more accurate prediction of postoperative lung function of lung cancer patients.

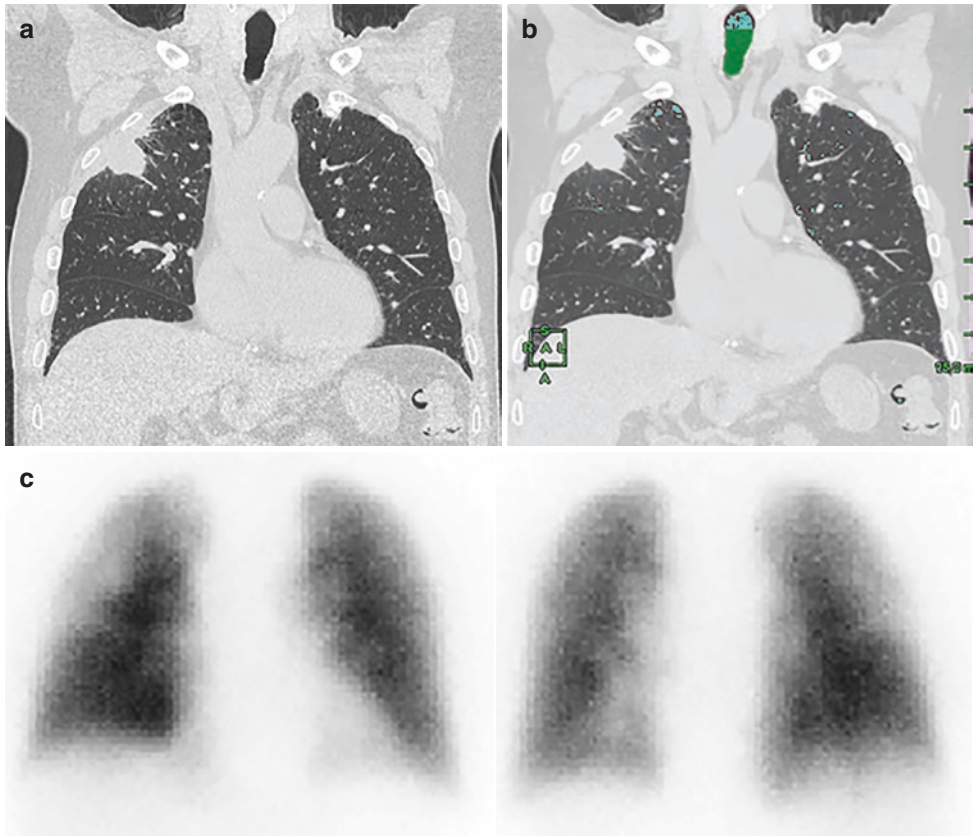


Fig. 4 A 62-year-old male patient with invasive adenocarcinoma in the right upper lobe. (**a**) Thin-section multiplanar reformatted (MPR) image at coronal plane demonstrates lung cancer in the right upper lobe. Bullae and pulmonary emphysema shows in the apex and peripheral lungs. (**b**) On quantitatively assessed thin-section MPR image, pulmonary emphysema is determined as sky blue pixels, whose CT numbers are equal to or less than -950HU. (**c**) Perfusion scan (*L* to *R*: anterior to posterior) shows heterogeneous uptakes of ^{99m}Tc-MAA within both lungs due to pulmonary emphysema and bullae. In addition, uptake within right upper lung field is decreased due to lung cancer. (**d**) Ventilation scan (*L* to *R*: anterior to posterior) demonstrates heterogeneous uptakes of ^{81m}Krypton (^{81m}Kr) within both lungs. Moreover, uptake within right upper lung field is decreased due to lung cancer. (**e**) Perfusion SPECT at coronal plane matched with thin-section MPR image shows homogeneous uptakes of ^{99m}Tc-MAA within both lungs. In addition, uptake within right upper lung field is reduced due to lung cancer. (**f**) Ventilation SPECT at coronal plane matched with thin-section MPR image demonstrates homogeneous uptakes of ^{81m}Kr within both lungs. Moreover, uptake within right upper lung field is reduced due to lung cancer. (**g**) Perfusion SPECT/CT at coronal plane matched with thin-section MPR image shows homogeneous uptakes of ^{99m}Tc-MAA within both lungs. In addition, uptake within right upper lung field is reduced due to lung cancer. (**h**) Ventilation SPECT/CT at coronal plane matched with thin-section MPR image demonstrates homogeneous uptakes of ^{81m}Kr within both lungs. Moreover, uptake within right upper lung field is reduced due to lung cancer. (**i**) Xe-CT obtained by DE-CT technique at same coronal plane shows homogeneous xenon-enhancement except lung cancer in both lungs. (**j**) Xe-CT obtained by subtraction technique at same coronal plane shows homogeneous xenon-enhancement except lung cancer in both lungs. In addition, subtraction technique demonstrates higher xenon-enhancement than DE-CT technique, and can more clearly visualize regional difference of xenon distribution as CT number change within lung than DE-CT technique

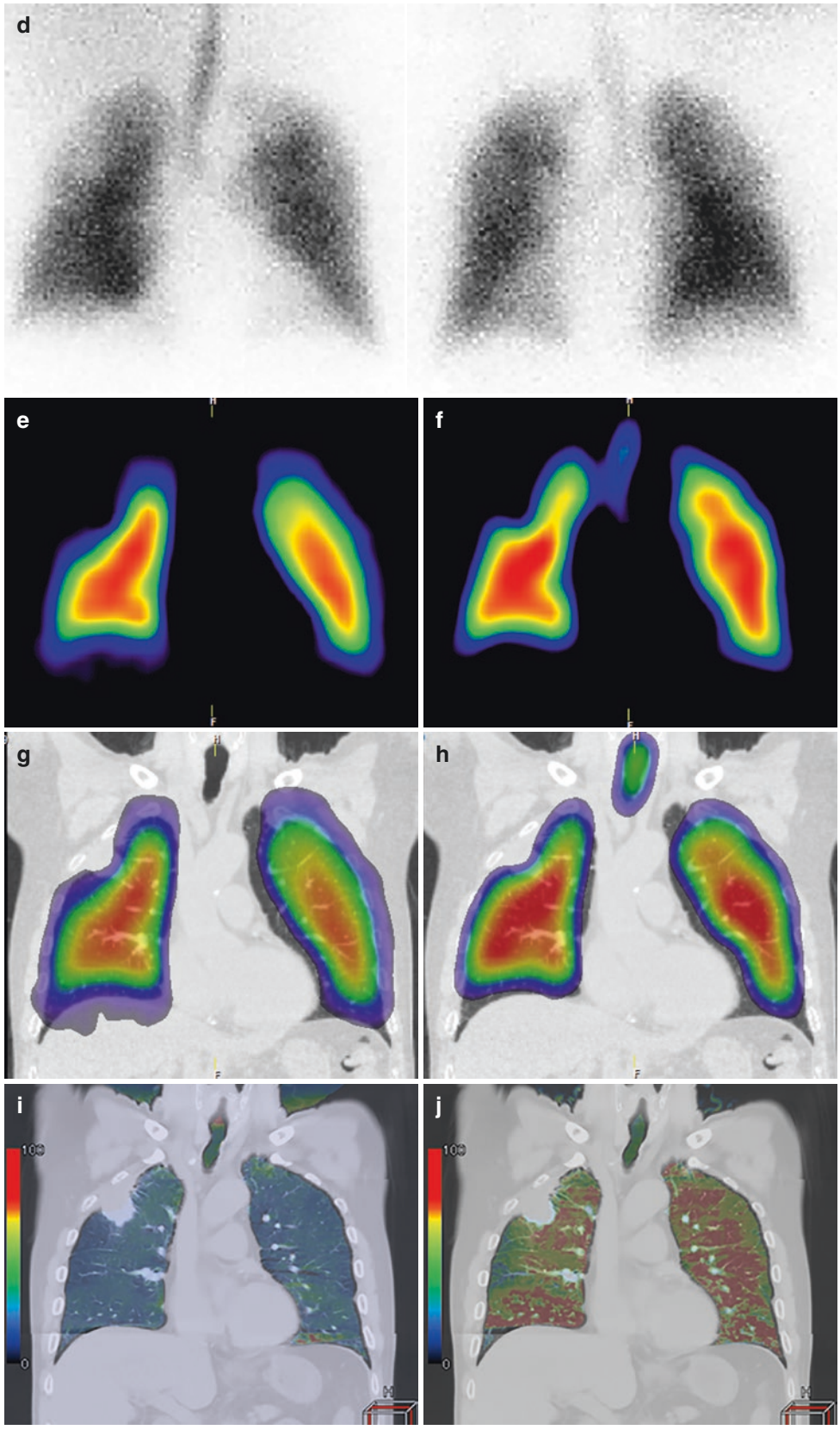


Fig. 4 (continued)

3 Pulmonary Functional Imaging for Differentiating Malignant from Benign Lesions

3.1 Background for Contrast Enhancement

3.1.1 Pathological Background

Unless a vascular supply is established during their early developmental stages, malignant lesions will not dramatically increase in size due to the balance between formation and loss of tumor cells. Initially, malignant tumors do not have the potential to generate vessels (Folkman 1992) and contain only minor and preexisting vessels encased by the tumor growth until new tumor vessels are developed resulting from stimulation of angiogenic factors, many of which have been identified so far. The following structural abnormality characteristics of tumor vessels have been reported in the literature (Less et al. 1991; Delorme and Knopp 1998): (1) caliber variations with dilated and narrowed segments in a single branch, (2) elongation and coiling, (3) nonhierarchical vascular networks, vascular rings, and sinusoids, (4) normal, pre-capillary architecture with dichotomous branching and reduced size and diameter of the higher-order branches, and (5) incomplete vascular walls without muscular layers, gaps in the endothelium, incomplete basal membranes, and direct tumor-to-blood contact.

The degree of abnormality of the vascular anatomy probably depends on whether structural maturation can keep pace with angiogenesis. Although anaplastic tumors present a chaotic network of irregular vessel-like spaces without mature or even recognizable elements, highly differentiated tumors have almost normal architectures. These structural abnormalities cause several functional impairments. First, the transcapillary permeability is increased, thus allowing extravasation of red blood cells, and this in turn causes hemoconcentration and greater viscous flow resistance. However, a different mechanism appears to be associated with vesico-vacuolar organelles, which help various substances pass across endothelial cells and may be involved in the transcapillary exchange of iodinated and gadolinium contrast agents. Moreover, vascular endothelial growth factor (VEGF) has been shown to increase vascular permeability and its overexpression is characteristic of malignant nodules and tumors (Dvorak et al. 1995). VEGF is also considered to be essential for angiogenesis since it performs a crucial role in the proliferation and migration of endothelial cells. Histologic evaluations of the relationship between microvessel density and VEGF expression have shown the utility of predicting metastases and consequent poor prognoses (Fontanini et al. 1997; Han et al. 2001; Tanaka et al. 2001; Mineo et al. 2004). In addition, a few reports have suggested that several dynamic CE-CT and/or MR indices reflecting microvascular density and VEGF expression may be useful for distinguishing malignant from benign nodules as well as for the diagnosis of metastatic lymph nodes (Fujimoto et al. 2003; Yi et al. 2004). The second functional impairment caused by structural abnormalities in hypervascular tumors is an increase in the total vascular cross-sectional area and thus a decrease in peripheral flow resistance. At the local areas of stasis within malignant nodules and tumors, these luminal irregularities may increase flow resistance regionally, depending on hemoconcentration and increased interstitial pressure (Delorme and Knopp 1998). The main factors contributing to interstitial hypertension are increased vascular permeability and lack of lymphatic drainage, while the interstitial space in tumors is usually three to five times larger than normal, which leads to compression of vessels inside the tumor (Delorme and Knopp 1998). The third impairment is due to the development of arteriovenous shunts, resulting in some of the blood bypassing the capillary bed within malignant tumor tissue. Consequently, despite a low global flow resistance and a high global blood flow, various parts of the tumor may be deprived of their blood supply. Tissue with only venovenous flow will be hypoxic due to slow flow velocity and low oxygen saturation of the blood supply (Delorme and Knopp 1998). The variety of pathogenetic and angiogenetic phenomena described here make it

clear why the effects of such functional mechanisms are not consistent throughout the tumor and may even be highly inconsistent, both spatially and temporally.

3.1.2 Pharmacokinetic Background

Iodinated and gadolinium (Gd) contrast media are generally used for not only conventional CE-CT and MR methods but also functional imaging methods for oncologic patients. While there are three tissue compartments, intravascular, interstitial, and intracellular spaces, in any organ (Jain and Gerlowski 1986; Dean et al. 1988), contrast enhancement of a given tissue is related to the degree of retention of contrast material in only the intravascular or extravascular spaces, or both, during a specific time frame. The characteristics of transport of these contrast media through the lung involve only intravascular and interstitial space because their designation of extravascular space does not differentiate interstitial from intracellular space. Therefore, neither of the two contrast media enters the intracellular space to a sufficient degree to be significant (Dean et al. 1988; Nordby et al. 1989), and reference will be made only to the interstitial space.

As for the pharmacokinetic background of contrast enhancement, pharmacokinetic analysis has clearly demonstrated that the degree of enhancement of CT number or signal intensity following contrast material injection depends on perfusion, relative blood volume, capillary surface area, and permeability as well as the volume of extravascular fluid in the tissue. Initial changes in the density-time course curve as well as in the signal intensity (or relative enhancement ratio)-time course curve during the first transit of contrast media are thought to be associated with a combination of perfusion (blood flow per unit of tissue), increase in the extracellular space for accumulation of contrast material, and permeability of capillaries (Littleton et al. 1990; Frouge et al. 1994; Sipkins et al. 1998; Ohno et al. 2002, 2008, 2011a, 2013). All these components have been reported to increase more markedly in malignant lesions than in benign lesions.

3.1.2.1 Normal Lung Tissue

While the wash-in of contrast medium into the intravascular space of the lung normally takes place through both the dual pulmonary and bronchial arterial systems, by far the major proportion, accounting for approximately 97% of the intravascular volume, is supplied by the pulmonary arterial circulation, while only 3% is derived from the systemic bronchial circulation (Littleton et al. 1990). Therefore, bronchial arterialization in normal lung contributes little to the wash-in concentration of contrast media.

On the other hand, washout from the intravascular space is uniquely different from that from other tissues due to the presence of a dual circulation. The major outflow in this case is through the pulmonary veins, which are supplied by the systemic system via the bronchopulmonary veins (Littleton et al. 1990).

The rate of outflow of contrast material from the intravascular space to the extravascular or interstitial spaces generally depends on temporal differences in the quantities of contrast media uptake typical of each tissue and its blood supply (Kormano and Dean 1976). On the other hand, washout from the interstitial space takes place via the lymphatic vessels and in the form of capillary backflow. Molecular transport across the interstitial space is realized through convection and diffusion, which are related to other physiologic parameters, such as capillary permeability, hydrostatic pressure, and temperature (Swabb et al. 1974; Kormano and Dean 1976; Nugent and Jain 1984; Jain and Gerlowski 1986; Littleton et al. 1990). The volumes of the intravascular and interstitial spaces in the normal lung are approximately equal, so that contrast medium transport produces a uniform background blush image throughout the entire lung, and the contrast media are excreted through the kidneys except for a small recirculating component.

3.1.2.2 Malignant and Benign Lesions

The time course of contrast media distribution through malignant lesions is entirely different from that through the normal lung and shows distinct changes in both the intravascular and interstitial spaces in response to the previously

described pathological changes. Wash-in to the intravascular space of malignant lesion is markedly reduced and the flow impeded, as can be expected in view of the abnormal structure of the blood supply as compared with that of benign lesions.

Generally speaking, primary lung cancers are mainly supplied by bronchial arteries with contributions derived to various degrees from pulmonary circulation (Milne 1967, 1976; Milne and Zerhouni 1987). In addition, findings of recent studies have demonstrated that the contribution from pulmonary circulation and the shift of the blood supply from the pulmonary capillary bed to the bronchial artery may be the result of histological changes from adenocarcinoma in situ to invasive adenocarcinoma (Milne and Zerhouni 1987). In metastatic lung lesions, on the other hand, the contribution by pulmonary circulation varies, up to 100% in some peripherally localized metastases (Milne 1967, 1976). While bronchial arteries of tumors increase in size and number to augment the bronchial flow by as much as 20–30%, this is not sufficient to compensate for the loss of blood normally supplied by pulmonary circulation (Milne 1967, 1976). Moreover, the structure of these tortuous ectatic vessels may result in relative obstruction of flow.

The microvasculature within primary malignant and benign lesions is also distinct and varied. A few investigators (Zieliński and Kulig 1984; Zieliński et al. 1984) have described eight different patterns of microvessels, including dense interlacing capillary beds containing ectatic and sinusoidal segments, varicose vessels, and interspersed venous lakes. The most luxuriant growth of vessels was found at the periphery, and other spatial variations occurring in abnormal vascular patterns were also noted, although these features depend on histological subtype (Zieliński and Kulig 1984; Zieliński et al. 1984). Furthermore, the intravascular space available in malignant or benign lesions is compromised by the fact that the contribution from the pulmonary artery system is usually reduced, and this deficit is only partially compensated for by the bronchial artery system despite an increase in the size and number of bronchial arteries (Littleton et al. 1990).

It has been suggested that washout from malignant or benign lesions is quite different. Washout from the intravascular space in normal lung takes place primarily through the pulmonary veins, but in malignant lesions, drainage via the pulmonary veins is reduced because of nonexistent or fewer pulmonary arteries. There are indications that the bronchopulmonary veins may be drained to some extent through the pulmonary veins. However, the major venous outflow occurs through the bronchial veins to the right atrium, although in benign nodules supply and washout may be mainly realized through bronchial circulation. Moreover, a markedly large interstitial space has been observed in some human and experimental malignant tumors (Littleton et al. 1990). It has been suggested that the most important feature of washout from the interstitial space of malignant or benign nodules or tumors is a near absence or significant reduction of lymphatic outflow.

Because of the impeded flow-through pattern in the intravascular and interstitial spaces, the stage would appear to be set for greater retention of contrast media in both types of nodules or tumors than in normal lung tissue (Littleton et al. 1990). The markedly reduced contribution to the intravascular space by wash-in from the pulmonary arteries is only partially compensated for by the increased supply from the bronchial artery system (Littleton et al. 1990). At the same time, the volume of microcirculation increases proportionately with reduced flow rates compared with those in normal lung, while washout is further impeded by the lack of a lymphatic components and relative obstruction in the bronchial venous system (Littleton et al. 1990). These features further contribute to retention of contrast media.

3.1.2.3 Inflammatory Lesions with High- and Low-Level Biological Activity

The transport of contrast media through an area of an acutely inflammatory lesion is also quite different from that in either normal lung tissue or malignant lesions. Acute inflammation has three major characteristics: (1) alterations in vascular

caliber leading to an increase in blood flow; (2) structural changes in the microvasculature allowing the plasma proteins and leukocytes to leave the circulation; and (3) emigration of the leukocytes from microcirculation and their accumulation at the focus of injury (Cotan et al. 1999). These processes increase blood flow and permeability of vessels and depend on the phase of the inflammatory process.

The intravascular space in actively infectious nodules or lesions is reduced. In most of the inflammatory pulmonary processes studied, diffuse thrombosis at the arteriolar level has been noted in the pulmonary circulation, so that the inflammatory process is actually sequestered from the pulmonary arterial circulation. The pathological finding consists of an increase in the size and number of bronchial arteries. In addition, previously reported studies of acute pneumonia and bronchiectasis have detected diminished or absent pulmonary blood flow or a definite dilatation of bronchial arteries and an increase in bronchopulmonary anastomoses (Liebow et al. 1949; Wagner Jr et al. 1964; Deffebach et al. 1987; Littleton et al. 1990). Injection of contrast media into pulmonary arteries was found to result in obliteration at the arteriolar level throughout the consolidated area or at certain levels within the nodule. Cavitating tuberculosis features dilated bronchial arteries surrounding the walls of the cavity, so that the microvasculature in acute inflammatory nodules is composed of a dense capillary network derived from the bronchial arterial system. Extensive thrombosis of pulmonary arteries takes place in the early stages of the disease. The bronchial arteries also supply other granulomatous lesions, including organizing pneumonia, with high-level biological activity, while, due to extensive thrombosis, pulmonary circulation cannot supply the inflammatory tissues. As a result, inflammatory nodules or granulomatous nodules, as well as organizing pneumonia with high- and low-level biological activity, receive a variety of contributions from pulmonary circulation depending on their inflammatory activities (Nugent and Jain 1984; Charan et al. 1985; Littleton et al. 1990). These pharmacokinetical changes result in a significant reduction in the volume of the intravascular space under inflammatory conditions as compared with that in normal lung because of the loss of pulmonary arterial circulation. This deficit is only partially compensated for in most inflammatory cases by an increase in the number and size of bronchial vessels. Flow of contrast media through the intravascular space in acutely inflammatory nodules and organizing pneumonia with high-level biological activity therefore takes place through relatively straight vessels with a normal configuration and is therefore probably not impeded.

As for the interstitial spaces of inflammatory nodules or granulomas, including organizing pneumonia with high- and low-level biological activity, washout of contrast media from the interstitial space is enhanced by an increase in interstitial flow based on convection and diffusion to dilated lymphatic vessels with marked acceleration of lymphatic flow (Littleton et al. 1990). Rapid diffusion occurs from the interstitial space back into the intravascular space, while outflow through pulmonary and bronchial veins is enhanced due to the increase in the number of anastomoses between the bronchial and pulmonary veins. This means that retention is unlikely for most inflammatory processes in the lung, a finding contrary to popular assumptions based on the observation of the highly vascular nature of these lesions (Littleton et al. 1990). Engorgement is introduced from the bronchial arterial system, but this vascular response does not compensate for the reduction in volume of the intravascular space occasioned by the loss of the pulmonary arterial flow. In addition, flow through both the intravascular and interstitial spaces is accelerated and enhanced by the active lymphatic flow, which is not seen in the normal lung and is absent from others (Littleton et al. 1990). Retention of contrast media in inflammatory nodules or granulomas including organizing pneumonia with high- and low-level biological activity thus approximates that of normal lung and depends on the inflammatory stage and pulmonary and bronchial circulatory conditions.

3.2 Dynamic CE-CT and Dynamic CE-MR Imaging Without Ultra-Short TE

Measurement of the degree of enhancement of pulmonary lesions on dynamic CE-CT has proved to be helpful for differentiation of malignant from benign lesions based on differences in vascularity, vasculatures, blood flow patterns, microvessel density, etc. (Swensen et al. 2000; Tateishi et al. 2002; Yi et al. 2004; Jeong et al. 2005; Cronin et al. 2008a, b; Ohno et al. 2008). Several studies using dynamic CE-CT for distinguishing malignant from benign nodules in both small and large patient populations have reported sensitivities ranging from 93 to 99%, specificities from 42 to 90%, and accuracies from 77 to 92% (Swensen et al. 2000; Yi et al. 2004; Jeong et al. 2005; Cronin et al. 2008a, b; Ohno et al. 2008) (Table 3). However, this method has not been widely used, probably because of the relatively high radiation dose.

Since the clinical application of Gd contrast media, dynamic CE-MR imaging is still being

Table 3 Comparison of solitary pulmonary nodule diagnosis using dynamic CE-CT, dynamic CE-MR imaging, dynamic first-pass contrast-enhanced perfusion area-detector CT and FDG-PET or PET/CT

Source	No. of cases	Methods	Parameters	SE (%)	SP (%)	AC (%)	PPV (%)	NPV (%)
Swensen et al. (2000)	356	Dynamic CT using single-detector CT	Net enhancement	98	58	77	68	96
Ohno et al. (2002)	58	Dynamic MRI using 3D radiofrequency spoiled GRE (3D fast field echo: 3D FFE) with ultra-short TE ≤ 2 ms	Maximum relative enhancement ratio	100	75	91	88	100
			Slope of enhancement ratio	100	85	95	93	100
Yi et al. (2004)	131	Dynamic CT using 4-detector CT	Net enhancement	99	54	78	71	97
Kim et al. (2004)	54	Multislice fast multiplanar spoiled GRE	Peak percentage increase in signal intensity	100	76	85	72	100
		Dynamic CT	Maximum density increment	89.5	68	76	63.0	91.3
Schaefer et al. (2004)	58	2D T1-weighted in-phase GRE	Maximum peak	96	88	92	90	95
			Slope	96	75	86	81	95
			Washout	52	100	75	100	65
Jeong et al. (2005)	107	Dynamic CT using 4- or 16-detector CT	Wash-in combined with washout	94–98	86–90	92	86–88	95–98
Zou et al. (2008)	68	T1-weighted turbo (fast) SE	Steepest slope in time–signal intensitycurve (%SI/s) combined withenhancement of signal intensity (%SI) at fourth minute on time–signal intensity curve (modified)	93	89	93	93	89
Cronin et al. (2008a)	N/A (meta-analysis)	Dynamic CT	N/A	93	76	N/A	80	95
		Dynamic MRI	N/A	99	62	N/A	83	95
		FDG-PET	N/A	99	67	N/A	91	90
		^{99m}Tc-depreotide SPECT	N/A	98	61	N/A	80	96

(continued)

Table 3 (continued)

Source	No. of cases	Methods	Parameters	SE (%)	SP (%)	AC (%)	PPV (%)	NPV (%)
Ohno et al. (2008)	175	Dynamic CT using 16-detector CT	Maximum enhancement combined with absolute loss of enhancement	93.4	42.0	80.7	83.0	67.7
			Net enhancement combined with absolute loss of enhancement	93.4	52.0	83.2	85.5	72.2
			Slope of enhancement combined with absolute loss of enhancement	93.4	48.0	82.2	84.5	70.6
			Maximum relative enhancement ratio	96.0	54.0	85.6	86.4	81.8
			Slope of enhancement ratio	96.0	64.0	88.1	89.0	84.2
		FDG-PET	SUV_{max}	93.4	54.0	83.7	86.0	73.0
Li et al. (2010)	77	Dynamic CT using 64-detector row CT	Perfusion	91.3	86.4	88.2	93.3	82.6
			Peak enhancement intensity	93.5	81.8	88.2	91.5	88.2
			Blood volume	93.5	90.9	92.6	95.6	92.6
Ohno et al. (2011a)	50	Dynamic first-pass perfusion ADCT	Perfusion using single-input maximum slope model	98	79	90	86	96
			Extraction fraction using Patlak plot model	88	82	86	86	84
			Blood volume ~~by~~ using Patlak plot model	86	54	72	71	78
		FDG-PET/CT	SUV_{max}	91	52	74	71	81
Ohno et al. (2013)	52	Dynamic first-pass perfusion ADCT	Total perfusion using dual-input maximum slope model	86.0	79.5	83.3	86.0	79.5
			Pulmonary arterial perfusion using dual-input maximum slope model	70.2	76.9	72.9	81.6	63.8
			Systemic arterial perfusion using dual-input maximum slope model	80.7	53.8	69.8	71.9	65.6
			Perfusion using single-input maximum slope model	64.9	69.2	66.7	75.5	57.4
		FDG-PET/CT	SUV_{max}	63.2	56.4	60.4	67.9	51.2
Ohno et al. (2015b)	230	Dynamic first-pass perfusion ADCT	Total perfusion using dual-input maximum slope model	92	71	84	83	86
			Pulmonary arterial perfusion using dual-input maximum slope model	90	26	65	66	63
			Systemic arterial perfusion using dual-input maximum slope model	89	26	65	65	61
			Nodule perfusion using single-input maximum slope model	91	28	67	66	67
		Dynamic MRI using 3D FFE with ultra-short TE $\leq$ 2 ms	Maximum relative enhancement ratio	92	49	76	74	81
			Slope of enhancement ratio	93	49	76	74	82
		FDG-PET/CT	SUV_{max}	89	31	67	67	65

SE sensitivity, SP, specificity, *AC* accuracy, *PPV* positive predictive value, *NPV* negative predictive value

recommended as useful for distinguishing malignant from benign nodules and tumors (Ohno et al. 2002, 2008; Kim et al. 2004; Schaefer et al. 2004; Kono et al. 2007; Cronin et al. 2008a, b; Zou et al. 2008). These authors have recommended dynamic MR imaging be used for two-dimensional (2D) or multislice (MS) T1-weighted SE or turbo SE sequences or for various types of 2D, MS or three-dimensional (3D) T1-weighted gradient-echo (GRE) sequences, and that enhancement patterns within nodules and/or parameters determined from signal intensity-time course curves be assessed visually. These curves represent the first transit and/or recirculation and washout of contrast media under breath holding or 8 min of repeated breath holding (Ohno et al. 2002, 2008; Kim et al. 2004; Schaefer et al. 2004; Kono et al. 2007; Cronin et al. 2008a, b; Zou et al. 2008). Based on these findings, together with other study results, one meta-analysis concluded in 2008 that there were no significant differences in diagnostic performance among dynamic CE-CT, dynamic CE-MR imaging using various sequences including two-dimensional (2D) or multislice (MS) T1-weighted SE or turbo SE sequences or various types of 2D, MS or three-dimensional (3D) T1-weighted gradient-echo (GRE) sequences, FDG-PET and technetium 99 m (^{99m}Tc) depreotide single-photon emission computed tomography (SPECT) (Cronin et al. 2008a). This study concluded that 45 studies, comprising 22 using FDG PET, 10 using dynamic CT, 7 using ^{99m}Tc-depreotide SPECT, and 6 using dynamic MR imaging met the inclusion criteria (Cronin et al. 2008a). Sensitivities, specificities, positive predictive values, negative predictive values, diagnostic odds ratios, and areas under the receiver operating characteristic (ROC) curve for the studies using FDG PET were, respectively, 0.95 (95% confidence interval [CI]: 0.93, 0.98), 0.82 (95% CI: 0.77, 0.88), 0.91 (95% CI: 0.88, 0.93), 0.90 (95% CI: 0.85, 0.94), 97.31 (95% CI: 6.26, 188.37), and 0.94 (95% CI: 0.83, 0.98); for dynamic CT they were 0.93 (95% CI: 0.88, 0.97), 0.76 (95% CI: 0.68, 0.97), 0.80 (95% CI: 0.74, 0.86), 0.95 (95% CI: 0.93, 0.98), 39.91 (95% CI: 1.21, 81.04), and 0.93 (95% CI: 0.81, 0.97); for ^{99m}Tc-depreotide SPECT, 0.95 (95% CI: 0.93, 0.97), 0.82 (95% CI: 0.78, 0.85), 0.90 (95% CI: 0.83, 0.97), 0.91 (95% CI: 0.84, 0.98), 84.50 (95% CI: 34.28, 134.73), and 0.94 (95% CI: 0.83, 0.98); and for dynamic MR imaging, 0.94 (95% CI: 0.91, 0.97), 0.79 (95% CI: 0.73, 0.86), 0.86 (95% CI: 0.83, 0.89), 0.93 (95% CI: 0.90, 0.96), 60.59 (95% CI: 5.56, 115.62), and 0.94 (95% CI: 0.83, 0.98) (Cronin et al. 2008a). These findings demonstrate there were no significant differences in diagnostic performance among the methods for differentiating malignant from benign lesions in routine clinical practice (Cronin et al. 2008a).

In view of the results shown in this section, pulmonary functional imaging is now considered to be a new and promising tool for distinguishing malignant from benign lesions in lung. In the following sections, the new techniques for pulmonary functional imaging using new CT and MR systems are introduced and discussed.

3.3 3D Dynamic First-Pass Contrast-Enhanced MR Imaging with Ultra-Short TE Equal to or Less Than 2.0 ms

Although dynamic MR imaging had been performed by using 2D or MS T1-weighted SE or turbo SE sequences or using 2D or MS 3D T1-weighted GRE sequences with various parametric setting obtained from various vendors, 3D dynamic first-pass CE-MR imaging with ultra-short TE equal to or less than 2.0 ms has been suggested as useful and applied since 2002 (Ohno et al. 2002, 2008). This procedure has also been used as 3D dynamic first-pass perfusion MR imaging for not only assessing lung parenchyma, pulmonary nodules, or mass perfusions but also for evaluation of therapeutic effect or recurrence in lung cancer patients treated with conservative therapy (Ohno et al. 2002, 2004b, c, 2005b, 2007c, d, 2008, 2010, 2012a).

Table 3 shows the reported capability of dynamic CE-MR imaging with ultra-short TE equal to or less than 2.0 ms for distinguishing malignant from benign nodules.

This technique was first introduced in 2002 (Ohno et al. 2002), and when used for the diagnosis of pulmonary nodules, sensitivity was 100%, specificity 75–85%, and accuracy 91–95% (Ohno et al. 2002).

Another study directly compared diagnostic performance among the above MR imaging technique, dynamic CE-CT, and positron emission tomography (PET) fused with CT (PET/CT) for the diagnosis or management of pulmonary nodules (Ohno et al. 2008). In addition, it may be more relevant to differentiate pulmonary nodules requiring further intervention and treatment (malignant nodules and benign nodules with high biological activities) from those requiring no further evaluation (benign nodules with low biological activities) rather than to differentiate between malignant and other nodules. When feasibility threshold values were adopted for nodule diagnosis, the specificity (64.0%) and accuracy (88.1%) of the slope of enhancement ratio were significantly higher than those of dynamic CT indices (specificity: 42–52%, $p < 0.05$; accuracy: 80.7–83.2, $p < 0.05$). In addition, accuracy of the slope of enhancement was also significantly higher than that for SUV_{max} (specificity: 54%, $p < 0.05$; accuracy: 83.7%, $p < 0.05$) (Ohno et al. 2008). When feasibility threshold values were adopted for nodule management in this study, the specificity (82.1%) and accuracy (93.6%) of the slope of the enhancement ratio were significantly higher than those of dynamic CT indices (specificity: 43.6–48.7%, $p < 0.05$; accuracy: 84.2–85.6, $p < 0.05$) and SUV_{max} (specificity: 66.7%, $p < 0.05$; accuracy: 88.6%, $p < 0.05$) (Ohno et al. 2008). As a result, 3D dynamic CE-perfusion MR imaging with ultra-short TE equal to or less than 2.0 ms is currently considered one of the most promising methods in this setting (Fig. 5 and 6). However, a subsequent study demonstrated that quantitatively assessed dynamic first-pass CE-perfusion area-detector CT (ADCT) had better potential than semiquantitative assessment using the aforementioned 3D dynamic CE-perfusion MR imaging method in the same setting (Ohno et al. 2015b). It can therefore be expected that further technical improvement will provide opportunities in the near future for improvement of the potential of quantitative evaluation of MR indices for more accurate diagnosis and management of pulmonary nodules similar to those attainable with dynamic first-pass CE-perfusion ADCT.

3.4 Dynamic First-Pass CE-Perfusion CT Using Multidetector-Row and Area-Detector CT Systems

Quantitative assessment of data obtained with dynamic CE-CT using a 320-detector row CT system with an area-detector system has been tried for assessing lung nodules and tumors to deal with a variety of clinical questions (Ohno et al. 2011a, 2013, 2015b; Yuan et al. 2013; Yabuuchi et al. 2018). Although CT with 64 or fewer detector rows can also be used for dynamic first-pass perfusion CT examination with and without the helical scan (i.e., shuttle scan) technique (Ng et al. 2006a, 2006b, 2010; Tacelli et al. 2010, 2013; Li et al. 2010; Mandeville et al. 2012), only an ADCT system is thought to be able to perform a real dynamic first-pass perfusion because this system encompasses an extensive range while obtaining isotropic volume data within a 16-cm area without helical scanning (Ohno et al. 2011a, 2013, 2015b; Yuan et al. 2013; Yabuuchi et al. 2018). Thus, whole-organ perfusion CT data can be obtained by means of continuous dynamic scanning without any risk of miss-registration, thus making it possible to evaluate pulmonary nodules or tumors qualitatively and/or quantitatively (Ohno et al. 2011a, 2013, 2015b; Yuan et al. 2013; Yabuuchi et al. 2018).

Several studies have tested dynamic first-pass perfusion CT for pulmonary nodules with 64- or 320-detector row CT, and Table 3 shows the findings for their diagnostic performance (Li et al. 2010; Ohno et al. 2011a, 2013, 2015b), with sensitivity ranging from 64.9% to 98%, specificity from 26% to 90.9%, and accuracy from 65% to 92.6% (Li et al. 2010; Ohno et al. 2011a, 2013, 2015b). In addition, a few studies directly compared the diagnostic performance of quantitatively assessed dynamic first-pass CE-ADCT

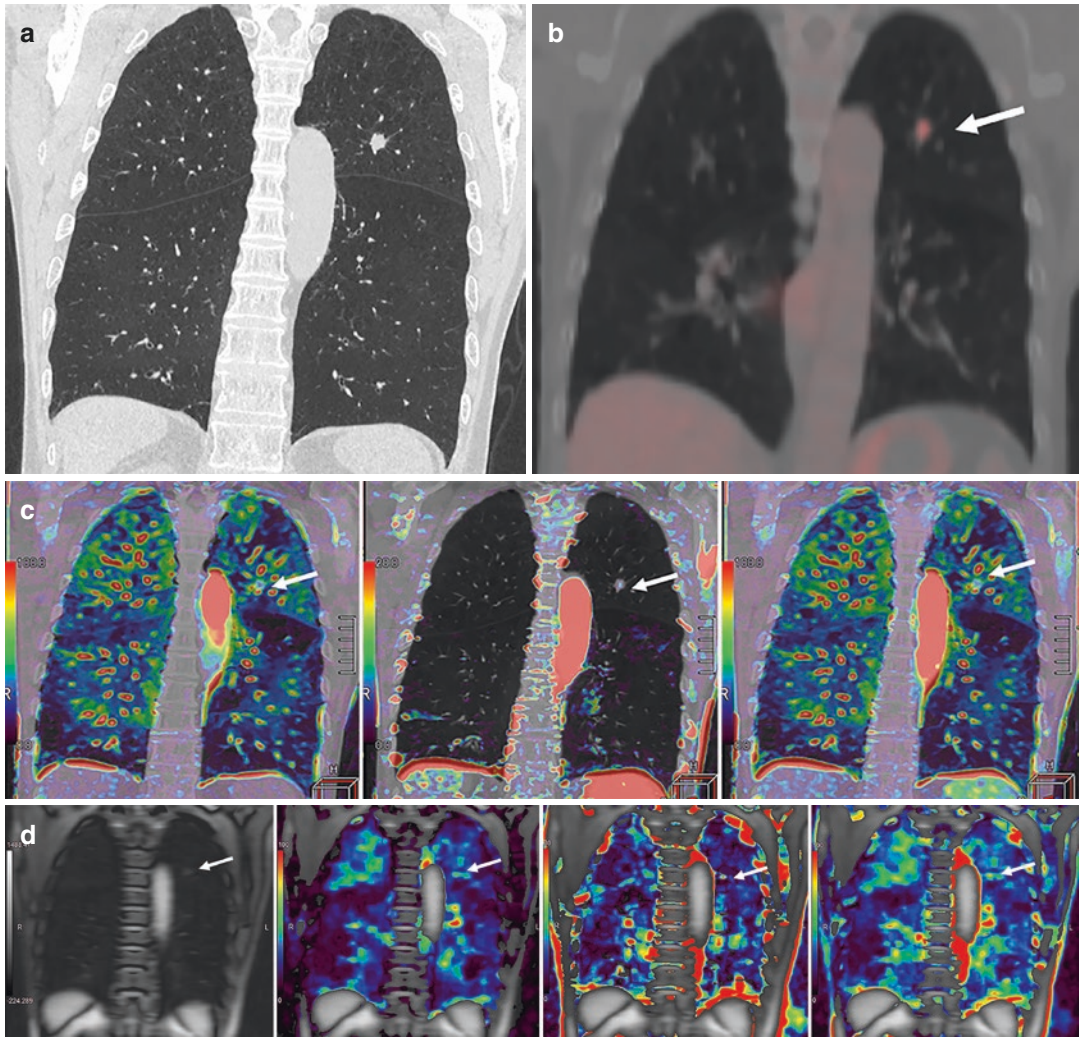


Fig. 5 A 75-year-old male patient with invasive adenocarcinoma. (**a**) Thin-section multiplanar reformatted (MPR) image at coronal plane demonstrates a nodule (arrow) in the left upper lobe. The longest nodule diameter was measured as 10 mm. The nodule was diagnosed as invasive adenocarcinoma. (**b**) FDG-PET/CT shows a nodule (arrow) in the left upper lobe. SUV_{max} was determined as 2.3, and considered as benign nodule such as organizing pneumonia. This case was false-negative case on PET/CT. (**c**) (*L* to *R*: pulmonary arterial, systemic arterial, and total perfusion maps generated from dynamic first-pass CE-perfusion ADCT analyzed by dual-input maximum slope method): Each perfusion parameter of nodule (arrow) on each perfusion parameter map was evaluated as follows: pulmonary arterial perfusion, 32 ml/100 ml/min, 10 ml/100 ml/min, and 42 ml/100 ml/min. On each perfusion parameter map evaluation, the nodule was considered as malignant nodule, and this case was also determined as true-positive case. (**d**) (*L* to *R*: original MR image at 0 s and pulmonary arterial, systemic arterial, and total perfusion maps generated from dynamic first-pass CE-perfusion MR imaging with ultra-short TE equal to or less than 2.0 ms analyzed by dual-input maximum slope method): Each perfusion parameter of nodule (arrow) on each perfusion parameter map was evaluated as follows: pulmonary arterial perfusion, 32 ml/100 ml/min, 18 ml/100 ml/min, and 50 ml/100 ml/min. This case was considered as malignant nodule on each perfusion parameter map evaluation, and determined as true-positive case on each perfusion assessment

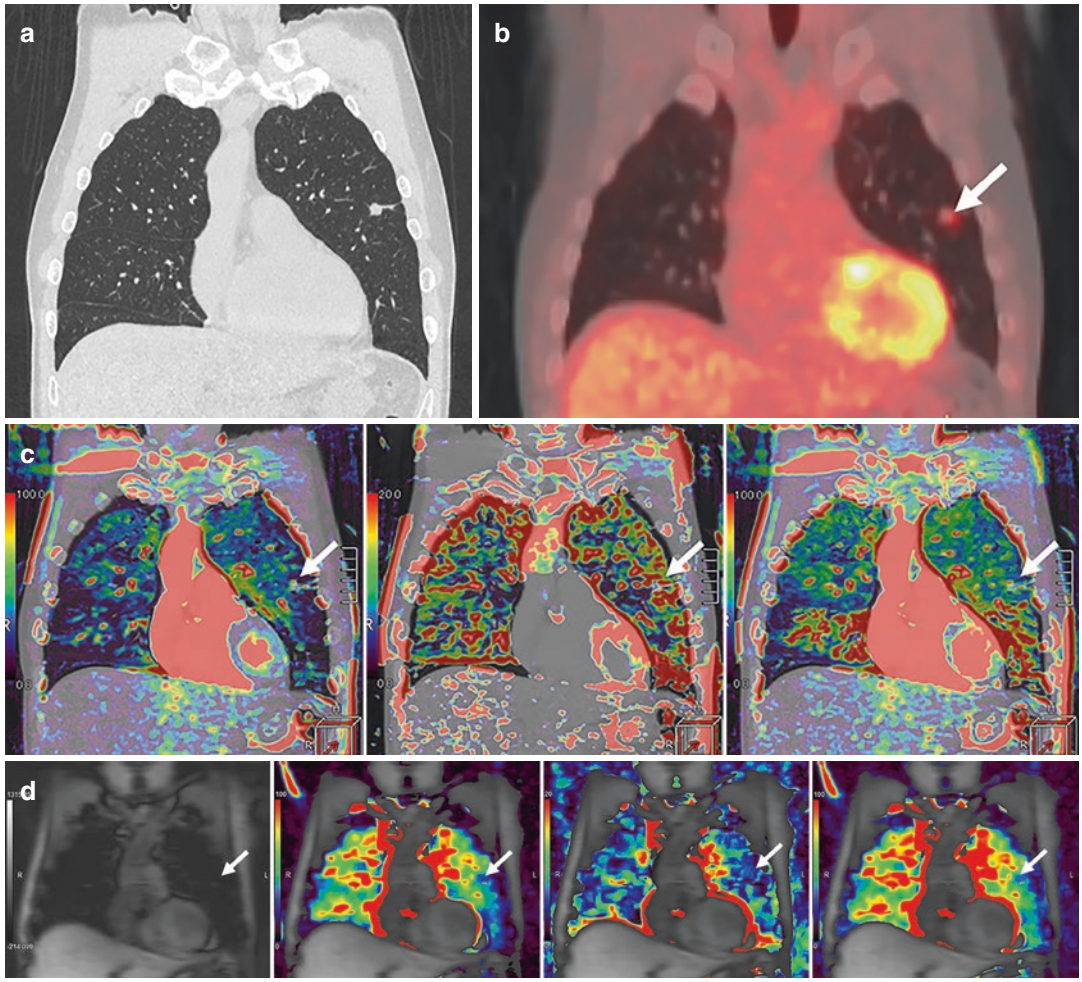


Fig. 6 A 73-year-old male patient with organizing pneumonia. (**a**) Thin-section multiplanar reformatted (MPR) image at coronal plane demonstrates a nodule (arrow) with pleural tag in the left upper lobe. The longest nodule diameter was measured as 10 mm. The nodule was diagnosed as invasive adenocarcinoma. (**b**) FDG-PET/CT shows a nodule (arrow) in the left upper lobe. SUV_{max} was determined as 3.0, and considered as malignant nodule. This case was false-negative case on PET/CT. (**c**) (*L* to *R*: pulmonary arterial, systemic arterial, and total perfusion maps generated from dynamic first-pass CE-perfusion ADCT analyzed by dual-input maximum slope method): Each perfusion parameter of nodule (arrow) on each perfusion parameter map was evaluated as follows: pulmonary arterial perfusion, 19 ml/100 ml/min, 6 ml/100 ml/min, and 25 ml/100 ml/min. The nodule was considered as benign nodule on systemic arterial and total perfusion map evaluations, although pulmonary arterial perfusion map assessment suggested as malignant nodule. This case was determined as true-negative on systemic arterial and total perfusion map evaluations, although pulmonary arterial perfusion map assessment was evaluated as false-positive case. (**d**) (*L* to *R*: original MR image at 0 s and pulmonary arterial, systemic arterial, and total perfusion maps generated from dynamic first-pass CE-perfusion MR imaging with ultra-short TE equal to or less than 2.0 ms analyzed by dual-input maximum slope method): Each perfusion parameter of nodule (arrow) on each perfusion parameter map was evaluated as follows: pulmonary arterial perfusion, 13 ml/100 ml/min, 5 ml/100 ml/min, and 18 ml/100 ml/min. The nodule was considered as benign nodule on systemic arterial and total perfusion map evaluations, although pulmonary arterial perfusion map assessment suggested as malignant nodule. This case was determined as true-negative on systemic arterial and total perfusion map evaluations, although pulmonary arterial perfusion map assessment was evaluated as false-positive case

with that of PET/CT (Ohno et al. 2011a, 2013, 2015b) and reported that quantitative assessment of nodule perfusion by single- or dual-input maximum slope models as well as of extraction fraction by means of the Patlak plot model were significantly more specific and accurate than SUV_{max} evaluation by means of PET/CT, although other models also warrant testing in this setting (Ohno et al. 2011a, 2013).

Most recently, the findings of a comparison among dynamic first-pass CE-perfusion ADCT, dynamic CE-MR imaging with ultra-short TE equal to or less than 2.0 ms, and PET/CT suggest that dynamic first-pass CE-ADCT is more useful than PET/CT and can also be considered to be potentially slightly superior to dynamic CE-MR imaging with ultra-short TE in this setting (Ohno et al. 2015b) (Fig. 5 and 6). When used for distinguishing malignant from benign nodules, area-detector CT indices obtained by means of the dual-input maximum slope method were compared with those obtained with other methods, and it was found that the specificity and/or accuracy of total perfusion obtained from dynamic first-pass contrast-enhanced ADCT was significantly higher than that of others obtained from dynamic first-pass contrast-enhanced MR indices and SUV_{max} ($p < 0.05$). Moreover, a comparison between dynamic MR indices and other indices showed that the specificity and accuracy of both dynamic MR indices were significantly better than those of SUV_{max} and other ADCT indices except for total perfusion ($p < 0.05$) (Ohno et al. 2015b). On the other hand, a comparison of the capability for differentiating between nodules necessitating aggressive intervention and treatment from those requiring only follow-up examination, the specificity and/or accuracy or total perfusion was significantly better than those of the others ($p < 0.05$). In addition, a comparison of dynamic MR indices with SUV_{max} demonstrated that the specificity and accuracy of both dynamic MR indices were significantly better than those of SUV_{max} ($p < 0.05$) (Ohno et al. 2015b). Therefore, dynamic first-pass CE-perfusion ADCT may be the most accurate and clinically practicable method for differentiating malignant from benign nodules and nodules requiring further intervention and treatment from those requiring no further evaluation.

In addition to being used for differentiation of malignant from benign pulmonary nodules, dynamic first-pass CE-perfusion ADCT was also employed for distinguishing metastatic from nonmetastatic lymph nodes and N-stage assessment of NSCLC patients (Ohno et al. 2017b). Area under the ROC curve (Az) values of systemic arterial perfusion (Az = 0.89), permeability surface (Az = 0.78), and SUV_{max} (Az = 0.85) were significantly larger than the Az values of total perfusion (Az = 0.70, $p < 0.05$) and distribution volume (Az = 0.55, $p < 0.05$) (Ohno et al. 2017b). A comparison between N-stage assessments for each index and final diagnosis showed that agreement for systemic arterial perfusion calculated by using the dual-input maximum slope model was substantial ($\kappa = 0.70$, $p < 0.0001$), and agreement for SUV_{max} was moderate ($\kappa = 0.60$, $p < 0.0001$) (Ohno et al. 2017b). As for differentiation of malignant from benign lesions, dynamic first-pass CE-perfusion ADCT proved to be as useful as FDG PET/CT for the differentiation of metastatic from nonmetastatic lymph nodes and assessment of N stage for NSCLC patients. In addition, the previously mentioned clinical questions are considered to constitute useful indications for pulmonary functional imaging of patients with pulmonary nodules or masses as well as NSCLC at this time point.

4 Prediction of Treatment Outcome and Recurrence for Lung Cancer Patients Treated with Conservative Therapy

The standard evaluation of treatment response in the oncologic field is based on the response evaluation criteria in solid tumors (RECIST), which evaluate changes in tumor size on CT (Eisenhauer et al. 2009). As previously reported for FDG-PET/CT, several studies have reported that perfu-

sion CT is a promising tool for monitoring and evaluating early response for lung cancer patients or predicting prognosis after chemotherapy (Ng et al. 2006a, b, 2010; Tacelli et al. 2010, 2013; Ohno et al. 2016b, 2017a; Yabuuchi et al. 2018). In addition, it has been suggested that dynamic CE-MR imaging including the use of perfusion MR and diffusion weighted imaging (DWI) are effective for treatment response prediction or evaluation for thoracic oncology patients (Ohno et al. 2005b, 2012b; Giesel et al. 2006, 2008; de Langen et al. 2011; Yabuuchi et al. 2011). It has further been suggested that dynamic CE-perfusion CT and CE-MR imaging using the perfusion imaging technique are effective for assessment of tumor angiogenesis (Ohno et al. 2014, 2015a, 2018a, b), so that it has been speculated that the quantitative and/or semiquantitative parameters provided by this technique can be useful for prediction of prognosis for adenocarcinomas (Ohno et al. 2004c) and of treatment response and recurrence after conservative therapy for lung cancer patients (Ohno et al. 2005b, 2016b, 2017a; Yabuuchi et al. 2018).

4.1 Dynamic CE-MR Imaging with Ultra-Short TE Equal to or Less Than 2.0 ms

Although dynamic CE-MR imaging has been mostly tested for its capability for prediction of the effect of various conservative therapies on oncologic patients (Ohno et al. 2005b; Giesel et al. 2006, 2008; de Langen et al. 2011), a few investigators used this technique for evaluation of therapeutic effect and recurrence in lung cancer patients for the same clinical purposes (Ohno et al. 2005b; de Langen et al. 2011) (Table 4). Moreover, to examine the applicability of the technique to pulmonary functional imaging, a study was conducted to evaluate the utility of dynamic CE-MR imaging with ultra-short TE equal to or less than 2.0 ms for the prediction of recurrence in lung cancer patients treated with conservative therapy (Ohno et al. 2005b) (Fig. 7). A total of 114 consecutive patients with NSCLC underwent dynamic CE-MR imaging after chemoradiotherapy and calculation of dynamic MR indexes for recurrence prediction in NSCLC patients. The findings of this study showed that the maximum relative enhancement ratio and the slope of enhancement for the local control group were significantly lower than those for the local failure group ($p < 0.05$). Using 0.08/s as the threshold value for the slope of enhancement, the sensitivity and specificity for differentiation between the two groups were 90.9% and 91.3%, respectively. When the slope of enhancement was used for estimation of prognosis after therapy, the mean survival period for the group with a slope of enhancement ≤0.08/s was significantly longer than that seen in the group with a slope of enhancement >0.08/s ($p < 0.0001$). Therefore, dynamic CE-MR imaging using 3D dynamic CE-perfusion MR imaging potentially is of prognostic value for NSCLC patients after chemoradiotherapy, but further evaluations are warranted to demonstrate its clinical relevance in this setting.

4.2 Dynamic First-Pass CE-Perfusion CT and ADCT

Dynamic CE-CT analyzed by means of perfusion software has been recommended during recent years as useful for quantitative assessment or prediction of treatment response by NSCLC patients treated with chemo- or chemoradiotherapy (Ng et al. 2006a, b, 2010; Tacelli et al. 2010, 2013). However, the temporal resolution of this procedure might be not appropriate for quantitative assessment of tumor perfusion on CT because it was shown that real pulmonary perfusion could be evaluated by using a quantitative perfusion analysis model introduced in 2000, which uses an electron-beam CT with higher temporal resolution and sharper bolus profile of contrast media injection (Schoepf et al. 2000). Such developments have made it possible to clinically apply dynamic first-pass CE-perfusion ADCT examination since 2011 (Ohno et al. 2011a, 2013, 2015a, 2016b, 2017a, b; Yabuuchi et al. 2018).

Table 4 Recurrence prediction and therapeutic effect prediction capabilities for dynamic contrast-enhanced perfusion MRI and CT

Source	No. of cases	Method	Parameters	Differentiation between responders and nonresponders			Disease (or progression) free survival (mean ± standard deviation, months)		Overall survival (mean ± standard deviation, months)	
				SE (%)	SP (%)	AC (%)	Responder	Nonresponder	Responder	Nonresponder
Ohno et al. (2005a)	114	Dynamic MRI using 3D FFE with ultra-short TE ≤ 2 ms	Maximum relative enhancement ratio	54.5	91.3	84.2	N/A	N/A	N/A	N/A
			Slope of enhancement	90.9	91.3	91.2			26.1 ± 2.0	14.8 ± 1.2
de Langen et al. (2011)	44	Dynamic MRI using 3D T1-weightd GRE with different flip angle	Heterogeneity of tumor K^{trans} distribution (K^{trans} SD)	N/A	N/A	N/A	7.0	2.3	N/A	N/A
		$H2^{15}O$-PET	Perfusion (F)				12.5	2.9		
		FDG-PET	SUV				9.7	2.8		
Ohno et al. (2016b)	66	Dynamic first-pass CE-perfusion ADCT	Total perfusion using dual-input maximum slope model	88.2	84.4	86.4	15.6 ± 0.8	10.4 ± 1.1	25.3 ± 1.2	18.7 ± 1.4
			Pulmonary arterial perfusion using dual-input maximum slope model	41.2	96.9	68.2	13.2 ± 0.9	12.7 ± 0.9	24.6 ± 1.7	22.8 ± 1.5
			Systemic arterial perfusion using dual-input maximum slope model	79.4	80.6	78.8	15.2 ± 0.9	11.0 ± 1.1	24.6 ± 1.3	22.0 ± 2.0
			Perfusion using single-input maximum slope model	41.2	96.9	68.2	13.6 ± 0.9	12.8 ± 0.9	23.8 ± 1.8	23.2 ± 1.5
			Distribution volume using Patlak plot model	94.1	68.8	81.8	14.5 ± 0.8	10.7 ± 1.5	24.1 ± 1.3	19.6 ± 1.7
Ohno et al. (2017a)	53	Dynamic first-pass CE-perfusion ADCT	Total perfusion using dual-input maximum slope model	80	71.4	80	18.4 ± 1.5	9.3 ± 0.8	36.6 ± 2.7	23.3 ± 2.9
			Pulmonary arterial perfusion using dual-input maximum slope model	66	67.9	70.4	N/A		N/A	
			Systemic arterial perfusion using dual-input maximum slope model	88	78.6	88	20.3 ± 1.4	8.8 ± 0.7	38.8 ± 3.5	25.8 ± 2.2
			Perfusion using single-input maximum slope model	40	85.7	82.8	N/A		N/A	
		PET/CT	SUV_{max}	92	67.9	90.5	18.8 ± 1.4	9.0 ± 0.8	35.0 ± 2.3	27.5 ± 2.6

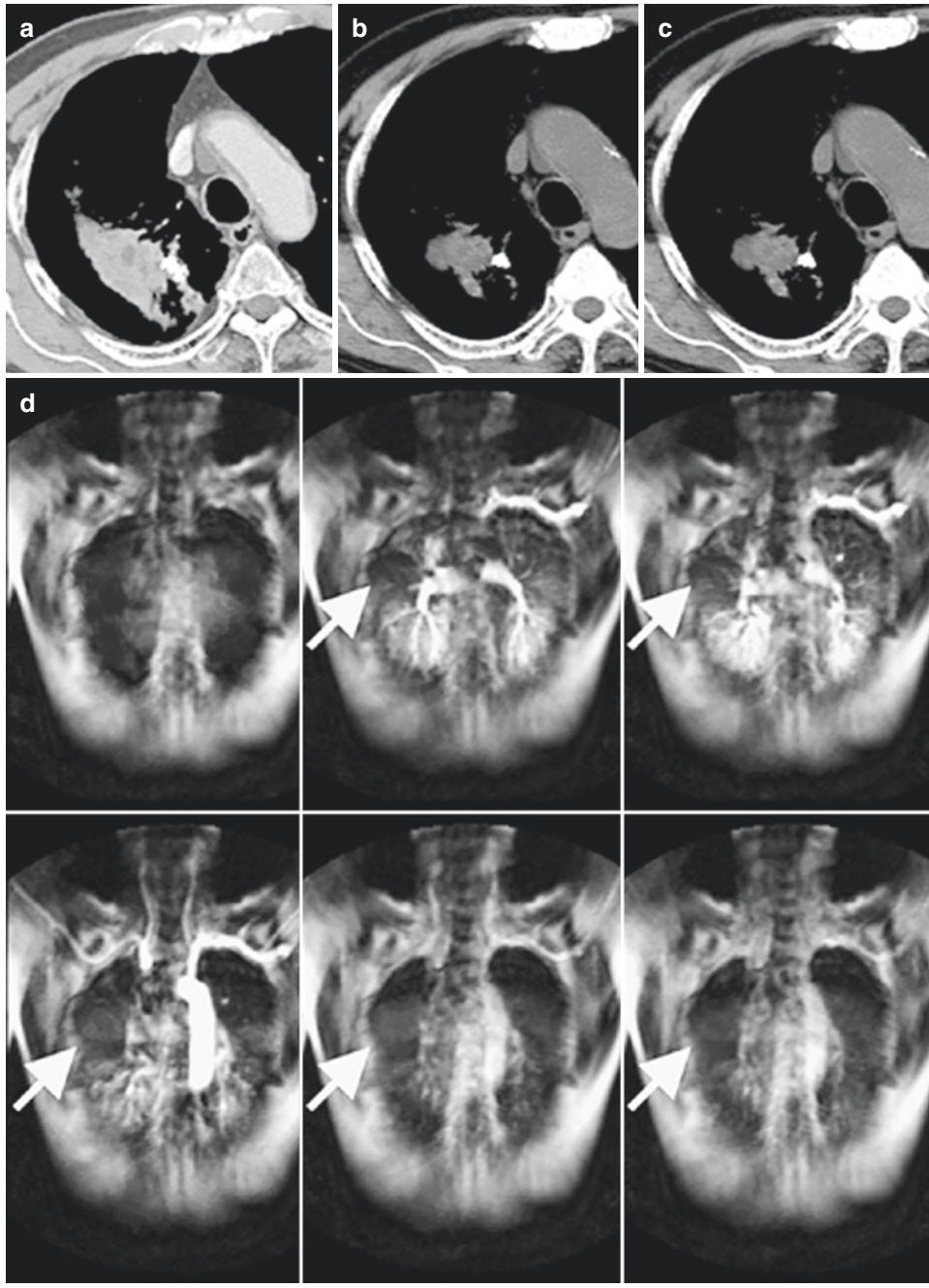


Fig. 7 A 68-year-old male patient with adenocarcinoma (T2N2M0: stage IIIA) (Permission obtained from Ohno et al. 2005b). (**a**) Chest CT before therapy shows a mass with calcification in the right lung. The greatest diameter of the mass is 4.5 cm. (**b**) On chest CT after therapy, the greatest diameter of the mass is 3.5 cm, and the therapeutic effect is determined as NC by WHO criteria. (**c**) A post-therapy chest CT after 60 months shows no recurrence of the primary lesion. Distant failure is not demonstrated in the follow-up examinations after 60 months. Therefore, this patient was assigned to the local control group. The survival period of this patient was 65 months. (**d**) On dynamic MRI (first line left to right: t = 0 s; t = 4.4 s; t = 6.6 s; second line left to right: t = 8.8 s, t = 9.9 s, t = 16.5 s), the tumor (arrow) demonstrates a perfusion defect in the pulmonary circulation phase, and little tumor enhancement in the systemic circulation phase. The maximum relative enhancement ratio is 0.15, and the slope of enhancement is 0.019/s. This case was evaluated as local control group

The radiation dose used for this technique can be reduced while maintaining the accuracy of quantitative perfusion matrix evaluations for NSCLC patients (Ohno et al. 2016c). This has resulted in reports by a few investigators of the success of quantitative prediction of the therapeutic effect of conservative therapy for NSCLC patients during recent years (Ohno et al. 2016b, 2017a; Yabuuchi et al. 2018) (Table 4) (Fig. 8).

One study (Ohno et al. 2017a) described an appropriate mathematical model for use in this setting. This study involved 53 consecutive Stage IIIB NSCLC patients treated with chemoradiotherapy, who underwent dynamic first-pass CE-perfusion ADCT. For each targeted lesion, the pulmonary arterial and systemic arterial perfusions as well as total perfusion were calculated with the dual-input maximum slope method, permeability surface and distribution volume with the Patlak plot method, and tumor perfusion with the single-input maximum slope method. In addition, each patient also underwent PET/CT for assessment of SUV_{max} at the same lesion. A stepwise regression test was then performed, the findings of which demonstrated that therapeutic effect ($r^2 = 0.63$, $p = 0.01$) was significantly affected by the following three factors in order of magnitude of impact: systemic arterial perfusion, total perfusion, and SUV_{max}. In addition, Kaplan-Meier analyses demonstrated that mean progression-free survival was significantly different for the responder and nonresponder groups as determined with the aid of the feasible threshold values for systemic arterial perfusion ($p = 0.008$) and SUV_{max} ($p = 0.03$). Mean overall survival was also significantly different for the responder and nonresponder groups as determined with the feasible threshold values for total perfusion ($p = 0.003$) and systemic arterial perfusion ($p = 0.04$). Further investigation showed that dynamic first-pass CE-perfusion ADCT and PET/CT are useful for treatment response prediction for NSCLC patients treated with chemoradiotherapy. Moreover, the dual-input maximum slope model rather than the single-input maximum slope or Patlak Plot models is better for assessment of tumor perfusion in this setting (Ohno et al. 2016b, 2017a).

In contrast to the abovementioned study, Yabuuchi et al. (2018) used the same CT technique with the same mathematical method for a comparison of the capability for early prediction of the therapeutic effect for NSCLC patients of bevacizumab treatment, two-agent platinum-based therapy without bevacizumab, and other non-bevacizumab treatment groups. In this study, 66 patients with stage III or IV NSCLC who underwent chemotherapy were enrolled. Patients were separated into three groups: those who underwent chemotherapy with bevacizumab ($n = 20$), two-agent platinum-based therapy without bevacizumab ($n = 25$), and other non- bevacizumab treatments ($n = 21$). Before treatment, pulmonary artery perfusion (PAP) and bronchial artery perfusion (BAP) of the tumors were calculated with the dual-input maximum slope model and statistically assessed. After two courses of chemotherapy in the bevacizumab treatment group, pretreatment BAP was independently correlated with the posttreatment tumor reduction rate ($p = 0.006$). Pretreatment BAP was found to be significantly associated with a high cumulative risk of death ($p = 0.006$) and disease progression after chemotherapy ($p = 0.015$). Pretreatment PAP and clinical parameters were determined not to be significant predictors of therapeutic effect or prognosis for the three treatment groups. The authors concluded that pretreatment BAP derived from dual-input perfusion CT seems to be a promising tool for enhancing the prediction of responses to chemotherapy with bevacizumab for patients with NSCLC (Yabuuchi et al. 2018).

In consideration of the findings of the abovementioned studies, quantitatively assessed dynamic CE-perfusion ADCT can be considered to be one of the new radiological and functional methods for prediction of treatment response and recurrence in NSCLC patients treated with conservative therapy. In addition, further improvements in the clinical application of CT systems, contrast media injection protocols, and software for analyses can be expected to provide clinicians with the tools for more accurate evaluation of treatment of lung cancer patients in the near future.

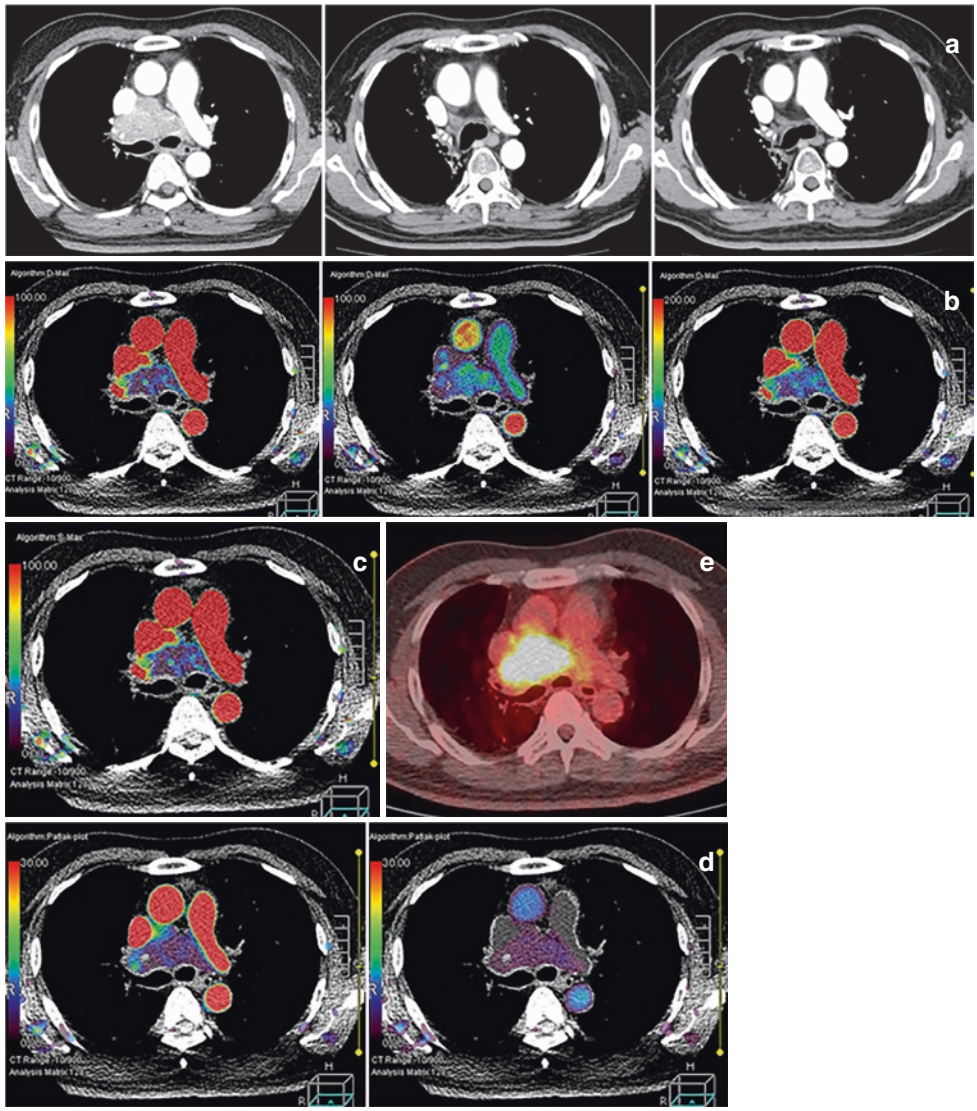


Fig. 8 Perfusion CT and PET/CT in Lung cancer after chemoradiotherapy from EJR. 1-year-old male patient with squamous cell carcinoma treated with chemoradiotherapy and assessed as PR. Progression-free and overall survivals were 24 and 32 months. (Permission obtained from Ohno et al. 2017a). (**a**) Contrast-enhanced CT (*L* to *R*: CT images obtained at pretreatment, posttreatment, and 24 months after treatment) shows lung cancer in mediastinum. This case was assessed as PR by RECIST ver.1.1. (**b**) Dynamic first-pass CE-perfusion ADCT assessed with the dual-input maximum slope method provides perfusion maps (*L* to *R*: pulmonary arterial perfusion, systemic arterial perfusion, and total perfusion maps) for the same targeted lesion. Pulmonary arterial perfusion, systemic arterial perfusion, and total perfusion were 19.9 ml/100 ml/min, 40.1 ml/100 ml/min, and 61.1 ml/100 ml/min, respectively. This case was assessed as a RECIST-responder in the (CR + PR) group for each index, and as true-positive. (**c**) Dynamic first-pass CE-perfusion ADCT assessed with the single-input maximum slope method provides a perfusion map at same targeted lesion. Perfusion was assessed as 29.3 ml/100 ml/min, and the patient was categorized as a RECIST-responder in the (CR + PR) group. This case was assessed as true-positive on the basis of perfusion. (**d**) Dynamic first-pass CE-perfusion ADCT assessed with the Patlak plot method provides perfusion maps (*L* to *R*: distribution volume for permeability surface maps) for the same targeted lesion. Distribution volume and permeability surface were determined as 4.2 ml/100 ml and 3.2 ml/100 ml/min, respectively. (**e**): PET/CT demonstrates high uptake of FDG, and SUV_{max} was evaluated as 3.0. This case was evaluated as a RECIST-responder in the (CR + PR) group, and assessed as true-positive

5 Conclusion

Since the middle 1990s, pulmonary functional imaging methods have been developed, tested, and demonstrated for their clinical relevance, mainly for chronic obstructive pulmonary diseases, airway diseases, and pulmonary vascular diseases. Lung cancer imaging has mainly progressed by the use of morphological assessment on thin-section CT and glucose metabolism evaluation on FDG-PET or PET/CT. As the only perfusion studies using nuclear medicine with planar imaging, SPECT and SPECT/CT have played a role in functional evaluation of lung cancer patients. In the last couple of decades, however, advances in CT and MR system development have made it possible to apply several functional imaging methods used for lung cancer patients to answer several clinical questions. Several investigators are currently engaged in promoting further progress in pulmonary functional imaging by means of not only CT but also MR imaging and nuclear medicine studies with new PET tracers. Such progress is believed to further demonstrate the clinical relevance of these methods and result in improved management of lung cancer patients.

References

Beckles MA, Spiro SG, Colice GL, Rudd RM, American College of Chest Physicians (2003) The physiologic evaluation of patients with lung cancer being considered for resectional surgery. Chest 123(1 Suppl):105S–114S

Bohlsen D, Talakic E, Fritz GA, Quehenberger F, Tillich M, Schoellnast H (2016) First pass dual input volume CT-perfusion of lung lesions: The influence of the CT-value range settings on the perfusion values of benign and malignant entities. Eur J Radiol 85(6):1109–1114

Bolliger CT, Jordan P, Solèr M, Stulz P, Grädel E, Skarvan K, Elsasser S, Gonon M, Wyser C, Tamm M et al (1995) Exercise capacity as a predictor of postoperative complications in lung resection candidates. Am J Respir Crit Care Med 151(5):1472–1480

Bolliger CT, Jordan P, Solèr M, Stulz P, Tamm M, Wyser C, Gonon M, Perruchoud AP (1996) Pulmonary function and exercise capacity after lung resection. Eur Respir J 9(3):415–421

Bolliger CT, Gückel C, Engel H, Stöhr S, Wyser CP, Schoetzau A, Habicht J, Solèr M, Tamm M, Perruchoud AP (2002) Prediction of functional reserves after lung resection: comparison between quantitative computed tomography, scintigraphy, and anatomy. Respiration 69(6):482–489

British Thoracic Society; Society of Cardiothoracic Surgeons of Great Britain and Ireland Working Party (2001) BTS guidelines: guidelines on the selection of patients with lung cancer for surgery. Thorax 56(2):89–108

Brunelli A, Charloux A, Bolliger CT, Rocco G, Sculier JP, Varela G, Licker M, Ferguson MK, Faivre-Finn C, Huber RM, Clini EM, Win T, De Ruysscher D, Goldman L, European Respiratory Society and European Society of Thoracic Surgeons Joint Task Force on Fitness for Radical Therapy (2009) ERS/ESTS clinical guidelines on fitness for radical therapy in lung cancer patients (surgery and chemoradiotherapy). Eur Respir J 34(1):17–41

Brunelli A, Kim AW, Berger KI, Addrizzo-Harris DJ (2013) Physiologic evaluation of the patient with lung cancer being considered for resectional surgery: Diagnosis and management of lung cancer, 3rd ed: American College of Chest Physicians evidence-based clinical practice guidelines. Chest 143(5 Suppl):e166S–e190S

Chae EJ, Song JW, Seo JB, Krauss B, Jang YM, Song KS (2008) Clinical utility of dual-energy CT in the evaluation of solitary pulmonary nodules: initial experience. Radiology 249(2):671–681

Chae EJ, Song JW, Krauss B, Song KS, Lee CW, Lee HJ, Seo JB (2010) Dual-energy computed tomography characterization of solitary pulmonary nodules. J Thorac Imaging 25(4):301–310

Chae EJ, Kim N, Seo JB, Park JY, Song JW, Lee HJ, Hwang HJ, Lim C, Chang YJ, Kim YH (2013) Prediction of postoperative lung function in patients undergoing lung resection: dual-energy perfusion computed tomography versus perfusion scintigraphy. Investig Radiol 48(8):622–627

Charan NB, Turk GM, Dhand R (1985) The role of bronchial circulation in lung abscess. Am Rev Respir Dis 131(1):121–124

Charloux A, Brunelli A, Bolliger CT, Rocco G, Sculier JP, Varela G, Licker M, Ferguson MK, Faivre-Finn C, Huber RM, Clini EM, Win T, De Ruysscher D, Goldman L, European Respiratory Society and European Society of Thoracic Surgeons Joint Task Force on Fitness for Radical Therapy (2009) Lung function evaluation before surgery in lung cancer patients: how are recent advances put into practice? A survey among members of the European Society of Thoracic Surgeons (ESTS) and of the Thoracic Oncology Section of the European Respiratory Society (ERS). Interact Cardiovasc Thorac Surg 9(6):925–931

Chiro GD, Brooks RA, Kessler RM, Johnston GS, Jones AE, Herdt JR, Sheridan WT (1979) Tissue signatures with dual-energy computed tomography. Radiology 131(2):521–523

Ciliberto M, Kishida Y, Seki S, Yoshikawa T, Ohno Y (2018) Update of MR Imaging for Evaluation of Lung Cancer. Radiol Clin N Am 56(3):437–469

Colice GL, Shafazand S, Griffin JP, Keenan R, Bolliger CT, American College of Chest Physicians (2007) Physiologic evaluation of the patient with lung cancer being considered for resectional surgery: ACCP evidenced-based clinical practice guidelines (2nd edition). Chest 132(3 Suppl):161S–177S

Cotan RS, Kumar V, Collins TC (1999) Acute and chronic inflammation. In: Cotran RS, Kumar V, Collins T, Robbins SL (eds) Robbins pathologic basis of disease, 6th edn. Saunders, Philadelphia, PA, pp 50–88

Cronin P, Dwamena BA, Kelly AM, Carlos RC (2008a) Solitary pulmonary nodules: meta-analytic comparison of cross-sectional imaging modalities for diagnosis of malignancy. Radiology 246(3): 772–782

Cronin P, Dwamena BA, Kelly AM, Bernstein SJ, Carlos RC (2008b) Solitary pulmonary nodules and masses: a meta-analysis of the diagnostic utility of alternative imaging tests. Eur Radiol 18(9):1840–1856

David EA, Marshall MB (2012) Physiologic evaluation of lung resection candidates. Thorac Surg Clin 22(1):47–54

Dean PB, Niemi P, Kivisaari L, Kormano M (1988) Comparative pharmacokinetics of gadolinium DTPA and gadolinium chloride. Investig Radiol 23(Suppl 1):S258–S260

Deffebach ME, Lakshminarayan S, Kirk W, Butler J (1987) Bronchial circulation and cyclooxygenase products in acute lung injury. J Appl Physiol (1985) 63(3):1083–1088

Delorme S, Knopp MV (1998) Non-invasive vascular imaging: assessing tumour vascularity. Eur Radiol 18(4):517–527

Dvorak HF, Brown LF, Detmar M, Dvorak AM (1995) Vascular permeability factor/vascular endothelial growth factor, microvascular hyperpermeability, and angiogenesis. Am J Pathol 146(5):1029–1039

Eisenhauer EA, Therasse P, Bogaerts J, Schwartz LH, Sargent D, Ford R, Dancey J, Arbuck S, Gwyther S, Mooney M, Rubinstein L, Shankar L, Dodd L, Kaplan R, Lacombe D, Verweij J (2009) New response evaluation criteria in solid tumours: revised RECIST guideline (version 1.1). Eur J Cancer 45(2):228–247

Flohr TG, McCollough CH, Bruder H, Petersilka M, Gruber K, Süss C, Grasruck M, Stierstorfer K, Krauss B, Raupach R, Primak AN, Küttner A, Achenbach S, Becker C, Kopp A, Ohnesorge BM (2006) First performance evaluation of a dual-source CT (DSCT) system. Eur Radiol 16(2):256–266

Folkman J (1992) The role of angiogenesis in tumor growth. Semin Cancer Biol 3(2):65–71

Fontanini G, Vignati S, Boldrini L, Chinè S, Silvestri V, Lucchi M, Mussi A, Angeletti CA, Bevilacqua G (1997) Vascular endothelial growth factor is associated with neovascularization and influences progression of non-small cell lung carcinoma. Clin Cancer Res 3(6):861–865

Frouge C, Guinebretière JM, Contesso G, Di Paola R, Bléry M (1994) Correlation between contrast enhancement in dynamic magnetic resonance imaging of the breast and tumor angiogenesis. Investig Radiol 29(12):1043–1049

Fujimoto K, Abe T, Müller NL, Terasaki H, Kato S, Sadohara J, Kono R, Edamitsu O, Ishitake T, Hayashi A, Rikimaru T, Hayabuchi N (2003) Small peripheral pulmonary carcinomas evaluated with dynamic MR imaging: correlation with tumor vascularity and prognosis. Radiology 227(3):786–793

Genant HK, Boyd D (1977) Quantitative bone mineral analysis using dual energy computed tomography. Investig Radiol 12(6):545–551

Giesel FL, Bischoff H, von Tengg-Kobligk H, Weber MA, Zechmann CM, Kauczor HU, Knopp MV (2006) Dynamic contrast-enhanced MRI of malignant pleural mesothelioma: a feasibility study of noninvasive assessment, therapeutic follow-up, and possible predictor of improved outcome. Chest 129(6):1570–1576

Giesel FL, Choyke PL, Mehndiratta A, Zechmann CM, von Tengg-Kobligk H, Kayser K, Bischoff H, Hintze C, Delorme S, Weber MA, Essig M, Kauczor HU, Knopp MV (2008) Pharmacokinetic analysis of malignant pleural mesothelioma-initial results of tumor microcirculation and its correlation to microvessel density (CD-34). Acad Radiol 15(5):563–570

Giordano A, Calcagni ML, Meduri G, Valente S, Galli G (1997) Perfusion lung scintigraphy for the prediction of postlobectomy residual pulmonary function. Chest 111(6):1542–1547

Han H, Silverman JF, Santucci TS, Macherey RS, d'Amato TA, Tung MY, Weyant RJ, Landreneau RJ (2001) Vascular endothelial growth factor expression in stage I non-small cell lung cancer correlates with neoangiogenesis and a poor prognosis. Ann Surg Oncol 8(1):72–79

Hirose Y, Imaeda T, Doi H, Kokubo M, Sakai S, Hirose H (1993) Lung perfusion SPECT in predicting postoperative pulmonary function in lung cancer. Ann Nucl Med 7(2):123–126

Horeweg N, Scholten ET, de Jong PA, van der Aalst CM, Weenink C, Lammers JW, Nackaerts K, Vliegenthart R, ten Haaf K, Yousaf-Khan UA, Heuvelmans MA, Thunnissen E, Oudkerk M, Mali W, de Koning HJ (2014) Detection of lung cancer through low-dose CT screening (NELSON): a prespecified analysis of screening test performance and interval cancers. Lancet Oncol 15(12):1342–1350

Howington JA, Blum MG, Chang AC, Balekian AA, Murthy SC (2013) Treatment of stage I and II non-small cell lung cancer: Diagnosis and management of lung cancer, 3rd ed: American College of Chest Physicians evidence-based clinical practice guidelines. Chest 143(5 Suppl):e278S–e313S

Infante M, Cavuto S, Lutman FR, Passera E, Chiarenza M, Chiesa G, Brambilla G, Angeli E, Aranzulla G, Chiti A, Scorsetti M, Navarria P, Cavina R, Ciccarelli M, Roncalli M, Destro A, Bottoni E, Voulaz E, Errico V, Ferraroli G, Finocchiaro G, Toschi L, Santoro A, Alloisio M, DANTE Study Group (2015) Long-term follow-up results of the DANTE trial, a randomized study of lung cancer screening with spiral

computed tomography. Am J Respir Crit Care Med 191(10):1166–1175

Iwasawa T, Saito K, Ogawa N, Ishiwa N, Kurihara H (2002) Prediction of postoperative pulmonary function using perfusion magnetic resonance imaging of the lung. J Magn Reson Imaging 15(6):685–692

Jain RK, Gerlowski LE (1986) Extravascular transport in normal and tumor tissues. Crit Rev Oncol Hematol 5(2):115–170

Jeong YJ, Lee KS, Jeong SY, Chung MJ, Shim SS, Kim H, Kwon OJ, Kim S (2005) Solitary pulmonary nodule: characterization with combined wash-in and washout features at dynamic multi-detector row CT. Radiology 237(2):675–683

Jett JR, Schild SE, Kesler KA, Kalemkerian GP (2013) Treatment of small cell lung cancer: diagnosis and management of lung cancer, 3rd ed: American College of Chest Physicians evidence-based clinical practice guidelines. Chest 143(5 Suppl):e400S–e419S

Kazerooni EA, Armstrong MR, Amorosa JK, Hernandez D, Liebscher LA, Nath H, McNitt-Gray MF, Stern EJ, Wilcox PA (2015) ACR CT accreditation program and the lung cancer screening program designation. J Am Coll Radiol 12(1):38–42

Kazerooni EA, Armstrong MR, Amorosa JK, Hernandez D, Liebscher LA, Nath H, McNitt-Gray MF, Stern EJ, Wilcox PA (2016) ACR CT accreditation program and the lung cancer screening program designation. J Am Coll Radiol 13(2 Suppl):R30–R34

Kim JH, Kim HJ, Lee KH, Kim KH, Lee HL (2004) Solitary pulmonary nodules: a comparative study evaluated with contrast-enhanced dynamic MR imaging and CT. J Comput Assist Tomogr 28(6):766–775

Kim HS, Lee KS, Ohno Y, van Beek EJ, Biederer J (2015) PET/CT versus MRI for diagnosis, staging, and follow-up of lung cancer. J Magn Reson Imaging 42(2):247–260

Ko JP, Brandman S, Stember J, Naidich DP (2012) Dual-energy computed tomography: concepts, performance, and thoracic applications. J Thorac Imaging 27(1):7–22

Kono R, Fujimoto K, Terasaki H, Müller NL, Kato S, Sadohara J, Hayabuchi N, Takamori S (2007) Dynamic MRI of solitary pulmonary nodules: comparison of enhancement patterns of malignant and benign small peripheral lung lesions. AJR Am J Roentgenol 188(1):26–36

Kormano M, Dean PB (1976) Extravascular contrast material: the major component of contrast enhancement. Radiology 121(2):379–382

Koyama H, Ohno Y, Seki S, Nishio M, Yoshikawa T, Matsumoto S, Sugimura K (2013) Magnetic resonance imaging for lung cancer. J Thorac Imaging 28(3):138–150

Kozower BD, Larner JM, Detterbeck FC, Jones DR (2013) Special treatment issues in non-small cell lung cancer: Diagnosis and management of lung cancer, 3rd ed: American College of Chest Physicians evidence-based clinical practice guidelines. Chest 143(5 Suppl):e369S–e399S

Kristersson S, Lindell SE, Svanberg L (1972) Prediction of pulmonary function loss due to pneumonectomy using 133 Xe-radiospirometry. Chest 62(6):694–698

de Langen AJ, van den Boogaart V, Lubberink M, Backes WH, Marcus JT, van Tinteren H, Pruim J, Brans B, Leffers P, Dingemans AM, Smit EF, Groen HJ, Hoekstra OS (2011) Monitoring response to antiangiogenic therapy in non-small cell lung cancer using imaging markers derived from PET and dynamic contrast-enhanced MRI. J Nucl Med 52(1):48–55

Less JR, Skalak TC, Sevick EM, Jain RK (1991) Microvascular architecture in a mammary carcinoma: branching patterns and vessel dimensions. Cancer Res 51(1):265–273

Li Y, Yang ZG, Chen TW, Yu JQ, Sun JY, Chen HJ (2010) First-pass perfusion imaging of solitary pulmonary nodules with 64-detector row CT: comparison of perfusion parameters of malignant and benign lesions. Br J Radiol 83(993):785–789

Liebow AA, Hales MR, Lindskog GE (1949) Enlargement of the bronchial arteries, and their anastomoses with the pulmonary arteries in bronchiectasis. Am J Pathol 25(2):211–231

Lipscomb DJ, Pride NB (1977) Ventilation and perfusion scans in the preoperative assessment of bronchial carcinoma. Thorax 32(6):720–725

Littleton JT, Durizch ML, Moeller G, Herbert DE (1990) Pulmonary masses: contrast enhancement. Radiology 177(3):861–871

Lu GM, Zhao Y, Zhang LJ, Schoepf UJ (2012) Dual-energy CT of the lung. AJR Am J Roentgenol 199(5 Suppl):S40–S53

MacMahon H, Austin JH, Gamsu G, Herold CJ, Jett JR, Naidich DP, Patz EF Jr, Swensen SJ, Fleischner Society (2005) Guidelines for management of small pulmonary nodules detected on CT scans: a statement from the Fleischner Society. Radiology 237(2):395–400

MacMahon H, Naidich DP, Goo JM, Lee KS, Leung ANC, Mayo JR, Mehta AC, Ohno Y, Powell CA, Prokop M, Rubin GD, Schaefer-Prokop CM, Travis WD, Van Schil PE, Bankier AA (2017) Guidelines for management of incidental pulmonary nodules detected on CT images: from the Fleischner Society 2017. Radiology 284(1):228–243

Mandeville HC, Ng QS, Daley FM, Barber PR, Pierce G, Finch J, Burke M, Bell A, Townsend ER, Kozarski R, Vojnovic B, Hoskin PJ, Goh V (2012) Operable non-small cell lung cancer: correlation of volumetric helical dynamic contrast-enhanced CT parameters with immunohistochemical markers of tumor hypoxia. Radiology 264(2):581–589

Markos J, Mullan BP, Hillman DR, Musk AW, Antico VF, Lovegrove FT, Carter MJ, Finucane KE (1989) Preoperative assessment as a predictor of mortality and morbidity after lung resection. Am Rev Respir Dis 139(4):902–910

Micke P, Faldum A, Metz T, Beeh KM, Bittinger F, Hengstler JG, Buhl R (2002) Staging small cell lung cancer: veterans Administration Lung Study Group versus International Association for the Study of Lung

Cancer—what limits limited disease? Lung Cancer 37(3):271–276
Millner MR, McDavid WD, Waggener RG, Dennis MJ, Payne WH, Sank VJ (1979) Extraction of information from CT scans at different energies. Med Phys 6(1):70–71
Milne EN (1967) Circulation of primary and metastatic pulmonary neoplasms. A postmortem microarteriographic study. Am J Roentgenol Radium Therapy, Nucl Med 100(3):603–619
Milne EN (1976) Pulmonary metastases: vascular supply and diagnosis. Int J Radiat Oncol Biol Phys 1(7–8):739–742
Milne EN, Zerhouni EA (1987) Blood supply of pulmonary metastases. J Thorac Imaging 2(4):15–23
Mineo TC, Ambrogi V, Baldi A, Rabitti C, Bollero P, Vincenzi B, Tonini G (2004) Prognostic impact of VEGF, CD31, CD34, and CD105 expression and tumour vessel invasion after radical surgery for IB-IIA non-small cell lung cancer. J Clin Pathol 57(6):591–597
Naidich DP, Bankier AA, MacMahon H, Schaefer-Prokop CM, Pistolesi M, Goo JM, Macchiarini P, Crapo JD, Herold CJ, Austin JH, Travis WD (2013) Recommendations for the management of subsolid pulmonary nodules detected at CT: a statement from the Fleischner Society. Radiology 266(1): 304–137
National Lung Screening Trial Research Team, Aberle DR, Adams AM, Berg CD, Black WC, Clapp JD, Fagerstrom RM, Gareen IF, Gatsonis C, Marcus PM, Sicks JD (2011) Reduced lung-cancer mortality with low-dose computed tomographic screening. N Engl J Med 365(5):395–409
Nawa T, Nakagawa T, Mizoue T, Kusano S, Chonan T, Hayashihara K, Suito T, Endo K (2012) A decrease in lung cancer mortality following the introduction of low-dose chest CT screening in Hitachi, Japan. Lung Cancer 78(3):225–228
Ng QS, Goh V, Fichte H, Klotz E, Fernie P, Saunders MI, Hoskin PJ, Padhani AR (2006a) Lung cancer perfusion at multi-detector row CT: reproducibility of whole tumor quantitative measurements. Radiology 239(2):547–553
Ng QS, Goh V, Klotz E, Fichte H, Saunders MI, Hoskin PJ, Padhani AR (2006b) Quantitative assessment of lung cancer perfusion using MDCT: does measurement reproducibility improve with greater tumor volume coverage? AJR Am J Roentgenol 187(4):1079–1084
Ng QS, Goh V, Milner J, Sundin J, Wellsted D, Saunders MI, Hoskin PJ (2010) Quantitative helical dynamic contrast enhanced computed tomography assessment of the spatial variation in whole tumour blood volume with radiotherapy in lung cancer. Lung Cancer 69(1):71–76
Nordby A, Tvedt KE, Halgunset J, Kopstad G, Haugen OA (1989) Incorporation of contrast media in cultured cells. Investig Radiol 24(9):703–170
Nugent LJ, Jain RK (1984) Extravascular diffusion in normal and neoplastic tissues. Cancer Res 44(1):238–244
Ohno Y (2014) New applications of magnetic resonance imaging for thoracic oncology. Semin Respir Crit Care Med 35(1):27–40
Ohno Y, Hatabu H, Takenaka D, Adachi S, Kono M, Sugimura K (2002) Solitary pulmonary nodules: potential role of dynamic MR imaging in management initial experience. Radiology 224(2):503–511
Ohno Y, Hatabu H, Higashino T, Takenaka D, Watanabe H, Nishimura Y, Yoshimura M, Sugimura K (2004a) Dynamic perfusion MRI versus perfusion scintigraphy: prediction of postoperative lung function in patients with lung cancer. AJR Am J Roentgenol 182(1):73–78
Ohno Y, Hatabu H, Murase K, Higashino T, Kawamitsu H, Watanabe H, Takenaka D, Fujii M, Sugimura K (2004b) Quantitative assessment of regional pulmonary perfusion in the entire lung using three-dimensional ultrafast dynamic contrast-enhanced magnetic resonance imaging: preliminary experience in 40 subjects. J Magn Reson Imaging 20(3): 353–365
Ohno Y, Hatabu H, Takenaka D, Uematsu H, Ohbayashi C, Higashino T, Nogami M, Yoshimura M, Fujii M, Sugimura K (2004c) Dynamic MR imaging: value of differentiating subtypes of peripheral small adenocarcinoma of the lung. Eur J Radiol 52(2):144–150
Ohno Y, Hatabu H, Higashino T, Nogami M, Takenaka D, Watanabe H, Van Cauteren M, Yoshimura M, Satouchi M, Nishimura Y, Sugimura K (2005a) Oxygen-enhanced MR imaging: correlation with postsurgical lung function in patients with lung cancer. Radiology 236(2):704–711
Ohno Y, Nogami M, Higashino T, Takenaka D, Matsumoto S, Hatabu H, Sugimura K (2005b) Prognostic value of dynamic MR imaging for non-small-cell lung cancer patients after chemoradiotherapy. J Magn Reson Imaging 21(6):775–783
Ohno Y, Koyama H, Takenaka D, Nogami M, Kotani Y, Nishimura Y, Yoshimura M, Yoshikawa T, Sugimura K (2007a) Coregistered ventilation and perfusion SPECT using krypton-81m and Tc-99m-labeled macroaggregated albumin with multislice CT utility for prediction of postoperative lung function in non-small cell lung cancer patients. Acad Radiol 14(7):830–838
Ohno Y, Koyama H, Nogami M, Takenaka D, Matsumoto S, Yoshimura M, Kotani Y, Sugimura K (2007b) Postoperative lung function in lung cancer patients: comparative analysis of predictive capability of MRI, CT, and SPECT. AJR Am J Roentgenol 189(2):400–408
Ohno Y, Murase K, Higashino T, Nogami M, Koyama H, Takenaka D, Kawamitu H, Matsumoto S, Hatabu H, Sugimura K (2007c) Assessment of bolus injection protocol with appropriate concentration for quantitative assessment of pulmonary perfusion by dynamic contrast-enhanced MR imaging. J Magn Reson Imaging 25(1):55–65
Ohno Y, Hatabu H, Murase K, Higashino T, Nogami M, Yoshikawa T, Sugimura K (2007d) Primary pulmonary hypertension: 3D dynamic perfusion MRI for

quantitative analysis of regional pulmonary perfusion. AJR Am J Roentgenol 188(1):48–56

Ohno Y, Koyama H, Takenaka D, Nogami M, Maniwa Y, Nishimura Y, Ohbayashi C, Sugimura K (2008) Dynamic MRI, dynamic multidetector-row computed tomography (MDCT), and coregistered 2-[fluorine-18]-fluoro-2-deoxy-D-glucose-positron emission tomography (FDG-PET)/CT: comparative study of capability for management of pulmonary nodules. J Magn Reson Imaging 27(6):1284–1295

Ohno Y, Koyama H, Matsumoto K, Onishi Y, Nogami M, Takenaka D, Yoshikawa T, Matsumoto S, Sugimura K (2010) Dynamic MR perfusion imaging: capability for quantitative assessment of disease extent and prediction of outcome for patients with acute pulmonary thromboembolism. J Magn Reson Imaging 31(5):1081–1090

Ohno Y, Koyama H, Matsumoto K, Onishi Y, Takenaka D, Fujisawa Y, Yoshikawa T, Konishi M, Maniwa Y, Nishimura Y, Ito T, Sugimura K (2011a) Differentiation of malignant and benign pulmonary nodules with quantitative first-pass 320-detector row perfusion CT versus FDG PET/CT. Radiology 2258(2):599–609

Ohno Y, Koyama H, Nogami M, Takenaka D, Onishi Y, Matsumoto K, Matsumoto S, Maniwa Y, Yoshimura M, Nishimura Y, Sugimura K (2011b) State-of-the-art radiological techniques improve the assessment of postoperative lung function in patients with non-small cell lung cancer. Eur J Radiol 77(1):97–104

Ohno Y, Koyama H, Yoshikawa T, Nishio M, Matsumoto S, Matsumoto K, Aoyama N, Nogami M, Murase K, Sugimura K (2012a) Contrast-enhanced multidetector-row computed tomography vs time-resolved magnetic resonance angiography vs. contrast-enhanced perfusion MRI: assessment of treatment response by patients with inoperable chronic thromboembolic pulmonary hypertension. J Magn Reson Imaging 36(3):612–623

Ohno Y, Koyama H, Yoshikawa T, Matsumoto K, Aoyama N, Onishi Y, Sugimura K (2012b) Diffusion-weighted MRI versus 18F-FDG PET/CT: performance as predictors of tumor treatment response and patient survival in patients with non-small cell lung cancer receiving chemoradiotherapy. AJR Am J Roentgenol 198(1):75–82

Ohno Y, Nishio M, Koyama H, Fujisawa Y, Yoshikawa T, Matsumoto S, Sugimura K (2013) Comparison of quantitatively analyzed dynamic area-detector CT using various mathematic methods with FDG PET/CT in management of solitary pulmonary nodules. AJR Am J Roentgenol 200(6):W593–W602

Ohno Y, Nishio M, Koyama H, Miura S, Yoshikawa T, Matsumoto S, Sugimura K (2014) Dynamic contrast-enhanced CT and MRI for pulmonary nodule assessment. AJR Am J Roentgenol 202(3):515–529

Ohno Y, Koyama H, Yoshikawa T, Matsumoto S, Sugimura K (2015a) Lung cancer assessment using MR imaging: an update. Magn Reson Imaging Clin N Am 23(2):231–244

Ohno Y, Nishio M, Koyama H, Seki S, Tsubakimoto M, Fujisawa Y, Yoshikawa T, Matsumoto S, Sugimura K (2015b) Solitary pulmonary nodules: comparison of dynamic first-pass contrast-enhanced perfusion area-detector CT, dynamic first-pass contrast-enhanced MR imaging, and FDG PET/CT. Radiology 274(2):563–575

Ohno Y, Seki S, Koyama H, Yoshikawa T, Matsumoto S, Takenaka D, Kassai Y, Yui M, Sugimura K (2015c) 3D ECG- and respiratory-gated non-contrast-enhanced (CE) perfusion MRI for postoperative lung function prediction in non-small-cell lung cancer patients: a comparison with thin-section quantitative computed tomography, dynamic CE-perfusion MRI, and perfusion scan. J Magn Reson Imaging 42(2): 340–353

Ohno Y, Koyama H, Lee HY, Yoshikawa T, Sugimura K (2016a) Magnetic Resonance Imaging (MRI) and Positron Emission Tomography (PET)/MRI for Lung Cancer Staging. J Thorac Imaging 31(4):215–227

Ohno Y, Koyama H, Fujisawa Y, Yoshikawa T, Seki S, Sugihara N, Sugimura K (2016b) Dynamic contrast-enhanced perfusion area detector CT for non-small cell lung cancer patients: Influence of mathematical models on early prediction capabilities for treatment response and recurrence after chemoradiotherapy. Eur J Radiol 85(1):176–186

Ohno Y, Koyama H, Fujisawa Y, Yoshikawa T, Inokawa H, Sugihara N, Seki S, Sugimura K (2016c) Hybrid Type iterative reconstruction method vs. filter back projection method: Capability for radiation dose reduction and perfusion assessment on dynamic first-pass contrast-enhanced perfusion chest area-detector CT. Eur J Radiol 85(1):164–175

Ohno Y, Fujisawa Y, Koyama H, Kishida Y, Seki S, Sugihara N, Yoshikawa T (2017a) Dynamic contrast-enhanced perfusion area-detector CT assessed with various mathematical models: its capability for therapeutic outcome prediction for non-small cell lung cancer patients with chemoradiotherapy as compared with that of FDG-PET/CT. Eur J Radiol 86:83–91

Ohno Y, Fujisawa Y, Sugihara N, Kishida Y, Seki S, Koyama H, Yoshikawa T (2017b) Dynamic contrast-enhanced perfusion area-detector CT: preliminary comparison of diagnostic performance for N stage assessment with FDG PET/CT in non-small cell lung cancer. AJR Am J Roentgenol 209(5):W253–W262

Ohno Y, Yoshikawa T, Takenaka D, Fujisawa Y, Sugihara N, Kishida Y, Seki S, Koyama H, Sugimura K (2017c) Xenon-enhanced CT using subtraction CT: basic and preliminary clinical studies for comparison of its efficacy with that of dual-energy CT and ventilation SPECT/CT to assess regional ventilation and pulmonary functional loss in smokers. Eur J Radiol 86: 41–51

Ohno Y, Kauczor HU, Hatabu H, Seo JB, van Beek EJR, International Workshop for Pulmonary Functional Imaging (IWPFI) (2018a) MRI for solitary pulmonary nodule and mass assessment: current state of the art. J Magn Reson Imaging 47(6):1437–1458

Ohno Y, Fujisawa Y, Takenaka D, Kaminaga S, Seki S, Sugihara N, Yoshikawa T (2018b) Comparison of xenon-enhanced area-detector CT and krypton ventilation SPECT/CT for assessment of pulmonary functional loss and disease severity in smokers. AJR Am J Roentgenol 210(2):W45–W53

Olsen GN, Block AJ, Tobias JA (1974) Prediction of postpneumonectomy pulmonary function using quantitative macroaggregate lung scanning. Chest 66(1): 13–16

Pierce RJ, Copland JM, Sharpe K, Barter CE (1994) Preoperative risk evaluation for lung cancer resection: predicted postoperative product as a predictor of surgical mortality. Am J Respir Crit Care Med 150(4):947–955

Ramnath N, Dilling TJ, Harris LJ, Kim AW, Michaud GC, Balekian AA, Diekemper R, Detterbeck FC, Arenberg DA (2013) Treatment of stage III non-small cell lung cancer: diagnosis and management of lung cancer, 3rd ed: American College of Chest Physicians evidence-based clinical practice guidelines. Chest 143(5 Suppl):e314S–e340S

Ryo UY (1990) Prediction of postoperative loss of lung function in patients with malignant lung mass. Quantitative regional ventilation-perfusion scanning. Radiol Clin N Am 28(3):657–663

Saghir Z, Dirksen A, Ashraf H, Bach KS, Brodersen J, Clementsen PF, Døssing M, Hansen H, Kofoed KF, Larsen KR, Mortensen J, Rasmussen JF, Seersholm N, Skov BG, Thorsen H, Tønnesen P, Pedersen JH (2012) CT screening for lung cancer brings forward early disease. The randomised danish lung cancer screening trial: status after five annual screening rounds with low-dose CT. Thorax 67(4):296–301

Schaefer JF, Vollmar J, Schick F, Vonthein R, Seemann MD, Aebert H, Dierkesmann R, Friedel G, Claussen CD (2004) Solitary pulmonary nodules: dynamic contrast-enhanced MR imaging—perfusion differences in malignant and benign lesions. Radiology 232(2):544–553

Schoepf UJ, Bruening R, Konschitzky H, Becker CR, Knez A, Weber J, Muehling O, Herzog P, Huber A, Haberl R, Reiser MF (2000) Pulmonary embolism: comprehensive diagnosis by using electron-beam CT for detection of emboli and assessment of pulmonary blood flow. Radiology 217(3):693–700

Sieren JC, Ohno Y, Koyama H, Sugimura K, McLennan G (2010) (2010). Recent technological and application developments in computed tomography and magnetic resonance imaging for improved pulmonary nodule detection and lung cancer staging. J Magn Reson Imaging 2(6):1353–1369

Silvestri GA, Gould MK, Margolis ML, Tanoue LT, McCrory D, Toloza E, Detterbeck F, American College of Chest Physicians (2007) Noninvasive staging of non-small cell lung cancer: ACCP evidenced-based clinical practice guidelines (2nd edition). Chest 132(3 Suppl):178S–201S

Sipkins DA, Cheresh DA, Kazemi MR, Nevin LM, Bednarski MD, Li KC (1998) Detection of tumor angiogenesis in vivo by alphaVbeta3-targeted magnetic resonance imaging. Nat Med 4(5):623–626

Smulders SA, Smeenk FW, Janssen-Heijnen ML, Postmus PE (2004) Actual and predicted postoperative changes in lung function after pneumonectomy: a retrospective analysis. Chest 125(5):1735–1741

Socinski MA, Evans T, Gettinger S, Hensing TA, VanDam SL, Ireland B, Stinchcombe TE (2013) Treatment of stage IV non-small cell lung cancer: Diagnosis and management of lung cancer, 3rd ed: American College of Chest Physicians evidence-based clinical practice guidelines. Chest 143(5 Suppl):e341S–e368S

Sudoh M, Ueda K, Kaneda Y, Mitsutaka J, Li TS, Suga K, Kawakami Y, Hamano K (2006) Breath-hold single-photon emission tomography and computed tomography for predicting residual pulmonary function in patients with lung cancer. J Thorac Cardiovasc Surg 131(5):994–1001

Swabb EA, Wei J, Gullino PM (1974) Diffusion and convection in normal and neoplastic tissues. Cancer Res 34(10):2814–2822

Swensen SJ, Viggiano RW, Midthun DE, Müller NL, Sherrick A, Yamashita K, Naidich DP, Patz EF, Hartman TE, Muhm JR, Weaver AL (2000) Lung nodule enhancement at CT: multicenter study. Radiology 214(1):73–80

Tacelli N, Remy-Jardin M, Copin MC, Scherpereel A, Mensier E, Jaillard S, Lafitte JJ, Klotz E, Duhamel A, Remy J (2010) Assessment of non-small cell lung cancer perfusion: pathologic-CT correlation in 15 patients. Radiology 257(3):863–871

Tacelli N, Santangelo T, Scherpereel A, Duhamel A, Deken V, Klotz E, Cortot A, Lafitte JJ, Wallyn F, Remy J, Remy-Jardin M (2013) Perfusion CT allows prediction of therapy response in non-small cell lung cancer treated with conventional and anti-angiogenic chemotherapy. Eur Radiol 23(8):2127–2136

Tanaka F, Otake Y, Yanagihara K, Kawano Y, Miyahara R, Li M, Yamada T, Hanaoka N, Inui K, Wada H (2001) Evaluation of angiogenesis in non-small cell lung cancer: comparison between anti-CD34 antibody and anti-CD105 antibody. Clin Cancer Res 7(11): 3410–3415

Tateishi U, Kusumoto M, Nishihara H, Nagashima K, Morikawa T, Moriyama N (2002) Contrast-enhanced dynamic computed tomography for the evaluation of tumor angiogenesis in patients with lung carcinoma. Cancer 95(4):835–842

Ueda K, Kaneda Y, Sudoh M, Mitsutaka J, Tanaka N, Suga K, Hamano K (2005) Role of quantitative CT in predicting hypoxemia and complications after lung lobectomy for cancer, with special reference to area of emphysema. Chest 128(5):3500–3506

Wagner HN Jr, Sabiston DC Jr, Iio M, Mcafee JG, Meyer JK, Langan JK (1964) Regional pulmonary blood flow in man by radioisotope scanning. JAMA 187: 601–603

Walter JE, Heuvelmans MA, de Jong PA, Vliegenthart R, van Ooijen PMA, Peters RB, Ten Haaf K, Yousaf-Khan U, van der Aalst CM, de Bock GH, Mali W, Groen

HJM, de Koning HJ, Oudkerk M (2016) Occurrence and lung cancer probability of new solid nodules at incidence screening with low-dose CT: analysis of data from the randomised, controlled NELSON trial. Lancet Oncol 17(7):907–916

Wu MT, Chang JM, Chiang AA, Lu JY, Hsu HK, Hsu WH, Yang CF (1994) Use of quantitative CT to predict postoperative lung function in patients with lung cancer. Radiology 191(1):257–262

Wu MT, Pan HB, Chiang AA, Hsu HK, Chang HC, Peng NJ, Lai PH, Liang HL, Yang CF (2002) Prediction of postoperative lung function in patients with lung cancer: comparison of quantitative CT with perfusion scintigraphy. AJR Am J Roentgenol 178(3):667–672

Wyser C, Stulz P, Solèr M, Tamm M, Müller-Brand J, Habicht J, Perruchoud AP, Bolliger CT (1999) Prospective evaluation of an algorithm for the functional assessment of lung resection candidates. Am J Respir Crit Care Med 159(5 Pt 1):1450–1456

Yabuuchi H, Hatakenaka M, Takayama K, Matsuo Y, Sunami S, Kamitani T, Jinnouchi M, Sakai S, Nakanishi Y, Honda H (2011) Non-small cell lung cancer: detection of early response to chemotherapy by using contrast-enhanced dynamic and diffusion-weighted MR imaging. Radiology 261(2):598–604

Yabuuchi H, Kawanami S, Iwama E, Okamoto I, Kamitani T, Sagiyama K, Yamasaki Y, Honda H (2018) Prediction of therapeutic effect of chemotherapy for NSCLC using dual-input perfusion CT analysis: comparison among bevacizumab treatment, two-agent platinum-based therapy without bevacizumab, and other non-bevacizumab treatment groups. Radiology 286(2):685–695

Yanagita H, Honda N, Nakayama M, Watanabe W, Shimizu Y, Osada H, Nakada K, Okada T, Ohno H, Takahashi T, Otani K (2013) Prediction of postoperative pulmonary function: preliminary comparison of single-breath dual-energy xenon CT with three conventional methods. Jpn J Radiol 31(6): 377–385

Yi CA, Lee KS, Kim EA, Han J, Kim H, Kwon OJ, Jeong YJ, Kim S (2004) Solitary pulmonary nodules: dynamic enhanced multi-detector row CT study and comparison with vascular endothelial growth factor and microvessel density. Radiology 233(1): 191–199

Yoshimoto K, Nomori H, Mori T, Kobayashi H, Ohba Y, Shibata H, Shiraishi S, Kobayashi T (2009) Prediction of pulmonary function after lung lobectomy by subsegments counting, computed tomography, single photon emission computed tomography and computed tomography: a comparative study. Eur J Cardiothorac Surg 35(3):408–413

Yuan X, Zhang J, Quan C, Cao J, Ao G, Tian Y, Li H (2013) Differentiation of malignant and benign pulmonary nodules with first-pass dual-input perfusion CT. Eur Radiol 23(9):2469–2474

Zieliński KW, Kulig A (1984) Morphology of the microvascular bed in primary human carcinomas of lung. Part I: Three dimensional pattern of microvascular network. Pathol Res Pract 178(3):243–250

Zieliński KW, Kulig A, Zieliński J (1984) Morphology of the microvascular bed in primary human carcinomas of lung. Part II. Morphometric investigations of microvascular bed of lung tumors. Pathol Res Pract 178(4):369–377

Zou Y, Zhang M, Wang Q, Shang D, Wang L, Yu G (2008) Quantitative investigation of solitary pulmonary nodules: dynamic contrast-enhanced MRI and histopathologic analysis. AJR Am J Roentgenol 191(1):252–259

Computational Approach toward Pulmonary Functional Imaging

William D. Lindsay Jr, Nicholas J. Tustison, and James C. Gee

Contents

1 **Quantitative Measurement of Lung Function: Metrics and Modalities** 300
1.1 Introduction 300
1.2 Measuring Ventilation 300
1.3 Measuring Perfusion 302
1.4 Measuring Respiratory Motion 305

2 **Computational Lung Image Analysis** 306
2.1 Introduction 306
2.2 Image Registration 306
2.3 Image Segmentation 308

3 **Computational Functional Biomarkers of Lung Diseases** 309
3.1 Introduction 309
3.2 Asthma 310
3.3 COPD 310
3.4 Cystic Fibrosis 311
3.5 Pulmonary Embolism 312

4 **Efforts Toward Automated Diagnosis and Prognosis of Lung Disease** 312
4.1 Introduction 312
4.2 Prediction of Disease Progression in COPD Patients 312
4.3 Predicting Malignancy of Pulmonary Nodules 313
4.4 Predicting Need for Lung Transplant in Cystic Fibrosis Patients 314

5 **Summary** 314

References 315

Abstract

Quantitative functional imaging has improved clinical understanding of lung disease, enhanced researchers' abilities to develop new treatments, and has the potential to improve care for millions of patients who suffer from COPD, asthma, cystic

W. D. Lindsay Jr · J. C. Gee (✉)
University of Pennsylvania, Philadelphia, PA, USA
e-mail: gee@mail.med.upenn.edu

N. J. Tustison
University of Virginia, Charlottesville, VA, USA

© Springer Nature Switzerland AG 2021

Y. Ohno et al. (eds.), *Pulmonary Functional Imaging*, Medical Radiology Diagnostic Imaging,
https://doi.org/10.1007/978-3-030-43539-4_14

fibrosis, and other diseases. While all imaging modalities rely on physics and computation, functional lung imaging is especially amenable to and dependent on computational approaches. Functional imaging modalities, such as hyperpolarized noble gas magnetic resonance imaging (MRI), inhaled contrast computed tomography (CT), and nuclear imaging, require complex processing strategies for synthesis, quantification, and computer-aided diagnosis. Early investigation into the use of such modalities for the development of computational metrics specifically tailored for the quantitative assessment of lung function has led to advanced machine learning strategies for classifying patients and predicting disease progression. Such developments will have a lasting impact on future diagnostic capabilities and the potential treatment of lung disease. In this chapter, we review these functional lung imaging modalities, their corresponding computational methodologies, and potential clinical significance.

1 Quantitative Measurement of Lung Function: Metrics and Modalities

1.1 Introduction

In order to better measure lung function, quantitative metrics derived from imaging have emerged alongside traditional lung function measurement tools such as pulmonary function testing (PFT). These quantitative measurements of lung function extend traditional methods and offer key benefits in clinical care and research. For example, quantitative metrics allow for fine-grained tracking of lung function over time. Quantitative metrics also allow for detailed characterization of lung response to various interventions, such as drugs, or to exercise. In this section, we review a variety of quantitative lung function metrics derived from various functional lung imaging modalities.

1.2 Measuring Ventilation

Lung ventilation, or the delivery of gas to the lung alveoli for gas exchange, is impaired in numerous pulmonary disease states such as chronic obstructive pulmonary disorder (COPD), asthma, and acute respiratory distress syndrome (ARDS). PFTs allow measurement of ventilation at a global level, but functional lung imaging modalities such as inspiration-expiration computed tomography (IE-CT), inhaled xenon contrast enhanced computed tomography (Xe-CT), and hyperpolarized magnetic resonance imaging (HP-MRI) permit the quantification of ventilation in a regional and even voxel-specific manner. Such localized quantification of ventilation can enhance the granularity for probing specific research questions which could ultimately lead to faster, more accurate clinical diagnoses and potentially improved patient outcomes. Specific metrics used to measure ventilation include ventilation defect percentage (VDP) and apparent diffusion coefficient (ADC).

Both VDP and ADC can be computed using HP-MRI which has been under investigation since the early 1990s (Kauczor and Chen 2001). In HP-MRI, the patient inhales a gaseous mixture of a hyperpolarized noble gas, typically xenon or helium. The hyperpolarized gas acts as a magnetic resonance contrast agent due to its enhanced polarity when compared to normal gases found in the atmosphere. Furthermore, in the lungs, traditional proton-based MRI provides minimal information because of the relative lack of protons in the lung parenchyma and gas-containing alveoli. HP-MRI, with pulse sequences tuned to the gas atom instead of protons, offers an opportunity for better delineation of lung structure as well as function.

VDP, defined as the ratio of ventilation defect volume to total lung volume, has been used by a variety of groups for reporting research findings (Hughes et al. 2018; Woodhouse et al. 2005; He et al. 2014). Multiple strategies have been employed by researchers to calculate VDP from various imaging modalities. Early strategies involved thresholding lung voxels based on an intensity value corresponding to the magnitude

of ventilation at that position (Woodhouse et al. 2005). Improvements on this method, such as segmentation and removal of tissue that does not participate in gas exchange such as large airways, have been made by multiple groups resulting in improved quantification (Kirby et al. 2012). Improvement in calculation of VDP has also been facilitated by the development of automated and semiautomated methods for providing such ventilation-based segmentation. Prior to these technical developments, standard practice involved subjective scoring of lung defects by trained radiologists. From these ventilation segmentation images both local and global ventilation can be quantified. Local ventilation can be measured by the average normalized image intensity within a given region whereas global ventilation can be measured by computing the VDP of the whole lungs or specific lung regions. Ventilation defects are common in functional lung diseases and the change in VDP over time can be used to assess disease progression or response to therapy. VDP is also sensitive to exercise-induced bronchoconstriction (Zha et al. 2016). VDP can vary from permanent to transient, and a decrease in VDP in response to certain pharmacologic therapies can be diagnostic of certain diseases. VDP has been used as a biomarker for smoking, COPD (Kirby et al. 2014), asthma (Busacker et al. 2009; Svenningsen et al. 2014; Trivedi et al. 2017), and other lung diseases.

ADC, a measure of the restriction to normal diffusion in a defined region, can be used to quantify ventilation from MR imaging. All molecules exhibit diffusion, a process of random motion, in a medium. In an unrestricted media, in a time interval t, a gas molecule will move a room mean square distance given by $L_0 = (2D_0t)^{½}$. D_0 is deemed the free diffusion coefficient and is specific to the gas and temperature. When calculated across an anatomic region using MR imaging, the diffusion coefficient is instead called "the apparent diffusion coefficient" (ADC). In restricted media, such as tissue with higher order structures like neurons or acini, diffusion is reduced, meaning gas molecules move a shorter distance in unit time on average and the region possesses a lower ADC. It has been suggested by Yablonskiy and others that diffusion-weighted He-3 MRI has the potential to measure diffusion at the level of the lung acinus, showing that the ADC of helium in regions containing acini in healthy human lungs is 0.20 cm^2/s, which is four times lower than the free diffusion coefficient of He-3 in air at 37 °C (Yablonskiy et al. 2002). MRI can be used to specifically measure diffusion and diffusion-weighted HP-MRI can be used to quantify restricted diffusion in small airspaces (Yablonskiy et al. 2002). Over the past decade, substantial work has been performed to assess ADC in various human lung diseases. For example, ADC measured using He-3 MRI has been shown to differentiate between lungs of normal subjects and subjects with COPD (Kirby et al. 2012).

Inspiration-expiration computed tomography (IE-CT) has been investigated as a way of quantifying ventilation from conventional CT images obtained during a patient's respiratory cycle. A large multi-institutional study, the COPDGene study (http://www.copdgene.org/), has yielded a large, openly available dataset of subjects who all received CT imaging at full inspiration and at residual expiratory value. One group of investigators employed a lung-mass preserving registration technique to co-register inspiration/expiration CT image pairs (Bhatt et al. 2017). This mapping has been used to quantify regional expansion of alveoli as a measure of regional ventilation (Bhatt et al. 2017).

IE-CT is not the only CT-based method to quantify ventilation. Inhaled xenon gas has been used as a contrast agent for CT imaging and can also be used to measure ventilation. Xenon has a higher atomic number than other gases typically found in the lung, and therefore can provide enhanced contrast against lung parenchyma. The CT attenuation in a specific lung region is a function of the density of xenon in that particular region, and therefore CT intensity can be used as an estimation of a region's local ventilation during inspiration of xenon (Chon et al. 2006, 2007). This enables local quantification of lung ventilation, thus permitting a more detailed classification of a patient's ventilation defects as global (common in asthma where bronchoconstriction

restricts airflow across the lung in a relatively uniform manner) or region-specific (common in COPD, where the elasticity of individual alveolar walls deteriorates).

While effective, these CT-based techniques involve delivery of ionizing radiation to the patient. HP-MRI, on the other hand, does not require subjecting the patient to ionizing radiation. However, there are challenges associated with producing hyperpolarized gas and with interpreting the images. It is difficult to synthesize hyperpolarized gas, and only certain laboratories and clinical centers have the resources to create it. Furthermore, there are specific challenges presented by hyperpolarized gas when trying to quantify ventilation. MR signal intensity depends not only on the density of the gas but also on local partial pressure in the lung, which is nonuniform. Because of this, HP-MRI intensities do not define an absolute measure of ventilation. However, computational techniques, such as the method featured in Fig. 1, enable segmentation of the lung into areas of similar ventilation with multiple groups demonstrating superior performance to human manual segmentations of the lung into areas of similar ventilation (Tustison et al. 2010).

1.3 Measuring Perfusion

When assessing pulmonary function, clinicians seek to quantify pulmonary perfusion in addition to ventilation. While ventilation represents the transit of gas from outside the body through the trachea and bronchi and into the alveolar space, perfusion represents the flow of blood through the alveolar capillaries, which is similarly crucial for effective gas exchange.

Many conditions affect lung perfusion, including pulmonary emboli, making proper quantification of lung perfusion an important method of accurate diagnosis. Quantification of perfusion in other organs such as the brain is of demonstrated clinical importance and methods for analysis are well established. However, methods of quantifying perfusion in the lung face a number of domain-specific challenges. For instance, the tissue density of lung parenchyma is significantly lower than that of the brain. These lung-specific tissue characteristics result in a significant difference between perfusion per unit volume and perfusion per unit mass, necessitating appropriate conversion for clinical interpretation. Furthermore, the lungs are large elastic organs and their position and density are heavily influenced by gravity. Nonconstant, voxel-wise changes in lung density must be accounted for to ensure accurate perfusion measurement. The lung also contains many large and medium sized blood vessels, which appear as areas of blood density on perfusion imaging but are not actively participating in gas exchange. For example, a regional lung perfusion measure might include signal from the blood inside of a large pulmonary artery in addition to the blood contained in capillaries in the surrounding lung parenchyma. In order to accurately measure the blood that reaches the alveoli and participates in gas exchange, these inactive regions must be taken into account.

Various imaging modalities are currently used in clinical practice to measure perfusion, with recently developed methods, such as dual-energy computed tomography, in clinical and preclinical development. A prominent, clinically relevant modality is single photon emission computed tomography (SPECT), where a radioactive tracer is injected into the patient through a peripheral vein. The radioactive tracer emits radioactive particles which are detected by an array of detectors. SPECT imaging can be combined with structural imaging (such as MR or CT) to provide additional anatomical information that is not available due to the inherently low spatial resolution of SPECT. Areas of high intensity on SPECT correspond to areas of theoretically high ventilation after taking into account some challenges described above such as gravity and large vessels that do not participate in gas exchange (Levin et al. 2017).

Another technique used to measure pulmonary perfusion is magnetic resonance angiography (MRA). MRA involves the injection of a T1-shortening contrast agent into a patient's peripheral vein followed by timed image acquisition of the lungs, to capture certain phases of the

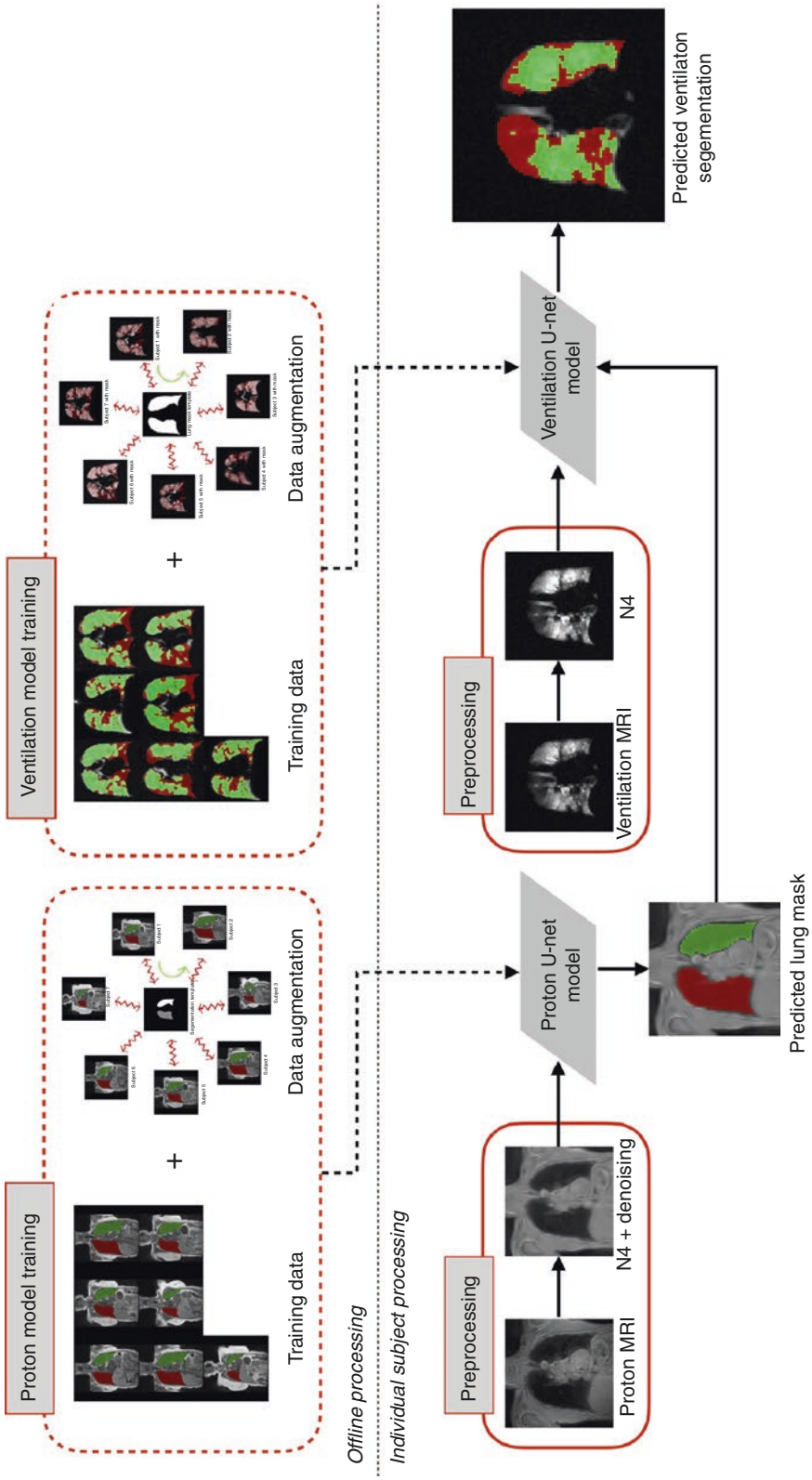


Fig. 1 A deep learning framework for ventilation segmentation (adapted from Tustison et al. 2019 with the author's permission)

pulmonary cycle (e.g., arterial, venous). From an MRA, multiple quantitative perfusion metrics can be calculated, including pulmonary blood flow, pulmonary blood volume, and mean transit time. In order to calculate these metrics, multiple image acquisitions throughout the cardiac cycle are required (Johns et al. 2017; Tsuchiya et al. 2018; Ohno et al. 2017a, b, c; Freed et al. 2016; Hecht and Rosenkrantz 2009).

In addition to contrast-based modalities, dual-energy CT (DECT) can be used to quantitatively measure pulmonary perfusion as shown in Fig. 2 (Hwang et al. 2017) without injection of a contrast agent. DECT refers to a form of CT imaging that uses X-rays from two different energy spectra. X-rays of different energies exhibit different attenuation profiles. When multiple energies are used together in one image, the differential attenuation between the two images can be used to provide superior contrast between different materials. In the case of lung imaging, DECT can be used to identify contrast agents such as iodine, as well as subtle differences in parenchymal tissue appearance. Three major DECT technologies are commercially available as shown in Fig. 3: dual-source CT scanners, rapid kVP switching scanners, and CT scanners which leverage energy-sensitive sandwich detectors. Dual-source scanners contain two X-ray tubes and two detectors. In addition to offering superior tissue contrast, dual-source CT scanners also provide enhanced temporal resolution, as two source-

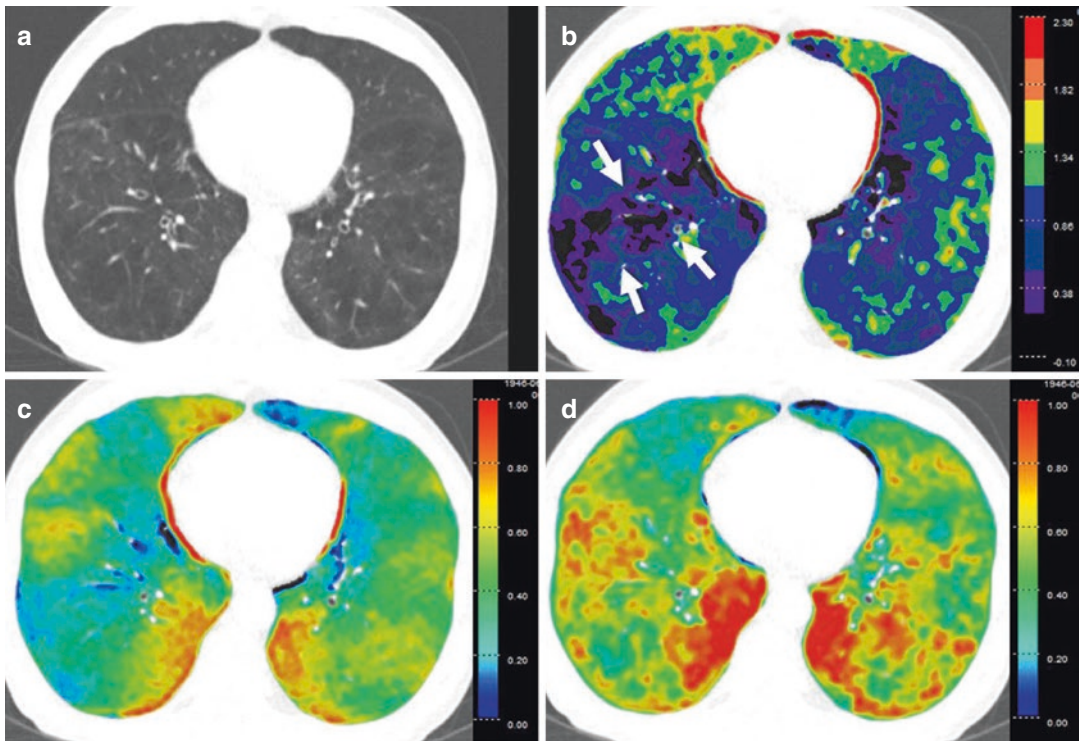


Fig. 2 (**a**–**d**) Combined ventilation perfusion DECT in a 59-year-old man with COPD. From combined xenon ventilation and iodine perfusion CT using DECT, the conventional VNC image (**a**), color-coded xenon ventilation/pulmonary PBV map (**b**), ventilation map (**c**), and pulmonary blood volume map (**d**) are generated. Lung parenchymal ventilation, perfusion, and ventilation-perfusion imbalance with high-resolution anatomic CT information can be simultaneously evaluated with combined ventilation and perfusion DECT. In both lower lobes, although emphysema is noted throughout the lung on the VNC image (**a**), variable ventilation and perfusion changes are evident. (**b–d**) Ventilation is decreased (blue color) (**c**), while perfusion is preserved (yellow and green color) (**d**) in the lateral segment of the right lower lobe, resulting in the mismatch of ventilation-perfusion relationship (arrows, violet and black color) (**b**). (Adapted from Hwang et al. 2017, used with author's permission)

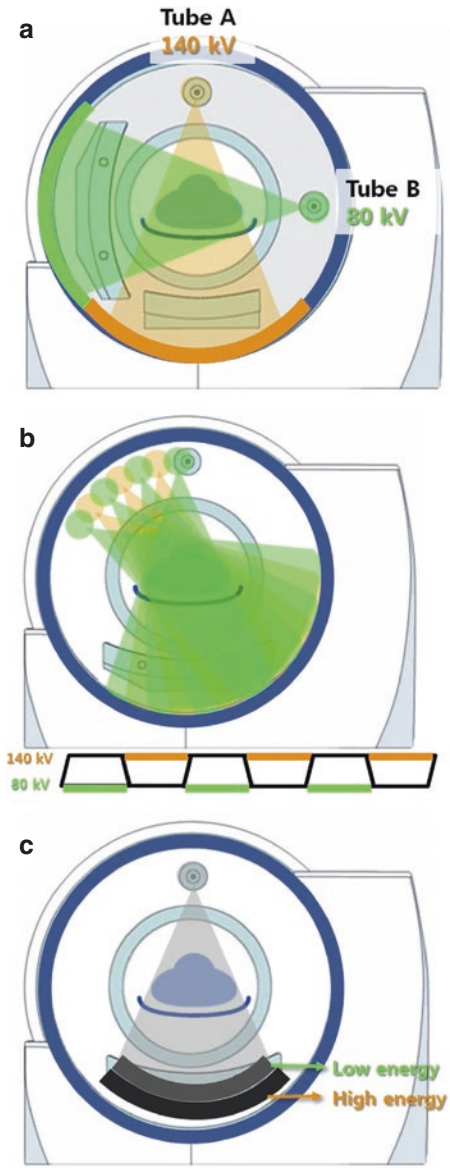


Fig. 3 (**a–c**) Diagrams of technical approaches for DECT data acquisition. (**a**) Diagram of dual-source CT system, which is composed of two X-ray tubes and two corresponding detectors offset by 90° in one gantry. Each tube is operated at different kilovoltage (e.g., 140 and 80 kV) and milliampere settings, and then two datasets at high- and low-energy spectra are obtained at corresponding detectors. (**b**) Diagram of rapid kVp switching system for DECT data acquisition. The tube voltage is rapidly switched between high and low energy in about 0.5 ms. (**c**) Diagram of the DECT data acquisition system with energy-sensitive layered detector and single X-ray tube at constant kVp. The layered detector comprises a thin top scintillator that absorbs lower energy photons and a bottom scintillator that absorbs the higher energy photons. (Adapted from Hwang et al. 2017, used with author's permission)

detector pairs are present, allowing twice as many image acquisitions per unit time. In scanners with rapid kVp switching, one X-ray tube and one detector are present and the voltage of the X-ray tube is electronically switched to generate different X-ray spectra. This results in a longer acquisition time and increased radiation to the patient. In scanners using energy-sensitive sandwich detectors, a single multi-spectral X-ray tube is used to generate X-rays of multiple energies. The sandwich detector contains multiple layered energy-specific detectors and allows both images to be acquired simultaneously. The presence of a single detector facilitates image registration (Hwang et al. 2017).

1.4 Measuring Respiratory Motion

The normal functioning of respiratory mechanics is crucial to healthy lung function and perturbations in the dynamics of respiratory motion can cause numerous pathologies. Traditional methods such as PFTs are limited to measuring global lung function and fail to capture important regional measurements of lung physiology. The combination of quantitative functional lung imaging and advanced image registration techniques provides researchers and clinicians with the ability to better understand lung motion in vivo both in normal and pathologic states.

In a detailed review, the progression from ex vivo study of animal models of lung disease to advanced functional imaging of in vivo human studies is discussed (Tustison et al. 2011a, 2011b). Lung diseases are often categorized into either restrictive lung disease or obstructive lung diseases. Restrictive lung diseases, for example, COPD, are characterized by reduced elasticity and local restriction of lung expansion.

Four-dimensional CT imaging, in which images of the lungs are acquired throughout the respiratory cycle, allows for precise quantification of respiratory motion. This imaging technique is often used during radiation therapy treatment planning, meaning large real world data sets can be acquired and analyzed. In work

by Werner et al., a radiation therapy dataset was used to model lung motion with a finite element method (Werner et al. 2009). During inspiration, the alveoli in the lung expand, drawing gas into the lung for gas exchange. This process deforms the lungs in three dimensions from their minimum volume at maximal expiration to their maximum volume at maximal inspiration. Deformable registration offers an opportunity to assess the local volumetric changes of the lung during respiratory motion. A commonly used metric is the determinant of the Jacobian matrix of the deformation map at a particular voxel. Areas of the lung with reduced deformation during inspiration have been shown to correspond to areas of ventilation defect (Bhatt et al. 2017). The tissue surrounding the area of ventilation defect, termed mechanically altered lung (MAL), is under increased mechanical stress and hypotheses have been made that this tissue is at high risk of becoming emphysematous during the progression of COPD (Bhatt et al. 2017). Specifically, the mechanical effect appeared to extend 2 mm in all directions from the lung region, spurring the recording of a metric called MAL2, which is the mean Jacobian determinant of the voxels within 2 mm of the emphysematous lung. This metric was shown to be associated with subsequent FEV1 decline (Bhatt et al. 2019).

2 Computational Lung Image Analysis

2.1 Introduction

While the introduction of new imaging modalities has advanced diagnosis and prognosis in lung disease, advances in computational analysis methods have also contributed to research efforts and clinical advancements. In this section, we discuss advanced image processing techniques applied to standard and emerging functional lung imaging modalities. We divide image processing into three broad subdomains: image registration, image segmentation, and feature extraction. In the corresponding subsections, we describe the basic technical underpinnings of each category before discussing domain-specific considerations required when working with functional pulmonary imaging.

2.2 Image Registration

Image registration is used to determine the correspondence function between two spatial domains typically measured using imaging techniques. In routine image registration tasks, the correspondence function is used to map one image on to the domain of another image. The set of possible correspondence functions is typically limited by certain criteria designed to preserve characteristics of the original image, such as shape or mass. For example, linear image registration allows for rotation, translation, scaling, and other affine transformations. Nonrigid, or deformable, registration permits local adjustment of the input image by easing the restrictions placed on allowable transformations. To help constrain deformable registration tasks, certain restrictions are often placed on allowable mappings to help maintain the original image's shape and other characteristics. In pulmonary imaging specifically, domain-specific registration algorithms have enabled large-scale research analyses of lung image datasets. For example, deformable registrations that allow discontinuous sliding motion, which are present during respiration, have been designed specifically for lung-specific motion (Schmidt-Richberg et al. 2012).

Years of development have led to Improvements in deformable registration algorithms which have enabled improved accuracy in determining spatial correspondence. For example, the symmetric normalization (SyN) algorithm for diffeomorphisms, which was originally developed for neuroimaging applications (Avants et al. 2008), has been applied to pulmonary imaging (Song et al. 2010; Sundaram et al. 2005) and further modified with a B-spline formulation, demonstrating superior performance in certain lung-specific applications (Tustison et al. 2013).

In functional lung imaging, there are specific image registration challenges that require unique solutions. For example, intra-subject registration

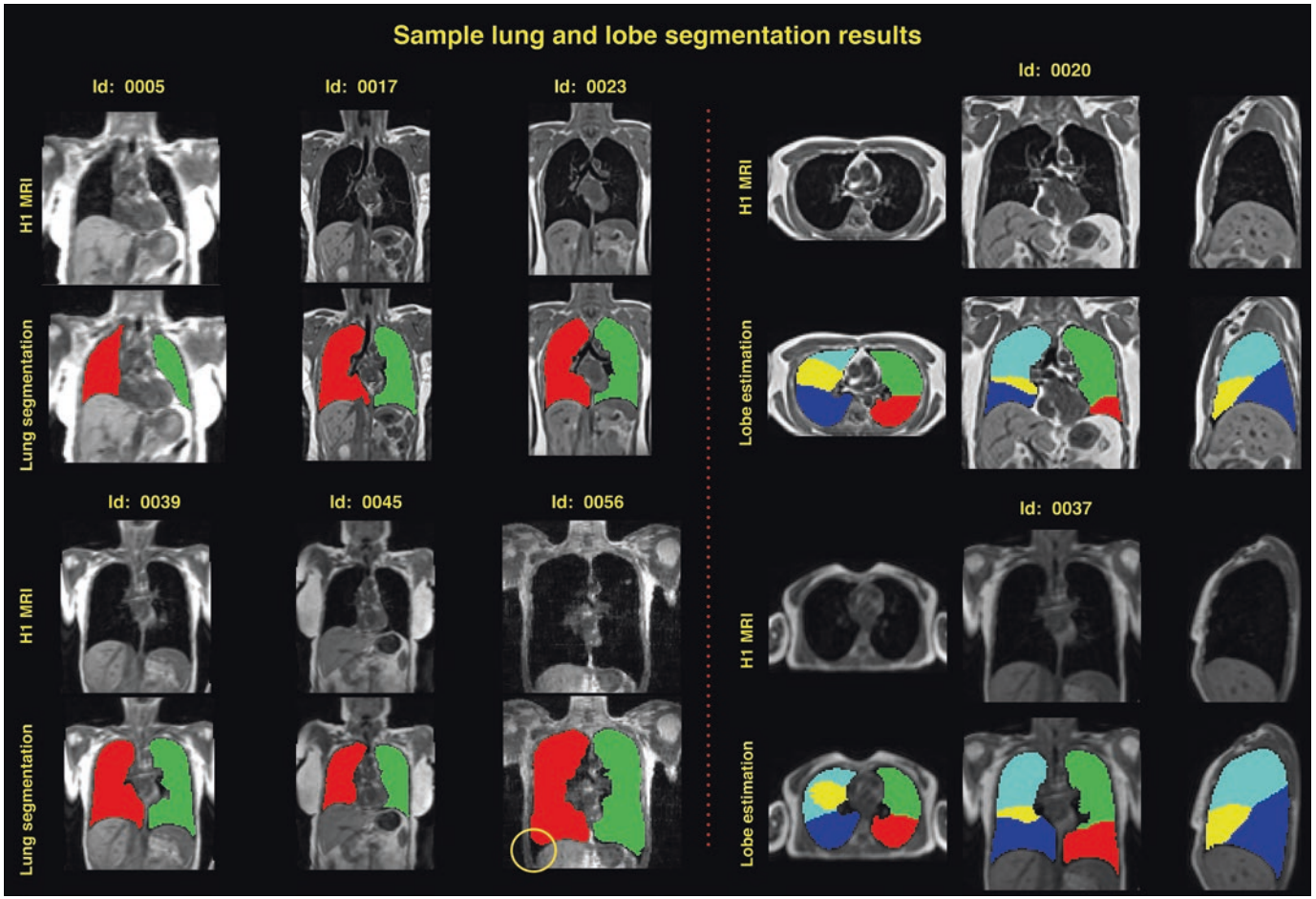


Fig. 4 Randomly selected results for the proposed lung segmentation and lobe estimation framework. The only exception is the lower right lung segmentation result (Id: 0056) which produced the minimum overlap measure due to the mis-segmentation of the basal portion of the right lung. (Left) Mid-coronal slices of randomly selected results of our applied lung segmentation methodology. (Right) Three canonical views of the lobe estimation results in two randomly selected subjects. (Adapted from Tustison et al. 2016 with author's permission)

of lung images acquired at different points in the tidal respiratory cycle is required to compensate for subject breathing. By warping a full inspiration breath hold image to a forced expiration image, researchers and clinicians can characterize regional lung expansion in a voxel-wise manner, which can provide insight into disease-specific lung function.

In work by Yin et al., a cubic B-spline-based method was also applied with success in a study of dynamic airway modeling (Yin et al. 2011). In this work, the authors categorize deformable pulmonary registration algorithms into two types: feature-based registration algorithms and intensity-based registration algorithms. Because both intensity- and feature-based methods have advantages and known limitations, hybrid feature and intensity-based methods have been developed. In Yin et al., all three methods (intensity, feature, and hybrid) are applied using repetitive, locally invertible B-splines (Yin et al. 2011).

In intensity-based registration methods, the global difference in image intensity is minimized, either directly with regularized voxel-wise subtraction or indirectly using mutual information or other methods. This measure of global "likeness" between image pairs is called the similarity function. The chosen similarity function is a key component of intensity-based registration methods. In feature-based registration methods, specific anatomic landmarks or structures (such as airways) define the mapping from one image to another. In intra-subject registrations (such as spatial normalization for all time points of the respiratory cycle), this technique is particularly successful, as the airways of an individual patient ought to be topologically equivalent throughout the respiratory cycle. For example, airway bifurcation points are commonly used as landmarks in feature-based registration of pulmonary images. These bifurcation points can be manually labeled by experts, but semiautomated landmark identification methods have also been successfully applied in pulmonary imaging (Murphy et al. 2008).

Although differentiable mappings between images are desirable, natural anatomic interfaces or boundaries between organs present an interesting challenge in the specific case of lung registration. For example, at the interface between the chest cavity and the lung parenchyma, sliding motion occurs during the respiratory cycle. Furthermore, the diaphragm, the muscle that provides the driving force for inspiration and expiration, interfaces with the lungs in a manner that can also allow discontinuous sliding motion. This has been highlighted as a particularly important consideration in tracking tumors during respiratory-gated radiation therapy (Werner et al. 2009).

2.3 Image Segmentation

Image segmentation is a crucial step in quantitative pulmonary image analysis. Image segmentation is the process of voxel-wise annotation of the various regions of an input image with label values indicative of categorization. Image segmentation has traditionally been performed by experts such as radiologists who manually annotate images. However, in high-throughput clinical and research environments with large datasets, manual labeling is often infeasible due to resource constraints. Manual labeling also suffers from intersubject biases and variation. Semiautomated and automated image segmentation techniques provide an alternative to manual segmentation and have been applied in a variety of computer vision tasks both inside and outside of medical imaging.

In medical imaging specifically, automated image segmentation techniques can be broadly classified as either atlas-based or machine learning-based. In atlas-based methods, the input image is compared to an atlas image that has been manually labeled by an expert. The source image is called an atlas and is registered to the image of the subject to be segmented. The atlas labels are then transferred to the input image using the resulting transformation. This process can be performed with multiple atlases, in which case a voxel on the input image will have multiple possible identities, one from each atlas. In this case, a voting algorithm (or other weighted consensus scheme) is used to determine each voxel's label.

This paradigm is called multi-atlas segmentation and a joint label fusion variant is the current state of the art across multiple medical imaging domains (Wang and Yushkevich 2013).

A downside of atlas-based methods is the requirement of highly detailed labeled atlases which require time demanding hand labeling. In various imaging fields, expertly labeled atlas has been developed and disseminated to the scientific community. In lung imaging specifically, researchers are developing templates and atlases to support multi-atlas-based lung segmentation methods. These atlases and templates include detailed functional lung atlases showing ventilation and perfusion defects expertly labeled by pulmonary radiologists (Tustison et al. 2016).

In machine learning-based image segmentation methods, a machine learning algorithm is trained to classify voxels in the input image. This category can be further divided into unsupervised techniques and supervised techniques. Unsupervised machine learning methods, such as k-means clustering, do not require training on a labeled training set, whereas supervised machine learning techniques require a training set of labeled examples. Supervised machine learning-based methods include various deep convolutional neural network (CNN) approaches. Although CNNs have achieved state-of-the-art classification accuracy on numerous computer vision and medical imaging tasks, they require significant quantities of data as well as substantial computing resources such as graphics processing units (GPUs).

In functional lung imaging, a common preprocessing task involves labeling the lung which is surrounded by other soft tissue structures such as the chest wall and shares borders with the diaphragm and mediastinal structures such as the heart and great vessels. More advanced segmentation tasks include segmenting lung substructures such as individual lobes of the lung, or segmenting and removing large airways or large blood vessels that do not participate in gas exchange or perfusion.

Another crucial segmentation task required for metric calculation involves partitioning the lung into regions of low and high ventilation. Simple intensity thresholding can provide some quantification of lung ventilation (Campana et al. 2009), but this method has numerous limitations and fails to incorporate important spatial information such as location in the lung and proximity to areas of high or low ventilation. An alternative segmentation approach designed specifically for helium-3 lung images iterates between estimating a Gaussian mixture model of the intensity histogram and Markov random field smoothing of local voxel-wise neighborhoods (Tustison et al. 2011a, 2011b). Deep learning-based methods for functional lung image quantification have been developed that achieve accuracy parity with human labeling. Due to the sample size requirements of the CNN, data augmentation is often applied. Tustison and colleagues also introduced a novel template-based data augmentation strategy specifically for functional lung imaging and have made this method available through the open-source ANTsRNet, a growing repository of well-known deep learning architectures (Tustison et al. 2019).

3 Computational Functional Biomarkers of Lung Diseases

3.1 Introduction

Various functional lung imaging biomarkers, summarized in Table 1, are currently under investigation across multiple diseases. These biomarkers are calculated from functional lung images and offer insight into lung disease progression, severity, and initial diagnosis. These biomarkers are noninvasive and can potentially reduce unnecessary invasive procedures for patients. Computational biomarkers also offer researchers new tools to study lung diseases with exacting detail, potentially improving our ability to understand the pathophysiology underlying these diseases. In this section, we review examples of biomarkers derived from functional lung images that have been investigated in a collection of lung diseases including asthma, COPD, ARDS, pulmonary embolism, and lung cancer.

Table 1 Example functional biomarkers and related disease states

Biomarker	Description	Disease
Ventilation defect percentage (VDP)	Percentage of lung volume receiving inadequate ventilation	COPD, asthma
Mechanically affected lung (MAL)	Lung tissue volume adjacent to area of ventilation defect	COPD
Pulmonary perfused blood flow (PBV)	Quantification of the volume of blood flowing to a particular volume of pulmonary tissue	PE
Lung clearance index (LDI)	Quantitative measurement of the efficiency of gas mixture in the lung	Cystic fibrosis
FDG-PET avidity	Measure of uptake of FDG tagged PET tracer	Lung cancer

3.2 Asthma

Asthma is a prominent disease characterized clinically by airway inflammation leading to hyperresponsiveness and airflow limitation. It is estimated in the USA alone that there are 26 million people living with asthma (CDC "2016 National Health Interview Survey (NHIS) Data"). Despite significant efforts to characterize asthma using clinical history and spirometric variables, a proper classification of patients has eluded experts.

Quantitative functional lung imaging offers a new opportunity to measure disease and various investigators have shown that quantitative functional imaging features are correlated with spirometric measurements (de Lange et al. 2016), are important in determining disease severity, and can be useful in classifying patients into distinct disease phenotypes. For example, an early study demonstrated that quantitative imaging features extracted from HP-MRI contain more information about asthma characterization than do traditional spirometry and clinical history features using a mutual information-based feature selection strategy (Tustison et al. 2010). Detailed analyses of image features and traditional clinical metrics such as FEV1/FVC, fraction of exhaled nitric oxide, and metrics derived methacholine challenge results have also been performed. One group demonstrated an association between ventilation defect percentage and airway remodeling metrics and inflammation metrics, but not with FEV1 (Svenningsen et al. 2014). Although this study was limited to adult asthma patients, an independent study highlighted the discriminative value ventilation defect percentage in predicting disease severity in a cohort of children with mild and severe asthma (Altes et al. 2016).

PET-CT with fluorodeoxyglucose (FDG) is a clinically accepted method for measuring cellular activity. FDG PET has shown promise as a biomarker for lung inflammation in asthma. For example, studies have demonstrated an association between FDG-PET avidity and conditions known to cause increased inflammation such as sarcoidosis (Jones et al. 1997), COPD (Madsen 2013), and cystic fibrosis (Chen et al. 2006). Relating to asthma specifically, research has shown that neutrophils are the primary source of increased FDG uptake in the lung (Fahy 2009). Neutrophils, along with eosinophils, have also been shown to be involved in the inflammatory process underlying asthma (Fahy 2009).

3.3 COPD

In COPD, a major limitation of current diagnostic tests is their inability to separate patients into clinically significant subphenotypes. A partition of patients into meaningful subphenotypes would allow for better targeting of existing therapies. Conventional lung function measurements such as those provided by PFTs yield a global assessment of lung function. COPD is a structural disease of lung parenchyma and is often heterogeneous. Thus, a region-specific characterization of disease extent may better reflect the underlying condition of a patient and improve prognostic abilities. Quantitative imaging biomarkers for COPD would also enable improved ability to track disease progression. Historical data could then be used to train machine learning models to accurately predict exacerbations,

enabling proactive instead of reactive therapeutic management. In a comprehensive review article, one group describes the various biomarkers under investigation for COPD (Hoffman et al. 2016).

Pulmonary vascular changes are well-characterized phenomena observed in the natural course of COPD. Therefore, investigators have hypothesized that pulmonary vascular changes could have value as biomarkers for COPD progression. Investigators have demonstrated that heterogeneous pulmonary vascular changes can serve as a biomarker for smokers who are susceptible to centrilobular emphysema (Alford 2010). These pulmonary vascular metrics include increased coefficient of variation (CV) in regional pulmonary blood flow (PBF) and mean transit time (MTT). Advanced CT methods, such as dual-energy CT, have allowed for increased temporal resolution, allowing for more accurate measurement of pulmonary vascular metrics (Kong et al. 2014; Fuld et al. 2013).

Impaired ventilation is also a hallmark of COPD and has been thoroughly investigated as a biomarker for disease and disease progression (Hoffman et al. 2016). Xenon gas regional wash-in and washout kinetic studies using CT imaging have been performed and provide valuable insight into ventilation defects (Chon et al. 2006). Other methods of measuring ventilation have been developed that do not require any inhaled contrast agents. The SPIROMICS CT protocol (Ding et al. 2012) involves acquisition of high-resolution CT images of the lungs at TLC and RV. This protocol combined with image registration techniques allows for computation of voxel-wise ventilation maps (Yin et al. 2011).

3.4 Cystic Fibrosis

Cystic fibrosis (CF) is an autosomal recessive disease characterized by airway obstruction, neutrophil inflammation, and persistent infection. Caused by a mutation in both alleles of the cystic fibrosis transmembrane conductance regulator (CFTR) gene, CF is the most common inherited disorder in Caucasian populations (Adler et al. 2008). The pathology of CF manifests in various lung dysfunctions all eventually leading to respiratory failure.

CF is characterized by intermittent exacerbations, or flairs, which are often caused by external infections. Exacerbations can also be caused by host inflammatory response. Because of the established role of inflammation in causing CF symptoms (Gibson et al. 2003), the ability to quantitatively and noninvasively measure lung inflammation could lead to better understanding and prediction of CF exacerbations.

The current gold standard for measuring lung inflammation in CF is bronchoalveolar lavage (BAL), an invasive and costly test (Chen et al. 2006). However, recent imaging studies have leveraged FDG-PET scanning of the lung to measure regional inflammation in CF patients (Chen et al. 2006). Importantly, this work demonstrated a correlation between BAL regional neutrophil levels and FDG uptake (Chen et al. 2006). Another common measurement used in assessing CF disease exacerbation is FEV1. While FEV1 is the most commonly used metric in tracking progressive lung function decline in CF, it is well known that FEV1 is not as sensitive to resistance in small airways (Aurora et al. 2004). Instead a more specific marker called the lung clearance index (LCI) has been developed. LCI is computed from a multiple breath inert gas washout study, which is a method for quantifying the efficiency of gas mixing in the lung. Imaging researchers have demonstrated that scores derived from MR imaging correlate with LCI and offer a potentially region-specific imaging biomarker for CF (Stahl et al. 2016). A noninvasive way to assess regional ventilation defects would allow for more detailed tracking of CF progression and measurement of the effects of newly developed disease interventions. In one study, researchers demonstrated the ability of hyperpolarized helium-3 MRI to measure changes in ventilation defect after administration of ivacaftor, a CFTR potentiator in patients suffering from CF (Altes et al. 2017).

Multivolume MRI and CT techniques have also been used to quantify structural and func-

tional changes in young children and adolescents with CF (Pennati et al. 2018). In this study, researchers demonstrated the potential of inspiratory-expiratory MR and CT imaging to identify and classify lung ventilation defects. As a nonionizing technique, MRI is a particularly compelling monitoring tool for CF patients, who require disease surveillance throughout their lifetimes.

3.5 Pulmonary Embolism

Pulmonary embolism occurs when an embolism, typically originating from the lower extremities, travels through the systemic vasculature to the heart and into the pulmonary vasculature, where it becomes lodged, obstructing perfusion to a part of the lung. This blockage of perfusion is often not accompanied by a corresponding change in regional ventilation causing ventilation-perfusion mismatch. The traditional method of assessing regional lung perfusion and ventilation is through SPECT imaging, where a radioactive tracer is injected into the patient's peripheral vasculature and images of the lung are acquired. With advancements in CT- and MR-based functional pulmonary imaging, there is an opportunity to address some of the inherent spatial resolution concerns associated with SPECT imaging.

High-speed single-energy CT imaging has been used to quantify lung perfusion using first pass kinetics (Chon et al. 2006). Dual-energy CT has the advantage of having double the temporal resolution compared with single acquisition CT imaging, which allows for fine-grained assessment of pulmonary parenchymal blood flow using the metric pulmonary perfused blood volume (PBV) (Hwang et al. 2017). Dual-energy CT has benefits above and beyond having multiple source-detector pairs. By leveraging the benefits of two different energy spectra (which are absorbed by tissues in differing manner), DECT can obtain even more information that can be used to characterize pulmonary structure and function in the setting of pulmonary embolism.

4 Efforts Toward Automated Diagnosis and Prognosis of Lung Disease

4.1 Introduction

The development of the previously discussed functional imaging modalities and quantitative imaging metrics has enhanced investigation of a variety of lung pathologies including asthma, cystic fibrosis, COPD, pulmonary embolism, and lung cancer. In this section, we discuss efforts to use quantitative functional pulmonary imaging to predict disease diagnosis, disease exacerbation, and disease complications. While the value of automated diagnosis is well established, there is also a strong potential benefit of being able to predict other disease-related events such a complication or treatment failure. In this case, supportive or prophylactic therapies could be used to influence the natural history of the disease and prevent patient suffering and mortality.

4.2 Prediction of Disease Progression in COPD Patients

Prediction models for COPD exacerbation have long been sought by clinicians and researchers. Such models would enable physicians to provide prophylactic treatment to patients, avoiding short-term respiratory distress. Reduction in the number of COPD exacerbations has also been shown to be disease modifying (Donaldson and Wedzicha 2006), reducing a patient's risk of COPD-related mortality.

Early efforts to predict COPD exacerbations have been based on clinical features such as smoking status and spirometric features such as FEV1. These efforts have modeled various end points associated with COPD exacerbation such as "COPD-related hospitalization," "Outpatient treatment for COPD exacerbation," or "Exacerbation as defined by symptomatic criteria" (Guerra et al. 2017). Methods applied include logistic regression, cox regression, linear regression, and random forests (Guerra et al. 2017),

with area under the ROC curve measurements ranging from 0.58 to 0.81.

Inclusion of features derived from pulmonary functional imaging has great promise for developing more reliable, more accurate predictive models of COPD exacerbation. In an analysis of COPD exacerbations in the COPDGene cohort, investigators found association between COPD exacerbation with a collection of functional imaging metrics including total lung emphysema percentage, segmental bronchial wall thickness, alongside conventional features like FEV1 and smoking history and current smoking status (Han et al. 2011). These methods hold the promise of improved accuracy over conventional methods, though further evaluation is required.

4.3 Predicting Malignancy of Pulmonary Nodules

Assessment of pulmonary nodules requires careful consideration of nodule size, location, and appearance discernible from conventional CT imaging. This has motivated commercial development of computational systems to facilitate tracking and monitoring of these various imaging biomarkers. There remains, however, a wealth of additional information about nodules and surrounding lung tissue which can be explored using pulmonary functional imaging. For example, FDG-PET imaging of lung nodules, when fused with standard CT imaging as depicted in Fig. 5, has been shown to provide

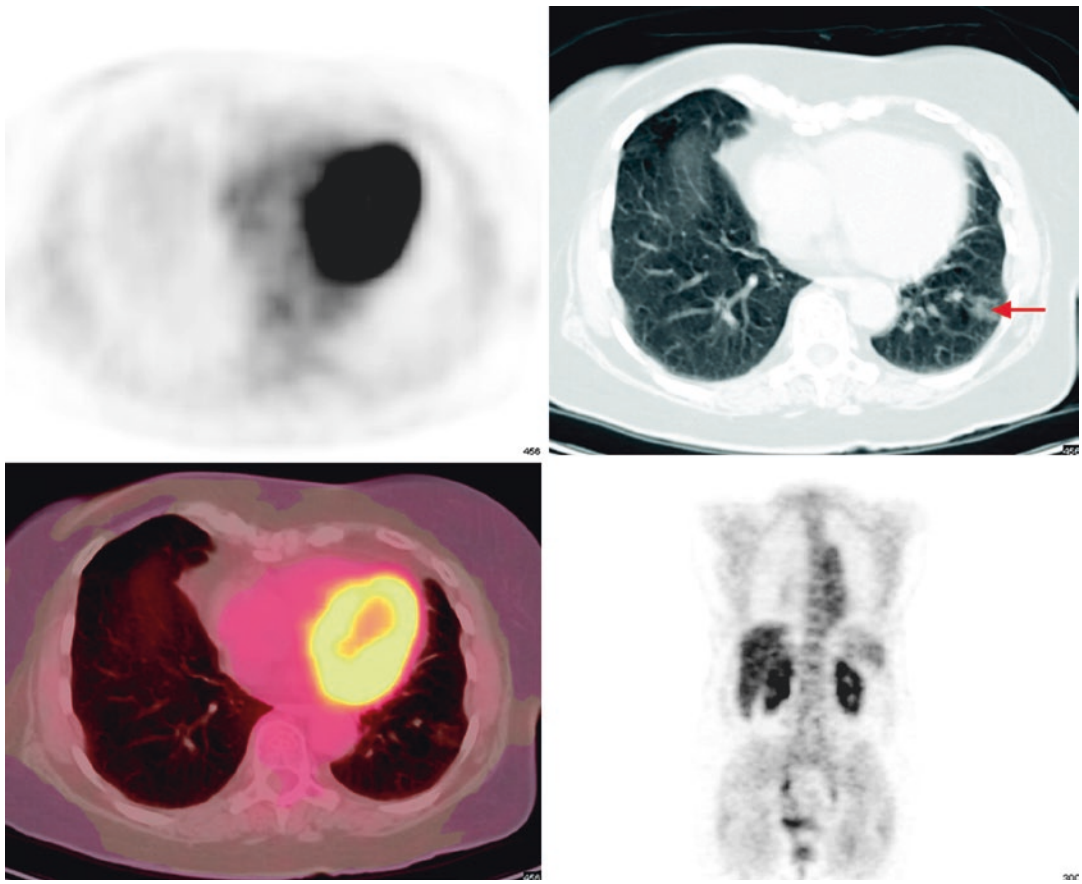


Fig. 5 Opacification in left lower lung field on CT (arrow). On PET and fusion images there is no 18F-FDG uptake. Lesion was scored as 4 on CT and 0 on PET and interpreted as benign on PET/CT. Lesion was resected and pathology revealed an adenocarcinoma with BAC features. (Adapted from Kim et al. 2007 with author's permission)

additional diagnostic value to radiologists when determining whether a nodule is malignant or benign (Hillner et al. 2007; Kim et al. 2007). Certain lung pathologies, such as infection or inflammation, may result in increased immune cell activity leading to increased uptake of FDG and hence higher intensity of FDG-PET imaging. This information may be used to help rule out inflammatory or infectious etiologies of lung nodules.

Furthermore, certain tumors exhibit marked differences in vasculature when compared to surrounding lung parenchyma or nonmalignant nodules. By using contrast enhanced CT or MR imaging, these vascular differences can be better appreciated. Advanced functional imaging modalities can measure perfusion and pulmonary vascular changes in a fine-grained manner and have been shown to assist in the diagnosis of malignant lung nodules. MR imaging has also been studied as a potential screening and diagnostic modality for primary lung cancer, showing acceptable sensitivity and potentially superior specificity to CT (Biederer et al. 2017).

MR imaging has also been used to characterize malignant nodules and masses (Ohno 2018). Various MR modalities including DWI, non-dynamic contrast enhanced methods, and dynamic contrast enhanced methods, have been evaluated in both the detection and characterization of lung masses and nodules, demonstrating the potential for this technology to complement existing clinical practice.

4.4 Predicting Need for Lung Transplant in Cystic Fibrosis Patients

Cystic fibrosis (CF) is characterized by progressive pulmonary decline and eventual pulmonary failure. Although novel therapies for CF have been developed in the last decade, the average life expectancy for a patient with CF remains low at only 40 years. In an effort to prolong life expectancy, lung transplants are often performed. However, a lung transplant is a dangerous procedure and the number of qualifying CF patients exceeds donor supply. Therefore, a way to identify CF patients with the greatest need for a lung transplant is needed.

Existing efforts to predict CF exacerbation and lung failure have relied primarily on FEV1. Consensus guidelines by the International Society of Heart and Lung Transplantation recommend referring CF patients for lung transplant when FEV1 drops below 30% of the patient's predicted normal FEV1 value (Weill et al. 2015). However, in this group of patients with an FEV1 below 30%, there is substantial variability in mortality. Some patients suffer, while others live long beyond expected life span. Using variables extracted from electronic medical records, laboratory values, and pulmonary function testing, investigators were able to create a predictive model for three-year mortality with a better positive predictive value and negative predictive value than FEV1 value alone (Alaa and van der Schaar 2018).

5 Summary

Advances in computational image analysis in concert with advancements in functional imaging techniques and methods have resulted in informative research and novel clinical methods for the diagnosis and assessment of pulmonary disease. In this chapter, we reviewed the myriad computational metrics that have emerged as putative biomarkers for diseases such as asthma, CF, COPD, pulmonary embolism, and lung cancer. We have discussed emerging functional imaging modalities such as hyperpolarized gas MRI and inhaled contrast CT and reviewed novel uses of existing technologies, such as DECT to quantify ventilation and perfusion in a voxel-wise manner. We have also discussed a number of exciting translational research projects leveraging these methods, metrics, and modalities to diagnose and better treat disease.

Perhaps most promising methods based on deep learning are drawing significant interest from the community and offer the potential of improved diagnostic and prognostic abilities. Indeed, a bounty of deep learning-based methods

has been presented across numerous domains, regularly demonstrating superior classification accuracy when compared against conventional methods. While these methods require continued rigorous investigation, their possible clinical translation has exciting ramifications for the field of functional lung imaging, and indeed medicine overall.

References

Adler AI, Shine BSF, Chamnan P, Haworth CS, Bilton D (2008) Genetic determinants and epidemiology of cystic fibrosis-related diabetes: results from a British cohort of children and adults. Diabetes Care 31(9):1789–1794. https://doi.org/10.2337/dc08-0466

Alaa AM, Mihaela van der S (2018) "Prognostication and risk factors for cystic fibrosis via automated machine learning." Scientific Reports 8(1). https://doi.org/10.1038/s41598-018-29523-2

Alford SK, Edwin JR van Beek, Geoffrey Mc, Eric AH (2010) "Heterogeneity of pulmonary perfusion as a mechanistic image-based phenotype in emphysema susceptible smokers." Proc Natl Acad Sci 107(16):7485. https://doi.org/10.1073/pnas.0913880107

Altes TA, Mugler JP, Ruppert K, Tustison NJ, Gersback J, Szentpetery S, Meyer CH, de Lange EE, Teague GW (2016) Clinical correlates of lung ventilation defects in asthmatic children. J Allergy Clin Immunol 137(3):789–796.e7. https://doi.org/10.1016/j.jaci.2015.08.045

Altes TA, Johnson M, Fidler M, Botfield M, Tustison NJ, Levia-Salinas C, de Lange EE, Froh D, Mugler JP (2017) Use of hyperpolarized helium-3 MRI to assess response to ivacaftor treatment in patients with cystic fibrosis. J Cyst Fibros 16(2):267–274. https://doi.org/10.1016/j.jcf.2016.12.004

Aurora P, Bush A, Gustafsson P, Oliver C, Wallis C, Price J, Stroobant J, Carr S, Stocks J (2004) Multiple-breath washout as a marker of lung disease in preschool children with cystic fibrosis. Am J Respir Crit Care Med 171(3):249–256. https://doi.org/10.1164/rccm.200407-895OC

Avants B, Epstein CL, Grossman M, Gee JC (2008) Symmetric diffeomorphic image registration with cross-correlation: evaluating automated labeling of elderly and neurodegenerative brain. Med Image Anal 12(1):26–41. https://doi.org/10.1016/j.media.2007.06.004

Bhatt SP, George RW, Eric AH, John DN, Sandeep B, Alejandro AD, Craig JG, Edwin KS, Raúl San JE, David AL (2019) "Imaging advances in chronic obstructive pulmonary disease. Insights from the Genetic Epidemiology of Chronic Obstructive Pulmonary Disease (COPDGene) Study." Am J Respir Crit Care Med 199(3):286–301. https://doi.org/10.1164/rccm.201807-1351SO

Bhatt SP, Bodduluri S, Hoffman EA, Newell JD, Sieren JC, Dransfield MT, Reinhardt JM (2017) Computed tomography measure of lung at risk and lung function decline in chronic obstructive pulmonary disease. Am J Respir Crit Care Med 196(5):569–576. https://doi.org/10.1164/rccm.201701-0050OC

Biederer J, Ohno Y, Hatabu H, Schiebler ML, Van Beek EJR, Vogel-Claussen J, Kauczor H-U (2017) Screening for lung cancer: does MRI have a role? Eur J Radiol 86:353–360. https://doi.org/10.1016/j.ejrad.2016.09.016

Busacker A, Newell JD, Keefe T, Hoffman EA, Granroth JC, Castro M, Fain S, Wenzel S (2009) A multivariate analysis of risk factors for the air-trapping asthmatic phenotype as measured by quantitative CT analysis. Chest 135(1):48–56. https://doi.org/10.1378/chest.08-0049

Campana L, Kenyon J, Zhalehdoust-Sani S, Tzeng Y-S, Albert M, Lutchen KR (2009) Probing airway conditions governing ventilation defects in asthma via hyperpo- larized MRI image functional modeling. J Appl Physiol 106(4):1293–1300. https://doi.org/10.1152/japplphysiol.91428.2008

CDC (2016) National Health Interview Survey (NHIS) Data

Chen, Delphine L., Ferkol, Thomas W., Mintun, Mark A., Pittman, Jessica E., Rosenbluth, Daniel B., Schuster, and Daniel P. "Quantifying pulmonary inflammation in cystic fibrosis with positron emission tomography." Am J Respir Crit Care Med, 173(12)2006: 1363–1369. doi: https://doi.org/10.1164/rccm.200506-934OC.

Chon D, Beck KC, Larsen RL, Shikata H, Hoffman EA (2006) Regional pulmonary blood flow in dogs by 4D-X-ray CT. J Appl Physiol 101(5):1451–1465. https://doi.org/10.1152/japplphysiol.01131.2005

Chon D, Kenneth CB, Brett AS, Hidenori S, Osama IS, Eric AH (2007) "Effect of low-xenon and krypton supplementation on signal/noise of regional CT-based ventilation measurements." J Appl Physiol 102(4):1535–44. https://doi.org/10.1152/japplphysiol.01235.2005

Ding L, Ley TJ, Larson DE, et al. (2012) Clonal evolution in relapsed acute myeloid leukaemia revealed by whole-genome sequencing. Nature 481(7382):506–510. Published 2012 Jan 11. https://doi.org/10.1038/nature10738

Donaldson GC, Wedzicha JA (2006) COPD exacerbations. I. Epidemiol Thorax 61(2):164–168

Fahy JV (2009) Eosinophilic and neutrophilic inflammation in asthma: insights from clinical studies. Proc Am Thorac Soc 6(3):256–259. https://doi.org/10.1513/pats.200808-087RM

Freed BH, Collins JD, François CJ, Barker AJ, Cuttica MJ, Chesler NC, Markl M, Shah SJ (2016) MR and CT imaging for the evaluation of pulmonary hypertension. JACC Cardiovasc Imaging 9(6):715–732

Fuld MK, Ahmed FH, Susan EH, Abhay AD, Junfeng G, Eric AH (2013) "Pulmonary perfused blood volume with dual-energy CT as surrogate for pulmonary perfusion assessed with dynamic multidetector CT." Radiology 267(3):747–756. https://doi.org/10.1148/radiol.12112789

Gibson RL, Burns JL, Ramsey BW (2003) Pathophysiology and management of pulmonary infections in cystic fibrosis. Am J Respir Crit Care Med 168(8): 918–951. https://doi.org/10.1164/rccm.200304-505SO

Guerra B, Gaveikaite V, Bianchi C, Puhan MA (2017) Prediction models for exacerbations in patients with COPD. Eur Respir Rev 26(143):160061. https://doi.org/10.1183/16000617.0061-2016

Han MLK, Kazerooni EA, Lynch DA, Liu LX, Murray S, Curtis JL, Criner GJ, Kim V, Bowler RP, Hanania NA, Anzueto AR, Make BJ, Hokanson JE, Crapo JD, Silverman EK, Martinez FJ, Washko GR (2011) Chronic obstructive pulmonary disease exacerbations in the COPDGene study: associated radiologic phenotypes. Radiology 261(1):274–282. https://doi.org/10.1148/radiol.11110173

He M, Kaushik SS, Robertson SH, Freeman MS, Virgincar RS, McAdams HP, Driehuys B (2014) Extending semiautomatic ventilation defect analysis for hyperpolarized 129Xe ventilation MRI. Acad Radiol 21(12):1530–1541. https://doi.org/10.1016/j.acra.2014.07.017

Hecht EM, Rosenkrantz A (2009) Pulmonary MR angiography techniques and applications. Magn Reson Imaging Clin N Am 17(1):101–131

Hillner BE, Siegel BA, Liu D, Shields AF, Gareen IF, Lucy H (2007) Impact of positron emission tomography/computed tomography and positron emission tomography (PET) alone on expected management of patients with cancer: initial results from the National Oncologic PET Registry. J Clin Oncol 26:2155–2161. https://doi.org/10.1200/JCO.2007.14.5631

Hoffman EA, Lynch DA, Barr GR, Van Beek EJR, Parraga G (2016) Pulmonary CT and MRI phenotypes that help explain chronic pulmonary obstruction disease pathophysiology and outcomes: CT and MRI of COPD. J Magn Reson Imaging 43(3):544–557. https://doi.org/10.1002/jmri.25010

Hughes PJC, Horn FC, Collier GJ, Biancardi A, Marshall H, Wild JM (2018) Spatial Fuzzy C-means thresholding for semiautomated calculation of percentage lung ventilated volume from hyperpolarized gas and ^{1}H MRI: SFCM-based segmentation of lung MRI. J Magn Reson Imaging 47(3):640–646. https://doi.org/10.1002/jmri.25804

Hwang HJ, Hoffman EA, Lee CH, Goo JM, Levin DL, Kauczor H-U, Seo Joon B (2017) The role of dual-energy computed tomography in the assessment of pulmonary function. Eur J Radiol 86:320–334. https://doi.org/10.1016/j.ejrad.2016.11.010

Johns CS, Swift AJ, Hughes PJC, Ohno Y, Schiebler M, Wild JM (2017) Pulmonary MR angiography and perfusion imaging—A review of methods and applications. Eur J Radiol 86:361–370. https://doi.org/10.1016/j.ejrad.2016.10.003

Jones HA, Sriskandan S, Peters AM, Pride NB, Boobis AR, Haslett C (1997) Dissociation of neutrophil emigration and metabolic activity in lobar pneumonia and bronchiectasis. Eur Respir J 10(4):9

Kauczor HU, Chen XJ (2001) Pulmonary ventilation imaged by magnetic resonance: at the doorstep of clinical application. Eur Respir J:16

Kim SK, Allen-Auerbach M, Goldin J, Fueger BJ, Dahlbom M, Brown M, Czernin J, Schiepers C (2007) Accuracy of PET/CT in characterization of solitary pulmonary lesions. J Nucl Med 48(2):214–220

Kirby M, Heydarian M, Svenningsen S, Wheatley A, McCormack DG, Etemad-Rezai R, Parraga G (2012) Hyperpolarized 3He magnetic resonance functional imaging semiautomated segmentation. Acad Radiol 19(2):141–152. https://doi.org/10.1016/j.acra.2011.10.007

Kirby M, Pike D, Coxson HO, McCormack DG, Parraga G (2014) Hyperpolarized 3He ventilation defects used to predict pulmonary exacerbations in mild to moderate chronic obstructive pulmonary disease. Radiology 273(3):887–896. https://doi.org/10.1148/radiol.14140161

Kong X, Hui XS, Guang ML, Felix GM, Kevin TD, U Joseph S, Long JZ. (2014) "Xenon-enhanced dual-energy CT lung ventilation imaging: Techniques and Clinical Applications." AJR Am J Roentgenol 202(2):309–317. https://doi.org/10.2214/AJR.13.11191

de Lange EE, Altes TA, Patrie JT, Gaare JD, Knake JJ, Mugler JP, Platts-Mills TA (2016) Evaluation of asthma with hyperpolarized helium-3 MRI. Chest J 130(4):1055–1062. https://doi.org/10.1378/chest.130.4.1055

Levin DL, Schiebler ML, Hopkins SR (2017) Physiology for the pulmonary functional imager. Eur J Radiol 86:308–312. https://doi.org/10.1016/j.ejrad.2016.09.027

Madsen PH, Hess S, Høilund-Carlsen PF, Alavi A (2013) Positron emission tomography in chronic obstructive pulmonary disease. Hell J Nucl Med. 2013;16(2):121–124

Murphy K, Ginneken B, Pluim JP, Klein S, Staring M (2008) Semi-automatic reference standard construction for quantitative evaluation of lung CT registration Proc. MICCAI (New York: Springer) pp. 1006–13

Ohno Y, Fujisawa Y, Koyama H, Kishida Y, Seki S, Sugihara N, Yoshikawa T (2017a) Dynamic contrast-enhanced perfusion area-detector CT assessed with various mathematical models: its capability for therapeutic outcome prediction for non-small cell lung cancer patients with chemoradiotherapy as compared with that of FDG-PET/CT. Eur J Radiol 86:83–91. https://doi.org/10.1016/j.ejrad.2016.11.008

Ohno Y, Yoshikawa T, Takenaka D, Fujisawa Y, Sugihara N, Kishida Y, Seki S, Koyama H, Sugimura K (2017b) Xenon-enhanced CT using subtraction CT: basic and

preliminary clinical studies for comparison of its efficacy with that of dual-energy CT and ventilation SPECT/CT to assess regional ventilation and pulmonary functional loss in smokers. Eur J Radiol 86:41–51. https://doi.org/10.1016/j.ejrad.2016.10.035

Ohno Y, Yoshikawa T, Kishida Y, Seki S, Karabulut N (2017c Mar) Unenhanced and contrast-enhanced MR angiography and perfusion imaging for suspected pulmonary thromboembolism. AJR Am J Roentgenol 208(3):517–530

Ohno Y, Kauczor H-U, Hatabu H, Seo JB, van Beek EJR, and for the International Workshop for Pulmonary Functional Imaging (IWPFI) (2018) MRI for solitary pulmonary nodule and mass assessment: current state of the art: MRI for solitary pulmonary nodule and mass. J Magn Reson Imaging 47(6):1437–1458. https://doi.org/10.1002/jmri.26009

Pennati F, Roach DJ, Clancy JP, Brody AS, Fleck RJ, Aliverti A, Woods JC (2018) Assessment of pulmonary structure-function relationships in young children and adolescents with cystic fibrosis by multivolume proton-MRI and CT: noncontrast MRI in CF lung disease. J Magn Reson Imaging 48(2):531–542. https://doi.org/10.1002/jmri.25978

Schmidt-Richberg A, Werner R, Handels H, Ehrhardt J (2012) Estimation of slipping organ motion by registration with direction-dependent regularization. Med Image Anal 16(1):150–159. https://doi.org/10.1016/j.media.2011.06.007

Song G, Tustison NJ, Avants BB, Gee JC (2010) Lung CT image registration using diffeomorphic transformation models. Medical image analysis for the clinic: a grand challenge. pp 23–32

Stahl M, Wielpütz MO, Graeber SY, Joachim C, Sommerburg O, Kauczor H-U, Puderbach M, Eichinger M, Mall MA (2016) Comparison of lung clearance index and magnetic resonance imaging for assessment of lung disease in children with cystic fibrosis. Am J Respir Crit Care Med 195(3):349–359. https://doi.org/10.1164/rccm.201604-0893OC

Sundaram TA, Avants BB, Gee JC (2005) Towards a dynamic model of pulmonary parenchymal deformation: evaluation of methods for temporal reparameterization of lung data. Med Image Comput Comput Assist Interv 8:328–335

Svenningsen S, Kirby M, Starr D, Coxson HO, Paterson NAM, McCormack DG, Parraga G (2014) What are ventilation defects in asthma? Thorax 69(1):63–71. https://doi.org/10.1136/thoraxjnl-2013-203711

Trivedi A, Hall C, Hoffman EA, Woods JC, Gierada DS, Castro M (2017) Using imaging as a biomarker for asthma. J Allergy Clin Immunol 139(1):1–10. https://doi.org/10.1016/j.jaci.2016.11.009

Tsuchiya N, van Beek EJ, Ohno Y, Hatabu H, Kauczor HU, Swift A, Vogel-Claussen J, Biederer J, Wild J, Wielpütz MO, Schiebler ML (2018) Magnetic resonance angiography for the primary diagnosis of pulmonary embolism: a review from the international workshop for pulmonary functional imaging. World J Radiol 10(6):52–64

Tustison NJ, Altes TA, Song G, de Lange EE, Mugler JP 3rd, Gee JC (2010) Feature analysis of hyperpolarized helium-3 pulmonary MRI: a study of asthmatics versus nonasthmatics. Magn Reson Med 63(6):1448–1455. https://doi.org/10.1002/mrm.22390

Tustison NJ, Cook TS, Song G, Gee JC (2011a) Pulmonary kinematics from image data: a review. Acad Radiol 18(4):402–417. https://doi.org/10.1016/j.acra.2010.10.019

Tustison NJ, Avants BB, Flors L, Altes TA, de Lange EE, Mugler JP 3rd, Gee JC (2011b) Ventilation-based segmentation of the lungs using hyperpolarized 3He MRI. J Magn Reson Imaging 34(4):831–841. https://doi.org/10.1002/jmri.22738

Tustison NJ, Brian BA (2013) "Explicit B-spline regularization in diffeomorphic image registration." Frontiers in Neuroinformatics 7. https://doi.org/10.3389/fninf.2013.00039

Tustison NJ, Qing K, Wang C, Altes TA, Mugler JP (2016) Atlas-based estimation of lung and lobar anatomy in proton MRI: atlas-based estimation of lung and lobar anatomy in proton MRI. Magn Reson Med 76(1):315–320. https://doi.org/10.1002/mrm.25824

Tustison NJ, Avants BB, Lin Z, Feng X, Cullen N, Mata JF, Flors L, Gee JC, Altes TA, Mugler Iii JP, Qing K (2019) Convolutional neural networks with template-based data augmentation for functional lung image quantification. Acad Radiol 26(3):412–423. https://doi.org/10.1016/j.acra.2018.08.003

Wang H, Paul AY (2013) "Multi-Atlas segmentation with joint label fusion and corrective learning—an open source implementation." Frontiers in Neuroinformatics 7. https://doi.org/10.3389/fninf.2013.00027

Weill D, Christian B, Paul AC, John HD, R Duane D, Shaf K, David JL, et al. (2015) "A consensus document for the selection of lung transplant candidates: 2014—an update from the pulmonary transplantation council of the international society for heart and lung transplantation." J Heart Lung Transplant: The Official Publication of the International Society for Heart Transplantation 34(1):1–15. https://doi.org/10.1016/j.healun.2014.06.014

Werner R, Ehrhardt J, Schmidt R, Handels H (2009) Patient-specific finite element modeling of respiratory lung motion using 4D CT image data. Med Phys 36(5):1500–1511. aapm.onlinelibrary.wiley.com. https://doi.org/10.1118/1.3101820

Woodhouse N, Wild JM, Paley MNJ, Fichele S, Said Z, Swift AJ, van Beek EJR (2005) Combined helium-3/proton magnetic resonance imaging measurement of ventilated lung volumes in smokers compared to never-smokers. J Magn Reson Imaging 21(4):365–369. https://doi.org/10.1002/jmri.20290

Yablonskiy DA, Sukstanskii AL, Leawoods JC, Gierada DS, Bretthorst L, Lefrak SS, Cooper JD, Conradi MS (2002) Quantitative in vivo assessment of lung micro-

structure at the alveolar level with hyperpolarized 3He diffusion MRI. Proc Natl Acad Sci 99(5):3111–3116. https://doi.org/10.1073/pnas.052594699

Yin Y, Hoffman EA, Ding K, Reinhardt JM, Lin C-L (2011) A cubic B-spline-based hybrid registration of lung CT images for a dynamic airway geometric model with large deformation. Phys Med Biol 56(1):203–218. https://doi.org/10.1088/0031-9155/56/1/013

Zha W, Niles DJ, Kruger SJ, Dardzingski BJ, Cadman RV, Mummy DG, Nagle SK, Fain SB (2016) Semiautomated ventilation defect quantification in exercise-induced bronchoconstriction using hyperpolarized helium-3 magnetic resonance imaging. Acad Radiol 23(9):1104–1114. https://doi.org/10.1016/j.acra.2016.04.005

Image-Based Phenotyping, Deep Learning (DL), and Artificial Intelligence (AI) Applications in Clinical and Research Radiology and Chest Imaging

Vladimir I. Valtchinov, Joon Beom Seo, Tomoyuki Hida, and Hiroto Hatabu

Contents

1 **Image-Based Phenotyping** 320
1.1 Figures (Two Figures from Radiology 2018 with Permission) 322

2 **Deep Learning (DL) and Artificial Intelligence (AI) Applications in Clinical and Research Radiology** 323
2.1 Availability of Large, Annotated Sets of Labeled Data for Training and Testing 326
2.2 Deep Learning Algorithms Need Real-World Testing 327
2.3 Black-Box Nature: Why Do DL NNs Work? 328
2.4 Interpretation: Develop and Implement Algorithms that Self-Explain themselves 328

3 **Current Application of Deep Learning in Chest Imaging** 329
3.1 Chest Radiography 329
3.2 Computed Tomography 330

4 **Conclusion** 331

References 331

V. I. Valtchinov
Center for Pulmonary Functional Imaging, Brigham and Women's Hospital and Harvard Medical School, Boston, MA, USA

Department of Biomedical Informatics, Harvard Medical School, Boston, MA, USA

J. B. Seo
University of Ulsan College of Medicine, Asan Medical Center, Seoul, South Korea

T. Hida · H. Hatabu (✉)
Center for Pulmonary Functional Imaging, Brigham and Women's Hospital and Harvard Medical School, Boston, MA, USA
e-mail: hhatabu@bwh.harvard.edu

Abstract

Image-based phenotyping with genomic correlation is opening a new window to the groundbreaking and innovative research field by combining genetic and morphologic data. The natural extensions of the works with visual review of CT scans by radiologists are applications of deep learning and artificial intelligence. We introduce the main concepts and core ideas and briefly review the history and current state-of-the-art artificial intelligence (AI) and deep learning (DL) appli-

© Springer Nature Switzerland AG 2021

Y. Ohno et al. (eds.), *Pulmonary Functional Imaging*, Medical Radiology Diagnostic Imaging,
https://doi.org/10.1007/978-3-030-43539-4_15

cations in clinical and research radiology. Unsupervised and supervised general approaches are reviewed. We spell out the technical, knowledge discovery, regulatory, and ethical challenges for the wider and seamless adoption of AI in clinical radiology practice. We advocate for parallel development of deterministic and probabilistic approaches to supplement the rapid advancements in deep learning and simulation technique applications which often serve as "black box" with limited clinical insight behind the results they provide. The current applications of deep learning in chest imaging are also summarized.

1 Image-Based Phenotyping

Sixty years after the discovery of double helical structure of DNA, molecular biology drives precision and personalized medicine, drastically changing how we manage and care for patients. However, it gradually became apparent that genomic information alone is not enough to explain all clinical phenomena. Phenotyping approaches using imaging modality, i.e., image-based phenotyping, play an important and complementary role to genotyping. Image-based phenotyping with genomic correlation opens a groundbreaking and innovative research field by combining genetic and morphologic data (Hatabu 2011, 2015; Hatabu et al. 2018).

First, in 2010, a group of pulmonologists approached us to review a few thousand CT scans from COPDGene study in the hunt for early or subclinical pulmonary fibrosis. We decided to work together for 3 months to systematically review the presence of subtle and mild interstitial lung abnormalities among 2416 CT scans of COPDGene NIH-supported multi-center trial using the sequential scoring method (Washko et al. 2010). The effort resulted in one of the first publications of the subject related to ILA (interstitial lung abnormality) in New England Journal of Medicine in 2011 (Washko et al. 2011). The ILA is defined as nondependent changes affecting more than 5% of any lung zone and included nondependent ground-glass or reticular abnormalities, diffuse centrilobular nodularity, nonemphysematous cysts, honeycombing, and traction bronchiectasis. To our surprise, ILA is present on 8% of the subjects, and associated with reduced total lung capacity. Among 194 subjects with ILA, 37 were centrilobular, 107 were subpleural, 38 were mixed centrilobular and subpleural, and 12 were radiographic interstitial lung disease (ILD). In the later studies, more and more evidences are accumulating to indicate subpleural subtype (55%; 107/194) may be the most important subtype including the subjects, who subsequently progress to pulmonary fibrosis. Jin GY et al. investigated 884 CT scans from National Lung Screening Trial at a single site and found ILA in 86 (9.7%) (Jin et al. 2013). ILA is also associated with reduced exercise capacity (Doyle et al. 2012). In 2011, a single-nucleotide polymorphism (SNP) (rs35705950) in the promoter region of the gene encoding mucin 5B (MUC5B) was reported to be associated with both familial and sporadic idiopathic pulmonary fibrosis (Seibold et al. 2011). The minor allele of SNP rs35705950, located 3 kb upstream of the *MUC5B* transcription start site, was present at a frequency of 34% among subjects with familial interstitial pneumonia, 38% among subjects with IPF, and 9% among controls (allelic association with familial interstitial pneumonia, $P = 1.2 \times 10^{-15}$; allelic association with IPF, $P = 2.5 \times 10^{-37}$). The *MUC5B* expression in the lung was 14.1 times as high in subjects who had IPF as in those who did not ($p < 0.001$), and MUC5B protein was expressed in lesions of IPF (Seibold et al. 2011). The minor allele of SNP rs35705950 was present in approximately 20% of European population (Mucin 5, Subtype B, Tracheobronchial: MUC5B n.d.). To test the hypothesis that subjects with the MUC5B variant in the general population would have an increased prevalence of ILA and ILD, we approached Dr. Schwartz's group in Denver. As a result, we started examining ILA in 2633 CT scans obtained as part of the Framingham Heart Study (FHS), and completed in 2013. Of the 2633 CT scans, 177 (7%) had ILA, 1086 (41%) were indeterminate, and 1370 (52%) did not have ILA (Hunninghake et al. 2013). As compared with subjects without ILA, the subjects with ILA were

found to be older, had increased exposure to tobacco smoke, and were twice more likely to report having a chronic cough and shortness of breath. The subjects with ILA had decreased diffusion capacity carbon monoxide by 12% and total lung capacity by 9% compared with those without ILA. More than half of the subjects with ILA had a CT-derived total lung capacity of less than 80% of the predicted value, consistent with a restrictive lung deficit. The minor allele frequency of the MUC5B promoter SNP (rs3570950) was 10.5%. After adjustment for covariates, for each copy of the MUC5B, the odds of ILA were 2.8 times greater as compared with those without ILA. ILA was strongly associated with age. The prevalence of ILA was 2% in subjects who were 50 years of age or younger, and was 9% in subjects who were over the age of 50 years. Of 177 subjects with ILA, 42 (27%) could be classified as having architectural distortion, who had 6.3 times greater odds compared with subjects without ILA.

How about mortality in subjects with ILA? To address this question, CT scans from four different prospective cohort studies including FHS (n = 2633), AGES-Reykjavik Study (n = 5320), COPDGene (n = 2068), and ECLIPSE (n = 1670) were systematically reviewed. In all 4 separate research cohorts, ILA was associated with a greater risk of all-cause mortality (Putman et al. 2016) (Fig. 1). In the AGES-Reykjavik cohort, the higher rate of mortality could be explained by a higher rate of death due to respiratory disease, in particular due to pulmonary fibrosis (Putman et al. 2016). Does ILA progress over time? In the study with 1867 subjects from FHS cohort with serial CT scans of 6-year interval, 37 (2%) had stable to improving ILA, and 118 (6%) had ILA with progression (Araki et al. 2016a) (Fig. 2). ILA progression was associated with increased rate of pulmonary function decline and increased risk of death (Araki et al. 2016a). How about histopathology of ILA? Miller ER et al. investigated histopathology in 424 patients who had lung nodule resection and had a CT scan within 3 months before surgery. ILA was present in 26 (6%). The patients with ILA had increased rates of pulmonary fibrosis in general and subpleural interstitial fibrosis, fibroblastic foci, honeycombing/UIP, and atypical adenomatous hyperplasia. The patients with ILA were more likely to have subpleural fibrosis [OR 2.1] and AAH [OR, 1.7] compared with patients without ILA (Miller et al. 2018). Of the 26 cases of ILA, 3 (12%) were centrilobular, 17 (65%) were subpleural, and 6 (23%) were mixed. No case of fibrosis, fibroblastic foci, or honeycombing was identified in patients with centrilobular predominant ILA, while association between AAH and ILA appeared to be limited to centrilobular predominant ILA (Miller et al. 2018). How about relationship between ILA and ARDS? Putman RK et al. examined 227 patients who had CT scan at least 7 days before ICU admission. ILA was present in 19 (8%), who were more likely to be diagnosed with ARDS compared with patients without ILA: 74% vs. 15% ($p < 0.0001$) (Putman et al. 2017). Nishino M et al. reported that the stage VI non-small cell lung cancer patients with ILA on the pretreatment CT scans had shorter overall survival compared with those who do not have ILA (Nishino et al. 2015).

When new therapies for fibrotic lung diseases have been emerged with positive clinical trials outcomes (Richeldi et al. 2014; King Jr. et al. 2014; Raghu et al. 2018), and researchers and clinicians started to think that patients for early treatment or prevention of developing pulmonary fibrosis may be included among the subjects with ILA, the abovementioned works with large cohorts of CT scans with genetic and prognostic correlations gradually made the concept of ILA recognized (Hatabu et al. 2018).

At the same time, we have also systematically reviewed CT scans from the Framingham Heart Study (FHS) with special interests in the noncardiac thoracic findings including normal thymus, anterior mediastinal mass, paraseptal emphysema, cysts, and asbestos plaques (Araki et al. 2016b, 2015a, b, c, 2017). This was probably the first experience for the human being to observe lungs noninvasively in a few thousand population.

The natural extensions of the works with visual review of CT scans by radiologists are applications of deep learning and artificial intelligence (Kim et al. 2015; Pankratz et al. 2017; Jacob et al. 2016, 2017; Ash et al. 2018; Humphries et al. 2017). In the following portion of this chapter, the applications of deep learning and artificial intelli-

gence in clinical research in radiology in general as well as the current applications of deep learning in chest imaging will be summarized.

1.1 Figures (Two Figures from Radiology 2018 with Permission)

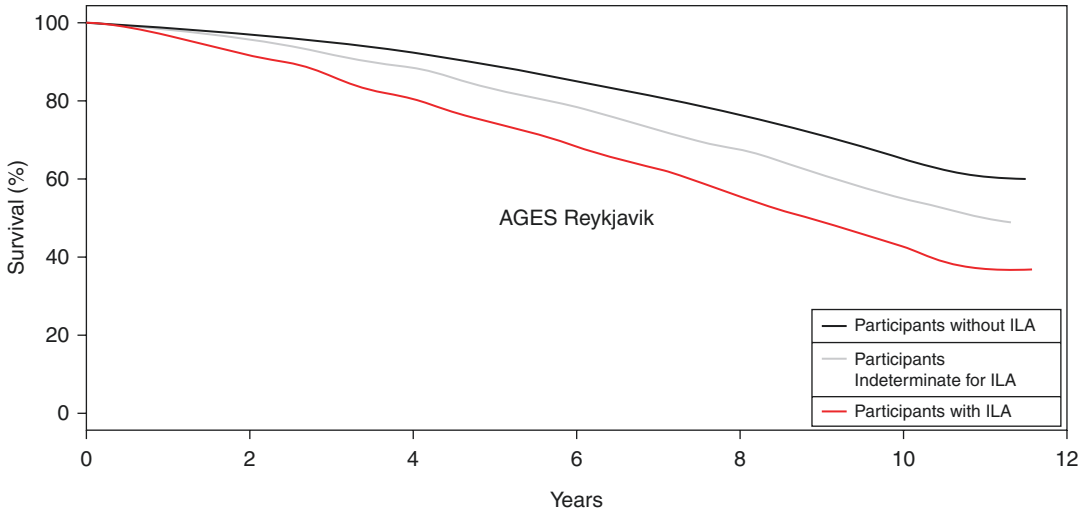


Fig. 1 Survival rates by ILA status for the AGES-Reykjavik study. *X*-axis indicates the duration of follow-up in years up to 12 years. *Y*-axis indicates survival range from 100 to 0%. Hazard ratio was 1.3 [1.2–1.4; 95% CIs; $p < 0.001$] between participants with ILA and participants without ILA from the adjusted Cox proportional hazards model including adjustments for age, sex, body mass index, pack-years of smoking, and current or former smoking status. AGES indicates the Age Gene/Environment Susceptibility; ILA, interstitial lung abnormalities. Created from the data published in reference (Putman et al. 2016) (Putman RK, Hatabu H, Araki T, et al. Association between interstitial lung abnormalities and all-cause mortality. JAMA 2016; 315:672–681)

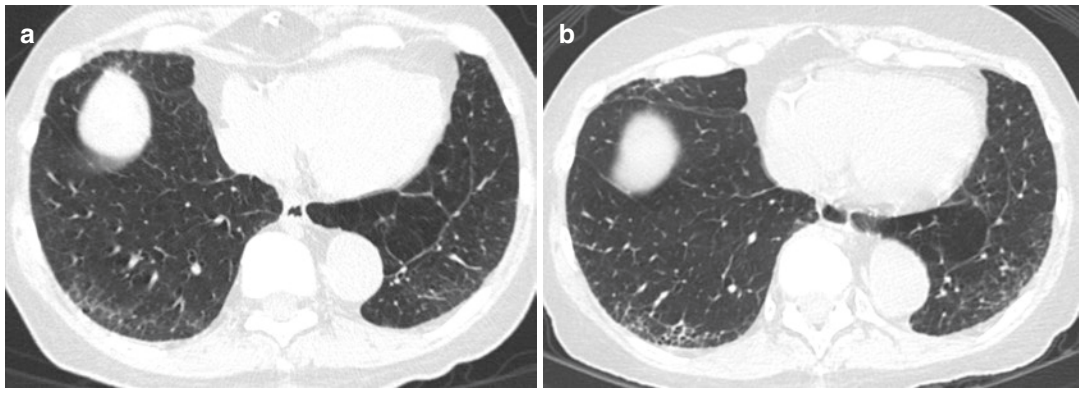


Fig. 2 A 73-year-old female participant in the COPDGene Study. (Reproduced from Reference (Hatabu et al. 2018) with permission). (**a**) Baseline non-contrast chest CT scan of the chest shows mild ground-glass abnormalities with interlobular septal thickening with subpleural distribution. (**b**) CT scan performed five and half years later demonstrates reticular and ground-glass opacities with mild traction bronchiectasis and architectural distortion indicating progression. Over this time period, the participant experienced increase in respiratory symptoms and decrease in total lung capacity

2 Deep Learning (DL) and Artificial Intelligence (AI) Applications in Clinical and Research Radiology

The birth date and place of AI are considered as the Dartmouth Artificial Intelligence (AI) conference in 1956 in New Hampshire. At this meeting, organized and spearheaded by the legendary late professor of computer science at Stanford John McCarthy, a group of leading researchers in their fields gathered to discuss and define topics in chaos and complexity theory, machines that are capable of learning ("thinking machines"), neuron nets and simulations, etc. for which John McCarty has coined a new term: Artificial Intelligence (A Proposal for the Dartmouth Summer Research Project on Artificial Intelligence [Internet] 2019).

Today, a good example of how our understanding of AI has evolved is given for example by the AI definition in the open-source encyclopedia Wikipedia, where it is defined as follows (Artificial Intelligence n.d.): "Artificial intelligence (AI), sometimes called machine intelligence, is intelligence demonstrated by machines, in contrast to the natural intelligence displayed by humans and other animals." In addition, it is widely recognized that the definition of AI changes rather quickly over time depending on the tasks we have already learned to do. The scope of AI is disputed: as machines become increasingly capable, tasks considered as requiring "intelligence" are often removed from the definition, a phenomenon known as the "AI Effect," leading to the quote known as the Tesler's Theorem, "AI is whatever hasn't been done yet" (Artificial Intelligence 2019).

In this text we will focus our attention on a branch of AI called deep learning and its research and clinical applications in radiology. In deep learning models, a large number of interconnected simple units are used to form multiple layers that are capable of extracting "features" from the input of increasingly sophisticated level of details, generating representations of the imaging data. We review the general concepts of an artificial neural network and more specifically the one type that has been extensively used in radiology applications, the convolutional neural network (CNN). We also provide brief account of the training process of these networks, which is the process of incorporating the patterns extracted from data into the very architecture of the neural networks.

Artificial neural networks (ANNs) are machine learning models based on concepts put forward back as early as 1950s (Bishop 2000). After they went through a significant and fast development periods, limitations slowed down the rate of new development, before a massive comeback has started in around 2000s (LeCun et al. 2015; Salakhutdinov and Hinton 2012; Hinton 2007). ANNs consist of a multitude of interconnected processing units, called neurons, usually organized in layers (see Fig. 3). A traditional ANN typically used in the practice of machine learning contains just a few (2 or 3) layers of neurons. Many "model neurons" were proposed over the years, ranging from biophysical models based on the ion channel structure of the physical human neuron (Hodgkin-Huxley model (Hodgkin and Huxley 1952)) to simple "integrate-and-fire" models based on the insight that time-resolved electrical activity (known as an action potential or spike) is a threshold process (Gerstner and Naud 2009). A typical neuron simply multiplies each input by a certain factor (weight), then adds all the products for all the inputs and applies a pre-selected filter function at the end (Bishop 2000; Gerstner and Naud 2009).

Even though each neuron performs a deceivingly simple and rudimentary operation, it is the interconnected nature of the network or its "collective behavior" (note that every node from one layer is connected to every node on the neighboring layers, this is a feature of the ANN architecture) that allows for the performance of an arbitrarily complex and sophisticated computations and modeling the implementation of complicated functions.

At least two main reasons combined to create the "perfect storm" so the popularity of DL approaches exploded recently (LeCun et al. 2015; Schmidhuber 2015).

On the one hand, the progress in digital image capture and storage via digital camera via smart-

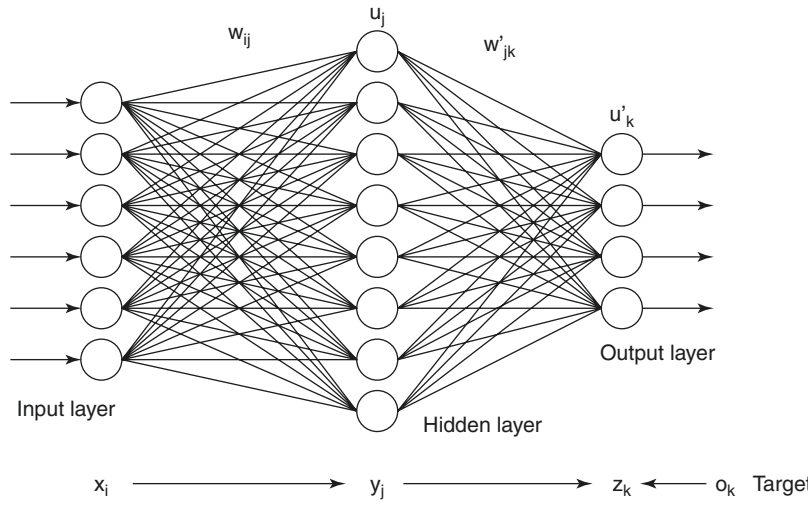


Fig. 3 Schematic representation of an ANN. From (Artificial Neural Networks are Changing the World 2015)

phones has created unparalleled opportunities for collection, aggregation, and labeling of every-day-pixel data sets that could be further structured and made available with a relative ease using common internet technologies. Specifically for radiology, the wide adoption and availability of PACS (Picture Archiving and Communication Systems) (Khorasani 2004, 2008) based on Dicom communication format (Current Edition – DICOM Standard n.d.) have led to rapid accumulation of high-fidelity diagnostic medical images that can be relatively easily annotated based on actual clinical findings (for example, by cross-examining the clinical findings in the radiology reports), utilizing routine IRB (Institutional Review Board) processes put forward across many institutions in the US (Enfield and Truwit 2008). It has been however the example of the ImageNet (Russakovsky et al. 2014) library of annotated images that has led the charge of providing a sufficient in size and sufficiently annotated database of images that have become the standard source against which algorithms are evaluated.

The second main reason was the advent of the Graphics Processing Units (GPU) and the realization that they can be used to off-load a lot of the mathematical operations from the general-purpose CPU systems. This has first become obvious in the computer gaming industry where massive amounts of video resources were required for a smooth 3D scene rendering capabilities which required ability to mathematically manipulate massive matrices (Goodfellow et al. 2016). The realization that the special kind of network architecture and the way of processing pixel data in neural nets can take advantage of the GPU resources (Raina et al. 2009) has led to speeding the network learning tens even hundreds of times. This in turn led to the development of "deeper" algorithms (by adding layers to the network architectures, see Fig. 4) ultimately leading to the explosion of best-of-class results computer networks were able to achieve, at par and sometimes exceeding human experts' abilities.

The practice of radiology's standard workflow is well suited for utilization of AI tools and technologies (Mazurowski et al. 2018; Choy et al. 2018; Hosny et al. 2018). To a large degree it is based on human interpretation of pictorial data using knowledge about imaging technologies, human anatomy, and also factoring in prior experience, and as such is very conducive to automation procedures where algorithms preprocess the imaging data to enhance existing features and discover new insights. In this section, we will review some recent, state-of-the-art applications of AI and DL to radiology-related tasks.

A lot of the everyday radiology clinical image interpretation tasks can be cast as classification tasks. Diagnostic medical images can be classified according to multiple clinical criteria: a)

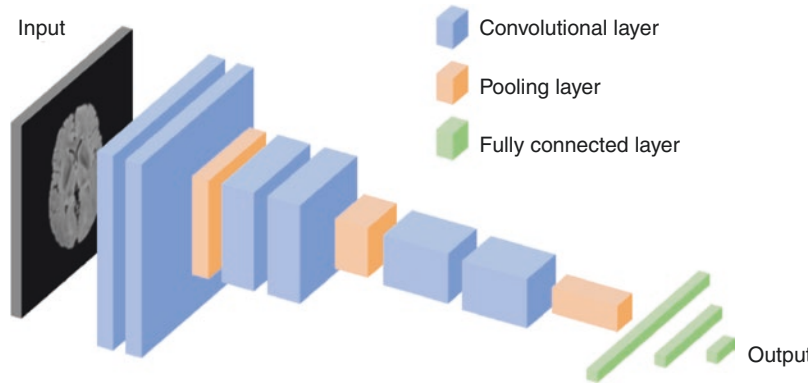


Fig. 4 Convolutional neural network schematics. From (Mazurowski et al. 2018)

presence or absence of lesions (abnormality), b) further classify the lesion as benign or malignant, or c) according to the status of mutations or genomics data, etc. DL-based classifiers are becoming the approach of choice when it comes to analyzing medical pixel data. Most of them use variations and differently organized deep neural architectures using CNNs; the number of learning layers is adapted to the amount of abstracted "features" to be learned by the network and also depends on the available annotated imaging databases to train the network (cf. Fig. 4). As massive data sets of radiological images are still the exception rather than the rule for applying DL in radiology, a lot of earlier studies have resorted to (unsupervised) features extraction with transfer learning (Choy et al. 2018). To just mention a few examples, breast cancer screening might be one of the areas where deep learning is expected to be incorporated into radiology practice quickly (Mikolov et al. 2013). Several studies have shown the diagnostic value of machine learning techniques in different breast imaging modalities, including mammography (Karimi et al. 2017), US (Chen et al. 2018), MRI (Kohli et al. 2015), and tomosynthesis (Bennett and Hauser 2013). Pulmonary nodules detection and classification represent another area of active research with early results within the inter-observer variation of human experts (Ciompi et al. 2017), as well as the bone age detection and characterization of pediatric patients using radiographs (Lee et al. 2017).

We should also mention here the deep learning classifier study by Esteva et al. from early 2017 which achieved a human-dermatologist accuracy of two classificaiton tasks: classifying keratinocyte carcinomas vs. benign seborrheic keratoses, and secondly, an example of most-malignant skin cancer, malignant melanomas vs. nevi. The results were verified against classification performance of 21 board-certified dermatologists using biopsy-confirmed clinical images, and represents one of the first use cases of successfully using DL approaches classifying clinical images (Esteva et al. 2017).

Image registration is a task that has also attracted a lot of applications of DL methods. Registration is defined as the problem of aligning two sets of images (or volumes) of usually a different type in the 3D space, so that the same location on the images is projected on the same anatomical location. For example, a recent study has introduced a Deep Learning Image Registration (DLIR) network and shown that for registration of cardiac cine MRI and registration of chest CT performance of the DLIR framework is comparable to conventional image registration while being several orders of magnitude faster (de Vos et al. 2019). Another approach utilized nonrigid image registration through a learning approach via a CNN architecture that, in contrast to all other work, directly estimates the displacement vector field from a pair of input images using chest CT follow-up images. In another approach, chest CT follow-up examinations were registered by training a CNN to predict three-dimensional displacement vector fields between the fixed and moving image pairs (Sokooti et al. 2017). Yet another supervised-learning-based

study put forward a CNN-based network which was optimized to correct for the respiratory motion in 3D abdominal MR images by predicting spatial transforms probabilistically (Lv et al. 2018). In a different application of DL techniques using unsupervised learning, a CNN was trained from scratch to generate a families of coordinate transformation to minimize the degree of dissimilarity between misaligned image pairs (de Vos et al. 2019).

Generation of set of images with predetermined global image quality and controlled enhancements characteristics (with the added benefit of being free of any specific patient identity, i.e., are de-identified by default) has become an important task in quantitative imaging and radiologic research. It has naturally attracted applications of several deep learning methods. For example, image encoders via convolutional NNs were used to extract a set of main "features" from brain MRI images of a given patient, and then generate new "similar" images via embedding the same "feature" set in them (Chartsias et al. 2018). Another application of the same ideas of controlled image generation is found in image reconstruction of low-dose CT images, in a study in which a generation process was designed to obtain CT images of "normal dose" using images of low-dose CT imaging protocols, via a CNN, to quantitatively compare clinical soft-read utility and quality of interpretation (Chen et al. 2017). To study the inverse process, another study put forward a deep CNN trained with low-dose abdominal CT images for reconstruction of normal-dose CT (Kang et al. 2017).

Non-pixel data manipulation and handling also plays a central role in the radiology clinical and research activities. As the output of the clinical imaging interpretation is often a free-text report, application of NLP (Natural Language Processing) techniques is required to structure the medical narrative text. Hidden-Markov Models (HMMs) are usually state of the art in building and implementing real-time NLP processors (Savova et al. 2010; Garla et al. 2011), with deep learning approaches to natural language processing quickly becoming more widespread (Choy et al. 2018; Collobert et al. 2011a). Most commonly, DL implementations of NLP follow the approach to model phrases as ordered (vector) representation of words which can be learned via an unsupervised NN model (Mikolov et al. 2013; Kim 2014). Examples of this general approach are flagging radiology reports using the International Coding of Diseases (ICD9) ontology via auto-encoding by using a publicly available corpus (Karimi et al. 2017); in another such study the authors classified CT radiology reports as representing presence or absence of pulmonary embolism (PE) (Chen et al. 2018).

Deep learning and AI approaches have also been applied to enhancing various existing radiology clinical decision support (CDS) processes and supporting tools. For example, it is believed that intelligent CDS systems could be utilized to catch errors, for example, in protocoling of the imaging examinations, thus driving down the probability of adverse events and improving the quality of care (Kohli et al. 2015). Further improvements and potential for optimizing human clinical decisions could in principle be obtained by studying the results of artificial intelligence simulation frameworks designed to operate in uncertain environment (Bennett and Hauser 2013).

Next, we will review some of the challenges the widespread adoption of AI and DL methods in radiology face. We attempt to outline and summarize the most important technical, knowledge discovery, regulatory and ethical hurdles and open questions, and also provide thoughts for moving forward.

2.1 Availability of Large, Annotated Sets of Labeled Data for Training and Testing

It has been widely recognized that the successful development and QA/validation of best-performing DL models relevant to clinical practice of radiology depends on the availability of a large cohorts of annotated imaging studies. The importance of the ImageNET (Russakovsky et al. 2014) imaging library to the development of the deep learning techniques and NN architectures

cannot be overstated. Similarly, for medical imaging DL development, availability of a large corpus of relevant medical imaging data will be critical to speed of adoption and quality of DL models developed. Transfer learning approaches can and have been utilized to scale the available smaller imaging cohorts to sizes that are required for optimal application of deep learning NNs (see Fig. 5). Specifically, in order to expand the image sample for training of a deep learning algorithm, several approaches have been put forward, including image augmentation (LeCun et al. 2015; Krizhevsky et al. 2012) and multi-window conversion (Lee et al. 2019). Image augmentation creates additional case and control images through simple image transformations that do not change the image label, including horizontal/vertical flipping, rotation, scaling, cropping, translation, and adding Gaussian noise (LeCun et al. 2015; Mazurowski et al. 2018; Krizhevsky et al. 2012). Multi-window conversion mimics clinical manipulation of window-width (WW) or window-level (WL) display settings during clinical interpretation (Lee et al. 2019), a process which can be algorithmically modeled by transforming the images by generating multiple 8-bit grayscale images with different window-levels.

Several initiatives along those lines have already been put in place. CheXNet, a convolutional neural network, was trained on ChestX-ray14, currently the largest publicly available chest X-ray dataset, containing over 100,000 frontal-view X-ray images with 14 diseases (Rajpurkar et al. 2018). Another notable initiative is based at the Center for Advanced Imaging Innovation and Research (CAI2R), in the Department of Radiology at NYU School of Medicine and NYU Langone Health in partnering with Facebook AI Research (FAIR) on fastMRI—a collaborative research project to investigate the use of AI to make MRI scans up to 10× faster. NYU Langone and FAIR are providing open-source AI models, baselines, and evaluation metrics (Zbontar et al. 2018).

2.2 Deep Learning Algorithms Need Real-World Testing

Related to the question of availability and quality of training and testing datasets, a recent MGH-team study has found that although DL algorithms may yield record-breaking performances on carefully selected datasets, AI algorithms need to be tested on real-world cases prior to being deployed in clinical practice (Deep-Learning Algorithms Need Real-World Testing [Internet] n.d.). The authors compared the performance of their intracranial hemorrhage (ICH) detection algorithm on real-world cases with the initial dataset used to test the algorithm and found that performance of the deep learning model declined significantly on the real-world cases. Notably, however, they showed that a simple retraining of the DL algorithm can improve the specificity when a better balance of training cases is used.

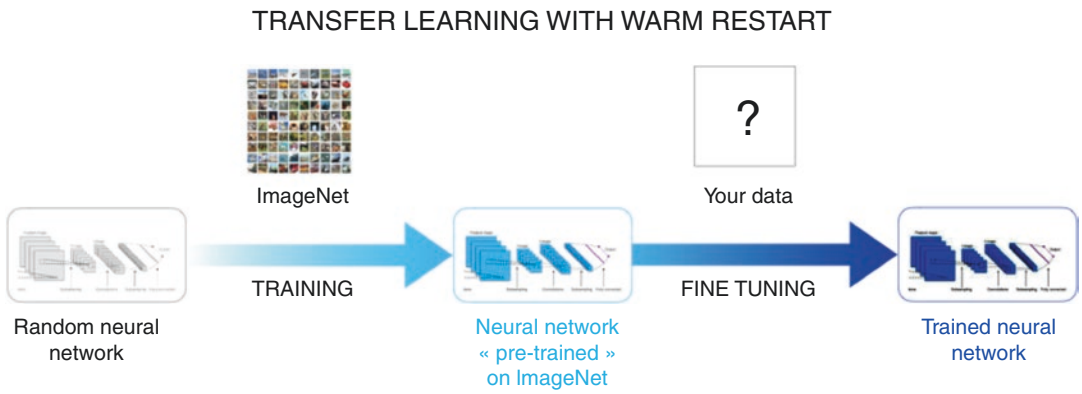


Fig. 5 Transfer learning (TF) schematic representation. From (Wainrib 2017)

2.3 Black-Box Nature: Why Do DL NNs Work?

Here we would like to take a wider look at some of the recently uncovered insights shedding some light on the question why DL and the deep NN architectures are so successful in approximating and learning data.

Deep learning methods have been applied, with large success, to a number of difficult machine learning and classification tasks stemming from complex real-life problems (LeCun et al. 2015; Collobert et al. 2011a; Beam and Kohane 2016). Notable recent applications include computer vision (i.e., optical character recognition) (LeCun et al. 1998), speech recognition (Mikolov et al. 2011), natural language processing (Collobert et al. 2011b), medical images analysis (image segmentation, feature extraction, and classification) (Krizhevsky et al. 2012; Wong and Bressler 2016), clinical and molecular data biomarkers discovery and verification (Syafiandini et al. 2017), often leading to performance record-setting. An attractive feature of the approach is its ability to be applied to both unsupervised and supervised learning tasks (Schmidhuber 2015). The unsupervised learning application holds the promise of a much better scalability across data domains, a very highly desirable feature having in mind the pace at which new biomedical data is generated.

Neural networks, and the deep NN approach in particular, have been shown to be based on a sound theoretical foundation (Bishop n.d.; Hertz et al. 1991), and are broadly modeled after principles believed to represent the high-level cognition functions of the human brain. For example, in the neocortex, associated with a lot of cognitive abilities, the sensory signals propagate through a complex local, modular hierarchy which learns to represent observations over time (Lee and Mumford 2003; Lee et al. 1998)—a design principle that has led to the general definition and construction of convolution NNs used for, i.e., image classification and feature extraction (Krizhevsky et al. 2012). However, it has been somewhat of an undecided question what are the more fundamental reasons for the superior performance of the DL networks and approach compared to frameworks with the same number of fitting parameters but without the deep-layered architecture (Bengio et al. 2012; Mehta and Schwab 2014).

Recently, it was suggested that one possible explanation for the success of the DL architecture is rooted in the general observation that the DL design and processing can be thought as a coarse-graining procedure of extracting more and more abstract features from the data by applying the transformations on each layer of the network (LeCun et al. 2015). Moreover, it has been conjectured that this is reminiscent of the Renormalization Group (RG) approach in statistical physics to model the behavior of highly complex, irreversible critical phenomena systems. At a high level, the RG procedure consists of extracting features/variables relevant at larger-and-larger length scales, thus averaging out the short-scale parameters which do not matter at the larger scales (Mehta and Schwab 2014). Furthermore, an exact mapping was provided between a flavor of the RG approach ("real-space" renormalization using Variational Renormalization Group, (Efrati et al. 2014)) and a DL architecture as exemplified by Restricted Boltzmann Machines (RBMs) utilized in, i.e., the construction of Deep Belief Networks (DBNs) (Salakhutdinov and Hinton 2012).

2.4 Interpretation: Develop and Implement Algorithms that Self-Explain themselves

It is becoming increasingly clear and accepted that the black-box nature of the deep learning algorithms is a rather limiting factor in the rapid and wider acceptance of such approaches into the clinical practice of radiology (Hosny et al. 2018; Lee et al. 2017). Ability for AI algorithms and human experts to co-exist and jointly deliver, i.e., better image interpretation regardless of unavoidable variations in imaging protocoling and image

quality, workflow, level of access to priors and complete medical record, etc. is becoming the consensus across the radiology establishment, replacing the early paranoia that AI (i.e., "the Robot Radiologist") will replace radiologists as interpreters of medical images (Opinion: Rise of the Robot Radiologists [Internet] n.d.).

A number of recent developments have launched and implemented the idea of so-called self-explaining DL algorithms. In the CheXNet example, the convolutional neural network trained on largest publicly available chest X-ray dataset ChestX-ray14 has been designed to self-explain its findings. It displays the probability of pneumonia along with a heatmap localizing the areas of the image most indicative of pneumonia (Rajpurkar et al. 2018). Similarly, a recent study from MGH Department of Radiology and Harvard Applied Sciences Department reported on the development of an understandable deep learning system that detects acute intracranial hemorrhage (ICH) and classifies five ICH subtypes from unenhanced head computed-tomography scans. The system includes an attention map and a prediction basis retrieved from training data to enhance explainability, and an iterative process that mimics the workflow of radiologists (Lee et al. 2019).

Another, more general approach to increase the explainability of the AI-based algorithms was put forward via the introduction of Concept Activation Vectors (CAVs). CAVs provide an interpretation of a neural net's internal state in terms of human-friendly concepts with the key idea being to view the high-dimensional internal state of a neural net as an aid (Kim et al. 2017). The authors show how to use CAVs as part of a technique, Testing with CAVs (TCAV), that uses directional derivatives to quantify the degree to which a user-defined concept is important to a classification result, i.e., how sensitive a prediction of zebra is to the presence of stripes. Using the domain of image classification as a testing ground, they describe how CAVs may be used to explore hypotheses and generate insights for a standard image classification network as well as a medical application.

3 Current Application of Deep Learning in Chest Imaging

3.1 Chest Radiography

Deep learning algorithm can be applied to help radiologist interpreting chest radiograph. Chest radiograph is the most commonly used first-line diagnostic imaging test for the patient suspicious of pulmonary or cardiac diseases. Although this study is very useful, efficient, and cost efficient, correct interpretation of chest radiograph is not easy, requiring experience and medical knowledge. Nowadays, increased workloads with inherent difficulty in interpretation is associated with considerable inter- and intra-reader variability, missed lesions, and reporting delays (McAdams et al. 2006). Deep learning algorithm has the potential to help radiologists interpret chest radiographs more efficiently and correctly, by highlighting the area of potential abnormalities or providing preliminary report.

Detection of nodules on chest radiographs is one of promising applications of deep learning technology. Although chest radiograph is widely used as a tool to detect early lung cancer, due to the confounding factors of anatomic complexity and so on, lung cancer screening using chest radiographs has failed to show its value, with reports of 40% of missing nodules (Finigan and Kern 2013; Quekel et al. 1999). Many CAD systems using traditional image processing technologies have been developed to help radiologists detect nodule. These methods have shown sensitivities about 70% with 1 or 1.3 false-positive CAD marks per images, which still need further improvement of accuracy to be accepted clinically (Schalekamp et al. 2014; Li et al. 2015). Newly developed CAD systems using deep learning algorithm showed much better accuracy for nodule detection. Recently, Nam et al. developed and validated a new deep learning-based CAD system using internal and external data with radiograph classification and nodule detection performances ranging 0.92–0.99 of area under the receiver-operating characteristic curve and 0.831–0.924 of jackknife alternative free-

response receiver-operating characteristic figure of merit, respectively (Nam et al. 2019).

Diagnosis of pulmonary tuberculosis is of great importance in public health and chest radiography is a highly sensitive tool for triaging and screening for current and previous pulmonary tuberculous infection. However, in countries where the prevalence of tuberculosis in high, the number of experienced chest radiologists is limited, which impairs the usage of chest radiograph as screening tool (Melendez et al. 2016). Accordingly, there have been considerable efforts to develop traditional CAD system to help detection or diagnosis of tuberculosis on chest radiograph with acceptable performance of an area under the curve ranging from 0.71 to 0.84 (Pande et al. 2016). Recent study using deep learning algorithm showed much better performance with an area under the curve of 0.99 in detection of pulmonary tuberculosis, although further validation with external data is necessary (Lakhani and Sundaram 2017).

In routine clinical practice, chest radiograph may contain many different patterns of abnormalities, such as consolidation, nodule, pleural effusion, pneumothorax, and cardiomegaly. Therefore, it is necessary to develop the CAD system to detect multiple abnormal patterns at the same time. There have been several promising studies on this task reported with accuracies ranging from 0.56 to 0.88 (Wang et al. 2017; Cicero et al. 2017). Although further development and validation are needed, this technology will be of great help for radiologists by improving overall performance and efficiency.

3.2 Computed Tomography

Chest CT, providing cross-sectional images, allows for three-dimensional visualization of abnormal lesions with much higher sensitivity and lower inter-reader variability than chest radiograph. Progressive increased number of chest CT exams each year is becoming huge clinical burden to chest radiologists. Therefore, development of effective CAD system to help radiologist reduce reading time for each study with enhanced accuracy is critically necessary.

Since the National Lung Screening Trial announced a significant improvement in lung cancer mortality in high-risk populations, screening of lung cancer with low-dose chest CT has been widely accepted (Aberle et al. 2011; Oudkerk et al. 2017). It has resulted in increased CT studies, which requires expert analysis by radiologist for the detection and classification of nodules. Even with promising results in detection and classification of lung nodule using traditional CAD system, complex pipelines of algorithm including preprocessing, segmentation, feature extraction, and so on, often requiring human intervention, hampered wide usage of CAD system in clinical practice (Goo 2005). Deep learning technology is promising alternate to tradition CAD system, by providing seamless process of nodule detection and classification without human interactions. Recent studies showed that the deep learning algorithm provided much better performance in detection of nodules when compared with traditional CAD system (Hua et al. 2015; Setio et al. 2016; Hamidian et al. 2017; Jiang et al. 2018; Masood et al. 2018). Characteristics of detected nodule on CT, mainly size and nodule type, are closely associated with the likelihood of malignancy. CAD system is beneficial in classification of nodules with reduction of inter-reader variability. Clompe et al. introduced a deep learning-based system for nodule type classification based on lung-RADS system with acceptable performance within inter-reader variability among four experienced human readers (Ciompi et al. 2017). Several studies suggested that deep learning algorithm may be helpful to determine the likelihood of malignancy (Nibali et al. 2017; Zhao et al. 2018; Shen et al. 2017).

A more fundamental application of deep learning technology is the segmentation of organ or region of interest on chest CT. This is particularly useful in quantitative assessment of disease components in diffuse lung diseases, such as chronic obstructive lung disease and diffuse interstitial lung disease. Lung and lobe segmentation are usually the first step of quantitative

assessment of these diseases. Traditional imaging processing methods are mostly semiautomatic requiring human interaction. Several recent studies introduced new deep learning algorithm for lung and lobe segmentation with improved performance (Harrison et al. 2017; George et al. 2017). Robust and reliable airway segmentation is also important for quantitative assessment of chronic obstructive pulmonary disease and asthma. Traditional airway segmentation algorithms have limitations in that they are significantly influenced by morphologic changes and show limited performance in extracting peripheral airways (Lo et al. 2012). Using deep learning algorithm, more peripheral airways can be segmented with less errors such as air leak or early termination (Yun et al. 2019). Quantitative assessment of regional disease patterns on CT of interstitial lung disease is another potential clinical application for deep learning technology. Thin section CT is a very sensitive tool to detect various disease patterns in interstitial lung disease such as ground-glass opacity, reticulation, and/or honeycombing. However, it is prone to high inter- and intra-reader variability. Therefore, automatic detection and classification of different ILD patterns may be highly beneficial for quantitative assessment of disease components. Several reports showed that deep learning method is promising in classifying different regional patterns with accuracy more than 85% when compared with reference standard generated by experts (Anthimopoulos et al. 2016; Kim et al. 2018; Gao et al. 2018).

4 Conclusion

Sixty years after the discovery of double helical structure of DNA, molecular biology drives precision and personalized medicine, changing care for patients. Phenotyping approaches using imaging modality, i.e., image-based phenotyping, play an important and complementary role to genotyping. We have reviewed main concepts, core ideas, and the current state-of-the-art AI and DL applications in clinical and research radiology. We underlined the challenges for the wider and seamless adoption of AI in clinical radiology practice. We advocate for accelerated development of deterministic and probabilistic approaches to parallel the rapid advancements in deep learning and simulation technique applications. It seems the initial focus of radiology AI applications on image interpretation-related tasks has the potential to expand into a much wider array of tasks touching upon almost every aspect of the modern radiology practice. The current applications of deep learning in chest imaging including chest radiograph and CT are reviewed.

References

A Proposal for the Dartmouth Summer Research Project on Artificial Intelligence [Internet] (1956) [cited 2018 November 29]. http://www-formal.stanford.edu/jmc/history/dartmouth/dartmouth.html

Aberle DR, Adams AM, Berg CD, Black WC, Clapp JD, Fagerstrom RM et al (2011) Reduced lung-cancer mortality with low-dose computed tomographic screening. N Engl J Med 365(5):395–409

Anthimopoulos M, Christodoulidis S, Ebner L, Christe A, Mougiakakou S (2016) Lung pattern classification for interstitial lung diseases using a deep convolutional neural network. IEEE Trans Med Imaging 35(5):1207–1216

Araki T, Nishino M, Gao W, Dupuis J, Washko GR, Hunninghake GM et al (2015a) Anterior mediastinal masses in the Framingham heart study: prevalence and CT image characteristics. Eur J Radiol 2:26–31

Araki T, Nishino M, Zazueta OE, Gao W, Dupuis J, Okajima Y et al (2015b) Paraseptal emphysema: prevalence and distribution on CT and association with interstitial lung abnormalities. Eur J Radiol 84(7):1413–1418

Araki T, Nishino M, Gao W, Dupuis J, Putman RK, Washko GR et al (2015c) Pulmonary cysts identified on chest CT: are they part of aging change or of clinical significance? Thorax 70(12):1156–1162

Araki T, Putman RK, Hatabu H, Gao W, Dupuis J, Latourelle JC et al (2016a) Development and progression of interstitial lung abnormalities in the Framingham heart study. Am J Respir Crit Care Med 194(12):1514–1522

Araki T, Nishino M, Gao W, Dupuis J, Hunninghake GM, Murakami T et al (2016b) Normal thymus in adults: appearance on CT and associations with age, sex, BMI and smoking. Eur Radiol 26(1):15–24

Araki T, Yanagawa M, Sun FJ, Dupuis J, Nishino M, Yamada Y et al (2017) Pleural abnormalities in the Framingham heart study: prevalence and CT image features. Occup Environ Med 74(10):756–761

Artificial Intelligence (2019) Wikipedia [Internet]. [cited 2019 February 9]. https://en.wikipedia.org/w/index.php?title=Artificial_intelligence&oldid=882350706

Artificial Neural Networks are Changing the World (2015) What are they? - ExtremeTech [Internet] [cited 2019 February 10]. https://www.extremetech.com/extreme/215170-artificial-neural-networks-are-changing-the-world-what-are-they

Ash SY, Harmouche R, Ross JC, Diaz AA, Rahaghi FN, Vegas Sanchez-Ferrero G et al (2018) Interstitial features at chest CT enhance the deleterious effects of emphysema in the COPD gene cohort. Radiology 288(2):600–609

Beam AL, Kohane IS (2016) Translating Artificial Intelligence Into Clinical Care. JAMA 316(22):2368–2369

Bengio Y, Courville A, Vincent P (2012) Representation Learning: a Review and new perspectives. ArXiv12065538 Cs [Internet]. [cited 2016 November 10]. http://arxiv.org/abs/1206.5538

Bennett CC, Hauser K (2013) Artificial intelligence framework for simulating clinical decision-making: a Markov decision process approach. Artif Intell Med 57(1):9–19

Bishop C (2000) Neural networks for pattern recognition, 7-th edn. Oxford University Press, Oxford

Chartsias A, Joyce T, Giuffrida MV, Tsaftaris SA (2018) Multimodal MR synthesis via modality-invariant latent representation. IEEE Trans Med Imaging 37(3):803–814

Chen H, Zhang Y, Zhang W, Liao P, Li K, Zhou J et al (2017) Low-dose CT via convolutional neural network. Biomed Opt Express 8(2):679–694

Chen MC, Ball RL, Yang L, Moradzadeh N, Chapman BE, Larson DB et al (2018) Deep learning to classify radiology free-text reports. Radiology 286(3):845–852

Choy G, Khalilzadeh O, Michalski M, Do S, Samir AE, Pianykh OS et al (2018) Current applications and future impact of machine learning in radiology. Radiology 288(2):318–328

Cicero M, Bilbily A, Colak E, Dowdell T, Gray B, Perampaladas K et al (2017) Training and validating a deep convolutional neural network for computer-aided detection and classification of abnormalities on frontal chest radiographs. Investig Radiol 52(5):281–287

Ciompi F, Chung K, van Riel SJ, Setio AAA, Gerke PK, Jacobs C et al (2017) Towards automatic pulmonary nodule management in lung cancer screening with deep learning. Sci Rep 7:46479

Collobert R, Weston J, Bottou L, Karlen M, Kavukcuoglu K, Kuksa P (2011a) Natural language processing from scratch. ArXiv11030398 Cs [Internet]. [cited 2017 April 18]. http://arxiv.org/abs/1103.0398

Collobert R, Weston J, Bottou L, Karlen M, Kavukcuoglu K, Kuksa P (2011b) Natural language processing (almost) from scratch. J Mach Learn Res 12:2493–2537

Current Edition – DICOM Standard (2019). https://www.dicomstandard.org/current/. Accessed 1 Sep 2019

Deep-Learning Algorithms Need Real-World Testing [Internet] (2018) [cited 2019 February 27]. https://www.auntminnie.com/index.aspx?sec=rca&sub=rsna_2018&pag=dis&ItemID=123871

Doyle TJ, Washko GR, Fernandez IE, Nishino M, Okajima Y, Yamashiro T et al (2012) Interstitial lung abnormalities and reduced exercise capacity. Am J Respir Crit Care Med 185(7):756–762

Efrati E, Wang Z, Kolan A, Kadanoff LP (2014) Real-space renormalization in statistical mechanics. Rev Mod Phys 86(2):647–667

Enfield KB, Truwit JD (2008) The purpose, composition, and function of an institutional review board: balancing priorities. Respir Care 53(10):1330–1336

Esteva A, Kuprel B, Novoa RA, Ko J, Swetter SM, Blau HM et al (2017) Dermatologist-level classification of skin cancer with deep neural networks. Nature 542(7639):115–118

Finigan JH, Kern JA (2013) Lung cancer screening: past, present and future. Clin Chest Med 34(3):365–371

Gao M, Bagci U, Lu L, Wu A, Buty M, Shin HC et al (2018) Holistic classification of CT attenuation patterns for interstitial lung diseases via deep convolutional neural networks. Comput Methods Biomech Biomed Eng Imaging Vis 6(1):1–6

Garla V, Lo Re V 3rd, Dorey-Stein Z, Kidwai F, Scotch M, Womack J et al (2011) The Yale cTAKES extensions for document classification: architecture and application. J Am Med Inform Assoc 18(5):614–620

George K, Harrison AP, Jin D, Xu Z, Mollura DJ (2017) Pathological pulmonary lobe segmentation from ct images using progressive holistically nested neural networks and random walker. In: Cardoso MJ, Arbel T, Carneiro G, Syeda-Mahmood T, JMRS T, Moradi M et al (eds) Deep learning in medical image analysis and multimodal learning for clinical decision support DLMIA 2017, ML-CDS 2017 lecture notes in computer science. 10553. Springer, Cham, pp 195–203

Gerstner W, Naud R (2009) Neuroscience. How good are neuron models? Science (New York, NY) 326(5951):379–380

Goo JM (2005) Computer-aided detection of lung nodules on chest CT: issues to be solved before clinical use. Korean J Radiol 6(2):62–63

Goodfellow I, Bengio Y, Courville A (2016) Deep learning. The MIT Press, Cambridge, MA

Hamidian S, Sahiner B, Petrick N, Pezeshk A (2017) 3D convolutional neural network for automatic detection of lung nodules in chest CT. Proc SPIE Int Soc Opt Eng 10134

Harrison AP, Xu Z, George K, Lu L, Summers RM, Mollur DJ (2017) Progressive and multi-path holistically nested neural networks for pathological lung segmentation from CT images. In: Descoteaux M, Maier-Hein L, Franz A, Jannin P, Collins DL, Duchesne S (eds) Medical image computing and computer assisted intervention – MICCAI 2017 MICCAI 2017 lecture notes in computer science. 10435. Springer, Cham, pp 621–629

Hatabu H (2011) Lung volumes and emphysema in smokes with interstitial lung abnormalities Fleischner Society Meeting; Jun 27; Speyer, Germany

Hatabu H (2015) Image-based phenotyping of lung disease. 7th International workshop for pulmonary functional imaging; Sep 29; Edinburgh, UK

Hatabu H, Hunninghake GM, Lynch DA (2018) Interstitial lung abnormality: recognition and perspectives. Radiology 181684

Hertz J, Palmer RG, Krogh A (1991) Introduction to the theory of neural computation, 1st edn. Perseus Publishing, New York

Hinton GE (2007) To recognize shapes, first learn to generate images. Prog Brain Res 165:535–547

Hodgkin AL, Huxley AF (1952) A quantitative description of membrane current and its application to conduction and excitation in nerve. J Physiol 117(4):500–544

Hosny A, Parmar C, Quackenbush J, Schwartz LH, Aerts H (2018) Artificial intelligence in radiology. Nat Rev Cancer 18(8):500–510

Hua KL, Hsu CH, Hidayati SC, Cheng WH, Chen YJ (2015) Computer-aided classification of lung nodules on computed tomography images via deep learning technique. Onco Targets Ther 8:2015–2022

Humphries SM, Yagihashi K, Huckleberry J, Rho BH, Schroeder JD, Strand M et al (2017) Idiopathic pulmonary fibrosis: data-driven textural analysis of extent of fibrosis at baseline and 15-month follow-up. Radiology 285(1):270–278

Hunninghake GM, Hatabu H, Okajima Y, Gao W, Dupuis J, Latourelle JC et al (2013) MUC5B promoter polymorphism and interstitial lung abnormalities. N Engl J Med 368(23):2192–2200

Jacob J, Bartholmai BJ, Rajagopalan S, Kokosi M, Nair A, Karwoski R et al (2016) Automated quantitative computed tomography versus visual computed tomography scoring in idiopathic pulmonary fibrosis: validation against pulmonary function. J Thorac Imaging 31(5):304–311

Jacob J, Bartholmai BJ, Rajagopalan S, Kokosi M, Nair A, Karwoski R et al (2017) Mortality prediction in idiopathic pulmonary fibrosis: evaluation of computer-based CT analysis with conventional severity measures. Eur Respir J 49(1)

Jiang H, Ma H, Qian W, Gao M, Li Y (2018) An automatic detection system of lung nodule based on multigroup patch-based deep learning network. IEEE J Biomed Health Inform 22(4):1227–1237

Jin GY, Lynch D, Chawla A, Garg K, Tammemagi MC, Sahin H et al (2013) Interstitial lung abnormalities in a CT lung cancer screening population: prevalence and progression rate. Radiology 268(2):563–571

Kang E, Min J, Ye JC (2017) A deep convolutional neural network using directional wavelets for low-dose X-ray CT reconstruction. Med Phys 44(10):e360–ee75

Karimi S, Dai X, Hassanzadeh H, Nguyen A (2017) Automatic diagnosis coding of radiology reports: a comparison of deep learning and conventional classification methods. BioNLP 2017. Association for Computational Linguistics, Vancouver, Canada, pp 328–332

Khorasani R (2004) Integrating PACS into the virtual electronic medical record: the time is now. Acad Radiol 11(6):607–608

Khorasani R (2008) Business continuity and disaster recovery: PACS as a case example. J Am Coll Radiol 5(2):144–145

Kim Y. Convolutional neural networks for sentence classification. ArXiv14085882 Cs [Internet]. 2014 [cited 2019 February 27]. http://arxiv.org/abs/1408.5882

Kim SY, Diggans J, Pankratz D, Huang J, Pagan M, Sindy N et al (2015) Classification of usual interstitial pneumonia in patients with interstitial lung disease: assessment of a machine learning approach using high-dimensional transcriptional data. Lancet Respir Med 3(6):473–482

Kim B, Wattenberg M, Gilmer J, Cai C, Wexler J, Viegas F, et al. (2017) Interpretability beyond feature attribution: quantitative testing with concept activation vectors (TCAV). ArXiv171111279 Stat [Internet]. [cited 2019 February 26]. http://arxiv.org/abs/1711.11279

Kim GB, Jung KH, Lee Y, Kim HJ, Kim N, Jun S et al (2018) Comparison of shallow and deep learning methods on classifying the regional pattern of diffuse lung disease. J Digit Imaging 31(4):415–424

King TE Jr, Bradford WZ, Castro-Bernardini S, Fagan EA, Glaspole I, Glassberg MK et al (2014) A phase 3 trial of pirfenidone in patients with idiopathic pulmonary fibrosis. N Engl J Med 370(22):2083–2092

Kohli M, Dreyer KJ, Geis JR (2015) Rethinking radiology informatics. AJR Am J Roentgenol 204(4):716–720

Krizhevsky A, Sutskever I, Hinton GE (2012) ImageNet classification with deep convolutional neural networks. Proceedings of the 25th International Conference on Neural Information Processing Systems, vol 1. Curran Associates Inc., Lake Tahoe, Nevada, pp 1097–1105

Lakhani P, Sundaram B (2017) Deep learning at chest radiography: automated classification of pulmonary tuberculosis by using convolutional neural networks. Radiology 284(2):574–582

LeCun Y, Bottou L, Bengio Y, Haffner P (1998) Gradient-based learning applied to document recognition. Proc IEEE 86(11):2278–2324

LeCun Y, Bengio Y, Hinton G (2015) Deep learning. Nature 521(7553):436–444

Lee TS, Mumford D (2003) Hierarchical Bayesian inference in the visual cortex. J Opt Soc Am A Opt Image Sci Vis 20(7):1434–1448

Lee TS, Mumford D, Romero R, Lamme VA (1998) The role of the primary visual cortex in higher level vision. Vis Res 38(15–16):2429–2454

Lee H, Tajmir S, Lee J, Zissen M, Yeshiwas BA, Alkasab TK et al (2017) Fully automated deep learning system for bone age assessment. J Digit Imaging 30(4):427–441

Lee H, Yune S, Mansouri M, Kim M, Tajmir SH, Guerrier CE et al (2019) An explainable deep-learning algorithm for the detection of acute intracranial haemorrhage from small datasets. Nat Biomed Eng 3:173–182

Li F, Engelmann R, Armato SG 3rd, MacMahon H (2015) Computer-aided nodule detection system: results in an unselected series of consecutive chest radiographs. Acad Radiol 22(4):475–480

Lo P, van Ginneken B, Reinhardt JM, Yavarna T, de Jong PA, Irving B et al (2012) Extraction of airways from CT (EXACT'09). IEEE Trans Med Imaging 31(11):2093–2107

Lv J, Yang M, Zhang J, Wang X (2018) Respiratory motion correction for free-breathing 3D abdominal MRI using CNN-based image registration: a feasibility study. Br J Radiol 91(1083):20170788

Masood A, Sheng B, Li P, Hou X, Wei X, Qin J et al (2018) Computer-assisted decision support system in pulmonary cancer detection and stage classification on CT images. J Biomed Inform 79:117–128

Mazurowski MA, Buda M, Saha A, Bashir MR (2018) Deep learning in radiology: an overview of the concepts and a survey of the state of the art. [cited 2018 November 26]. https://arxiv.org/abs/1802.08717

McAdams HP, Samei E, Dobbins J 3rd, Tourassi GD, Ravin CE (2006) Recent advances in chest radiography. Radiology 241(3):663–683

Mehta P, Schwab DJ (2014) An exact mapping between the Variational Renormalization Group and Deep Learning. ArXiv14103831 Cond-Mat Stat [Internet]. [cited 2016 November 10]. http://arxiv.org/abs/1410.3831

Melendez J, Sanchez CI, Philipsen RH, Maduskar P, Dawson R, Theron G et al (2016) An automated tuberculosis screening strategy combining X-ray-based computer-aided detection and clinical information. Sci Rep 6:25265

Mikolov T, Deoras A, Povey D, Burget L, Černocký J (2011) Strategies for training large scale neural network language models. 2011 IEEE Workshop on Automatic Speech Recognition Understanding p. 196–201

Mikolov T, Sutskever I, Chen K, Corrado G, Dean J (2013) Distributed representations of words and phrases and their compositionality. ArXiv13104546 Cs Stat [Internet]. [cited 2019 February 27]. http://arxiv.org/abs/1310.4546

Miller ER, Putman RK, Vivero M, Hung Y, Araki T, Nishino M et al (2018) Histopathology of interstitial lung abnormalities in the context of lung nodule resections. Am J Respir Crit Care Med 197(7):955–958

Mucin 5, Subtype B, Tracheobronchial: MUC5B (2019) OMIM no. 600770 [Internet]. Johns Hopkins University, Baltimore, MD. http://www.omim.org/entry/600770?search=600770&highlight=600770

Nam JG, Park S, Hwang EJ, Lee JH, Jin KN, Lim KY et al (2019) Development and validation of deep learning-based automatic detection algorithm for malignant pulmonary nodules on chest radiographs. Radiology 290(1):218–228

Nibali A, He Z, Wollersheim D (2017) Pulmonary nodule classification with deep residual networks. Int J Comput Assist Radiol Surg 12(10):1799–1808

Nishino M, Cardarella S, Dahlberg SE, Araki T, Lydon C, Jackman DM et al (2015) Interstitial lung abnormalities in treatment-naive advanced non-small-cell lung cancer patients are associated with shorter survival. Eur J Radiol 84(5):998–1004

Opinion: Rise of the Robot Radiologists [Internet] (2018) The Scientist Magazine®; [cited 2019 February 27]. https://www.the-scientist.com/news-opinion/opinion%2D%2Drise-of-the-robot-radiologists-64356

Oudkerk M, Devaraj A, Vliegenthart R, Henzler T, Prosch H, Heussel CP et al (2017) European position statement on lung cancer screening. Lancet Oncol 18(12):e754–ee66

Pande T, Cohen C, Pai M, Ahmad KF (2016) Computer-aided detection of pulmonary tuberculosis on digital chest radiographs: a systematic review. Int J Tuberc Lung Dis 20(9):1226–1230

Pankratz DG, Choi Y, Imtiaz U, Fedorowicz GM, Anderson JD, Colby TV et al (2017) Usual interstitial pneumonia can be detected in transbronchial biopsies using machine learning. Ann Am Thorac Soc 14(11):1646–1654

Putman RK, Hatabu H, Araki T, Gudmundsson G, Gao W, Nishino M et al (2016) Association between interstitial lung abnormalities and all-cause mortality. JAMA 315(7):672–681

Putman RK, Hunninghake GM, Dieffenbach PB, Barragan-Bradford D, Serhan K, Adams U et al (2017) Interstitial lung abnormalities are associated with acute respiratory distress syndrome. Am J Respir Crit Care Med 195(1):138–141

Quekel LG, Kessels AG, Goei R, van Engelshoven JM (1999) Miss rate of lung cancer on the chest radiograph in clinical practice. Chest 115(3):720–724

Raghu G, van den Blink B, Hamblin MJ, Brown AW, Golden JA, Ho LA et al (2018) Effect of recombinant human pentraxin 2 vs placebo on change in forced vital capacity in patients with idiopathic pulmonary fibrosis: a randomized clinical trial. JAMA 319(22):2299–2307

Raina R, Madhavan A, Ng AY (2009) Large-scale deep unsupervised learning using graphics processors. Proceedings of the 26th Annual International Conference on Machine Learning; Montreal, Quebec, Canada; p. 873–80

Rajpurkar P, Irvin J, Ball RL, Zhu K, Yang B, Mehta H et al (2018) Deep learning for chest radiograph diagnosis: a retrospective comparison of the CheXNeXt algorithm to practicing radiologists. PLoS Med 15(11):e1002686

Richeldi L, du Bois RM, Raghu G, Azuma A, Brown KK, Costabel U et al (2014) Efficacy and safety of nintedanib in idiopathic pulmonary fibrosis. N Engl J Med 370(22):2071–2082

Russakovsky O, Deng J, Su H, Krause J, Satheesh S, Ma S, et al. (2014) ImageNet large scale visual recognition challenge. ArXiv14090575 Cs [Internet]. [cited 2019 February 6]. http://arxiv.org/abs/1409.0575

Salakhutdinov R, Hinton G (2012) An efficient learning procedure for deep Boltzmann machines. Neural Comput 24(8):1967–2006

Savova GK, Masanz JJ, Ogren PV, Zheng J, Sohn S, Kipper-Schuler KC et al (2010) Mayo clinical text analysis and knowledge extraction system (cTAKES): architecture, component evaluation and applications. J Am Med Inform Assoc 17(5):507–513

Schalekamp S, van Ginneken B, Koedam E, Snoeren MM, Tiehuis AM, Wittenberg R et al (2014) Computer-aided detection improves detection of pulmonary nodules in chest radiographs beyond the support by bone-suppressed images. Radiology 272(1):252–261

Schmidhuber J (2015) Deep learning in neural networks: an overview. Neur Netw 61:85–117

Seibold MA, Wise AL, Speer MC, Steele MP, Brown KK, Loyd JE et al (2011) A common MUC5B promoter polymorphism and pulmonary fibrosis. N Engl J Med 364(16):1503–1512

Setio AA, Ciompi F, Litjens G, Gerke P, Jacobs C, van Riel SJ et al (2016) Pulmonary nodule detection in CT images: false positive reduction using multi-view convolutional networks. IEEE Trans Med Imaging 35(5):1160–1169

Shen W, Zhou M, Yang F, Yu D, Dong D, Yang C et al (2017) Multi-crop convolutional neural networks for lung nodule malignancy suspiciousness classification. Pattern Recogn 61:663–673

Sokooti H, Vos BD, Berendsen F, BPF L, Išgum I, Staring M (2017) Nonrigid image registration using multi-scale 3D convolutional neural networks. In: Descoteaux M, Maier-Hein L, Franz A, Jannin P, Collins DL, Duchesne S (eds) Medical image computing and computer assisted intervention - MICCAI 2017. Springer International, pp 232–239

Syafiandini AF, Wasito I, Fitriawan A, Amien M, Yazid S (2017) Identification of gene expression linked to malignancy of human colorectal carcinoma using restricted boltzmann machines. In: ICBBB '17 Proceedings of the 7th International Conference on Bioscience, Biochemistry and Bioinformatics [Internet]. ACM.; [17-21], New York, NY. https://doi.org/10.1145/3051166.3051177

de Vos BD, Berendsen FF, Viergever MA, Sokooti H, Staring M, Isgum I (2019) A deep learning framework for unsupervised affine and deformable image registration. Med Image Anal 52:128–143

Wainrib G (2017) Transfer learning and the rise of collaborative artificial intelligence [Internet]. Medium; [cited 2019 February 10]. https://medium.com/owkin/transfer-learning-and-the-rise-of-collaborative-artificial-intelligence-41f9e2950657

Wang X, Peng Y, Lu L, Lu Z, Bagheri M, Summers RM (2017) ChestX-ray8: hospital-scale chest X-ray database and benchmarks on weakly-supervised classification and localization of common thorax diseases. 2017 IEEE Conference on Computer Vision and Pattern Recognition (CVPR); 21–26 July 2017; Honolulu, HI: IEEE

Washko GR, Lynch DA, Matsuoka S, Ross JC, Umeoka S, Diaz A et al (2010) Identification of early interstitial lung disease in smokers from the COPD Gene study. Acad Radiol 17(1):48–53

Washko GR, Hunninghake GM, Fernandez IE, Nishino M, Okajima Y, Yamashiro T et al (2011) Lung volumes and emphysema in smokers with interstitial lung abnormalities. N Engl J Med 364(10):897–906

Wong TY, Bressler NM (2016) Artificial intelligence with deep learning technology looks into diabetic retinopathy screening. JAMA 316(22):2366–2367

Yun J, Park J, Yu D, Yi J, Lee M, Park HJ et al (2019) Improvement of fully automated airway segmentation on volumetric computed tomographic images using a 2.5 dimensional convolutional neural net. Med Image Anal 51:13–20

Zbontar J, Knoll F, Sriram A, Muckley MJ, Bruno M, Defazio A, et al. (2018) fastMRI: an open dataset and benchmarks for accelerated MRI. ArXiv181108839 Phys Stat [Internet]. [cited 2019 February 27]. http://arxiv.org/abs/1811.08839

Zhao X, Liu L, Qi S, Teng Y, Li J, Qian W (2018) Agile convolutional neural network for pulmonary nodule classification using CT images. Int J Comput Assist Radiol Surg 13(4):585–595

Future of Pulmonary Functional Imaging

Yoshiharu Ohno and Hiroto Hatabu

Contents

1 **Introduction** 338

2 **Ventilation Imaging** 338
2.1 Nuclear Medicine Examination 338
2.2 Hyperpolarized Noble Gas MR Imaging 339
2.3 Fluorinated Gas MR Imaging 340
2.4 Oxygen-Enhanced MR Imaging 340
2.5 Xenon-Enhanced Ventilation CT 341

3 **Perfusion Imaging** 342
3.1 Nuclear Medicine Examination 342
3.2 Non-Contrast-Enhanced and Contrast-Enhanced MR Angiography and Perfusion MR Imaging 343
3.3 CE-Multi-Energy CT for Pulmonary Perfusion Assessment 344
3.4 Dynamic First-Pass CE-Perfusion Area-Detector CT (ADCT) 345
3.5 Pulmonary Hemodynamic Evaluation by Phase-Contrast MR Imaging 345

4 **Biomechanics Evaluation as Pulmonary Functional Imaging** 346
4.1 CT-Based Biomechanics Assessment 346
4.2 MR-Based Biomechanics Assessment 346

5 **Challenges of New Methods for Future Pulmonary Functional Imaging** 348

6 **Conclusion** 349

References 350

Y. Ohno (✉)
Department of Radiology, Fujita Health University School of Medicine, Toyoake, Japan

Joint Research Laboratory of Advanced Medical Imaging, Fujita Health University School of Medicine, Toyoake, Japan
e-mail: yohno@fujita-hu.ac.jp

H. Hatabu
Center for Pulmonary Functional Imaging, Department of Radiology, Brigham and Women's Hospital and Harvard Medical School, Boston, MA, USA

Abstract

The morphological evaluation of the lung is important in the clinical evaluation of pulmonary diseases. However, the disease process may primarily result in change in pulmonary function without changing pulmonary structure, especially in its early phase. In such cases, the traditional imaging approaches to pulmonary morphology may not provide insight into the underlying pathophysiology.

© Springer Nature Switzerland AG 2021

Y. Ohno et al. (eds.), *Pulmonary Functional Imaging*, Medical Radiology Diagnostic Imaging,
https://doi.org/10.1007/978-3-030-43539-4_16

Therefore, we try to assess pulmonary diseases and functions utilizing not only nuclear medicine but also computed tomography (CT) and magnetic resonance imaging (MRI) with various technical approaches. Moreover, positron emission tomography (PET) with new tracers is going to be available within the next decade, which is being tested for demonstrating its clinical relevance in radiology and pulmonary medicine. In this chapter, we overview the state-of-the-art methods and future direction of: (1) ventilation imaging, (2) perfusion imaging, and (3) biomechanics evaluation as pulmonary functional imaging. We also discuss the potential challenges in future pulmonary functional imaging.

1 Introduction

When we evaluate patients with pulmonary diseases, the morphological evaluation is important because of the close relationship between structural changes of the lung and pathophysiology of the diseases. Such correlations between pulmonary morphology and functions are the foundation for diagnostic imaging modalities including chest radiograph and computed tomography (CT), which play a significant role in diagnosis and management of the patient with pulmonary disease. However, the underlying disease process may result primarily in a change in pulmonary function without substantial changes in pulmonary morphology or structure, especially in the relatively early phase of the disease. In such cases, the traditional pulmonary imaging approaches may not provide enough insight into underlying pathological process. Therefore, we have tried to assess pulmonary disease from the point of view of gas exchange using nuclear medicine, CT, and magnetic resonance imaging (MRI) with various technical approaches.

The principle function of the lung is gas exchange. It is necessary for the lung to achieve the function of gas exchange effectively, the flow of air to the alveoli (ventilation) and the flow of blood to the capillary (perfusion) have to happen in a coordinated manner. Therefore, pulmonary function can be evaluated as a combination of imaging of ventilation and imaging of perfusion with reference or framework of anatomical imaging with spatial information and temporal information. A great advantage of pulmonary functional imaging is the ability to examine these processes on a regional basis, which is different from the traditional measures of pulmonary functions, such as spirometry, which evaluates the whole lung as a single unit. As many diseases begin regionally, their functional effects are often masked by normal lung elsewhere until the disease has progressed to involve substantial portions of the lung parenchyma. Pulmonary functional imaging may significantly improve our ability to evaluate the diseases before they lead to global changes in function and morphology. In addition to the evaluation of pulmonary disease, function imaging may also have a significant impact upon our understanding of pulmonary physiology. As stated, many of the traditional methods for the evaluation of physiology lack spatial or temporal resolution. Therefore, pulmonary functional imaging offers new, noninvasive, methods to evaluate regional physiology with high spatial and temporal resolution. Moreover, new techniques on not only CT and MR imaging but also PET with new tracers has been available since 2000, and also tested for demonstrating their clinical relevance in not only radiology but also pulmonary medicine. In this chapter, we mention the state-of-the-art methods and future direction of (1) ventilation imaging, (2) perfusion imaging, and (3) biomechanics evaluation as pulmonary functional imaging. We also describe potential challenges in future pulmonary functional imaging.

2 Ventilation Imaging

2.1 Nuclear Medicine Examination

For ventilation imaging, nuclear medicine study has been played for a long time as only method for assessing ventilation utilizing krypton-81m (^{81m}Kr), xenon-133 (^{133}Xe), and technetium-99m

(^{99m}Tc) gases. In general, nuclear medicine ventilation study has been considered as low spatial resolution and less anatomical information until single-photon emission computed tomography (SPECT) examination is added. Therefore, SPECT fused with CT (SPECT/CT) has been suggested as useful for evaluation of ventilation and structure changes in various pulmonary diseases. However, ^{133}Xe has been less frequently used recently.

In this situation, gallium-68 (^{68}Ga-) carbon nanoparticles or aerosol, "Galligas," is suggested as new technique for ventilation study on positron emission tomography (PET) or PET fused with PET/CT (Hofman et al. 2011; Ament et al. 2013; Callahan et al. 2014; Oehme et al. 2014). With this technique, PET/CT using ^{68}Ga-labeled tracers allow for quantitative procedures to improve ventilation imaging in clinical and investigational assessment, when compared with currently applied krypton-81m ventilation scintigraphy, SPECT or SPECT/CT.

2.2 Hyperpolarized Noble Gas MR Imaging

As the substitution of nuclear medicine ventilation scan, hyperpolarized noble gas MR imaging and oxygen-enhanced MR imaging have been studied since 1990s (Albert et al. 1994; Edelman et al. 1996; Kauczor et al. 1998; Ramirez et al. 2000). Hyperpolarized noble gas MR imaging can be performed with helium-3 (^{3}He) and xenon-129 (^{129}Xe). They have been extensively tested for assessment of disease severity and therapeutic effect evaluation in various pulmonary diseases (Fain et al. 2007; Kruger et al. 2016). They provide regional ventilation difference in cystic fibrosis, asthma, and chronic obstructive pulmonary disease (COPD) on static hyperpolarized noble gas MR imaging (Altes et al. 2001; Altes and Salerno 2004; Fain et al. 2007; Sun et al. 2011; Svenningsen et al. 2013; Capaldi et al. 2016; Kruger et al. 2016), dynamic gas movement by dynamic gradient-echo sequence (Salerno et al. 2001; Altes and Salerno 2004; Fain et al. 2007; Kruger et al. 2016), and regional gas diffusion to determine alveolar sizes (Salerno et al. 2002; Fain et al. 2006, 2007; van Beek et al. 2009; Kirby et al. 2012; Capaldi et al. 2016; Kruger et al. 2016) with higher spatial resolution or temporal resolution than nuclear medicine studies. In addition, hyperpolarized noble gas MR imaging with ^{129}Xe can provide additional information such as xenon polarization transfer contrast (XTC) and depolarization map is derived which are believed to reflect the regional lung parenchyma density, when compared with hyperpolarized noble gas MR imaging with ^{3}He (Ruppert et al. 2000; Fain et al. 2007; Kruger et al. 2016). Therefore, hyperpolarized noble gas MR imaging has been expected as useful for not only ventilation imaging but also quantitatively assessed lung structure changes in some pulmonary diseases.

However, these techniques had not been clinically set, yet. Drawbacks of these techniques are their dependence on polarizer and multinuclear technology that is not widely available (Kruger et al. 2016). The global quantities of ^{3}He are also very limited, leading to high cost (Cho 2009). This fact has necessitated migration to the more widely available ^{129}Xe nucleus. The technical challenges of this migration have been made easier by advances in ^{129}Xe SEOP polarization (Kruger et al. 2016). Most typically, hyperpolarized ^{129}Xe MR imaging uses enriched ^{129}Xe isotope from the natural abundance of 26% to ≤85% to compensate for lower gyromagnetic ratio and achievable polarization compared to ^{3}He gas (Kruger et al. 2016). Therefore, all the major types of hyperpolarized ^{3}He MR imaging have now been replicated robustly with enriched hyperpolarized ^{129}Xe MR imaging for future clinical set. With considering these drawbacks for clinical set of hyperpolarized noble gas MR imaging in the all over the world, fluorinated gas MR imaging might be regarded as an attractive alternative for the clinical setting. Therefore, we discuss the current situation and future direction of fluorinated gas MR imaging in the next section.

2.3 Fluorinated Gas MR Imaging

With considering the future of gas MR imaging except oxygen-enhanced MR imaging, Fluorine-19 (^{19}F) MR imaging may be more promising approach for ^{19}F MR imaging using inhaled inert fluorinated gases is a lung imaging technique currently under development that can potentially provide a more economical alternative to hyperpolarized noble gas MR imaging (Adolphi and Kuethe 2008; Couch et al. 2013, 2019; Gutberlet et al. 2018). Inert fluorinated gases are nontoxic, abundant, relatively inexpensive, and the technique can be performed on any MRI scanner with broadband multinuclear imaging capabilities (Adolphi and Kuethe 2008; Couch et al. 2013, 2019; Gutberlet et al. 2018). Feasibility studies have been reported in human lungs, demonstrating breath-hold images with gas mixtures containing 79% sulfur hexafluoride (SF_6) or perfluoropropane (C_3F_8 or PFP) and 21% oxygen (O_2) (Couch et al. 2013; Halaweish et al. 2013). SF_6 and PFP are nontoxic, abundant, and relatively inexpensive. A report suggested the cost estimates for ^{3}He, ^{129}Xe, and ^{19}F gases (Kruger et al. 2016). The per-liter cost of ^{3}He and enriched ^{129}Xe is much higher than ^{19}F gases, but the cost of naturally abundant xenon is similar to SF_6 and PFP. Since a typical imaging session using ^{19}F MR imaging might use several liters of SF_6 or PFP, the total cost of a single study might be approaching the cost of an enriched hyperpolarized noble gas MR imaging with ^{129}Xe; however, the advantage of ^{19}F gas MR imaging is that the gases are imaged using thermal equilibrium polarization and a polarizer system is not required (Couch et al. 2019). In addition, ^{19}F gas MR imaging can visualize regional difference of ventilation as well as air trapping and potentially provides functional information that is similar to images obtained from hyperpolarized noble gas MR imaging (Adolphi and Kuethe 2008; Couch et al. 2013, 2019; Halaweish et al. 2013; Gutberlet et al. 2018). Overall, ^{19}F gas MR imaging is expected to complement existing proton-based structural imaging techniques, and the combination of structural and functional lung MR imaging will provide useful outcome measures in the future management of pulmonary diseases based on not only academic but also clinical purposes. Therefore, further investigations will be extensively performed in the next few decades for clinical set as one of the pulmonary functional imaging in routine clinical practice.

2.4 Oxygen-Enhanced MR Imaging

Oxygen-enhanced (O_2-enhanced) MR imaging has been suggested as one of the pulmonary functional MR imaging since 1996 (Edelman et al. 1996; Hatabu et al. 2001; Tadamura et al. 1997; Ohno et al. 2001a, b, 2002, 2005, 2008a, b, 2011a, 2012a, b, 2014a, b; Jobst et al. 2015; Triphan et al. 2015, 2017; Kruger et al. 2016; Fuseya et al. 2018). Molecular oxygen is weakly paramagnetic with a magnetic moment of 2.8 Bohr magnetons. O_2 modulates the MR imaging signal of blood and fluid through two different mechanisms: the paramagnetic property of deoxyhemoglobin and the paramagnetic property of molecular oxygen itself (Young et al. 1981; Brooks and Di Chiro 1987). Because deoxyhemoglobin is compartmentalized in red blood cell (RBC), tissue water protons do not have access to coordination sites, which is required for spin-lattice interactions causing T1 shortening (Young et al. 1981; Brooks and Di Chiro 1987). Therefore, deoxyhemoglobin with RBC has a T2*-shortening effect with little T1-shortening effect (Young et al. 1981; Brooks and Di Chiro 1987). Dissolved molecular oxygen will shorten the T1 relaxation time of pulmonary venous blood because molecular oxygen is paramagnetic. The areas of the lung affected by pulmonary emphysema were pathologically characterized as having a decrease in pulmonary capillary beds, abnormal permanent enlargement of the air spaces distal to the terminal bronchiole, accompanied by destruction of their walls, and without obvious fibrosis. O_2-enhanced MR imaging can

demonstrate not only regional oxygen enhancement based on oxygen diffusion from alveoli to capillary bed, but also oxygen uptake based on ventilation as well as respiration, and is suggested as useful for evaluation of various pulmonary diseases such as asthma, COPD, cystic fibrosis, interstitial lung disease, and lung cancer (Ohno et al. 2001b, 2002, 2005, 2008a, b, 2011a, 2012a, b, 2014a, b; Jobst et al. 2015; Triphan et al. 2015, 2017; Fuseya et al. 2018). Moreover, O_2-enhanced MR imaging is a proton-based technique and considered as one of the key techniques for pulmonary functional imaging because no other imaging method can demonstrate oxygen uptake based on respiration itself, although it is not able to directly visualize O_2 itself. However, drawbacks of O_2-enahnced MR imaging are low signal intensity changes due to oxygen inhalation and time consuming to cover entire lung because 2D sequence rather than 3D sequence had been applied in the past studies. In addition, many studies were assessed as semiquantitative assessment, and a few studies were applied quantitative evaluation (Edelman et al. 1996; Ohno et al. 2001a, b, 2002, 2005, 2008a, b, 2011a, 2012a, b, 2014a, b; Jobst et al. 2015; Triphan et al. 2015, 2017; Fuseya et al. 2018). Therefore, further developments of O_2-enhanced MR imaging for 3D acquisition to cover entire lung and quantitative analysis for oxygen uptake evaluation are warranted, and further investigation on the application of the abovementioned new techniques has to be performed for enhancing clinical relevance of O_2-enhanced MR imaging in the next few decades.

2.5 Xenon-Enhanced Ventilation CT

Dual-energy CT (DE-CT) techniques using dual X-ray sources, dual-layer detectors, or fast kilovoltage-switching methods had been suggested since 1970s (Genant and Boyd 1977; Chiro et al. 1979; Millner et al. 1979) and have been clinically applied since 2008 (Flohr et al. 2006; Chae et al. 2008, 2010a; Yanagita et al. 2013; Kong et al. 2014; Lee et al. 2017a, b). Although their CT systems and data acquisition methods are different, all these techniques make it possible to display xenon distribution maps as ventilation-weighted images with Xe in various pulmonary diseases (Flohr et al. 2006; Chae et al. 2008, 2010a, Yanagita et al. 2013; Kong et al. 2014, Lee et al. 2017a, b).

In contrast to Xe-enhanced ventilation CT using dual-energy CT technique, Xe-enhanced ventilation CT can be obtained by using subtraction CT method (Ohno et al. 2017a, 2018a). In addition, the subtraction CT method for visualization of Xe enhancement is potentially superior to the DE-CT method, and can more clearly demonstrate regional Xe ventilation on Xe-enhanced CT as well as be effectively matched with ^{81m}Kr SPECT/CT (Ohno et al. 2017a, 2018a). The subtraction CT method requires well-organized nonrigid registration software for visualization of Xe on unenhanced and contrast-enhanced CT with Xe but does not need specific equipment such as dual-source X-ray tube, fast tube voltage switching, and dual-layer detector systems. Xe-enhanced ventilation CT by using dual-energy and subtraction CT techniques provide regional ventilation difference with higher spatial resolution than nuclear medicine and all MR techniques and similar spatial resolution to thin-section CT, and may be one of the best methods for ventilation assessment in pulmonary diseases, although only drawbacks are ionizing radiation exposure and non-refoundation by health insurance. Currently, Xe is allowed to be used only for brain perfusion CT examination and refunded by health insurance. On the other hand, iterative reconstruction techniques as well as other radiation dose reduction methods are currently applicable for radiation dose reduction for CT examination in routine clinical practice. With considering the abovementioned situations for Xe-enhanced ventilation CT, it would be better for us to demonstrate more clinical relevance for pulmonary ventilation imaging and try to obtain Food and Drug Administration (FDA) approval in not only Japan

and Korea but also the USA and Europe and clinically set as routine CT examination within this decade.

3 Perfusion Imaging

3.1 Nuclear Medicine Examination

Pulmonary perfusion scan as well as SPECT and SPECT/CT has been clinically applied for not only pulmonary thromboembolism as well as other pulmonary vascular diseases, but also lung cancer as well as COPD. However, spatial resolution of perfusion study and application of ^{99m}Tc-macro aggregated albumin (MAA) have not been changed, and clinicians currently apply this technique as limited clinical situation.

Since late 1980s, PET is suggested as a noninvasive, quantitative method to assess pulmonary perfusion and ventilation in vivo. Three methods had been suggested as useful for pulmonary perfusion assessment on PET. The first is ^{13}N2-saline bolus injection method (Rhodes et al. 1989a, b; Sandiford et al. 1995; Mijailovich et al. 1997; Treppo et al. 1997; Musch et al. 2002; Musch and Venegas 2005; Vidal Melo et al. 2002, 2010). On $^{13}N_2$-bolus injection, accurate estimates of regional perfusion and regional shunt can be derived by applying a mathematical model to the pulmonary kinetics of a $^{13}N_2$-saline bolus. When breathing is resumed, specific alveolar ventilation can be calculated from the tracer washout rate, because $^{13}N_2$ is eliminated almost exclusively by ventilation. Because of the rapid elimination of the tracer, $^{13}N_2$ infusion scans can be followed by $^{13}N_2$ inhalation scans that allow determination of regional gas fraction in acute lung injury, pulmonary embolism, and COPD (Rhodes et al. 1989a, b; Sandiford et al. 1995; Mijailovich et al. 1997; Treppo et al. 1997; Musch et al. 2002; Musch and Venegas 2005; Vidal Melo et al. 2002, 2010).

The second method that allows assessment of regional pulmonary blood flow is based on the intravenous administration of $H_2{}^{15}O$ as the radiotracer (Mintun et al. 1986; Schuster et al. 1995; Musch and Venegas 2005). This method is based on a single compartment model of the distribution of tracer and relies on two basic assumptions: the tracer is biologically inert, and the tracer is freely and rapidly diffusible in the lung, so that the concentration of tracer in the pulmonary venous blood that flows out of a region is equal to the concentration of tracer in the tissue, divided by the tissue-blood partition coefficient of the tracer (i.e., the tracer leaves the lung at equilibrium with lung tissue). This assumption has been demonstrated to hold even for very high values of regional pulmonary blood flow (Mintun et al. 1986; Schuster et al. 1995; Musch and Venegas 2005).

The third is albumin microspheres radiolabeled with ^{68}Ga (i.e., ^{68}Ga-labeled microspheres), which was firstly reported to obtain lung perfusion scans since 1975 (Chesler et al. 1975; Hnatowich 1976; Bailey et al. 2016). A point of difference from ^{99m}Tc imaging to note is that the shorter physical half-life of ^{68}Ga means that a perfusion scan subsequent to a ventilation study contains less of a ventilation contribution that would be present when using ^{99m}Tc. From the abovementioned studies, it was suggested that acceptable lung perfusion images could be obtained in humans with as little as $\leq$20MBq (0.5mCi) of ^{68}Ga-labeled microspheres. Others simplified the radiolabeling process of the albumin using a diethylenetriami-nepentaacetic acid chelator and enhanced the labeling techniques (Wagner and Welch 1979; Even and Green 1989; Bailey et al. 2016). Other aspects of lung function, apart from perfusion, were also imaged with ^{68}Ga and PET. Mintun, and subsequently Schuster, used the intravenous injection of ^{68}Ga-transferrin to study the flux of radiolabeled proteins across the pulmonary endothelium (Mintun et al. 1987; Schuster et al. 1995, 1998). The former mentioned methods, combined with measurements derived from PET images of pulmonary blood flow and volume, have been used to quantify acute lung injury and pulmonary edema, pulmonary thromboembolism, lung cancer with radiation therapy, etc. (Schuster et al. 2002; Hofman et al. 2011; Ament et al. 2013; Hardcastle et al. 2015; Bailey et al. 2016). With

current situation of PET imaging for pulmonary perfusion assessment, all techniques are under development, not covered by health insurance and warranted to further investigation for clinical set in future.

3.2 Non-Contrast-Enhanced and Contrast-Enhanced MR Angiography and Perfusion MR Imaging

Since 1990s, non-contrast-enhanced and contrast-enhanced MR angiography and perfusion MR imaging have been suggested as useful for visualization of pulmonary vasculature and blood flow by various methods (Matsuoka et al. 2008a; Liszewski et al. 2013; Ohno et al. 2016a; Johns et al. 2017). Currently, there are two major methods for assessment of pulmonary vasculature and blood flow. One is non-contrast-enhanced (CE-) MR examination, which is used as proton within blood as endogenous tracer, and the other is CE-MR examination that used gadolinium contrast media as intravenous injected tracer. As former method for MR angiography, the balanced steady-state free precession (bSSFP) sequence, 3D electrocardiogram-gated (ECG-gated) fresh blood imaging (3D FBI) using 3D fast spin-echo (SE)-based sequence, and arterial spin labeling technique with SE and gradient-recalled echo (GRE) type sequences have been suggested as useful for assessment of pulmonary vasculatures (Ohno et al. 2014c, 2016a, 2017b; Johns et al. 2017). Currently, these techniques are being tried to be applied at each MR scanner by all MR vendors and would be better to be applied in pulmonary vascular disease patients with low renal function or contraindication of gadolinium contrast media in routine clinical practice.

On the other hand, CE-MR examination for angiography has been suggested as useful and clinically applied for diagnosis or assessment of not only pulmonary vascular disease but also other diseases including lung cancer, etc. in the last few decades (Hatabu et al. 2000; Tadamura and Hatabu 2001; Ohno et al. 2014c, 2016a, 2017b). It is usually called as "time-resolved CE-MR angiography" or "4D CE-MR angiography" after clinical installation of parallel imaging techniques (Ohno et al. 2014c, 2016a, 2017b, Johns et al. 2017), and widely applied in routine clinical practice, when compared with non-CE-MR angiography. Moreover, time-resolved CE-MR angiography is also applied as substitution or complementary role for CE-CT angiography and perfusion scan, SPECT or SPECT/CT in routine clinical practice because this technique can clearly demonstrate not only pulmonary vasculature but also pulmonary parenchymal perfusion as a single examination. Therefore, this examination is considered as clinically set and would be better to be applied in patients with cardiopulmonary diseases in routine clinical practice.

As well as non-CE- and CE-MR angiography, non-CE- and dynamic CE-perfusion MR imaging have been tested since the late 1990s. As non-CE-perfusion MR imaging, signal targeting with alternating radiofrequency (STAR) technique with a half-Fourier single shot turbo spin-echo (HASTE) sequence (Chen et al. 1997; Hatabu et al. 2000), arterial spin tagging imaging (Roberts et al. 1999), arteria spin labeling imaging such as flow sensitive alternating inversion recovery (FAIR) and FAIR with an extra radiofrequency pulse (FAIRER) imaging (Mai and Berr 1999), and ECG-gated fast-spin-echo perfusion MR imaging that were generated as subtraction imaging between systolic and diastolic phases (Ogasawara et al. 2004) had been tested in not only healthy volunteers but also patients with different pulmonary diseases However, all these techniques were 2D acquisition and time consuming. Therefore, these techniques have not been clinically applied since the times that they were introduced. Since 2009, non-contrast-enhanced perfusion and ventilation assessment of the human lung by means of Fourier decomposition (FD) technique in proton MRI had been tested in not only healthy volunteer but also patients with pulmonary diseases (Bauman et al. 2009, 2013a, b; Sommer et al. 2013; Schönfeld et al. 2015; Voskrebenzev et al. 2018). Although FD technique is 2D acquisition

technique, it can provide perfusion-weighted and ventilation-weighted images at same time and performed at proton-based MR technique. Therefore, this technique is considered as new pulmonary functional imaging method, has been extensively tested by a few investigators, and would be better to be clinically set in future. In contrast to the abovementioned 2D non-CE-perfusion MR imaging, 3D ECG- and respiratory-gated non-CE-perfusion MR imaging had been introduced and demonstrate its utility for prediction of postoperative lung function in non-small cell lung cancer patients and had similar potential for assessment of regional perfusion with dynamic CE-perfusion MR imaging (Ohno et al. 2015a). This technique is considered as only one method for 3D non-CE-perfusion MR imaging, currently trying to clinically set by several investigators, would be better to be applied to various pulmonary diseases, and will demonstrate the clinical relevance based on these study results in near future. Therefore, in contrast to non-CE-MR and CE-MR angiography, non-CE- MR perfusion imaging would be better to be considered as preclinical situation or under development, when considering clinical applications (Ohno et al. 2014c, 2016a, 2017b, Johns et al. 2017).

From the semiquantitative and qualitative assessment of pulmonary circulation assessment, dynamic first-pass CE-perfusion MR imaging had been extensively tested in patients with various pulmonary diseases by many investigators in the last few decades (Hatabu et al. 1996a, b, 1999; Levin et al. 2001; Ohno et al. 2004a, b, 2007, 2010, 2012c, 2015a, b; Johns et al. 2017). With applying indicator dilution therapy and deconvolution analysis, quantitatively assessed pulmonary blood flow, pulmonary blood volume, and mean transit time can be measured on dynamic first-pass CE-perfusion MR imaging (Hatabu et al. 1999; Levin et al. 2001; Ohno et al. 2004a, b, 2007, 2010, 2012c, 2015a, b). By using the abovementioned methods, quantitatively assessed perfusion parameters can be applied as image-based biomarkers for not only diagnosis but also disease severity assessment and patients' management in various pulmonary diseases.

Currently, all MR scanners, whose field strengths are equal to or higher than 1.5Tesla, from each vendor can perform dynamic first-pass CE-perfusion MR imaging with and without parallel imaging technique. On the other hand, there are no commercially available software for quantitative assessment of pulmonary perfusion parameter, and all previously reported studies applied the investigators' proprietary software. Therefore, it is necessary for us to encourage vendors to provide appropriate sequence, bolus injection protocol, and commercially available software for widening clinical set of this technique within the next decade.

3.3 CE-Multi-Energy CT for Pulmonary Perfusion Assessment

CE-multi-energy CT has been suggested as having a potential to visualize perfused lung as iodine distribution maps within the lungs in patients with pulmonary vascular diseases since 2008, although acquisition methods are varied such as dual-source CT system and single-source CT with ultrafast tube voltage switching or dual-layer detector system (Lu et al. 2012). With these techniques, several investigators had been reported the utility for assessment of acute or chronic pulmonary thromboembolism, acute or chronic pulmonary hypertension, pulmonary nodule and lung cancer patients (Chae et al. 2010b, c, 2013; Hoey et al. 2011; Hong et al. 2013; Dournes et al. 2014; Meyer et al. 2015; Giordano et al. 2017; Masy et al. 2018). Although this technique can be easily clinical set, this technique has a few major drawbacks. Firstly, this technique cannot quantitatively evaluate regional perfusion and can semiquantitatively assess regional perfused lung condition as iodine distribution map because iodine distribution map is affected by iodine injection protocol, cardiac output, bronchial circulation, etc. Therefore, appropriate bolus injection protocol would be better to be determined (Fuld et al. 2013). Secondly, this technique is possible to perform at CT systems with two X-ray tubes, X-ray tube with ultrafast

tube voltage switching, or two layers detector provided by a few CT vendors, and cannot be applied to all CT systems. However, CT systems with X-ray tube with ultrafast tube voltage switching and two layers detector provide multi-energy CT images by raw data base domain image reconstruction, although CT system with dual source system provide dual-energy CT images by non-raw data base domain image reconstruction. Therefore, former methods have more potential than the later method to evaluate regional perfusion-based information with detecting a little difference of iodine contrast media by mono-energetic imaging. In addition, many clinical applications have been tested and could play a complementary role in cardiopulmonary disease assessments, along with other advanced imaging modalities (Kalisz et al. 2017). Therefore, multi-energy CT techniques offer advantages over conventional CT techniques, particularly for improving vascular contrast, decreasing artifacts, improving tissue differentiation, and reducing radiation burden. Therefore, further investigation of these techniques will demonstrate further clinical relevance and new applications for cardiopulmonary diseases within the next decade.

3.4 Dynamic First-Pass CE-Perfusion Area-Detector CT (ADCT)

Quantitatively analyzed dynamic first-pass CE-perfusion CT by means of electron-beam CT was firstly reported in normal individuals and patients with pulmonary thromboembolism in 2010 (Schoepf et al. 2000). However, dynamic first-pass CE-perfusion CT had not been clinically applied until area-detector CT (ADCT) systems were introduced (Ohno et al. 2011b, 2013, 2015b, 2016a, b, 2017c, d; Yabuuchi et al. 2018). ADCT is a 320-detector row CT system with area detector and can obtain isotropic volume data of lung parenchyma and nodules or masses simultaneously within a 160 mm area without helical scan. Thus, dynamic first-pass CE-perfusion ADCT data can be obtained by means of continuous dynamic scanning, allowing for qualitative and quantitative evaluation of perfusion of pulmonary nodules (Ohno et al. 2011b, 2013, 2015b, 2016a, b). For these reasons, ADCT systems are now being used for not only morphologic examinations but also functional assessments, especially real first-pass evaluation of perfusion with in a pulmonary nodule or mass by using different mathematical models (Ohno et al. 2011b, 2013, 2015b, 2016b, 2017c, d; Yabuuchi et al. 2018). In addition, this technique has been suggested as more useful for diagnosis of pulmonary nodule, N-stage evaluation, and therapeutic effect prediction in NSCLC than PET/CT (Ohno et al. 2011b, 2013, 2015b, 2016a, b, 2017c, d; Yabuuchi et al. 2018). Therefore, this technique has a potential to be the candidate for one of the most feasible pulmonary functional imaging methods and can provide the opportunity for morphological and functional information with the highest spatial resolution and temporal resolution. Drawbacks are ionizing radiation and difficulty for obtaining whole lung perfusion information at single examination in this time. However, radiation dose reduction of this technique may be achieved with keeping the measurement accuracy of each perfusion parameter, when applied newly developed and clinically applied iterative reconstruction algorithm (Ohno et al. 2016c). In addition, a proprietary software with appropriate perfusion CT examination protocol including bolus injection of contrast media is suggested as having the potential for assessing whole lung perfusion as single examination (Ohno et al. 2016a). Therefore, further development in not only protocol but also software may give us the chance for clinical set of dynamic first-pass CE-perfusion ADCT examination in the next several years.

3.5 Pulmonary Hemodynamic Evaluation by Phase-Contrast MR Imaging

As the substitution of cardiac echography, phase-contrast MR imaging with velocity sensitizing gradients can be used to quantitatively map the blood flow in the major vessels in the lungs in 2

or 3 dimensions and can provide insight into pulmonary vascular resistance and nonsteady and turbulent flow in the pulmonary arteries in mainly pulmonary arterial hypertension due to various cardiopulmonary diseases (Sanz et al. 2007; Reiter et al. 2015, 2016; Johns et al. 2017; Nagao et al. 2017). Recent developments with 3D view shared phase-contrast methods allow 3D time-resolved imaging of blood flow in the pulmonary arteries and allow for the acquisition of 4D flow in the pulmonary arteries (Reiter et al. 2015, 2016; Barker et al. 2015, Nagao et al. 2017).

When considering clinical application, this technique is one of the most easily applicable MR techniques in this time point because MR sequences as well as commercially available analysis software are provided by almost all MR vendors as well as workstation vendors, etc. Only drawback might be limited potential for analysis of peripheral vessels within lung and no potential for pulmonary parenchymal perfusion. Therefore, this technique may be better to be clinically applied with other perfusion MR imaging techniques for assessment of pulmonary parenchymal perfusion with or without pulmonary vasculatures in pulmonary diseases.

4 Biomechanics Evaluation as Pulmonary Functional Imaging

4.1 CT-Based Biomechanics Assessment

CT is the fundamental tool for diagnosis of thoracic diseases. For assessment of CT-based motion analysis, inspiratory/expiratory CT had been clinically applied for assessment of air trapping for some pulmonary diseases and tested for quantitative assessment of lung volume, airway dimension, emphysema cluster assessment, etc. (Kauczor et al. 2000, 2002; Arakawa et al. 2003; Zaporozhan et al. 2005; Matsuoka et al. 2007, 2008b, c; Ley-Zaporozhan et al. 2008; Yamashiro et al. 2010; Nishio et al. 2014, 2015; Lee et al. 2015; Koyama et al. 2016; Martinez et al. 2017). On the other hand, most current CT devices are not fast enough to acquire large lung volumes in real time (Biederer et al. 2010). Two different methods are available to overcome this limitation. Prospective 4D-CT uses respiratory-gated image acquisition in reference to an external motion indicator, producing a single "motion-free" 3D image at the selected respiratory phase. Retrospective 4D-CT continuously acquires images from all respiratory phases, which are then sorted into appropriate phase bins defined by the signal of an external motion indicator. This results in a set of motion-free 3D images at different phases of the breathing cycle. An external motion indicator or surrogate is necessary to label the image projections with motion status and timestamp, facilitating the sorting of image projections. With these techniques, 4D-CT is being tried to be applied for radiation oncology field. As a third option, the ADCT scanner has only recently become available for real 4D ventilation CT by using time-resolved step-and-shoot acquisition. Recently, real 4D ventilation CT has been tested for quantitative assessment of airway and lung parenchyma in animal model, smokers, COPD, and lung cancer (Yamashiro et al. 2015, 2016, 2017; Sakuma et al. 2017; Hashimoto et al. 2018). This technique is now under evaluation as one of the new methods for pulmonary functional imaging and warranted for further investigations to demonstrate clinical relevance in near future.

4.2 MR-Based Biomechanics Assessment

MR imaging is a tool not relying on ionizing radiation, and thus allowing for repeated and prolonged measurements to be made. Recent advances in MR technology have made it possible to assess diaphragmatic and chest wall motion, static and dynamic lung volumes, as well as regional lung function. Even though existing studies show large heterogeneity in design and applied methods, it becomes evident that MR imaging is capable to visualize pulmonary function as well as diaphragmatic and thoracic wall

movement, providing new insights into lung physiology.

Several studies were designed to answer basic physiological questions about diaphragmatic configuration and function as static thoracic MR images in sagittal and coronal orientations (Paiva et al. 1992; Gauthier et al. 1994; Gierada et al. 1995; Cluzel et al. 2000). From the analyzed contours of thorax and diaphragm, lung volumes were calculated and judged to be in good agreement with spirometric measurement. However, all these studies have the limitation that image acquisition was performed in a supine position, leaving the question open whether the findings would be transferable to a normal upright position. A study was addressed by an open MR system to dynamically image subjects in the sitting as well as supine position during slow maximal respiration and showed that diaphragmatic excursion is significantly greater when sitting than in the supine position, especially in the posterior region (Takazakura et al. 2004). However, the MR system has been not available in not only academic, but also clinical purposes. Therefore, other methods have been tried to clinical set.

For static lung volume evaluations, a few studies demonstrated methods for estimation of lung volume in normally breathing non-sedated infants with wheezing and bronchitis (Chapman et al. 1990) and emphysema patients scheduled for lung volume reduction surgery (Gierada et al. 1998) as well as healthy volunteers (Qanadli et al. 1999). A limitation of all the studies is the small number of subjects included and the lack of control groups. In summary, these studies found that the satisfactory visualization and calculation of static lung volumes is possible from 2D MR images using complex reconstruction algorithms, and limited functional information could be gained from these studies.

In contrast to static lung volume assessment, dynamic lung volume evaluation was tested with applying parallel imaging and fast sequences with high temporal resolution for real-time visualization of lung and chest wall motion (Suga et al. 1999, 2000). Compared to healthy controls, patients with emphysema showed a flattened diaphragm and a reduced, irregular respiratory motion of both chest wall and diaphragm. Repetition of dynamic MR imaging after lung volume reduction surgery significantly improved these parameters. Other studies used dynamic MRI to visualize chest wall and diaphragmatic movement with instantaneous spirometric measurements (Kondo et al. 2000, 2005; Plathow et al. 2004a). In addition, the influence of tumor location on the local chest wall and diaphragmatic movement is also evaluated as evident when applying this method in lung cancer and malignant mesothelioma (Plathow et al. 2004b, c, 2006). Further, the introduction of dynamic 3D MR imaging, using an isotropic time-resolved 3D gradient echo pulse sequence for volumetric assessment of the breathing cycle (Plathow et al. 2005), improved the correlation between spirometric data and MR-volumetric data. However, the lower temporal resolution of the sequence only allowed for a dynamic examination during slow maximum inspiration and expiration. Therefore, 3D sequences had been applied with parallel imaging techniques for improving correlations between MR-based volumetric evaluations and pulmonary function test results (Kolb et al. 2016).

Pulmonary parenchymal strain and mechanical properties of the lung had been proposed for regional functional assessment, and much effort has been undertaken to study these aspects with imaging. The thoracic wall and the diaphragm provide sufficient signal to be relatively easy to track. However, motion analysis on these structures is only a surrogate for pulmonary motion and function. Approaches to assess pulmonary tissue motion directly are challenging due to the limited signal provided. Nevertheless, two promising techniques have been evaluated. The first uses grid tagging, a technique widely applied in MR motion analysis of not only heart but also lung. In the lung, the fast signal decay of the grid due to the large number of susceptibility artifacts at the tissue/air interfaces presents the main challenge. Despite these difficulties, the feasibility of this technique has been shown by several studies (Chen et al. 2001; Napadow et al. 2001; Voorhees et al. 2005; Cai et al. 2007, 2009; Cui et al. 2018). In summary, this technique appears very promising for direct assessment of regional alterations

of tissue motion and thus regional pulmonary function. The second approach, registration of serial images, has to cope with the limited signal of pulmonary tissue and thus low signal-to-noise ratio, especially in dynamic imaging. So far, this technique has only been evaluated in healthy volunteers and mice (Gee et al. 2003; Sundaram and Gee 2005; Sundaram et al. 2005; Kiryu et al. 2008). This ability to detect motion changes over time appears promising for serial imaging of patients for the assessment of disease progression. The major limitations of registration methods in MR imaging remain the poor signal and contrast from solid tissue and blood vessels. If this limitation could be overcome, registration would even be possible on 3D images, which would eliminate the problem of through-plane motion. Another advantage of the registration approach is that it is not dependent on a specific imaging sequence and thus should profit directly from new developments in MR sequences.

Currently, MR-based biomechanics assessment has been mainly challenged for radiation oncology rather than pulmonary functional imaging. The lack of ionizing radiation makes MR-based biomechanics assessment available for experimental work with healthy subjects. For this, MR-based biomechanics assessment is just being discovered and the optimization of dedicated sequence protocols are strongly encouraged. Moreover, further investigations are warranted for demonstrating clinical relevance for not only motion tracking for radiation oncology but also pulmonary functional imaging in near future.

5 Challenges of New Methods for Future Pulmonary Functional Imaging

Although the abovementioned techniques have been tried to be applied in the routine clinical practice, some investigators as well as medical industries are continuously developing and testing new functional imaging methods. In this section, we strive to introduce some of them and their potential to contribute future pulmonary functional imaging.

When considering CT, two new CT systems have been introduced since 2015. One is multi-energy CT with photon-counting detector (PCD), and the other is ultra-high-resolution CT with thinner detector than currently clinically available detectors (Kakinuma et al. 2015; Leng et al. 2017; Symons et al. 2017; Bartlett et al. 2019; Hata et al. 2018; Honda et al. 2018; Kopp et al. 2018; Tanabe et al. 2018; Yanagawa et al. 2018). On the former CT system with PCD (Leng et al. 2017; Symons et al. 2017), two different imaging modes with ultra-high resolution (UHR), both capable of discriminating multi-energy information, have been implemented on the whole-body research CT with PCD. This system is currently started to be testing for improvement of special resolution (Leng et al. 2017; Bartlett et al. 2019; Kopp et al. 2018), radiation dose reduction (Symons et al. 2017), although its' clinical relevance and contribution to pulmonary functional imaging has not been addressed. On the other hand, latter CT system has thinner detector system (i.e. 0.25mm detector collimation×160 detector row=40mm) and can reconstruct CT images as three different matrixes such as 512×512, 1024×1024, and 2048×2048 matrixes. With this system, a larger matrix size maintained the spatial resolution and improved the image quality and assessment of lung diseases, despite an increase in image noise, when compared to a 512 matrix (Kakinuma et al. 2015; Hata et al. 2018; Honda et al. 2018; Yanagawa et al. 2018). In addition, the wall thickness in the small airway showed a lower value with the 1024 × 1024 scans versus the 512 × 512 scans, when applying this system in COPD subjects (Tanabe et al. 2018). Therefore, this system may be useful for morphological-based functional evaluation in COPD and airway diseases, although further investigations are warranted to determination of real clinical significance for ultra-high resolution CT in near future.

In contrast to CT, pulmonary functional MR imaging has been shifting from functional to metabolic evaluations and from 1.5 Tesla (T) MR systems to 3 T MR systems. Although 3T system has severe susceptibility artifact and decrease image quality, it is able to improve image quality of non-contrast-enhanced MR angiography and

perfusion imaging due to increased T1 relaxation time of blood by arterial spin labeling technique, etc. (Ohno et al. 2014c, 2015a; Walker et al. 2015; Tibiletti et al. 2016; Sá et al. 2017), demonstrate pulmonary parenchyma on pulmonary MR imaging with ultra-short TE (UTE) less than 200μs as well as thin-section CT (Ohno et al. 2016d, 2017e; Wielpütz et al. 2018), and determine regional perfusion-based information as subtraction between unenhanced and contrast-enhanced MR imaging with UTE as well as perfusion SPECT (Ohno et al. 2019). Moreover, 3T MR system can also provide metabolic information by chemical exchange saturation transfer (CEST) imaging (Ohno et al. 2016e, 2018b). CEST imaging was introduced as a new type of method, which has drawn considerable attention as a novel mechanism to produce modified tissue contrast for MR imaging based upon exchangeable protons (-NH, -OH, -SH, others) on endogenous or exogenous molecules. Currently, amid proton ($-NH_3$) transfer (APT) weighted CEST imaging has been tested to differentiate malignant from benign lesions in patients with thoracic oncology as well as pulmonary nodule (Ohno et al. 2016d, 2018b). Furthermore, a few investigators tried to develop sodium (^{23}Na) MR imaging for the quantification of tissue sodium concentration, and enables the investigation of tissue viability in not only brain but also others including lung at 7T MR system because ^{23}Na plays a key role in many physiological processes (Platt et al. 2018). However, the clinical results as well as clinical relevance of MR imaging by ^{23}Na has not been determined. In addition, clinical application of 7T MR system has not been achieved. Therefore, these techniques will open new MR-based pulmonary functional imaging with various information in near future.

When considering nuclear medicine study, there are two important progresses. One is the clinical application of PET fused with MR imaging (PET/MRI), and the other is the development of new tracer. The former is currently applied for thoracic oncology patients including non-small cell lung cancer, thymic epithelial tumor, and malignant mesothelioma (Ohno et al. 2015c, 2016f, 2017f, 2018c, d; Schaarschmidt et al. 2016, 2017; Kirchner et al. 2019). However, this technique has not been applied for pulmonary functional imaging; its potential for contributing to not only thoracic oncology but also pulmonary functional imaging will be tested in the next decades. On the other hands, the latter is being continuously tried and tested as basic studies in the last few decades. As basic researches, several investigators have been testing nanoparticles for assessing inflammation (Pérez-Campaña et al. 2014), nano theranosis for primary and metastatic lung tumor (Key et al. 2014; Black et al. 2016), and ^{68}Ga-siderophores and monoclonal antibody JF5 for aspergillus fumigatus infection imaging (Petrik et al. 2012; Thornton 2018). Moreover, many traces were also tested for pulmonary inflammatory or thoracic oncologic imaging as *in vivo* studies, although human studies have not been performed (Locke et al. 2009; Lamare et al. 2011; Tsuji et al. 2012; Nishii et al. 2013; Ebenhan et al. 2014; Burger et al. 2014; Gao et al. 2015; Jørgensen et al. 2017; Zhang et al. 2017; Jiang et al. 2018; Li et al. 2018). Therefore, these traces as well as new others will be tested and their clinical significances for pulmonary functional imaging will be demonstrated in the next few decades.

6 Conclusion

State-of-the-art pulmonary ventilation imaging, perfusion imaging, and biomechanics evaluation are reviewed with their future challenges. The imaging techniques are gradually but steadily shifting from nuclear medicine to CT and MRI, from those with qualitative assessment to those with quantitative assessment. In addition, they are still developing and under evaluation for clinical relevance not only in radiology but also in the multi-disciplinary fields of pulmonology, pulmonary physiology, pathophysiology, thoracic surgery, and radiation oncology. The combination of imaging method with various image analyses using bioengineering is also important for future clinical setting. Furthermore, new imaging techniques that are under development and/or testing will emerge in future. Although efforts of

many researchers and clinicians have resulted in many different approaches for functional imaging, the real breakthrough toward significant clinical applications with strong impact remains to be achieved. Such obstacles in front of us motivated us to produce this book for the younger and future challengers in the field of pulmonary functional imaging.

References

Adolphi NL, Kuethe DO (2008) Quantitative mapping of ventilation-perfusion ratios in lungs by 19F MR imaging of T1 of inert fluorinated gases. Magn Reson Med 59(4):739–746

Albert MS, Cates GD, Driehuys B, Happer W, Saam B, Springer CS Jr, Wishnia A (1994) Biological magnetic resonance imaging using laser-polarized 129Xe. Nature. 370(6486):199–201

Altes TA, Powers PL, Knight-Scott J, Rakes G, Platts-Mills TA, de Lange EE, Alford BA, Mugler JP 3rd, Brookeman JR (2001) Hyperpolarized 3He MR lung ventilation imaging in asthmatics: preliminary findings. J Magn Reson Imaging. 13(3):378–384

Altes TA, Salerno M (2004) Hyperpolarized gas MR imaging of the lung. J Thorac Imaging. 19(4): 250–258

Ament SJ, Maus S, Reber H, Buchholz HG, Bausbacher N, Brochhausen C, Graf F, Miederer M, Schreckenberger M (2013) PET lung ventilation/perfusion imaging using (68)Ga aerosol (Galligas) and (68)Ga-labeled macroaggregated albumin. Recent Results Cancer Res. 194:395–423

Arakawa H, Stern EJ, Nakamoto T, Fujioka M, Kaneko N, Harasawa H (2003) Chronic pulmonary thromboembolism. Air trapping on computed tomography and correlation with pulmonary function tests. J Comput Assist Tomogr. 27(5):735–742

Bailey DL, Eslick EM, Schembri GP, Roach PJ (2016) (68)Ga PET ventilation and perfusion lung imaging-current status and future challenges. Semin Nucl Med. 46(5):428–435

Barker AJ, Roldán-Alzate A, Entezari P, Shah SJ, Chesler NC, Wieben O, Markl M, François CJ (2015) Four-dimensional flow assessment of pulmonary artery flow and wall shear stress in adult pulmonary arterial hypertension: results from two institutions. Magn Reson Med 73(5):1904–1913

Bartlett DJ, Koo CW, Bartholmai BJ, Rajendran K, Weaver JM, Halaweish AF, Leng S, McCollough CH, Fletcher JG (2019) High-resolution chest computed tomography imaging of the lungs: impact of 1024 matrix reconstruction and photon-counting detector computed tomography. Invest Radiol. 54(3): 129–137

Bauman G, Puderbach M, Deimling M, Jellus V, Chefd'hotel C, Dinkel J, Hintze C, Kauczor HU, Schad LR (2009) Non-contrast-enhanced perfusion and ventilation assessment of the human lung by means of fourier decomposition in proton MRI. Magn Reson Med. 62(3):656–664

Bauman G, Scholz A, Rivoire J, Terekhov M, Friedrich J, de Oliveira A, Semmler W, Schreiber LM, Puderbach M (2013a) Lung ventilation- and perfusion-weighted Fourier decomposition magnetic resonance imaging: in vivo validation with hyperpolarized 3He and dynamic contrast-enhanced MRI. Magn Reson Med. 69(1):229–237

Bauman G, Puderbach M, Heimann T, Kopp-Schneider A, Fritzsching E, Mall MA, Eichinger M (2013b) Validation of Fourier decomposition MRI with dynamic contrast-enhanced MRI using visual and automated scoring of pulmonary perfusion in young cystic fibrosis patients. Eur J Radiol. 82(12):2371–2317

Biederer J, Hintze C, Fabel M, Dinkel J (2010) Magnetic resonance imaging and computed tomography of respiratory mechanics. J Magn Reson Imaging. 32(6):1388–1397

Black KC, Ibricevic A, Gunsten SP, Flores JA, Gustafson TP, Raymond JE, Samarajeewa S, Shrestha R, Felder SE, Cai T, Shen Y, Löbs AK, Zhegalova N, Sultan DH, Berezin M, Wooley KL, Liu Y, Brody SL (2016) In vivo fate tracking of degradable nanoparticles for lung gene transfer using PET and Ĉerenkov imaging. Biomaterials. 98:53–63

Brooks RA, Di Chiro G (1987) Magnetic resonance imaging of stationary blood: a review. Med Phys. 14(6):903–913

Burger IA, Zitzmann-Kolbe S, Pruim J, Friebe M, Graham K, Stephens A, Dinkelborg L, Kowal K, Schibli R, Luurtsema G, Maas B, Horn-Tutic M, Haerle SK, Wiegers J, Schaefer NG, Hany TF, von Schulthess GK (2014) First clinical results of (D)-18F-Fluoromethyltyrosine (BAY 86-9596) PET/CT in patients with non-small cell lung cancer and head and neck squamous cell carcinoma. J Nucl Med. 55(11):1778–1785

Cai J, Altes TA, Miller GW, Sheng K, Read PW, Mata JF, Zhong X, Cates GD Jr, de Lange EE, Mugler JP 3rd, Brookeman JR (2007) MR grid-tagging using hyperpolarized helium-3 for regional quantitative assessment of pulmonary biomechanics and ventilation. Magn Reson Med. 58(2):373–380

Cai J, Sheng K, Benedict SH, Read PW, Larner JM, Mugler JP 3rd, de Lange EE, Cates GD Jr, Miller GW (2009) Dynamic MRI of grid-tagged hyperpolarized helium-3 for the assessment of lung motion during breathing. Int J Radiat Oncol Biol Phys. 75(1):276–284

Callahan J, Hofman MS, Siva S, Kron T, Schneider ME, Binns D, Eu P, Hicks RJ (2014) High-resolution imaging of pulmonary ventilation and perfusion with 68Ga-VQ respiratory gated (4-D) PET/CT. Eur J Nucl Med Mol Imaging. 41(2):343–349

Capaldi DP, Zha N, Guo F, Pike D, McCormack DG, Kirby M, Parraga G (2016) Pulmonary imaging

biomarkers of gas trapping and emphysema in COPD: (3)He MR imaging and CT parametric response maps. Radiology. 279(2):597–608

Chae EJ, Seo JB, Goo HW, Kim N, Song KS, Lee SD, Hong SJ, Krauss B (2008) Xenon ventilation CT with a dual-energy technique of dual-source CT: initial experience. Radiology. 248(2):615–624

Chae EJ, Seo JB, Lee J, Kim N, Goo HW, Lee HJ, Lee CW, Ra SW, Oh YM, Cho YS (2010a) Xenon ventilation imaging using dual-energy computed tomography in asthmatics: initial experience. Invest Radiol. 45(6):354–361

Chae EJ, Seo JB, Jang YM, Krauss B, Lee CW, Lee HJ, Song KS (2010b) Dual-energy CT for assessment of the severity of acute pulmonary embolism: pulmonary perfusion defect score compared with CT angiographic obstruction score and right ventricular/left ventricular diameter ratio. AJR Am J Roentgenol. 194(3):604–610

Chae EJ, Song JW, Krauss B, Song KS, Lee CW, Lee HJ, Seo JB (2010c) Dual-energy computed tomography characterization of solitary pulmonary nodules. J Thorac Imaging. 25(4):301–310

Chae EJ, Kim N, Seo JB, Park JY, Song JW, Lee HJ, Hwang HJ, Lim C, Chang YJ, Kim YH (2013) Prediction of postoperative lung function in patients undergoing lung resection: dual-energy perfusion computed tomography versus perfusion scintigraphy. Invest Radiol. 48(8):622–627

Chapman B, O'Callaghan C, Coxon R, Glover P, Jaroszkiewicz G, Howseman A, Mansfield P, Small P, Milner AD, Coupland RE (1990) Estimation of lung volume in infants by echo planar imaging and total body plethysmography. Arch Dis Child. 65(2):168–170

Chen Q, Siewert B, Bly BM, Warach S, Edelman RR (1997) STAR-HASTE: perfusion imaging without magnetic susceptibility artifact. Magn Reson Med. 38(3):404–408

Chen Q, Mai VM, Bankier AA, Napadow VJ, Gilbert RJ, Edelman RR (2001) Ultrafast MR grid-tagging sequence for assessment of local mechanical properties of the lungs. Magn Reson Med. 45(1):24–28

Chesler DA, Hales C, Hnatowich DJ, Hoop B (1975) Three-dimensional reconstruction of lung perfusion image with positron detection. J Nucl Med. 16(1):80–82

Chiro GD, Brooks RA, Kessler RM, Johnston GS, Jones AE, Herdt JR, Sheridan WT (1979) Tissue signatures with dual-energy computed tomography. Radiology. 131(2):521–523

Cho A (2009) Physics. Helium-3 shortage could put freeze on low temperature research. Science 326:778–779

Cluzel P, Similowski T, Chartrand-Lefebvre C, Zelter M, Derenne JP, Grenier PA (2000) Diaphragm and chestwall: assessment of the inspiratory pump with MR imaging-preliminary observations. Radiology 215(2):574–583

Couch MJ, Ball IK, Li T, Fox MS, Littlefield SL, Biman B, Albert MS (2013) Pulmonary ultrashort echo time 19F MR imaging with inhaled fluorinated gas mixtures in healthy volunteers: feasibility. Radiology. 269(3):903–909

Couch MJ, Ball IK, Li T, Fox MS, Biman B, Albert MS (2019) 19 F MRI of the lungs using inert fluorinated gases: challenges and new developments. J Magn Reson Imaging. 49(2):343–354

Cui T, Miller GW, Mugler JP 3rd, Cates GD Jr, Mata JF, de Lange EE, Huang Q, Altes TA, Yin FF, Cai J (2018) An initial investigation of hyperpolarized gas tagging magnetic resonance imaging in evaluating deformable image registration-based lung ventilation. Med Phys. 45(12):5535–5542

Dournes G, Verdier D, Montaudon M, Bullier E, Rivière A, Dromer C, Picard F, Billes MA, Corneloup O, Laurent F, Lederlin M (2014) Dual-energy CT perfusion and angiography in chronic thromboembolic pulmonary hypertension: diagnostic accuracy and concordance with radionuclide scintigraphy. Eur Radiol. 24(1):42–51

Ebenhan T, Zeevaart JR, Venter JD, Govender T, Kruger GH, Jarvis NV, Sathekge MM (2014) Preclinical evaluation of 68Ga-labeled 1,4,7-triazacyclononane-1,4,7-triacetic acid-ubiquicidin as a radioligand for PET infection imaging. J Nucl Med. 55(2): 308–314

Edelman RR, Hatabu H, Tadamura E, Li W, Prasad PV (1996) Noninvasive assessment of regional ventilation in the human lung using oxygen-enhanced magnetic resonance imaging. Nat Med. 2(11):1236–1239

Even GA, Green MA (1989) Gallium-68-labeled macroaggregated human serum albumin, 68Ga-MAA. Int J Rad Appl Instrum B. 16(3):319–321

Fain SB, Panth SR, Evans MD, Wentland AL, Holmes JH, Korosec FR, O'Brien MJ, Fountaine H, Grist TM (2006) Early emphysematous changes in asymptomatic smokers: detection with 3He MR imaging. Radiology. 239(3):875–883

Fain SB, Korosec FR, Holmes JH, O'Halloran R, Sorkness RL, Grist TM (2007) Functional lung imaging using hyperpolarized gas MRI. J Magn Reson Imaging. 25(5):910–923

Flohr TG, McCollough CH, Bruder H, Petersilka M, Gruber K, Süss C, Grasruck M, Stierstorfer K, Krauss B, Raupach R, Primak AN, Küttner A, Achenbach S, Becker C, Kopp A, Ohnesorge BM (2006) First performance evaluation of a dual-source CT (DSCT) system. Eur Radiol. 16(2):256–268

Fuld MK, Halaweish AF, Haynes SE, Divekar AA, Guo J, Hoffman EA (2013) Pulmonary perfused blood volume with dual-energy CT as surrogate for pulmonary perfusion assessed with dynamic multidetector CT. Radiology. 267(3):747–756

Fuseya Y, Muro S, Sato S, Tanabe N, Sato A, Tanimura K, Hasegawa K, Uemasu K, Kubo T, Kido A, Fujimoto K, Fushimi Y, Kusahara H, Sakashita N, Ohno Y, Togashi K, Mishima M, Hirai T (2018) Complementary regional heterogeneity information from COPD patients obtained using oxygen-enhanced MRI and chest CT. PLoS One. 13(8):e0203273

Gao S, Wu H, Li W, Zhao S, Teng X, Lu H, Hu X, Wang S, Yu J, Yuan S (2015) A pilot study imaging integrin αvβ3 with RGD PET/CT in suspected lung cancer patients. Eur J Nucl Med Mol Imaging. 42(13):2029–2037

Gauthier AP, Verbanck S, Estenne M, Segebarth C, Macklem PT, Paiva M (1994) Three-dimensional reconstruction of the in vivo human diaphragm shape at different lung volumes. J Appl Physiol. 76(2): 495–506

Gee J, Sundaram T, Hasegawa I, Uematsu H, Hatabu H (2003) Characterization of regional pulmonary mechanics from serial magnetic resonance imaging data. Acad Radiol. 10(10):1147–1152

Genant HK, Boyd D (1977) Quantitative bone mineral analysis using dual energy computed tomography. Invest Radiol. 12(6):545–551

Gierada DS, Curtin JJ, Erickson SJ, Prost RW, Strandt JA, Goodman LR (1995) Diaphragmatic motion: fast gradient-recalled-echo MR imaging in healthy subjects. Radiology 194(3):879–884

Gierada DS, Hakimian S, Slone RM, Yusen RD (1998) MR analysis of lung volume and thoracic dimensions in patients with emphysema before and after lung volume reduction surgery. AJR Am J Roentgenol. 170(3):707–714

Giordano J, Khung S, Duhamel A, Hossein-Foucher C, Bellèvre D, Lamblin N, Remy J, Remy-Jardin M (2017) Lung perfusion characteristics in pulmonary arterial hypertension (PAH) and peripheral forms of chronic thromboembolic pulmonary hypertension (pCTEPH): Dual-energy CT experience in 31 patients. Eur Radiol. 27(4):1631–1639

Gutberlet M, Kaireit TF, Voskrebenzev A, Lasch F, Freise J, Welte T, Wacker F, Hohlfeld JM, Vogel-Claussen J (2018) Free-breathing dynamic 19F gas MR imaging for mapping of regional lung ventilation in patients with COPD. Radiology. 286(3):1040–1051

Halaweish AF, Moon RE, Foster WM, Soher BJ, McAdams HP, MacFall JR, Ainslie MD, MacIntyre NR, Charles HC (2013) Perfluoropropane gas as a magnetic resonance lung imaging contrast agent in humans. Chest. 144(4):1300–1310

Hardcastle N, Hofman MS, Hicks RJ, Callahan J, Kron T, MacManus MP, Ball DL, Jackson P, Siva S (2015) Accuracy and Utility of Deformable Image Registration in (68)Ga 4D PET/CT assessment of pulmonary perfusion changes during and after lung radiation therapy. Int J Radiat Oncol Biol Phys. 93(1):196–204

Hnatowich DJ (1976) Labeling of tin-soaked albumin microspheres with 68Ga. J Nucl Med. 17(1):57–60

Hashimoto M, Nagatani Y, Oshio Y, Nitta N, Yamashiro T, Tsukagoshi S, Ushio N, Mayumi M, Kimoto T, Igarashi T, Yoshigoe M, Iwai K, Tanaka K, Sato S, Sonoda A, Otani H, Murata K, Hanaoka J, investigators of ACTIve study group (2018) Preoperative assessment of pleural adhesion by four-dimensional ultra-low-dose computed tomography (4D-ULDCT) with adaptive iterative dose reduction using three-dimensional processing (AIDR-3D). Eur J Radiol 98:179–186

Hata A, Yanagawa M, Honda O, Kikuchi N, Miyata T, Tsukagoshi S, Uranishi A, Tomiyama N (2018) Effect of matrix size on the image quality of ultra-high-resolution CT of the lung: comparison of 512×512, 1024×1024, and 2048×2048. Acad Radiol. 25(7):869–876

Hatabu H, Gaa J, Kim D, Li W, Prasad PV, Edelman RR (1996a) Pulmonary perfusion and angiography: evaluation with breath-hold enhanced three-dimensional fast imaging steady-state precession MR imaging with short TR and TE. AJR Am J Roentgenol. 167(3):653–635

Hatabu H, Gaa J, Kim D, Li W, Prasad PV, Edelman RR (1996b) Pulmonary perfusion: qualitative assessment with dynamic contrast-enhanced MRI using ultra-short TE and inversion recovery turbo FLASH. Magn Reson Med. 36(4):503–508

Hatabu H, Tadamura E, Levin DL, Chen Q, Li W, Kim D, Prasad PV, Edelman RR (1999) Quantitative assessment of pulmonary perfusion with dynamic contrast-enhanced MRI. Magn Reson Med. 42(6): 1033–1038

Hatabu H, Tadamura E, Prasad PV, Chen Q, Buxton R, Edelman RR (2000) Noninvasive pulmonary perfusion imaging by STAR-HASTE sequence. Magn Reson Med. 44(5):808–812

Hatabu H, Tadamura E, Chen Q, Stock KW, Li W, Prasad PV, Edelman RR (2001) Pulmonary ventilation dynamic MRI with inhalation of molecular oxygen. Eur J Radiol 37:172–178

Hoey ET, Mirsadraee S, Pepke-Zaba J, Jenkins DP, Gopalan D, Screaton NJ (2011) Dual-energy CT angiography for assessment of regional pulmonary perfusion in patients with chronic thromboembolic pulmonary hypertension: initial experience. AJR Am J Roentgenol. 196(3):524–532

Hofman MS, Beauregard JM, Barber TW, Neels OC, Eu P, Hicks RJ (2011) 68Ga PET/CT ventilation-perfusion imaging for pulmonary embolism: a pilot study with comparison to conventional scintigraphy. J Nucl Med. 52(10):1513–1519

Honda O, Yanagawa M, Hata A, Kikuchi N, Miyata T, Tsukagoshi S, Uranishi A, Tomiyama N (2018) Influence of gantry rotation time and scan mode on image quality in ultra-high-resolution CT system. Eur J Radiol. 103:71–75

Hong YJ, Kim JY, Choe KO, Hur J, Lee HJ, Choi BW, Kim YJ (2013) Different perfusion pattern between acute and chronic pulmonary thromboembolism: evaluation with two-phase dual-energy perfusion CT. AJR Am J Roentgenol. 200(4):812–817

Jiang L, Song D, Chen H, Zhang A, Wang H, Cheng Z (2018) Pilot study of 64CuCl2 for PET imaging of inflammation. Molecules 23(2):E502

Jobst BJ, Triphan SM, Sedlaczek O, Anjorin A, Kauczor HU, Biederer J, Ley-Zaporozhan J, Ley S, Wielpütz MO (2015) Functional lung MRI in chronic obstructive pulmonary disease: comparison of T1 mapping,

oxygen-enhanced T1 mapping and dynamic contrast enhanced perfusion. PLoS One. 10(3):e0121520

Johns CS, Swift AJ, Hughes PJC, Ohno Y, Schiebler M, Wild JM (2017) Pulmonary MR angiography and perfusion imaging-A review of methods and applications. Eur J Radiol. 86:361–370

Jørgensen NP, Alstrup AK, Mortensen FV, Knudsen K, Jakobsen S, Madsen LB, Bender D, Breining P, Petersen MS, Schleimann MH, Dagnæs-Hansen F, Gormsen LC, Borghammer P (2017) Cholinergic PET imaging in infections and inflammation using 11C-donepezil and 18F-FEOBV. Eur J Nucl Med Mol Imaging. 44(3):449–458

Kakinuma R, Moriyama N, Muramatsu Y, Gomi S, Suzuki M, Nagasawa H, Kusumoto M, Aso T, Muramatsu Y, Tsuchida T, Tsuta K, Maeshima AM, Tochigi N, Watanabe S, Sugihara N, Tsukagoshi S, Saito Y, Kazama M, Ashizawa K, Awai K, Honda O, Ishikawa H, Koizumi N, Komoto D, Moriya H, Oda S, Oshiro Y, Yanagawa M, Tomiyama N, Asamura H (2015) Ultra-high-resolution computed tomography of the lung: image quality of a prototype scanner. PLoS One. 10(9):e0137165

Kauczor H, Surkau R, Roberts T (1998) MRI using hyperpolarized noble gases. Eur Radiol. 8(5):820–827

Kauczor HU, Hast J, Heussel CP, Schlegel J, Mildenberger P, Thelen M (2000) Focal airtrapping at expiratory high-resolution CT: comparison with pulmonary function tests. Eur Radiol. 10(10):1539–1546

Kauczor HU, Hast J, Heussel CP, Schlegel J, Mildenberger P, Thelen M (2002) CT attenuation of paired HRCT scans obtained at full inspiratory/expiratory position: comparison with pulmonary function tests. Eur Radiol. 12(11):2757–2763

Key J, Kim YS, Tatulli F, Palange AL, O'Neill B, Aryal S, Ramirez M, Liu X, Ferrari M, Munden R, Decuzzi P (2014) Opportunities for nano theranosis in lung cancer and pulmonary metastasis. Clin Transl Imaging. 2(5):427–437

Kirby M, Svenningsen S, Owrangi A, Wheatley A, Farag A, Ouriadov A, Santyr GE, Etemad-Rezai R, Coxson HO, McCormack DG, Parraga G (2012) Hyperpolarized 3He and 129Xe MR imaging in healthy volunteers and patients with chronic obstructive pulmonary disease. Radiology. 265(2): 600–610

Kirchner J, Sawicki LM, Nensa F, Schaarschmidt BM, Reis H, Ingenwerth M, Bogner S, Aigner C, Buchbender C, Umutlu L, Antoch G, Herrmann K, Heusch P (2019) Prospective comparison of 18F-FDG PET/MRI and 18F-FDG PET/CT for thoracic staging of non-small cell lung cancer. Eur J Nucl Med Mol Imaging. 46(2):437–445

Kiryu S, Sundaram T, Kubo S, Ohtomo K, Asakura T, Gee JC, Hatabu H, Takahashi M (2008) MRI assessment of lung parenchymal motion in normal mice and transgenic mice with sickle cell disease. J Magn Reson Imaging. 27(1):49–56

Kalisz K, Halliburton S, Abbara S, Leipsic JA, Albrecht MH, Schoepf UJ, Rajiah P (2017) Update on Cardiovascular Applications of Multienergy CT. Radiographics. 37(7):1955–1974

Kolb C, Wetscherek A, Buzan MT, Werner R, Rank CM, Kachelrie M, Kreuter M, Dinkel J, Heuel CP, Maier-Hein K (2016) Regional lung ventilation analysis using temporally resolved magnetic resonance imaging. J Comput Assist Tomogr. 40(6):899–906

Kondo T, Kobayashi I, Taguchi Y, Ohta Y, Yanagimachi N (2000) A dynamic analysis of chest wall motions with MRI in healthy young subjects. Respirology. 5(1):19–25

Kondo T, Kobayashi I, Taguchi Y, Hayama N, Tajiri S, Yanagimachi N (2005) An analysis of the chest wall motions using the dynamic MRI in healthy elder subjects. Tokai J Exp Clin Med. 30(1):15–20

Kong X, Sheng HX, Lu GM, Meinel FG, Dyer KT, Schoepf UJ, Zhang LJ (2014) Xenon-enhanced dual-energy CT lung ventilation imaging: techniques and clinical applications. AJR Am J Roentgenol. 202(2):309–317

Kopp FK, Daerr H, Si-Mohamed S, Sauter AP, Ehn S, Fingerle AA, Brendel B, Pfeiffer F, Roessl E, Rummeny EJ, Pfeiffer D, Proksa R, Douek P, Noël PB (2018) Evaluation of a preclinical photon-counting CT prototype for pulmonary imaging. Sci Rep. 8(1):17386

Koyama H, Ohno Y, Fujisawa Y, Seki S, Negi N, Murakami T, Yoshikawa T, Sugihara N, Nishimura Y, Sugimura K (2016) 3D lung motion assessments on inspiratory/expiratory thin-section CT: Capability for pulmonary functional loss of smoking-related COPD in comparison with lung destruction and air trapping. Eur J Radiol. 85(2):352–359

Kruger SJ, Nagle SK, Couch MJ, Ohno Y, Albert M, Fain SB (2016) Functional imaging of the lungs with gas agents. J Magn Reson Imaging. 43(2):295–315

Lamare F, Hinz R, Gaemperli O, Pugliese F, Mason JC, Spinks T, Camici PG, Rimoldi OE (2011) Detection and quantification of large-vessel inflammation with 11C-(R)-PK11195 PET/CT. J Nucl Med. 52(1):33–39

Lee E, Seo JB, Lee HJ, Chae EJ, Lee SM, Oh SY, Kim N (2015) Quantitative assessment of global and regional air trappings using non-rigid registration and regional specific volume change of inspiratory/expiratory CT scans: studies on healthy volunteers and asthmatics. Korean J Radiol. 16(3):632–640

Lee SM, Seo JB, Hwang HJ, Kim N, Oh SY, Lee JS, Lee SW, Oh YM, Kim TH (2017a) Assessment of regional emphysema, air-trapping and Xenon-ventilation using dual-energy computed tomography in chronic obstructive pulmonary disease patients. Eur Radiol. 27(7):2818–2827

Lee SW, Lee SM, Shin SY, Park TS, Oh SY, Kim N, Hong Y, Lee JS, Oh YM, Lee SD, Seo JB (2017b) Improvement in ventilation-perfusion mismatch after bronchoscopic lung volume reduction: quantitative image analysis. Radiology. 285(1):250–260

Leng S, Gutjahr R, Ferrero A, Kappler S, Henning A, Halaweish A, Zhou W, Montoya J, McCollough C (2017) Ultra-high spatial resolution, multi-energy CT using photon counting detector technology. Proc SPIE Int Soc Opt Eng 10132:101320Y

Levin DL, Chen Q, Zhang M, Edelman RR, Hatabu H (2001) Evaluation of regional pulmonary perfusion using ultrafast magnetic resonance imaging. Magn Reson Med. 46(1):166–171

Ley-Zaporozhan J, Ley S, Unterhinninghofen R, Weinheimer O, Saito Y, Kauczor HU, Szabo G (2008) Quantification of lung volume at different tidal volumes and positive end-expiratory pressures in a porcine model by using retrospective respiratory gated 4D-computed tomography. Invest Radiol. 43(6):461–469

Li J, Zheng H, Fodah R, Warawa JM, Ng CK (2018) Validation of 2-18F-fluorodeoxysorbitol as a potential radiopharmaceutical for imaging bacterial infection in the lung. J Nucl Med. 59(1): 134–139

Liszewski MC, Hersman FW, Altes TA, Ohno Y, Ciet P, Warfield SK, Lee EY (2013) Magnetic resonance imaging of pediatric lung parenchyma, airways, vasculature, ventilation, and perfusion: state of the art. Radiol Clin North Am. 51(4):555–582

Locke LW, Chordia MD, Zhang Y, Kundu B, Kennedy D, Landseadel J, Xiao L, Fairchild KD, Berr SS, Linden J, Pan D (2009) A novel neutrophil-specific PET imaging agent: cFLFLFK-PEG-64Cu. J Nucl Med. 50(5):790–797

Lu GM, Zhao Y, Zhang LJ, Schoepf UJ (2012) Dual-energy CT of the lung. AJR Am J Roentgenol. 199(5 Suppl):S40–S53

Mai VM, Berr SS (1999) MR perfusion imaging of pulmonary parenchyma using pulsed arterial spin labeling techniques: FAIRER and FAIR. J Magn Reson Imaging. 9(3):483–487

Martinez CH, Diaz AA, Meldrum C, Curtis JL, Cooper CB, Pirozzi C, Kanner RE, Paine R 3rd, Woodruff PG, Bleecker ER, Hansel NN, Barr RG, Marchetti N, Criner GJ, Kazerooni EA, Hoffman EA, Ross BD, Galban CJ, Cigolle CT, Martinez FJ (2017) Han MK; SPIROMICS Investigators. Age and small airway imaging abnormalities in subjects with and without airflow obstruction in SPIROMICS. Am J Respir Crit Care Med. 195(4):464–472

Masy M, Giordano J, Petyt G, Hossein-Foucher C, Duhamel A, Kyheng M, De Groote P, Fertin M, Lamblin N, Bervar JF, Remy J, Remy-Jardin M (2018) Dual-energy CT (DECT) lung perfusion in pulmonary hypertension: concordance rate with V/Q scintigraphy in diagnosing chronic thromboembolic pulmonary hypertension (CTEPH). Eur Radiol. 28(12): 5100–5110

Matsuoka S, Kurihara Y, Yagihashi K, Nakajima Y (2007) Quantitative assessment of peripheral airway obstruction on paired expiratory/inspiratory thin-section computed tomography in chronic obstructive pulmonary disease with emphysema. J Comput Assist Tomogr. 31(3):384–389

Matsuoka S, Hunsaker AR, Gill RR, Jacobson FL, Ohno Y, Patz S, Hatabu H (2008a) Functional MR imaging of the lung. Magn Reson Imaging Clin N Am. 16(2):275–289

Matsuoka S, Kurihara Y, Yagihashi K, Hoshino M, Watanabe N, Nakajima Y (2008b) Quantitative assessment of air trapping in chronic obstructive pulmonary disease using inspiratory and expiratory volumetric MDCT. AJR Am J Roentgenol. 190(3): 762–769

Matsuoka S, Kurihara Y, Yagihashi K, Hoshino M, Nakajima Y (2008c) Airway dimensions at inspiratory and expiratory multisection CT in chronic obstructive pulmonary disease: correlation with airflow limitation. Radiology. 248(3):1042–1049

Mijailovich SM, Treppo S, Venegas JG (1997) Effects of lung motion and tracer kinetics corrections on PET imaging of pulmonary function. J Appl Physiol (1985) 82(4):1154–1162

Millner MR, McDavid WD, Waggener RG, Dennis MJ, Payne WH, Sank VJ (1979) Extraction of information from CT scans at different energies. Med Phys. 6(1):70–71

Mintun MA, Ter-Pogossian MM, Green MA, Lich LL, Schuster DP (1986) Quantitative measurement of regional pulmonary blood flow with positron emission tomography. J Appl Physiol (1985) 60(1):317–326

Mintun MA, Dennis DR, Welch MJ, Mathias CJ, Schuster DP (1987) Measurements of pulmonary vascular permeability with PET and gallium-68 transferrin. J Nucl Med. 28(11):1704–1716

Musch G, Layfield JD, Harris RS, Melo MF, Winkler T, Callahan RJ, Fischman AJ, Venegas JG (2002) Topographical distribution of pulmonary perfusion and ventilation, assessed by PET in supine and prone humans. J Appl Physiol (1985) 93(5):1841–1851

Musch G, Venegas JG (2005) Positron emission tomography imaging of regional pulmonary perfusion and ventilation. Proc Am Thorac Soc. 2(6):522–527. 508-9

Meyer M, Haubenreisser H, Sudarski S, Doesch C, Ong MM, Borggrefe M, Schoenberg SO, Henzler T (2015) Where do we stand? Functional imaging in acute and chronic pulmonary embolism with state-of-the-art CT. Eur J Radiol. 84(12):2432–2437

Nagao M, Yamasaki Y, Abe K, Hosokawa K, Kawanami S, Kamitani T, Yamanouchi T, Yabuuchi H, Fukushima K, Honda H (2017) Energy efficiency and pulmonary artery flow after balloon pulmonary angioplasty for inoperable, chronic thromboembolic pulmonary hypertension: analysis by phase-contrast MRI. Eur J Radiol. 87:99–104

Napadow VJ, Mai V, Bankier A, Gilbert RJ, Edelman R, Chen Q (2001) Determination of regional pulmonary parenchymal strain during normal respiration using spin inversion tagged magnetization MRI. J Magn Reson Imaging. 13(3):467–474

Nishii R, Higashi T, Kagawa S, Kishibe Y, Takahashi M, Yamauchi H, Motoyama H, Kawakami K, Nakaoku T, Nohara J, Okamura M, Watanabe T, Nakatani K, Nagamachi S, Tamura S, Kawai K, Kobayashi M (2013) Diagnostic usefulness of an amino acid tracer, α-[N-methyl-(11)C]-methylaminoisobutyric acid ((11)C-MeAIB), in the PET diagnosis of chest malignancies. Ann Nucl Med. 27(9):808–821

Nishio M, Matsumoto S, Koyama H, Ohno Y, Sugimura K (2014) Airflow limitation in chronic obstructive pulmonary disease: ratio and difference of percentage of low-attenuation lung regions in paired inspiratory/expiratory computed tomography. Acad Radiol. 21(10):1262–1267

Nishio M, Matsumoto S, Tsubakimoto M, Nishii T, Koyama H, Ohno Y, Sugimura K (2015) Paired inspiratory/expiratory volumetric CT and deformable image registration for quantitative and qualitative evaluation of airflow limitation in smokers with or without copd. Acad Radiol. 22(3):330–336

Oehme L, Zöphel K, Golgor E, Andreeff M, Wunderlich G, Brogsitter C, de Abreu MG, Kotzerke J (2014) Quantitative analysis of regional lung ventilation and perfusion PET with (68)Ga-labelled tracers. Nucl Med Commun. 35(5):501–510

Ogasawara N, Suga K, Zaki M, Okada M, Kawakami Y, Matsunaga N (2004) Assessment of lung perfusion impairment in patients with pulmonary artery-occlusive and chronic obstructive pulmonary diseases with noncontrast electrocardiogram-gated fast-spin-echo perfusion MR imaging. J Magn Reson Imaging. 20(4):601–611

Ohno Y, Chen Q, Hatabu H (2001a) Oxygen-enhanced magnetic resonance ventilation imaging of lung. Eur J Radiol. 37(3):164–171

Ohno Y, Hatabu H, Takenaka D, Adachi S, Van Cauteren M, Sugimura K (2001b) Oxygen-enhanced MR ventilation imaging of the lung: preliminary clinical experience in 25 subjects. AJR Am J Roentgenol. 177(1):185–194

Ohno Y, Hatabu H, Takenaka D, Van Cauteren M, Fujii M, Sugimura K (2002) Dynamic oxygen-enhanced MRI reflects diffusing capacity of the lung. Magn Reson Med. 47(6):1139–1144

Ohno Y, Hatabu H, Higashino T, Takenaka D, Watanabe H, Nishimura Y, Yoshimura M, Sugimura K (2004a) Dynamic perfusion MRI versus perfusion scintigraphy: prediction of postoperative lung function in patients with lung cancer. AJR Am J Roentgenol. 182(1):73–78

Ohno Y, Hatabu H, Murase K, Higashino T, Kawamitsu H, Watanabe H, Takenaka D, Fujii M, Sugimura K (2004b) Quantitative assessment of regional pulmonary perfusion in the entire lung using three-dimensional ultrafast dynamic contrast-enhanced magnetic resonance imaging: Preliminary experience in 40 subjects. J Magn Reson Imaging. 20(3):353–365

Ohno Y, Hatabu H, Higashino T, Nogami M, Takenaka D, Watanabe H, Van Cauteren M, Yoshimura M, Satouchi M, Nishimura Y, Sugimura K (2005) Oxygen-enhanced MR imaging: correlation with postsurgical lung function in patients with lung cancer. Radiology. 236(2):704–711

Ohno Y, Hatabu H, Murase K, Higashino T, Nogami M, Yoshikawa T, Sugimura K (2007) Primary pulmonary hypertension: 3D dynamic perfusion MRI for quantitative analysis of regional pulmonary perfusion. AJR Am J Roentgenol. 188(1):48–56

Ohno Y, Koyama H, Nogami M, Takenaka D, Matsumoto S, Obara M, Sugimura K (2008a) Dynamic oxygen-enhanced MRI versus quantitative CT: pulmonary functional loss assessment and clinical stage classification of smoking-related COPD. AJR Am J Roentgenol. 190(2):W93–W99

Ohno Y, Iwasawa T, Seo JB, Koyama H, Takahashi H, Oh YM, Nishimura Y, Sugimura K (2008b) Oxygen-enhanced magnetic resonance imaging versus computed tomography: multicenter study for clinical stage classification of smoking-related chronic obstructive pulmonary disease. Am J Respir Crit Care Med. 177(10):1095–1102

Ohno Y, Koyama H, Matsumoto K, Onishi Y, Nogami M, Takenaka D, Yoshikawa T, Matsumoto S, Sugimura K (2010) Dynamic MR perfusion imaging: capability for quantitative assessment of disease extent and prediction of outcome for patients with acute pulmonary thromboembolism. J Magn Reson Imaging. 31(5):1081–1090

Ohno Y, Koyama H, Matsumoto K, Onishi Y, Nogami M, Takenaka D, Matsumoto S, Sugimura K (2011a) Oxygen-enhanced MRI vs. quantitatively assessed thin-section CT: pulmonary functional loss assessment and clinical stage classification of asthmatics. Eur J Radiol. 77(1):85–91

Ohno Y, Koyama H, Matsumoto K, Onishi Y, Takenaka D, Fujisawa Y, Yoshikawa T, Konishi M, Maniwa Y, Nishimura Y, Ito T, Sugimura K (2011b) Differentiation of malignant and benign pulmonary nodules with quantitative first-pass 320-detector row perfusion CT versus FDG PET/CT. Radiology. 258(2): 599–609

Ohno Y, Koyama H, Yoshikawa T, Matsumoto K, Aoyama N, Onishi Y, Takenaka D, Matsumoto S, Nishimura Y, Sugimura K (2012a) Comparison of capability of dynamic O2-enhanced MRI and quantitative thin-section MDCT to assess COPD in smokers. Eur J Radiol. 81(5):1068–1075

Ohno Y, Nishio M, Koyama H, Yoshikawa T, Matsumoto S, Takenaka D, Sugimura K (2012b) Oxygen-enhanced MRI, thin-section MDCT, and perfusion SPECT/CT: comparison of clinical implications to patient care for lung volume reduction surgery. AJR Am J Roentgenol. 199(4):794–802

Ohno Y, Koyama H, Yoshikawa T, Nishio M, Matsumoto S, Matsumoto K, Aoyama N, Nogami M, Murase K, Sugimura K (2012c) Contrast-enhanced multidetector-row computed tomography vs. Time-resolved magnetic resonance angiography vs. contrast-enhanced perfusion MRI: assessment of treatment response by patients with inoperable chronic thromboembolic pulmonary hypertension. J Magn Reson Imaging. 36(3):612–623

Ohno Y, Nishio M, Koyama H, Fujisawa Y, Yoshikawa T, Matsumoto S, Sugimura K (2013) Comparison of quantitatively analyzed dynamic area-detector CT using various mathematic methods with FDG PET/CT in management of solitary pulmonary nodules. AJR Am J Roentgenol. 200(6):W593–W602

Ohno Y, Nishio M, Koyama H, Yoshikawa T, Matsumoto S, Seki S, Tsubakimoto M, Sugimura K (2014a) Oxygen-enhanced MRI for patients with connective tissue diseases: comparison with thin-section CT of capability for pulmonary functional and disease severity assessment. Eur J Radiol. 83(2):391–397

Ohno Y, Nishio M, Koyama H, Seki S, Yoshikawa T, Matsumoto S, Obara M, van Cauteren M, Sugimura K (2014b) Asthma: comparison of dynamic oxygen-enhanced MR imaging and quantitative thin-section CT for evaluation of clinical treatment. Radiology. 273(3):907–916

Ohno Y, Nishio M, Koyama H, Yoshikawa T, Matsumoto S, Seki S, Sugimura K (2014c) Journal Club: Comparison of assessment of preoperative pulmonary vasculature in patients with non-small cell lung cancer by non-contrast- and 4D contrast-enhanced 3-T MR angiography and contrast-enhanced 64-MDCT. AJR Am J Roentgenol. 202(3):493–506

Ohno Y, Seki S, Koyama H, Yoshikawa T, Matsumoto S, Takenaka D, Kassai Y, Yui M, Sugimura K (2015a) 3D ECG- and respiratory-gated non-contrast-enhanced (CE) perfusion MRI for postoperative lung function prediction in non-small-cell lung cancer patients: A comparison with thin-section quantitative computed tomography, dynamic CE-perfusion MRI, and perfusion scan. J Magn Reson Imaging. 42(2): 340–353

Ohno Y, Nishio M, Koyama H, Seki S, Tsubakimoto M, Fujisawa Y, Yoshikawa T, Matsumoto S, Sugimura K (2015b) Solitary pulmonary nodules: Comparison of dynamic first-pass contrast-enhanced perfusion area-detector CT, dynamic first-pass contrast-enhanced MR imaging, and FDG PET/CT. Radiology. 274(2):563–575

Ohno Y, Koyama H, Yoshikawa T, Takenaka D, Seki S, Yui M, Yamagata H, Aoyagi K, Matsumoto S, Sugimura K (2015c) Three-way Comparison of Whole-Body MR, Coregistered whole-body FDG PET/MR, and integrated whole-body FDG PET/CT imaging: TNM and stage assessment capability for non-small cell lung cancer patients. Radiology. 275(3):849–861

Ohno Y, Koyama H, Lee HY, Miura S, Yoshikawa T, Sugimura K (2016a) Contrast-enhanced CT- and MRI-based perfusion assessment for pulmonary diseases: basics and clinical applications. Diagn Interv Radiol. 22(5):407–421

Ohno Y, Koyama H, Fujisawa Y, Yoshikawa T, Seki S, Sugihara N, Sugimura K (2016b) Dynamic contrast-enhanced perfusion area detector CT for non-small cell lung cancer patients: Influence of mathematical models on early prediction capabilities for treatment response and recurrence after chemoradiotherapy. Eur J Radiol. 85(1):176–186

Ohno Y, Koyama H, Fujisawa Y, Yoshikawa T, Inokawa H, Sugihara N, Seki S, Sugimura K (2016c) Hybrid Type iterative reconstruction method vs. filter back projection method: Capability for radiation dose reduction and perfusion assessment on dynamic first-pass contrast-enhanced perfusion chest area-detector CT. Eur J Radiol. 85(1):164–175

Ohno Y, Koyama H, Yoshikawa T, Seki S, Takenaka D, Yui M, Lu A, Miyazaki M, Sugimura K (2016d) Pulmonary high-resolution ultrashort TE MR imaging: Comparison with thin-section standard- and low-dose computed tomography for the assessment of pulmonary parenchyma diseases. J Magn Reson Imaging. 43(2):512–532

Ohno Y, Yui M, Koyama H, Yoshikawa T, Seki S, Ueno Y, Miyazaki M, Ouyang C, Sugimura K (2016e) Chemical exchange saturation transfer mr imaging: preliminary results for differentiation of malignant and benign thoracic lesions. Radiology. 279(2):578–589

Ohno Y, Koyama H, Lee HY, Yoshikawa T, Sugimura K (2016f) Magnetic resonance imaging (MRI) and positron emission tomography (PET)/MRI for lung cancer staging. J Thorac Imaging. 31(4):215–227

Ohno Y, Yoshikawa T, Takenaka D, Fujisawa Y, Sugihara N, Kishida Y, Seki S, Koyama H, Sugimura K (2017a) Xenon-enhanced CT using subtraction CT: Basic and preliminary clinical studies for comparison of its efficacy with that of dual-energy CT and ventilation SPECT/CT to assess regional ventilation and pulmonary functional loss in smokers. Eur J Radiol. 86:41–51

Ohno Y, Yoshikawa T, Kishida Y, Seki S, Karabulut N (2017b) Unenhanced and contrast-enhanced MR angiography and perfusion imaging for suspected pulmonary thromboembolism. AJR Am J Roentgenol. 208(3):517–530

Ohno Y, Fujisawa Y, Koyama H, Kishida Y, Seki S, Sugihara N, Yoshikawa T (2017c) Dynamic contrast-enhanced perfusion area-detector CT assessed with various mathematical models: Its capability for therapeutic outcome prediction for non-small cell lung cancer patients with chemoradiotherapy as compared with that of FDG-PET/CT. Eur J Radiol. 86:83–91

Ohno Y, Fujisawa Y, Sugihara N, Kishida Y, Seki S, Koyama H, Yoshikawa T (2017d) Dynamic contrast-enhanced perfusion area-detector CT: preliminary comparison of diagnostic performance for N stage assessment with FDG PET/CT in non-small cell lung cancer. AJR Am J Roentgenol. 209(5):W253–W262

Ohno Y, Koyama H, Yoshikawa T, Kishida Y, Seki S, Takenaka D, Yui M, Miyazaki M, Sugimura K (2017e) Standard-, reduced-, and no-dose thin-section radiologic examinations: comparison of capability for nodule detection and nodule type assessment in patients suspected of having pulmonary nodules. Radiology. 284(2):562–573

Ohno Y, Yoshikawa T, Kishida Y, Seki S, Koyama H, Yui M, Kassai Y, Aoyagi K, Kaminaga S, Sugimura K (2017f) Diagnostic performance of different imaging modalities in the assessment of distant metastasis and local recurrence of tumor in patients with non-small cell lung cancer. J Magn Reson Imaging. 46(6):1707–1717

Ohno Y, Fujisawa Y, Takenaka D, Kaminaga S, Seki S, Sugihara N, Yoshikawa T (2018a) Comparison of xenon-enhanced area-detector CT and krypton venti-

lation SPECT/CT for assessment of pulmonary functional loss and disease severity in smokers. AJR Am J Roentgenol. 210(2):W45–W53

Ohno Y, Kishida Y, Seki S, Yui M, Miyazaki M, Koyama H, Yoshikawa T (2018b) Amide proton transfer-weighted imaging to differentiate malignant from benign pulmonary lesions: Comparison with diffusion-weighted imaging and FDG-PET/CT. J Magn Reson Imaging. 47(4):1013–1021

Ohno Y, Kishida Y, Seki S, Koyama H, Yui M, Aoyagi K, Yoshikawa T (2018c) Comparison of interobserver agreement and diagnostic accuracy for IASLC/ITMIG Thymic epithelial tumor staging among co-registered FDG-PET/MRI, Whole-body MRI, integrated FDG-PET/CT, and conventional imaging examination with and without contrast media administrations. Acad Radiol. S1076-6332(17)30542-1

Ohno Y, Yui M, Aoyagi K, Kishida Y, Seki S, Koyama H, Yoshikawa T (2018d) Whole-body MRI: comparison of its capability for TNM staging of malignant pleural mesothelioma with that of coregistered PET/MRI, integrated FDG PET/CT, and conventional imaging. AJR Am J Roentgenol. 212(2):311–319

Ohno Y, Yui M, Chen Y, Kishida Y, Seki S, Yoshikawa T (2019) Gadolinium-based blood volume mapping from MRI with ultrashort TE versus CT and SPECT for predicting postoperative lung function in patients with non-small cell lung cancer. AJR Am J Roentgenol. 212(1):57–66

Paiva M, Verbanck S, Estenne M, Poncelet B, Segebarth C, Macklem PT (1992) Mechanical implications of in vivo human diaphragm shape. J Appl Physiol. 72(4):1407–1412

Pérez-Campaña C, Gómez-Vallejo V, Puigivila M, Martin A, Calvo-Fernández T, Moya SE, Larsen ST, Gispert JD, Llop J (2014) Assessing lung inflammation after nanoparticle inhalation using 2-deoxy-2-[18F]fluoro-D-glucose positron emission tomography imaging. Mol Imaging Biol. 16(2):264–273

Petrik M, Franssen GM, Haas H, Laverman P, Hörtnagl C, Schrettl M, Helbok A, Lass-Flörl C, Decristoforo C (2012) Preclinical evaluation of two 68Ga-siderophores as potential radiopharmaceuticals for Aspergillus fumigatus infection imaging. Eur J Nucl Med Mol Imaging. 39(7):1175–1183

Plathow C, Ley S, Fink C, Puderbach M, Heilmann M, Zuna I, Kauczor HU (2004a) Evaluation of chest motion and volumetry during the breathing cycle by dynamic MRI in healthy subjects: comparison with pulmonary function tests. Invest Radiol. 39(4):202–209

Plathow C, Fink C, Ley S, Puderbach M, Eichinger M, Schmähl A, Kauczor HU (2004b) Measurement of diaphragmatic length during the breathing cycle by dynamic MRI: comparison between healthy adults and patients with an intrathoracic tumor. Eur Radiol. 14(8):1392–1399

Plathow C, Ley S, Fink C, Puderbach M, Hosch W, Schmähl A, Debus J, Kauczor HU (2004c) Analysis of intrathoracic tumor mobility during whole breathing cycle by dynamic MRI. Int J Radiat Oncol Biol Phys. 59(4):952–959

Plathow C, Schoebinger M, Fink C, Ley S, Puderbach M, Eichinger M, Bock M, Meinzer HP, Kauczor HU (2005) Evaluation of lung volumetry using dynamic three-dimensional magnetic resonance imaging. Invest Radiol. 40(3):173–179

Plathow C, Klopp M, Schoebinger M, Thieke C, Fink C, Puderbach M, Ley S, Weber MA, Sandner A, Claussen CD, Herth F, Tuengerthal S, Meinzer HP, Kauczor HU (2006) Monitoring of lung motion in patients with malignant pleural mesothelioma using two-dimensional and three-dimensional dynamic magnetic resonance imaging: comparison with spirometry. Invest Radiol. 41(5):443–448

Platt T, Umathum R, Fiedler TM, Nagel AM, Bitz AK, Maier F, Bachert P, Ladd ME, Wielpütz MO, Kauczor HU, Behl NGR (2018) In vivo self-gated 23 Na MRI at 7 T using an oval-shaped body resonator. Magn Reson Med. 80(3):1005–1019

Qanadli SD, Orvoen-Frija E, Lacombe P, Di Paola R, Bittoun J, Frija G (1999) Estimation of gas and tissue lung volumes by MRI: functional approach of lung imaging. J Comput Assist Tomogr. 23(5):743–748

Ramirez MP, Sigaloff KC, Kubatina LV, Donahue MA, Venkatesh AK, Albert MS (2000) Physiological response of rats to delivery of helium and xenon: implications for hyperpolarized noble gas imaging. NMR Biomed. 13(4):253–264

Rhodes CG, Valind SO, Brudin LH, Wollmer PE, Jones T, Hughes JM (1989a) Quantification of regional V/Q ratios in humans by use of PET. I. Theory. J Appl Physiol (1985) 66(4):1896–1904

Reiter G, Reiter U, Kovacs G, Olschewski H, Fuchsjäger M (2015) Blood flow vortices along the main pulmonary artery measured with MR imaging for diagnosis of pulmonary hypertension. Radiology. 275(1): 71–79

Reiter U, Reiter G, Fuchsjäger M (2016) MR phase-contrast imaging in pulmonary hypertension. Br J Radiol. 89(1063):20150995

Rhodes CG, Valind SO, Brudin LH, Wollmer PE, Jones T, Buckingham PD, Hughes JM (1989b) Quantification of regional V/Q ratios in humans by use of PET. II. Procedure and normal values. J Appl Physiol (1985) 66(4):1905–1913

Roberts DA, Gefter WB, Hirsch JA, Rizi RR, Dougherty L, Lenkinski RE, Leigh JS Jr, Schnall MD (1999) Pulmonary perfusion: respiratory-triggered three-dimensional MR imaging with arterial spin tagging--preliminary results in healthy volunteers. Radiology. 212(3):890–895

Ruppert K, Brookeman JR, Hagspiel KD, Mugler JP 3rd. (2000) Probing lung physiology with xenon polarization transfer contrast (XTC). Magn Reson Med. 44(3):349–357

Sá RC, Henderson AC, Simonson T, Arai TJ, Wagner H, Theilmann RJ, Wagner PD, Prisk GK, Hopkins SR (2017) Measurement of the distribution of ventilation-perfusion ratios in the human lung with

proton MRI: comparison with the multiple inert-gas elimination technique. J Appl Physiol (1985) 123(1): 136–146

Sakuma K, Yamashiro T, Moriya H, Murayama S, Ito H (2017) Parietal pleural invasion/adhesion of subpleural lung cancer: quantitative 4-dimensional CT analysis using dynamic-ventilatory scanning. Eur J Radiol. 87:36–44

Salerno M, Altes TA, Brookeman JR, de Lange EE, Mugler JP 3rd. (2001) Dynamic spiral MRI of pulmonary gas flow using hyperpolarized (3)He: preliminary studies in healthy and diseased lungs. Magn Reson Med. 46(4):667–677

Salerno M, de Lange EE, Altes TA, Truwit JD, Brookeman JR, Mugler JP 3rd. (2002) Emphysema: hyperpolarized helium 3 diffusion MR imaging of the lungs compared with spirometric indexes--initial experience. Radiology. 222(1):252–260

Sandiford P, Province MA, Schuster DP (1995) Distribution of regional density and vascular permeability in the adult respiratory distress syndrome. Am J Respir Crit Care Med. 151(3 Pt 1):737–742

Sanz J, Kuschnir P, Rius T, Salguero R, Sulica R, Einstein AJ, Dellegrottaglie S, Fuster V, Rajagopalan S, Poon M (2007) Pulmonary arterial hypertension: noninvasive detection with phase-contrast MR imaging. Radiology. 243(1):70–79

Schaarschmidt BM, Sawicki LM, Gomez B, Grueneisen J, Hoiczyk M, Heusch P, Buchbender C (2016) Malignant pleural mesothelioma: initial experience in integrated (18)F-FDG PET/MR imaging. Clin Imaging. 40(5):956–960

Schaarschmidt BM, Grueneisen J, Metzenmacher M, Gomez B, Gauler T, Roesel C, Heusch P, Ruhlmann V, Umutlu L, Antoch G, Buchbender C (2017) Thoracic staging with 18F-FDG PET/MR in non-small cell lung cancer - does it change therapeutic decisions in comparison to 18F-FDG PET/CT? Eur Radiol. 27(2):681–688

Schoepf UJ, Bruening R, Konschitzky H, Becker CR, Knez A, Weber J, Muehling O, Herzog P, Huber A, Haberl R, Reiser MF (2000) Pulmonary embolism: comprehensive diagnosis by using electron-beam CT for detection of emboli and assessment of pulmonary blood flow. Radiology. 217(3):693–700

Schönfeld C, Cebotari S, Voskrebenzev A, Gutberlet M, Hinrichs J, Renne J, Hoeper MM, Olsson KM, Welte T, Wacker F, Vogel-Claussen J (2015) Performance of perfusion-weighted Fourier decomposition MRI for detection of chronic pulmonary emboli. J Magn Reson Imaging. 42(1):72–79

Schuster DP, Kaplan JD, Gauvain K, Welch MJ, Markham J (1995) Measurement of regional pulmonary blood flow with PET. J Nucl Med. 36(3): 371–377

Schuster DP, Markham J, Welch MJ (1998) Positron emission tomography measurements of pulmonary vascular permeability with Ga-68 transferrin or C-11 methylalbumin. Crit Care Med. 26(3):518–525

Schuster DP, Stark T, Stephenson J, Royal H (2002) Detecting lung injury in patients with pulmonary edema. Intensive Care Med. 28(9):1246–1253

Suga K, Tsukuda T, Awaya H, Takano K, Koike S, Matsunaga N, Sugi K, Esato K (1999) Impaired respiratory mechanics in pulmonary emphysema: evaluation with dynamic breathing MRI. J Magn Reson Imaging. 10(4):510–520

Suga K, Tsukuda T, Awaya H, Matsunaga N, Sugi K, Esato K (2000) Interactions of regional respiratory mechanics and pulmonary ventilatory impairment in pulmonary emphysema: assessment with dynamic MRI and xenon-133 single-photon emission CT. Chest. 117(6):1646–1655

Sun Y, O'Sullivan BP, Roche JP, Walvick R, Reno A, Baker D, Mansour JK, Albert MS (2011) Using hyperpolarized 3He MRI to evaluate treatment efficacy in cystic fibrosis patients. J Magn Reson Imaging. 34(5):1206–1211

Sundaram TA, Gee JC (2005) Towards a model of lung biomechanics: pulmonary kinematics via registration of serial lung images. Med Image Anal. 9(6):524–537

Sundaram TA, Avants BB, Gee JC (2005) Towards a dynamic model of pulmonary parenchymal deformation: evaluation of methods for temporal reparameterization of lung data. Med Image Comput Comput Assist Interv. 8:328–335

Sommer G, Bauman G, Koenigkam-Santos M, Draenkow C, Heussel CP, Kauczor HU, Schlemmer HP, Puderbach M (2013) Non-contrast-enhanced preoperative assessment of lung perfusion in patients with non-small-cell lung cancer using Fourier decomposition magnetic resonance imaging. Eur J Radiol. 82(12):e879–e887

Svenningsen S, Kirby M, Starr D, Leary D, Wheatley A, Maksym GN, McCormack DG, Parraga G (2013) Hyperpolarized (3) He and (129) Xe MRI: differences in asthma before bronchodilation. J Magn Reson Imaging. 38(6):1521–1530

Symons R, Pourmorteza A, Sandfort V, Ahlman MA, Cropper T, Mallek M, Kappler S, Ulzheimer S, Mahesh M, Jones EC, Malayeri AA, Folio LR, Bluemke DA (2017) Feasibility of dose-reduced chest CT with photon-counting detectors: initial results in humans. Radiology. 285(3):980–989

Tadamura E, Hatabu H, Li W, Prasad PV, Edelman RR (1997) Effect of oxygen inhalation on relaxation times in various tissue. JMRI 7:220–225

Tadamura E, Hatabu H (2001) Assessment of pulmonary perfusion using a subtracted HASTE image between diastole and systole. Eur J Radiol 37:179–183

Takazakura R, Takahashi M, Nitta N, Murata K (2004) Diaphragmatic motion in the sitting and supine positions: healthy subject study using a vertically open magnetic resonance system. J Magn Reson Imaging 19(5):605–659

Tanabe N, Oguma T, Sato S, Kubo T, Kozawa S, Shima H, Koizumi K, Sato A, Muro S, Togashi K, Hirai T (2018) Quantitative measurement of airway dimensions using

ultra-high resolution computed tomography. Respir Investig. 56(6):489–496

Thornton CR (2018) Molecular imaging of invasive pulmonary aspergillosis using ImmunoPET/MRI: the future looks bright. Front Microbiol. 9:691

Tibiletti M, Bianchi A, Stiller D, Rasche V (2016) Pulmonary perfusion quantification with flow-sensitive inversion recovery (FAIR) UTE MRI in small animal imaging. NMR Biomed. 29(12):1791–1799

Treppo S, Mijailovich SM, Venegas JG (1997) Contributions of pulmonary perfusion and ventilation to heterogeneity in V(A)/Q measured by PET. J Appl Physiol (1985) 82(4):1163–1176

Triphan SM, Breuer FA, Gensler D, Kauczor HU, Jakob PM (2015) Oxygen enhanced lung MRI by simultaneous measurement of T1 and T2 * during free breathing using ultrashort TE. J Magn Reson Imaging. 41(6):1708–1714

Triphan SM, Jobst BJ, Anjorin A, Sedlaczek O, Wolf U, Terekhov M, Hoffmann C, Ley S, Düber C, Biederer J, Kauczor HU, Jakob PM, Wielpütz MO (2017) Reproducibility and comparison of oxygen-enhanced T1 quantification in COPD and asthma patients. PLoS One. 12(2):e0172479

Tsuji AB, Kato K, Sugyo A, Okada M, Sudo H, Yoshida C, Wakizaka H, Zhang MR, Saga T (2012) Comparison of 2-amino-[3-^{11}C]isobutyric acid and 2-deoxy-2-[^{18}F]fluoro-D-glucose in nude mice with xenografted tumors and acute inflammation. Nucl Med Commun. 33(10):1058–1064

van Beek EJ, Dahmen AM, Stavngaard T, Gast KK, Heussel CP, Krummenauer F, Schmiedeskamp J, Wild JM, Søgaard LV, Morbach AE, Schreiber LM, Kauczor HU (2009) Hyperpolarised 3He MRI versus HRCT in COPD and normal volunteers: PHIL trial. Eur Respir J. 34(6):1311–1321

Vidal Melo MF, Harris RS, Layfield D, Musch G, Venegas JG (2002) Changes in regional ventilation after autologous blood clot pulmonary embolism. Anesthesiology. 97(3):671–681

Vidal Melo MF, Winkler T, Harris RS, Musch G, Greene RE, Venegas JG (2010) Spatial heterogeneity of lung perfusion assessed with (13)N PET as a vascular biomarker in chronic obstructive pulmonary disease. J Nucl Med. 51(1):57–65

Voorhees A, An J, Berger KI, Goldring RM, Chen Q (2005) Magnetic resonance imaging-based spirometry for regional assessment of pulmonary function. Magn Reson Med. 54(5):1146–1154

Voskrebenzev A, Gutberlet M, Klimeš F, Kaireit TF, Schönfeld C, Rotärmel A, Wacker F, Vogel-Claussen J (2018) Feasibility of quantitative regional ventilation and perfusion mapping with phase-resolved functional lung (PREFUL) MRI in healthy volunteers and COPD, CTEPH, and CF patients. Magn Reson Med. 79(4):2306–2314

Wagner SJ, Welch MJ (1979) Gallium-68 labeling of albumin and albumin microspheres. J Nucl Med. 20(5):428–433

Walker SC, Asadi AK, Hopkins SR, Buxton RB, Prisk GK (2015) A statistical clustering approach to discriminating perfusion from conduit vessel signal contributions in a pulmonary ASL MR image. NMR Biomed. 28(9):1117–1124

Wielpütz MO, Lee HY, Koyama H, Yoshikawa T, Seki S, Kishida Y, Sakai Y, Kauczor HU, Sugimura K, Ohno Y (2018) Morphologic characterization of pulmonary nodules with ultrashort TE MRI at 3T. AJR Am J Roentgenol. 210(6):1216–1225

Yabuuchi H, Kawanami S, Iwama E, Okamoto I, Kamitani T, Sagiyama K, Yamasaki Y, Honda H (2018) Prediction of therapeutic effect of chemotherapy for NSCLC using dual-input perfusion CT analysis: comparison among bevacizumab treatment, two-agent platinum-based therapy without bevacizumab, and other non-bevacizumab treatment groups. Radiology. 286(2):685–695

Yamashiro T, Matsuoka S, Bartholmai BJ, San José Estépar R, Ross JC, Diaz A, Murayama S, Silverman EK, Hatabu H, Washko GR (2010) Collapsibility of lung volume by paired inspiratory and expiratory CT scans: correlations with lung function and mean lung density. Acad Radiol. 17(4):489–495

Yamashiro T, Tsubakimoto M, Nagatani Y, Moriya H, Sakuma K, Tsukagoshi S, Inokawa H, Kimoto T, Teramoto R, Murayama S (2015) Automated continuous quantitative measurement of proximal airways on dynamic ventilation CT: initial experience using an ex vivo porcine lung phantom. Int J Chron Obstruct Pulmon Dis. 10:2045–2054

Yamashiro T, Moriya H, Tsubakimoto M, Matsuoka S, Murayama S (2016) Continuous quantitative measurement of the proximal airway dimensions and lung density on four-dimensional dynamic-ventilation CT in smokers. Int J Chron Obstruct Pulmon Dis. 11:755–764

Yamashiro T, Moriya H, Matsuoka S, Nagatani Y, Tsubakimoto M, Tsuchiya N, Murayama S (2017) Asynchrony in respiratory movements between the pulmonary lobes in patients with COPD: continuous measurement of lung density by 4-dimensional dynamic-ventilation CT. Int J Chron Obstruct Pulmon Dis. 12:2101–2109

Yanagawa M, Hata A, Honda O, Kikuchi N, Miyata T, Uranishi A, Tsukagoshi S, Tomiyama N (2018) Subjective and objective comparisons of image quality between ultra-high-resolution CT and conventional area detector CT in phantoms and cadaveric human lungs. Eur Radiol. 28(12):5060–5068

Yanagita H, Honda N, Nakayama M, Watanabe W, Shimizu Y, Osada H, Nakada K, Okada T, Ohno H, Takahashi T, Otani K (2013) Prediction of postoperative pulmonary function: preliminary comparison of single-breath dual-energy xenon CT with three conventional methods. Jpn J Radiol. 31(6): 377–385

Young IR, Clarke GJ, Bailes DR, Pennock JM, Doyle FH, Bydder GM (1981) Enhancement of relaxation rate

with paramagnetic contrast agents in NMR imaging. J Comput Tomogr. 5(6):543–547

Zaporozhan J, Ley S, Eberhardt R, Weinheimer O, Iliyushenko S, Herth F, Kauczor HU (2005) Paired inspiratory/expiratory volumetric thin-slice CT scan for emphysema analysis: comparison of different quantitative evaluations and pulmonary function test. Chest. 128(5):3212–3220

Zhang Z, Ordonez AA, Smith-Jones P, Wang H, Gogarty KR, Daryaee F, Bambarger LE, Chang YS, Jain SK, Tonge PJ (2017) The biodistribution of 5-[18F]fluoropyrazinamide in Mycobacterium tuberculosis-infected mice determined by positron emission tomography. PLoS One. 12(2):e0170871